Cover Page

Universiteit Leiden

Author: Matthee, J.J.A.
Title: Identifying the origins of galaxy formation
Issue Date: 2018-09-19

Identifying the origins of galaxy formation

Proefschrift

ter verkrijging van
de graad van Doctor aan de Universiteit Leiden
op gezag van Rector Magnificus prof. mr. C.J.J.M Stolker,
volgens besluit van het College voor Promoties
te verdedigen op woensdag 19 september 2018
klokke 10:00 uur

door **Jorryt Johan Anton Matthee**

geboren te Utrecht
in 1990

Promotiecommissie

Promotor:	Prof. dr. Huub Röttgering	
Promotor:	Prof. dr. Joop Schaye	
Co-promotor:	Dr. David Sobral	(Lancaster University)

Overige leden:	Prof. dr. Richard Ellis	(University College London)
	Prof. dr. Andrea Ferrara	(Scuola Normale Superiore Pisa)
	Prof. dr. Marijn Franx	
	Dr. Jacqueline Hodge	
	Prof. dr. Paul van der Werf	

For those born in less favourable spacetime locations

Front cover: Logarithmic spiral where the radius of each quarter increases with growth factor $\phi = \frac{1+\sqrt{5}}{2}$, the golden ratio. From small to large: temperature fluctuations of the cosmic microwave background observed by the *Planck* satellite; simulated large-scale structure of dark matter in the universe in the EAGLE simulation; NASA/*Hubble Space Telescope* image of *The Pillars of Creation* in the Eagle nebula based on observations in the [S II], Hα and [O III] filters; artist impression of the CR7 galaxy, ESO/Kornmesser; part of the COSMOS field imaged in the near-infrared using *J*, *H* and *K* filters on VIRCAM as part of the UltraVISTA survey; simulated large-scale structure of the universe in dark matter, gas and stars in the EAGLE simulation.

Back cover: From bottom-left to top-right: stylised photograph from the Isaac Newton Telescope on La Palma; drawing from the Moon by Galileo Galilei in 1610 based on the first astronomical usage of a telescope; drawing of Saturn by Christiaan Huygens in 1698; illustration of the NASA/*GALEX* satellite; drawing of the Whirlpool galaxy (M51) by Lord Rosse in 1850; illustration of the spectrum of a Lyman-α photon; hexagonal cut-outs of observations used in this thesis from the INT, Subaru and the *HST*.

Contents

Chapter 1
Introduction

1.1 Historical, physical and methodological framework

1.1.1 History and cosmology

The topic of this thesis is the formation and evolution of galaxies. Galaxies are the locations where gas that resides in a reservoir in the circumgalactic medium (CGM) condensates, originating from the intergalactic medium (IGM; e.g. White & Rees 1978), and where molecular clouds, stars, planets and black holes form. In between stars, the gas in galaxies (the interstellar medium; ISM) is chemically enriched by stellar winds and supernova explosions at the end stages of the lives of stars. The gas reservoir in the ISM is used to form stars, but it can also lose mass due to galactic winds. Winds can be driven by supernova explosions and/or energetic radiation and jet flows originating from supermassive black holes. The gas reservoir can also gain mass due to inflows of accreted material. All these different states of matter (hot gas, cold gas, stars, accretion disks around black holes) emit photons that can be observed with different sensitivities.

A striking observation of large samples of galaxies is that there is a clear bi-modality in several properties that describe the galaxy population in the present-day Universe, but it is observed to already exist at $z \sim 1$, roughly the half of the age of the Universe (Bell et al., 2004). This bi-modality is predominantly expressed in galaxies' colours (a blue cloud and a red sequence) and morphologies (spiral galaxies such as Andromeda and the Milky Way and elliptical galaxies). Blue galaxies tend to have a spiral structure (e.g. Strateva et al., 2001), while red galaxies tend to be elliptical galaxies residing in over-dense regions (e.g. Peng et al., 2010). The origin of galaxy bi-modality lies in the relation between galaxy mass, the dominant mode of stellar mass growth (in situ star formation versus growth through merging) and the rate at which this happens (Trayford et al., 2016). Besides understanding the details of this bi-modality, a number of *big questions* dominate present-day extra-galactic astronomy. These include the exact interplay between feedback from star formation and supermassive black hole growth and gas in the ISM and CGM; the connection between galaxies observed at different cosmic times; the physics determining the mass distribution of stars that are formed in molecular clouds (the stellar initial mass function, IMF); the properties of the first stellar populations and the sources responsible for the reionization of the Universe.

Since the understanding that the Universe extends beyond the Milky Way (e.g. Curtis, 1917; Hubble, 1926), it rapidly became clear that galaxies reside in an expanding Universe whose dynamics are determined by the different contributors to the energy density and the Einstein equation (e.g. Carroll, 2001). Therefore, galaxy formation occurs in a cosmological framework that prescribes the formation of structure on the largest scales. Currently, the cold dark matter + dark energy (ΛCDM) model is the best tested model that can fit properties of the cosmic microwave background (which depends on the formation of structure in

the early Universe) with only a small number of parameters (e.g. Planck Collaboration et al., 2014). However, ΛCDM has important ingredients that dominate the energy density at current cosmic time, but which nature are poorly understood: dark matter and dark energy. Dark matter is assumed to be a collisionless form of matter that does not interact with *ordinary* baryonic matter besides gravitational interactions, while dark energy is assumed to be a constant number in the Einstein equation, causing accelerated expansion of the Universe at late cosmic times. It is important to stress that calculations of distances to extragalactic sources, and the age of the Universe where we observe them, depend on the cosmological model and the contents of the Universe. These distances and ages change when model parameters as the Hubble parameter or the matter density are revised.

Throughout this work, I assume a flat Universe with a dark energy density relative to the critical density $\Omega_\Lambda = 0.7$, a total matter (dark + baryonic) density $\Omega_M = 0.3$ and Hubble parameter $H_0 = 70$ km s^{-1} Mpc^{-1}. In this cosmology, the current age of the Universe is 13.462×10^9 yr. At redshift $z = 1$ (when the Universe had half its current size, $a = \frac{1}{1+z}$ where a is the scale factor), the Universe was 5.74×10^9 yr old, while $z = 7$ marks the first 750 million years. At $z = 7$, the luminosity distance is 68995.3 Mpc and the proper angular diameter distance is 5.227 kpc/$''$. I will use the CGS unit system combined with common astrophysical quantities, in particular parsec (pc, the distance at which the annual parallax of a star is $1''$, 3.08568×10^{18} cm) and solar mass (M$_\odot$, 1.9891×10^{33} g).

1.1.2 Methodology

While research in astrophysics follows standard scientific methodology of developing theories through empirical tests and falsification of hypotheses, a crucial difference to other branches of physics (e.g. particle physics) is that research in astrophysicists typically does not involve controlled-experiments. In astrophysics, the Universe itself is the laboratory and typical changes in the properties of stars and galaxies occur on timescales that are far beyond those that can be observed.[1] Therefore, testing theoretical models of how galaxies form and evolve is severely complicated, simply because predictions can not be tested in the measurable future. Theories of galaxy formation are therefore tested with observations of galaxy ensembles at different points in cosmic time. Fundamental observations include the (evolution of the) galaxy stellar mass function (e.g. Baldry et al., 2012), the cosmic star formation history (e.g. Sobral et al., 2013; Madau & Dickinson, 2014), the relation between stellar mass and star formation rate (SFR; e.g. Brinchmann et al. 2004; Whitaker et al. 2012), the stellar mass - halo mass relation (e.g. Behroozi et al., 2013b), the galaxy mass-size relation (e.g. van der Wel et al., 2014) and the mass - metallicity relation in both the stellar and gas-phase (e.g. Tremonti et al., 2004; Gallazzi et al., 2005; Erb et al., 2006).

---

[1] Notable exceptions include gamma-rays bursts and their after-glows (timescales $\sim$ seconds to hours), the explosions of stars as supernova (timescales $\sim$ months) and variable accretion onto supermassive black holes (timescales $\sim$ months).

Observations of galaxy-ensembles can often not uniquely discriminate between models (e.g. Abramson et al., 2016). One approach to study the time-evolution of galaxies is to connect different galaxy populations observed at different points of time in cosmic time and link 'progenitors' with their 'descendants' by matching cumulative number densities (e.g. van Dokkum et al., 2010; Torrey et al., 2015). This approach has difficulties with galaxy mergers and differences between star formation histories of individual galaxies (e.g. Abramson et al. 2016 and Chapter 11). A complementary approach is to simulate galaxies in a cosmological environment in a computer, reproducing observations at specific times in the Universe (e.g. Hopkins et al., 2014; Schaye et al., 2015; Pillepich et al., 2018). This way galaxies and their environments can be traced throughout cosmic time. However, as important physical processes happen over a large dynamical range, several processes can not be simulated from first principles and invoke calibrations and assumptions as discussed in §1.2.2.
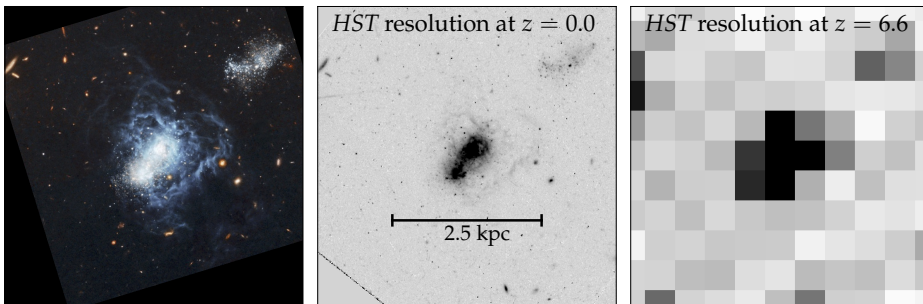
Figure 1.1: The young, low-metallicity dwarf galaxy I Zwicky 18, that is observed at a distance of $\approx$ 18 Mpc. The *left* panel shows the coloured image based on the *HST*/ACS F660W and F814W imaging (Credit: NASA, ESA, and A. Aloisi (ESA & STScI)) This image highlights the blue colours corresponding to the young age and metallicity of the galaxy and also the luminous Hɪɪ regions. The *center* panel shows the grey-scale *HST*/ACS F702W image illustrating the highest resolution at which these galaxies can be observed with current-instrumentation in the optical. The *right* panel, based on R band SDSS imaging, shows the resolution at which *HST* would observe this galaxy if it was at $z = 6.6$ (at a luminosity distance of 64458 Mpc).

Another important methodological limitation arises from practical and observational reasons. Due to their distance, the angular resolution of observations is currently only sufficient to resolve individual stars in the closest neighbouring galaxies, even when using space telescopes that do not suffer from atmospheric distortions. This means that the light emitted by different stars and phases of gas are blurred in observations of the vast majority of galaxies. Observations of galaxies in the early Universe – the prime topic of this thesis – suffer significantly from this limitation. This is illustrated in Figure 1.1, which shows the low metallicity galaxy I Zw 18, which is at a distance of $\approx$ 18 Mpc from the Milky Way. The left panel shows the composite image from the *Hubble Space Telescope (HST)*, in which several distinct star-forming regions and star clusters can be identified. The right panel shows the spatial resolution at which I Zw 18 would be observed by *HST* if it was at a redshift of $z = 6.6$, similar to several objects

that are the subjects in Chapters 2–6, ignoring the effects of surface brightness dimming. By comparing this panel with the center panel one can immediately notice the loss of information on < 1 kpc scales.

Another limitation besides spatial resolution is the simple fact that galaxies in the distant Universe appear very faint, such that measurements are typically only available for the brightest spectral features and typically only performed at the position where the rest-frame UV emission peaks. Because of this, derived properties such as star formation rates and gas-phase metallicities are typically measured using calibrations that are performed on galaxies and/or H_{II} regions in the local Universe (e.g. Kennicutt, 1998; Pettini & Pagel, 2004). The validity of such calibrations depend on the validity of underlying assumptions such as the IMF, the burstiness of star formation, chemical abundances, gas densities and temperatures.

1.2 Galaxy formation: theoretical perspective

1.2.1 Structure formation in a ΛCDM Universe

As dark matter is the dominant contributor to the mass density of the Universe (Planck Collaboration et al., 2016a; Hildebrandt et al., 2017), structure formation is dominated by the gravitational collapse of over-dense regions in the primordial dark matter distribution. Gravitational collapse results in the formation of dark matter haloes, in which baryonic gas and stars (which costitute galaxies) are embedded. On the largest scales, connections between haloes form the cosmic web, with filaments extending between knots (typically called clusters). Collapse is halted when a halo is virialized, occurring once the self-gravity is balanced by random (thermal) motions. This happens once the matter density reaches an overdensity of around 200 compared to the critical density of the Universe, approximately confirmed by numerical simulations (e.g Cole & Lacey, 1996). Structures form hierarchically, meaning that small halos form earliest and merge into more massive halos at later times.

Observationally, it is challenging to measure the large-scale distribution of dark matter directly, as dark matter does not interact with baryons. Therefore, galaxies are used as tracers of the large-scale structure. As a consequence, testing the ΛCDM cosmological model in the present-day Universe requires detailed knowledge of the interplay between the growth of dark matter halos and galaxy formation. This contrasts to cosmological tests that use the cosmic microwave background (e.g. Planck Collaboration et al., 2014), which is emitted at a time when density fluctuations are in the linear regime and galaxies did not yet form.

Compared to dark matter physics, which only includes the collisionless interactions from gravity, the baryonic physics that is involved in galaxy formation is significantly complicated. Even though the total energy-density of the baryons is small compared to the dark matter energy-density, its intricate physics can have important effects on galactic, extra-galactic and even cosmological scales (e.g. Schaller et al., 2015b). Therefore, obtaining a complete understanding of galaxy formation is not only a goal on its own, but also mandatory for testing
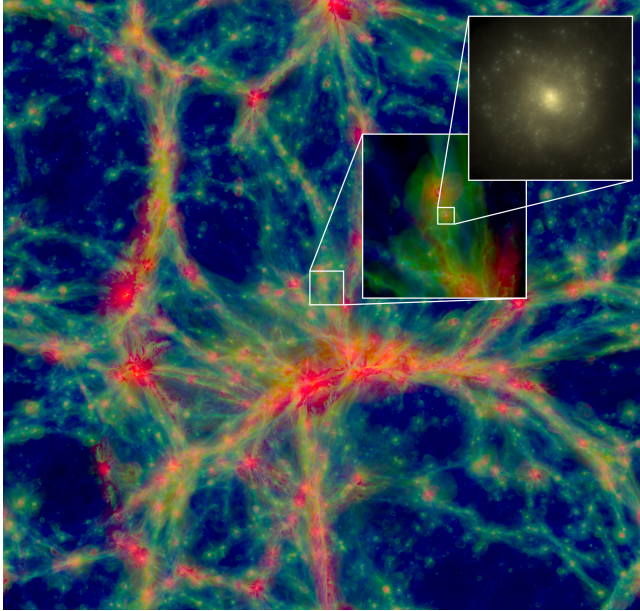
Figure 1.2: The simulated cosmic web in the EAGLE simulation ($100 \times 100 \times 20$ cMpc), coloured by the temperature of the gas, ranging from $T \lesssim 10^{4.5}$ K (blue) to $T \gtrsim 10^{5.5}$ K (red). Galaxies reside in dark matter haloes that are embedded in a large-scale cosmic web. The gas temperature is highest in clusters in the knots of the cosmic web. Inset figures illustrate the dynamic range probed in the simulation, by zooming in on the direct environment of a halo ($10 \times 10 \times 10$ cMpc) and on the spiral morphology of a simulated galaxy with a mass similar to the Milky Way ($60 \times 60 \times 60$ ckpc). *Figure from Schaye et al. 2015*.

cosmological models and the physics of gravity on the largest scales.

1.2.2   Gas cooling, star and black formation and feedback

In the early Universe, baryons trace the dark matter density closely. However, baryons are able to lose energy by emitting radiation (called cooling), allowing them to collapse further towards the center of dark matter haloes. Gas can cool through a range of mechanisms, such as atomic cooling, Compton cooling, molecular cooling and cooling by bremsstrahlung. Each of these mechanisms is dominant at a range of certain densities and temperatures (e.g. Gnat & Sternberg, 2007). Eventually, gas that cools sufficiently collapses into molecular clouds, in which stars eventually form (White & Rees, 1978). Therefore, on long timescales, the growth of stellar mass traces the amount of gas that has accreted onto a galaxy. Galaxies and halos are not isolated, complicating this picture slightly. A smaller galaxy can fall into a large halo, becoming a satellite of the central galaxy of that halo, which can have an important impact on the evolution of the satellite.

Using a simple calculation that combines the number density of dark matter

halos with the mass-dependency of gas-cooling efficiency, one can obtain a rude estimate of the stellar mass function of galaxies. This estimate over-predicts the number of low-mass galaxies and the number of high-mass galaxies significantly (e.g. Oppenheimer et al., 2010; Genel et al., 2014). This problem is called the 'overcooling problem'. The implication is that there has to be a mechanism that reduces the efficiency at which gas is converted into stars (named 'feedback'; see Fig. 1.3). As both low and high masses are affected, it is likely that multiple mechanisms govern the star formation histories of galaxies, depending on the mass-scale at which they are important.

Galaxy formation is highly non-linear, with different physical processes acting on each other simultaneously. Therefore, galaxy formation can not be solved analytically, but requires large numerical computer simulations. The simulations are discretised in either mass (particles; using a method called smoothed particle hydrodynamics; SPH, e.g. Springel 2005), in volume (grid-cells) or in a hybrid implementation (moving-mesh; as in e.g. Pillepich et al. 2018). The size of cosmological simulations are on the order of 10^{4-6} cMpc^3 and they are run with initial conditions similar to those in the observed Universe.
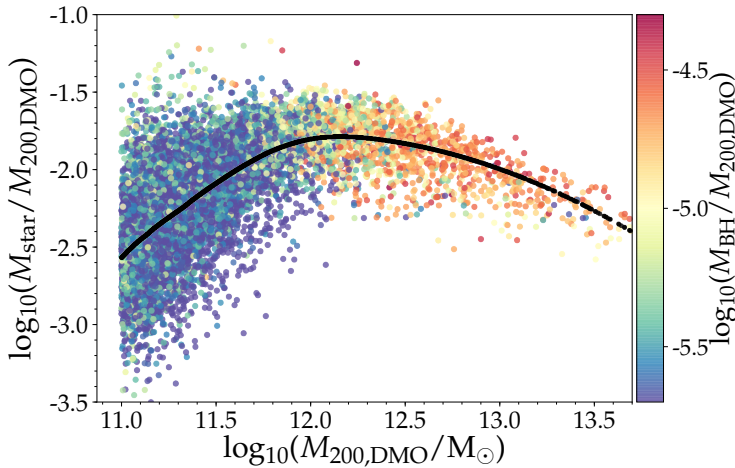
Figure 1.3: The efficiency of galaxy formation, quantified by the stellar mass - halo mass ratio as a function of halo mass of central galaxies in the EAGLE hydrodynamical cosmological simulation at $z = 0.1$ (as in Chapter 10). The points are colored by the relative supermassive black hole mass compared to the halo mass and thus illustrate the efficiency of black hole formation. The black line shows the median galaxy formation efficiency for each halo mass, highlighting that the efficiency peaks at $M_{200,\text{DMO}} \approx 2 \times 10^{12}$ M$_\odot$, which is similar to the estimated halo mass of the Milky Way. At low masses, feedback associated to star formation prevents significant amounts from accreting onto central supermassive black holes (e.g. Bower et al. 2017), leading to low black hole formation efficiencies, but an increasing galaxy formation efficiency. At high halo masses, the black hole formation efficiency increases at the cost of a declining galaxy formation efficiency due to the feedback associated with the growth of supermassive black holes, that can no longer be halted.

Large cosmological volumes initially only included dark matter particles that interact only through gravity (e.g. Springel et al., 2005b). In such simulations,

galaxy properties were 'painted' in dark matter structures using simple ana-
lytical prescriptions (e.g. Benson, 2010; Henriques et al., 2013). More recently,
hydrodynamical simulations also include baryonic particles, simultaneously mod-
elling the growth of structure, the dynamics of gas and the formation of galaxies
(e.g. Schaye et al., 2015; Pillepich et al., 2018). Due to computational limitations,
the number of simulation elements (e.g. particles) is around 10^7. This implies
a resolution of about 10^6 $M_\odot$, meaning that several physical processes, such as
the formation and evolution of stars and black holes, supernovae, gas cooling
and chemical enrichment, are unresolved. These processes are implemented us-
ing subgrid models, which include parameters that are not known from first
principles and hence need to be calibrated. Typically, simulations calibrate the
parameters of the different subgrid models in order to reproduce several key ob-
servations of the Universe, such as the galaxy stellar mass function and galaxy
sizes in the EAGLE simulation (e.g. Schaye et al., 2015).

The most important physics that are currently encoded in subgrid models are
related to feedback from the growth of stars and black holes. Feedback mecha-
nisms are physical processes that add energy to gas (called heating). Examples
include photo-heating (e.g. radiation feedback from young, massive stars) or
shock-heating (e.g. jets from Active Galactic Nuclei, AGN). AGN are powered
by accretion of gas on supermassive black holes that form in galaxy centres (Ko-
rmendy & Richstone, 1995). Black hole masses are correlated with the stellar
mass in galactic bulges (Magorrian et al., 1998), indicating that the growth of
stars and black holes are related (e.g. Booth & Schaye, 2011).

Stellar heating sources (supernovae and hot radiation from massive stars)
are typically important in low mass galaxies, while AGN heating is most
likely only responsible for feedback in the most massive galaxies (see Fig. 1.3).
Understanding which physical principles determines these mass scales and how
feedback events couple to gas are current areas of research. For example, it is
uncertain whether short-lived quasar mode AGN feedback can expel significant
amounts of cold gas (e.g. Croton et al., 2006; Hopkins et al., 2006, 2008), whether
longer sustained radio-mode AGN feedback has the most important role in
keeping the gas heated (e.g. Best et al., 2005; Bower et al., 2008; Guo et al., 2011),
or whether both mechanisms are required.

As galaxies are not isolated, environmental processes can influence the mor-
phology and the star formation history of a galaxy (e.g. Dressler, 1980; Lewis
et al., 2002; Peng et al., 2010, 2012; Darvish et al., 2015). For example, the pres-
ence of a close companion during a merger can boost the formation of stars
temporarily. Moreover, once a satellite enters the halo of a massive galaxy, it
can lose its gas by ram-pressure stripping (e.g. Gunn & Gott, 1972; Abadi et al.,
1999), the satellite can accrete gas less efficiently (strangulation; e.g. van den
Bosch et al., 2008) and tidal interactions during close encounters may disrupt
entire galaxies (such as the Antennae galaxies). Besides feedback mechanisms
originating in galaxies themselves, environmental processes are thus also im-
portant in influencing the growth of galaxies. Observational evidence includes
the fact that the passive fraction in satellite galaxies is generally higher at fixed

mass, and the passive fraction decreases with the distance to the central galaxy (e.g Muzzin et al., 2014).

As current cosmological hydrodynamical simulations are not run fully from first physical principles, their predictive power is limited. This means that the major purposes of these simulations are i) to identify which physical processes may be relevant at different scales, ii) to be able to follow the evolution of individual galaxies through time, iii) to be able to connect observables (such as stellar light) to properties that can much less easily be observed (dark matter mass, hot baryonic gas), iv) to test biases and limitations of observations by mimicking selection functions and v) to identify which relations between observables are new tests of several aspects of the galaxy formation model. The main predictive power of simulations depends on which observables have been used to calibrate the simulations. For example, the EAGLE simulation, that is studied in Chapters 10-12 of this thesis, has been tuned to reproduce stellar properties of galaxies in the present-day Universe (stellar mass and size in particular; e.g. Crain et al. 2015), meaning that its most predictive power lies towards the properties of gas and dark matter around galaxies and the properties of galaxies in the early Universe.
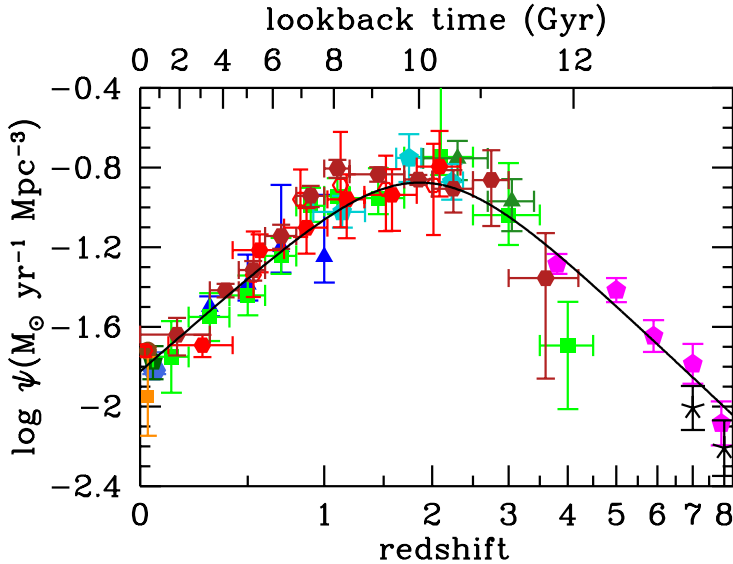
Figure 1.4: The history of the cosmic star formation rate density as estimated using various ways to measure the SFR (different colours and symbols). Below redshift $z < 2$ there is agreement between radio, FIR, UV and emission line surveys that the CSFR increases up to $z \sim 2$. Above $z > 3$, UV surveys indicate a decline in the CSFR. The rise in the CSFR in the first ≈ 3 Gyr follows the assembly of halos, while the decline in the last 10 Gyr is a result of declining cooling rates in hot halos, the overall exhaustion of neutral hydrogen gas and AGN feedback. *Figure from Madau & Dickinson 2014.*

1.2.3   The star formation history of the Universe

A fundamental measurement of galaxy formation is the cosmic star formation history, which describes how the stellar mass formed per year in an average volume of the Universe depends on cosmic time (see Fig. 1.4). A variety of observations agrees that the cosmic star formation rate (CSFR) was higher in the past and that it has been declining since the last 10 Gyrs (e.g. Lilly et al., 1996; Hopkins & Beacom, 2006; Sobral et al., 2013; Madau & Dickinson, 2014). On average, a galaxy with the same stellar mass was forming stars roughly ten times faster at redshift $z = 2$ (when the Universe was ≈ 3 Gyr old; a period called the *peak of star formation rate density* or the *cosmic noon*) than galaxies with the similar stellar mass do at the current cosmic time (e.g. Whitaker et al., 2012).

Beyond $z \sim 2$ observations indicate that the CSFR density declines up to the highest redshifts where galaxies are observed ($z \sim 10$, e.g. Bouwens et al. 2015a). A caveat is that observations in the *cosmic dawn* ($z > 6$) are predominantly limited to the rest-frame UV and hence rely on (uncertain) dust corrections.

Theoretically, the evolution of the CSFR density is understood by the accretion rate of gas on halos (the primary limiting factor at $z > 3$; Schaye et al. 2010) and the interplay between star formation and the strength and mechanism of feedback (e.g. Madau & Dickinson, 2014). The peak of the CSFR is determined by the halo mass at which galaxy formation peaks (e.g. Behroozi et al., 2013b; Moster et al., 2013), which is influenced predominantly by the gas cooling rate of hot, high mass halos and AGN feedback associated with the growth of supermassive black holes. Additional physical processes that affect the CSFR are photo-ionization in the epoch of reionization (mostly impacting low mass halos) and increased cooling due to stellar metal yields (mostly impacting galaxy formation at late times; e.g. Schaye et al. 2010)

1.2.4   Chemical enrichment

One of the key properties of galaxies is the chemical abundance of the ISM, which controls the metal content of the proto-stellar clouds in which stars and planets form. The cosmological mean metal content follows the star formation history and increases with increasing cosmic time (e.g. Madau & Dickinson, 2014). The evolution of the ISM of individual galaxies is however more complex. While the ISM is chemically enriched by supernovae and stellar winds in the late stages of stellar evolution (such as the AGB phase), the metallicity may also be lowered due to dilution from inflowing pristine (metal-poor) gas and/or outflows of metal enriched gas.

Observations of large samples of galaxies show that the typical gas-phase oxygen abundance increases with cosmic time, at least for galaxies with $M_{star} < 10^{10}$ $M_{\odot}$ (Zahid et al., 2013). However, most of this evolution may be explained by higher gas fractions (i.e. hydrogen masses) in the early Universe (e.g. Brown et al., 2018), such that the oxygen mass could be relatively constant. As the specific SFR of a galaxy is high for galaxies with a high gas fraction (e.g. Bothwell et al., 2013), galaxies' gas-phase metallicity is anti-correlated with specific SFR. This means that the scatter in the mass-metallicity relation is reduced when vari-

Table 1.1: The abundance relative to iron in the stellar ejecta from a single stellar population with so-lar metallicity as a function of its age, based on Wiersma et al. (2009b). *Absolute* values are uncertain by a factor two due to uncertainties in the yields and SN Ia rates.

Element	10 Myr	100 Myr	500 Myr	1 Gyr	5 Gyr
C	3.6	2.8	3.2	3.2	2.5
N	2.0	2.1	2.1	2.0	1.6
O	4.6	3.6	3.3	3.1	2.4
Fe	1.0	1.0	1.0	1.0	1.0

ations in specific SFR are accounted for (e.g. Lara-López et al., 2010; Mannucci et al., 2010). Hence, galaxies reside on a three-dimensional relation between mass, growth rate and chemical enrichment (see Chapter 12).

Although the exact stellar yields of different elements are uncertain due to the complexity of modelling stellar properties in the AGB phase and supernova explosions (e.g. Portinari et al., 1998), it is clear that different metal species are produced predominantly by stars of different masses (Wiersma et al., 2009b). As the stellar lifetime depends on stellar mass, this means that different chemical elements are produced on different time-scales associated to an episode of star formation activity in a galaxy (e.g. Tinsley, 1979).

For example, C, N and O abundances (relative to iron) of the stellar ejecta of a single stellar population with solar metallicity are listed in Table 1.1. Oxygen is only produced in massive stars (> 8 M$_\odot$) that end their lives as Type II su-pernovae (SNe), resulting in enrichment time-scales of ~ 10 Myr. As significant amounts (of roughly 30 %) of carbon and nitrogen are produced in the AGB phases of intermediate mass stars ($0.8 - 8.0$ M$_\odot$), their enrichment occurs on $\approx 200 - 500$ Myr (note that nitrogen is a secondary element, meaning that more nitrogren-rich stars also have increasingly higher nitrogen yields). Due to a sig-nificant contribution from the Type Ia SNe that occur in binary systems, 20-30% of the iron yields of a single stellar population occurs on long time-scales of $\gtrsim 2$ Gyr. Therefore, while gas is rapidly enriched with oxygen, it takes significantly longer for gas to be enriched with iron, with varying oxygen to iron ratios as a result. As a result, the α-enhancements of stars (the ratio of α-elements, such as oxygen, to iron) encode differences in the entire star formation histories of galaxies (e.g. Trager et al., 2000; Conroy et al., 2014). This is discussed in more detail in Chapters 11 and 12.

1.2.5 Reionization

Once the first generations of stars formed, ionizing photons produced in their host galaxies heated the IGM to temperatures that began to ionize hydrogen atoms. This cosmological phase-transition is called reionization (see Fig. 1.5 for an illustrated timeline of this process). As ionized photons damp the power spec-trum of the cosmic microwave background (CMB; e.g. Reichardt 2016), rough constraints on the average time when the Universe reionized can be obtained
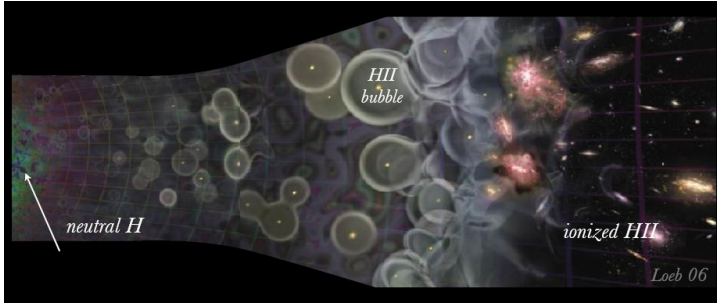
Figure 1.5: Illustration of the history of the Universe, focused on the timeline of reionization. As the first structures formed in a neutral IGM, ionizing photons produced by stars and AGN in early galaxies reionized the Universe. Reionization likely occurred bottom-up, with the first HII regions arising in the over-dense regions where the earliest galaxies formed. Measuring the detailed timeline and topology of reionization is the main aim of future 21-cm observations. *Figure from Loeb 2006.*

from CMB measurements.

Initially, the *WMAP* satellite measured an optical depth $\tau = 0.089 \pm 0.014$ (Bennett et al., 2013), indicating a mean reionization redshift $z = 10.6 \pm 1.1$ that requires early structure formation and/or ionizing photons contributed by extreme objects. The *Planck* satellite, which obtained higher resolution observations that can better remove foreground contaminants, revised these measurements to a lower optical depth $\tau = 0.058 \pm 0.012$, resulting in a later mean reionization redshift $z = 8.8 \pm 0.9$ (Planck Collaboration et al., 2016b). However, how reionization exactly occurred in different cosmological environments is currently poorly constrained observationally.

While future 21-cm observations may accurately map out the evolution of the neutral hydrogen power spectrum (e.g. Loeb & Barkana, 2001), the currently most accurate measurements of the neutral fraction of the IGM are obtained using the Lyα forest absorption lines and Gunn-Peterson trough in the spectra of high-redshift quasars (e.g. Fan et al., 2006; Becker et al., 2015). Unfortunately, the Gunn-Peterson trough saturates at low neutral hydrogen fractions of $x_{\mathrm{HI}} < 10^{-3}$ and can not be used at $z \gtrsim 6$. Alternative, but more uncertain probes of the neutral fraction are the Lyα damping wing in (rare) quasars at $z > 7$ (e.g. Miralda-Escudé, 1998; Bañados et al., 2018), the evolution of the strength and width of the Lyα emission line in galaxies (e.g. Hu et al., 2010; Ouchi et al., 2010; Stark et al., 2010; Pentericci et al., 2014) and the clustering of Lyman-α emitters (Ouchi et al., 2018).

Observations indicate that the mean neutral fraction decreased rapidly from ≈ 100 % at $z > 9$ (when the Universe was less than 500 Myr old) to $\approx 50(10)$ % at $z = 7(6.5)$ (at cosmic times about 750-800 Myr) and down to an almost completely ionized Universe with a neutral fraction of only ≈ 0.01 % at $z \approx 5$ (Universe 1 Gyr old). This means that the reionization of the Universe occurred relatively rapidly in ≈ 400 Myrs.

Current observational and theoretical efforts are aimed at understanding the patchiness of reionization and mapping out which kind of galaxies contributed

the majority of ionizing photons. Although quasars emit large numbers of ionizing photons that dominate the UV background after the reionization era (Becker & Bolton, 2013), their number densities are likely too low to contribute significantly to the ionizing photon budget at $z > 6$ (e.g. Parsa et al., 2018). Star-forming galaxies on the other hand are abundant and produce significant amounts of ionizing photons (e.g. Robertson et al., 2013; Bouwens et al., 2015b). However, it is unclear how many ionizing photons produced by short-lived massive stars can escape from their birth-clouds and eventually contribute to the ionizing background, and how this depends on galaxy mass. This problem can be mitigated if a significant fraction of massive stars reside in binary systems, which continue to emit ionizing photons on longer time-scales (e.g. Rosdahl et al., 2018). Understanding whether stars could have reionized the Universe requires detailed observations of the properties of the stellar populations in early galaxies and the properties of gas in and around them.

1.3 Galaxy formation: observational perspectives

1.3.1 Observational tools

Modern extragalactic astrophysics is not confined to wavelength ranges visible to the human eye, but includes observations spanning the entire electromagnetic spectrum using a range of instruments and techniques. The goals of this section are to give a broad overview of different wavelengths that are accessible and most commonly used in the study of distant galaxies and how observations are used to infer their properties.

Due to poor atmospheric transmission or strong atmospheric emission, sensitive observations in the X-ray ($\lambda \approx 0.1 - 10$nm), ultra-violet (UV; $\lambda \approx 120 - 300$nm) and infrared (IR; $\lambda \approx 3 - 600\mu$m) require telescopes outside the atmosphere of the Earth. Observations in the optical and near-IR ($\lambda \approx 300 - 800$nm and $\lambda \approx 0.8 - 2.5\mu$m, respectively) can be performed from Earth, although atmospheric OH line-emission adds considerable amounts of background to near-IR observations and turbulence in the atmosphere blurs images. As observations are sensitive to cloud coverage and atmospheric turbulence, ideal locations are high mountain peaks above the atmospheric inversion layer, near the vicinity of stabilising conditions due to the presence of large oceans. Examples include the islands La Palma (Canary islands, Spain) and the big island of Hawaii (USA), and mountain ranges in Chile. Sub-mm ($\lambda \approx 0.5 - 3.5$mm) and radio ($\lambda \approx 0.7 - 1000$cm) observations can be obtained with single dishes and interferometers. Sub-mm observatories require low humidity levels and are hence located on the driest places on Earth, such as the ALMA telescope in the Atacama desert in Chile at an altitude of 5000m. Currently, optical instruments are the most sensitive (in terms of reaching the lowest flux density noise levels), but interferometric (radio and sub-mm) observations can reach higher spatial resolutions.

For the purpose of this thesis, the two observational techniques that are mostly employed are imaging and spectroscopy in the optical and NIR. Imag-

Figure 1.6: The 2.5m Isaac Newton Telescope in its dome on Observatorio Roque de los Muchachos on La Palma. The telescope has an equatorial mount designed for its initial location in the UK and modifications had been made in order to use the telescope at lower latitudes. The Wide Field Camera is mounted on the prime focus and cooled by liquid nitrogen. *Credit: Isaac Newton Group.*

ing is performed using filters that transmit only a specific wavelength range, resulting in transmission-weighted mean flux densities in specific wavelength intervals. The optical and NIR wavelength regimes are typically split in ≈ 9 broad-band filters (such as the $ugriz$ SDSS system in the optical and the $YJHK$ filters in the NIR). Narrow- and medium-band filters deliver more detailed spectral information, at the expense of costing more observing time in order to obtain full wavelength coverage. In practice, different filters are combined depending on the specific science questions.

A significant fraction of this thesis is based on narrow-band imaging that is used to select emission line galaxies at specific redshift intervals (mostly using the Lyman-α line (e.g. Chapter 2), but also other emission lines; see Chapter 9). A part of this thesis is based on observations using the NB392 filter mounted on the Wide Field Camera (WFC) on the 2.5m Isaac Newton Telescope (INT, Fig. 1.6). The NB392 filter has been specifically designed for the purpose of measuring the Lyα emission line for a sample of galaxies selected through their Hα emission line (Sobral et al., 2013). These observations therefore combine measurements in the bluest and reddest parts of the optical to near-IR wavelengths observable from Earth. A particular challenge in these observations is that the CCD that is used to monitor the guide-star during an exposure is placed behind the filter. Due to the narrow width of the filter ($\Delta\lambda = 5.2$nm), the reduced quantum efficiency in the blue ($\lambda = 392$nm) and the scarceness of bright stars in typical extra-galactic survey fields, the majority of exposures are un-guided and

therefore have short exposure times. Consequently, few stars are available per image to perform photometric and astrometric calibration and these therefore have to be performed with care (see Chapter 7 for details). Even though the INT has been superseded by two generations of telescopes with larger mirrors, our observations show that, when a significant fraction of observing time is available, relatively old telescopes[2] can still deliver competitive data-sets, even for galaxies in the very distant Universe.
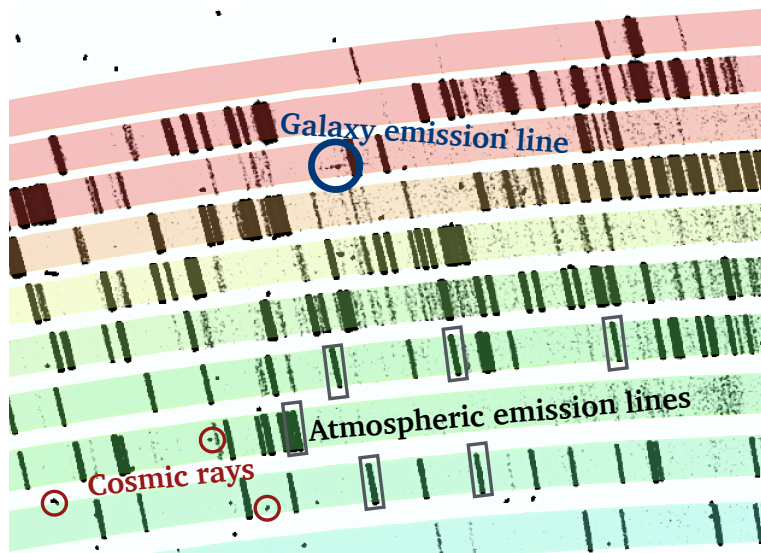
Figure 1.7: Example annotated single raw CCD image from a part of the optical coverage of the X-SHOOTER echelle spectrograph (program 100.A-0213, PI: Matthee). The shaded coloured regions show the pixels on which light from the spectrograph that falls through the slit is dispersed and that the observed wavelength increases from bottom to top. In each coloured band, the vertical offset position is related to the position on the sky. A galaxy emission line (encircled in blue; see Chapter 6) is identified at 923 nm (implying a look-back time of 12.6 Gyr) and can be separated from cosmic rays (red circles) due to its position and wavelength extent. Observations typically use multiple exposures at slightly different positions to over-come contamination from CCD effects and cosmic rays. Real emission lines are observed at the same wavelength and at positions consistent with the offsets between multiple images, while cosmic rays are not. Strong atmospheric emission lines are observed on all slit-positions for a given wavelength (a few are highlighted with grey boxes).

Spectroscopic techniques, on the other hand, disperse the light over a large number of spectral resolution elements. This allows detailed measurements of specific spectral features as absorption and/or emission lines. Typical spectroscopic instruments can either only observe a single target (through a slit) at high spectral resolution, or multiple (few tens) at moderate spectral resolution. A spectroscopic instrument that is used frequently in this thesis is X-SHOOTER, mounted at the Cassegrain focus of UT2 of the VLT. The key ability of the X-SHOOTER echelle spectrograph is that it can obtain a spectrum over a wide

---

[2] The INT, located at Herstmonceux Castle in Sussex in the United Kingdom from 1967-1979, saw first light in 1984 after its relocation to La Palma. The WFC on the INT saw first light in 1997.

wavelength range of $0.3 - 2.5\mu$m in a single observation at relatively high spectral resolution (see Fig. 1.7 for an example image), although on an object-by-object basis. For the purpose of high-redshift galaxies ($z > 2$), X-SHOOTER is particularly efficient as it can identify low-redshift interlopers in galaxy samples easily, it provides a high resolution spectrum of the Lyα profile and it simultaneously measures the properties of multiple emission lines (e.g. Chapters 4 and 6). Contrarily, observations with other instruments require sources to be observed with different instruments/telescopes, each with their own characteristics, on different observing nights and hence varying atmospheric conditions and other practicalities such as source acquisition (pointing the telescope at exactly the same location), etc.

The latest developments in spectroscopy are being made on integral field unit spectrographs (IFUs) such as MUSE on a Nasmyth focus on UT4 on the VLT. IFUs combine imaging with spectroscopy and deliver a spectrum for each pixel in the (often limited) spatial coverage. The major benefits of this technique are that spatial information is obtained and that targets do not have to be pre-selected. Therefore, this technique is particularly suited to study spatially resolved galaxies, but it is also very efficient in identifying objects for which the line-emission is offset from the continuum emission (hence easily missed by slit spectroscopy) and objects that are very faint in continuum emission, but with strong emission lines. The downsides are that spatial coverage is significantly smaller than imaging cameras and that the spectral resolution and wavelength coverage are less than that of e.g. X-SHOOTER.

The observations that I performed and/or analysed in this thesis include imaging in the optical and near-IR from ground and space (using the *HST*, *Spitzer*, VLT, Subaru, CFHT, INT, UKIRT and KPNO telescopes, Chapters 2–4, 6 and 9), slit-spectroscopy in the optical-near-IR (using the VLT and Keck, Chapters 4 and 6), interferometry in the sub-mm (using ALMA, Chapter 5), X-ray imaging and UV imaging from space (using *Chandra* and *GALEX*, Chapters 7–9). They therefore span 6 orders of magnitude in wavelengths, from 2.5nm to 2mm.

1.3.2   What do galaxy colours tell us

The majority of physical information that one can retrieve from the properties of galaxies comes from the analysis of their spectral energy distribution (SED). An SED can be described as the wavelength dependency of the intensity of light and which determines the colours of galaxies when observed in various photometric filters. As a complete overview of the properties that determine galaxies' SEDs is beyond the scope of this introduction, I will focus on the wavelength ranges and properties that are related to the Chapters in this thesis using an example SED.

A simulated galaxy SED is shown in Fig. 1.8, where the contributions from different components of the galaxy are highlighted in blue (light from stars), red (dust emission) and grey (ionized gas). As the stellar population in this example SED is young, the stellar light is dominated by hot O and B stars and thus shows

a moderately blue slope around $\lambda = 0.1 - 0.4 \mu$m. Hot stars ionize gas, that cools through nebular recombination lines and nebular continuum free-free emission (grey lines). Luminous emission lines include the hydrogen Lyα, Hα and Hβ lines, the oxygen [OIII]$_{5007}$ and [OIII]$_{88\mu m}$ lines, and the carbon [CII]$_{158\mu m}$ line (which also has a significant contribution from cool neutral gas as its ionization energy is lower than hydrogen). UV photons are absorbed by dust grains in the ISM that re-emit their thermal energy in the far-infrared ($\lambda \approx 10 - 200 \mu$m). Dust emission can typically be parametrised by a modified black-body spectrum (e.g. da Cunha et al., 2013), which shape and peak depend on the luminosity-weighted temperature distribution of the dust (e.g. Magnelli et al., 2014).

The example SED in Fig. 1.8 represents a galaxy with a very young stellar populations and a low amount of dust (similar to the galaxies discussed in the major part of this thesis). However, an SED can be very different depending on galaxy properties. In particular, the observed stellar emission is highly sensitive to the age of the stellar population and the amount of dust that is present (e.g. Conroy, 2013). As dust preferentially absorbs photons with a high energy (Calzetti et al., 2000), a higher dust content results in redder colours in wavelengths dominated by stellar emission. Hot, massive stars die earlier than cooler, less massive stars. Therefore, stellar populations become redder as they age, and the stellar light will mostly be emitted red-wards of the Balmer break ($\lambda > 0.4 \mu$m). The stellar emission is also sensitive to the metallicity of stars (as the iron abundance determines the opacity of stellar envelopes and hence the temperature in the atmosphere), the IMF (the relative abundance of massive to low mass stars determines the ratio of red to blue flux), the fraction of binary stars and stellar rotation (that both result in hotter, bluer stellar atmospheres; e.g. Eldridge et al. 2017).

While several physical processes may lead to degenerate observables (for example, a red galaxy colour could either be due to old stars or a significant dust attenuation), such degeneracies can be over-come by observing over a larger wavelength range (a strongly dust obscured galaxy would for example be expected to be much brighter in the far infrared), or using detailed spectroscopic features, such as absorption lines that are sensitive to the age and metal contents of stars (e.g. Conroy, 2013).

1.3.3 The physics encoded in nebular emission lines

The strengths of nebular emission lines are sensitive to the properties of the (ionized) gas in the ISM, such as the ionization parameter, the hardness of the ionizing radiation, the gas density and the chemical abundance. Therefore, measurements of the relative strengths of emission lines can be used to estimate these detailed properties. Spatially resolved emission line measurements can furthermore be used to probe the dynamics of the gas using the Doppler effect.

As illustrated in Fig. 1.8, the brightest emission lines in the rest-frame 0.1-0.7 μm range (observable with X-SHOOTER out to $z \sim 2$) include the hydrogen recombination lines, in particularly in the Lyman and Balmer series. Lyman-α is intrinsically the brightest emission line, but suffers from scattering and extinc-
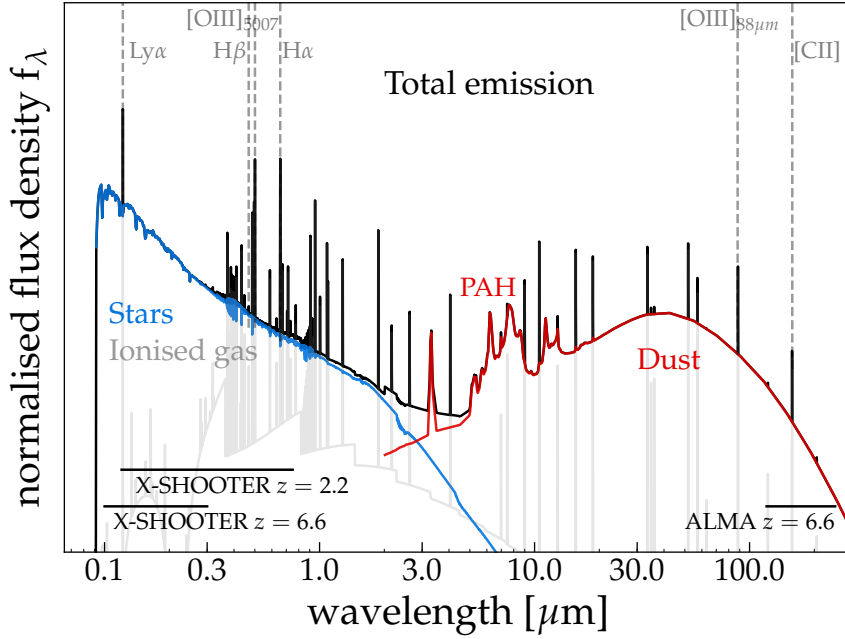
Figure 1.8: Example spectral energy distribution of a star-forming galaxy over the wavelength range of $\lambda = 0.1 - 300\mu$m, based on modelling with the CIGALE software package (Burgarella et al. 2005). The blue line shows the blue, weakly attenuated stellar light of a young stellar population. The luminosity and slope of the stellar light depend on the SFR, the stellar age, metallicity and the dust attenuation. The red line shows the radiation emitted by heated dust particles in the neutral and ionized gas of the galaxy. The dust emission can be modelled as a modified blackbody curve. A hotter dust temperature, for example due to a lower dust opacity as a result of a lower dust-to-metal ratio, would shift the peak to shorter wavelengths. The grey line shows the nebular emission in Hɪɪ regions. The relative strengths of nebular emission lines depend on chemical abundances, electron densities and the ionizing spectrum. A significant fraction of the light is emitted in narrow emission lines that are the subject of this study, e.g. the hydrogen Lyα and Hα emission lines and the fine-structure [CII] line emitted at 157.7μm. The wavelength ranges that are currently observable with spectroscopy (for example with X-SHOOTER) and with ALMA (in the high transmission region of band 6) are indicated by horizontal lines.

tion (discussed in detail in Section 1.3.4).

The strength of hydrogen recombination lines is directly related to the intrinsic number of produced ionizing photons and the escape fraction (e.g. Schaerer 2003 and Chapter 8) and can hence be used as indicators of the SFR (Kennicutt, 1998). The relative intrinsic ratios between the Balmer lines are well known and do not vary significantly (Osterbrock, 1989). Therefore, any deviation from the intrinsic ratio can be explained by different attenuations at the wavelengths of the emission lines. Hence, the Balmer 'decrement' is a reliable way to estimate the dust-attenuation in galaxies (Reddy et al., 2015).

Besides hydrogen, strong emission lines in the rest-frame optical are also emitted by (multiply) ionized oxygen and nitrogen, such as $[OIII]_{4959,5007}$, $[OII]_{3727}$ and $[NII]_{6548,6583}$. Together with hydrogen lines, these lines can be used to estimate the gas-phase metallicity (e.g. Pettini & Pagel, 2004; Tremonti et al., 2004; Erb et al., 2006). However, as these emission lines all have different ionization energies, their relative strengths are also sensitive to the ionization parameter (Kewley & Ellison, 2008). Reliable measurements of metallicity need to overcome this problem, by for example directly measuring the temperature of the gas (e.g. Andrews & Martini, 2013a). On the other hand, because of their different ionization energies, the relative strengths of these lines can also be used to identify the dominant ionizing source (i.e. a star-forming population, a power-law AGN spectrum or shocks; e.g. Baldwin et al. 1981a).

Deep, high resolution observations can also deliver measurements of other gas properties such as electron densities (e.g. using the density sensitive doublets $[OII]_{3726,3729}$ and $[SII]_{6716,6731}$; Sanders et al. 2016), the kinematics and covering fraction of gas (using low and high-ionization metal absorption lines such as $SiII_{1260}$, $SiIV_{1393,1403}$ and CII_{1334}; e.g. Henry et al. 2015), relative C/O and N/O abundances (using high-ionization emission lines as $OIII]_{1661,1666}$, $CIII]_{1907,1909}$ and $NIV]_{1488}$; e.g. Stark et al. 2014; Amorín et al. 2017). The properties of hot, massive stars can also be constrained (e.g. using P-Cygni features in the NV_{1240} and $HeII_{1640}$ lines; e.g. Gräfener & Vink 2015).

Besides using the strengths of emission lines to infer gas properties, physical information is also encoded in the width of the lines (such as the velocity dispersion) and particularly in the relative velocities of spatially resolved lines, which can be used to map out the dynamics (e.g. Swinbank et al., 2012). Dynamical information can particularly be useful to constrain the mass distribution in galaxies and the origin of pressure support in galactic disks (e.g. Förster Schreiber et al., 2009; Burkert et al., 2010; Turner et al., 2017).

1.3.4 Studying galaxy formation with the Lyα emission line

The HI Lyman-α (Lyα, $\lambda_0 = 1215.67$ Å) emission line, emitted when an electron in a hydrogen atom decays from the $n = 2$ to $n = 1$ state, is intrinsically the brightest nebular emission line emitted from star-forming galaxies (e.g. Partridge & Peebles, 1967; Charlot & Fall, 1993). As it is a rest-frame UV line, it is redshifted into the favourable optical window at redshifts $z = 2 - 7$, making it an ideal tool to find and study galaxies in the first 3 Gyr of cosmic history.

However, being a rest-frame UV photon, Lyα is sensitive to absorption by dust. Moreover, interpretation of Lyα luminosity is significantly challenged by its resonant nature (e.g. Dijkstra, 2017).

The absorption cross-section at the core of the Lyα line is $\sigma \approx 1 \times 10^{-14}$ cm^{-2} and only decreases to $\sigma < 10^{-21}$ cm^{-2} at > 1000 km s^{-1} away from line-centre. As re-emission after an absorption event occurs almost instantaneously, Lyα photons resonantly scatter in the presence of neutral hydrogen. As a result, Lyα photons undergo a random-walk in a neutral medium, leading to diffusion in real and frequency space and, in some cases, a double-peaked line-profile (Adams, 1972; Neufeld, 1990).

As scattering significantly increases the path length, the likelihood of Lyα photons being absorbed by dust is increased. Another consequence of scattering is that Lyα photons are spread out over a larger scale than the HII regions in which the photons are produced. This lowers the surface brightness, decreasing the contrast with respect to the night sky background and therefore lowering the observability. The Lyα escape fraction (the fraction of produced Lyα photons that is observed) depends strongly on the limiting surface brightness and aperture that is used (e.g. Wisotzki et al. 2016 and Chapter 7). As a result, the Lyα escape fraction is poorly understood.

Simultaneously, the observed spatial and spectral profile of Lyα emission also present an opportunity to constrain the properties of gas in and around galaxies (e.g. Verhamme et al., 2008), in particular the distribution of neutral hydrogen gas (e.g. Steidel et al., 2011; Mas-Ribas & Dijkstra, 2016). The Lyα line profile is shaped by the HI column density distribution and velocity structure along the line of sight and therefore caries information on the ionization state and porosity of the gas (e.g. Gronke & Dijkstra, 2016). Consequently, the Lyα spectral profile can be used to estimate the fraction of ionizing photons that escape from the ISM (Verhamme et al., 2015), which is one of the key unknowns in understanding the epoch of reionization (e.g. Robertson et al., 2013; Madau, 2017). An example of such an application is presented in Chapter 6.

While early searches for Lyα emission from distant galaxies were unsuccessful (e.g. Koo, 1986; Pritchet, 1994), likely due to lower than expected Lyα escape fractions (e.g. Hayes 2015 and Chapter 7) and small observed areas (Pritchet & Hartwick, 1987; Lowenthal et al., 1990), Lyα searches (mostly through narrow-band surveys) have been very efficient in identifying large samples at $z \approx 2 - 6.5$ since the early 2000s (e.g. Malhotra & Rhoads, 2002; Shimasaku et al., 2006; Dawson et al., 2007; Gronwall et al., 2007; Ouchi et al., 2008).

Current observational efforts are i) extending samples at $z = 0 - 2$, at which the Lyα line is still in the observed UV wavelengths and hence requires observations from space (e.g. Wold et al., 2017), ii) identifying galaxies at redshifts above $z > 6.5$, challenged by the increasing neutral fraction of the IGM that decreases the Lyα escape fraction, atmospheric OH line-emission that hinders spectroscopy and the need of near-IR detectors that are less sensitive than optical detectors (e.g. Matthee et al., 2014; Zheng et al., 2017; Ouchi et al., 2018) and iii) pushing towards much fainter sensitivities between $z = 3 - 6$ with integral field spectroscopic instruments as MUSE, e.g. Bacon et al. 2017, that also allow
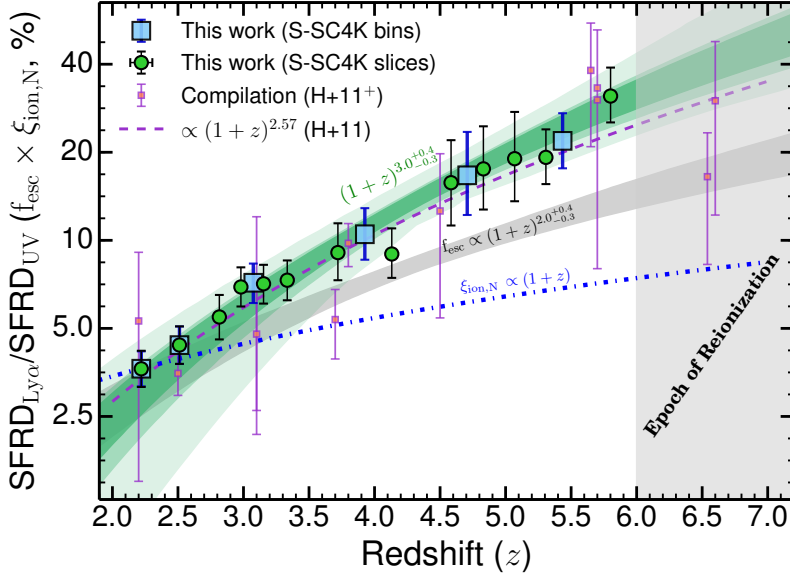
Figure 1.9: The evolution of the ratio between the Lyα and UV luminosity density, inferred from integration Lyα and UV luminosities to a fixed luminosity limit. The ratio is sensitive to both the number of Lyα photons that escape from galaxies and the number of Lyα photons that are produced per unit UV luminosity. Recent measurements from Sobral et al. 2018b agree with early estimates from Hayes et al. 2011. Most of the evolution is driven by an evolving escape fraction due to a decreasing dust content with redshift (as $(1 + z)^2$), but the number of produced Lyα photons per unit UV luminosity also increases with $(1 + z)$, as inferred from the evolution of specific SFRs. *Figure from Sobral et al. 2018b.*

for detailed studies of surface brightness profiles and identification of fainter galaxies.

A global picture of the evolution of Lyα emissivity in the Universe can be obtained by integrating Lyα luminosity functions and comparing the volume averaged Lyα luminosity with the UV luminosity density (e.g. Hayes et al., 2011; Sobral et al., 2018b). While the UV luminosity density rises quickly in the first 3 Gyr (following the increase in the global star formation rate density; e.g. Bouwens et al. 2015a), the Lyα luminosity density is roughly constant between $z = 2$ and $z = 6$ (between 0.5-3 Gyr of cosmic time). As illustrated in Fig. 1.9, this indicates that the global Lyα escape fraction increases from ≈ 3 % at $z = 2$ to ≈ 30 % at the end of reionization, $z \approx 6$ and that the produced number of ionizing photons per unit UV luminosity increases by a factor ≈ 2.5 over the same period. This likely means that galaxies in the early Universe are less dusty, allowing more Lyα photons to escape. At the same time relatively more Lyα photons are being produced due to either higher temperatures in the atmospheres of metal-poor stars or because star formation activity may occur in many short bursts (e.g. Sobral et al. 2018b). Therefore, while a Lyman-α emitting galaxy is not a typical galaxy at the peak of star formation history, the majority of galaxies in the very early Universe are strong Lyman-α emitters (e.g. Stark et al., 2011; Curtis-Lake

et al., 2012).

More detailed investigations on the properties driving the Lyman-α escape fraction in individual galaxies have been performed using 'analogues' in the local Universe (e.g. Atek et al., 2008; Hayes, 2015; Henry et al., 2015; Yang et al., 2016). Although there is significant scatter in correlations, these studies indicate that the Lyα escape fraction is higher for galaxies with a lower dust content, gas-phase metallicity, mass, outflow velocity and, most importantly, H$\textsc{i}$ column density. This means that galaxies that are selected through their bright Lyα emission typically have a low mass, low dust content and metallicity and correspondingly have young stellar populations. Hence, Lyα emitters are ideally suited to study the properties of low-metallicity early stellar populations and the early phases of galaxy formation and chemical enrichment.

1.3.5   Sample selection methods

Several techniques exist to obtain samples of galaxies in the distant Universe. These techniques can roughly be classed in three categories: identification of spectral breaks in the rest-frame UV or optical continuum, infrared continuum selection and emission line selection.

Examples of the first category are the Lyman-break selection (e.g. Koo & Kron, 1980; Steidel et al., 1996), which identifies the drop in the continuum below $\lambda_0 = 912$ Å (or $\lambda_0 = 1216$ Å at high-redshifts where the IGM transmission at the Lyman-Werner region is low) using the observed colours in broadband filters, or the BzK-criterion, which allows the selection of galaxies through the location of their redshifted Balmer break (Daddi et al., 2004). While the Lyman-break selection is highly efficient in identifying large samples of galaxies up to $z \approx 10$ (e.g. Bouwens et al., 2015a), it is susceptible to contaminants such as extremely dust obscured galaxies and brown dwarf stars in the Milky Way (e.g. Bowler et al., 2014). Another caveat is that the Lyman-break selection is biased against dust-obscured galaxies.

Galaxies can also be selected based on their strong infrared or sub-mm emission (e.g. Blain et al., 1999), typically associated with high, dust-obscured star formation activity. While typical sub-mm surveys are much less sensitive than optical surveys and source confusion due to limited spatial resolution is significant, sub-mm surveys are able to identify heavily obscured galaxies that are missed by optical surveys. Both strategies are therefore highly complementary.

Emission line selections, encompassing the third category, typically use narrow-band imaging, blind slit or grism spectroscopy or blind integral field spectroscopy in the optical and near-IR, but interferometric sub-mm data may also be used (e.g. Aravena et al., 2016). The most common emission lines that are used to select galaxies are the strong Lyα, [OII]$_{3727}$, [OIII]$_{5007}$ and Hα lines (e.g. Ly et al. 2007; Ouchi et al. 2010; Sobral et al. 2013; Khostovan et al. 2015 and Chapter 9), but selections on the FIR [CII] line or other rest-frame UV lines besides Lyα are also possible (Maseda et al., 2017; Stroe et al., 2017). Emission line selection is biased towards galaxies that have ongoing star formation or AGN activity and is not sensitive to passive galaxies. Similarly to the Lyman-break se-

lection, rest-frame UV emission line samples may miss heavily obscured galaxies (Oteo et al., 2015).

While the specific emission line that is observed in a narrow-band needs to be identified with additional photometric or spectroscopic observations, a benefit of narrow-band observations is that observational techniques are well tested and can cover large parts of the sky efficiently. Another advantage is that narrow-bands can be designed to observe in wavelength windows with high atmospheric transparency and low levels of atmospheric emission, which is particularly important in the near-IR (e.g. Sobral et al., 2013, 2015a). While blind spectroscopy directly provides additional spectroscopic information and emission line properties, the downside is that observations are expensive and limited to small regions on the sky. These limitations can be mitigated with grism spectroscopy, but at the cost of source-confusion and low spectral resolution.

1.4   This thesis, outlook

1.4.1   Challenges & Open questions

The motivation and aims of this thesis can be understood in the context of the fundamental underlying questions that are among the key goals of modern astrophysics.

The first question that is the main driver of Chapters 2 to 9 in this thesis is *how do galaxies form?* When were the first stars born? What were their properties? How did early stellar generations impact the gas in early galaxies? How and when was gas enriched with chemical elements and how did this affect the formation of later stellar generations? How and when did the Universe reionize? What are the main drivers of reionization and where did it start? When and how did the first supermassive black holes form? While none of these questions will be fully answered here, the exploratory observational research of this part of this thesis helps formulating more accurate, testable questions.

The second set of questions is related to *how do galaxies grow, and what makes their growth histories different?* This is the main question behind Chapters 10, 11 and 12 and is approached from a theoretical perspective. Galaxies are observed with a wide variety of properties such as their sizes, their colours, their morphologies and their environments. What is the main driver of these differences? How can it be that galaxies with the same stellar mass (and hence a similar gravitational potential and thus similar local initial conditions in the early Universe) may have completely different colours, star formation rates and stellar populations? To what degree is galaxy formation chaotic, meaning that seemingly unimportant differences in initial conditions (i.e. density perturbations) drive large differences between galaxies at later times? What is the origin behind strong scaling relations, such as the relation between galaxy stellar mass and star formation rate?

1.4.2   This thesis

The Chapters in this thesis can roughly be divided in three topics: i) the identification, confirmation and spectroscopic investigation of luminous Lyman-α emitters in the early Universe (Chapters 2–6), ii) calibration of the Lyman-α and Lyman-Continuum emission at the peak of star formation history (Chapters 7–9) and iii) exploration of the origin of scatter in galaxy scaling relations in the cosmological hydrodynamical EAGLE simulation (Chapters 10–12).

Luminous Lyman-α emitters in the early Universe (Chapters 2-6)

Samples of luminous distant galaxies are required to observationally study the formation of galaxies in the epoch of reionization. To this aim, we performed a very wide field survey for Lyα emitters at $z = 6.6$ using a large compilation of data-sets from different telescopes – the largest Lyα survey at its time. This search, described in Chapter 2, revealed that the number of very luminous galaxies is higher than initially was expected based on extrapolations from earlier, smaller surveys.

Due to their luminosity, the distances of a sample of four newly discovered extremely luminous galaxies were reliably measured using spectroscopy in Chapters 3 and 4. The measured distances correspond to look-back times of over more than 12.5 Gyr, meaning that these galaxies are observed in the first billion years of cosmic time. Chapters 3 and 4 also discuss the properties of these galaxies that can be derived using high-resolution imaging with *HST* and near-IR spectroscopy. In particular, the results in these Chapters show that luminous Lyα emitters are often resolved into multiple separate components and that they contain young, highly ionizing sources with high temperatures and low metallicities. The brightest of these, named COSMOS Redshift 7 (CR7) presented the best evidence to date (in 2015) of containing a population of stars with an extremely low metallicity. However, subsequent observations with ALMA (Chapter 5), revealed that traces of carbon are present ubiquitously in all three components of CR7, indicating that early stellar populations have already enriched the ISM. ALMA moreover reveals that we are witnessing the build-up of a galaxy in the early Universe through the accretion of smaller galaxies.

Chapter 6 presents the properties of another luminous galaxy at the same distance as CR7. The complex Lyα profile from this galaxy presents a challenge to theories about the reionization of the Universe, as it indicates that the galaxy resides in a large highly ionized region, created by the ionizing radiation produced by the stars that are forming within it. Simultaneously, this is also the first object that shows that star-forming galaxies actively contributed to the reionization of the Universe.

Calibration of Lyα and Lyman-Continuum at the peak of star formation history (Chapters 7-9)

Currently, spectroscopic observations of galaxies in the distant Universe ($z > 3$) are mostly limited to the Lyα emission line, which is hard to interpret due to

its complex nature. As Lyα is an efficient tool to select distant galaxies and to study the epoch of reionization (Dijkstra et al. 2014, but also Chapters 2 and 6), calibrating correlations between galaxy properties and the Lyα escape fraction is necessary. Moreover, the escape fraction of ionizing photons, an important unknown for galaxy reionization studies, can not directly be observed in the distant Universe, and needs to be calibrated as well.

To calibrate these escape fractions, we designed a survey at the peak of star formation history at a redshift $z = 2.2$, where the Lyα escape fraction can directly be measured using Hα. Hα can be used to measure directly the intrinsic Lyman-Continuum radiation, while escaping Lyman-Continuum radiation is observable using UV observations. The dual narrow-band technique that is used in this survey is presented in Chapters 7 and 9, while UV observations are presented in Chapter 8.

These Chapters present individual objects that show the highest escape fractions and form the tip of the iceberg of the full population. The population averaged escape fraction, inferred through stacking techniques, is remarkably low. We find that the Lyα escape fraction anti-correlates with mass and the SFR, and is higher for galaxies with less dust content. Chapter 6 furthermore also shows that the majority of Lyα emission escapes at large distances from galaxies through resonant scattering in neutral hydrogen around galaxies. In Chapter 7, we predict that the production efficiency of ionizing photons was higher in the early Universe, which may facilitate the contribution from star-forming galaxies to cosmic reionization.

The origin of scatter in galaxy scaling relations (Chapters 10-12)

Large observational surveys of galaxies in the nearby Universe have revealed that galaxies reside on several tight scaling relations, such as the relation between stellar mass and metallicity and the relation between stellar mass and SFR. However, the physical origin of the existence of these relations is unclear.

To understand the physics encoded in scaling relations, we study the origin of their scatter in simulated galaxies in the cosmological hydrodynamical EAGLE simulation in Chapters 10, 11 and 12. In Chapter 10 we focus on which property determines the efficiency of galaxy formation by correlating the residuals in the stellar mass - halo mass relation at the present-day with dark matter halo properties in a matched dark matter only simulation (that not affected by galaxy formation physics, hence enabling to identify causation besides correlation). We find that a combination of halo mass and formation time correlates more strongly with galaxies' stellar mass compared to halo mass alone, indicating that halo properties that combine both halo mass and profile (such as the binding energy) are the most fundamental in determining galaxy properties. However, a significant fraction of the scatter remains unexplained by any dark matter halo property, indicating that galaxy formation is a partly chaotic process.

In Chapter 11, we focus on understanding the scatter in the stellar mass - SFR relation, and hence understanding which properties diversify the growth rates

of galaxies (i.e. their star formation histories). While SFRs fluctuate on short time-scales, long time-scale coherences exist between the present-day SFR and the star formation history driven by differences in halo formation time. This has implications for the relation between galaxy mass, growth rate and chemical evolution, as presented in Chapter 12. In particular, we predict, based on the EAGLE simulation, that the most fundamental three dimensional scaling relation of star-forming galaxies is a relation between stellar mass, SFR and the α-enhancement. Future observations can test this prediction, providing a detailed test of state-of-the-art galaxy formation models.

CHAPTER 2

Identification of the brightest Lyα emitters at z = 6.6: implications for the evolution of the luminosity function in the reionization era

Using wide field narrow-band surveys, we provide a new measurement of the $z = 6.6$ Lyman-α Emitter (LAE) luminosity function (LF), which constraints the bright end for the first time. We use a combination of archival narrow-band NB921 data in UDS and new NB921 measurements in SA22 and COSMOS/UltraVISTA, all observed with the Subaru telescope, with a total area of ~ 5 deg^2. We exclude lower redshift interlopers by using broad-band optical and near-infrared photometry and also exclude three supernovae with data split over multiple epochs. Combining the UDS and COSMOS samples we find no evolution of the bright end of the Lyα LF between $z = 5.7$ and 6.6, which is supported by spectroscopic follow-up, and conclude that sources with *Himiko*-like luminosity are not as rare as previously thought, with number densities of $\sim 1.5 \times 10^{-5}$ Mpc^{-3}. Combined with our wide-field SA22 measurements, our results indicate a non-Schechter-like bright end of the LF at $z = 6.6$ and a different evolution of *observed* faint and bright LAEs, overcoming cosmic variance. This differential evolution is also seen in the spectroscopic follow-up of UV selected galaxies and is now confirmed for Lyα emitters, and we argue that it may be an effect of re-ionisation. Using a toy-model, we show that such differential evolution of the LF is expected, since brighter sources are able to ionise their surroundings earlier, such that Lyα photons are able to escape. Our targets are excellent candidates for detailed follow-up studies and provide the possibility to give a unique view on the earliest stages in the formation of galaxies and re-ionisation process.

2.1   Introduction

The Lyman-α (Lyα) emission line (1216 Å) is a powerful tool to study the formation of galaxies in the early Universe. This is because it has been predicted to be emitted by young "primeval" galaxies (Partridge & Peebles, 1967; Pritchet, 1994), but also because it is redshifted into optical wavelengths at $z > 2$, where most rest-frame optical emission lines are impossible to observe with current instrumentation.

Indeed, the Lyα line has been used to spectroscopically confirm high redshift candidate galaxies up to $z \sim 7.5$ obtained with the Lyman-break technique (e.g. Steidel et al., 1996; Finkelstein et al., 2013; Schenker et al., 2014), which is based on broad-band photometry using e.g. WFC3 on the *Hubble Space Telescope* (HST). Galaxies selected this way are called Lyman-Break Galaxies (LBGs) and the current largest sample contains already 10,000s (e.g. Bouwens et al., 2015a).

Narrow-band surveys select emission line-galaxies at specific redshift slices and are therefore used to search for Lyα emitters (LAEs) directly. Samples of LAEs have now been established from $z \sim 2 - 7$ through narrow-band surveys (e.g. Cowie & Hu, 1998; Rhoads et al., 2000; Fynbo et al., 2001; Rhoads et al., 2003; Malhotra & Rhoads, 2004; Taniguchi et al., 2005; Shimasaku et al., 2006; Westra et al., 2006; Nilsson et al., 2007; Ouchi et al., 2008, 2010; Hu et al., 2010; Kashikawa et al., 2011; Shibuya et al., 2012; Konno et al., 2014), but also through spectroscopic surveys (e.g. HETDEX, VUDS and MUSE; Hill et al., 2008; Cassata et al., 2015; Bacon et al., 2015). Limited samples of LAEs at lower redshifts and the local Universe also exist that are detected through e.g. GALEX or HST (e.g. Hayes et al., 2007; Deharveng et al., 2008; Cowie et al., 2010).

While part of the difference between LAEs and LBGs is just the way they are detected, there are also differences in their average properties. There exists an anti-correlation between the UV brightness and the Lyα Equivalent Width (EW) (Ando et al., 2006; Stark et al., 2010), indicating that the brightest LBGs are typically not LAEs, and that the UV continuum for most LAEs is very hard to detect, even in the deepest broad-band images (Bacon et al., 2015). Spectroscopic follow-up of LBG selected galaxies has shown that the typical Lyα EW increases with increasing redshift up to $z \sim 6.5$. This is likely due to LBGs being younger on average and less dustier at higher redshift (Stark et al., 2010; Schenker et al., 2012; Cassata et al., 2015). This picture is consistent with the evolution of the luminosity function (LF) of the different classes of galaxies. For LAEs, the Lyα LF is remarkably constant between $z = 3 - 6$ (e.g. Shimasaku et al., 2006; Dawson et al., 2007; Gronwall et al., 2007; Ouchi et al., 2008), while the UV LF of LBGs declines to higher redshifts in a reasonably uniform way due to the decline in the global star formation activity in galaxies (Ellis et al., 2013; Bouwens et al., 2015a; McLeod et al., 2015a). This also indicates that the Lyα emission line generally brightens with increasing redshift.

From these observations, the picture has emerged that Lyα is preferentially observed at a specific phase during a galaxy's evolution. Since Lyα is produced by recombination radiation from hydrogen clouds around very massive, young (< 10 Myr) stars (e.g. Schaerer, 2003), and Lyα is easily absorbed and re-scattered

(leading to lower surface brightnesses), on average LAEs are believed to be young starbursts, while LBGs on average are slightly more evolved galaxies with a higher dust content (e.g. Verhamme et al., 2008). Ono et al. (2010) find that the UV slope of $z = 6 - 7$ LAEs is very steep ($\beta = -3$), while Bouwens et al. (2014) find that the UV slope of LBGs at similar redshifts is typically slightly shallower ($\beta = -2.2$). From clustering measurements, Gawiser et al. (2007); Ouchi et al. (2010) and Bielby et al. (2016) agree on an average LAE halo mass of $\sim 10^{11}$ M$_\odot$ from $z = 3 - 7$. For LBGs alternatively, the typical halo mass is one order of magnitude higher at these redshifts (e.g. Ouchi et al., 2003; Hamana et al., 2004; Ouchi et al., 2005; Hildebrandt et al., 2009), more typical of "Milky Way" dark matter haloes of 10^{12} M$_\odot$.

Near the re-ionisation redshift, physical processes start to play a role which are additional to intrinsic changes in the properties of galaxies, since Lyα is easily absorbed by a neutral Inter Galactic Medium (IGM). While LAEs can be an important source of ionising photons for re-ionisation, one of the main interests in studying LAEs at this epoch is observable effects of a higher neutral IGM opacity. Besides evolution of the luminosity function, these observables include an increased observed clustering in a more neutral IGM, and attenuated line-profile. The observed clustering of LAEs increases since the observability is favoured when sources are in overlapping ionised spheres (McQuinn et al., 2007), while the line-profile becomes more asymmetric due to absorption and re-scattering of Lyα photons in a more neutral medium (Dijkstra et al., 2007).

At $z > 7$ spectroscopic follow-up of LBGs is remarkably less successful (Fontana et al., 2010; Stark et al., 2010; Pentericci et al., 2011; Ono et al., 2012; Treu et al., 2013; Pentericci et al., 2014; Caruana et al., 2014), indicating either a lower intrinsic escape of Lyα (e.g. Dijkstra et al., 2014), an increased column density of absorbing clouds (Bolton & Haehnelt, 2013), or a higher neutral fraction of the IGM (Santos, 2004; Dijkstra et al., 2007; Schenker et al., 2014; Taylor & Lidz, 2014; Tilvi et al., 2014). There is also evidence for an increased opacity to Lyα photons from the Lyα LF, which is observed to decline very rapidly (Ouchi et al., 2010; Konno et al., 2014). Searches for LAEs at $z = 7.7$ and $z = 8.8$ have been unsuccessful in spectroscopically confirming any of the candidates (Willis & Courbin, 2005; Cuby et al., 2007; Willis et al., 2008; Sobral et al., 2009b; Hibon et al., 2010; Tilvi et al., 2010; Clément et al., 2012; Krug et al., 2012; Jiang et al., 2013a; Faisst et al., 2014; Matthee et al., 2014). However, these studies are still limited by their sensitivity since Lyα is shifted into the near-infrared (NIR). Most of these studies only probe tiny areas in the sky, meaning that bright sources might be missed.

Typically, research is so far limited to ~ 1 deg^2 areas (e.g. Ouchi et al., 2008, 2010), where cosmic variance, especially for the observability of Lyα around the re-ionisation epoch, can play a large role. To make further progress, we are carrying out an extensive set of wide-field narrow-band observations to study the evolution of Lyα emitters from the epoch of re-ionisation ($z \sim 6 - 9$) up to the peak of the cosmic star formation history ($z \sim 2 - 3$). Our aim is to explore the evolution of the bright end which is so far uncharted and for which spectroscopic follow-up is easier and gives a better comparison to to surveys at
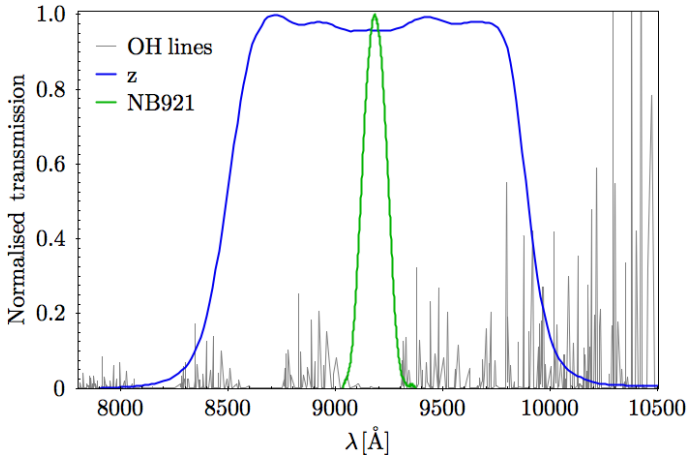
Figure 2.1: Filter transmission profiles of the NB921(blue) and z (green) filters, normalised to the maximum transmission. Atmospheric OH emission lines are shown in grey (Rousselot et al., 2000). The narrow-band is located in a wavelength region that is free of strong atmospheric emission, allowing sensitive observations and facilitating spectroscopic follow-up.

the highest redshifts.

In this paper, we focus at the $z = 6.6$ Lyα LF because of its importance to the study of re-ionisation. The widest narrow-band survey at that redshift to date has been presented by Ouchi et al. (2010), which reaches a Lyα luminosity of $\sim 10^{42.5}$erg s^{-1} over a ~ 0.9 deg^2 area. The brightest Lyα emitter in their sample, *Himiko*, with a luminosity of 3.5×10^{43} erg s^{-1} (Ouchi et al., 2009, 2013), has been seen as a very rare source, a triple merger, one of its kind. Because there has been only one very bright source known, the error on its number density is large, such that there is a factor 30 offset between the fitted luminosity function and the data. We have obtained wide field observations to further constrain the number density of bright Lyα emitters.

We introduce our data and sample selection in §2. Using our data set, we re-produce the Ouchi et al. (2010) sample and add new $z = 6.6$ Lyα candidates from deep archival Subaru data in the COSMOS field and new shallow wide-field data in SA22 in §3. Our estimates of the completeness of our selection procedure and description of the corrections made to the luminosity function are shown in §4. This leads to a new estimate of the luminosity function in §5 (supported by spectroscopic confirmation of the two brightest LAEs in COSMOS; Sobral et al. 2015b), where we find that the combined luminosity function has a non Schechter-like bright end. We discuss the evolution and implication for re-ionisation in §6. The main results are shown in Fig. 2.6, which shows our new estimate of the $z = 6.6$ Lyα LF, and Fig. 2.7, where we compare the evolution between $z = 5.7$ and $z = 6.6$.

Throughout the paper, we use a 737 ΛCDM cosmology (H$_0$ = 70 km s^{-1} Mpc^{-1}, $\Omega_M = 0.3$, $\Omega_\Lambda = 0.7$) and magnitudes are measured in 2″ diameter

apertures in the AB system.

2.2 Observations & Data reduction

2.2.1 Imaging

Optical imaging data was obtained with Subaru's Suprime-Cam (Miyazaki et al., 2002) using the NB921 narrow-band filter (Fig. 8.2). The Suprime-Cam is composed by 10 CCDs with a combined field of view of $34' \times 27'$ and with chip gaps of $\sim 15''$. The NB921 filter has a central wavelength of 9196 Å and a FWHM of 132 Å and is located in a wavelength region free of OH line-emission in the atmosphere (see Fig. 8.2).

We obtained archival ultra-deep observations in UKIDSS-UDS (02:18:00 −05:00:00, J2000) and COSMOS-UltraVISTA (10:00:00 +02:00:00, J2000) and SA22 (22:00:00 +00:00:00, J2000) and took new data in a wide area (~ 4.5 deg^2) in SA22 on May 28-29 2014, observing program S14A-086 (PI: Sobral). These fields were chosen for their multi-wavelength coverage and low Galactic foreground emission. Apart from providing a large total area, the combination of ultra-deep and shallower surveys allows us to sample a wide range of luminosities.

In UDS, there are 5 sub-fields with a total integration time ranging from 7.8 to 10.5 hours (see Table 2.1). This exposure time is obtained after stacking individual exposures of 1.2ks, with a small dithering pattern. The seeing FWHM ranges from $0.8 - 0.9$". We mask regions around bright stars, where spherical artefacts boost the fluxes artificially. We also mask horizontal and vertical stripes caused by blooming of a saturated bright object (see Fig. 2.3). This is the same raw data as used to study Lyα emitters at $z = 6.6$ by Ouchi et al. (2010).

In the four pointings in COSMOS, the total integration time ranges from 2.2 to 3 hours, with individual exposure time of 1.2ks, such that the total number of exposures per field is smaller (ranging from 7 to 9). In two pointings, the seeing is particularly good (0.3"), the other two have seeing FWHM of 0.6". Similar to in UDS, we mask spherical halo-regions around bright stars, and vertical and horizontal blooming-stripes (depending on the position angle rotation of the Suprime-cam pointing).

The deep SA22 data consists of 27 exposures of 1.2ks at a single pointing with small dithering in perfect seeing conditions (FWHM 0.3"). We mask a small noisy region and blooming patterns. The wide SA22 data consists of 19 pointings of 3 exposures of 120s in very good seeing conditions (FWHM 0.5"). Because of the limited number of exposures, a significant area has a lower signal to noise due to the dithering pattern. Another minor issue is that the astrometric corrections and calibration of the zero-point are less accurate in certain detectors due to the low signal to noise. We conservatively mask all these regions and also mask regions around bright stars and are left with a final coverage of 2.7 deg^2.

The total area after masking is 4.66 deg^2. An overview of the observations is given in Table 2.1.

Table 2.1: Observation log for the NB921 optical imaging in the COSMOS, SA22 Deep and Wide and UKIDSS UDS fields. Depths are based on empty aperture measurements and take correlations in the background into account. The UDS data have been analysed by Ouchi et al. (2010). The area is the area after masking (see §2.1). * Note that we have 19 pointings in SA22-WIDE, all with similar observing conditions.

Field	R.A. (J2000)	Dec. (J2000)	Int.time (ks)	FWHM (")	Area (deg^2)	Depth (3σ)	Dates
COSMOS-1	10:01:28	+02:25:51	10.8	0.3	0.24	25.8	2009 Dec 19
COSMOS-2	09:59:35	+02:27:01	8.78	0.3	0.24	25.9	2009 Dec 19,20
COSMOS-3	10:01:24	+01:58:00	10.8	0.6	0.24	25.9	2009 Dec 21
COSMOS-4	09:59:29	+01:58:42	7.80	0.6	0.24	25.7	2009 Dec 21
S-DEEP	22:19:14	+00:11 24	32.1	0.3	0.17	26.4	2009 Sep 15-17
S-W-[1-19]*	22:16:19	+00:10:00	0.36	0.5	2.72	24.3	2014 May 28-29
UDS C	02:18:00	-05:00:00	30.0	0.8	0.14	26.4	2005 Oct 29, Nov 1, 2007 Oct
UDS N	02:18:00	-04:35:00	37.8	0.9	0.18	26.4	2005 Oct 30,31, Nov 1, 2006 Nov 11,12
UDS S	02:18:00	-05:25:00	37.1	0.8	0.19	26.4	18, 2007 Oct 11,12 2005 Aug 29, Oct 29, 2006 Nov 18, 2007 Oct 12
UDS E	02:19:47	-05:00:00	29.3	0.8	0.16	26.4	2005 Oct 31, Nov 1, 2006 Nov 18, 2007 Oct 11,12
UDS W	02:16:13	-05:00:00	28.1	0.8	0.14	26.4	2006 Nov 18, 2007 Oct 11,12

2.2.2   Data reduction

The NB921 imaging data was reduced with SDFRED2 package (Ouchi et al., 2004). The sequential steps in the reduction are:

1. **Overscan and bias subtraction:** for each image, a median value for the overscan region was determined and subtracted in each line of pixels. The bias was subtracted by assuming that it has the same value as the overscan.

2. **Flat fielding:** flat frames are obtained by observing a uniform light source and are required to correct variations in pixel-to-pixel sensitivity across the camera. By dividing the images by these flat frames, the background becomes flat and luminous patterns caused by differences in the sensibility of the pixels are removed.

3. **Point spread function homogenisation:** the point spread function (PSF) measures the response of the detector to a point-like source. PSF sizes were obtained by measuring the FWHM of the point-like sources of each frame. The target PSF for homogenisation was defined as the one with more occurrences and the frames with PSF smaller than the target were smoothed with a gaussian.

4. **Sky background subtraction:** a mesh pattern was computed to represent the sky background, the pattern was interpolated and subtracted on each frame.

5. **Bad pixel masking:** defects with the detector and problems with the observations may cause data in some pixels to become corrupted. A mask is applied to these pixels.

6. **Astrometric calibrations**: we correct each image for astrometric distortions using Scamp (Bertin, 2006), which fits a polynomial solution by matching detected sources with the 2MASS catalog in the J band (Skrutskie et al., 2006). It also takes into account that images have different integration times and attributes a different weight to each image.

7. **Stacking**: Once each individual frame has been reduced, we stack the different jittered frames for each pointing.

8. **Cosmic ray rejection:** cosmic rays are rejected automatically based on the standard deviation in the pixel values in a 1" aperture. The standard deviation is typically a hundred times higher for cosmic rays than for real sources. We use a very conservative cut since we do not want to risk rejecting real sources, meaning that our sample will still be somewhat contaminated by cosmic rays. Partly because of this, we inspect all our final candidates visually.

Table 2.2: 3σ depths of broad-band coverage of our survey-fields obtained using empty $2''$ aperture measurements. The SXDF data is presented in Furusawa et al. (2008), the COSMOS data in Ilbert et al. (2009) and UltraVISTA in McCracken et al. (2012).

Field	Optical	Depths	NIR	Depths
UDS	$BVRiz$	28.3, 28.4, 27.8, 27.2, 26.6	JHK	25.7, 24.5, 24.4
COSMOS	$BViz$	27.6, 27.0, 26.9, 25.8	$YJHK$	25.9, 25.4, 25.1, 24.7
SA22	$ugriz$	26.2, 26.3, 26.0, 25.7, 24.5	JK	24.4, 23.9

2.2.3 Photometric calibration & survey depths

Once we obtained the reduced data for each pointing, we set the zero-point (ZP) to a magnitude of 30 (AB). This is done by extracting sources with SExtractor (Bertin & Arnouts, 1996) with high detection thresholds ($> 20\sigma$) and match these sources with public catalogues in UDS (Cirasuolo et al., 2007), COSMOS (Ilbert et al., 2009) and our own catalog in SA22 (based on K detected sources in UKIDSS-DXS; Matthee et al., 2014; Sobral et al., 2015a), using STILTS (Taylor, 2006). We only include sources with narrow-band magnitudes brighter than 19, such that our detections are at sufficient high signal to noise, and fainter than 16, since brighter sources are saturated in our data. In each pointing, we use roughly 500 sources. We then set the ZP by correcting the cropped mean difference between the magnitudes in our images and the ones in the catalogue.

We estimate our survey depth by measuring the root mean square (rms) of the background in a million empty apertures with $2''$ diameters, placed at random places in the image, avoiding sources which are detected at $> 3\sigma$. Empty aperture measurements take into account that the background noise is correlated and are thus more robust than if the background is measured on a pixel by pixel basis (c.f. Milvang-Jensen et al., 2013). Also, empty apertures can still include very faint sources below our detection threshold, so this is a conservative upper limit. The depths of the narrow-band images are listed in Table 2.1. The 3σ depths are 26.4 in UDS, 25.8 in COSMOS, 26.4 in the deep pointing in SA22 and 24.3 in the wide pointings in SA22.

2.2.4 Multi-wavelength data and photometry

For UDS, deep z-band data (26.6, 3σ) is available from the Subaru Extreme Deep Field (SXDF) project (Furusawa et al., 2008), as well as data in the optical bands B, V, R and i, with 3σ limits: 28.3, 28.4, 27.8 and 27.2 respectively (see Table 2.2). This multi-wavelength data is essential to identify different line-emitters. The images in the optical and NB921 are all aligned, because all are from a single survey, telescope and instrument. Furthermore, UKIDSS NIR J, H, K data (Lawrence et al., 2007) is available for 60 % of the coverage, with 3σ depths 25.4, 24.7 and 24.9. For NIR photometry, we use Swarp (Bertin, 2010) to align the NIR images to the NB921 images and interpolate the NIR images, since the pixel

scale is slightly larger (UKIRT WFCAM; Casali et al., 2007) than the Suprime-Cam pixel scale.

The COSMOS field is one of the best studied extra-galactic fields with > 30 bands coverage (Ilbert et al., 2009), ranging from X-ray to radio. We use deep optical *BViz* data from Subaru imaging, with 3σ depths of 27.6, 27.0, 26.9 and 25.8 (Table 2.2) which is available through the COSMOS archive[1]. We align the optical images to the narrow-band images using SWARP. NIR data in $YJHK_s$ is available from UltraVISTA DR2 (McCracken et al., 2012) with 5σ depths 25.4, 25.1, 24.7 and 24.8. The pixel scale of VISTA's VIRCAM is 0.15″/px, so we degrade the images to the pixel scale of the narrow-band images (0.2″/px) and align them.

The SA22 field is covered by CFHTLS and UKIDSS DXS surveys. SA22 is W4 in CFHTLS[2] and is imaged in *ugriz* with MegaCam, which has a field of view of 1 x 1 deg^2 and a pixel scale of 0.187″/pixel. The near-infrared UKIDSS DXS survey has imaged it in *J* and *K* filters with UKIRT/WFCAM. Note that the multi-wavelength data is not as deep as in the other two fields (typically 1-2 magnitudes shallower), and there is also no Spitzer/IRAC data available. This limits the search for LAEs in the deep pointing since the uncertainty in the *z*-band is much higher than the uncertainty in NB921. For the brightest objects (including all reliable detections in the Wide coverage), this is less of a problem. As before, we align the optical and near-infrared images to our narrow-band pointings using SWARP, including degrading the pixel scale to that of the narrow-band imaging.

For all fields, photometry is extracted using SEXTRACTOR in dual-mode with the NB921 image as detection image and within a 2″ circular aperture. In the case of a non-detection in any of the broad-bands, we assign 1σ limits. We then use the *i*-band to correct our *z*-band such that the median narrow-band excess is zero for all sources by fitting a linear relation between the $(i - z)$ colour and the narrow-band excess. Since the narrow-band filter is almost in the center of the broad-band filter, the correction is small, $z_{cor} = z - 0.13(i - z) + 0.286$. For sources undetected in the *i* band we assign the median correction of $+0.03$.

2.3 Selecting Lyman-α emitters at $z = 6.6$

In the NB921 data, Lyman-α emitters need to be selected as line-emitters at $z = 6.55 \pm 0.055$. This requires multi-wavelength coverage of the fields, which is available through a combination of large (public) surveys. First of all, we require broad-band photometry over the same wavelength coverage as the narrow-band, which is in this case the *z*-band.

Line-emitters are selected based on two criteria (e.g. Sobral et al., 2013): the first is that the narrow-band excess must be high enough. Since the observed equivalent width of emission lines increases with redshift and the intrinsic EW of Lyα is high ($\sim 100 - 200$ Å), we expect Lyman-α emitters to have a high

---

[1] Capak et al. (2007); http://irsa.ipac.caltech.edu/data/COSMOS/
[2] http://www.cfht.hawaii.edu/Science/CFHTLS/

narrow-band excess. We follow previous searches (e.g. Ouchi et al., 2010) and use an excess criterion of $z - NB921 > 1$, corresponding to a $z = 6.6$ rest-frame EW of 38 Å. This limit is also chosen to minimise contamination by lower redshift interlopers, although we will also lower this criterion and comment on the differences. To convert the narrow-band excess to the observed EW, we first transform magnitudes (m_i) to flux densities in each filter (f_i) with the standard AB convention:

$$f_i = \frac{c}{\lambda_{i,center}^2} 10^{-0.4(m_i+48.6)} \tag{2.1}$$

In this equation, c is the speed of light and $\lambda_{i,center}$ is the central wavelength in each filter, which are 9183.8 Å and 8781.7 Å for the narrow-band (NB) and broad-band (BB) respectively.

Using Eq. 1, we use the following equations to convert to EW and line-flux respectively:

$$EW = \Delta\lambda_{NB} \frac{f_{NB} - f_{BB}}{f_{BB} - f_{NB}\frac{\Delta\lambda_{NB}}{\Delta\lambda_{BB}}} \tag{2.2}$$

Here, f_{NB} and f_{BB} are the flux-densities, $\Delta\lambda_{NB}$ and $\Delta\lambda_{BB}$ the filter-widths, 135.1 Å and 1124.6 Å, respectively. In this formula, the numerator is the difference in narrow-band and broad-band flux and the denominator the continuum, which is corrected for the contribution from the narrow-band flux. The formula breaks down at a certain NB excess depending on the specific filters, and thus we set the EW of those sources to > 1500 Å. The line-flux is computed using:

$$f_{line} = \Delta\lambda_{NB} \frac{f_{NB} - f_{BB}}{1 - \frac{\Delta\lambda_{NB}}{\Delta\lambda_{BB}}} \tag{2.3}$$

The second criterion for selecting emission line galaxies is that the excess should be significant, meaning that it is not dominated by errors in the narrow-band and broad-band photometry. We will follow the methodology presented in Bunker et al. (1995) and the equation from Sobral et al. (2013) to compute the excess significance (Σ):

$$\Sigma = \frac{1 - 10^{-0.4(BB-NB)}}{10^{-0.4(ZP-NB)}\sqrt{\pi r_{ap}^2 (\sigma_{px,BB}^2 + \sigma_{px,NB}^2)}} \tag{2.4}$$

In this case, BB is the z-band magnitude after correction using the i band (see next subsections), NB the magnitude in NB921, ZP the zero-point of the images, which is set to a 30 AB magnitude. σ_{px} is the root mean squared (rms) of background pixel values in the data of the respective filters and r_{ap} is the aperture radius in pixels. Our depths are estimated using empty aperture based rms values, which takes correlations in the background into account. For the selection of emitters however, we use pixel based rms values for consistency with previous surveys, but also check that our results are robust when using empty aperture-based Σ values.

After selecting a sample of line-emitters, we use multi-wavelength data to distinguish high redshift candidate LAEs. In addition to the z-band, we also need bands in bluer wavelengths in order to apply the Lyman break technique to select high redshift sources. In this case this means that there should be no detection in the B, V, u, g and r filters and a strong break in the $(i - z)$ colours. Measurements in redder wavelengths, such as in the near-infrared (NIR) J, H and K filters, can provide valuable insight in the nature of the candidates and possibly help excluding lower-redshift interlopers. Finally, Spitzer-IRAC data can be used as further constraints on excluding dusty low redshift interlopers (generally with bright IRAC detections and red colours), or as a further evidence for the source being at $z = 6.6$, since at that redshift the [3.6] and [4.5] μm bands are contaminated in such a way that sources with strong nebular emission (EW > 1000 Å) are expected to have blue $[3.6] - [4.5]$ colours (e.g. Stark et al., 2013; Smit et al., 2014, 2015).

In addition to using colours for our selection and characterisation of Lyα candidates, we also compute photometric redshifts using EAZY v1.1 (Brammer et al., 2008), which includes the contribution of emission lines (although typically not strong enough for the observed extreme emission lines galaxies). We include optical and near-infrared photometry and we use it to identify possible lower redshift interlopers.

The details of our selection per field are presented in §3.1 for UDS, §3.2 for COSMOS and §3.3 for SA22.

2.3.1 Selecting LAEs in UDS

We use our photometry described in §2.4 and select line-emitters using the following criteria:

1. **z − NB921 > 1**

2. **Σ > 3**

3. Pass visual inspection

After the first two criteria, we have 1514 line-emitter candidates (see Table 2.3 for the numbers after each step). We check each line-emitter candidate visually in the NB921 image and exclude 122. Furthermore, 25 candidates are excluded since their excess is unphysically high, meaning that their (non-)detection in the z-band is in disagreement with the flux solely contributed by the measured narrow-band flux by more than 3σ. Most of the excluded candidates have their flux boosted by artifacts from bright stars, such as haloes or spikes (even after masking), others are excluded because they reflect read-out noise (since the images are so deep) and there are CCD-grid like patterns.

In total, we find 1367 line-emitters, which selection is shown in Fig. 9.2. This sample is dominated by Hβ/[OIII] at $z = 0.83$, [OII] emitters at $z = 1.46$ and Hα at $z = 0.40$ (based on photometric redshifts), even though the high excess criterion is already used to minimise this number. These lower redshift emitters are described for example in Sobral et al. (2013), which also shows a
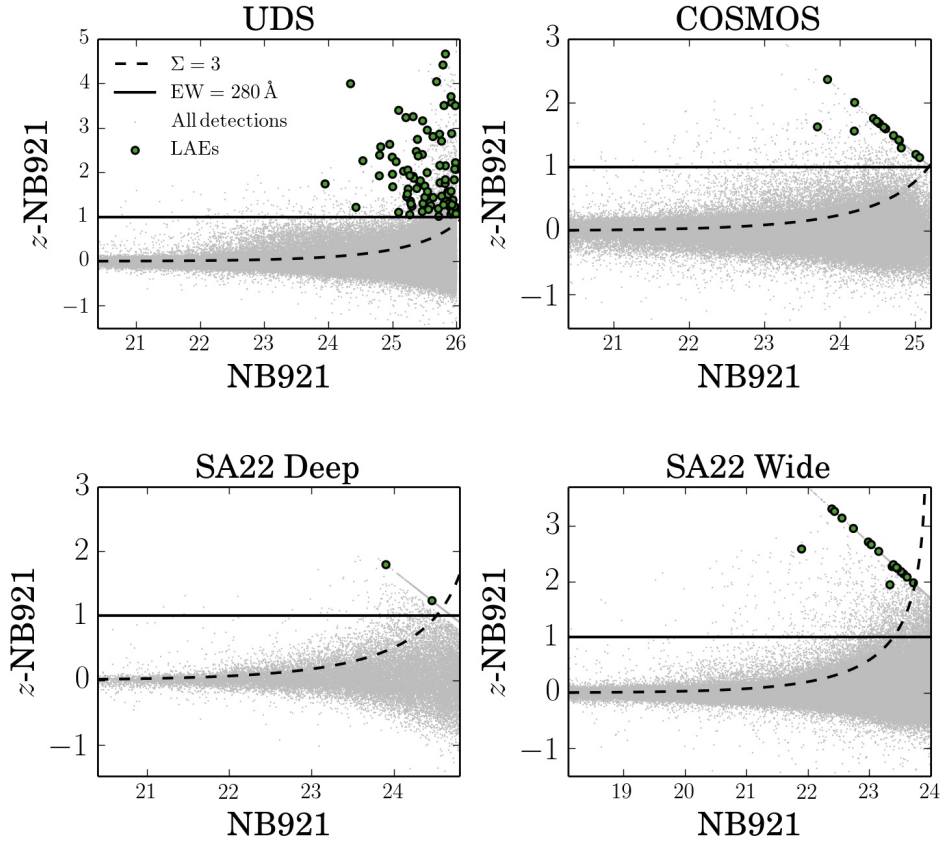
Figure 2.2: Narrow-band excess versus narrow-band magnitude. This figure shows the selection of line-emitters in our different fields. The grey points show all detected objects (after removing cosmic rays, visually identified spurious sources and sources for which the excess is unphysical) and the green points show the selected LAEs in each field. The selection consists of an EW cut (solid horizontal line) and a criterion to determine whether the excess is significant (dashed lines). The EW cut corresponds to a restframe EW of 38 Å at $z = 6.56$, and the significance cut corresponds to 3Σ. After visual removal of spurious sources and cosmic rays and optical and near-infrared broadband criteria, we find 99 LAEs in UDS, 15 in COSMOS, 2 in SA22-Deep and 19 in SA22-Wide. While the narrow-band imaging in UDS and SA22-Deep have similar depth, the number in UDS is higher due to a roughly 5 times larger area and (most importantly) deeper z-band imaging. There are less candidates in COSMOS due to shallower narrow-band imaging. The imaging in SA22-Wide is even shallower, but this is compensated by a much larger area.

photometric redshift distribution. To select Lyα candidates, we exclude low redshift sources and select high-redshift candidates using the Lyman-break technique:

$$B > 28.7 \wedge V > 28.2 \wedge (i - z > 1.3 \vee i > 27.2)$$

The Lyman-break technique is based on the absence of flux blue-ward of the Lyman limit (912 Å) and we therefore require our sources not to be detected at wavelengths below $912 \times (6.6 + 1) = 6930$ Å. This results in non-detections in B and V, and a strong $(i - z)$ break (or a non-detection in i as well). The $(i - z)$ criterion, adapted from Ouchi et al. (2010) takes the Gunn-Peterson trough at $z = 6.6$ into account. For consistency with the analysis from Ouchi et al. (2010), we use 2σ limits in order to minimise the number of potential interlopers (we show our 3σ limits in Table 2.2).

Finally, we use the NIR photometry to identify possible low-redshift interlopers which are extremely reddened by dust. For these sources, the Lyman-break is mimicked by the reddening from dust. However, it is possible to identify these interlopers based on their colours red-ward of the narrow-band. We exclude candidates which have $J - K > 0.5$ (empirically determined as a conservative lower limit) and are detected in the NIR by $> 3\sigma$, which results in only 1 additional lower redshift interloper. This source, which is likely an [OII] or [OIII]/Hβ emitter, has an observed EW of 1050 Å. This additional step is not applied by Ouchi et al. (2010), but it makes little difference for these luminosities. It is however important for shallower narrow-band surveys, as will be shown in the following sections. The public SpUDS-IRAC catalogue (Kim et al., 2011) is based on a conservative magnitude limit and therefore does not contain faint enough objects, such that there is no match with any of the LAE candidates within a 2″ radius, not even *Himiko*. It is however detected in deeper IRAC data (Ouchi et al., 2013).

We find a total of 99 Lyman-α candidates in UDS and show the positions in the UDS panel in Fig. 2.3. The size of the symbols of the Lyα candidates scales with the logarithm of the line-flux.

Lowering the EW criterion

We retrieve 37 additional LAEs by lowering our excess (EW) criterion to $z - NB921 > 0.5$, but keeping the other conditions fixed. The risk of lowering the EW criterion is that the number of lower redshift interlopers increases. We use the NIR information and photometric redshift to exclude lower-redshift interlopers, because these will generally be very dusty (in order to mimic the Lyman-break) and thus bright and red in the NIR. In §3.1, we found only 1 interloper if we use an excess criterion of $z - NB921 = 1$. If we lower the criterion to $z - NB921 > 0.5$, we remarkably find only 4 interlopers, where we expected to find more. However, most of the additional 37 LAEs are very faint in the z-band, with magnitudes of ~ 25.5. This means that they need to have a very red colour ($z - J > 1$ or $z - K > 2$) to be detected in the near-infrared, since our detection limits are $\sim 24 - 25$ (see Table 2.2). Therefore, it is likely that a fraction

of interlopers which do not have those extreme colours might be missed.

Because of their low excess, the additional LAEs have faint luminosities and thus affect mostly the faint end slope in the luminosity function. However, since we do not include these luminosities in the luminosity function due to their low completeness, the specific EW criterion used has little to no effect in our results.

Comparison to Ouchi et al. (2010)

The UKIDSS-UDS NB921 data has been analysed by Ouchi et al. (2010), who found 207 LAE candidates in UDS. The difference of 108 in number of candidates arises since we are even more conservative in our masked regions, limiting magnitude, and visually checking each candidate. However, when applying an analysis similar to Ouchi et al.'s, we find a very similar luminosity function (See §5.1 and §5.2). From the 16 spectroscopically confirmed LAEs by Ouchi et al. (2010), we have 15 LAEs in our first selection. The remaining source has a slightly lower excess in our analysis because we do not use MAG-AUTO. Even though Lyα is sometimes observed to be more extended than continuum emission (e.g. Steidel et al., 2011; Momose et al., 2014), we choose to use aperture photometry for all our measurements. This is motivated by our line-flux completeness estimate in §5.1 and a comparison with detection completeness in §5.1.1. However, by lowering our excess criterion to 0.9, we also select this source. Since we recover the luminosity function and the spectroscopically confirmed LAEs, we find that our sample of LAEs is in agreement with the sample from Ouchi et al. (2010) and that we fully recover their results.

2.3.2   Selecting LAEs in COSMOS

With the photometry presented in §2.4, we select line-emitters in the COSMOS field using:

1. **$z - \text{NB921} > 1$**

2. **$\Sigma > 3$**

3. Pass visual inspection

With the first two criteria, we find a total of 1633 candidate line-emitters, although immediately exclude 1070 sources for which the excess is unphysically high (see Table 2.3 for the numbers after each step). We visually inspect the remaining ones and exclude a further 165. The number of candidates excluded based on an unphysical excess or visual checks is considerably higher than in UDS, which is caused by a high number of cosmic rays. The automatic rejection of cosmic rays is less successful because the number of raw exposures is roughly three times lower than in UDS. Other spurious sources have their flux boosted by haloes or spikes caused by bright stars. The difference with UDS is caused by the z-band photometry, which is now relatively deeper compared to the narrowband photometry. Our cut is slightly more conservative in this field than in UDS since we prefer completeness and robustness over the number of sources. We

Table 2.3: Number of sources in each selection step, for each field. The final numbers of LAE candidates are printed in bold. *The number between parentheses shows the number of spectroscopically confirmed LAEs. When comparing the fields, it can be seen that there are relatively more line-emitters selected as high-redshift source in UDS. This is because the UDS observations are deeper and the sample therefore exists of fainter observed sources, which generally are at higher redshifts. The number of interlopers identified based on near-infrared colours is relatively high in SA22, where the constraints on the Lyman-break are weaker due to shallower optical photometry. We could only check for variability in the COSMOS field and a small part of the SA22 field.

Field	Selection step	Number of sources
UDS	Candidate excess sources	1514
0.81 deg^2	Spurious/Un-physical	147
NB921 < 26.4	Line-emitters	1367
	Lyman-break selected	100
	Red near-infrared	1
	Final LAE candidates	**99 (15)***
COSMOS	Candidate excess sources	1633
0.96 deg^2	Spurious/Un-physical	1235
NB921 < 25.8	Line-emitters	398
	Lyman-break selected	19
	Red near-infrared	2
	Variable sources	2
	Final LAE candidates	**15 (2)***
SA22-Deep	Candidate excess sources	359
0.17 deg^2	Spurious/Un-physical	2
NB921 < 26.4	Line-emitters	357
	Lyman-break selected	6
	Red near-infrared	4
	Final LAE candidates	**2**
SA22-Wide	Candidate excess sources	1674
2.72 deg^2	Spurious/Un-physical	929
NB921 < 24.3	Line-emitters	745
	Lyman-break selected	25
	Red near-infrared	5
	Variable sources	1
	Final LAE candidates	**19**

also rely on the UDS sample for the faintest luminosities (because of the deeper imaging) in our determination of the luminosity function and use COSMOS for brighter sources. They agree in number densities (Fig. 2.4) indicating that this approach is correct.

In total, we have 398 line-emitters. The photo-z distribution is peaked at [OIII]/Hβ at $z = 0.83$, with a smaller peak at Hα at $z = 0.40$ and one around [OII] at $z = 1.46$. 10 have spectroscopic redshifts, of which 9 are [OIII]/Hβ and 1 [OII], see Sobral et al. (2013). In order to select LAEs, we apply the following criteria to select high redshift line-emitters (see also §3.1):

$$B > 27.9 \land V > 27.3 \land (i - z > 1.3 \lor i > 27.0)$$

The optical limits are 2σ limits (also applied to UDS) computed by our empty aperture measurements, but consistent with Muzzin et al. (2013). We use the deep near-infrared data to identify dusty lower-redshift interlopers with red near-infrared colours and identify two likely [OIII] or [OII] emitters, which have $J - K = 1.53$ and $J - K = 1.8$ and observed EW of 420 Å and 350 Å, respectively.

In addition to this, we are able to check our sources for variability. We have publicly available data from Sobral et al. (2013) which has been taken one year later than the COSMOS NB921 data and reaches a 3σ depth of ~ 25, which is similar to the magnitudes of our faintest Lya candidates. By comparing the magnitudes, we exclude the two brightest candidates (NB921 ~ 21.5), because they are completely undetected in the data from Sobral et al. (2013). This means that their brightness changes by ~ 5 magnitudes and that they are thus likely supernovae. This means that similar surveys are expected to have roughly 2 SNe per 0.9 deg^2 as contaminants to their sample of LAEs, except if the data has been split over multiple epochs. This may be very important to interpret results at higher redshift (e.g. Faisst et al., 2014; Matthee et al., 2014) and shows how important it is to have data spread over time.

We match our remaining LAE candidates to sources in the S-COSMOS-IRAC catalogue and find one match. This match is our brightest candidate, nicknamed "COSMOS REDSHIFT 7; *CR7*". After these steps, we find 15 Lyman-α candidates in COSMOS, of which two remarkably bright sources - brighter than *Himiko* - and show their positions in Fig. 2.3. The size of the symbols of the Lyα candidates scales with the logarithmic of the line-flux.

We find no additional candidates when relaxing the excess criterion. This is because the narrow-band is not as deep as in UDS, while especially the near-infrared constraints are stronger. Therefore, the exclusion of lower redshift interlopers is more successful, especially since we have shown in §3.1.1 that the additional candidates are typically very faint, and therefore not present in our slightly shallower COSMOS imaging.

Spectroscopic follow-up: bright sources in COSMOS

In UDS, there are 16 spectroscopic confirmed LAEs by Ouchi et al. (2010) using Keck/DEIMOS. For COSMOS, we have obtained spectroscopic follow-up for

our brightest two candidates using Keck/DEIMOS and DDT program 294.A-5018 on VLT/X-SHOOTER and VLT/FORS2 presented in Sobral et al. (2015b). Both of these are confirmed Lyα emitters, at redshifts $z = 6.604$ and $z = 6.541$, respectively. We nicknamed these galaxies *CR7* (see above) and *MASOSA*[3]. *CR7* is detected at only half of the narrow-band filter transmission, leading to a 2″ luminosity of 5.8×10^{43} erg s^{-1}, which is a factor 2 higher than our estimate from the photometry. Based on MAG-AUTO, the luminosity is 9.6×10^{43} erg s^{-1}, and thus a factor 2.5 brighter than *Himiko*. This is a lower limit since the COSMOS NB921 observations are shallower than in UDS and might therefore miss some lower surface brightness regions and it assumes the z-band continuum being flat. It is so extreme that is even detected individually in the $zYJHK$ bands and detected at 5σ in the near-infrared stack, with $YJHK = 24.9$. It is also detected in IRAC, with a blue $[3.6] - [4.5]$ colour, consistent with the $[3.6]$ μm flux being boosted by strong Hβ/[OIII] line-emission (e.g. Smit et al., 2015). Because of these broad-band detections, the source can be selected as a Lyman-break galaxy. Indeed, *CR7* is present in the bright $z \sim 7$ UltraVISTA catalogs from Bowler et al. (2012, 2014). However, the Lyα EW is much larger than the values used for the SED fitting (see Sobral et al. (2015b)), meaning that the result from their SED fit requires revision and explaining the high χ^2.

MASOSA (with a Lyα luminosity of at least 3×10^{43} erg s^{-1}, both in a 2″ aperture and MAG-AUTO) is not detected in any of the near-infrared bands, and also not in the stacked image (meaning $YJHK > 26.7$). *MASOSA* is undetected in the z-band, meaning that the luminosity is a lower limit. It is only brighter than *Himiko* when measured in 2″ apertures, but this could also be due to our fainter narrow-band imaging in COSMOS than in UDS. It is not extended (diameter ~ 0.9″), while *CR7* and *Himiko* show an extent of ~ 3″ in diameter. This means that the sources are of a different nature and therefore interesting targets for follow-up study with e.g. *HST*.

None of our LAE candidates are in the zCOSMOS (Lilly et al., 2009) or UDSz (Bradshaw et al., 2013; McLure et al., 2013) catalogues, which we also did not expect, since they would likely be interlopers in that case. As expected, none of our LAE candidates except for *CR7*, are in the UV selected $z \sim 7$ galaxy catalogue from Bowler et al. (2014), since they are not detected in broad-band photometry. None of the other sources in the Bowler et al. (2014) catalogue are selected as line-emitters.

2.3.3 Selecting LAEs in SA22 Wide & Deep

Using our photometry described in §2.4, we select line-emitters using the following criteria:

1. **$z - \mathbf{NB921} > 1$**

2. **$\Sigma > 3$**

3. Pass visual inspection

---

[3] The nickname *MASOSA* consists of the initials of the first three authors of this paper.
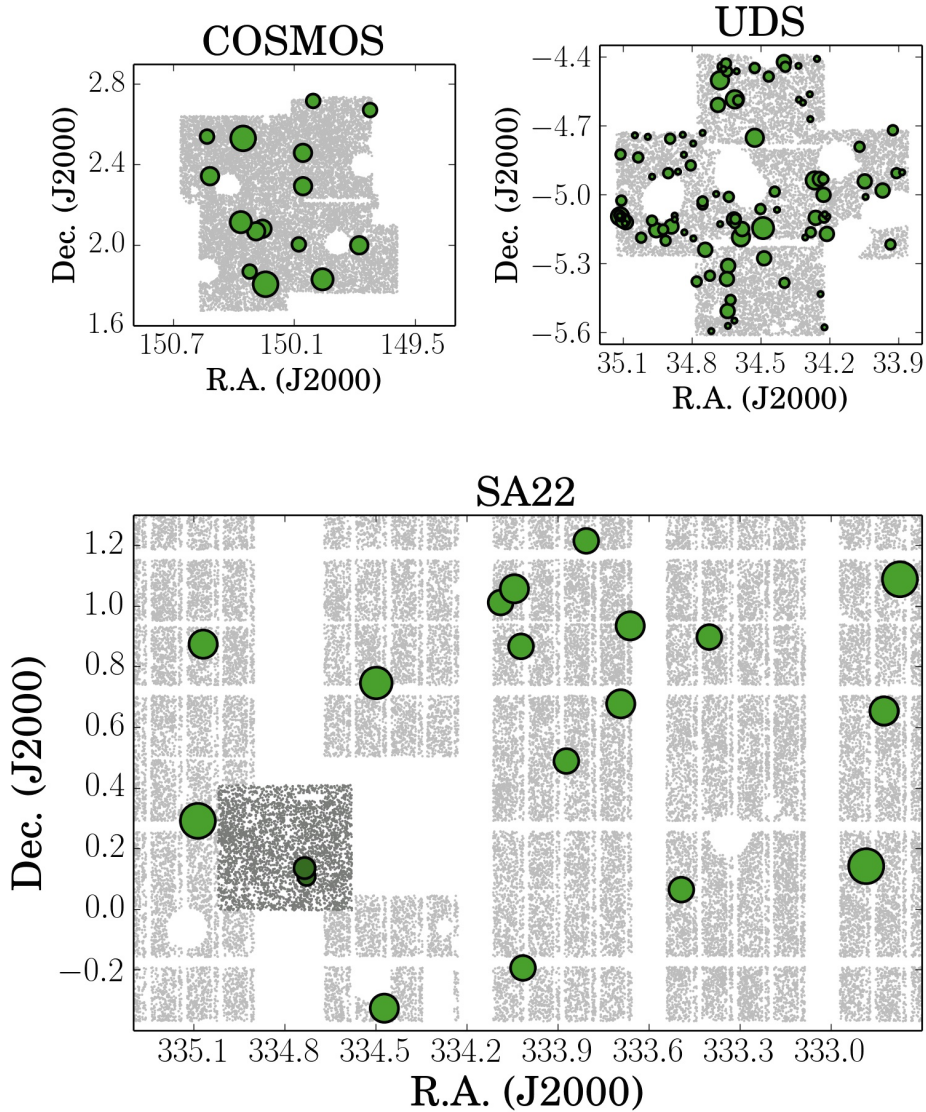
Figure 2.3: Position on the sky of the three survey fields. The three panels show the relative areas of the three fields. Grey dots show all detections with $NB921 < 22$, highlighting the masked regions due to bright stars and masked noisy areas due to our pointing strategy (such as the grid pattern in SA22). In SA22, the detections in the Deep region have a slightly darker colour. The green symbols show the positions of our LAEs. The size of these symbols scales with the line-flux (luminosity), following size $\sim (\log_{10}(L_{Ly\alpha}))^{3/5}$, and has the same limits and range for all the three fields. From this, it can be seen that UDS is significantly deeper since it has many more LAEs with small symbols. Two LAE candidates in SA22 are not visible in the image because they overlap with other symbols due to a small separation on the sky (~ 4").

After these steps, we find 1674 line-emitters in SA22-Wide, from which we exclude 359 for having an unphysically high excess, and 347 emitters in SA22-Deep (see the corresponding panels in Fig. 9.2, and Table 2.3) and apply the following criteria to select high redshift line-emitters:

$$u > 26.4 \wedge g > 26.5 \wedge r > 26.2 \wedge (i - z > 1.3 \vee i > 25.9)$$

The optical limits are 2σ limits and the $(i - z)$ criterion is similar to that in the other fields. We visually check each LAE candidate in the NB921 images and exclude a further 560 in SA22-Wide and 2 in SA22-Deep. Most of these objects are cosmic rays which were not detected automatically and sources which have their flux boosted by haloes or spikes caused by bright stars and are thus not real excess sources. In SA22-Wide our Σ-value from pixel based measurements corresponds to a 3 Σ if we measured the background with empty apertures, and to 1.5 Σ in SA22-Deep. These differences are caused by a different limiting narrow-band magnitude. There is one LAE candidate in SA22-Wide that is in the small overlapping region with SA22-Deep. This source happens to be variable, as it is undetected in the SA22-Deep data. We could not check the major part of the SA22-Wide field for variability and therefore use a statistical correction to the luminosity function using our empirical results from the COSMOS region, where we found 2 variable sources (likely supernovae) per 0.9 deg^2. The area is 2.72 deg^2, so we weight our number densities down by 6 sources.

Since the optical photometry in SA22 is shallower than in the other fields (see Table 2.2), there is a higher chance of our candidates being lower redshift interlopers, since the Lyman-break constraints are not as stringent. Using the near-infrared J and K data, we identify objects with significantly red NIR colours ($J - K > 0.5$). In SA22-Deep, we exclude 4 out of our 6 LAE candidates based on optical colours only, and are thus left with 2 LAEs. These four lower redshift interlopers can be called extreme emission line galaxies, since their observed EW is ~ 400 Å. In SA22-Wide, we exclude 5 interlopers out of the 24 LAE candidates from the near-infrared photometry. Because the SA22-Wide candidates are brighter, possible interlopers are easier to exclude based on their optical colours. Therefore, this number is relatively lower than in SA22-Deep. In total, we find 2 LAEs in SA22-Deep, and 19 LAE candidates in SA22-Wide. Their spatial position is shown in Fig. 2.3, where the size of the symbols scales with the logarithm of the line-flux.

The LAE candidates in SA22-Wide are particularly bright, with luminosities $3 - 16 \times 10^{43}$ erg s^{-1}, if they are at $z = 6.6$. We note that four candidates are in pairs, separated only by $\sim 3 - 5''$ in the sky (such that only one point is seen in the Fig. 2.3). Once these candidates are spectroscopically confirmed, this sample will allow us to study the variety of bright LAEs.

2.4   Number counts, completeness and corrections for filter profile bias

Our main diagnostic is the luminosity function and its evolution with redshift. The luminosity function shows the volume number density of Lyα emitters with a certain (observed) luminosity. In this section, we derive the observed number counts and all other input values for the luminosity function. This is because in addition to the raw number counts per bin, there are important corrections to be made, since our observations and analysis introduce biases and systematic errors, for which we correct in the following subsections.

The probed volume can be calculated using the FWHM of the filter, since that puts a lower limit and an upper limit to the Lyα emission-line redshift, which are 6.50 and 6.61 respectively. We calculate the volume then as the difference in comoving spherical volumes within the upper and lower redshift limits, and multiply this by the fraction of the sky that is our survey area. We find a comoving volume of 9.02×10^5 Mpc^3 deg^{-2}, corresponding to 7.4×10^5 Mpc^3 in UDS, 8.7×10^5 Mpc^3 in COSMOS, 1.5×10^5 Mpc^3 in SA22-Deep and 2.5×10^6 Mpc^3 in SA22-Wide. In total our volume is 42.6×10^5 Mpc^3.

2.4.1   Line-flux completeness

Our selection of line-emitters relies on the measured narrow-band excess and the excess significance. This means that photometric errors can lead to missing real Lyα emitters at $z = 6.6$, especially at the faintest luminosities. The result is that our sample is incomplete. How incomplete our survey is at a given luminosity (line-flux) depends on the survey depth, source extraction and selection method. We can measure the incompleteness with a simulation based on a sample of observed sources which are consistent with being at high redshift ($z > 3$, using Lyman-break criteria), but are not detected as line-emitters. This sample is detected and analysed in exactly the same way as our sample of Lyα candidates and has similar narrow-band magnitude distribution. To these sources ($> 1,000$ in total in the three deep fields, and $> 10,000$ in SA22-Wide) we artificially add line-flux by changing their NB921 and z-band magnitude correspondingly, and test whether it is then selected as a line-emitter based on the updated excess and excess significance. The completeness is then obtained for each line-flux by measuring the fraction of sources which is selected as line-emitter after adding the flux (e.g. Sobral et al., 2012). We show the line-flux for which our fields are complete up to 80 % in Table 2.4. These fluxes correspond to luminosities from 6.37×10^{42} erg s^{-1} (UDS) up to 4.9×10^{43} erg s^{-1} (SA22-Wide). Note that even though the narrow-band photometry has similar depths in SA22-Deep and UDS, the line-flux completeness is very different due to a different broad-band limit. This means that a measure of completeness based on detection only will give inconsistent results.

For each luminosity bin, we correct the number of sources by dividing by the completeness. We also divide the poissonian errors by this completeness value.

Table 2.4: The line-flux for which our completeness is 80 %, shown in our different fields. This depends on both the NB921 and z band depths. Note that, because of this, even though the narrow-band photometry has similar depths in SA22-Deep and UDS, the line-flux completeness is very different due to a different broad-band limit. This highlights the need for line-flux completeness over detection completeness.

Field	80% completeness flux
UDS	1.3×10^{-17} erg s^{-1} cm^{-2}
COSMOS	4.4×10^{-17} erg s^{-1} cm^{-2}
SA22-Deep	7.4×10^{-17} erg s^{-1} cm^{-2}
SA22-Wide	10.0×10^{-17} erg s^{-1} cm^{-2}

Only bins with a completeness higher than 40 % are included in the luminosity function. The completeness correction is strongest for the faintest luminosities, and thus increases the number density mostly at low luminosities.

Detection completeness in SA22

In order to access the quality of our data in our wide SA22 survey, we use our three spectroscopically confirmed bright LAEs to estimate the detection completeness. By placing them at random positions in our images and see whether we recover them, we know whether our data is sufficient to observe these luminous sources and we can furthermore check our line-flux completeness procedure (see above) and compare the two.

We produce small cutout images ($5'' \times 5''$) around *CR7*, *Himiko* and *MASOSA* and add them to 100 random positions per pointing in SA22, excluding masked regions. After this, we run SExtractor with identical settings as used on the original images and compute the fraction of our input sources that is detected. We repeat this 1000 times per image and use the average recovered fraction as detection completeness. On average, we find a detection completeness of 44 %, with a standard deviation of 20 % in different pointings.

The detection completeness is highest for *MASOSA*, 64 %, around the average for *CR7*, 43 %, and lowest for *Himiko*, 27 %. This is because the first source is not extended, while the other two are extended and therefore have lower surface brightnesses. Note that we do not exclude pixel positions with actual sources or regions with a slightly lower signal to noise, which both decreases the completeness. The average detection completeness is remarkably similar to our estimated line-flux completeness (which is 46 % for the average line-flux of the three sources). The large variation in detection completeness between the different sources, which have almost the same $2''$ magnitude, highlights the need for a completeness based on line-flux, instead of detection.
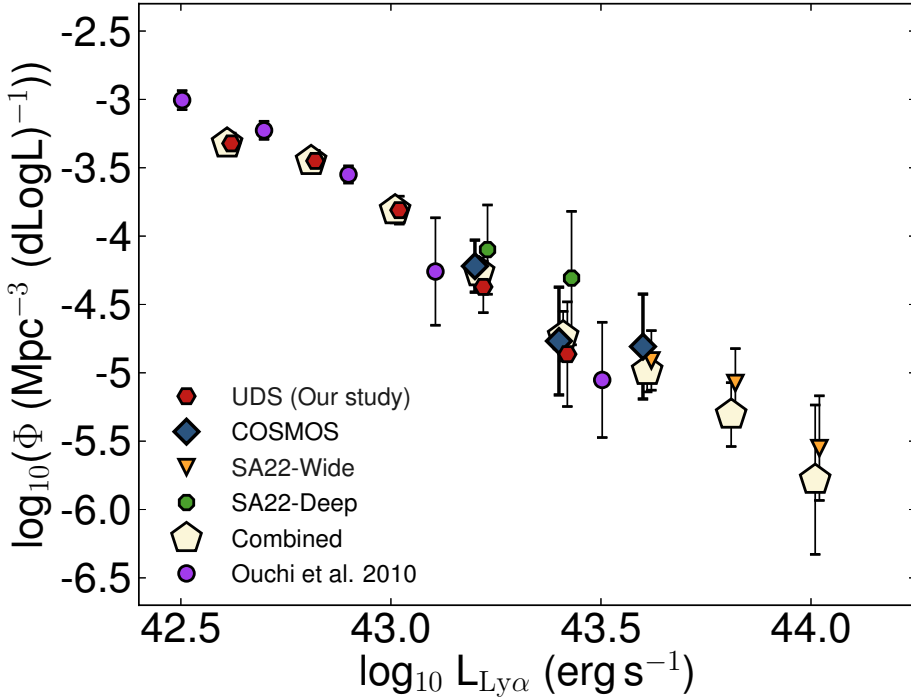
Figure 2.4: Number counts in our three fields, compared to the bins from Ouchi et al. (2010). The bins are only corrected for completeness. Our bins in UDS vary with this from Ouchi et al. (2010) because we use luminosities based on 2″ apertures and apply a different completeness correction. The SA22-Wide bins are corrected for contamination from variable sources and supernovae, empirically calibrated in COSMOS. Note the good agreement between measurements from all fields, although some variance is found which is likely due to cosmic variance.

Table 2.5: Correction factors for the number densities at $z = 6.6$. These corrections are made for the bias arising from the observations through the filter profile not being a top-hat. Because of the filter profile, luminous LAEs can be observed as faint LAEs, meaning that their real number densities are higher than observed. This is particularly important for when comparing narrow-band LAE searches with IFU based LAE searches.

| Luminosity bin	Number density correction factor
42.5	0.99
42.7	1.07
42.9	1.18
43.1	1.32
43.3	1.51
43.5	1.77
43.7	2.08
43.9	2.79
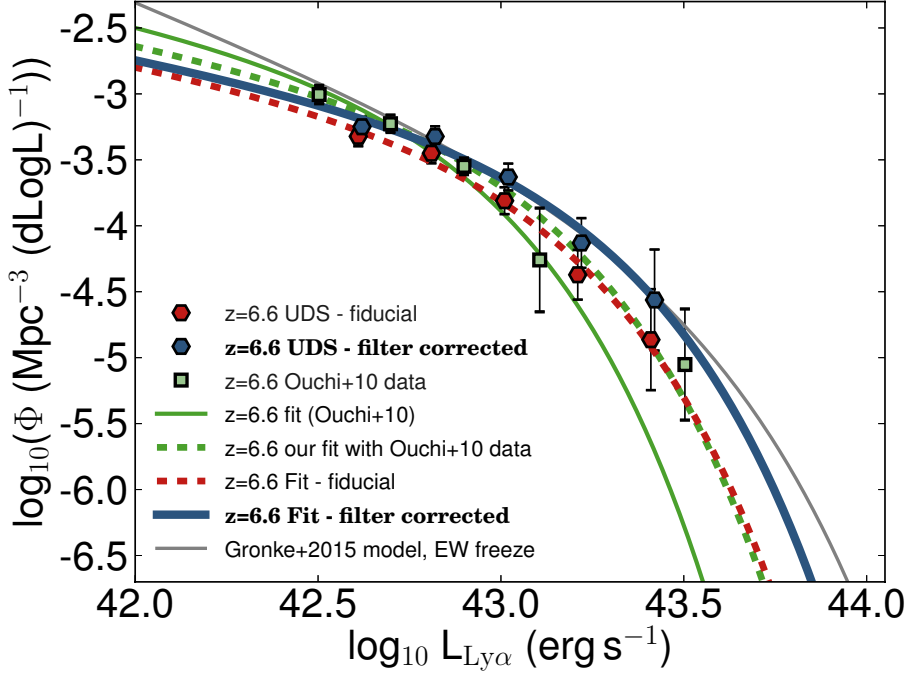
Figure 2.5: Luminosity function at $z = 6.6$: comparison of number densities and fits with and without filter profile correction. We compare our number densities in UDS with those of Ouchi et al. (2010), which are largely based on the UDS field as well. We show that our red hexagons (before correcting for the filter profile) agree well with the green squares from Ouchi et al. (2010), whose fit to the data is shown as a solid green line. The dashed green line shows our fit to their total data (fixing $\alpha = -1.5$ in Eq. 5), which differs significantly from their published fit. The fit to our data (α fixed to -1.5; dashed red line) again agrees well, indicating that our results are similar. The effect of the filter profile correction is shown by comparing the blue hexagons with the red hexagons. The effect is that the number density of bright line-emitters is higher, while the number density of faint line-emitter is slightly lower. The blue line shows the fit to the bins after correcting for the filter profile, which again highlights the effect of the correction. The grey line shows a model prediction by Gronke et al. (2015a) which is based on the LBG LF and a Lyα EW distribution, frozen at $z = 6.0$. It is remarkable that there it agrees well with the blue curve, despite not being a fit.

Table 2.6: Values to our Schechter fits to the luminosity functions. Because of our limited depth, we fix the faint end slope to either -2 or -1.5 and only keep $\Phi^\star$ and $L^\star$ as free parameters.

Data-set	α *fixed*	$\log_{10}(\Phi^\star)$ [Mpc^{-3}]	$\log_{10}(L^\star)$ [erg s^{-1}]	χ^2_{red}
UDS + COSMOS + SA22	-2.0	$-4.52^{+0.10}_{-0.12}$	$43.61^{+0.09}_{-0.06}$	3.14
UDS + COSMOS	-2.0	$-4.13^{+0.10}_{-0.13}$	$43.31^{+0.09}_{-0.65}$	2.49
UDS	-2.0	$-4.16^{+0.19}_{-0.44}$	$43.34^{+0.38}_{-0.13}$	1.78
UDS + COSMOS + SA22 without filter correction	-2.0	$-4.40^{+0.10}_{-0.13}$	$43.42^{+0.10}_{-0.07}$	1.75
UDS without filter correction	-2.0	$-3.97^{+0.15}_{-0.21}$	$43.12^{+0.15}_{-0.09}$	1.31
Ouchi et al. (2010) data, our fit	-2.0	$-3.78^{+0.13}_{-0.18}$	$43.06^{+0.13}_{-0.08}$	0.48
UDS + COSMOS + SA22	-1.5	$-3.93^{+0.06}_{-0.05}$	$43.33^{+0.04}_{-0.03}$	6.65
UDS + COSMOS	-1.5	$-3.62^{+0.06}_{-0.06}$	$43.05^{+0.06}_{-0.04}$	2.07
UDS	-1.5	$-3.56^{+0.10}_{-0.11}$	$43.01^{+0.10}_{-0.11}$	0.95
UDS + COSMOS + SA22 without filter correction	-1.5	$-3.91^{+0.06}_{-0.07}$	$43.20^{+0.05}_{-0.04}$	3.87
UDS without filter correction	-1.5	$-3.53^{+0.09}_{-0.10}$	$42.88^{+0.07}_{-0.05}$	0.68
Ouchi et al. (2010) data, our fit	-1.5	$-3.35^{+0.08}_{-0.08}$	$42.84^{+0.07}_{-0.05}$	0.71

2.4.2   Number densities

We show our number densities in Fig. 2.4 and compare with the number densities from Ouchi et al. (2010) (purple circles), which is based majorly on UDS. Our UDS points agree with those of Ouchi et al. (2010), while the SA22-Deep and COSMOS bins (which are spectroscopically confirmed) converge at brighter luminosities and are also consistent with Ouchi et al. (2010). Our SA22-Wide number densities are more uncertain, since there is no spectroscopic confirmation yet and the photometric constraints are weaker than in the other fields. However, even if there are still some contaminants, these further highlight a departure from a Schechter function (already indicated by our spectroscopically confirmed sample) at high luminosities and indicate that the observed Lyα luminosity function at $z = 6.6$ can be fitted by a powerlaw (e.g. the pentagons in Fig. 2.4). The powerlaw fit is: $\log_{10}(\frac{\Phi}{\mathrm{Mpc}^{-3}}) = 68.38 - 1.68 \log_{10}(\frac{L_{\mathrm{Ly}\alpha}}{\mathrm{erg\,s}^{-1}})$.

Since we have only two sources in SA22-Deep and since this agrees very well UDS and COSMOS, we will include them when we refer to the UDS+COSMOS sample in the remainder of the text. We will also refer to the SA22-Wide results as SA22.

Since our LF estimate is based on binning the data, we suffer from Eddington bias (e.g. Ilbert et al., 2013). As luminosities have photometric errors, these uncertainties scatter sources from one bin to the next bin. However, due to the shape of the LF (more sources in the fainter bins than in the bright bins), the luminosity uncertainties move more sources into the luminous end than vice versa.

Table 2.7: Power-law fits to the number densities of the functional form: $\log_{10}(\frac{\Phi}{\mathrm{Mpc}^{-3}}) = a + b\log_{10}(\frac{L_{\mathrm{Ly}\alpha}}{\mathrm{erg\,s}^{-1}})$. The first two rows show the results from a fit to the corrected number densities (Fig. 2.6) and the second to the observed number densities (Fig. 2.4).

Data-set	a	b	χ^2_{red}
UDS + COSMOS + SA22	62.07 ± 3.45	-1.53 ± 0.08	2.75
UDS + COSMOS	60.84 ± 5.00	-1.50 ± 0.12	4.72
UDS + COSMOS + SA22 before filter correction	68.38 ± 4.58	-1.68 ± 0.11	1.62
UDS + COSMOS before filter correction	66.26 ± 6.10	-1.63 ± 0.14	2.67

Therefore, this bias tends to overestimate the number of luminous sources and underestimates the fainter sources. It could therefore overestimate the bright end. We are aware of this bias, but do not apply a correction in order for consistency with previous surveys and since its effect are similar between different redshifts.

2.4.3 Filter profile bias correction

Since our filter is not a perfect top-hat, the exact redshift of the Lyα emission line influences the observed luminosity. This means that intrinsic luminous LAEs which are detected at the edges of the filter (where the transmission is lower) are observed as fainter LAEs. It also means that the probed volume depends on the luminosity, since luminous sources can be detected over a larger redshift range, but will be observed as fainter sources. For example, our brightest spectroscopically confirmed source in COSMOS, *CR7*, is actually detected at only 50 % of the transmission and is thus even brighter than our photometric estimate.

Corrections for this effect are derived with a simulation, similar to Sobral et al. (2013) for Hα line-emitters. We use the Schechter fit of our UDS+COSMOS data to generate a million Lyα emitters and assume that they have a random redshift between the edges of the filter. We then convolve the luminosities with the filter profile into an observed population. Corrections are then obtained by comparing the number of sources in each luminosity bin before and after applying the filter-profile. The result of our correction is that the number-density of luminous sources is increased, while it decreases at low luminosities. We note explicitly that this correction is required to remove the bias from observation strategy, since e.g. an IFU survey without a filter would not suffer from this bias, and that it is not related to any intrinsic effect of the sources. We show the correction factors for $z = 6.6$ in Table 2.5.

Comparison to Ouchi et al. (2010): effect of the filter profile correction

There are two reasons for the small differences between our UDS and Ouchi's number densities (Fig. 2.4): the first is that our completeness correction is based
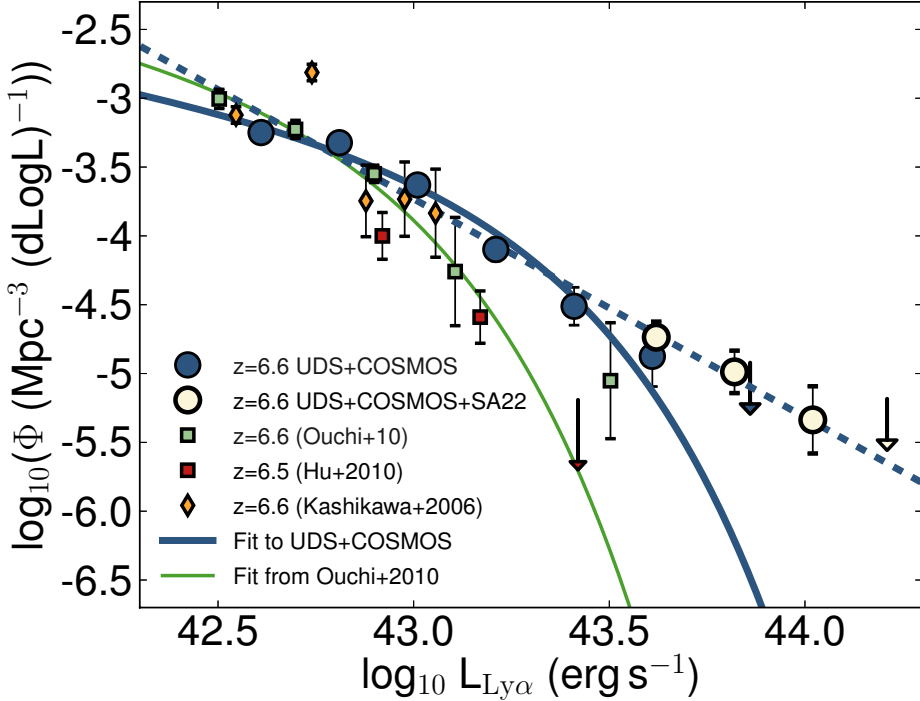
Figure 2.6: The Lyman-α luminosity function at $z = 6.6$ compared to literature data. Our most robust luminosity function is shown as a solid blue line. This is a Schechter fit to our combined UDS and COSMOS data (blue circles, see also Table 2.6), for which the brightest LAEs have all been confirmed spectroscopically. Our additional SA22 data is shown in open circles and is consistent with the upper limits from our robust sample. We also place upper limits (blue and open arrow) at the luminosity bin just brighter than the most luminous observed sources, meaning that there is less than one of these in the probed volume. The dashed blue line is our power-law fit (see Table 2.7) to the data from all three fields. The fit from Ouchi et al. (2010) at $z = 6.6$ differs for two main reasons (see also Fig. 2.5), namely practically not including the brightest bin to their fit (due to very large errors, as the fit contains only a single source) and not correcting for different biases caused by the filter profile. This is also the major reason why our results are slightly different with the results from Kashikawa et al. (2006) (ochre diamonds) and Hu et al. (2010) (red squares). Other reasons are cosmic variance, since they only probed small areas (Kashikawa et al.), and small (spectroscopic) completeness (Hu et al.).

on line-flux and the selection of emitters, while their completeness correction is based on detection completeness and narrow-band magnitudes. The other difference is that Ouchi et al. (2010) uses MAG-AUTO to estimate narrow-band magnitudes (which are used to compute luminosities), while we use the magnitude in 2″ apertures. As Lyα is often extended, MAG-AUTO might have been a better choice. We however chose to consistently use the 2″ aperture since we also used this for our (important) line-flux completeness correction. Using MAG-AUTO would mean the introduction of an additional uncertainty. We compare the luminosities derived with both 2″ apertures and MAG-AUTO for the spectroscopic confirmed sample in UDS and find that corrections of +0.11 dex can be used to statistically correct the luminosities. This is used in Fig. 2.4 and in all other following luminosity functions. Our results do not strongly depend on this correction.

The effect of the filter profile correction on the luminosity function derived by Ouchi et al. (2010) is shown in Fig. 2.5. We first fit a Schechter function to our UDS data, both before and after correcting for the profile (respectively the dashed red and solid blue line, see also Table 2.6) and then compare this fit to the Schechter function from Ouchi et al. (2010). Because the brightest bin in their sample contains only one source (Himiko), the error on the bin is extreme. Therefore, the fit from Ouchi et al. predicts a 30 times lower number density of bright LAEs than observed. We also fit a Schechter function to their data in log space (green dashed line). Note that we fix α to −1.5 in all our fits, similar to previous searches (e.g. Ouchi et al., 2008), since even the deepest UDS data is too shallow to constrain α accurately. However, in Table 2.6 we also provide fit values for an α fixed to −2. From Fig. 2.5 it is clear that, first of all, our luminosity function is in agreement with Ouchi et al. (2010) if we use similar corrections and include their brightest bin to the fit (as can be seen by comparing the two dashed lines in Fig. 2.5). Second, the effect of the filter profile is highlighted by comparing the solid blue to the dashed red line: after correcting for observational biases from the filter profile, the number density increases mostly at brightest luminosities.

2.5 Lyα Luminosity function at $z = 6.6$

In this section, we present the $z = 6.6$ Lyα LF from our combined analysis in UDS, COSMOS and SA22. As a functional form, we use the well-known Schechter function:

$$\phi(L)dL = \phi^{\star}(L/L^{\star})^{\alpha} \exp(-L/L^{\star})d(L/L^{\star}) \qquad (2.5)$$

We convert our observed line-fluxes to luminosities by assuming a luminosity distance corresponding to a redshift of 6.56, which is the redshift of the center of the filter. We combine the luminosities in bins with widths of 0.2 dex and count the number of sources within each bin and correct this number for incompleteness. The errors on the bins are taken to be Poissonian. The number of sources is divided by the probed volume, such that we obtain a number density.

We then apply our corrections for the filter profile bias. Only data where the completeness is at least 40 % is included. The resulting luminosity function is shown in Fig. 2.6, where we also compare with other published $z = 6.6$ LAE data. The evolution between $z = 5.7$ and $z = 6.6$ is shown in Fig. 2.7, while the left panel of Fig. 2.8 shows the evolution towards $z = 7.3$. We are cautious about interpreting the results from SA22 because of the less stringent photometric criteria, even though they fully agree with results from the other fields. The results from UDS and COSMOS however, are confirmed by spectroscopy.

It is interesting to compare these results with the model from Gronke et al. (2015a), which is shown as the black line in Fig. 2.5. This model uses the UV LF and a probability distribution (PDF) of Lyα EWs to predict the Lyα LF. The EW distribution generally evolves with redshift, but in this case, it is frozen to the EW PDF at $z = 6.0$, because of possible effects from re-ionisation. It is remarkable that the prediction from Gronke et al. (2015a) seems to be consistent with our blue points. Differences arise because of their steeper faint end slope (~ -2.2), which is largely unconstrained by the depth of our current data of LAEs. The agreement highlights the need for the correction of the filter profile bias when comparing narrow-band derived LFs with LFs derived from spectroscopy (either follow-up or blind IFU).

As noted in §5.2.1, our results in UDS differ by those from Ouchi et al. (2010) at brighter luminosities due to a different treatment of the brightest bin in the fit (solid green line) and by correcting for the filter profile (which effect is shown in Fig. 2.5). This explains also the differences (although largely within the errors) with Kashikawa et al. (2006), although cosmic variance plays a role because of their limited survey area. As noted by Kashikawa et al. (2011), the difference between the results from Hu et al. (2010) and the others is due to incompleteness of the sample of Hu et al. (2010), since they rely on spectroscopic follow-up with too short integration times.

Before correcting for the filter profile, our results in COSMOS agree with those from Ouchi et al. (2010) (see Fig. 2.4), but even after correcting for the filter profile, our combined UDS+COSMOS LF agrees with the brightest bin of Ouchi et al. (2010), and disagrees only slightly with the second brightest bin. Our SA22 results are not yet confirmed spectroscopically and are thus upper limits when viewed most conservatively. There is however excellent agreement with the spectroscopically confirmed COSMOS sources and with the upper limits from the UDS+COSMOS sample (blue arrow in Fig. 2.6). If all (or even only a fraction) of these very bright Lyα emitters in SA22 are confirmed, this indicates that the observed Lyα luminosity function at $z = 6.6$ can be fitted by a powerlaw (e.g. the pentagons in Fig. 2.4), similar to the UV luminosity function at $z = 6 - 7$ (e.g. Bowler et al., 2014).

Now we have used a combination of wide and ultra-deep fields, we have established a new LF at $z = 6.6$ (see Table 2.6) and will compare this with results in the literature at lower redshift. To be conservative, we will use our fit to the UDS+COSMOS sample for comparison, although our results are only strengthened by the results from SA22.
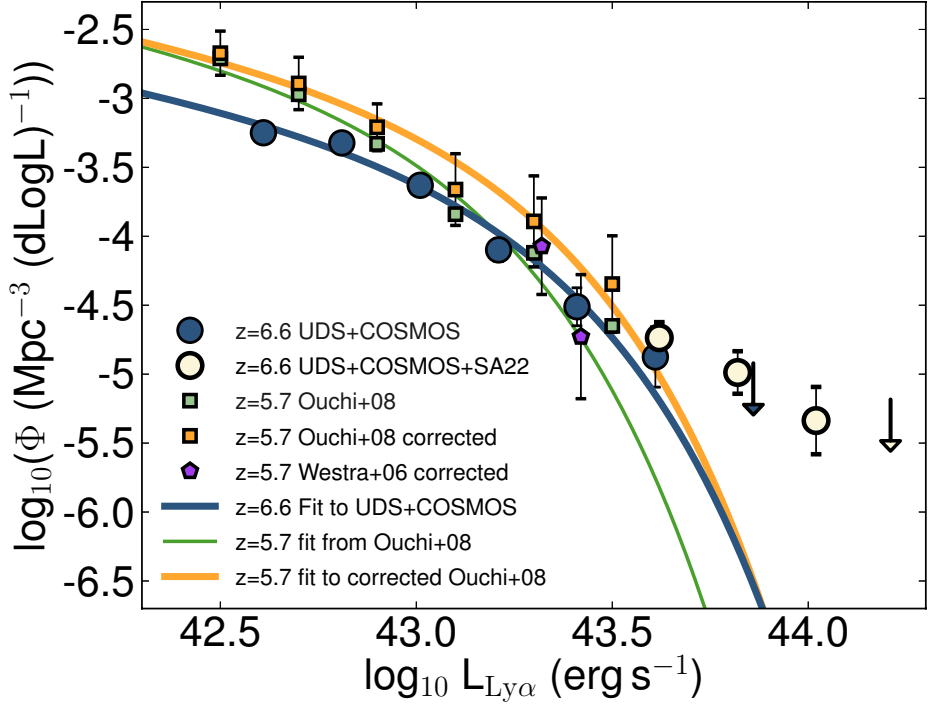
Figure 2.7: Evolution of the Lyα luminosity function from $z = 6.6$ to $z = 5.7$. We compare our $z = 6.6$ LF (blue solid line) to published data and fits to the data at $z = 5.7$. We apply a filter profile correction to the data from Ouchi et al. (2008) at $z = 5.7$ (green: uncorrected, ochre: corrected) and fit a Schechter function to the corrected data (orange solid line). We also show the spectroscopically confirmed results from Westra et al. (2006) at $z = 5.7$. Comparing the orange solid line to the blue solid line shows that the LF evolves only at the faint end and not (as has been claimed by Ouchi et al. (2010)) at all luminosities. In fact, we find no evolution for $L > 10^{43.5}$ erg s^{-1}. We show in §6.2 that this may be a consequence of re-ionisation. We do not show our fit which includes the SA22 data-points, since there is no comparison available at $z = 5.7$. This motivates the need for larger volumes at $z = 5.7$ as well, in order to see if there is evolution at the bright end.

2.5.1   The z = 5.7 − 6.6 evolution of the LF

Previous studies (e.g. van Breukelen et al., 2005; Ajiki et al., 2006; Shimasaku et al., 2006; Gronwall et al., 2007; Ouchi et al., 2008) have found that the observed Lyα luminosity function is remarkably constant between $z = 3 - 6$. While the LBG LF declines over this redshift range, the implication is that the strength of the Lyα line increases with redshift, which is also confirmed spectroscopically (e.g. Stark et al., 2010). At $z > 6$, there is evidence both from a declining success-rate of spectroscopic observations of LBGs (e.g. Schenker et al., 2012), and also for a drop in the Lyα LF (Ouchi et al., 2010; Konno et al., 2014).

In our independent analysis we confirm evolution of the Lyα LF from $z = 5.7$ to $z = 6.6$, although only robustly at fainter luminosities, $L_{Lyα} < 10^{43}$ erg s^{-1}, see Fig. 2.7. As a comparison at $z = 5.7$, we use data-points from Ouchi et al. (2008) (green squares in Fig. 2.7), complemented with the wide area survey from Westra et al. (2006). We were not able to compare our results to the number densities of Murayama et al. (2007) at $z = 5.7$ (2 deg^2 in COSMOS) since they do not correct for completeness. As discussed above, we apply a correction for the filter profile, based on a generated sample of a million LAEs following the $z = 5.7$ Schechter function from Ouchi et al. (2008). The result is shown as the orange squares in Fig. 2.7. For the data from Westra et al. (2006), we only show the corrected bins. We then fit a new Schechter function to the corrected points, shown as a solid orange line. The evolution between $z = 5.7$ and $z = 6.6$ can be seen by comparing the orange and blue solid lines. At fainter luminosities ($L_{Lyα} \sim 10^{42.5}$ erg s^{-1}) the observed number density of LAEs declines by a factor ~ 3, while there is no evolution at the bright end $L_{Lyα} > 10^{43.5}$ erg s^{-1}). Note that we only compare to our $z = 6.6$ sample based on UDS and COSMOS and that these results at the bright end are confirmed spectroscopically. Addition of the SA22 bins only strengthens the conclusion, but it is not yet possible to compare the SA22 results with lower redshifts, since there is no comparable data-set at $z < 6$. Even without the filter profile correction, we find differential evolution of the luminosity function. We will discuss explanations for this differential evolution in the discussion in §6.1 and §6.2.

When adding even higher redshift data from $z = 7.0$ (Iye et al., 2006; Ota et al., 2010) and $z = 7.3$ (Shibuya et al., 2012; Konno et al., 2014) narrow-band surveys (see the left panel of Fig. 2.8), the LF keeps decreasing at luminosities smaller than 10^{43} erg s^{-1}. Note that these bins consist of just a handful of sources and that we have not corrected them for the bias due to the filter profile. As the survey areas of these surveys are below 0.3 deg^2, they are all limited severely by cosmic variance and it is therefore not possible to compare the evolution at the bright end. A few additional shallower pointings will be useful to constrain the evolution of the bright end as well, and confirm or neglect a continuing differential evolution.

2.6 Discussion

2.6.1 LF evolution and re-ionisation

The evolution of the observed Lyα LF can be caused by different processes:
i) an intrinsic dimming of the Lyα EW. As the cosmic star formation rate density derived from UV observations at $z > 6$ continues to decline with redshift (e.g. Bouwens et al., 2015a; McLeod et al., 2015a), the production rate of Lyα can decrease due to a lower star formation rate, since Lyα is emitted by the recombination of hydrogen atoms which are photo-ionised by massive, young, short-lived stars. However, the cosmic star formation rate is already declining from at least $z > 3$, while the observed Lyα LF is constant between $z = 3 - 6$, indicating an increase in Lyα EW with increasing redshift (see also Stark et al. (2010)) and it is hard to explain a sudden reversal of this trend. Furthermore, the star formation towards higher redshifts can be partly contributed by formation of metal free Pop III stars, which are predicted to produce copious amounts of Lyα emission (Schaerer, 2003).

ii) the observed drop in the Lyα LF can be explained by a lower escape of Lyα in the interstellar medium of galaxies (Dayal & Ferrara, 2012; Dijkstra et al., 2014). This escape fraction is largely unconstrained, although first direct measurements of matched Hα-Lyα observations at $z = 2.2$ indicate an average escape of 5 % (Hayes et al., 2010). However, other, more indirect measurements of the escape fraction in LAEs is in general higher (30 %, e.g. Wardlow et al., 2014; Kusakabe et al., 2015). Using a joint analysis of the evolution of the Lyα and LBG luminosity functions, Hayes et al. (2011) finds that the volumetric (statistical) Lyα escape fraction increases with redshift up to $z = 6$ and decreases at higher redshift, although this result is based on the integration of the Lyα LF from Ouchi et al. (2010). As we show, in this paper, their large error on the bright end results in an underestimate of the luminosity density. The intrinsic Lyα escape fraction can be measured directly at $z > 3$ once infrared spectroscopy of the Hα line with the *James Webb Space Telescope* is possible. It is thought that the primary factor in driving the escape fraction is the neutral hydrogen column density (e.g. Nakajima et al., 2012), but kinematics and dust production can also have a role. Similar to the intrinsic dimming of Lyα EW, it is hard to explain a reversal of the trend highlighted by Hayes et al. (2011), i.e. an increase up to $z \sim 6$ and a decline afterwards.

iii) a sudden decrease in the observability of Lyα can possibly be explained by an increase in the incidence of dense pockets of neutral hydrogen in the line of sight (e.g. Lyman Limit Systems or Damped Lyman-α absorbers). Bolton & Haehnelt (2013) argue that the majority of optically thick gas along lines of sight is present in absorption systems, although again, there is no definite explanation why there should be a sudden increase, or why this increase depends strongly on Lyα luminosity.

iv) the most quoted reason (e.g. Santos, 2004; Haiman & Cen, 2005; McQuinn et al., 2007; Choudhury et al., 2015; Jensen et al., 2014) is that the observed decrease in both the evolution in the Lyα LF and the declining spectroscopic success-rate in LBG follow-up, is caused by an increased neutral fraction of the
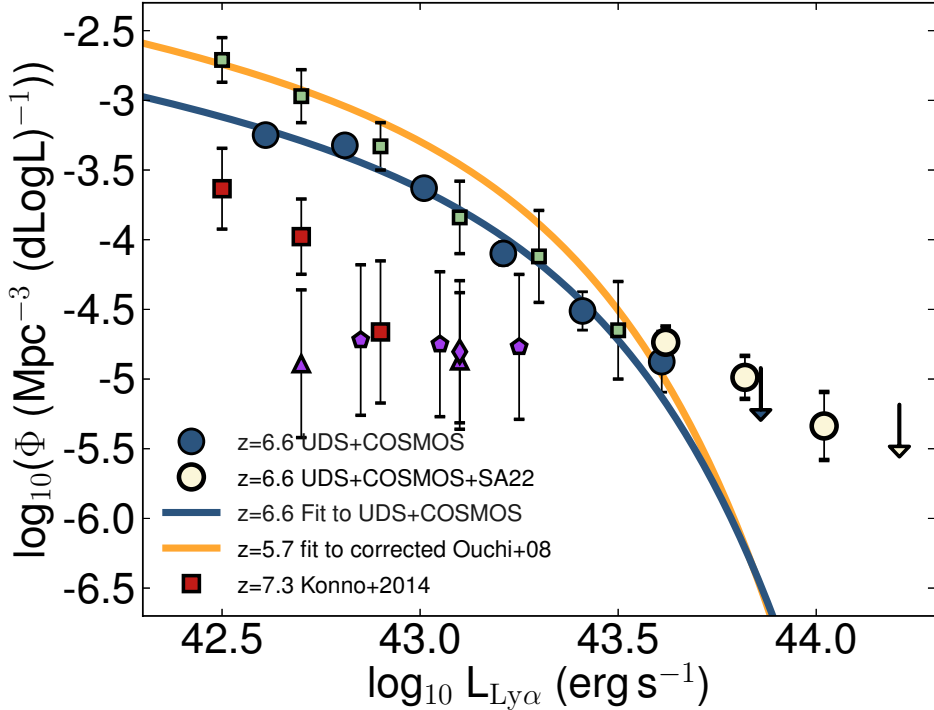
Figure 2.8: Evolution of the luminosity function evolution from $z = 7.3$ to $z = 5.7$. We compare our $z = 6.6$ LF (blue solid line) to published data at $z > 7$ Konno et al. (2014) (red squares) Shibuya et al. (2012); Ota et al. (2010); Iye et al. (2006) (purple triangles, pentagons and diamond, respectively). We also show our LF fit to the corrected $z = 5.7$ data (orange solid line) and the green squares show the number densities at $z = 5.7$ from Ouchi et al. (2008). Note that the errors on the $z > 7$ data are still significant and that the surveys are limited to small areas, meaning that the LF is still unconstrained at luminosities $> 10^{43.3}$ erg/s. A few additional, shallower pointings with the Subaru S-Cam and the NB101 ($z = 7.3$) filter would place useful constraints on the evolution of the Lyα LF at these epochs.

IGM, which leads to a higher opacity to Lyα photons. Mesinger et al. (2015) however argue that re-ionisation can not be the only driver of the observed changing opacity to Lyα and Konno et al. (2014) mention that the neutral IGM fraction required to explain their observed evolution of the Lyα LF (see left panel of Fig. 2.8) is in tension with results from the polarisation of the Cosmic Microwave Background (CMB) (Planck Collaboration et al., 2014), with a mean re-ionisation redshift of $z = 11.1$. On the other hand, Choudhury et al. (2015) argue that the most recent CMB results are not in disfavour with a re-ionisation epoch that ends between $z = 6 - 7$. The latest Planck results suggest a re-ionisation redshift of $z = 8.8$ (Planck Collaboration et al., 2016a), but this result is model dependent.

A lot of these explanations are very degenerate with the currently available observational data and can only be solved by disentangling the effect from galaxy formation (e.g. a varying intrinsic production or escape of Lyα photons) with a cosmological cause (re-ionisation of the IGM). One way to overcome this is to study the clustering properties of LAEs in wide area surveys, as is the goal of the HyperSuprimeCam survey on the Subaru telescope (see also §6.2). Jensen et al. (2014) show that an increased (observed) clustering signal of LAEs is indicative of a more neutral IGM, because Lyα is preferentially observed in an ionised region and more clustered LAEs will lead to a larger ionised region around them. Mimicking this clustering signal is unlikely by changes in the intrinsic escape fraction or production of Lyα. Another measurement which will overcome the degeneracy is to measure the intrinsic Lyα escape fraction directly using spectroscopic Hα measurements, for example possible with a matched narrow-band survey to Lyα with a wide field camera which is sensitive to 2-5 micron radiation in space (since the night sky background is very high in these wavelength regions).

In the next section, we argue that our observed differential evolution of the Lyα LF can be explained by a simple model for re-ionisation, although we do not claim that this is the only possibility.

2.6.2 Toy-model for the evolution of the Lyα LF

Since the process of re-ionisation likely has a patchy nature, where the Universe is ionised either bottom-up (overdense, early collapsing regions first) or top-down (voids first), there is an observable effect in the evolution of the Lyα LF. Haiman & Cen (2005) argue that the observability of bright LAEs is less attenuated by a neutral IGM than faint LAEs, since the ionised spheres around these are typically larger. This indicates that the evolution of the LF happens mostly at the faint end, where a smaller neutral fraction is sufficient to prevent the observability. This scenario is similar to our observations: most of the evolution between $z = 5.7$ and $z = 6.6$ happens at fainter luminosities, see Fig. 2.7.

We use the following toy-model to show that a differential evolution indeed follows from some basic assumptions about how the process of re-ionisation happened. We first assume that the intrinsic Lyα LF at $z = 6.6$ (without IGM absorption) is similar to the $z = 5.7$ LF from Ouchi et al. (2008). Using this LF, we generate a sample of LAEs with a minimum luminosity $10^{41.5}$ erg s^{-1} and con-
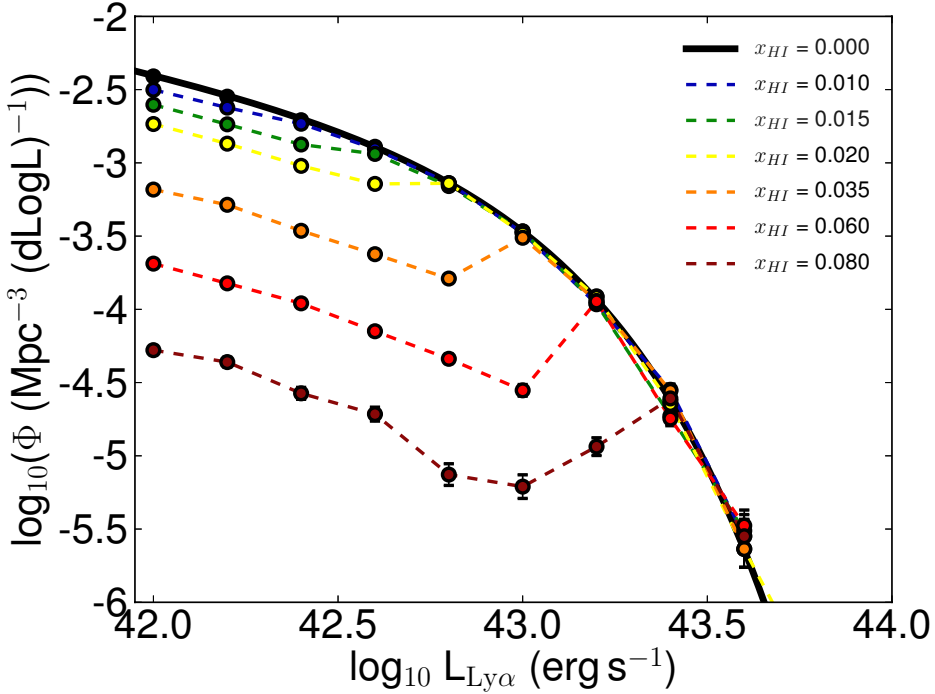
Figure 2.9: Toy-model evolution of the luminosity function in a neutral IGM. The black line shows the input LF, which is the $z = 5.7$ LF from Ouchi et al. (2008). We fix the parameters controlling the age and number of escaping ionising photons from LAEs (to age = 100 Myr, $f_{esc,ion}$ = 5% and $f_{esc,Ly\alpha}$ = 30 %) and investigate how a changing neutral fraction (X_{HI}) influences the observed LF. As can be seen, the evolution starts at the faintest luminosities only and gradually towards higher luminosities. The highest luminosities ($> 10^{43.5}$ erg s^{-1}) are still observable. Faint LAEs are observable if they are in the ionised sphere of a neighbouring, luminous source. Therefore, the observed faint-end slope depends on the clustering. The turnover luminosity, at which LAEs can ionise their own surrounding enough, depends on our input parameters and the neutral fraction. Note that our specific values for the neutral fraction are arbitrary since our input parameters are largely undetermined, and they are only showed for illustration purposes. While typical models require much larger changes in the neutral fraction (e.g. Dijkstra 2014), our values are particularly low because we assume that all Lyα emission is absorbed when the ionised sphere is < 1 Mpc, while in reality only part of the line-emission is absorbed, and we ignore other processes such as galaxy outflows which can increase the observability of Lyα.

sider three cases: First, we place them at random positions in our survey area, but also vary this to clustered positions, where the clustering has a functional form varying from 'low' clustering (powerlaw) to 'high' clustering (exponential). In case of the powerlaw clustering, the probability $p(x)$ that a LAE has a neighbouring LAE within a distance x, scales with $p(x) \sim -x$, while this scales with $p(x) \sim e^{-x}$ in the case of exponential clustering. This means that for the powerlaw clustering, the expected number of neighbours within 1 Mpc is 2 times higher than based on a random spatial distribution, while it is 13 times higher for the exponential clustering.

Assuming that the LAEs are the only source of an ionised region around them (without any contribution from fainter neighbouring sources), we use the following formula for the radius of their Strömgren sphere at $z = 6.56$ from Cen & Haiman (2000):

$$R_S = 4.3 \, x_{\text{IGM}}^{-1/3} \, (\frac{f_{esc,ion} N_{\gamma,em}}{1.3 \times 10^{57} \text{s}^{-1}})^{1/3} \, (\frac{t}{2 \times 10^7 \text{yr}})^{1/3} \text{ Mpc} \qquad (2.6)$$

where x_{IGM} is the neutral hydrogen fraction in the IGM, $f_{esc,ion}$ the escape fraction of ionising radiation, $N_{\gamma,em}$ the number of ionising photons per second and t the time the emitter has been emitting ionising radiation. Under basic assumptions, we calculate the number of ionising photons by converting the Lyα to Hα luminosity with:

$$L(H\alpha) = \frac{L(Ly\alpha)}{8.6 f_{esc,Ly\alpha}} \text{ erg s}^{-1} \qquad (2.7)$$

Here, $f_{esc,Lya}$ is the intrinsic Lyα escape fraction and the 8.6 value corresponds to case B recombination (Osterbrock, 1989). Under the same case B recombination assumption and using a Salpeter IMF, the Hα luminosity is then converted to the number of ionising photons using (e.g. Orsi et al., 2014):

$$N_{\gamma,em} = \frac{L(H\alpha)}{1.37 \times 10^{-12}} \text{ s}^{-1} \qquad (2.8)$$

According to Cen & Haiman (2000), it takes an ionised sphere of roughly 1 Mpc for Lyα to redshift out of resonance wavelength. Therefore, we use the above formalism to compute the ionised regions around LAEs, which can overlap if the sources are clustered, and check which LAEs can be observed, by being able to travel at least 1 Mpc through an ionised region through any sightline. As an output, we compile the observed Lyα LF and compare this to the input. Our results depend obviously on our choice for the Lyα escape fraction, the age of LAEs and the neutral fraction. However, we are only interested in qualitatively investigating the effect of this toy-model on the observed evolution of the LF, so the specific values are not that important, also because they all have the same powerlaw-scaling in Eq. 6. Our simulation likely breaks down when there is a strong dependence of intrinsic Lyα luminosity on age, escape fraction or clustering (halo mass), since this would affect the relative sizes of ionised spheres and thus the observability of LAEs.

After running our simulation 2000 times (to overcome sampling errors) for each set of clustering strengths and other input parameters, we find that the effect is that without clustering, brighter LAEs are more likely to be observed, since they are powerful enough to ionise their own surroundings. Changing any of the parameters except for clustering only varies the intrinsic Lyα luminosity at which a LAE is able to ionise its surrounding enough. A stronger clustering leads to an increase in the number of observed faint LAEs, since they likely reside in ionised regions of larger LAEs, or are able to ionise a large enough region with some close neighbours themselves.

Our results of the simulation are illustrated in the right panel of Fig. 2.8. In this Figure, we fixed the parameters t, $f_{esc,ion}$ and $f_{esc,Ly\alpha}$ to 100 Myr, 5 % and 30 %, respectively, and also fixed the clustering (to the maximum, exponential clustering strength) and only vary the neutral fraction. Our input LF (which is the same in the fully ionised case) is the LF at $z = 5.7$ from Ouchi et al. (2008). One can see that once the neutral fraction increases, the majority of the evolution happens at luminosities below 10^{43} erg s^{-1}, although the exact position depends on the specific neutral medium. This turnover point also depends on our choice of input parameters and therefore, since these are all uncertain, we do not use our model for estimates of the neutral fraction at $z = 6.6$. The turnover point corresponds to the luminosity at which a LAE is able to create a Strömgren sphere of 1 Mpc. However, even in the most neutral fraction, there are still faint LAEs which can be observed. This is due to clustering, since they are located in the ionised regions of larger LAEs. The faint-end slope depends on the clustering, being the strongest if ionising sources are highly clustered. Concluding, the right panel of Fig. 2.8 shows that in our simple toy-model for how re-ionisation happens and affects the observability of LAEs, the differential evolution that we observe between $z = 5.7$ and $z = 6.6$ can be explained by a higher neutral fraction of the IGM. It also shows that towards higher redshifts, where the Universe keeps becoming more neutral, strategies aiming at detecting LAEs benefit more from a wide-field approach, since LAEs are easier to be observed as they are able to ionise their own surroundings sufficiently.

Note that our specific values for the neutral fraction are arbitrary since our input parameters are largely undetermined. We therefore do not aim to use our model to quantitatively measure the neutral fraction, but to qualitatively explain our observations. While typical models require much larger changes in the neutral fraction to significantly reduce Lyα emission (e.g. Dijkstra, 2014), our values are particularly low. This is because we assume that all Lyα emission is absorbed when the ionised sphere is < 1 Mpc, while in reality only the blue part of the line-emission is absorbed, and the red wing broadens due to resonant scattering. We also ignore other processes which can increase the observability of Lyα, such as galaxy outflows.

The observed differential evolution for Lyα selected galaxies is also seen in the spectroscopic follow-up of Lyman-break galaxies. For example, Ono et al. (2012) finds that the drop in the fraction of UV selected galaxies which are detected in Lyα at $z > 6$ is stronger for UV faint galaxies, using a compilation of surveys. This is particularly interesting as at lower redshift, UV faint galaxies

tend to have a higher Lyα fraction (e.g. Stark et al., 2010). As mentioned by Ono et al. (2012), this differential drop indicates that re-ionisation happens first in over-dense regions and is qualitatively consistent with our observations of the Lyα LF.

2.6.3 Future surveys

We can use our number counts, shown in Fig. 2.4, to estimate the expected number of sources in future surveys such as the extragalactic Hyper Suprime-Cam (HSC) survey, which the Subaru telescope will undertake. Due to its large field of view (1.5 deg^2), the HSC is suited excellently for pushing to a survey with a similar depth as the narrow-band data in UDS and a > 10 deg^2 area, and even wider areas for slightly shallower surveys. From our spectroscopic confirmed sample only (and without the filter correction), we find that the observed number density at 5×10^{43}erg s^{-1}, the luminosity of our brightest source in COSMOS, is roughly 30 times higher than based on the LF from Ouchi et al. (2010) (see Fig. 2.5). The HSC survey[4] has a planned deep component of ~ 30 deg^2 (part of which is SA22) to a NB921 depth of 25.6 and an ultra-deep component (in UDS and COSMOS) of ~ 3.6 deg^2 to a depth of 26.2. If we use our power-law fit from §5.1, we therefore expect that ~ 60 bright LAEs ($> 5 \times 10^{43}$erg s^{-1}) will be found in total. These bright sources will be excellent targets for follow-up with *JWST*, to study the Lyα escape fraction directly with Hα measurements, and to study the metallicity and ionisation state with other nebular emission lines. The HSC survey will also be able to study our brightest LAEs to more detail, because it will be able to observe the more extended, lower surface brightness regions because of deeper survey limits. Furthermore, the HSC survey will also obtain additional wide observations with the $z = 5.7$ Lyα filter, such that the SA22 results at the highest luminosities can be compared.

Another survey which recently started observations is the *Javalambre Physics of the Accelerating Universe Astronomical Survey (J-PAS)* (Benitez et al., 2014), which will survey 8500 deg^2 with 54 narrow-band filters, from 3500 Å up to a wavelength of 10000 Å, to a depth of ~ 22.5. Its goal is to study dark energy at redshifts $z < 1$, but it is also interesting for extragalactic studies of quasars and LAEs due to its very wide area and large set of narrow-band filters. If we use our powerlaw fit (Table 2.7) and extrapolate it to a luminosity of 10^{45} erg s^{-1} (e.g. the Lyα luminosity of the $z = 7.085$ quasar (Mortlock et al., 2011)), we estimate that it will find 230 bright LAEs per NB filter. A caveat however is that excluding interlopers is challenging with the depth of the optical imaging and without the availability of near-infrared data.

The brightest LAEs detected with optical surveys (e.g. up to $z \sim 7.3$) are the best comparison with samples of even higher redshift LAEs. To date however, no LAE has been detected in the near-infrared (e.g. $z = 7.7$ and $z = 8.8$; Faisst et al., 2014; Matthee et al., 2014), but upcoming surveys will increase both the sensitivities (which is a main difficulty due to the high sky background) and probed volumes. Nevertheless, our results, showing little to no evolution at

---

[4] www.naoj.org/Projects/HSC/surveyplan.html

the bright end, encourage further searches for the brightest LAEs, at least at $z \sim 7 - 8$. Eventually, the Euclid satellite will perform a deep spectroscopic survey over a wide area (40 deg^2, 5×10^{-17}erg cm^{-2} s^{-1}) in the near-infrared, which will detect bright $z > 7.3$ LAEs if they exist.

2.7   Conclusions

The main conclusions of this work are:

- Using a combination of wide and ultra-deep surveys in SA22, UDS and COSMOS with the NB921 filter on the Subaru telescope, we obtain a large sample of LAEs at $z = 6.6$, spanning the largest dynamical range of luminosities to date, and derive a new luminosity function, which overcomes cosmic variance at the bright end because of our large and independent volumes.

- We identify lower redshift interlopers (including extreme emission line galaxies at $z = 1 - 2$) with near-infrared data. This way we find a number of extreme emission line galaxies with rest-frame EWs of > 400 Å.

- In total, we find 99+15+19 (UDS, COSMOS, SA22) LAE candidates at $z = 6.6$. Of these, 18 are confirmed spectroscopically. 16 in UDS by Ouchi et al. (2010) and 2 in COSMOS by Sobral et al. (2015b). These two sources are the brightest LAEs at $z = 6.6$ so far and confirm that sources with a luminosity similar to *Himiko* are not as rare as previously thought, and have number densities of $\sim 1.5^{+1.2}_{-0.9} \times 10^{-5}$ Mpc^{-3}.

- In our wide-field shallow SA22 data-set, we find 19 LAEs which are even brighter than the ones in UDS and COSMOS, although these have no spectroscopic follow-up yet. Even if there is significant contamination from low redshift interlopers or variable objects, all our results still hold.

- After reproducing the analysis from Ouchi et al. (2010), we find that the main difference with our results is that we can more accurately include the brightest objects in our fit of the luminosity function and that we do a correction for our observational biases originating from the filter profile. We have additionally varied our EW criteria and used near-infrared data to exclude lower redshift interlopers, but find that this does not cause significant differences with the previous results for the ultra-deep surveys. For the deep COSMOS and shallower SA22 data, near-infrared data is however crucial.

- Comparing our $z = 6.6$ data to lower redshift data at $z = 5.7$, we confirm that there is evolution of the number density of the fainter LAEs. However, there is no evolution at the bright end and there is also evidence that the Lyα LF deviates from a Schechter function at the brightest luminosities.

- Based on our toy-model, we argue that this differential evolution can be a sign of re-ionisation not being completed yet. Our model assumes that LAEs are only observed if they are in an ionised sphere which is large enough for the Lyα photons to redshift out of resonance wavelength, and that they are the only source of ionising radiation. Because of this, we preferentially observe the brightest LAEs, which have been able to ionise their own surrounding enough to be observable. Faint LAEs can only be observed if they are in the ionised spheres of more luminous LAEs, or when they are strongly clustered.

- Additional wide field data at $z = 5.7$ and $z = 7.3$ will provide useful constraints on the evolution of the brightest LAEs around the re-ionisation epoch.

- Finally, we use our results to make predictions for the upcoming Hyper Suprime Cam surveys at the Subaru telescope and also for upcoming very wide, cosmological surveys such as *J-PAS* and *Euclid*.

Acknowledgments

CHAPTER 3

Spectroscopic properties of luminous Lyα emitters at $z \approx 6 - 7$ and comparison to the Lyman-break population

We present spectroscopic follow-up of candidate luminous Lyα emitters (LAEs) at $z = 5.7 - 6.6$ in the SA22 field with VLT/X-SHOOTER. We confirm two new luminous LAEs at $z = 5.676$ (SR6) and $z = 6.532$ (VR7), and also present *HST* follow-up of both sources. These sources have luminosities $L_{Ly\alpha} \approx 3 \times 10^{43}$ erg s^{-1}, very high rest-frame equivalent widths of $EW_0 \gtrsim 200$ Å and narrow Lyα lines (200-340 km s^{-1}). VR7 is the most UV-luminous LAE at $z > 6.5$, with $M_{1500} = -22.5$, even brighter in the UV than CR7. Besides Lyα, we do not detect any other rest-frame UV lines in the spectra of SR6 and VR7, and argue that rest-frame UV lines are easier to observe in bright galaxies with low Lyα equivalent widths. We confirm that Lyα line-widths increase with Lyα luminosity at $z = 5.7$, while there are indications that Lyα lines of faint LAEs become broader at $z = 6.6$, potentially due to reionisation. We find a large spread of up to 3 dex in UV luminosity for $> L^\star$ LAEs, but find that the Lyα luminosity of the brightest LAEs is strongly related to UV luminosity at $z = 6.6$. Under basic assumptions, we find that several LAEs at $z \approx 6 - 7$ have Lyα escape fractions $\gtrsim 100$ %, indicating bursty star-formation histories, alternative Lyα production mechanisms, or dust attenuating Lyα emission differently than UV emission. Finally, we present a method to compute ξ_{ion}, the production efficiency of ionising photons, and find that LAEs at $z \approx 6 - 7$ have high values of $\log_{10}(\xi_{ion}/\mathrm{Hz}\ \mathrm{erg}^{-1}) \approx 25.51 \pm 0.09$ that may alleviate the need for high Lyman-Continuum escape fractions required for reionisation.

3.1   Introduction

Observations of galaxies in the early Universe help to constrain the properties
of the first stellar populations and black holes and to understand the reionisa-
tion process and sources responsible for that. However, because of their high
redshift, these galaxies are very faint and their rest-frame spectral features (i.e.
UV lines) shift to near-infrared wavelengths. This makes spectroscopic obser-
vations challenging and currently limited to the brightest sources. Therefore, it
has only been possible to study a few galaxies in detail (e.g. Ouchi et al., 2013;
Sobral et al., 2015b; Stark et al., 2015a,b; Zabl et al., 2015). Most of these galaxies
are strong Lyman-α (Lyα, $\lambda_{0,vac} = 1215.67$ Å) emitters (LAEs). This is partly by
selection, as LAEs can easily be identified with wide-field narrow-band surveys
(e.g. Konno et al., 2014; Matthee et al., 2015) and are easier to follow-up spectro-
scopically, but also because the fraction of UV-bright galaxies with strong Lyα
emission increases with redshift (e.g. Curtis-Lake et al., 2012; Stark et al., 2017),
such that a large fraction of Lyman-break galaxies at $z \approx 5-6$ (after reionisation)
are typically also classed as LAEs (e.g. Pentericci et al., 2011; Stark et al., 2011;
Cassata et al., 2015), see e.g. Dayal & Ferrara (2012) for a theoretical perspective.

Lyα photons undergo resonant scattering by neutral hydrogen resulting in
significant uncertainties when using Lyα luminosities to study intrinsic prop-
erties of galaxies (e.g. Hayes, 2015). The fraction of observed Lyα photons de-
pends on the spatial distribution of neutral hydrogen and the characteristics of
the emitter (e.g. Matthee et al., 2016; Sobral et al., 2017). Hence, high resolution
measurements of the Lyα line-profile and measurements of the extent of Lyα can
provide information on the properties of both the inter-stellar medium (ISM)
and the circum-galactic medium (CGM) (e.g. Møller & Warren, 1998; Steidel
et al., 2011; Verhamme et al., 2015; Arrigoni Battaia et al., 2016; Gronke & Dijk-
stra, 2016). Furthermore, the prevalence of Lyα emitters and the Lyα equivalent
width (EW) distribution can be used to study the neutral fraction of the inter-
galactic medium (IGM) in the epoch of reionisation (e.g. Dijkstra, 2014; Hutter
et al., 2014).

Several observations of LAEs indicate an increasingly neutral fraction at $z >$
6.5: at fixed UV luminosity, the fraction of typical Lyman-break galaxies with
strong Lyα emission (observed in a slit) is observed to decrease with redshift (e.g.
Pentericci et al., 2014; Tilvi et al., 2014); the observed number density of LAEs
decreases at $z > 6$ (e.g. Konno et al., 2014; Matthee et al., 2015; Zheng et al., 2017)
and at fixed central Lyα luminosity, there is more extended Lyα emission around
faint LAEs at $z = 6.6$ than at $z = 5.7$ (Momose et al., 2014; Santos et al., 2016).
These observations all indicate that a relatively larger fraction of Lyα photons are
scattered out of the line of sight at $z > 6.5$ than at $z < 6.5$. Hence, the galaxies
that are still observed with high Lyα luminosities at $z > 7$ (e.g. Oesch et al., 2015;
Zitrin et al., 2015; Schmidt et al., 2016) are likely the signposts of early ionised
bubbles (e.g. Stark et al., 2017).

Matthee et al. (2015) performed a survey of LAEs at $z = 6.6$, increasing the
available number of bright LAEs that allowed detailed study. Two LAEs from
this sample ('CR7' and 'MASOSA') have been spectroscopically confirmed in

Sobral et al. (2015b). Several more recent wide-area surveys at $z = 6.6$ and $z = 6.9$ are now also identifying LAEs with similar luminosities (e.g. Hu et al., 2016; Shibuya et al., 2018; Zheng et al., 2017). CR7 and 'Himiko' (Ouchi et al., 2009) have been the subject of detailed spectroscopic studies (e.g. Ouchi et al., 2013; Sobral et al., 2015b; Zabl et al., 2015; Bowler et al., 2017b), which indicate that their ISM is likely metal poor and in high ionisation state. Such ISM conditions are similar to those in LAEs at $z \sim 2 - 3$ (e.g. Song et al., 2014; Trainor et al., 2015; Hashimoto et al., 2017a; Nakajima et al., 2016; Trainor et al., 2016), although we note that the Lyα luminosities of the latter samples are typically an order of magnitude fainter. In order to obtain a comparison sample to those at $z \sim 7$, Santos et al. (2016) undertook a comparable survey at $z = 5.7$, just after the end of reionisation. A major limitation is that the nature of the most luminous LAEs is currently unknown. Are they powered by active galactic nuclei (AGN) or star formation? What are their metallicities?

In this paper, we present follow-up observations of candidate luminous LAEs at $z = 5.7$ and $z = 6.6$ using VLT/X-SHOOTER, which is a high resolution spectrograph with a wavelength coverage of $\lambda = 0.3 - 2.5\mu$m. We assess the interloper and success fractions and use these to update the number densities of the most luminous LAEs. We present the properties of the Lyα lines, UV continua of newly confirmed luminous LAEs, and constrain rest-frame UV nebular lines. Together with a compilation of spectroscopically confirmed LAEs and Lyman-break galaxies (LBGs) from the literature, we study the evolution of Lyα line-widths between $z = 5.7 - 6.6$ and the relation between Lyα luminosity and UV luminosity. Finally, we explore the ionising properties (such as the production efficiency of ionising photons) using an empirical relation to estimate the Lyα escape fraction (e.g. Sobral et al., 2017).

The initial sample of luminous LAEs at $z = 5.7$ and $z = 6.6$, the observations and data reduction are presented in §3.2. We present the results in §3.3, which include updated number densities. In §3.4 we present the properties of newly confirmed LAEs. The properties of the sources are discussed and compared to the more general galaxy population at $z \approx 6 - 7$ in §11.7. This section includes a comparison of their Lyα line-widths (§3.5.1), the UV line-ratios to Lyα (§3.5.2) and their UV luminosity (§3.5.3). We discuss their production efficiency of ionising photons in §3.5.3. Finally, we summarise our conclusions in §5.8. Throughout the paper we use a flat ΛCDM cosmology with $\Omega_M = 0.3$, $\Omega_\Lambda = 0.7$ and $H_0 = 70$ km s^{-1} Mpc^{-1}.

3.2 Sample & Observations

3.2.1 Sample

The target sample includes candidate luminous LAEs selected through NB816 and NB921 narrow-band imaging with Subaru/Suprime-Cam in the SA22 field over co-moving volumes of 6.3×10^6 Mpc^3 and 4.3×10^6 Mpc^3 at $z = 5.7$ and

$z = 6.6$ as described in Santos et al. (2016) and Matthee et al. (2015), respectively.[1] The data in the SA22 field is very wide-field, yet shallow and single-epoch, and is aimed at identifying the brightest LAEs. Even though the expected number of contaminants and transients is significant, these sources are bright enough to be confirmed (or refuted) in relatively small amounts of telescope time.

The initial potential target samples included 6 objects at $z = 5.7$ and 21 at $z = 6.6$. Before choosing the final targets to follow-up spectroscopically, we investigated the individual exposures, instead of only inspecting the final reduced NB image. Nine sources from the NB921 sample were moving solar-system objects whose position changed by $\approx 0.2 - 0.5''$ between individual exposures. The stacked image of these sources then resulted in a slightly extended object. Such extended objects in the NB image resemble confirmed LAEs at $z = 6.6$ (e.g. Himiko and CR7), leading to their misidentification as candidates. We note that point-like sources may however still be other types of transients/variables. Six other sources from the NB921 sample have been identified as a detector artefact in a single exposure, which coincides with positive noise peaks in the other exposure. Due to PSF-homogenisation these artefacts were then not identified in our visual inspections of the final stack. These checks were also performed for the NB816 candidates, and were excluded already before the final analysis of Santos et al. (2016). These issues do not influence the search for LAE candidates in the fields with deeper coverage (COSMOS and UDS), as those fields have been observed with many more individual exposures. The final selection results in a sample of 6 LAE candidates at $z = 5.7$ and 6 at $z = 6.6$, all in the SA22 field, see Table 3.1.

3.2.2 Observations

We observed the candidate LAEs with the X-SHOOTER echelle spectrograph, mounted on UT2 of the VLT (Vernet et al., 2011). X-SHOOTER simultaneously takes a high resolution spectrum with a UVB, VIS and a NIR arm, providing a wavelength coverage from 300 nm to 2480 nm.

Observations were done under clear skies with a seeing ranging from 0.7-0.9'', using 0.9'' slits in the NIR and VIS arm and a slow read-out speed without binning. This leads to a spectral resolution of 1.2 Å ($R \approx 7400$) and 3.6 Å ($R \approx 4000$) in the VIS and NIR arm, respectively. We first acquired a star (with I-band magnitudes 16-17 AB) and applied a blind offset to the target. In order to improve the NIR sky subtraction, we use the standard `AutoNodOnSlit` procedure, which nods between two positions A and B along the slit, offset by 3.5''. This is repeated two times in an ABBA pattern. At each position, we take a 730 s exposure in the VIS arm and four 195 s exposures in the NIR arm. This results in a total exposure time of 2.92 ks in VIS and 3.12 ks in NIR in a single observing block. Several sources have been observed in two or three observing blocks, doubling or tripling the total exposure time, see Table 3.1.

---

[1] This sample already included the confirmed LAEs Himiko (Ouchi et al., 2013), MASOSA and CR7 (Sobral et al., 2015b). It furthermore includes 14 other spectroscopically confirmed LAEs at $z = 6.6$ from Ouchi et al. (2010) and 46 spectroscopic confirmed LAEs at $z = 5.7$ from Ouchi et al. (2008), Hu et al. (2010) and Mallery et al. (2012).

Table 3.1: Targeted sample of LAE candidates at $z = 5.7 - 6.6$. Candidates selected in NB816 are from Matthee et al. (2015), while candidates selected in NB921 are from Santos et al. (2016). $L_{Ly\alpha}$ is the estimated $Ly\alpha$ luminosity from NB imaging. We also list the observation dates from ESO program ID 097.A-0943, the total on-source exposure times and the telluric standard stars that have been used for flux-calibration. The final column identifies the classification of the targets, with 1 = $Ly\alpha$, 2 = [OIII], 3 = transient and 4 = star. Sources that are confirmed spectroscopically as $Ly\alpha$ emitters are shown in bold. We provide flux calibrated reduced spectra of SR6 and VR7 with the published version of the paper.

ID	R.A. J2000	Dec. J2000	$L_{Ly\alpha,NB}$ 10^{43} erg s^{-1}	Dates 2016	$t_{exp,VIS}$ ks	$t_{exp,NIR}$ ks	Telluric	Class
SA22-NB816-9442	22:18:00.68	+01:04:30.53	8.4	5 Aug	2.92	3.12	GD153	2
SA22-NB816-366911	22:13:00.92	+00:36:24.17	4.1	7 and 31 Aug	5.84	6.24	GD153, EG274	3
SA22-NB816-360178	22:12:54.85	+00:32:54.76	3.8	3 Sep	2.92	3.12	GD71	4
SA22-NB816-390412	22:15:01.22	+00:46:24.25	3.7	28 Aug	5.84	6.24	Feige110	3
SR6	22:19:49.76	+00:48:23.90	3.4	2 Sep	5.84	6.24	GD71	1
SA22-NB816-508969	22:21:09.92	+00:47:19.52	3.3	3 Sep	2.92	3.12	GD71	3
VR7	22:18:56.36	+00:08:07.32	2.4	12, 16 Jun, 12 Jul	8.76	9.36	GD153	1
SA22-NB921-D10845	22:18:54.82	+00:06:24.26	1.2	14 Jul, 2, 3 Aug	8.76	9.36	GD153, EG274	3
SA22-NB921-W210761	22:14:38.63	+00:56:02.98	4.1	2 Aug	2.92	3.12	EG274	3
SA22-NB921-W219795	22:15:29.18	+00:29:17.90	3.8	3 Aug	2.92	3.12	EG274	3
SA22-NB921-W6153	22:20:20.79	+00:17:27.96	11.0	2 Aug	2.92	3.12	EG274	3
SA22-NB921-W209855	22:16:05.05	+00:51:59.23	3.8	3 Aug	2.92	3.12	EG274	3

3.2.3   Data reduction

Data have been reduced with the recipes from the standard X-SHOOTER pipeline (Modigliani et al., 2010), which includes corrections for the bias from read-out noise (VIS arm) and dark current (NIR arm), sky subtraction and wavelength calibration. Since wavelength calibration is done in air, we convert the wavelengths to vacuum wavelengths following Morton (1991). The standard stars GD71, GD153, EG274 and Feige110 have been observed with a 5″ slit for flux calibration. We use the X-SHOOTER pipeline to combine the exposures from single observing blocks. In the case that a source has been observed with multiple observing blocks, we co-add the frames by weighting the sky background and by correcting for slight positional variations based on the position of the peak of observed Lyα lines.

3.2.4   Extraction

We extract 1D spectra in the VIS (NIR) arm by summing the counts in 10 (8) spatial pixels, corresponding to 1.6 (1.68)″, along the wavelength direction. These extraction boxes optimise the S/N in confirmed emission-line galaxies in our data-set. Slit losses are estimated by convolving the NB image to the PSF of spectroscopic observations and measuring the fraction of the flux that is retrieved within the slit compared to the flux measured with Mag-auto. Typical slit losses are $\approx 50 - 60$ %. We measure the effective spectral resolution at $\sim 0.9\,\mu$m and $\sim 1.6\,\mu$m by measuring the FWHM of well separated, isolated skylines and find $R = 7500$ and $R = 4400$, respectively. We note that due to this high resolution, instrumental line-broadening of the emission-lines from the sources discussed in this paper are negligible.

The line-flux sensitivity is measured as a function of line-width as follows. First, we select the sub-range of wavelengths in the collapsed 1D spectra that are within 30 nm from the targeted wavelength. Then, we measure the flux in 5000 randomly placed positions in this sub-range, with kernels corresponding to the targeted wavelength. We then calculate the noise as the r.m.s. of the 5000 measured fluxes. Note that, in the presence of skylines, this depth is a conservative estimate as it includes flux from skyline residuals, which could increase the noise by a factor $\approx 2 - 3$ depending on the specific wavelength.

3.3   Results

3.3.1   NB816 targets - candidate LAEs at $z = 5.7$

Out of the six brightest candidate LAEs at $z = 5.7$ that we observed with X-SHOOTER, one is reliably confirmed as a Lyman-α emitter, one is identified as [OIII] interloper, one is identified as brown dwarf star interloper and three are not detected, indicating that their NB detection was likely due to a transient or variable source, see Table 3.1 for a summary.
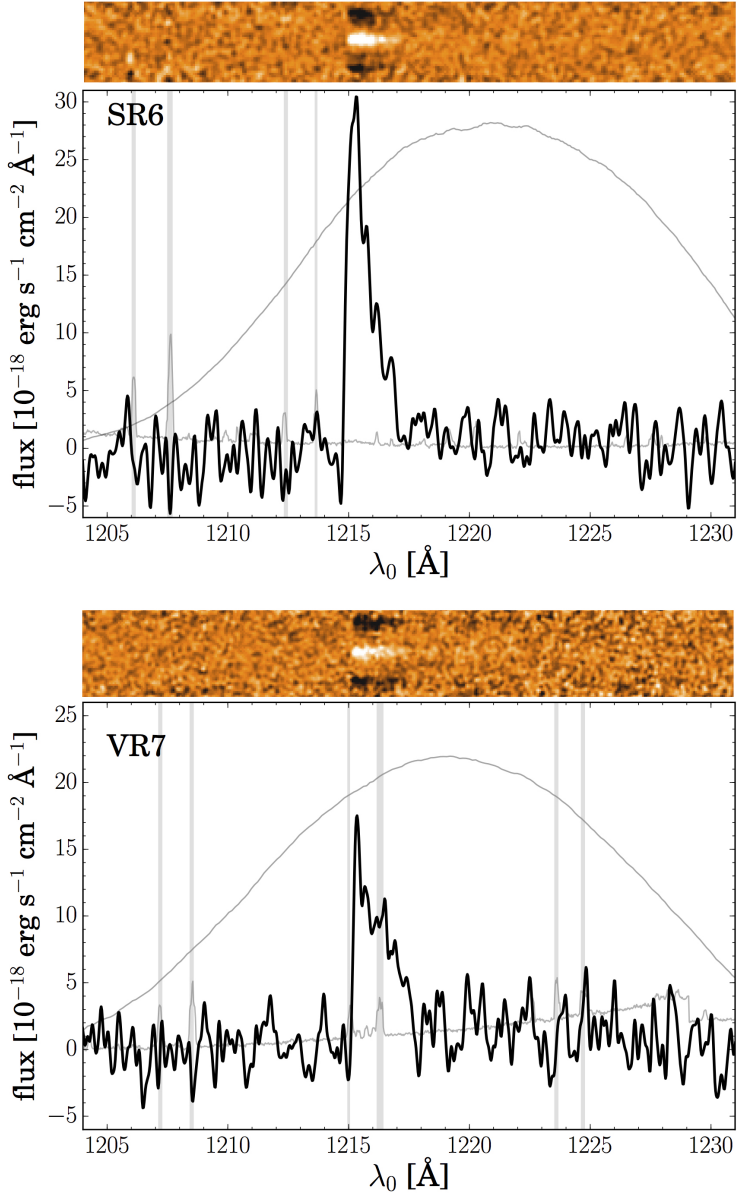
Figure 3.1: Rest-frame X-SHOOTER spectra of the newly confirmed luminous LAEs SR6 at $z = 5.676$ and VR7 at $z = 6.532$, zoomed in on the Lyα line. In the background we show the NB816/NB921 filter transmission (normalised arbitrarily for visualisation purposes), which illustrates that these sources are detected at ≈ 75 % and ≈ 92 % of the peak filter transmission in the original data, respectively. We also illustrate the position of atmospheric OH-lines in the background, based on the noise map provided by the X-SHOOTER pipeline. The Lyα line of VR7 is slightly contaminated by a faint sky-line at $\lambda_0 \approx 1216.3$ Å (observed $\lambda \approx 9161$ Å).

SA22-NB816-9442 is identified as an [OIII] emitter at $z = 0.638$. The flux observed in NB816 can be attributed to both the 4959 and 5007 Å lines. We measure a combined line-flux of $0.8 \pm 0.1 \times 10^{-16}$ erg s^{-1} cm^{-2} and observed EW > 393 Å. We do not detect an emission-line or continuum in the expected wavelength range or anywhere else in the spectrum of SA22-NB816-366911 and SA22-NB816-390412. This may indicate that these sources are variable/transients, as they are also not detected in any of the broad-band images. Matthee et al. (2015) confirmed two of such transients in 0.9 deg^2 of similar NB data. Hence, it is not unlikely that our selection picked up three transients in the 3.6 deg^2 coverage (see also Hibon et al. 2010).

Although we do not detect a clear emission line in the NB816 wavelength coverage in SA22-NB816-508969 and SA22-NB816-360178, we detect a faint trace of continuum in the center of the slits. For SA22-NB816-508969 this continuum is detected at low significance, making it challenging to classify the object. The continuum features, such as the peak-wavelength, of SA22-NB816-360178 resemble those of a star with an effective temperature of $T \approx 3500 - 3700$ K, or a K or M-type star (Kurucz, 1992). This interpretation is also strengthened by the point-like morphology in the available imaging.

The X-SHOOTER spectrum reliably confirms SR6[2] as a Lyman-α emitter at $z = 5.676 \pm 0.001$ (using the peak of Lyα), due to the asymmetric line-profile (see Fig. 3.1) and non-detection of flux blue-wards of the line. After correcting the VIS spectrum for slit losses of 56 % (estimated from NB imaging), we measure a line-flux of $7.6 \pm 0.4 \times 10^{-17}$ erg s^{-1} cm^{-2}, consistent within the errors with the NB estimate of $9.2 \pm 1.2 \times 10^{-17}$ erg s^{-1} cm^{-2}. We also identify faint [OII] emission from a foreground source at $z = 1.322$ offset by 2.4″ in the slit. We discuss the detailed properties of SR6 in §3.4.1.

3.3.2   NB921 targets - candidate LAEs at $z = 6.6$

Out of the six luminous LAE candidates at $z = 6.6$ in the SA22 field, we confirm one as a LAE, while we firmly rule out the others at the expected line-fluxes from the NB921 imaging.

Based on its asymmetric line-profile, the source VR7[3] is confirmed reliably as a LAE at $z = 6.532 \pm 0.001$ (corresponding to the wavelength of peak Lyα emission, see Fig. 3.1). After correcting for an estimated 54 % of slit losses, we measure a line-flux of $4.9 \pm 0.5 \times 10^{-17}$ erg s^{-1} cm^{-2}, which agrees well with the NB estimate of $4.8 \pm 1.2 \times 10^{-17}$ erg s^{-1} cm^{-2}. We present detailed properties of this source in §3.4.2.

We do not detect an emission-line or a continuum feature in the VIS spectra of SA22-NB921-D10845, SA22-NB921-W210761, SA22-NB921-W219795, SA22-NB921-W6153 or SA22-NB921-W209855, see Table 3.1 for a summary. We measure the sensitivity of the spectra as a function of redshift and velocity width of

---

[2] SA22 Redshift 6, the brightest LAE at $z = 5.7$ in the SA22 field.

[3] Named after Vera Rubin, and chosen to resemble the name of LAE COSMOS Redshift 7 (CR7, Matthee et al. 2015), as it was the fifth (V) luminous LAE confirmed at $z \approx 6.6$ by the time of discovery.

the line. For a line-width of 200 km s^{-1}, the 1σ limiting flux for wavelengths within the NB921 filter is $\approx 4.5(3.2) \times 10^{-18}$ erg s^{-1} cm^{-2} for sources observed with 1 (2) observing blocks (see Table 3.1). The sensitivity decreases by a factor ≈ 3 for a line-width of 600 km s^{-1}. However, even with such broad lines, the expected line-fluxes estimated from NB imaging would have been detected at the $> 3\sigma$ level. This means that these sources are likely transients (note that Matthee et al. 2015 estimated that ~ 6 transients were likely to be found within their sample), and that we can confidently rule out these six sources as Lyα emitters at $z = 6.6$. Therefore our results agree very well with the estimates from Matthee et al. (2015) on the fraction of transient interlopers.

3.3.3 Updated number densities of the most luminous LAEs at $z \approx 6 - 7$

Based on the spectroscopic follow-up, we provide a robust update on the number densities of luminous LAEs at $z = 5.7 - 6.6$ and compare those with Santos et al. (2016). At $z = 5.7$, the number density of LAEs with $L_{Ly\alpha} = 10^{43.6\pm0.1}$ erg s^{-1} is $10^{-5.26^{+0.21}_{-0.17}}$ Mpc^{-3}, which is ≈ 0.25 dex lower than in Santos et al. (2016). At $z = 6.6$, we find that the number density at $L_{Ly\alpha} = 10^{43.4\pm0.1}$ erg s^{-1} is $10^{-4.89^{+0.22}_{-0.15}}$ Mpc^{-3} and $10^{-5.35^{+0.49}_{-0.22}}$ Mpc^{-3} at $L_{Ly\alpha} = 10^{43.6\pm0.1}$ erg s^{-1}. We note that all these number densities are consistent with the previous measurements within 1σ errors. The results here support little to no evolution in the bright-end of the Lyα luminosity function between $z = 5.7 - 6.6$, and even little to no evolution at $L_{Ly\alpha} \approx 10^{43.6}$ erg s^{-1} up to $z = 6.9$ (Zheng et al., 2017). After rejecting all candidate LAEs with a luminosity similar to CR7 (for which we measure a total luminosity of 8.5×10^{43} erg s^{-1} after correcting for the transmission curve of the NB921 filter), we constrain the number density of CR7-like sources to one per $\gtrsim 5 \times 10^6$ Mpc^3.

3.4 Properties of newly confirmed LAEs

3.4.1 SR6

SR6 is robustly confirmed to be a luminous Lyα emitter at $z = 5.676 \pm 0.001$ (Fig. 3.1). We measure a Lyα line-width of $v_{FWHM} = 236 \pm 16$ km s^{-1} and Lyα luminosity of $2.7 \pm 0.2 \times 10^{43}$ erg s^{-1}. We do not detect continuum in the X-SHOOTER spectrum (with a 1σ depth of 3.0×10^{-19} erg s^{-1} cm^{-2} Å^{-1}, smoothed per resolution element), such that we can only provide a lower limit on the EW, which is EW$_0 \gtrsim 250$ Å. Based on Kashikawa et al. (2006), we quantify the line-asymmetry with the S-statistic and weighted skewness parameters, for which we measure 0.69 ± 0.05 and 9.7 ± 0.8 Å, respectively, similar to other confirmed LAEs.

The foreground [OII] emitter identified in the slit at $z = 1.322 \pm 0.001$, spatially offset by $2.4''$, is slightly magnifying SR6. We follow McLure et al. (2006)

to compute the magnification from galaxy-galaxy lensing as follows:

$$\mu = \frac{d_{\text{proj.}}}{d_{\text{proj.}} - \theta_E},$$
(3.1)

where μ is the magnification, $d_{\text{proj.}}$ is the projected separation in arcsec and θ_E the Einstein radius in arcsec. Under the assumption of a Singular Isothermal Sphere, we compute θ_E as follows (e.g. Fort & Mellier, 1994):

$$\theta_E = 30'' \left(\frac{\sigma_{1D}}{1000\,\text{km}\,\text{s}^{-1}}\right)^2 \frac{D_{ds}}{D_s},$$
(3.2)

where σ_{1D} is the one-dimensional velocity dispersion of the foreground source, D_{ds} is the angular diameter distance from foreground source to the background source and D_s the angular diameter distance from observer to the background source. Using the measured $\sigma_{1D} = 130 \pm 20$ km s^{-1}, we estimate $\theta_E = 0.24''$, resulting in a small magnification of $\mu = 1.1$. We note that additional magnification by other foreground-sources is possible (for example by a faint source separated by $\sim 1''$, see Fig. 3.2), although these sources are likely lower mass due to their faintness, resulting in a further negligible magnification. This results in a magnification corrected Lyα luminosity of $2.5 \pm 0.3 \times 10^{43}$ erg s^{-1}.

After confirming Lyα, we investigate the optical and near-infrared spectra for the presence of other emission-lines in the rest-frame UV. In particular, we search for Nv, Civ, Heii, Oiii] and Ciii][4], and check for any other significantly detected potential line – but we do not detect any above 3σ significance. We measure limiting line-fluxes at the positions of the expected lines for a range of line-widths. For a line-width of $\sim 100 - 250$ km s^{-1} and typical velocity offset with respect to Lyα of -200 km s^{-1}, we find a 2σ limit of 2.0×10^{-17} erg s^{-1} cm^{-2} for Nv after correcting for the same slit losses as Lyα (corresponding to EW$_0$ < 48 Å). For the other lines (observed in the NIR slit), we estimate slit losses of 59 %. This assumes that these lines are emitted over the same spatial scales as Lyα. Because sources are un-detected in the NIR continuum, we can not estimate slit losses from the continuum emission itself. As Lyα is likely emitted over a larger spatial scale (e.g. Wisotzki et al., 2016), slit losses for the other rest-UV lines may be over-estimated (except potentially for Civ which is also a resonant line). Our upper limits are on the conservative side if this is indeed the case. For similar widths and offsets as Nv, we measure 2σ limiting line-fluxes of $(7.3, 3.6, 3.5, 3.9) \times 10^{-17}$ erg s^{-1} cm^{-2} for (Civ, Heii, Oiii], Ciii]), corresponding to EW$_0$ < $(174, 86, 84, 93)$ Å, respectively. These limits are not particularly strong because all lines are either observed around strong sky OH lines or at low atmospheric transmission, but also due to our modest exposure time and conservative way of measuring noise.

---

[4] In vacuum, the wavelengths of these lines are Nv$_{\lambda\lambda} = 1239, 1243$ Å, Civ$_{\lambda\lambda} = 1548, 1551$ Å, Heii$_\lambda = 1640$, Oiii]$_{\lambda\lambda} = 1661, 1666$ Å and Ciii]$_{\lambda\lambda} = 1907, 1909$ Å.
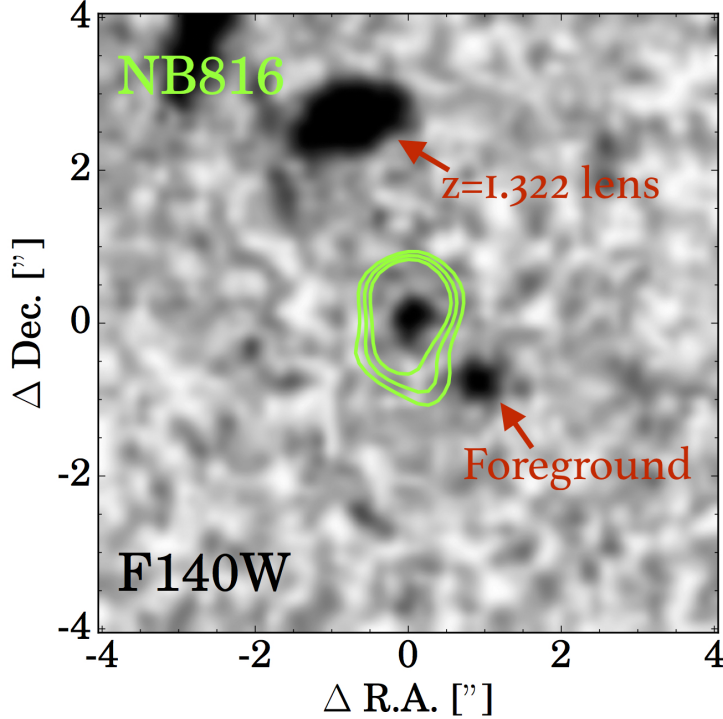
Figure 3.2: Rest-frame UV image of SR6 from follow-up with *HST* (see §3.4.1). Green contours (at 3, 4 and 5σ level) highlight the spatial scales at which we detect Lyα emission in the NB816 filter. The background image is the F140W image, which traces rest-frame wavelengths of ∼ 2000 Å. We note that the PSF of the NB816 imaging is significantly larger than the F098M imaging. SR6 is clearly detected in *HST* imaging, resulting in a (magnification corrected) UV luminosity of $M_{1500} = -21.1 \pm 0.1$ based on the F098M magnitude. *HST* imaging also reveals a foreground source at ∼ 1″ that can be identified in the ground-based optical imaging, which could slightly contribute to the flux measured in NB816, explaining why the flux inferred from the NB is slightly higher than the flux inferred from spectroscopy.

HST follow-up

We observed SR6 with our ongoing *HST*/WFC3 follow-up program (PI Sobral, program 14699), and is detected in the F098M and F140W filter, see e.g. Fig. 3.2, with a total integration time of 4076 s and 3176 s. The source is marginally resolved, consists of a single component that is separated by ≈ 0.2″ from the peak Lyα flux. We measure magnitudes of F098M=25.68 ± 0.13 and F140W=25.60 ± 0.10 in a 0.4″ aperture. Correcting for magnification, this results in $M_{1500} = -21.1 \pm 0.1$, which corresponds to a dust-uncorrected SFR $\approx 10 \ M_\odot \ yr^{-1}$ and is thus a $M^\star_{UV}$ source at that redshift (Bouwens et al., 2015a). Following the calibration from Schaerer et al. (2015), we estimate a stellar mass of $M_{star} \approx 4 \times 10^9 \ M_\odot$. The galaxy has a moderately blue UV slope, $\beta = -1.78 \pm 0.45$. In both *HST* filters, we measure a size of $r_{1/2} = 0.8 \pm 0.2$ kpc using SExtractor (corrected for PSF broadening following e.g. Curtis-Lake et al.

Table 3.2: Measurements of SR6 and VR7. Luminosity and EW are measured through spectroscopy. SFR_{UV} is based on the absolute UV magnitude, assuming negligible dust attenuation and a Chabrier IMF. Stellar mass is based on UV luminosity, following a calibration based on SED models presented in Schaerer et al. (2015). ξ_{ion} is computed as described in §3.5.3, which assumes $f_{esc,Ly\alpha} = 100\,\%$ for both sources, and is thus a lower limit. Line-flux 2σ limits are in 10^{-17} erg s^{-1} cm^{-2} and EW_0 limits are in Å.

Measurement	SR6	VR7
$z_{spec,Ly\alpha}$	5.676 ± 0.001	6.532 ± 0.001
$L_{Ly\alpha}/10^{43}$ erg s^{-1}	2.5 ± 0.3	2.4 ± 0.2
$EW_{0,spec}$/Å	> 65 Å	> 33 Å
$EW_{0,spec+phot}$/Å	210 ± 40 Å	35 ± 5 Å
$v_{FWHM,Ly\alpha}$/km s^{-1}	236 ± 16	340 ± 14
Skewness/Å	9.7 ± 0.8	6.9 ± 0.8
M_{1500}	-21.1 ± 0.1	-22.5 ± 0.1
$SFR_{UV}/M_\odot$ yr^{-1}	10	38
$M_{star}/M_\odot$	4×10^9	1.7×10^{10}
$\log_{10}(\xi_{ion}/$Hz erg$^{-1})$	$\gtrsim 25.25 \pm 0.23$	$\gtrsim 24.66 \pm 0.17$
β	-1.78 ± 0.45	-1.97 ± 0.31
$r_{1/2}$/kpc	0.9 ± 0.1	1.7 ± 0.1
f_{NV} ($EW_{0,NV}$)	< 2.0 (< 48)	< 1.0 (< 9)
f_{CIV} ($EW_{0,CIV}$)	< 7.3 (< 174)	< 2.3 (< 21)
f_{HeII} ($EW_{0,HeII}$)	< 3.6 (< 86)	< 2.3 (< 21)
$f_{OIII]}$ ($EW_{0,OIII]}$)	< 3.5 (< 84)	< 2.2 (< 20)
$f_{CIII]}$ ($EW_{0,CIII]}$)	< 3.9 (< 93)	< 2.1 (< 19)

2016; Ribeiro et al. 2016).

We use the *HST* photometry to estimate the continuum around Lyα and measure Lyα $EW_0 = 210 \pm 40$ Å. While the SFR, size and UV slope are typical, and not very different from UV selected galaxies at $z \approx 6 - 7$ (e.g. Bowler et al., 2017a), the extremely high Lyα EW is challenging to explain with simple stellar populations (e.g. Charlot & Fall, 1993), indicating an elevated production rate of ionising photons. Such high EWs are also found in numerous other Lyα surveys (e.g. Malhotra & Rhoads, 2002; Hashimoto et al., 2017a), although we note that those sources are typically of fainter luminosity. High EWs may be explained by extremely low metallicity stellar populations with young ages (e.g. Schaerer, 2003). Other explanations include AGN activity and contributions from cooling radiation (Rosdahl & Blaizot, 2012) and shocks (Taniguchi et al., 2015). However, these processes typically result in more extended Lyα emission, which is not observed with the current observational limits. Lyα EW may also be boosted in a clumpy ISM (e.g. Duval et al., 2014; Gronke & Dijkstra, 2014), but we note that measurements of the UV slope indicate little dust.

3.4.2   VR7

The source VR7 is a Lyα emitter at $z = 6.532 \pm 0.001$, see Fig. 3.1, with a Lyα luminosity of $2.4 \pm 0.2 \times 10^{43}$ erg s^{-1}. We do not detect continuum, allowing
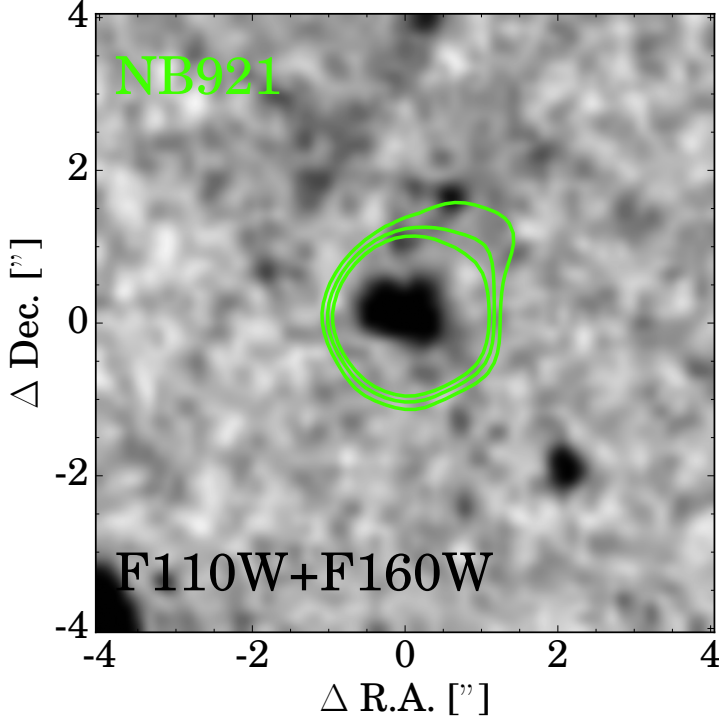
Figure 3.3: Rest-frame UV (F110W+F160W) image of VR7, which traces rest-frame wavelengths ~ 1500 Å. The green contours show the Lyα emission measured from NB921 (at 3, 4 and 5σ level). VR7 is elongated in the UV continuum, possibly due to two merging components. The absolute UV magnitude measured within a 2'' aperture centred on the Lyα peak is $M_{1500} = -22.5 \pm 0.1$, see 3.4.2.

us to place a lower limit on the equivalent width of $EW_0 > 33$ Å. The Lyα line-width is $v_{\rm FWHM} = 340 \pm 14$ km s^{-1}, the S-statistic is 0.33 ± 0.04, resulting in a Skewness of 6.9 ± 0.8 Å. This skewness is similar to those measured in fainter LAEs at $z = 6.5$ by Kashikawa et al. (2011).

We do not detect any emission-line besides Lyα in the optical or near-infrared spectrum, and place the following 2σ limits (assuming line-widths of ~ 200 km s^{-1}, narrower than Lyα, but similar to other studies): (1.0, 2.3, 2.3, 2.2, 2.1) $\times 10^{-17}$ erg s^{-1} cm^{-2} for (Nv, Civ, Heii, Oiii], Ciii]), see Table 10.1. These error estimates are also measured including sky OH lines, even though the lines themselves may avoid skylines, and are thus conservative. Assuming a continuum level of 1.3×10^{-19} erg s^{-1} cm^{-2} Å^{-1}, these flux limits translate into EW_0 limits of $<(9, 21, 21, 20, 19)$ Å, respectively.

HST follow-up

VR7 is detected at $\approx 3\sigma$ significance in the UKIDSS DXS J band imaging ($J = 24.2$), resulting in an absolute UV magnitude of $M_{1500} = -22.5 \pm 0.2$. This luminosity places the source in the transition region between luminous galaxies

Table 3.3: Compilation of Lyα line-widths of spectroscopically confirmed LAEs at $5.6 < z < 6.6$ included in Fig. 3.4. These sources are included in Fig. 3.4 in addition to the spectroscopically confirmed LAEs from Hu et al. (2010), Ouchi et al. (2010), Kashikawa et al. (2011) and Shibuya et al. (2018). More detailed information on these sources is included in Tables 3.4 and 3.5.

ID	Redshift	$v_{FWHM,Ly\alpha}$ km s^{-1}
SGP 8884	5.65	250 ± 30
SR6	5.67	236 ± 16
Ding-1	5.70	340 ± 100
S11 5236	5.72	300 ± 30
VR7	6.53	340 ± 14
MASOSA	6.54	386 ± 30
Himiko	6.59	251 ± 21
COLA1	6.59	194 ± 42
CR7	6.60	266 ± 15

and faint AGN (e.g. Willott et al., 2009; Matsuoka et al., 2016) and is ≈ 0.3 dex brighter than CR7 (e.g. Sobral et al., 2015b). We also obtained *HST*/WFC3 imaging in the F110W and F160W filters (PI Sobral, program 14699), with integration times of 2612 s and 5223 s. These observations reveal a relatively large elongated galaxy ($r_{1/2} = 1.7 \pm 0.1$ kpc, elongation of 1.4), with F110W=24.33 ± 0.09 and F160W=24.32 ± 0.10 in a 0.6″ aperture, see Fig. 3.3. We constrain the UV slope to $\beta = -1.97 \pm 0.31$. The UV luminosity corresponds to a SFR of 38 M$_\odot$ yr^{-1}, under the assumptions that the UV luminosity originates from star-formation (as noted above, we do not detect any signs of AGN activity such as CIV or MgII emission at the current detection limits), a Chabrier IMF and that dust attenuation is negligible. Based on the calibration from Schaerer et al. (2015), the stellar mass is M$_{star} \approx 1.7 \times 10^{10}$ M$_\odot$. Similar to SR6, we constrain the Lyα EW using *HST* photometry, and find EW$_0 = 35 \pm 5$ Å. Because of these properties, VR7 is an ideal target for further detailed follow-up observations.

3.5 Discussion

3.5.1 The evolution of Lyα line-widths

In order to investigate the nature of luminous LAEs at $z = 5.7 - 6.6$ using their Lyα line-profile, we compare the measurements with a reference sample of luminous LAEs at $z \approx 2 - 3$ (Sobral et al., 2018d). These comparison sources have been selected with wide-area narrow-band surveys (e.g. Sobral et al., 2017; Matthee et al., 2017c), and we match the minimum EW$_0$ criterion to > 20 Å. Even when we exclude broad-line AGN from the $z \approx 2 - 3$ sample, we find that luminous LAEs at $z = 5.7 - 6.6$ have Lyα line-widths (typically 290 ± 20 km s^{-1}) that are a factor 2-3 narrower than those at $z \approx 2 - 3$. These sources at lower redshift are a mix of narrow-line AGN and star-forming galaxies. This indicates that, besides non-detections of AGN associated lines as CIV or MgII, the Lyα
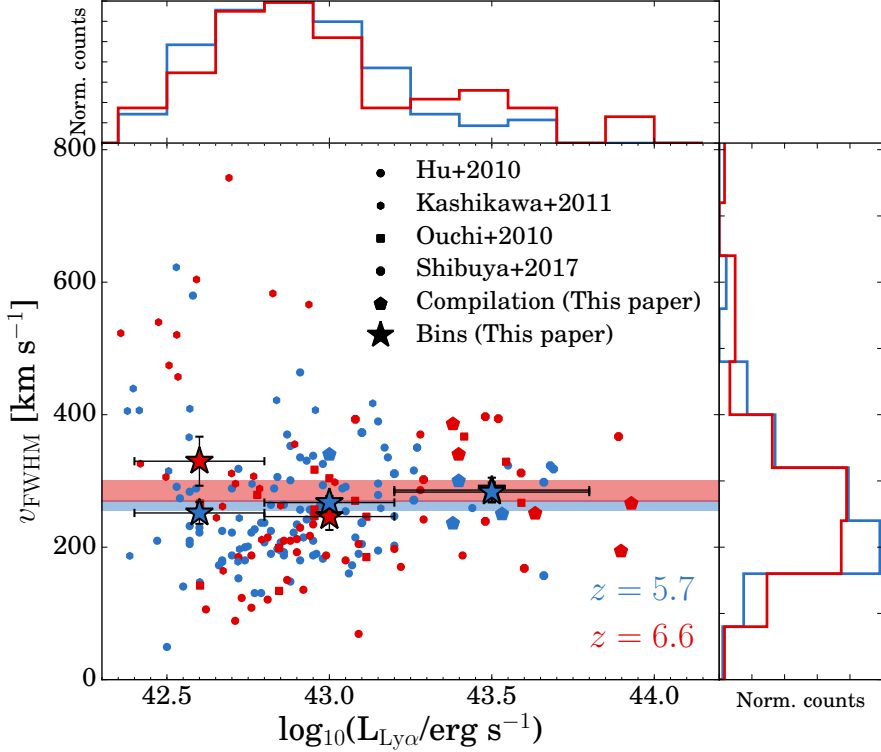
Figure 3.4: Lyα line-widths as a function of Lyα luminosity. Blue points show LAEs at $z = 5.7$, while red points show LAEs at $z = 6.6$. The red and blue horizontal bands indicate the mean line-widths and its error, while stars show the mean in bins of Lyα luminosity. At $z = 5.7$ Lyα line-widths increase slightly with increasing luminosity. While the average over the full sample indicates no significant evolution in line-widths from $z = 5.7 - 6.6$, the binned-averages indicate that line-widths of faint LAEs at $z = 6.6$ are a factor ~ 1.2 higher than at $z = 5.7$.

lines do not clearly indicate AGN activity in luminous LAEs at $z = 5.7 - 6.6$.

Due to resonant scattering, the presence of neutral hydrogen broadens Lyα emission lines (e.g. Kashikawa et al., 2006; Dijkstra et al., 2014). Theoretically, Haiman & Cen (2005) show that the observed Lyα line FWHM increase mostly at faint luminosities, $L_{Ly\alpha} \approx 10^{42}$ erg s^{-1}, with a more prominent evolution with higher neutral fraction and narrower intrinsic line-width. Therefore, evolution in the observed Lyα profiles at $z \gtrsim 6$ may provide hints on how reionisation happened. We investigate whether we find evidence for increasingly broad Lyα profiles as a function of redshift, by controlling for differences in Lyα luminosities.

In Fig. 3.4 we show the dependence of Lyα line-width on Lyα luminosity for samples at $z = 5.7$ and $z = 6.6$. We include samples from Hu et al. (2010), Ouchi et al. (2010), Kashikawa et al. (2011), Shibuya et al. (2018) and the compilation of Lyα selected sources from Table 3.3, which includes the two sources confirmed in this paper. This compilation also includes the luminous LAEs at $z = 5.7$ dis-

covered by Westra et al. (2006), studied in detail in Lidman et al. (2012), and the double-peaked LAE COLA1 at $z = 6.593$ discovered by Hu et al. (2016)[5]. While there is significant scatter, there are some interesting results. Firstly, the binned results indicate that line-widths at $z = 5.7$ increase slightly with increasing Lyα luminosity (at $\approx 3\sigma$ significance, see also Hu et al. 2010), while this is not necessarily the case at $z = 6.6$. In order to estimate the error on the bins as conservatively as possible, we combine the formal error ($\sigma/\sqrt{N}$, where σ is the observed standard deviation and N the number of sources in each bin) and the 1σ uncertainty on the mean estimated through bootstrap resampling the sample in the bins 1000 times in quadrature. By fitting a linear relation through the binned points at $z = 5.7$, we find that line-width increases with luminosity as:

$$v_{\mathrm{FWHM}} = 35^{+16}_{-13} \log_{10}\left(\frac{L_{\mathrm{Ly}\alpha}}{10^{43}\,\mathrm{erg\,s^{-1}}}\right) + 267^{+11}_{-11}\,\mathrm{km\,s^{-1}}. \qquad (3.3)$$

Secondly, the average values in bins of Lyα luminosity indicate that LAEs with luminosities $L_{\mathrm{Ly}\alpha} = 10^{42.4-42.8}$ erg s^{-1} have broader line-widths at $z = 6.6$ ($v_{\mathrm{FWHM}} \approx 330$ km s^{-1}) than at $z = 5.7$ ($v_{\mathrm{FWHM}} \approx 250$ km s^{-1}). We test the significance of these results by taking the uncertainties due to the limited sample size into account as follows. We bootstrap the sample in the low luminosity bins at both $z = 5.7$ and $z = 6.6$ 1000 times and we compute the mean v_{FWHM} in each realisation. The 1σ error on the mean is then the standard deviation of these 1000 measurements. At $z = 5.7$ we find $v_{\mathrm{FWHM}} = 252 \pm 17$ (error on mean) ± 112 (dispersion) km s^{-1}, while at $z = 6.6$ we find $v_{\mathrm{FWHM}} = 323 \pm 36$ (error on mean) ± 192 (dispersion) km s^{-1}. This means that the offset is only marginally significant. We also perform a Kolmogorov-Smirnov test on 1000 realisations of the sample where we have perturbed each measured v_{FWHM} with its uncertainty assuming that the uncertainty is gaussian. We find a mean P-value of 0.12 ± 0.05 and a KS-statistic of 0.27 ± 0.02. This means that the two distributions are not drawn from the same parent distribution at $\approx 85\,\%$ confidence level. This difference in the line-widths between the samples at $z = 5.7$ and $z = 6.6$ resembles the prediction from Haiman & Cen (2005) and may be used to constrain the neutral fraction of the IGM. As the dispersion is relatively large and the difference is significant at only $\approx 85\,\%$ confidence level, larger samples are required to better constrain this evolution.

The trends that Lyα line-width increases slightly with luminosity at $z = 5.7$

---

[5] In our analysis of COLA1, we find that it is detected at $> 5\sigma$ in the public HST F814W imaging (Koekemoer et al., 2007), with a magnitude of 26.2 ± 0.2. Even though the F814W filter has significant transmission above 920 nm, this magnitude indicates that a fraction of the flux density measured in F814W originates from $\lambda_0 < 1216$ Å. The F814W imaging also shows a neighbouring source within the PSF-FWHM of the NB921 imaging (data from Subaru program S13A-057; Sobral et al. 2013), indicating that the Lyα luminosity may be over-estimated. There is also a $\sim 2\sigma$ detection in the B band Suprime-Cam data. This tentative detection is unexpected for a source at $z = 6.6$ (because they trace below the Lyman break), and could indicate that the emission-line is the [OII]$_{3727,3729}$ doublet at $z = 1.477$ (similar to the photometric redshift of the source in the Laigle et al. 2016 catalogue). On the other hand, while the double-peak separation in the spectrum presented in Hu et al. (2016) may be explained with the [OII] doublet, the asymmetric red wing challenges this explanation. Thus, currently none of the scenarios is completely satisfactory. Follow-up observations in the NIR are required to fully distinguish between these scenarios (see Chapter 6).

and that the faintest LAEs may have broader Lyα lines at higher redshift, may explain why neither Hu et al. (2010), Ouchi et al. (2010) or Kashikawa et al. (2011) report increasing Lyα line-widths between $z = 5.7 - 6.6$. This is because they only studied the average over all luminosities (which does not change significantly), or probed a different Lyα luminosity regime. Interestingly, the luminosity at which line-widths may increase might correspond to the luminosity where the number density (at fixed Lyα spatial scale) drops most strongly between $z = 5.7 - 6.6$ (Matthee et al., 2015), and where there is relatively more extended Lyα emission at $z = 6.6$ than at $z = 5.7$ (Santos et al., 2016). This strengthens the idea that we are witnessing the effect of patchy reionisation affecting the number densities, line-widths and spatial extents of faint Lyα emitters at $z = 6.6$.

3.5.2   UV (metal) line-ratios to Lyα

As described in §3.4, no rest-UV metal-lines are detected in SR6 or VR7. Such lines have also not been detected in Himiko (Zabl et al., 2015) or CR7 (Sobral et al., 2015b). In this section we explore whether this is due to the limited depth of the observations or may be attributed to any peculiar physical condition (for example due to a low metallicity). As a comparison sample, we made a compilation of UV and Lyα selected galaxies at $z \gtrsim 6$ for which limits on other UV emission-lines besides Lyα are published, see Table 3.4. These sources have all been spectroscopically confirmed through their Lyα emission. All upper limits are converted to 2σ and we compute Lyα luminosities and absolute UV magnitudes based on the published observed magnitudes and fluxes in the case luminosities and absolute magnitudes have not been provided. We show limits on the strength of Nv, Civ, Heii, Oiii] and Ciii] compared to Lyα. A more detailed description on the compiled sample is provided in Appendix 3.A. In addition, we also compare our sources with a sample of luminous LAEs at $z \approx 2 - 3$ (Sobral et al., 2018d).

   Based on Tables 3.4 and 3.5, it is already clear that the limits on Ciii] and Civ with respect to Lyα for SR6 and VR7 are higher than, or at most similar to, known detections at $z \sim 6 - 7$, indicating that our observations are not deep enough. As we illustrate in Fig. 3.5, we find that the current detections and upper limits at $z \approx 6 - 7$ indicate that Civ/Lyα increases towards faint UV luminosities, while it decreases or stays constant at $z \approx 2 - 3$. Contrarily, relatively high Ciii]/Lyα ratios are detected among UV bright galaxies at $z \approx 6 - 7$, similarly to $z \approx 2 - 3$. In Fig. 3.6, we compare the ratios of Ciii] and Civ to Lyα as a function of the Lyα EW$_0$. This illustrates that the $z \approx 6 - 7$ galaxies with observed carbon lines ubiquitously have low Lyα EWs (note that this does not necessarily mean that they are UV bright, as we showed above). This is similar to the comparison sample at $z \approx 2 - 3$ and indicates that the observability of carbon lines may actually be related strongly to the observed strength of Lyα emission and thus on the Lyα escape fraction.

   We now compare the measured carbon-Lyα ratios to simple model predictions (Alegre et al. in prep), by correcting for Lyα escape fraction empirically. The physics driving the Lyα escape fraction are complex (e.g. Hayes, 2015; Henry

Table 3.4: Compilation of Lyα luminosities, EWs, absolute UV magnitudes and line-ratios between Lyα and rest-frame UV lines of Lyα (narrow-band) selected galaxies. Galaxies are ordered by increasing redshift (see Table 3.6). For the doublets C IV C III] and O III], we use the combined flux. Upper limits are at the 2σ level.

ID	$L_{Ly\alpha}$ erg s^{-1}	EW$_{0,Ly\alpha}$ Å	M$_{1500}$ AB	N v/Lyα	C IV/Lyα	He II/Lyα	O III]/Lyα	C III]/Lyα
Lyα selected								
SGP 8884	3.4×10^{43}	166	-	< 0.01	-	-	< 0.09	< 0.13
SR6	2.5×10^{43}	> 250	-21.1	< 0.26	< 0.96	< 0.47	< 0.46	< 0.51
Ding-3	0.7×10^{43}	62	-20.9	-	-	-	-	< 0.11
Ding-4	0.2×10^{43}	106	-20.5	-	-	-	-	< 0.31
Ding-5	2×10^{43}	79	-20.5	-	-	-	-	< 0.05
Ding-2	0.2×10^{43}	-	-22.2	-	-	-	-	< 0.31
Ding-1	1×10^{43}	21	-22.2	-	-	-	-	0.09
J233408	4.8×10^{43}	> 260	-20.8	< 0.05	0.08	< 0.01	< 0.01	-
S11 5236	2.5×10^{43}	160	-	< 0.03	< 0.13	-	< 0.21	< 0.18
J233454	4.9×10^{43}	217	-21.0	< 0.05	< 0.01	< 0.01	< 0.01	-
J021835	4.6×10^{43}	107	-21.7	< 0.07	< 0.02	< 0.03	< 0.01	-
WISP302	4.7×10^{43}	798	-19.6	-	-	< 0.41	-	< 0.29
VR7	2.4×10^{43}	> 196	-22.5	< 0.16	< 0.36	< 0.35	< 0.35	< 0.33
LAE SDF-LEW-1	1×10^{43}	872	> -22	-	< 0.01	< 0.02	-	-
J162126	7.8×10^{43}	99	-20.5	< 0.05	< 0.01	< 0.02	< 0.01	-
J160940	1.9×10^{43}	> 31	-22.1	< 0.14	< 0.19	< 0.30	< 0.49	-
J100550	3.9×10^{43}	> 107	-21.5	< 0.08	< 0.01	< 0.01	< 0.03	-
J160234	3.3×10^{43}	81	-21.9	< 0.11	< 0.12	< 0.16	< 0.23	-
Himiko	4.3×10^{43}	65	-22.1	< 0.03	< 0.10	< 0.05	-	< 0.08
CR7 (recalibrated)	8.5×10^{43}	211	-22.2	< 0.03	< 0.12	0.14 ± 0.06	< 0.09	< 0.11

Table 3.5: As Table 3.4, but for UV selected galaxies (Lyman-break galaxies).

| ID	$L_{Ly\alpha}$ erg s^{-1}	$EW_{0,Ly\alpha}$ Å	M_{1500} AB	Nv/Lyα	Civ/Lyα	Heii/Lyα	Oiii]/Lyα	Ciii]/Lyα
UV selected								
A383-5.2	0.7×10^{43}	138	-19.3	-	-	-	-	0.05 ± 0.01
RXCJ2248.7-4431-ID3	0.3×10^{43}	40	-20.1	< 0.05	0.42 ± 0.12	< 0.05	0.13 ± 0.04	< 0.11
RXCJ2248.7-4431	0.8×10^{43}	68	-20.2	< 0.48	0.45 ± 0.12	< 0.28	0.31 ± 0.12	< 0.09
SDF-46975	1.5×10^{43}	43	-21.5	< 0.13	-	-	-	-
IOK-1	1.1×10^{43}	42	-21.3	< 0.17	-	< 0.12	-	-
BDF-521	1.0×10^{43}	64	-20.6	< 0.26	-	< 0.16	-	-
A1703_zd6	0.3×10^{43}	65	-19.3	-	0.28 ± 0.03	< 0.07	0.06 ± 0.03*	-
BDF-3299	0.7×10^{43}	50	-20.6	< 0.26	-	-	-	-
GLASS-stack	1×10^{43}	210*	-19.7	< 0.4	< 0.3	< 0.2	< 0.2	< 0.2
EGS-zs8-2	0.5×10^{43}	9	-21.9	-	-	-	-	< 0.41
FIGS.GN1.1292	0.7×10^{43}	49	-21.2	0.85 ± 0.25	-	-	-	-
GN-108036	1.5×10^{43}	33	-21.8	< 0.33	-	-	-	0.09 ± 0.05
EGS-zs8-1	1.2×10^{43}	21	-22.1	-	-	-	-	0.46 ± 0.10
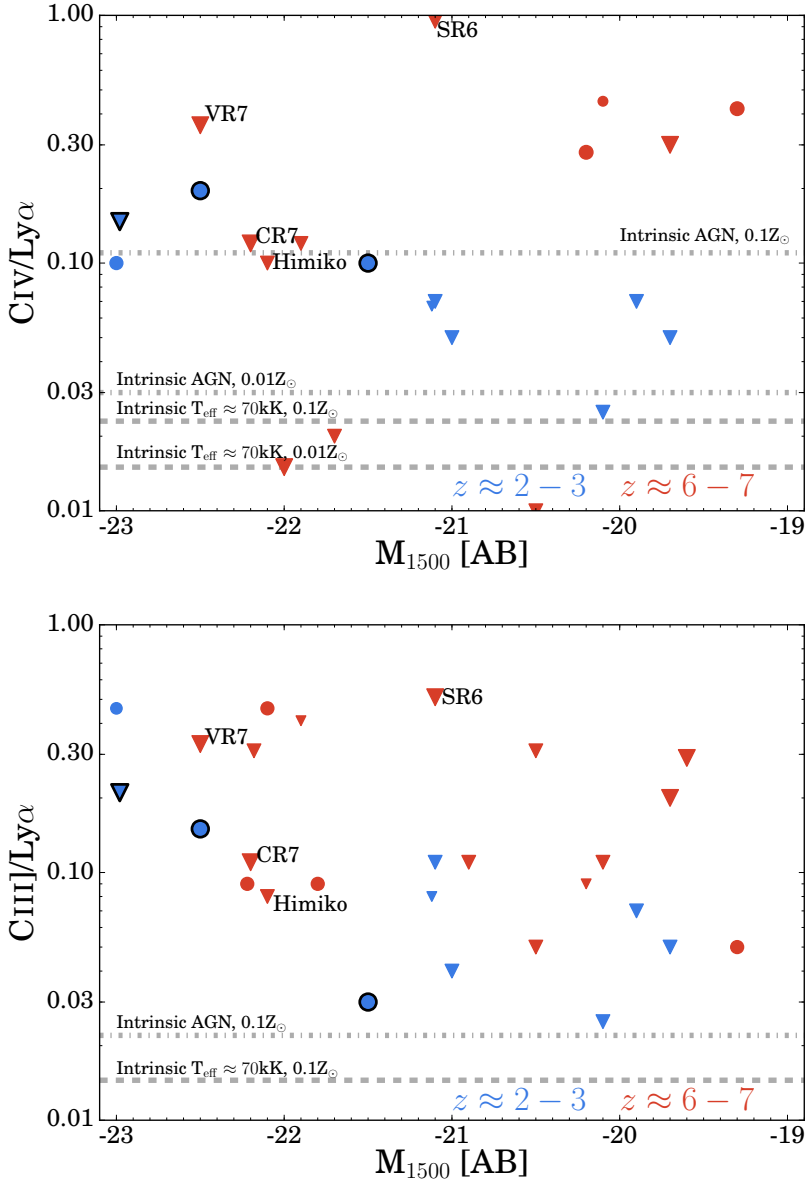
Figure 3.5: Observed CIV/Lyα and CIII]/Lyα ratios as a function of M$_{1500}$ for luminous LAEs at $z \approx 2 - 3$ (Sobral et al. 2018d) and the compilation of LAEs and LBGs at $z \approx 6 - 7$ from Table 3.4 with CIV and CIII] detections and/or upper limits. Upper limits are shown with down-ward pointing triangles, while detections are shown with circles. We highlight AGN in the $z \approx 2 - 3$ sample with black edges. The symbol sizes increase with increasing Lyα EW. Horizontal lines indicate estimated intrinsic line-ratios (Alegre et al. in prep), assuming a 100 % Lyα escape fraction. Galaxies with CIV detections at $z \approx 6 - 7$ have higher CIV/Lyα ratios than LAEs at $z \approx 2 - 3$ with similar UV luminosities. The limits on CR7 and Himiko are comparable to detections of similar sources at $z \approx 2 - 3$, but for which an AGN nature is confirmed.
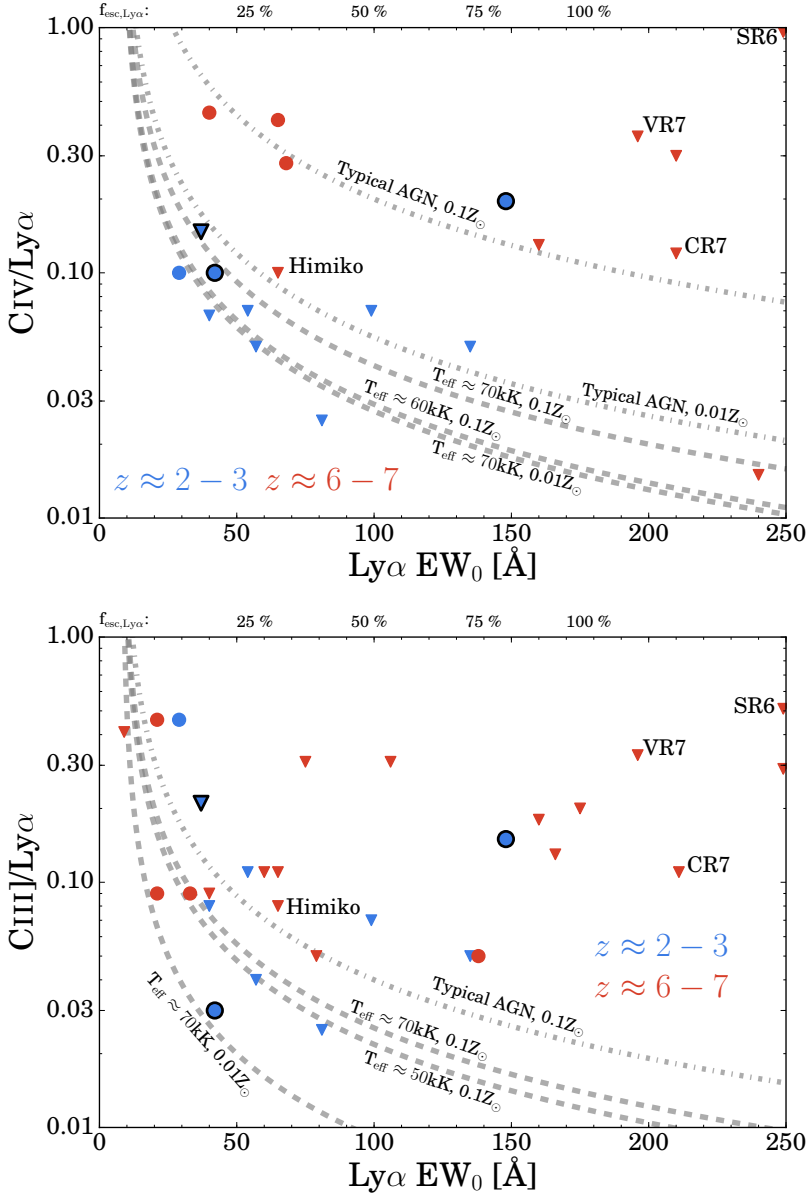
Figure 3.6: Observed CIV/Lyα and CIII]/Lyα ratios as a function of EW_{0,Lyff} for luminous LAEs at $z \approx 2 - 3$ (Sobral et al. 2018d) and the compilation of LAEs and LBGs at $z \approx 6 - 7$ from Table 3.4. Upper limits are shown with down-ward pointing triangles, while detections are shown with circles. We highlight AGN in the $z \approx 2 - 3$ sample with black edges. In dashed (dot-dashed) grey lines, we show expected observed line-ratios based on estimates with the star-forming (AGN) models from Eq. 3.5. It is clear that CIV and CIII] are most easily observed at $z \approx 6 - 7$ in galaxies with relatively low Lyα EWs and that the observations of e.g. CR7 and VR7 are not deep enough.

et al., 2015), with dust, Hɪ column density, outflows and (especially at $z > 6$) the neutral fraction of the IGM all playing an important role. However, a rough estimate of the Lyα escape fraction may be obtained from the Lyα EW_0, as for example shown at $z = 2.2$ in Sobral et al. (2017), see also e.g. Yang et al. (2017) at $z \sim 0$. Therefore, we use the EW_0 to provide a rough estimate of the Lyα escape fraction, and thus the intrinsic Lyα emission (that is, for example, strongly related to the ionising emissivity). An important caveat here is that the IGM transmission decreases between $z = 2.2 - 6.6$ at wavelengths around Lyα (even into the red wing, Laursen et al. 2011), such that the 'effective' Lyα escape fraction (including the effect from the IGM) may be under-estimated. On the other hand, this decreasing transmission may be mitigated in the presence of galactic outflows (e.g. Dijkstra et al., 2011). We fit the following relation to the data-points from Fig. 11 (right panel) in Sobral et al. (2017) to estimate the escape fraction:

$$f_{\text{esc,Ly}\alpha} = 0.006 \; EW_{\text{Ly}\alpha,0} - 0.05 \; [5 < EW_{\text{Ly}\alpha,0} < 175], \qquad (3.4)$$

where $f_{\text{esc,Ly}\alpha}$ is the Lyα escape fraction. Then, we use this relation to estimate observed line-ratios from their theoretically predicted values:

$$\frac{f_{\text{CIII}]}}{f_{\text{Ly}\alpha}} = \frac{\alpha}{f_{\text{esc,Ly}\alpha}} \quad ; \quad \frac{f_{\text{CIV}}}{f_{\text{Ly}\alpha}} = \frac{\alpha}{f_{\text{esc,Ly}\alpha}}, \qquad (3.5)$$

where α is the estimated intrinsic line-ratio with respect to Lyα. We use the results from CLOUDY (Ferland et al., 2013) modelling (to be presented in Alegre et al. in prep, but with a similar approach to Feltre et al. 2016) to model the intrinsic line-ratios. The ionisation sources in these models are either a range of black-bodies (with temperatures ranging from 20 kK to 150 kK, approximating stellar populations and including populations with extreme temperature > 70kK) and a range of power-laws (with spectral slopes of typical AGN), and the metallicities range from 0.001 $Z_\odot$ to solar, see also Sobral et al. (2018d). For CIV, we use models with values of α between 0.015 (for a blackbody with effective temperature ≈ 70kK and a metallicity of 0.01 $Z_\odot$) and $\alpha = 0.11$ (for a typical AGN power-law slope and a metallicity 0.1 $Z_\odot$). α decreases rapidly in the case of a lower metallicity or lower effective temperatures. For CIII], we use values from $\alpha = 0.005$ ($T_{\text{eff}} \approx 70$kK, Z= 0.01 $Z_\odot$) to $\alpha = 0.022$ for the same AGN model as described above. The results of this modelling is shown in dashed lines in Fig. 3.6.

We find that current CIV detections at $z \approx 6 - 7$ lie closer to expected line-ratios from AGN than those from star-forming galaxies (c.f. Mainali et al., 2017). However, we note that assuming a higher effective temperature of a stellar population would result in a higher CIV/Lyα ratio (compare for example the 60 kK, 0.1 $Z_\odot$ line with the 70 kK, 0.1 $Z_\odot$ line). Another issue is that Lyα luminosities from these sources are estimated from slits, such that a significant fraction may be missed due to (slightly) more extended emission. On the one hand, the detected CIII]/Lyα ratios are already close to those modelled with star-formation as powering source. The CIV limits observed in Himiko prefer a star-forming ionising source, or an AGN with a very low metallicity ($\approx 0.01 \; Z_\odot$). With the

current limits for SR6, CR7 and VR7 this analysis is not very meaningful, and we estimate that we would have to go a factor $5 - 10$ deeper to detect CIV or CIII].

3.5.3 UV luminosities and SFRs of luminous LAEs

In order to investigate how Lyα luminosity is related to the UV luminosity, which traces SFR of timescales of ~ 100 Myr, we use near-infrared data to measure rest-frame UV luminosities (M_{1500}) for LAEs at $z = 5.7 - 6.6$. In addition to the new sources presented in this paper, we also add remaining candidate LAEs at $z = 5.7 - 6.6$ from Matthee et al. (2015) and Santos et al. (2016) and several sources from the literature as described below.

Rest-frame absolute UV magnitudes of LAEs are estimated with Y and J band photometry, converted to rest-frame M_{1500} at $z = 5.7$ and $z = 6.6$ respectively. Y band imaging is available in the UltraVISTA (DR2) coverage of the COSMOS field (McCracken et al., 2012). J band imaging is available in the UDS field through UKIDSS UDS (we use DR8; Lawrence et al. 2007), in the COSMOS field through UltraVISTA and in the SA22 field through the UKIDSS DXS. Photometry is measured in $2''$ apertures with SEXTRACTOR (Bertin & Arnouts, 1996) in dual-image mode with the narrow-band image as detection image (i.e. the apertures are centred at the peak Lyα emission). Because the survey depth may vary from source to source (in particular in the COSMOS field due to the UltraVISTA survey design), we measure the depth locally. 2σ limits are assigned to sources that are undetected in the NIR imaging. We do not make any corrections for the fact that the effective wavelengths of the filters are not exactly at 1500 Å. However, for a typical UV slope of $\beta \approx -2.3$ (e.g. Ono et al., 2010; Jiang et al., 2013b), such a correction would only be on the order of $\Delta M_{1500} = 0.004\,(0.03)$ for LAEs at $z = 5.7\,(6.6)$. For a more extreme blue or relative red UV slope of $\beta = -3.0$ or $\beta = -1.0$, the correction would be up to 0.1 magnitude. We also add the information from LAEs in the Subaru Deep Field (Kashikawa et al., 2011) that have been observed with HST NIR imaging by Jiang et al. (2013b), LAEs observed by Ding et al. (2017), recently spectroscopically confirmed LAEs at $z = 5.7 - 6.6$ by Shibuya et al. (2018) and our compilation of UV selected galaxies between $z = 6.2 - 7.2$ with Lyα $EW_0 > 20$ Å (see Table 3.5, green symbols in the right panel of Fig. 3.7). In addition to the sources from this compilation, we also added two sources from Huang et al. (2016), see Table 3.6.

Fig. 3.7 clearly shows that at fixed Lyα luminosity, there is a large spread in UV luminosities, and vice versa (at both $z = 5.7$ and $z = 6.6$). Spectroscopically confirmed UV selected galaxies have similar $L_{Ly\alpha}$ luminosities as LAEs. Around $L^\star$ ($L_{Ly\alpha} \approx 10^{43}$ erg s^{-1}), absolute UV magnitudes can range from up to $3 \times M^\star_{1500}$ ($M_{1500} \approx -21.0$), down to $\approx 0.3 \times M^\star_{1500}$, with a 1σ spread of 0.9 dex. This means that relatively shallow, wide area Lyα surveys can be an efficient tool to select relatively UV-faint galaxies up to $z \approx 7$, thought to be signification contributors to the reionisation process (e.g. Robertson et al., 2013; Faisst et al., 2016). It also means that it is challenging to predict Lyα luminosities of UV-continuum selected galaxies, even outside the reionisation epoch.

Fig. 3.7 also shows that there is little evidence for a relation between the Lyα
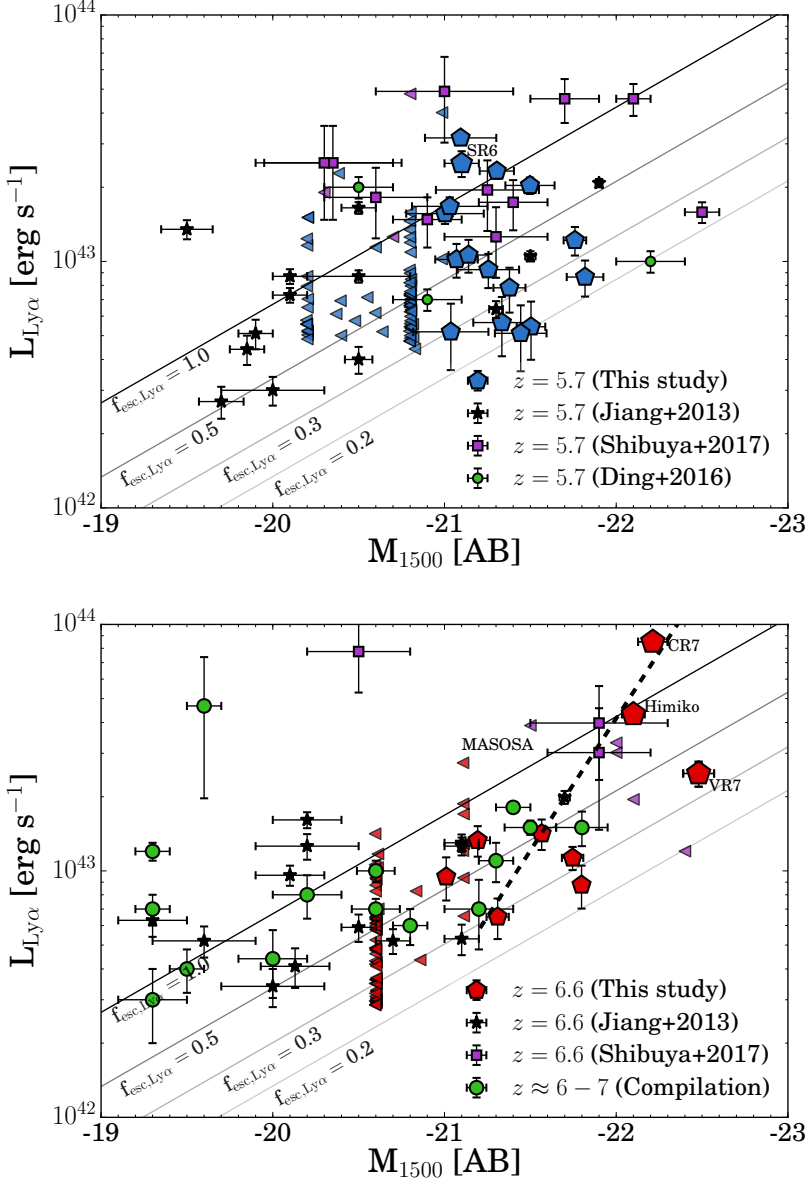
Figure 3.7: M_{1500} versus Lyα luminosity. Rest-frame absolute UV magnitudes are estimated from Y and J band photometry at $z = 5.7$ and $z = 6.6$, respectively. In the case of a non-detection, we show the local 2σ limit. Lines of constant Lyα escape fraction are computed assuming that $\text{SFR}_{UV}=\text{SFR}_{\text{H}\beta\text{ff}}$, case B recombination and no attenuation due to dust. Under these assumptions, several LAEs have escape fractions > 100 %. The sources included in this study are the LAEs from Jiang et al. (2013b), Matthee et al. (2015), Santos et al. (2016), Ding et al. (2017) and Shibuya et al. (2018) and the compilation at $z \approx 6 - 7$ comprises the UV-continuum selected galaxies in Table 3.6 between redshifts $z = 6.1$ and $z = 7.2$ and with Lyα EW> 20 Å. In the bottom panel, the dashed line shows a fit to LAEs with $M_{1500} < -21.2$. Note that Himiko and CR7 have multiple components in the rest-UV.

luminosity and M_{1500} for Lyα selected sources at $z = 5.7$ in our UV and Lyα luminosity range. As both M_{1500} and $L_{Ly\alpha}$ are, to first order, related to the SFR, we would have expected a correlation. To illustrate this, we show lines at constant Lyα escape fractions (based on the assumption that SFR$_{UV}$=SFR$_{H\beta ff}$, case B recombination with $T = 10000$K and $n_e = 100$ cm^{-3} and no attenuation due to dust). This result resembles the well known Ando et al. (2006) diagram, which reveals a deficiency of luminous LAEs with bright UV magnitudes between $z \approx 5 - 6$. More recently, other surveys also revealed that the fraction high EW Lyα emitters increases towards fainter UV magnitudes (e.g. Schaerer et al., 2011; Stark et al., 2011; Cassata et al., 2015). The lack of a strong correlation between M_{1500} and $L_{Ly\alpha}$ might indicate that the SFRs are bursty (because emission-line luminosities trace SFR over a shorter time-scale than UV luminosity), or that the Lyα escape fraction is anti-correlated with M_{1500} (such that Lyα photons can more easily escape from galaxies that are fainter in the UV). A possible explanation for the latter scenario is that slightly more evolved galaxies (which are brighter in the UV) have a slightly higher dust content (e.g. Bouwens et al., 2012), affecting their Lyα luminosity more than the UV luminosity. It is interesting to note that several galaxies lie above the 100 % Lyα escape fraction line. This implies bursty or stochastic star-formation (which is more likely in lower mass galaxies with faint UV luminosities, e.g. Mas-Ribas et al. 2016), alternative Lyα production mechanisms to star-formation (such as cooling), a higher ionising production efficiency (for example due to a top-heavy IMF or binary stars, e.g. Götberg et al. 2017), or dust attenuating Lyα in a different way than the UV continuum (e.g. Neufeld, 1991; Finkelstein et al., 2008; Gronke et al., 2016).

At $z = 6.6$, however, current detections indicate a relation between M_{1500} and $L_{Ly\alpha}$, albeit with significant scatter (Fig. 3.7). In order to be unbiased due to the depth of J band imaging, we fit a linear relation between $\log_{10}(L_{Ly\alpha})$ and M_{1500} for LAEs with $M_{1500} < -21.2$ using a least squares algorithm, resulting in:

$$\log_{10}(L_{Ly\alpha}/erg\,s^{-1}) = 20.8^{+4.2}_{-4.2} - 1.0^{+0.2}_{-0.2}\,M_{1500} \qquad (3.6)$$

This fit indicates that for LAEs at $z \approx 6.5 - 7$, M_{1500} and $L_{Ly\alpha}$ are related at 5σ significance in the current data (see also Jiang et al. 2013b). We measure a (large) 1σ scatter of 0.26 dex around this relation. We note that excluding UV selected galaxies results in a lower significance ($\approx 3.5\sigma$), but does not significantly change the fit parameters. The fitted slope between M_{1500} and $L_{Ly\alpha}$ is steeper than the slope that is expected at fixed $f_{esc,Ly ff}$, which could indicate that the Lyα escape fraction (or its production rate) increases towards brighter magnitudes (for Lyα selected sources). At fainter UV luminosities, we find that the slope is consistent with being flat (within the error-bars) and many of these sources only have upper limits on their UV magnitude. We also note that for a cut at high Lyα luminosity, no clear relation is seen between Lyα and UV luminosity. The presence of very luminous LAEs with luminous UV luminosities at $z = 6.6$ is at odds with the Ando et al. (2006) result, indicating additional physical processes playing a role.

We note that the most UV luminous sources at $z = 6.6$ have multiple UV-components (CR7, Himiko and VR7), which could help facilitating the escape of

Lyα photons. For example, outflows caused by earlier star formation episodes could boost the escape of Lyα photons through the ISM, while the same previous star formation episodes could have ionised a large enough fraction of the IGM around the galaxy such that Lyα can escape. This could be particularly important in the reionisation era at $z \gtrsim 6.5$. Similarly, Jiang et al. (2013c) found that their most UV-luminous LAE at $z = 5.7$ and 4 out of the 6 LAEs with $M_{1500} < -20.5$ at $z = 6.6$ are interacting/merging. Moreover, the galaxy IOK-1, a confirmed LAE at $z = 6.96$ (Iye et al., 2006) also consists of two UV-bright components. We note that the spectroscopic follow-up presented in Furusawa et al. (2016) included two luminous UV selected galaxies ($M_{1500} = -22.4, -22.7$) at $z \sim 7$ from Bowler et al. (2014), that have multiple components in the HST imaging (Bowler et al., 2017a). These sources are not detected with strong Lyα emission (with a limiting $L_{Ly\alpha} \lesssim 3 \times 10^{42}$ erg s^{-1}), indicating that while multiple components could boost Lyα observability, they do not imply observable Lyα emission at $z \sim 7$.

The production efficiency of ionising photons

We combine the Lyα and UV measurements to estimate ξ_{ion}, the ionising photon production efficiency, which is an important parameter in assessing the ionising budget from star-forming galaxies, particularly in the reionisation era (e.g. Robertson et al., 2013; Bouwens et al., 2016; Matthee et al., 2017b). Under the assumption that the escape fraction of ionising photons is close to zero, ξ_{ion} is defined as the number of produced ionising photons per second, per unit UV magnitude:

$$\xi_{ion} = \frac{Q_{ion}}{L_{UV}}, \tag{3.7}$$

where Q_{ion} is the number of emitted ionising photons per second, and L_{UV} the UV luminosity at $\lambda_0 \approx 1500$ Å. Ideally, Q_{ion} is estimated from Hα measurements, as $L_{H\alpha} = 1.36 \times 10^{-12} Q_{ion}$ under the assumption that $f_{esc,LyC} = 0$ % (e.g. Kennicutt, 1998). Unfortunately, Hα measurements can only be performed at $z > 2.5$ after the launch of the *James Webb Space Telescope (JWST)*. Therefore, we use the calibration of the Lyα escape fraction with EW$_0$ (see Eq. 3.4), which relates the Lyα luminosity to Hα luminosity under the assumption of case B recombination. Rewriting the equations results in:

$$\xi_{ion} = \frac{L_{Ly\alpha}}{8.7 \times 1.36 \times 10^{-12} \times f_{esc,Ly\alpha} \times L_{UV}}. \tag{3.8}$$

Here, the factor 8.7 is the case B recombination ratio between Lyα and Hα under typical ISM conditions of $T_e = 10,000$ K and $n_e = 350$ cm^{-3} (e.g. Henry et al., 2015). $f_{esc,Ly\alpha}$ is obtained through Eq. 3.4, with a maximum of 1.0 (for EW$_0 \gtrsim 175$ Å). L_{UV} is computed using the measured M_{1500}, assuming negligible dust attenuation (see Bouwens et al. 2016 for a discussion on how dust attenuation affects ξ_{ion}). This empirically motivated method to estimate ξ_{ion} can easily be tested with follow-up observations with *JWST*.

Using this prescription, we calculate values of $\log_{10}(\xi_{ion}/\text{Hz erg}^{-1}) \gtrsim 25.25 \pm$
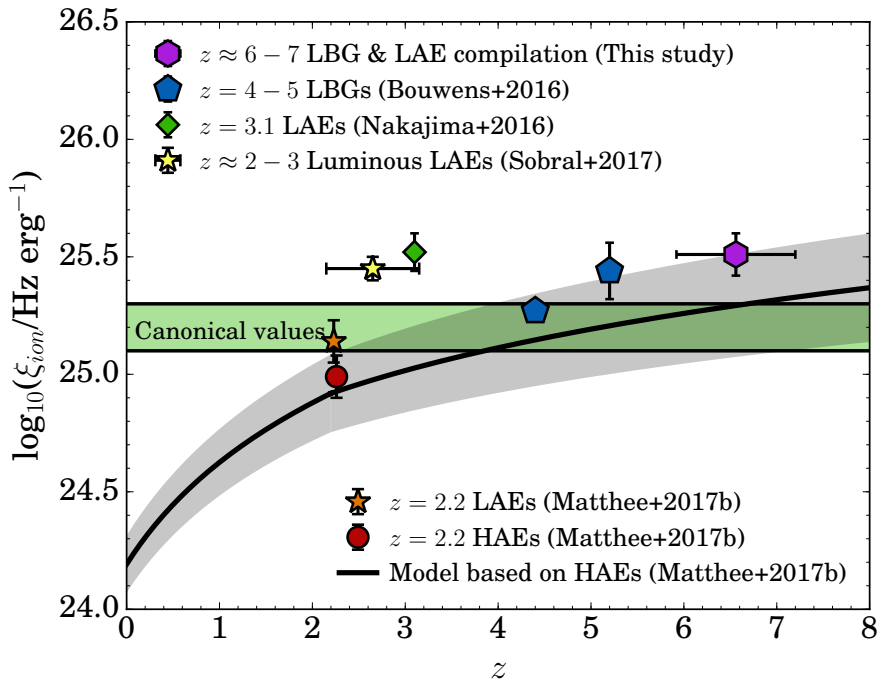
Figure 3.8: Production efficiency of ionising photons (ξ_{ion}) versus redshift for different compilations of galaxies, showing our results at $z \approx 6 - 7$ with a purple hexagon. The green region shows the canonical values from Robertson et al. (2013). The black line shows the modelled/predicted evolution of ξ_{ion} from Matthee et al. (2017b) based on the redshift evolution of the Hα EW and the relation between ξ_{ion} and Hα EW for Hα emitters (HAEs). It can be seen that at $z \approx 2 - 3$ LAEs have a significantly higher ξ_{ion} than the typical HAE/star-forming galaxy. Samples of LBGs at $z \approx 4 - 5$ and the compilation of LBGs and LAEs from Tables 3.4 and 3.5 at $z \approx 6 - 7$ show elevated values of ξ_{ion} compared to the canonical value, and qualitatively confirm the trend of the modeled evolution of ξ_{ion}.

0.23 and $\gtrsim 24.66 \pm 0.17$ for SR6 and VR7, respectively. We write these as upper limits because the Lyα EWs of SR6 and VR7 indicate $f_{esc,Ly\alpha} = 100$ %, which may be an over-estimate (in the case of 50 % Lyα escape, ξ_{ion} would increase by 0.3 dex). For CR7 and Himiko we measure $\log_{10}(\xi_{ion}/\text{Hz erg}^{-1}) \gtrsim 25.33 \pm 0.06$ and $\log_{10}(\xi_{ion}/\text{Hz erg}^{-1}) = 25.55 \pm 0.07$, respectively. Except for VR7, these values are similar to the measurements of faint LAEs at $z \approx 3$ (Nakajima et al., 2016) and $z \approx 4-5$ Lyman-break galaxies (Bouwens et al., 2016). The median value of ξ_{ion} for our compilation in Tables 3.4 and 3.5 is $\log_{10}(\xi_{ion}/\text{Hz erg}^{-1}) = 25.51 \pm 0.09$ (Fig. 3.8), which is similar to the mean value of the reference sample of luminous LAEs at $z \approx 2-3$, for which we measure a mean $\log_{10}(\xi_{ion}/\text{Hz erg}^{-1}) = 25.45 \pm 0.05$ using the same method, and slightly lower than those measured by Schaerer et al. (2016) in a sample of low redshift Lyman-Continuum leakers.

We also compare our method to the values of ξ_{ion} obtained independently by Stark et al. (2015b, 2017) using photo-ionisation modelling of UV metal lines. While we measure a higher value of $\log_{10}(\xi_{ion}/\text{Hz erg}^{-1}) = 26.63 \pm 0.36$ for EGS-zs8-2, our results for A1703_zd6, EGS-zs-1 (see Tables 3.4 and 3.5) and COS zs7-1 are $\log_{10}(\xi_{ion}/\text{Hz erg}^{-1}) = 25.52 \pm 0.18, 25.64 \pm 0.12$ and 25.63 ± 0.15, encouragingly consistent with the estimates from Stark et al. Under the model-assumptions, these results indicate that luminous Lyα emitters produce ionising photons a factor two more efficiently than typically assumed (e.g. Robertson et al., 2013), and similar to the estimated ξ_{ion} based on the evolution of the Hα EW / specific SFR (Matthee et al., 2017b), see Fig. 3.8. This implies that a significant amount of photons that reionised the Universe may have been produced in LAEs, in particular if the ISM conditions in these galaxies are also facilitating LyC photons to escape (e.g. Dijkstra et al., 2016b), which can be constrained with future observations with *JWST* (e.g. Zackrisson et al., 2017).

3.6   Conclusions

We have presented the results of X-SHOOTER follow-up observations of a sample of luminous LAE candidates at $z = 5.7 - 6.6$ in the SA22 field. We present the properties of newly confirmed LAEs (summarised in Table 10.1) and compare them with other LAEs and LBGs at similar redshifts. The main results are:

1. We spectroscopically confirm SR6, the most luminous LAE at $z = 5.676$ in the SA22 field. While SR6 has a high Lyα luminosity and extreme EW ($L_{Ly\alpha} = 2.5 \pm 0.3 \times 10^{43}$ erg s^{-1}, EW$_0 > 250$ Å), it has a typical UV continuum luminosity ($M_{1500} = -21.1 \pm 0.1$) and a narrow Lyα line (236 ± 16 km s^{-1}).

2. We confirm VR7, the most luminous LAE at $z = 6.532$, in the SA22 field ($L_{Ly\alpha} = 2.4 \pm 0.2 \times 10^{43}$ erg s^{-1}, EW$_0 > 196$ Å and $v_{FWHM} = 340 \pm 14$ km s^{-1}, see §3.4.2). Among the luminous LAEs known at $z \sim 6.5$, VR7 is also the most luminous in the UV found so far ($M_{1500} = -22.5 \pm 0.2$). Despite this luminosity, we do not detect any signs of AGN activity (such as C IV

or MgII emission) in the spectrum at the current depths ($f \lesssim 2 \times 10^{-17}$ erg s^{-1} cm^{-2}, EW $\lesssim 20$ Å). In contrast, essentially all LAEs at $z \approx 2 - 3$ with similar Lyα and UV luminosities are AGN.

3. Lyα line-widths increase slowly with Lyα luminosity at $z = 5.7$, while such a trend is not seen at $z = 6.6$. We find indications that the line-widths of LAEs with L$_{\text{Ly}\alpha} \approx 10^{42.5}$ erg s^{-1} increase between $z = 5.7 - 6.6$ (§3.5.1), although at relatively low statistical significance due to small sample sizes. This evolution occurs at the same luminosity where the number densities decrease, and Lyα spatial scales increase (Santos et al., 2016), all indicating patchy reionisation.

4. In §3.5.2, we argue empirically that rest-UV lines besides Lyα are most easily observed in galaxies with relatively low Lyα EWs. This explains why carbon lines have been detected in luminous UV-continuum selected sources, while they have not been easily detected in Lyα selected sources.

5. Combining our sources with a compilation of LAEs and LBGs at $z \approx 6 - 7$, we do not detect a clear relation between the Lyα luminosity and absolute UV magnitude at $z = 5.7$ indicating a lower Lyα escape fraction at brighter UV luminosities, for example due to dust (§3.5.3). There is a large dispersion in absolute UV magnitudes of $> L^\star$ LAEs of $\sigma = 0.9$ dex.

6. At $z = 6.6$, we find that, at M$_{1500} < -21$, the Lyα and UV luminosity are strongly correlated, while there is no evidence for a relation at fainter UV luminosities. This means that the Lyα escape fraction and/or its production rate increases strongly among luminous LAEs between $z = 5.7 - 6.6$. Most luminous LAEs show multiple components in the rest-UV. This could indicate that such merging systems could boost effective Lyα transmission through the IGM at $z > 6.5$, increasing the effective Lyα escape fraction.

7. Under basic assumptions, we find that several LAEs at $z \approx 6 - 7$ would have Lyα escape fractions $\gtrsim 100$ %, which could indicate bursty star-formation histories, alternative Lyα production mechanisms, a higher ionising production efficiency, or dust attenuating Lyα in a different way than the UV continuum.

8. Using an empirical relation to estimate the Lyα escape fraction, we present a method to compute ξ_{ion}, the production efficiency of ionising photons, based on Lyα and UV continuum measurements (§3.5.3). Our results indicate that luminous LAEs at $z \approx 6 - 7$ produce ionising photons efficiently, with a median $\log_{10}(\xi_{ion}/\text{Hz erg}^{-1}) = 25.51 \pm 0.09$, similar to other recent measurements of LAEs and LBGs at $z \approx 2 - 5$. These measurements will easily be testable with *JWST*.

In the future, significant improvements can be made by observing a statistical sample of homogeneously selected Lyα emitters at $z = 5.7 - 6.6$ with IFU spectroscopy with *JWST*, which can measure Hα up to $z = 6.6$. Such measurements can constrain any evolution in the effective Lyα escape fraction directly

(due to an increasingly neutral IGM), by controlling for the apertures/spatial scales and positions of the emission (hence the IFU), and allow us to test the empirical models to estimate Lyα escape fractions and ξ_{ion}. The bright, spectroscopically confirmed LAEs are the ideal targets to pioneer such studies as they already show extended/multiple component morphologies.

Acknowledgments

3.A   Galaxy compilation

Here we describe shortly the details of the sample of sources listed in Table 3.6. Part of this sample are narrow-band selected LAEs, where the Lyα flux is measured with a NB (except for WISP302, which is measured with the HST/WFC3

grism, Bagley et al. 2017). The other part of the sample are UV selected Lyman-break galaxies for which the Lyα flux and EW have been measured from slit spectroscopy, except for the grism measurements of RXCJ2248.7-4431 (Schmidt et al., 2017), the GLASS-stack (Schmidt et al., 2016) and FIGS_GN1_1292 (Tilvi et al., 2016). We note that due to extended Lyα emission and slit losses their Lyα luminosities may be under-estimated, in particular when Lyα is offset from the UV emission (e.g. Vanzella et al., 2017). For CR7, we use updated constraints on metal-lines from the recalibrated spectrum that is presented in Sobral et al. (2018a).

In the case Lyα luminosities are not published, we have computed them from the published line-flux and luminosity distance corresponding to the source redshift. For sources from Ding et al. (2017), we have used luminosities from their discovery-papers (Ouchi et al. 2005 and Shimasaku et al. 2006). If not published, M_{1500} is computed based on the observed magnitude in the band closest to a rest-frame $\lambda = 1500$ Å, corrected for the distance modulus and band-width spreading and for possible lensing magnification. In the case of emission-line doublets (such as CIII]$_{1907,1909}$), we use the sum of both lines, except in the case of the OIII] doublet of A1703_zd6, where only one component is measured due to adjacent skylines. Most measurements of/limits on rest-UV lines besides Lyα and Nv have been performed with slit spectroscopy from the ground and are thus significantly hampered by the sky OH emission lines in the near-infrared. This is less of an issue for grism data, although these are limited by their spectral resolution, and thus mostly sensitive to high EW lines. Another employed technique used a matched narrow-band that measures specific emission-lines at specific redshifts, for example CIII] at $z = 5.7$ (Cai et al., 2011, 2015; Ding et al., 2017).

Table 3.6: LAEs included in compilations of line-widths and rest-UV line-ratios.

ID	Redshift	Reference
Lyα selected		
SGP 8884	5.65	Westra et al. (2006); Lidman et al. (2012)
SR6	5.676	**This paper**
Ding-3	5.69	Ouchi et al. (2005); Ding et al. (2017)
Ding-4	5.69	Ouchi et al. (2005); Ding et al. (2017)
Ding-5	5.69	Ouchi et al. (2005); Ding et al. (2017)
Ding-2	5.692	Ouchi et al. (2005); Ding et al. (2017)
Ding-1	5.70	Shimasaku et al. (2006); Ding et al. (2017)
J233408	5.707	Shibuya et al. (2018)
S11 5236	5.72	Westra et al. (2006); Lidman et al. (2012)
J233454	5.732	Shibuya et al. (2018)
J021835	5.757	Shibuya et al. (2018)
WISP302	6.44	Bagley et al. (2017)
VR7	6.532	**This paper**
LAE SDF-LEW-1	6.538	Kashikawa et al. (2012)
J162126	6.545	Shibuya et al. (2018)
J160940	6.564	Shibuya et al. (2018)
J100550	6.573	Shibuya et al. (2018)
J160234	6.576	Shibuya et al. (2018)
Himiko	6.59	Ouchi et al. (2009); Zabl et al. (2015)
COLA1	6.593	Hu et al. (2016)
CR7	6.604	Sobral et al. (2015b)

Table 3.7: LBGs included in compilations of line-widths and rest-UV line-ratios.

ID	Redshift	Reference
UV selected		
WMH S	5.618	Willott et al. (2013)
WMH 13	5.983	Willott et al. (2013)
A383-5.2	6.0294	Richard et al. (2011); Stark et al. (2015a)
WMH 5	6.068	Willott et al. (2013)
RXCJ2248.7-4431-ID3	6.11	Mainali et al. (2017)
RXCJ2248.7-4431	6.11	Schmidt et al. (2017)
CLM 1	6.17	Cuby et al. (2003)
MACS0454-1251	6.32	Huang et al. (2016)
RXJ1347-1216	6.76	Huang et al. (2016)
SDF-46975	6.844	Ono et al. (2012)
IOK-1	6.96	Iye et al. (2006); Cai et al. (2011); Ono et al. (2012)
BDF-521	7.01	Vanzella et al. (2011); Cai et al. (2015)
A1703_zd6	7.045	Stark et al. (2015b)
BDF-3299	7.109	Vanzella et al. (2011)
GLASS-stack	$< 7.2 >$	Schmidt et al. (2016)
GN-108036	7.213	Ono et al. (2012); Stark et al. (2015a)
EGS-zs8-2	7.477	Stark et al. (2017)
FIGS_GN1_1292	7.51	Finkelstein et al. (2013); Tilvi et al. (2016)
EGS-zs8-1	7.73	Oesch et al. (2015); Stark et al. (2017)

CHAPTER 4

On the evidence for PopIII-like stellar populations in the most luminous Lyman-α emitters at the epoch of reionization

Here we present follow-up observations with X-SHOOTER and FORS2 on the VLT, and DEIMOS on Keck of the two most luminous Lyα candidates in the COSMOS field: 'MASOSA' and 'CR7'. We confirm very strong Lyα emission with S/N$>$ 10 at $z = 6.541$ and $z = 6.604$, respectively. MASOSA has a strong detection in Lyα with FWHM=$386 \pm 30 \, \mathrm{km\,s^{-1}}$ and a very high EW$_0$ (> 200Å), but undetected in the continuum, implying low stellar mass and a likely young stellar population. 'CR7', with an observed Lyα luminosity of $10^{43.92 \pm 0.05} \, \mathrm{erg\,s^{-1}}$ is the most luminous Lyα emitter ever found at $z > 6$ and is spatially extended (~ 16 kpc). 'CR7' reveals a narrow Lyα line with FWHM=$266 \pm 15 \, \mathrm{km\,s^{-1}}$ and is detected in the NIR (M$_{1500} = -22.2 \pm 0.1$, $\beta = -2.2 \pm 0.4$) and in *Spitzer*/IRAC (implying strong Hβ/[OIII] emission). We tentatively detect a narrow HeII1640Å emission line ($\approx 3\sigma$, FWHM $= 180 \pm 30 \, \mathrm{km\,s^{-1}}$, EW$_0 = 25 \pm 15$ Å), but no other emission-line in the rest-UV. We conclude that CR7 is best explained by a combination of an extremely metal poor and highly ionising population which dominates the rest-frame UV and the nebular emission and a more normal stellar population. *HST*/WFC3 observations show that the light is indeed spatially separated between a very blue component, coincident with the peak Lyα, and two fainter components (~ 5 kpc away). Our findings are consistent with theoretical predictions of a star-formation occurring in waves, with metal poor star formation migrating away from the original sites of star formation.

Proclaimer

Finding and observing the first generation of stars (PopIII stars) in the early Universe is one of the key goals of extragalactic astrophysics. So far, no PopIII stars have been observed directly, likely because they are only observable for a short time at very high redshift. In 2015, I contributed significantly to an article that presented a luminous galaxy at $z = 6.6$ with promising evidence that hot, low metallicity stellar populations, with properties resembling PopIII stars, resided within it (Sobral et al., 2015b). I identified this galaxy, that we named COSMOS Redshift 7, or CR7 (Matthee et al. 2015; Chapter 2). For the Sobral et al. (2015b) article, I particularly contributed to the photometric measurements, the writing of telescope proposals that lead to the observations, the interpretation of the data and I contributed to the writing of the manuscript.

The Sobral et al. (2015b) article had significant impact in the scientific community. Several research groups theoretically investigated the nature of CR7, leading to a number of articles whose results are summarised in Appendix A of this Chapter. In addition, independent observational investigations by Bowler et al. (2017b) and Shibuya et al. (2018) revisited some of the results from Sobral et al. (2015b), most importantly the strength and significance of the HeII emission line detection. The HeII line, combined with the non-detection of metal lines, has been fundamental for the interpretation that 'PopIII-like' stars reside in CR7. While detailed comparisons to Bowler et al. (2017b) and Shibuya et al. (2018) are presented in Appendices B and C of this Chapter, I note that the interpretation of 'PopIII-like' stars in CR7 is most reliably refuted by our [CII] detection with ALMA (Matthee et al. 2017e; Chapter 5).

Since 2015, new data, analysis methods and interactions with the community drove us to update parts of the Sobral et al. (2015b) article. These updates are presented in an article that Sobral, Matthee et al. submitted to *MNRAS*, but which is not yet accepted for publication. To simultaneously reflect the initial results and the natural advancement of science, the following Chapter is a version of the Sobral et al. (2015b) article rewritten slightly in the light of lessons learned over the past three years, while maintaining its structure, main result, discussion and conclusions that have motivated the interest in the community. I re-analysed and re-reduced the X-SHOOTER spectrum independently (§4.3.3; similar to the analysis in Chapter 6) and do not include SINFONI observations. A subsection is added that discusses differences with respect to the Sobral et al. (2015b) reduction, in particular focusing on the updated significance of the HeII line (§4.3.4). The main text uses the photometric data available at the time of writing the Sobral et al. (2015b) article for its relevance to the impact of the article and its influence on literature articles. However, a subsection is added with revised UltraVISTA DR3 photometry and their implications (§4.5.5).

4.1 Introduction

The study of the most distant sources such as galaxies, quasars and gamma ray bursts offers unique constraints on early galaxy and structure formation. Such

observations are particularly important to test and refine models of galaxy formation and evolution (e.g. Vogelsberger et al., 2014; Schaye et al., 2015) and to study the epoch of re-ionisation (e.g. Furlanetto et al., 2004; McQuinn et al., 2006; Iliev et al., 2006). Over the last two decades, considerable effort has been dedicated towards finding the most distant sources. More recently, and particularly due to the upgraded capabilities of *HST*, multiple candidate galaxies up to $z \sim 8 - 11$ (e.g. Bouwens et al., 2011; Ellis et al., 2013) have been found with deep broad-band photometry. However, spectroscopic confirmation is still limited to a handful of galaxies and quasars at $z > 6.5$ (e.g. Mortlock et al., 2011; Ono et al., 2012; Schenker et al., 2014; Finkelstein et al., 2013; Pentericci et al., 2014; Oesch et al., 2015), for both physical (galaxies becoming increasingly fainter) and observational reasons (the need for deep near-infrared exposures).

At these redshifts ($z > 6.5$), the Lyα line is virtually the only line available to confirm sources with current instruments. However, Lyα is easily attenuated by dust and neutral hydrogen in the inter-stellar and inter-galactic medium. Indeed, spectroscopic follow-up of UV-selected galaxies indicate that Lyα is suppressed at $z > 7$ (e.g. Caruana et al., 2014; Tilvi et al., 2014) and not a single $z > 8$ Lyα emitter candidate has been confirmed yet (e.g. Sobral et al., 2009b; Faisst et al., 2014; Matthee et al., 2014). If the suppression of Lyα is mostly caused by the increase of neutral hydrogen fraction towards higher redshifts, it is clear that $z \sim 6.5$ (just over 0.8 Gyrs after the Big Bang) is a crucial period, because re-ionisation should be close to complete at that redshift (e.g. Fan et al., 2006).

Narrow-band searches have been successful in detecting and confirming Lyα emitters at $z \sim 3 - 7$ (e.g. Cowie & Hu, 1998; Malhotra & Rhoads, 2004; Iye et al., 2006; Murayama et al., 2007; Hu et al., 2010; Ouchi et al., 2010). The results show that the Lyα luminosity function is constant from $z \sim 3$ to $z \sim 6$, but there are claims that the number density drops from $z \sim 6$ to $z \sim 6.6$ (e.g. Ouchi et al., 2010; Kashikawa et al., 2011) and that it drops at an even faster rate up to $z \sim 7$ (e.g. Shibuya et al., 2012; Konno et al., 2014). Moreover, the fact that the rest-frame UV luminosity function declines from $z \sim 3 - 6$ (e.g. Bouwens et al., 2015a) while the Lyα luminosity function (LF) is roughly constant over the same redshift range (e.g. Ouchi et al., 2008) implies that the cosmic average Lyα escape fraction is likely increasing, from $\sim 5\%$ at $z \sim 2$ (e.g. Hayes et al., 2010; Ciardullo et al., 2014), to likely $\sim 20 - 30\%$ around $z \sim 6$ (e.g. Cassata et al., 2015). Surprisingly, it then seems to fall sharply with increasing redshift beyond $z \sim 6.5$. Current results could be a consequence of re-ionisation not being completed at $z \sim 6 - 7$, particularly when taken together with the decline in the fraction of Lyman break selected galaxies with high EW Lyα emission (e.g. Tilvi et al., 2014; Caruana et al., 2014; Pentericci et al., 2014). However, it is becoming clear that re-ionisation by itself is not enough to explain the rapid decline of the fraction of strong Lyα emitters towards $z \sim 7$ (e.g. Dijkstra, 2014; Mesinger et al., 2015).

It is likely that re-ionisation was very heterogeneous/patchy (e.g. Pentericci et al., 2014), with the early high density regions re-ionising first, followed by the rest of the Universe. If that were the case, this process could have a distinguishable effect on the evolution of the Lyα luminosity function, and it may be that

the luminous end of the luminosity function evolves differently from the fainter end, as luminous Lyα emitters should in principle be capable of ionising their surroundings and thus are easier to observe. This is exactly what is found by Matthee et al. (2015), in agreement with spectroscopic results from Ono et al. (2012).

In addition to using Lyα emitters to study re-ionisation, they are also useful for identifying the most extreme, metal poor and young galaxies. Studies of Lyα emitters at $z > 2 - 3$ show that, on average, these sources are indeed very metal poor (Finkelstein et al., 2011; Nakajima et al., 2012; Guaita et al., 2013), presenting high ionisation parameters (high [O$\textsc{iii}$]/Hβ line ratios; Nakajima et al. 2013) and very low typical dust extinctions (e.g. Ono et al., 2010). Given these observations, Lyα searches should also be able to find metal-free, PopIII stellar populations (since galaxies dominated by PopIII emit large amounts of Lyα photons, e.g. Schaerer 2002, 2003). However, so far, although some candidates for PopIII stellar populations have been found (e.g. Jimenez & Haiman, 2006; Dijkstra et al., 2007; Nagao et al., 2008; Kashikawa et al., 2012; Cassata et al., 2013), and some metal poor galaxies have been confirmed (e.g. Prescott et al., 2009), they are all significantly more metal rich than the expected PopIII stars, and show e.g. C$\textsc{iii}$] and C$\textsc{iv}$ emission. For example, when there is no evidence for the presence of an AGN and no metal lines, the short-lived He$\textsc{ii}$1640Å emission line (the 'smoking gun' for PopIII stars in extremely high EW Lyman-α emitters without any metal emission line) was never detected with high enough EW (e.g. Nagao et al., 2008; Kashikawa et al., 2012).

Until recently, Lyα studies at the epoch of re-ionisation have been restricted to the more numerous, relatively faint sources of $L_{Ly\alpha} \sim 10^{42.5}$ erg s^{-1} (with some exceptions, e.g. $z = 5.7$ follow-up: Westra et al. 2006; Lidman et al. 2012; and 'Himiko': Ouchi et al. 2009). However, with the wide-field capabilities of current instruments (including Hyper Suprime-Cam; Miyazaki et al. 2012), the identification of luminous Lyα emitters will become increasingly easier. Recently, significant progress was made towards finding luminous Lyα emitters at $z = 6.6$ (Matthee et al., 2015), through a $\sim 5\,\mathrm{deg}^2$ narrow-band survey, which resulted in the identification of the most luminous Lyα emitters at the epoch of re-ionisation. Matthee et al. (2015) reproduced the Lyα luminosity function of Ouchi et al. (2010) for relatively faint Lyα emitters at $z = 6.6$ for the UDS field, who find a decrease in their number density compared to lower redshifts.

However, Matthee et al. (2015) find that the luminous end of the $z = 6.6$ LF resembles the $z = 3 - 5.7$ luminosity function, and is thus consistent with no evolution at the bright end since $z \sim 3$. Extremely luminous Lyα emitters at $z \sim 6.6$ are thus found to be much more common than expected, with space densities of $1.5^{+1.2}_{-0.7} \times 10^{-5}$ Mpc^{-3}. The results may mean that, because such bright sources can be observed at $z \sim 6.6$, we are witnessing preferential re-ionisation happening around the most luminous sources first. Such luminous sources may already be free (in their immediate surroundings) of a significant amount of neutral hydrogen, thus making their Lyα emission observable. Furthermore, these sources open a new window towards exploring the stellar populations of the most luminous Lyα emitters at the epoch of re-ionisation even before the *James*

Table 4.1: Observation log for the two luminous Lyα emitter candidates, CR7 (10 00 58.005 +01 48 15.251, J2000) and MASOSA (10 01 24.801 +02 31 45.340, J2000) using Keck/DEIMOS and VLT/FORS2 & X-SHOOTER (XSH).

Source	Exp. time [ks]	Dates	Features
CR7	DEIMOS: 5.4	28 Dec 2014	Lyα
CR7	XSH VIS: 8.1	22 Jan, 15 Feb 2015	Lyα
CR7	XSH NIR: 9.9	22 Jan, 15 Feb 2015	HeII 1640 Å (15 Feb only)
MASOSA	DEIMOS: 2.7	29 Dec 2014	Lyα
MASOSA	FORS2: 6.0	12 Jan 2015	Lyα

Webb Space Telescope (*JWST*) and $\sim 30 - 40$ m class telescopes (Extremely Large Telescopes, ELTs) become operational, as these are bright enough to be studied in unprecedented detail with e.g. *HST*, ALMA, VLT, Keck.

Here we present spectroscopy of the two most luminous Lyα emitters found so far at the epoch of re-ionisation ($z \sim 7$). This paper is organised in the following way. §2 presents the observations, the Lyα emitter sample, and the data reduction. §3 outlines the details of the optical and near-infrared spectroscopic observations and measurements with the VLT and Keck data. §4 presents the discovery of the most luminous Lyα emitters and comparison with previous studies. §5 discusses SED fitting, model assumptions and how *HST* high spatial resolution data corroborates our best interpretation of the data. §6 presents the discussion of the results. Finally, §7 outlines the conclusions. A $H_0 = 70 \, \mathrm{km \, s^{-1} \, Mpc^{-1}}$, $\Omega_M = 0.3$ and $\Omega_\Lambda = 0.7$ cosmology is used. We use a Salpeter (Salpeter, 1955) IMF and all magnitudes are in the AB system, unless noted otherwise.

4.2 Sample and Spectroscopic observations

4.2.1 The luminous Lyα candidates at $z = 6.6$

Matthee et al. (2015) used the Subaru telescope and the NB921 filter on Suprime-cam (Miyazaki et al., 2002) to survey $\sim 3 \, \mathrm{deg}^2$ in the SA22 (PI: D. Sobral), $\sim 1 \, \mathrm{deg}^2$ in COSMOS/UltraVISTA (PI: M. Ouchi) and $\sim 1 \, \mathrm{deg}^2$ in UDS/SXDF (PI: M. Ouchi) fields in order to obtain the largest sample of luminous Lyα emitters at the epoch of re-ionisation.

Out of the 135 Lyα candidates found in Matthee et al. (2015), we discover two very bright Lyα candidates in the COSMOS/UltraVISTA field: 'CR7' (COSMOS Redshift 7) and MASOSA[1]. MASOSA is particularly compact (0.7″), while CR7 is extended ($\sim 3''$). We show the location of the Lyα emitters within the COSMOS field footprint in Figure 4.1, in which the size of the symbols scales with luminosity. We also show their properties in Table 4.2.

---

[1] The nickname MASOSA consists of the initials of the first three authors of Matthee et al. (2015)

Thumbnails in various wavelengths ranging from observed optical to observed mid-infrared are shown in Figure 4.2. Both candidates show very high rest-frame Lyα EWs[2] in excess of > 200 Å. By taking advantage of the wealth of data in the COSMOS/UltraVISTA field (e.g. Capak et al., 2007; Scoville et al., 2007; Ilbert et al., 2009; McCracken et al., 2012), we obtain multi-band photometry for both sources. The measurements are given in Table 4.2. We re-measure the $3.6\,\mu$m and $4.5\,\mu$m photometry for CR7, in order to remove contamination from a nearby source. Such contamination is at the level of 10-20%, and is added in quadrature to the photometry errors.

We find that CR7 has very clear detections in the near-infrared and midinfrared (Figure 4.2), showing a robust Lyman-break (Steidel et al., 1996). CR7 is detected in *Spitzer*/IRAC, with colors as expected for a $z \sim 6.6$ source (Smit et al., 2014), likely due to contribution from strong nebular lines with EWs in excess of a few 100 Å in the rest-frame optical (see Figure 4.2). Because of the detections in the NIR and MIR, the rest-frame UV counterpart of CR7 was already identified as a $z \sim 6 - 7$ Lyman-break candidate (Bowler et al., 2012, 2014). However, because of its very uncommon NIR colors in the UltraVISTA DR2 data (i.e. excess in J relative to Y, H and K), the clear IRAC detections, and, particularly, without the NB921 data (Figure 4.2), it was classed as an unreliable candidate, possibly a potential interloper or cool star. MASOSA has a clear detection in the narrow-band and is weakly detected in z, but the z band detection can be fully explained by Lyα. It is not detected at $> 1\sigma$ in the NIR ($J > 25.7$, $H > 24.5$, $K > 24.4$), although a very weak signal is visible in the thumbnails (Figure 4.2). This indicates that the Lyα EW is very high and highlights that the Lyman-break selection can easily miss such sources, even if they are extremely bright and compact in Lyα, as MASOSA is not detected at the current depth of the UltraVISTA survey (Bowler et al., 2014).

4.2.2   Spectroscopic observations and data reduction

Spectroscopic observations were made with the Very Large Telescope (VLT)[3] using X-SHOOTER (for CR7) and FORS2 (for MASOSA). The choice of X-SHOOTER for CR7 was due to the fact that it was detected in the NIR and showed evidence for excess in the J band, likely indicating strong emission lines. Both sources were observed with DEIMOS on the Keck II telescope (see Table 4.1) as well. Spectra for both sources, obtained with both the VLT and Keck, are shown in Figure 4.3, including the spectra obtained by combining both data-sets.

DEIMOS/Keck observations

DEIMOS/Keck observations targeted both 'CR7' and 'MASOSA' in two different masks and two different nights. Observations were conducted on 28 and 29 December 2014. The seeing was $\sim 0.5''$ on the first night, when we observed

---

[2] EWs computed by using either z or Y lead to results in excess of 200 Å. We also present EWs computed based on Y band and from our spectroscopic follow-up in Table 4.2.

[3] Observations conducted under ESO DDT programs 294.A-5018 and 294.A-5039; PI: D. Sobral.
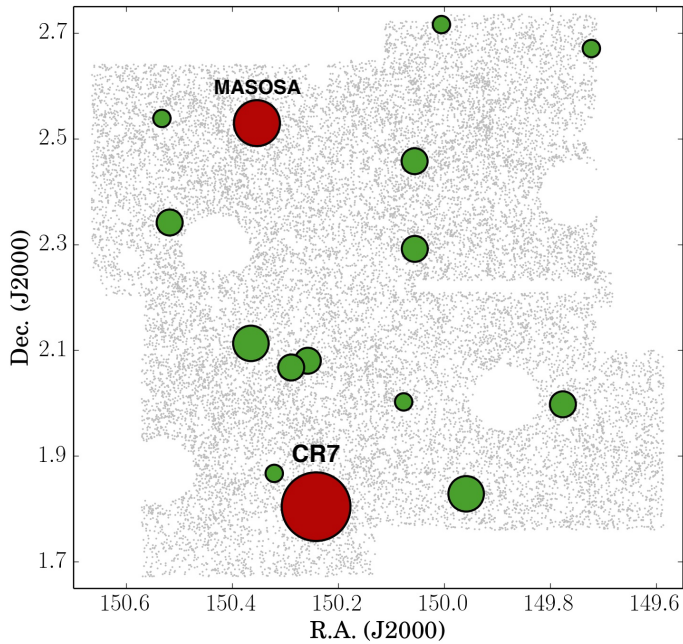
Figure 4.1: Projected positions on sky of all Lyα candidates (green circles) found in the COS-MOS/UltraVISTA field. The grey background points represent all detected sources with the NB921 filter, highlighting the masking applied (due to the presence of artefacts caused by bright stars and noisy regions, see Matthee et al., 2015). Lyα candidates are plotted with a symbol size proportional to their Lyα luminosity. CR7 and MASOSA are highlighted in red: these are the most luminous sources found in the field. Their coordinates are given in Table 4.1.
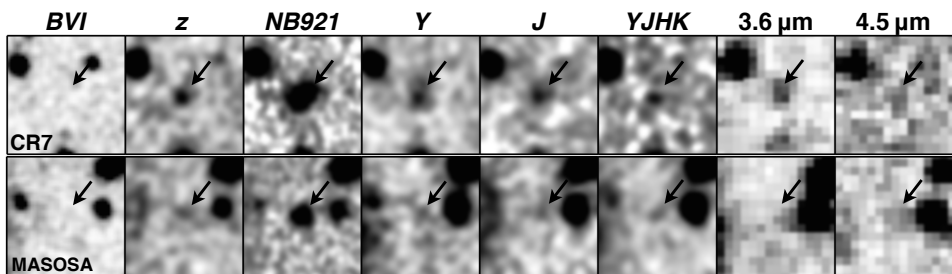
Figure 4.2: Thumbnails of both luminous Lyα emitters in the optical to MIR from left to right. Each thumbnail is $8 \times 8''$, corresponding to $\sim 44 \times 44$ kpc at $z \sim 6.6$. Note that while for MASOSA the Lyα emission line is detected by the NB921 filter at full transmission, for CR7 the Lyα is only detected at $\sim 50\%$ transmission. Therefore, the NB921 only captures $\sim 50\%$ of the Lyα flux: the observed flux coming from the source is $\sim 2\times$ larger.

'CR7', and $\sim 0.7''$ on the second night, when we observed 'MASOSA'. Observations were done under clear conditions with midpoint airmass of < 1.1 for both sources. We used a central wavelength of 7200 Å and the 600I grating, with a resolution of 0.65 Å pix^{-1}, which allowed us to probe from 4550 Å to 9850 Å. We used the 0.75$''$ slit.

For CR7, we obtained 4 individual exposures of 1.2 ks and one exposure of 0.6 ks, resulting in a total of 5.4 ks. For MASOSA, we obtained a total of 2.7 ks. A strong, extended and asymmetric line is clearly seen in every individual 1.2 ks exposure prior to any data reduction.

We reduced the data using the DEIMOS spec2d pipeline (Cooper et al., 2012; Newman et al., 2013). The observed spectra were flat-fielded, cosmic-ray-removed, sky-subtracted and wavelength-calibrated on a slit-by-slit basis. We used standard Kr, Xe, Ar and Ne arc lamps for wavelength solution and calibration. No dithering pattern was used for sky subtraction. The pipeline also generates 1D spectrum extraction from the reduced 2D per slit, and we use the optimal extraction algorithm (Horne, 1986). This extraction creates a one-dimensional spectrum of the target, containing the summed flux at each wavelength in an optimised window. We also extract the spectrum of both sources with varying apertures and at various positions, in order to take advantage of the fact that the sources are clearly spatially resolved. The final spectrum is shown in Figure 4.3.

FORS2/VLT observations

FORS2/VLT (Appenzeller et al., 1998) observations targeted 'MASOSA' and were obtained on 12 January and 11 February 2015. The seeing was 0.7$''$ and observations were done under clear conditions. We obtained individual exposures of 1 ks and applied 3 different offsets along the slit. In total, we obtained 6 ks. We used the OG590+32 filter together with the GRIS300I+11 Grism (1.62 Å pix^{-1}) with the 1$''$ slit. Lyα is clearly seen in each individual exposure of 1 ks.

We use the ESO FORS2 pipeline to reduce the data, along with a combination of Python scripts to combine the 2D and extract the 1D. The steps implements follow a similar procedure to that used for DEIMOS.

X-SHOOTER/VLT observations

Our X-SHOOTER/VLT (Vernet et al., 2011) observations targeted 'CR7' and were obtained on 22 January 2015 and 15 February 2015. The seeing varied between 0.8$''$ and 0.9$''$ and observations were done under clear conditions. We obtained individual exposures of 0.27 ks for the optical arm, while for NIR we used individual exposures of 0.11 ks. We nodded from an A to a B position, including a small jitter box in order to always expose on different pixels. We used 0.9$''$ slits for both the optical and near-infrared arms (resolution of $R \sim 7500$ and $R \sim 5300$, for the optical and near-infrared arms, respectively). In total, for the X-SHOOTER data, we obtained 8.1 ks in the optical and 9.9 ks in the NIR. The differences are driven by the slower read-out time in the optical CCD compared to the NIR detector.
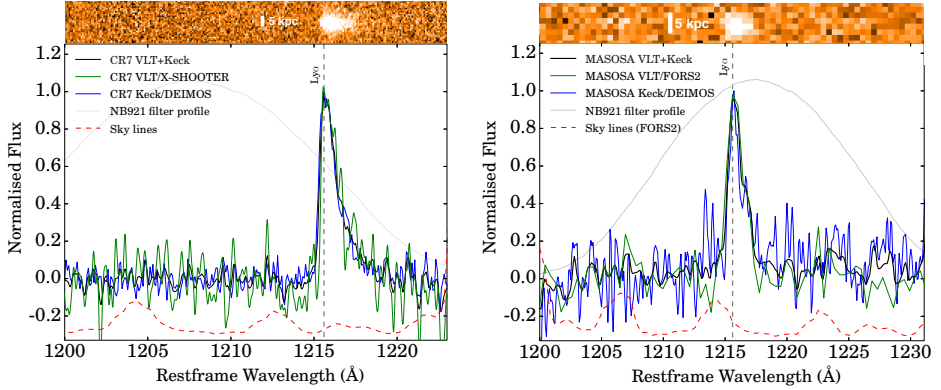
Figure 4.3: *Left*: 'CR7' 1-D and 2-D optical spectra, showing the strong and clear Lyα emission line. We also show the NB921 filter profile which was used to select the source. Note that Lyα is detected at the wing of the NB921 filter. Thus, while the NB921 photometry already implied the source was very luminous, its true luminosity was still underestimated by a factor of two. We show both our Keck/DEIMOS and VLT/X-SHOOTER spectra, which show perfect agreement, but with X-SHOOTER providing a higher spectral resolution. *Right*: 'MASOSA' 1-D and 2-D optical spectra (FORS2), showing the strong and clear Lyα emission line. We show both the VLT/FORS2 and Keck/DEIMOS spectra, showing they agree very well. The DEIMOS spectrum provides higher resolution, but both clearly reveal the asymmetry of the line, confirming it as Lyα without any doubt.

For the January observation a PA angle of 0 deg was used, together with an acquisition source at 10:01:03.156 +01:48:47.885 (J2000). Offsets of −77.266″ (R.A.) and −32.634″ (Dec.) were used to offset from the acquisition source to CR7. The acquisition for the first OB (OB1, 22 January 2015) was suspected to be relatively off-target due to an unreliable acquisition star centring (acquisition star was not centred in the slit), leading to an apparent lower Lyα flux. In order to avoid problems with acquisition, another acquisition source was used for the February observations: 10:01:00.227, 01:48:42.992 (J2000), applying an offset of −33.342″ (R.A.) and −27.742″ (Dec.) and this time with a PA angle of −39.76 deg, in order to better align the slit with the elongation of the Lyα 2D distribution obtained from the narrow-band imaging.

We use the X-SHOOTER pipeline to reduce the observations in the optical and NIR spectra separately (v2.4.8; Modigliani et al. 2010). Each observing block of one hour is reduced separately, including flux calibration using a standard star. We then median combine the reduced 2D spectra after centering each spectrum on the spatial pixel where the Lyα flux peaks, but we also inspect spectra of individual observation blocks. The final Lyα spectrum, for which we extracted the 1D spectrum using the native pixel scale that oversampled the line spread function, is shown in Figure 4.3.

Table 4.2: A summary of our results for CR7 and MASOSA. These include both the spectroscopic measurements, but also photometry. In order to provide an easy comparison, we also provide the measurements for Himiko, the other luminous source in the Matthee et al. (2015) sample, fully presented in Ouchi et al. (2013).

Measurement	CR7	MASOSA	Himiko
z_{spec} Lyα	$6.604^{+0.001}_{-0.003}$	6.541 ± 0.001	6.54
β UV slope	-2.3 ± 0.08	—	-2.0 ± 0.57
Lyα (FWHM, km s^{-1})	266 ± 15	386 ± 30	251 ± 21
Lyα (EW$_{0,\text{obs,Ycont}}$, Å)	211 ± 20	> 206	78 ± 8
Lyα (EW$_{0,\text{obs,spec}}$, Å)	> 230	> 200	—
Lyα (Log$_{10}$L, erg s^{-1})	43.93 ± 0.05	43.38 ± 0.06	43.40 ± 0.07
Lyα/NV	> 70	—	—
He$\textsc{ii}$/Lyα	0.11 ± 0.04	—	—
He$\textsc{ii}$ (EW$_0$, Å)	$25 \pm 15\ (> 20)$	—	—
He$\textsc{ii}$ (FWHM, km s^{-1})	180 ± 30	—	—
He$\textsc{ii}$/OIII]1663	> 2.5	—	—
He$\textsc{ii}$/CIII]1908	> 2	—	—
Photometry	CR7	MASOSA	Himiko
z	25.35 ± 0.20	26.28 ± 0.37	25.86 ± 0.20
NB921 2$''$ aperture	23.70 ± 0.04	23.84 ± 0.04	23.95 ± 0.02
NB921 $\textsc{mag-auto}$	23.24 ± 0.03	23.81 ± 0.03	23.55 ± 0.05
Y	24.92 ± 0.13	> 26.35	25.0 ± 0.35
J	24.62 ± 0.10	> 26.15	25.03 ± 0.25
H	25.08 ± 0.14	> 25.85	25.5 ± 0.35
K	25.15 ± 0.15	> 25.65	24.77 ± 0.29
3.6μm	23.86 ± 0.17	> 25.6	23.69 ± 0.09
4.5μm	24.52 ± 0.61	> 25.1	24.28 ± 0.19

4.3 Measurements and SED fitting

4.3.1 Redshifts

In both the VLT (FORS2 or X-SHOOTER) and Keck (DEIMOS) spectra for the two targets, we detect the very strong Lyα line (Figure 4.3) in emission, and no continuum either directly red-ward or blue-ward of Lyα. The very clear asymmetric profiles leave no doubts about them being Lyα and about the secure redshift (Figure 4.3). Particularly for CR7, the high S/N > 25 (combined Keck and VLT) at Lyα, despite the very modest exposure time for such a high-redshift galaxy, clearly reveals this source is unique.

Based on Lyα, we obtain redshifts of $z = 6.604$ for CR7 and $z = 6.541$ for MASOSA. The redshift determination yields the same answer for both our data-sets: X-SHOOTER and DEIMOS, for CR7 and FORS2 and DEIMOS, for MASOSA (see Figure 4.3, which shows the agreement). It is worth noting that for CR7 we find that the Lyα emission line is detected in a lower transmission region of the NB921 filter profile (50% of peak transmission). Therefore, the Lyα luminosity of CR7 is higher than estimated from the NB921 photometry, making the source even more luminous than thought.

4.3.2 Spectral line measurements

By fitting a Gaussian profile to the emission lines, we measure the EW (lower limits, as no continuum is detected) and FWHM. Emission line fluxes are obtained by using NB921 and Y photometry (similarly to e.g. Ouchi et al. 2009, 2013), in combination with the NB921 filter profile and the appropriate redshift. We also check that the integrated emission line (without any assumption on the fitting function) provides results which are fully consistent.

For MASOSA, we find no other line in the optical spectrum, and also find no continuum at any wavelength probed (see Figure 4.3). For CR7, we find no continuum either directly blue-ward or red-ward of Lyα in the optical spectrum (both in X-SHOOTER and DEIMOS; Figure 4.3).

4.3.3 Revised analysis of X-SHOOTER/NIR spectrum of CR7

We explore our X-SHOOTER NIR spectrum to look for any other emission lines in the spectrum of CR7. In order to extract 1D spectra, we first smooth the 2D spectrum with a gaussian kernel in the spatial direction with $\sigma = 0.4''$, which is similar to the seeing PSF FWHM of $\approx 0.8 - 0.9''$. Then, we bin the spectrum in the wavelength direction by a factor 3 in order to increase the S/N. This results in a pixel scale of 1.8 Å px^{-1}, still sampling the instrumental resolution with two pixels. The 1D spectrum is extracted using a box of 2.0$''$ in order to be able to identify slightly off-centred emission lines. In each binning step, the noise level estimated from the X-SHOOTER pipeline is propagated.

We mask all regions for which the error spectrum is too large ($> 1.5\times$ the error on OH line free regions), including the strongest OH lines. We then inspect

the spectrum for any emission lines. In the full stack, we find a tentative emission line at $\lambda_{obs,vacuum} = 12473$ Å (see Figure 4.4), slightly off-centred from the peak Lyα emission (0.8″ in the north-west direction)[4]. We find no other emission lines in the spectrum (Figure 4.4). The emission line found, at $z = 6.603 \pm 0.001$, corresponds to 1640.47 Å, and thus we associate it with He$\textsc{ii}$. For an optimal extraction of this flux, we shift the centre of our extraction box 0.8‴. Given the line flux ($1.7 \pm 0.5 \times 10^{-17}$ erg s^{-1} cm^{-2}), and the level of continuum estimated from e.g. Y and H bands, the spectrum indicates EW$_0 = 25 \pm 15$ Å, lower than the excess indicated by the UltraVISTA DR2 photometry (EW$_0 \sim 80$ Å). We find that the He$\textsc{ii}$1640 Å emission line is narrow (180 ± 30 km s^{-1} FWHM), and detected at $\approx 3\sigma$ in the fully combined X-SHOOTER data. Results based on the extraction of the full stack are presented in Table 4.2.

The He$\textsc{ii}$1640 Å emission line implies a small velocity offset of 100 ± 50 km s^{-1} between the peak of Lyα and He$\textsc{ii}$1640 Å (i.e., the Lyα peak is red-shifted by $+100$ km s^{-1} in respect to He$\textsc{ii}$, which could also be interpreted as an outflow). This means that, not surprisingly, we are only detecting the red wing of the Lyα line, while both the blue wing and any potential Lyα component with $< +160$ km s^{-1} is being likely absorbed and cannot be observed. This may imply that the intrinsic Lyα luminosity and the EW will be even larger than measured.

A more detailed analysis of individual one hour observation blocks reveals that the signal can almost solely be attributed to the third observation, performed using a different position angle than the other two. In this OB only, the line is detected at $\approx 4\sigma$ significance after smoothing and binning the spectrum as described above, and by propagating the noise-model from the pipeline. In this spectrum, shown in Fig. 4.4, the line has a line flux $2.3 \pm 0.6 \times 10^{-17}$ erg s^{-1} cm^{-2}, implying an EW$_0 = 35 \pm 20$ Å. This emphasises the need for spatially resolved spectroscopy in luminous galaxies such as CR7 and careful analysis once observations over multiple position angles are combined.

4.3.4   Comparison to Sobral et al. (2015b) X-SHOOTER measurements

The X-SHOOTER NIR measurements presented above differ from those originally published in the Sobral et al. (2015b) article. The two main differences are the redshift at which He$\textsc{ii}$ is detected and the strength of the He$\textsc{ii}$ line. The former determines the velocity offset between Lyα and He$\textsc{ii}$, while the latter is related to the measured EW and the significance of the detection. The origin of these differences is discussed here.

Our re-analysis of the X-SHOOTER data revealed a problem with the wavelength calibration in Sobral et al. (2015b) due to the use of outdated arc-calibration files. As a result, the wavelength solution was off by ~ 6 Å around the wavelength at which He$\textsc{ii}$ was detected. The Sobral et al. (2015b) article

---

[4] We note that while Sobral et al. (2015b) associated the emission line to clump A, our updated analysis indicates this may not be the case.

states an (air) wavelength of 12464 Å, that corresponds to a vacuum wavelength of 12468 Å, or a Heɪɪ redshift of $z = 6.600$. Here, we find that the wavelength of the line (in vacuum) is 12473 Å, corresponding to a Heɪɪ redshift of $z = 6.603$. This decreases the velocity offset between Heɪɪ and Lyα and also influences the comparison performed by Shibuya et al. (2018), see Appendix C.

Another difference between the X-SHOOTER reduction presented here and the one used in Sobral et al. (2015b) is that flux calibration has been performed with a standard star, while Sobral et al. (2015b) used the UltraVISTA DR2 J band photometry. As discussed below in §4.5.5, a more recent version of the UltraVISTA data reveals that the J band magnitude used for the calibration in Sobral et al. (2015b) was over-estimated by 0.5 magnitude, which translates into a significant over-estimate of the Heɪɪ line flux by a factor ≈ 2. This results in a lower revised Heɪɪ luminosity and EW.

In the Sobral et al. (2015b) analysis, the Heɪɪ line is detected at 6σ significance in the full stack, while we find 3σ here in the same data (full stack of the three observation blocks). The difference originates from the following: i) Sobral et al. (2015b) smoothed the data using a kernel that corresponds to the point spread function in the spatial direction and the line spread function in the wavelength direction (this kernel is larger than the smoothing kernel used in this analysis), ii) the noise estimate used in this analysis is the propagated pipeline error model, that potentially is overestimated (as can be seen in Fig. 4.4, more than 68 % of the points lie within the 1σ noise level; the overestimated propagated noise from the pipeline is discussed in detail in Zabl et al. 2015), Sobral et al. (2015b) contrarily estimate the noise on the actual data in skyline-free regions around the observed feature, iii) the red part of the Heɪɪ line is slightly contaminated by a weak skyline that had been masked in Sobral et al. (2015b), but increases the uncertainty of the flux measurement in this analysis. Therefore, the measurement that the line is detected at 3σ is on the conservative side.

How does the new X-SHOOTER analysis affect the interpretation of CR7 and how does it affect the discussion section of this Chapter compared to Sobral et al. (2015b)? In fact, it does not make much of a difference if one is willing to assume the detected feature is a real line. The reduced Heɪɪ luminosity reduces the hardness of the spectrum somewhat (which was challenging to explain even with the hottest PopIII stars, see §4.6.2) and a slightly lower mass of PopIII-like star formation is required (but within the same order of magnitude and hence likely still problematic to keep unpolluted from metals until $z = 6.6$, see the discussion in Appendix A). The lower Heɪɪ EW is still challenging to explain with 'normal' binary stellar populations, and requires a highly α-enhanced (iron poor) stellar population (Bowler et al., 2017b).

4.4 Discovery of the most luminous Lyα emitters

4.4.1 MASOSA

MASOSA is particularly compact (0.7″ in diameter, corresponding to 3.8 kpc diameter at $z = 6.541$). It is similar to sources now found by MUSE (e.g. Bacon
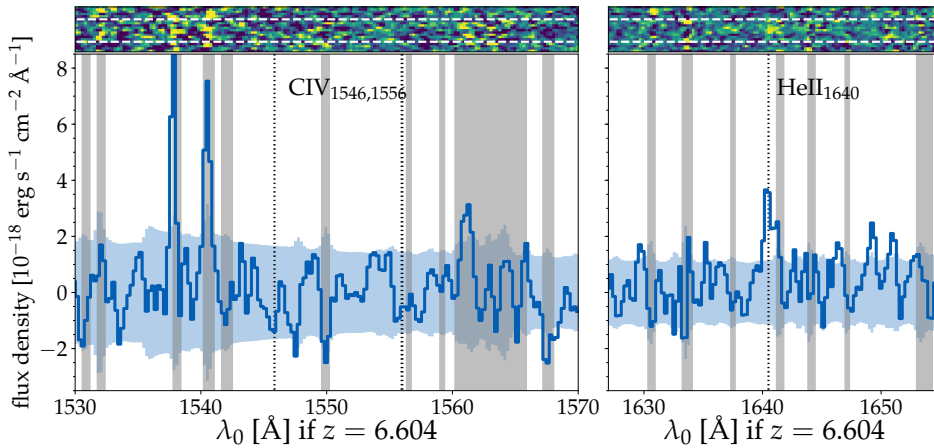
Figure 4.4: X-SHOOTER NIR spectrum of CR7, showing the tentative HeII detection. The Figure shows the spectrum from the observation in February (see text) and the extraction window, indicated by dashed white lines in the 2D spectrum, is shifted to center on the tentative line. The blue shaded region shows the 1σ noise level. The HeII1640 Å emission line is detected at 4σ using this method ($\approx 3\sigma$ in the full stack), while there is no detection of the CIV1546,1556 Å doublet. The dotted vertical line indicates the Lyα redshift. Sky lines were explicitly masked (illustrated with grey shaded regions), but some residuals are still visible, including those of two OH lines just redder of the HeII emission line, which show up as a slight flux increase and another one bluer of HeII, which has been slightly over-subtracted. No continuum is found in the NIR spectra, and that we would require significantly deeper observations in order to detect it simply based on the NIR photometry.

et al., 2015; Karman et al., 2015), that are completely undetected in the continuum and thus similar to typical Lyα emitters that have been found over the last years with e.g. Subaru/Suprime-cam. However, MASOSA is extremely bright in Lyα and thus separates it from the very faint sources found with MUSE in the HDF South and from other Lyα emitters. MASOSA is undetected in all continuum bands at all wavelengths and even the weak detection in z' can be fully explained by the luminous Lyα line and little to no continuum. The estimated rest-frame EW of the Lyα line from spectroscopy is very high (> 200 Å), thus implying a likely very metal-poor stellar population (Malhotra & Rhoads, 2002). Its nature is likely similar to other metal-poor Lyα emitters (Nagao et al., 2008; Ono et al., 2010, 2012). Given the very high equivalent width (EW) and no continuum detection, MASOSA is likely extremely young, metal-poor and likely contains low stellar mass ($< 10^9 \, \mathrm{M}_\odot$).

The Lyα emission line shows a FWHM of $386 \pm 30 \, \mathrm{km \, s^{-1}}$, and with tentative evidence for two components in the Lyα line (similar to what is found by Ouchi et al., 2010), potentially indicating a merger or radiative transfer effects (e.g. Verhamme et al., 2006). However, with the current ground-base imaging, and the faintness in the continuum, it is not possible to conclude anything about the potential merging nature of the source – only *HST* follow-up can investigate this. However, what is already clear is that MASOSA provides a new example of a relatively compact Lyα emitter with a similar luminosity to Himiko (Ouchi et al., 2009, 2013), but with a much more extreme EW, revealing that such high

luminosity sources present diverse properties and may have a diverse nature.

4.4.2 CR7

CR7 clearly stands out as the most luminous Lyα emitter at $z \sim 7$, with a luminosity of $L_{Ly\alpha} = 10^{43.93\pm0.05}$ erg s^{-1}, $\sim 3\times$ more luminous than any known Lyα emitter within the epoch of re-ionisation. It also presents a very high rest-frame EW of > 200 Å, and thus a likely intrinsic EW which is even higher because of absorption by the ISM. Our measurements are presented in Table 4.2.

CR7 is spatially extended: $3''$ in diameter, corresponding to ~ 15 kpc at $z = 6.6$, as seen from its narrow-band image, but also in the spectra. Both the X-SHOOTER and DEIMOS data confirm its spatial extent, with both of them agreeing perfectly on the redshift, extent and FWHM. While the Lyα line profile is narrow (FWHM≈ 270 km s^{-1}), and particularly for such high luminosity, we see evidence for potentially 2 or 3 components (double peaked Lyα emission and a redshifted component towards the South of the source) and/or signs of absorption (see Figure 4.3), which indicate a complex dynamical structure. It may also mean that the actual intrinsic FWHM is even narrower. However, such tentative evidence requires confirmation with further spectroscopy obtained over different angles, and particularly by exploring deep imaging with high enough spatial resolution with e.g. *HST*.

4.4.3 Comparison with Himiko

We find that CR7 may be seen as similar to Himiko (but much brighter in Lyα and much higher EW) due to both sources presenting a spatial extent of about $3''$ in diameter. Both could therefore be tentatively classed as Lyα "blobs" (e.g. Steidel et al., 2000; Matsuda et al., 2004; Steidel et al., 2011). However, we note that Himiko is detected at peak transmission in the NB and the NB imaging in which it is detected is 1 mag deeper (see Matthee et al., 2015) than the imaging used for the discovery of CR7. While the CR7 Lyα line profile is very narrow, it consists of 2 or potentially 3 components, which may indicate that the source is a double or triple merger, likely similar to Himiko in that respect as well (see §4.5.4 which shows this is very likely the case for CR7). However, a simpler explanation is radiation transfer, which can easily cause such bumps (e.g. Vanzella et al., 2010). There are other similarities to Himiko, including: detections in NIR and a blue IRAC color. CR7 is however a factor ~ 3 brighter in Lyα emission and has an excess in J-band (attributed to HeII emission). CR7 is also bluer ($\beta = -2.2 \pm 0.4$, either using $Y - H$ or $H - K$, following equation 1 of Ono et al. 2010) in the rest-frame UV when compared to Himiko (which shows $\beta \sim -2.0$, but note that Himiko shows a red colour from H to K which would imply $\beta \sim 0.2$ if those bands are used). While CR7 shows a tentative HeII1640 Å emission line, no significant HeII is detected in Himiko, even though Zabl et al. (2015) obtained very deep X-SHOOTER data.

MASOSA is quite different. While it has the highest Lyα peak brightness, it is not extended and not detected in NIR or IRAC. Therefore, MASOSA provides

also a new class of sources at the epoch of re-ionisation: as luminous as Himiko, but very compact and with no significant rest-frame UV or rest-frame optical detection at the current UltraVISTA depth.

4.5   SED fitting CR7

To interpret the photometry/SED of CR7 we exploit the SED-fitting code of Schaerer & de Barros (2009) and Schaerer & de Barros (2010), which is based on a version of the *Hyperz* photometric redshift code of Bolzonella et al. (2000), modified to take nebular emission into account. We have explored a variety of spectral templates including those from the GALAXEV synthesis models of Bruzual & Charlot (2003), covering different metallicities (solar, $Z_\odot$, to 1/200 $Z_\odot$) and star formation histories (bursts, exponentially declining, exponentially rising). A standard IMF with a Salpeter slope from 0.1 to 100 $M_\odot$ is assumed. We refer to these models as "standard"/"enriched" SED fits or "standard"/"enriched" models throughout this paper.
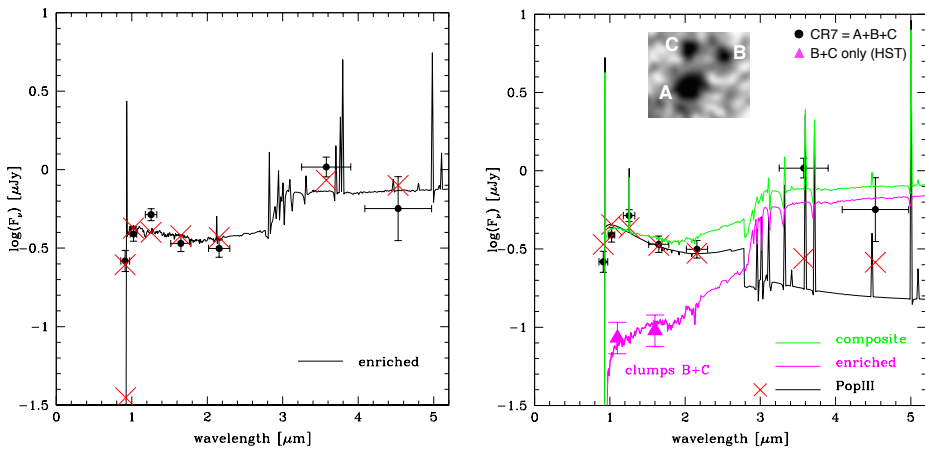

Figure 4.5: *Left*: The SED of 'CR7', from observed optical (rest-frame FUV) to observed MIR (rest-frame optical) and the best fit with a with a normal stellar population (not including extremely hot stars). Red crosses indicate the flux predicted for each broad-band filter for the best fit. The fit fails to reproduce the strong Lyα emission line and also the excess in J band, potentially boosted by HeII emission. Moreover, and even though the fit is unable to reproduce all the information available for the source, it requires an age of 700 Myr (the age of the Universe is 800 Myr at $z = 6.6$). In this case, the galaxy would have a SFR of $\sim 25\,M_\odot\,yr^{-1}$ and a stellar mass of $\sim 10^{10.3}\,M_\odot$. This is not able to explain the strong Lyα and the tentative HeII emission line. *Right*: Same observed SED of CR7 as in the left panel plus *HST* photometry for clumps B+C (magenta triangles). The black line shows a fit with a pure PopIII SED to the rest-frame UV part; the magenta line the SED of an old simple stellar population with 1/5 solar metallicity which matches the flux from clumps B+C; the green line shows the predicted SED summing the two populations after rescaling the PopIII SED by a factor 0.8. The composite SED reproduces well the observed photometry. Although there is a tension between the strength of the HeII line and nebular continuum emission (cf. text), a PopIII contribution is required to explain the HeII $\lambda1640$ line and the corresponding excess in the J-band. Although HeII has an unusually high EW (> 20 Å), we find no evidence for any other emission lines that would be characteristic of an AGN.

In addition, we also use synthetic spectra from metal-free ($Z < 10^{-4}$; PopIII) stellar populations assuming different IMFs (Salpeter, top-heavy), taken from Schaerer (2002, 2003). Constant SFR or bursts are explored in this case. We also explore SEDs from "composite" stellar populations, showing a superposition/mix of PopIII and more normal populations.

Nebular emission from continuum processes and emission lines are added to the spectra predicted as described in Schaerer & de Barros (2009). Nebular emission from continuum processes and emission lines are proportional to the Lyman continuum photon production. Whereas many emission lines are included in general, we only include H and He lines for the PopIII case (cf. Schaerer, 2003). The intergalactic medium (IGM) is treated with the prescription of Madau (1995). Attenuation by dust is described by the Calzetti law (Calzetti et al., 2000). We note that in our PopIII-like SED, the [OIII]4959,5007 lines are expected to be very weak due to small amounts of oxygen.

4.5.1 SED fitting with a normal population

Part of the photometry of CR7 is explained relatively well with "standard" models, as illustrated in Figure 4.5 (left panel). The shortcomings of these fits is that they cannot account for the relative excess in the UltraVISTA DR2 J band with respect to Y, H, and K, and that the Lyα emission is not strong enough to reproduce the entire flux observed in the NB921 filter. Both of these shortcomings thus relate to the presence of the strong emission lines (Lyα and HeII) observed in spectroscopy and also affecting the broad-band photometry.

The typical physical parameters derived from these SED fits which only include "normal" stellar populations indicate a stellar mass $M_* \sim 2 \times 10^{10}\,M_\odot$, SFR $\sim 25\,M_\odot\,\mathrm{yr}^{-1}$, and a fairly old age ($\sim 700$ Myr; the Universe is ~ 800 Myr old at $z = 6.6$). The SED fits and the derived parameters do not vary much for different star-formation histories (SFHs): both for exponentially declining and rising cases, the fits prefer long timescales (i.e. slowly varying SFHs). Whereas for exponentially declining SFHs and for constant SFR the best-fit attenuation is negligible ($A_V = 0$), a higher attenuation is needed for rising SFHs, as expected (cf. Schaerer & Pelló, 2005; Finlator et al., 2007). Depending on the assumed metallicity, this may reach from $A_V = 0.5$ (for 1/5 solar) to 0.25 (for 1/200 $Z_\odot$). The corresponding SFR is $\sim 30 - 40\,M_\odot\,\mathrm{yr}^{-1}$. The typical specific SFR, sSFR, obtained from these fits is sSFR $\sim 1.2 - 1.9\,\mathrm{Gyr}^{-1}$, as expected for a "mature" stellar population with SFH close to constant (c.f. González et al., 2014).

4.5.2 SED fitting with contribution from PopIII-like stars

The presence of strong Lyα and HeII emission lines, plus the absence of other UV metal emission lines (cf. above), may be due to exceptionally hot stars with a strong and hard ionizing flux, resembling that expected for PopIII stars (cf. Tumlinson et al., 2001; Schaerer, 2002). A fit with PopIII templates (from Schaerer, 2002, 2003) is shown in Figure 4.5 (right panel: black line). PopIII models (Schaerer, 2002, 2003) show that at 3.6 μm (for $z = 6.6$) there are strong HeII
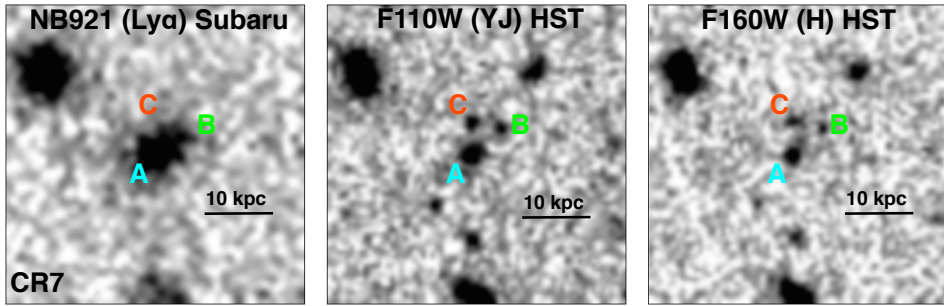
Figure 4.6: *Left:* CR7 with the NB921 filter/Suprime-cam imaging on Subaru, showing the extent of the Lyα but note that NB921 detects Lyα at only 50% transmission. *Middle:* HST imaging in *YJ*, revealing that CR7 clearly splits into 3 different components which we name A, B and C. *Right:* HST imaging in *H*, again revealing the 3 different components in CR7. We find that component A fully dominates the rest-frame UV and is coincident with the peak of Lyα emission and the location at which we detect strong HeII1640Å emission. The colours of clumps B and C are poorly constrained. Note that clumps B and C dominate the mass of the system in this SED model, and thus the actual mass centre of the system would be located between C and B, and significantly away from A.

and HeI lines, apart from Hβ, and that these Helium emission lines should have fluxes comparable to that of Hβ in the case of PopIII (Schaerer, 2002). Specifically, 3.6 μm should be contaminated by HeII4686, HeI4471 and HeI5016. For 4.5 μm, apart from Hα, the HeI5876 should be detected and could be comparable to Hβ. The general features of our fits with PopIII templates (considering bursts or constant SFR, as well as different IMFs) are the following:

- The UV rest-frame part of the SED is very well reproduced and a PopIII-like stellar population is required to "boost" the *J*-band flux (due to the presence of the HeII line) and for a stronger Lyα line due to a higher Lyman continuum flux (for the same UV flux). The exact strength of these emission lines is very sensitive to the "details" of the population, such as the upper end of the IMF, the age or star formation history (see more details in e.g. Raiter et al., 2010). The fits with PopIII also reproduce all other NIR detections: *Y*, *H* and *K* (see Figure 4.5).

- Populations with very strong line-emission also have a strong nebular continuum emission red-ward of Lyα and increasing towards the Balmer limit (see e.g. Schaerer, 2002). The observations (*H* and *K* band photometry) do not permit a much stronger contribution from the nebular continuum, as that would mean an increasing redder *H-K* colour, which is not observed. This limits the maximum strength of the predicted emission lines, except if the two emission processes (recombination line emission and nebular continuum emission, which is due to two-photon and free-bound emission) could be decoupled, and emission lines could be increased without significantly increasing the nebular continuum emission.

- All the available PopIII templates fitting the (rest-)UV part of the spectrum, predict a relatively low flux in the IRAC bands with or without accounting for emission lines. Therefore, a pure metal-free population does not seem

to be able to completely reproduce the observed rest frame UV–optical SED of this source. In any case, a PopIII only explanation would not seem very likely. Therefore, a metal-free population alone (without decoupling between recombination line emission and nebular continuum emission) is not able to reproduce the observed rest-frame UV-optical SED of this source.

4.5.3 PopIII and a more chemically evolved stellar population

As a consequence of our findings, we are led to consider a hybrid SED consisting of two populations (the source may well be a merger, and these components may well be completely separated, avoiding pollution by metals into the potentially metal-free region): a young metal-free stellar population and a more chemically evolved population. This can be fully confirmed by using *HST* and appropriate filters that can easily isolate Lyα, the rest-frame UV, and HeII.

A superposition of a young PopIII component dominating in the UV and an older population of "normal" metallicity (in this case, 0.2 $Z_\odot$) dominating the rest-frame optical flux of CR7 is shown in the right panel of Figure 4.5. In practice, we add 80% of a metal-free simple stellar population with an age of 16 Myr (shown by the black line; although younger ages of $\sim$ 5 Myr are preferred to produce the strongest HeII emission) to a 360 Myr old burst of 1/5 $Z_\odot$ (magenta curve), giving the total flux shown in green. As can be seen, an "old" population of $\sim 1.6 \times 10^{10}$ M$_\odot$ can make up for the missing rest-frame optical flux, whereas a young PopIII (or another kind of stellar population with extremely hot stars) burst can dominate the UV and the emission lines. There is some tension/uncertainty in the age or age spread of the metal-free population, as very young ages ($\lesssim$ 5 Myr) are preferred to produce the strongest HeII emission, whereas slightly older ages are preferred to avoid too strong nebular continuum emission (cf. above). For indication, the mass of the metal-free component would be 1×10^9 M$_\odot$ for a Salpeter IMF from 1 to 500 M$_\odot$, i.e. $\sim$ 6 % of mass of the old population. However, significantly less mass could be needed if the PopIII IMF was flat or top-heavy, lacking e.g. completely low mass stars (stars below 10 M$_\odot$). This could mean that $\sim 10^7$ M$_\odot$ of PopIII stars would be needed in order to fully explain the flux for an IMF peaking at ~ 60 M$_\odot$, or even less if the IMF peaks at even higher masses. This reveals that the presence of a young, metal-free population, forming for example in a yet un-polluted region of the galaxy, in an slightly evolved galaxy at $z = 6.6$, could reproduce the observed features of CR7 (consistent with theoretical predictions from e.g. Scannapieco et al., 2003; Tornatore et al., 2007).

4.5.4 *HST* imaging of CR7

In order for our best interpretation to be valid, CR7 would require to be clearly separated/resolved, with *HST* resolution, into at least two different spatial components: one being dominated by a PopIII-like stellar population (dominating the UV light but with only a very small fraction of the mass), and another, redder

Table 4.3: Resolved *HST* photometry, rest-frame UV magnitudes and UV slopes of the different components in CR7. F110W photometry is corrected for the contribution from Lyα emission using NB921 data.

Component	F110W	F160W	M_{1500}	β
Full	24.65 ± 0.05	24.70 ± 0.12	-22.2 ± 0.1	-2.2 ± 0.4
A	25.16 ± 0.05	25.25 ± 0.12	-21.6 ± 0.1	-2.3 ± 0.4
B	27.18 ± 0.15	26.88 ± 0.25	-19.6 ± 0.2	-1.0 ± 1.0
C	26.72 ± 0.10	26.80 ± 0.23	-20.1 ± 0.1	-2.3 ± 0.8

in the UV (and fully dominating the mass), with fluxes similar to those shown in Figure 4.5. While this requires more detailed follow-up, we find that CR7 has been fortuitously observed and is in the FoV of previous WFC3 observations in F110W (broad *YJ* filter that also contains Lyα) and F160W (*H*) of a different project (ID: 12578, PI: Forster-Schreiber). We explore such data in order to investigate the rest-frame UV morphology of CR7 and to conduct a first study of the rest-frame UV colours. Observations in F110W and F160W were obtained for 2.6 ks each.

We show the data in Figure 4.6, including a comparison with out NB921 imaging. Figure 4.7 presents a false-colour image combining data obtained with NB921, F110W and F160W. We find that CR7 is, beyond any doubt, split in different components (see Figures 4.6 and 4.7), in line with our best interpretation of a PopIII-like stellar population which dominates the UV, and a redder stellar population, found to be physically separated by at least 5 kpc (projected). In fact, we actually find three different components, which we label as A, B and C (see Figures 4.6 and 4.7). We obtain photometry for each of the clumps separately, in order to quantitatively test if they could explain the UV photometry predicted for the two components in §4.5.3. We use 0.4″ apertures for components B and C and 1″ for component A, more spatially extended. Our results are summarised in Table 4.3.

We find that the sum of the two redder, fainter clumps (B+C) matches our evolved stellar population remarkably well (see Figures 4.5 and 4.8). Note that the photometry of the two redder clumps was not used to derive such fit. We find that the central clump (A) is the one that dominates the rest-frame UV light (Figure 4.8). Figure 4.7 also shows the rest-frame colours of components A, B and C. The clumps are physically separated by ~ 5 kpc.

The *HST* imaging reveals that CR7 may be either a triple merger (similar to Himiko), and/or a system where we are witnessing a PopIII star formation wave, which may have moved from the reddest clump (C) to the other (B) and we are observing the brightest UV clump at the right time (A). It is therefore possible that the other clumps have emitted as much or even more of such radiation a few ~ 100 Myrs before, preventing what is now the site of young massive stars (A) to form before and potentially allowing for that pocket of metal free gas to remain metal free. There are of course, other potential interpretations of our observations. In §5.7 we discuss the different potential scenarios in detail.
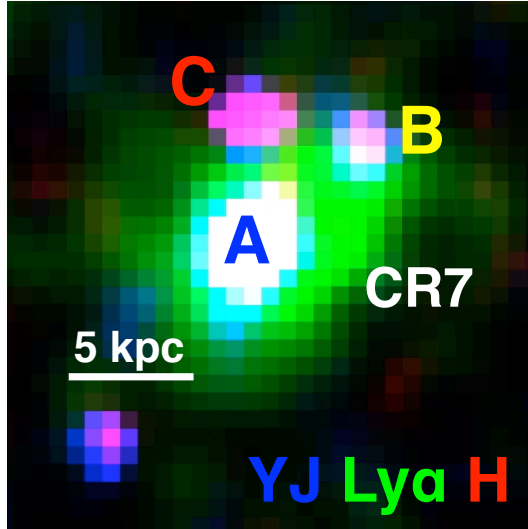
Figure 4.7: A false colour composite of CR7 by using NB921/Suprime-cam imaging (Lyα) and two *HST*/WFC3 filters: F110W (YJ) and F160W (H). This shows that while component A is the one that dominates the Lyα emission and the rest-frame UV light, the (likely) scattered Lyα emission seems to extend all the way to B and part of C, likely indicating a significant amount of gas in the system. Note that the reddest (in rest-frame UV) clump is C, with B having a more intermediate colour and with A being very blue in the rest-frame UV.

4.5.5   Differences when using UltraVISTA DR3

In addition to the indications of a HeII emission line in the spectrum, additional evidence for the presence of one or more strong emission lines in the NIR originates from a relatively bright *J* band magnitude compared to *Y* and *H* (Sobral et al., 2015b). This *J* band 'excess' had been measured in UltraVISTA DR2 (McCracken et al., 2012) data and resembles the colour excesses that are being found in galaxies at $z \sim 6 - 7$ with the *Spitzer*/IRAC filters, used to infer Hβ+[OIII] (e.g. Smit et al., 2014). Besides the Sobral et al. (2015b) article, indications of a *J* band excess were also found by Bowler et al. (2014), who identified CR7 independently as a Lyman-break galaxy candidate at $z \sim 7$, although with poorly fitted SED (due to this excess) and therefore unreliable redshift.

The evidence for a *J* band excess disappeared in the new UltraVISTA DR3 data (March 2016). Compared to DR2, the released data from UltraVISTA DR3 had been re-reduced and the exposure time around CR7 roughly doubled (private communication with the UltraVISTA team). While CR7's magnitude in the *Y* and *H* band does not change significantly, the difference in the *J* band magnitudes between DR2 and DR3 ranges from $+0.1$ and $+0.5$ magnitude (depending on the aperture).

The changes in the *J* band magnitude are larger than the measurement uncertainty provided in Table 4.2. The measurement uncertainty may have been under-estimated by a factor two (in flux density) due to correlated noise (private communication with the UltraVISTA team). Correlated noise originates from

resampling the data to a smaller pixel scale than the native pixel scale, and is known to be under-estimated by SExtractor. Furthermore, the variation in the *J* band magnitude is not statistically significant compared to the changes in the *J* band magnitude for all detections within a 5″ radius from CR7. Using these detections, we find that ≈ 5 % of the objects with similar brightness as CR7 have a *J*-band magnitude variation > 0.4 magnitude between DR2 and DR3. This implies that the largest change in CR7's *J* band magnitude is a 1.7σ fluctuation.

As a result, the evidence for the photometric excess is decreased with new photometry and the flux calibration of the X-SHOOTER spectrum in Sobral et al. (2015b) had been overestimated. As discussed in Bowler et al. (2017b), the high HeII EW of 80 Å Sobral et al. (2015b) is ruled out in the DR3 photometry, but an EW of ≈ 25 Å, similar to the revisited X-SHOOTER reduction, is possible within their conservatively measured uncertainties.

4.6   Discussion

CR7, with a luminosity of $L_{Ly\alpha} = 10^{43.93 \pm 0.05}\,\mathrm{erg\,s^{-1}}$ is ∼ 3× more luminous than any known Lyα emitter within the epoch of re-ionisation (e.g. Ouchi et al., 2013).

X-SHOOTER data provides a near-infrared spectrum, allowing to investigate the significant excess seen in the *J* band photometry from UltraVISTA DR2 (Mc-Cracken et al., 2012; Bowler et al., 2014), indicative of emission line(s). No continuum is detected in the NIR spectrum. However, and despite the relatively low integration time, a strong HeII1640 Å line was found (≈ 3σ, $\mathrm{EW_0} = 25 \pm 15$ Å), although not strong enough to explain the full observed excess in the *J* band (see Figure 4.5). HeII can only be produced if the intrinsic extreme UV spectrum is very hard, i.e., emits a large number of ionising photons with energies above 54.4 eV, capable of ionising He completely. The line we detect is also narrower than Lyα, with FWHM of $180 \pm 30\,\mathrm{km\,s^{-1}}$, as HeII1640 Å does not scatter easily as Lyα, as the line is not self-resonant.

While in principle there are a variety of processes that could produce both high EW Lyα and HeII1640Å, some of them are very unlikely to produce them at the luminosities we are observing, such as X-ray binaries or shocks. However, in principle, cooling radiation could produce strong Lyα emission with luminosities similar to those measured for CR7. Faucher-Giguère et al. (2010) provides predictions of the total Lyα cooling luminosity as a function of halo mass and redshift. Under the most optimistic/extreme assumptions, it would be possible to produce a Lyα luminosity of ∼ $10^{44}\,\mathrm{erg\,s^{-1}}$ for a dark matter halo mass of $M > 5 \times 10^{11}\,\mathrm{M_\odot}$. Since such dark matter haloes should have a co-moving number density of about ∼ $10^{-5}\,\mathrm{Mpc^{-3}}$ at $z \sim 6.6$, their number densities could potentially match the luminous Lyα emitters that we have found. However, in the case of cooling radiation, the HeII emission line should likely be weaker than what we measure (with intrinsic HeII/Lyα of 0.1 at most; e.g. Yang et al. 2006b), and cooling radiation in a massive dark matter halo should also result in a broader Lyα line than what we observe.
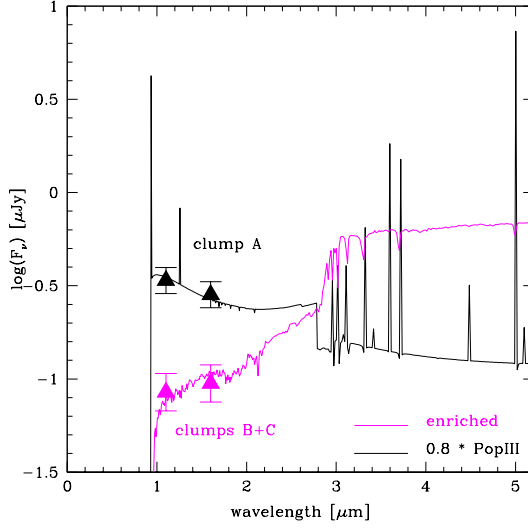
Figure 4.8: *HST* imaging in *YJ* and *H* allows us the physically separate CR7 in two very different stellar populations and show remarkable agreement with our best-fit composite SED derived in §4.5.3. While clump A (see e.g. Figure 4.7) is very blue and dominates the rest-frame UV flux, B+C may be somewhat redder and likely dominate the rest-frame optical and the mass. Note that we simply show the *HST* data together with our best fit composite model derived in §4.5.3 which was solely based on the full photometry and did not make use of any resolved *HST* data.

There are, nonetheless, four main sources known to emit an ionising spectrum that can produce high luminosity, high EW nebular Lyα and HeII as seen in our spectra (see also similar discussion in e.g. Prescott et al., 2009; Cai et al., 2011; Kashikawa et al., 2012):

1) strong AGN (many examples have been found, particularly on e.g. radio galaxies: De Breuck et al. 2000), with typical FWHM of lines being $\sim 1000\,\mathrm{km\,s^{-1}}$;

2) Wolf-Rayet (WR) stars (many cases known in e.g. SDSS: Shirazi & Brinchmann 2012; or see Erb et al. (2010) for a higher redshift example), with typical FWHM of lines being $\sim 3000\,\mathrm{km\,s^{-1}}$;

3) Direct collapse black hole (DCBH), which have been predicted and studied theoretically (e.g. Agarwal et al., 2013, 2016), although none has been identified yet, but they should produce strong HeII1640Å (Johnson et al., 2011);

4) PopIII-like, extremely hot and low metallicity stars (e.g. Schaerer, 2003; Raiter et al., 2010), which should produce high EW, narrow HeII emission lines (FWHM of a few $\sim 100\,\mathrm{km\,s^{-1}}$).

Many potential candidates for PopIII have been identified based on their colours and/or high EW Lyα, but either no HeII was found (e.g. Nagao et al., 2008), HeII was found but with clear signatures of AGN activity (De Breuck et al., 2000; Matsuoka et al., 2009), or HeII had very low EW (Cassata et al., 2013). Thus, so far, not a single source has been found with high EW Lyα, HeII detection with high EW, no AGN signatures, no WR star signatures (e.g. P-

Cygni profiles, broad lines, and many other metal lines e.g. Brinchmann et al. 2008; see also Gräfener & Vink 2015) and with no other metal lines.

4.6.1   The nature of CR7: AGN or WR stars?

In order to test the possibility of CR7 being an AGN, we start by checking X-ray data. We find no detection in the X-rays, with a limit of $< 10^{44}\,\mathrm{erg\,s^{-1}}$ (Elvis et al., 2009). We also find no radio emission, although the limit is much less stringent than the X-ray emission. The X-SHOOTER and DEIMOS spectra were carefully investigated for any metal lines, particularly NV, Oxygen and Carbon lines (see Table 4.2 and also Figure 4.4). No such lines were found, and thus we place 1σ upper limits on their fluxes, to constrain the nature of the source, finding, e.g. Lyα/NV > 70. Our Lyα and HeII emission lines are narrow (both FWHM$\sim 100 - 300\,\mathrm{km\,s^{1}}$), thus excluding broad-line AGN. Narrow-line AGNs with HeII emission typically have CIII]1909/HeII$\sim 1.5 \pm 0.5$ (e.g. De Breuck et al., 2000); such line ratio would result in a strong CIII]1909 detection in our X-SHOOTER spectrum (see Figure 4.4). We do not detect CIII]1909 and obtain an upper limit of CIII]1909/HeII< 0.5 (1σ; see Figure 4.4), which greatly disfavours the AGN hypothesis. The strong limit on Lyα/NV > 70 also disfavours the AGN hypothesis and points towards very low metallicities.

There are no indications of WR stars, due to the very narrow HeII line ($\sim 180\,\mathrm{km\,s^{-1}}$, compared to typical FWHM of $\sim 3000\,\mathrm{km\,s^{-1}}$ for WR stars, c.f. Brinchmann et al. 2008) and no other metal lines.

We note, nonetheless, that while CR7 is strongly disfavoured as an AGN, it shows characteristics of what has been predicted for a direct collapse black hole (e.g. Johnson et al., 2011; Agarwal et al., 2013, 2016). This is because it shows $\beta = -2.3$ (as predicted), no metal lines, and high luminosity. The detection of the other nearby sources about $\sim 5\,\mathrm{kpc}$ away (see Figure 4.6) are also a key prediction from Agarwal et al. 2015, while the relatively high observed HeII/Lyα would also match predictions for a direct collapse black hole (Johnson et al., 2011). However, CR7 does not show any broad line, as predicted by Agarwal et al. (2013), and the observed Lyα and HeII luminosities are higher by about ~ 2 orders of magnitude when compared to predictions by e.g. Johnson et al. (2011) for the case of $\sim 1 - 5 \times 10^{4}\,\mathrm{M_{\odot}}$ black holes. Another key distinction between a direct collapse black hole and stellar population(s) is X-ray emission: if it is a black hole, it must be emitting much more X-ray flux than a PopIII-like stellar population, and thus would likely be detectable with Chandra given the high line luminosities measured. Deeper Chandra observations could in principle test this.

4.6.2   On the hardness of the ionizing source of CR7

The theory of recombination lines relates, to first order, the ratio of HeII to Hydrogen recombination lines to the ratio between the ionizing photon flux above 54 eV, $Q(\mathrm{He^{+}})$, and that above 13.6 eV, $Q(H)$, the energies needed to

ionize He$^+$ and H respectively. For the relative intensity HeII/Lyα one thus has:

$$I(1640)/I(Ly\alpha) \approx 0.55 \times \frac{Q(\text{He}^+)}{Q(H)}, \qquad (4.1)$$

where the numerical factor depends somewhat on the electron temperature, here taken to be $T_e = 30$ kK (Schaerer, 2002). The observed line ratioHeII/Lyα $\approx$ 0.15 therefore translates to $Q(\text{He}^+)/Q(H) \approx 0.2$, which indicates a very hard ionizing spectrum.

For metal-free stellar atmospheres such a hardness is only achieved in stars with very high effective temperatures, typically $T_{\text{eff}} > 110$ kK (or > 70 kK for 1 σ lower limit), slightly hotter than the (already hot) zero-age main sequence predicted for PopIII stars which asymptotes to $T_{\text{eff}} \approx 100$ kK for the most massive stars (e.g. Schaerer, 2002).

For integrated stellar populations consisting of a ensemble of stars of different masses, a maximum hardness $Q(\text{He}^+)/Q(H) \approx 0.1$ is expected for zero or very low metallicities (Schaerer, 2002, 2003), higher than inferred from the observed HeII/Lyα ratio of CR7. This could indicate that only a fraction of the intrinsic Lyα emission is observed, or that a source with a spectrum other than predicted by the above PopIII models (e.g. an AGN) is responsible for the ionization or contributing at high energies (> 54 eV). In fact the observed HeII equivalent width of 25 ± 15 Å is in broad agreement with the equivalent width predicted for PopIII models (Schaerer, 2002). This supports the explanation that $\sim 75\%$ of the intrinsic Lyα emission may have escaped our observation, e.g. due to scattering by the IGM, internal absorption by dust, or due to a low surface brightness halo, processes which are known to affect in general Lyα emission (e.g. Atek et al., 2008; Dijkstra et al., 2011; Steidel et al., 2011). If the intrinsic Lyα emission is $\gtrsim 2 - 3$ times higher than observed, the hardness ratio is compatible with "standard" PopIII models. Future observations and detailed photoionization models may yield further insight on the properties of the ionizing source of CR7.

4.6.3 CR7: A PopIII-like stellar population?

As the AGN and WR stars hypothesis are strongly disfavoured (although we note that a direct collapse black hole could still explain most of our observations), could CR7 be dominated by a PopIII-like stellar population? For this to be the case, such stellar population would have to explain the detection, FWHMs, EWs and fluxes of Lyα and HeII (including the strong excess in J band), the UV continuum and continuum slope ($\beta = -2.2 \pm 0.4$) and the IRAC detections which imply very high EW rest-frame optical lines. We have shown in §4.5.3 and §4.5.4 that a composite of PopIII models (Schaerer, 2002, 2003; Raiter et al., 2010) with a more evolved stellar population can match all our observations, including spatially resolved *HST* data. This scenario requires that the majority of mass is in clumps B and C, which can be tested with future high resolution MIR imaging. We note that the intrinsic HeII/Lyα line ratio predicted for PopIII would be $\sim 0.05 - 0.1$ (Schaerer, 2002, 2003), but that can easily result in an observable

ratio of ~ 0.2 if a significant fraction of the Lyα line is absorbed.

A key question, of course, is whether it is even possible or expected to observe Lyman-α coming from PopIII stars alone, even if such line is ultra-luminous. The most massive PopIII stars should be short-lived (a few Myr), and, without any previous contribution to ionise their surroundings from e.g. neighbour star clusters or other nearby proto-galaxies, the most massive PopIII stars would have to be able to emit enough ionising photons to produce an ionised sphere larger than 1 Mpc after less than a few Myrs (Cen & Haiman, 2000), before the most massive stars reach the supernovae phase and likely start enriching the local environment. However, such process (for a single PopIII population in full isolation, and fully surrounded by neutral Hydrogen) should take at least ~ 3 Myrs to happen: this is simply set by the speed of light. However, if neighbouring sources (either PopIII or PopII stars) have already contributed towards ionising a local bubble, and if PopIII star formation can proceed in a wave-like pattern, likely from the highest density regions to the lowest densities, by the time later PopIII stars form (still in pristine gas which was not contaminated due to being sufficiently far away), they will be in ideal conditions to be directly observed in Lyα. Thus, it may be much more likely to observe potentially composite populations than to observe pure PopIII stellar populations. Furthermore, and despite the nature of the stellar populations, it is likely that the observability of very luminous Lyα emitters is strongly favoured in complex systems which already have older stellar populations like CR7 (that were able to ionise local bubbles before and thus allowing for strong Lyα emission from young stellar populations to be observable).

4.7   Conclusions

We presented the spectroscopic follow-up of the two most luminous $z \sim 6.6$ Lyα candidates in the COSMOS field ($L_{Ly\alpha} \sim 3 - 9 \times 10^{43}$ erg s^{-1}): 'MASOSA' and 'CR7'. These sources were identified in Matthee et al. (2015), revealing that such luminous sources are much more common than previously thought and have number densities of $\sim 1.5 \times 10^{-5}$ Mpc^{-3}. Our main results are:

- We used X-SHOOTER and FORS2 on the VLT, and DEIMOS on Keck, to confirm both candidates beyond any doubt. We find redshifts of $z = 6.604$ and $z = 6.541$ for 'CR7' and 'MASOSA', respectively. 'CR7' has an observed Lyα luminosity of $10^{43.93 \pm 0.05}$ erg s^{-1} ($\sim 3\times$ more luminous than Himiko) and is the most luminous Lyα emitter ever found at the epoch of re-ionisation.

- MASOSA has a strong detection in Lyα, with very high Lyα EW (EW$_0 >$ 200 Å), implying very low stellar mass and a likely young stellar population. It is, nonetheless, undetected in all other available bands and Lyα is also rather compact.

- CR7, with a narrow Lyα line with 266 ± 15 km s^{-1} FWHM, is detected in the NIR (rest-frame UV), with $\beta = -2.2 \pm 0.4$, an excess in publicly available

UltraVISTA DR2 *J* photometry compared to the *Y* and *H* bands, and it is strongly detected in *Spitzer*/IRAC.

- We detect a tentative HeII1640Å narrow emission line at $z = 6.603 \pm 0.001$ with X-SHOOTER in CR7, which contributes to the excess seen in the *J* band photometry. We find no other emission lines from the UV to the NIR in our X-SHOOTER spectra. No AGN line is seen, nor any signatures of WR stars, as the HeII1640Å emission line is narrow (FWHM $= 180 \pm 30\,\mathrm{km\,s^{-1}}$). The HeII emission line implies that we are seeing the peak of Lyα emission redshifted by $+100\,\mathrm{km\,s^{-1}}$ and thus that we are only seeing the red wing of the Lyα (the intrinsic Lyα flux is thus likely much higher than seen), or we are witnessing an outflow.

- Based on the narrowness of Lyα and HeII and the absence of CIV and NV, the AGN and WR stars interpretation of the nature of CR7 are strongly disfavoured. An alternative interpretation is that the source hosts a direct collapse black hole, although the lack of broad emission lines and the lack of X-ray detection also disfavours this interpretation. Given all the current data, we conclude that CR7 may host an unseen, extreme stellar population and it is therefore the strongest candidate for PopIII-like stellar population found so far.

- We find that CR7 cannot be described only by a PopIII-like stellar population, particularly due to the very strong IRAC detections. Our best interpretation of the full data (spectroscopy and photometry), which is fully consistent with many theoretical predictions, is a combination of a PopIII-like stellar population, which dominates the rest-frame UV and the emission lines, and an older, likely metal enriched stellar population, which is red, and that dominates the mass of the system. This interpretation fits remarkably well with high resolution *HST*/WFC3 imaging that reveals two red components, each about 5 kpc away from the peak of the rest-frame UV, Lyα and HeII1640 Å emission and that have the fluxes predicted by our SED fitting.

We may be witnessing, for the first time, direct evidence for the occurrence of waves of PopIII-like star formation which could happen from an original star cluster outwards (resulting from strong feedback which can delay PopIII star formation), as suggested by e.g. Tornatore et al. (2007). In this scenario, the reddest clump in CR7 (C, see Figures 4.7 and 4.8), which formed first (reddest and oldest), was likely responsible for not only starting to ionise a local bubble, but also for photoionisation feedback that may have prevented star-formation to occur in the vicinity of clump C. Star-formation likely proceeded to the second clump once stellar feedback from C declined (B, see Figure 4.7), with similar effects (preventing star-formation outside such region, but further ionising a local bubble), and we are observing source A (see Figure 4.7) at the right time to see an intense PopIII-like star formation episode. Most importantly, this scenario also provides a very simple explanation of why Lyα photons can easily escape the CR7 galaxy, as we see a significant amount of older stars which were able

to emit a significant amount of UV photons for a few hundred million years before observations, enough to ionise a bubble of $> 1\,\mathrm{Mpc}$ around the source. It may be that any previous episodes of star-formation could have prevented the gas around those star-forming regions to form stars. Furthermore, we note that while radiation is able to affect the surroundings as it travels fast, significant metal enrichment is very inefficient on scales larger than $\sim 1\,\mathrm{kpc}$ (e.g. Scannapieco et al., 2003; Tornatore et al., 2007; Ritter et al., 2014), both due to the larger time-scales for metals (from supernovae) to travel outwards (compared to the speed of light), but also due to the continued infall of metal-free gas from the cosmic web. It is therefore likely that in some cases, scales beyond 1-2 kpc of previous star formation activity can easily have the pristine gas necessary to allow PopIII to form (e.g. Ritter et al., 2012, 2014) even at $z \sim 6.6$, and to be detectable at redshifts even below $z \sim 5$ (e.g. Scannapieco et al., 2003; Tornatore et al., 2007). Tornatore et al. (2007), for example, predict that the peak of PopIII star formation rate density to occur at $z \sim 6 - 8$.

The spectroscopic confirmation of MASOSA and CR7, along with the high S/N spectroscopic and photometric data, allowed us to have a first glimpse into sources likely similar to Himiko and brighter, that are much more common than previously expected and have a remarkable nature. The follow-up of the full Matthee et al. (2015) Lyα sources at even higher luminosities found in the SA22 field will allow us to explore even more the diversity and nature of such unique targets. Such luminous Lyα emitters are the ideal first targets for JWST, particularly due to the likely very high EW and bright optical rest-frame emission lines, which may not be restricted to bright [OIII]5007, Hβ and Hα, but actually include HeII4686, HeI4471, HeI5016 and HeI5876. In the case of CR7, a composite of a PopIII-like stellar population and a likely enriched stellar population which is physically separated by $\sim 5\,\mathrm{kpc}$ (Figure 4.7) is currently strongly favoured, and it is possible that similar stellar populations will be found in the other Lyα emitters. We may have found an actual population with clear signatures of PopIII-like stars, besides CR7. JWST will, in only a short exposure time, clearly show if the rest-frame spectra is made up of only He+H lines, confirming PopIII beyond any doubt, or if [OIII] is also present and exactly where each of the lines is coming from.

Acknowledgments

ing and helpful discussions. The authors are grateful to ESO for the award of ESO DDT time (294.A-5018 & 294.A-5039). Observations are also based on data from W.M. Keck Observatory. The W.M. Keck Observatory is operated as a scientific partnership of Caltech, the University of California and the National Aeronautics and Space Administration. Based on observations obtained with MegaPrime/Megacam, a joint project of CFHT and CEA/IRFU, at the Canada-France-Hawaii Telescope (CFHT) which is operated by the National Research Council (NRC) of Canada, the Institut National des Science de l'Univers of the Centre National de la Recherche Scientifique (CNRS) of France, and the University of Hawaii. This work is based in part on data products produced at Terapix available at the Canadian Astronomy Data Centre as part of the Canada-France-Hawaii Telescope Legacy Survey, a collaborative project of NRC and CNRS. Based on data products from observations made with ESO Telescopes at the La Silla Paranal Observatory under ESO programme IDs 294.A-5018, 294.A-5039 and 179.A-2005, and on data products from the UltraVISTA consortium.

4.A   Summaries of articles interpreting CR7

Several theoretical articles have been written about the nature of CR7 after the publication from Sobral et al. (2015b). The findings of these articles are summarised below, in order of their publication date. I also comment on their validity after updated measurements of the HeII line strength and the ALMA results presented in Chapter 5.

- *'The brightest Lyα emitter: Pop III or black hole?'* (Pallottini et al., 2015). This article analyses recent cosmological hydrodynamical simulations and finds that several simulated galaxies indeed form PopIII stars from unpolluted pockets of pristine gas at relatively late cosmic times ($z = 6.0$). However, these pockets have an order of magnitude lower mass (in time windows of < 5 Myr) than required to explain the Sobral et al. (2015b) HeII luminosity. As PopIII stars only lead to strong HeII emission for < 10 Myr, the authors conclude that a PopIII explanation is highly unlikely. They conclude that a metal poor direct collapse black hole (that has a high HeII luminosity for a much longer time) is more likely. Even with the revised lower HeII luminosity, the simulations do not produce such a massive burst of PopIII star formation at $z = 6.6$. A caveat is that the simulation volume is limited to 10^3 Mpc^3 and therefore does not include simulated galaxies with similar mass as CR7, nor does it capture possible rare merger events. Regardless, other articles agree with Pallottini et al. (2015) that it is challenging to keep a large gas mass unpolluted until $z = 6.6$.

- *'Lyα Signatures from Direct Collapse Black Holes'* (Dijkstra et al., 2016a). The authors discuss the Lyα profile of CR7 in the context of Lyα photons originating from cooling radiation from the gravitational heating of a collapsing cloud and the photoionisation by a central source. The Lyα luminosity of CR7 indicates a black hole mass $> 10^7$ M$_\odot$, higher than the mass of a direct collapse black hole. The Lyα profile indicates a low neutral hydrogen

column density and outflows, and is similar to the Lyα profile of normal LAEs at $z \sim 2 - 3$. Hence, the Lyα properties indicate that the ISM in CR7 is already evolved and the current physical conditions are different from those in which the central supermassive black hole formed (in case CR7 is powered by this AGN). ALMA observations (Chapter 5) find a velocity shift that is in perfect agreement with the value estimated from the Lyα profile and a [CII]-UV luminosity ratio that is similar to the ISM in more normal galaxies, corroborating the findings of Dijkstra et al. (2016a).

· *'Formation of massive Population III galaxies through photoionization feedback: a possible explanation for CR7'* (Visbal et al., 2016). This article proposes that the ionising radiation emitted by clumps B and C (assuming they formed earlier than clump A) heated the gas cloud that eventually forms clump A. This prevents the gas cloud from collapsing and forming stars until $z \approx 6.6$. This way, a higher gas mass can remain unpolluted until $z = 6.6$, compared to the model from e.g. Pallottini et al. (2015) that ignores this effect. The authors find that the number density of observable PopIII galaxies that form this way is $\approx 10^{-7}$ Mpc^{-3} at $z = 6.6$, a factor ten lower than the number density of CR7. The updated HeII luminosity likely makes this scenario more likely, as a lower gas mass is required to be sufficiently photo-heated. On the other hand, this scenario requires assumptions about the ionising photon escape fraction from clumps B and C, and likely depends on a somewhat fine-tuned/rare combination of star formation histories of nearby halos. Regardless of the nature of CR7, the photoionization feedback mechanism could help delaying the formation of PopIII stars by delaying the collapse of pristine gas clouds in the environments of massive galaxies, facilitating their observability in future surveys.

· *'Evidence for a direct collapse black hole in the Lyman α source CR7'* (Smith et al., 2016b). This article explores 1D radiation-hydrodynamical simulations incorporating ionising radiation and Lyα feedback to study the impact of the spectrum of the ionising source on the observed properties of the Lyα line. This study focusses on the observed velocity offset and the surface brightness profile. They argue that the ionising spectrum of a stellar ionising source (similar to a blackbody with T=10^5 K) ionises its environment very efficiently, such that no velocity offset between the systemic redshift and the Lyα line would be observed. The observed velocity offset of $+160$ km s^{-1} in Sobral et al. (2015b), similar to the ALMA result, thus indicates a Compton thick AGN. The observed extended Lyα surface brightness profile also indicates the AGN scenario due to more resonant scattering in neutral hydrogen. The revised X-SHOOTER analysis reveals a slightly smaller velocity offset between the Lyα and HeII lines, although the velocity offset between Lyα and [CII] observed with ALMA agrees with the conclusion in Smith et al. (2016b). The authors conclude that future deep X-ray observations could help constraining the nature of CR7.

· *'Detecting direct collapse black holes: making the case for CR7'* (Agarwal et al., 2016). After performing their own deconfusion techniques to measure

Spitzer/IRAC photometry and performing their own SED fits of the individual components, the authors reconstruct the history of the local Lyman-Werner background around CR7 using the star formation histories of clumps B and C. They also use a halo merger tree, based on assuming $M_{halo} = 10^{12}$ $M_{\odot}$ for clump A at $z = 6.6$, to trace the formation of clump A's halo and the likelihood of metal pollution due to nearby star formation in the other two clumps. Combining these constraints, the authors find that a direct collapse black hole could have formed at $19 < z < 23$ in clump A with a resulting black hole mass of $\approx 4.4 \times 10^6$ $M_{\odot}$ at $z = 6.6$ after a sub-Eddington accretion period. The authors note that their SED fit can not explain the [3.6] flux at clump A, likely due to under-estimated Hβ+[OIII] emission (see also Appendix B and Bowler et al. 2017b). The presence of oxygen in clump A would require additional star formation and chemical enrichment between the time of BH formation and $z = 6.6$, but here it is not discussed whether this is theoretically possible.

- '*Ab Initio Cosmological Simulations of CR7 as an Active Black Hole*' (Smidt et al., 2016). This article presents a full hydrodynamical simulation that simulates a system similar to CR7, roughly reproducing the Lyα luminosity and line-profile. The authors find that the AGN heats the gas in the halo, preventing further star formation and chemical enrichment. This is at odds with the [CII] detection by ALMA and the inferred presence of strong Hβ+[OIII] by Bowler et al. (2017b), as discussed above in the summary of Agarwal et al. (2016). The authors also use their simulation to predict a synchrotron radio luminosity of $\approx 10^{40-41}$ erg s^{-1} in the AGN scenario, which can be tested with future observations.

- '*Exploring the nature of the Lyman-α emitter CR7*' (Hartwig et al., 2016). This article uses semi-analytical models to explore different formation scenarios of CR7 by randomly sampling dark matter merger trees. As the PopIII SFR density in their model peaks at $z \sim 15$ and chemical enrichment is efficient and ubiquitous (although ignoring photoionisation feedback that is proposed by Visbal et al. 2016), a PopIII scenario can not explain CR7s HeII luminosity at $z = 6.6$. The authors also argue that the metallicity (which they constrain to be Z$< 10^{-2}$ using CLOUDY modelling) is too low to explain CR7 with a black hole that formed as a PopIII remnant, as it would require a growth through mergers that would have chemically enriched the gas even further. Hence, the authors conclude that a black hole that formed in a low metallicity environment that remains metal poor (the case for a direct collapse black hole), is most likely. The revised HeII strength and the ALMA detection of [CII] emission allow for a higher, more normal metallicity in CR7. As a result, it is harder to determine the formation mechanism of the supermassive black hole, in case CR7 is powered by an AGN.

- '*The nature of the Lyman-α emitter CR7: a persisting puzzle*' (Pacucci et al., 2017). This is the first article that appeared after the Bowler et al. (2017b) article and therefore discusses whether the blue [3.6]-[4.5] IRAC colour in

component A could only indicate the presence of strong [OIII] emission. Instead, the authors find that the IRAC photometry of CR7 can also be explained by strong $HeI_{\lambda4714}$ and $HeII_{\lambda4687}$ emission, compatible with only a minor contribution from $[OIII]_{5007}$ emission. The authors therefore conclude that the current data are insufficient to distinguish between different AGN formation scenarios and detailed MIR spectroscopy is required.

·   *'Metallicity evolution of direct collapse black hole hosts: CR7 as a case study'* (Agarwal et al., 2017). This article addresses the issue whether metal pollution can take place after the formation of a supermassive black hole through direct collapse. They show that the star formation histories of clumps B and C from Agarwal et al. (2016) could pollute the metallicity in clump A to $\approx 1/100\ Z_{\odot}$ at $z = 6.6$, which is slightly higher than the metallicity inferred by Bowler et al. (2017b). Similar to Pacucci et al. (2017), this result implies that the current data do not rule out that the supermassive black hole in CR7 has not formed through a direct collapse. However, since the [CII]-UV ratio measured from ALMA indicates a metallicity that is $> 1/10\ Z_{\odot}$ (Chapter 5), additional star formation in clump A has likely occurred.

4.B   Comparison to Bowler et al. (2017b)

In their article *'No evidence for Population III stars or a Direct Collapse Black Hole in the $z = 6.6$ Lyman-α emitter 'CR7''*, Bowler et al. (2017b) re-analyse the photometric data of CR7. Compared to the analysis in this Chapter, Bowler et al. (2017b) analyse deeper *Spitzer*/IRAC [3.6] and [4.5] data and apply de-confusion methods. They also analyse new data from the UltraVISTA survey (DR3, versus DR2 in Sobral et al. 2015b).

As shown in Section 4.5.5, the *J* band photometry in the public UltraVISTA DR3 data is different from the public DR2 photometry, while photometry in other filters remains mostly unchanged. As also noted by Bowler et al. (2017b), this reduces the inferred strength of the HeII emission: $EW_0 = 40 \pm 30$ Å compared to the original value in Sobral et al. (2015b) of $EW_0 \approx 80$ Å. A lower HeII EW requires less exotic ionising populations and can plausibly be explained by a normal faint AGN or a low metallicity, α-enhanced binary stellar population. These results are consistent with our updated analysis from Sobral, Matthee et al. (submitted) and with the HeII EW presented in this Chapter.

As the PSF-FWHM of the *Spitzer*/IRAC data are considerably larger than the *HST*/WFC3 F110W and F160W data[5], the individual components of CR7, separated by $\approx 1''$, are significantly blended in the IRAC images. It is therefore challenging to measure the IRAC fluxes of the individual components. Typically, high-redshift studies use deblending techniques based on detailed knowledge of the IRAC PSF and a higher resolution image (e.g. Labbé et al., 2015), typically

---

[5] The mean FWHM of the IRAC [3.6] and [4.5] images are $1.95''$ and $2.02''$, mapped on a pixel scale of $1.2''$. The FWHM of *HST*/WFC3 images are $\approx 0.13''$ around 1200 nm, mapped on a $0.123''$ pixel scale.

from *HST*. A caveat of this technique is that it adopts that there are no strong colour gradients, as it assumes that the IRAC morphology is the same as the *HST*/WFC3 morphology. In practice, for a galaxy at $z = 6.6$, this means that the technique adopts no color gradients between $\lambda_0 \approx 1500$ Å and $\lambda_0 \approx 4500 - 6000$ Å. Therefore, this may not be the case if there is a strong Balmer break around 4000 Å due to an older stellar population or if there is differential dust attenuation.

Bowler et al. (2017b) applies such deconvolution technique to measure the IRAC fluxes for each of the three UV components of CR7 separately. They use the *HST*/WFC3 images as a high resolution prior and find that the majority of the flux in the [3.6] and [4.5] bands is associated to component A, that is the brightest in the UV. The [3.6]-[4.5] color is very blue ($-1.20^{+0.29}_{-0.32}$), which indicates strong Hβ+[OIII] line emission at the position of component A. Due to their faintness, the IRAC colours of the fainter UV components are poorly constrained. These measurements led Bowler et al. (2017b) to conclude that strong oxygen emission is present in component A from CR7, refuting an extreme 'PopIII' explanation. They also conclude that the majority of stellar mass is present in component A, contrarily to Sobral et al. (2015b) and Agarwal et al. (2016) who speculate/argue the majority of stellar mass resides in components B and C. Having a large fraction of the stellar mass outside the brightest UV component is a requirement for the direct collapse black hole scenario. Therefore, Bowler et al. (2017b) also rule out the direct collapse black hole scenario, and their most likely explanation of the nature of CR7 is a 'normal', faint AGN.

While the presence of a blue IRAC colour and hence Hβ+[OIII] line emission in CR7 had also been noted (but not quantfied) in Matthee et al. (2015), the main difference from the Bowler et al. (2017b) analysis with the Sobral et al. (2015b) analysis is that IRAC measurements are performed with deconvolution techniques and that SED fitting was performed on a component-by-component basis. In the main text of this Chapter and in Sobral et al. (2015b), the SED fitting was performed using blended ground based NIR and IRAC photometry, without using *HST* photometry. As discussed in the main text, a dual-component fit was required to simultaneously match the NIR and the IRAC photometry, leading to the assumption that the majority of mass did not coincide with the peak UV brightness. *HST* photometry was consistent with these fits, providing further confidence in their validity.

As discussed above, the method used in Bowler et al. (2017b) assumes that the three UV components have similar colours between $\approx 1500 - 5000$ Å. Without higher resolution MIR imaging (possible with *JWST*), this can currently not be tested. On the other hand, the ALMA measurements (Matthee et al. 2017e and Chapter 5) show that the highest dynamical mass within CR7 is co-located with component A. This is consistent with the result from Bowler et al. (2017b) and indicates that CR7 is an ongoing merger with several components whose light is dominated by 'normal' stellar populations. However, ALMA also reveals a [CII] emitting component that is not detected in the UV, but with similar dynamical mass as component A. This component is located between the three UV components of CR7 and could contribute to the IRAC photometry, but this

remains to be evaluated.

4.C   Comparison to Shibuya et al. (2018)

Shibuya et al. (2018) independently reduced and analysed the X-SHOOTER spectrum of CR7. While they confirm the Lyα line, the authors do not find an emission line at $> 2\sigma$ significance in the NIR spectrum. They measure a detection significance of $< 1\sigma$ at $\lambda = 1640$ Å in the full stack, ruling out the He II line as presented in Sobral et al. (2015b). They conclude no He II is observed in CR7.

A detailed comparison to the analysis of Shibuya et al. (2018) is challenging, as they do not specify over which spatial positions their 1D spectrum was extracted and whether their spectrum is converted to vacuum wavelength. Since we find that the centroid of the tentative line is slightly off-centred, the 1D spectrum of Shibuya et al. (2018) may miss part of the flux. Based on private communication with the authors and visual inspection of their Figure 8, it is clear that Shibuya et al. (2018) compare their data (reduced with correct wavelength calibration files) with those from Sobral et al. (2015b) that had been reduced with the wrong wavelength solution. Therefore, their measurement of $< 1\sigma$ significance at the position of He II had been performed at a different wavelength.

As noted in Shibuya et al. (2018) and as is visible in their Figure 8, they find tentative flux at a slightly redder wavelength – similar to the wavelength where we identify the tentative the He II line in the updated analysis in this Chapter. They measure that this flux is at the 1.8σ level, but (as they also note) this tentative line is contaminated by a nearby skyline (see also Fig. 4.4), in particular because they smooth in the wavelength direction. It is unclear how this affects their measured significance. Finally, as discussed in §4.3.3, we found in our revised analysis that the flux originates predominantly from a single observing block, such that its measured significance would increase if only this OB had been used.

Therefore, while the analysis of Shibuya et al. (2018) motivated us to revisit our own analysis, point out the inaccuracies in the wavelength calibrations and explore the origins of the tentative signal, we conclude too few details are given in Shibuya et al. (2018) to fully assess the differences between the analyses. While we agree that the significance may not be as high as initially presented, we leave it to the reader to conclude whether a line is 'detected'. Importantly, further observations that carefully take into account potential spatial variations of the spectrum are clearly required. Note that, compared to other studies in the literature, the ≈ 3 hours of VLT/X-SHOOTER time invested in the CR7 observations have been very modest. For example, Zabl et al. (2015) observed *Himiko* with X-SHOOTER for 10 hours, Laporte et al. (2017b) observed three $z \sim 7$ galaxies for 11-12 hours each and Vanzella et al. (2014) did not detect a $z \sim 7$ galaxy candidate combining 52 hours of integration time with VLT/FORS-2 from multiple programs.

CHAPTER 5

ALMA reveals metals yet no dust within multiple components in CR7

We present spectroscopic follow-up observations of CR7 with ALMA, targeted at constraining the infrared (IR) continuum and $[CII]_{158\mu m}$ line-emission at high spatial resolution matched to the *HST*/WFC3 imaging. CR7 is a luminous Lyα emitting galaxy at $z = 6.6$ that consists of three separated UV-continuum components. Our observations reveal several well-separated components of [CII] emission. The two most luminous components in [CII] coincide with the brightest UV components (A and B), blue-shifted by $\approx$ 150 km s^{-1} with respect to the peak of Lyα emission. Other [CII] components are observed close to UV clumps B and C and are blue-shifted by $\approx$ 300 and $\approx$ 80 km s^{-1} with respect to the systemic redshift. We do not detect FIR continuum emission due to dust with a 3σ limiting luminosity $L_{IR}(T_d = 35\,K) < 3.1 \times 10^{10}$ L$_\odot$. This allows us to mitigate uncertainties in the dust-corrected SFR and derive SFRs for the three UV clumps A, B and C of 28, 5 and 7 M$_\odot$ yr^{-1}. All clumps have [CII] luminosities consistent within the scatter observed in the local relation between SFR and L$_{[CII]}$, implying that strong Lyα emission does not necessarily anti-correlate with [CII] luminosity. Combining our measurements with the literature, we show that galaxies with blue UV slopes have weaker [CII] emission at fixed SFR, potentially due to their lower metallicities and/or higher photoionisation. Comparison with hydrodynamical simulations suggests that CR7's clumps have metallicities of $0.1 < Z/Z_\odot < 0.2$. The observed ISM structure of CR7 indicates that we are likely witnessing the build up of a central galaxy in the early Universe through complex accretion of satellites.

Matthee, Sobral, Boone, Röttgering, Schaerer, Girard,
Pallottini, Vallini, Ferrara, Darvish and Mobasher

5.1   Introduction

Characterising the properties of the interstellar medium (ISM) of the first genera-
tions of galaxies is one of the prime goals of observational astrophysics. With the
advent of the Atacama Large Millimetre Array (ALMA), direct measurements of
the ISM are now becoming possible for typical star-forming galaxies in the early
Universe ($z > 6$, e.g. Maiolino et al. 2015; Watson et al. 2015; Knudsen et al.
2017), in addition to studies of bright quasar hosts and galaxies with extreme
bursts of star-formation (e.g. Swinbank et al., 2012; Riechers et al., 2013; Wang
et al., 2013; Decarli et al., 2017; Riechers et al., 2017). These measurements are
very valuable in constraining models of early galaxy formation (e.g. Ceverino
et al., 2010; Hopkins et al., 2014; Pallottini et al., 2017a).

Rest-frame far-infrared continuum measurements (redshifted to sub-
millimetre wavelengths detectable by ALMA) can provide a direct determina-
tion of the dust mass, temperature and attenuation (e.g. da Cunha et al., 2015;
Bouwens et al., 2016; Scoville et al., 2016, 2017), and constrain the rate at which
dust has been produced (e.g. Hirashita et al., 2014; Michałowski, 2015; Mancini
et al., 2015, 2016). Combining measurements of emission lines in the far-infrared
such as the fine-structure lines $[CII]_{158\mu m}$, $[NII]_{205\mu m}$ and $[OIII]_{88\mu m}$ allows to
constrain the star formation rate (SFR), metallicity, density and ionisation state
of the gas, both at low redshift (e.g. Ferkinhoff et al., 2010; De Looze et al., 2014;
Herrera-Camus et al., 2015) and at high-redshift (e.g. Inoue et al., 2016; Carniani
et al., 2017). Furthermore, spatially resolved emission-line measurements can
probe the dynamical structure of the gas (e.g. Jones et al., 2017; Smit et al., 2018).

Besides quasar-hosts, dust continuum at $z > 6$ has been detected in a few
sources (Watson et al., 2015; Laporte et al., 2017a), but most sources show very
little dust (e.g. Schaerer et al., 2015; Bouwens et al., 2016). Observations of the
[CII] fine-structure cooling line indicate a large scatter in [CII] luminosities at
fixed SFR, particularly when compared to estimates based on the UV (e.g. De
Looze et al., 2014). While some sources have similar [CII] luminosities as those
on the local relation between SFR(UV) and $L_{[CII]}$, (e.g. Capak et al., 2015; Smit
et al., 2018; Jones et al., 2017), others have significantly fainter [CII] luminosities
at fixed UV SFR (e.g. Ouchi et al., 2013; Ota et al., 2014). A potential explanation
is that this is due to a selection bias. A large number of early sources observed
by the ALMA were selected based on their Lyα emission needed to measure
redshifts. Strong Lyα emission is typically associated with a high ionisation
state and/or lower metallicity (e.g. Nakajima et al., 2016; Trainor et al., 2016;
Matthee et al., 2017b; Stark et al., 2017), which should result in a deficit in [CII]
luminosity due to photo-dissociation (e.g. Vallini et al., 2015). This can be tested
with deeper [CII] observations of sources that span a wider parameter space
(e.g. Knudsen et al., 2017; Bradač et al., 2017).

Here we present deep spectroscopic observations of the COSMOS Redshift
7 galaxy (CR7) with ALMA, targeting the far-infrared dust continuum emission
and the [CII] line. CR7 has been identified as the most luminous Lyα emitter
(LAE) at $z = 6.6$ based on narrow-band imaging with Subaru/Suprime-Cam
(Matthee et al., 2015), with $L_{Ly\alpha} = 8.5 \times 10^{43}$ erg s^{-1} and $EW_{0,Ly\alpha} = 210$ Å

(Sobral et al., 2015b). Independently, Bowler et al. (2012, 2014) identified CR7 as a candidate luminous Lyman-break galaxy at $z \sim 6 - 7$ with ground-based near-infrared imaging. Hence, CR7 is also among the most UV-luminous galaxies known at $z \sim 7$, with $M_{1500} = -22.2 \pm 0.1$ (see Matthee et al. 2017d for even more luminous ones).

Besides strong Lyα emission, Sobral et al. (2015b) identified a narrow He$_{II}$ emission-line in near-infrared spectroscopic follow-up observations, and obtained limits on UV metal lines such as C$_{IV}$ and C$_{III}$]. *HST*/WFC3 near-infrared imaging revealed three separate rest-frame UV components, of which the brightest component (A) is closest to the peak of Lyα surface brightness on which spectroscopic observations were centred. The other two components (B and C) have photometric redshifts consistent with $z \gtrsim 6.5$.

These properties led to spectacular interpretations; clump A could contain low metallicity, hot ($T_{eff} \gtrsim 10^5$K) PopIII-like stars (e.g. Sobral et al., 2015b; Visbal et al., 2016) or a direct collapse black hole (e.g. Pallottini et al., 2015; Dijkstra et al., 2016a; Hartwig et al., 2016; Agarwal et al., 2016; Smidt et al., 2016; Smith et al., 2016b; Agarwal et al., 2017). However, in independent analyses, Bowler et al. (2017b) presented evidence of the possible presence of [O$_{III}$] line-emission inferred from deblended *Spitzer*/IRAC photometry. While the Bowler et al. (2017b) measurements are still consistent with a direct collapse or low metallicity AGN (e.g. Agarwal et al., 2017; Pacucci et al., 2017), the lower claimed significance of the He$_{II}$ line by Shibuya et al. (2018) removes most of the evidence for an AGN. As presented in detail in Sobral et al. (2018a), a re-analysis of old spectra and new near-infrared spectroscopy with the *HST*/WFC3 grism shows that the He$_{II}$ line is indeed at lower significance. Moreover, if present, it is at lower luminosity (by a factor ≈ 3) and does not spatially coincide with clump A, but rather is emitted in the direction of clump C. No UV metal lines are detected in clump A. This points towards a moderately low metallicity galaxy that is actively forming stars, without clear evidence for AGN activity (but see further details in Sobral et al. 2018a).

In this paper, we answer to the question of the presence of metals in CR7, and test whether the metallicity and dust content varies between different UV components. We summarise the UV properties of CR7 in §5.2. ALMA observations, data reduction, astrometry and sensitivity are discussed in §5.3. We investigate the resolved [C$_{II}$] emission in §5.4. Dust continuum measurements and their implications for the SFRs are detailed in §5.5. In §5.6, we discuss where the different clumps of CR7 are located in the SFR-L$_{[CII]}$ relation, and how this compares with other sources. We discuss the implication of our results in light of recent simulations in §5.7, where we also use these observations to update the interpretation of the nature of CR7. The conclusions of this work are summarised in §5.8. Throughout the paper, we assume a ΛCDM cosmology with $\Omega_M = 0.70$, $\Omega_\Lambda = 0.30$ and $H_0 = 70$ km s^{-1} Mpc^{-1}, and assume a Salpeter (1955) initial mass function (IMF) with mass limits 0.1 M$_\odot$ and 100 M$_\odot$.

5.2   UV properties of CR7

In the rest-frame UV, CR7 consists of three clumps (A, B and C, Sobral et al. 2015b), of which the brightest (A) coincides with the peak of Lyα emission, and is also spectroscopically confirmed at $z_{Ly\alpha} = 6.604$. UV components are separated by $\sim 1''$, corresponding to projected distances of ~ 5kpc. The latest photometry on the *HST*/WFC3 imaging in the F110W and F160W filters has been performed by Bowler et al. (2017b). We use this photometry to compute UV slopes of the three different clumps individually. The contribution of Lyα to the flux observed in the F110W filter is based on our Lyα narrow-band imaging as follows: we first correct the Subaru/S-Cam NB921 image for the contribution from the UV continuum by subtracting the z' image (which is calibrated such that a colour of z'-NB921=0 corresponds to a line flux of zero, see Matthee et al. 2015) and then use this Lyα image to measure the Lyα flux at the positions of clumps A, B and C. The Lyα flux is multiplied by a factor two to take into account that the NB921 filter transmission is 50 % at the wavelength of CR7's Lyα. We then convolve the apertures that have been used for *HST* photometry ($1''$, $0.4''$, $0.4''$, for clumps A, B and C respectively) with the PSF of the NB921 imaging ($0.6''$) and measure the Lyα flux in those PSF-convolved apertures. We measure Lyα fluxes of $8.3, 2.7, 1.3 \times 10^{-17}$ erg s^{-1} cm^{-2} in these apertures. Correcting the flux-density observed in the F110W for this line-flux contribution results in corrections of +0.15, +0.16 and +0.05 to the F110W magnitude (and M$_{1500}$) for clumps A, B and C, respectively. We measure UV slopes of $\beta = -2.3 \pm 0.4, -1.0 \pm 1.0$ and -2.3 ± 0.8, for the three clumps respectively (see Table 6.2).[1] Due to the shallow depth of the observations, the UV slopes of clumps B and C are only poorly constrained, and deeper observations particularly in the F160W filter are required to improve them.

Based on the rest-frame UV luminosities and UV slopes, we derive SFR$_{UV}$, where dust attenuation is estimated using the Meurer et al. (1999) attenuation law. We take the measurement uncertainties in the rest-UV magnitudes into account by perturbing these values 10,000 times (assuming the uncertainties are gaussian). In each realisation, we re-compute the UV luminosity and UV slope, and use these to derive dust-corrected SFR. We then obtain the median and the 1σ percentiles and use these to derive the asymmetric uncertainties. With this method, the SFRs are 29^{+23}_{-2}, 38^{+182}_{-32} and 7^{+19}_{-1} M$_\odot$ yr^{-1} for clumps A, B and C, respectively. The uncertainties in the dust corrected SFRs are large due to the propagation of errors in β. However, as we show in §5.5, these uncertainties are mitigated by constraints on the IR luminosity from our deep ALMA observations, which place firm limits on the dust-obscured SFR. Because of these constraints, our final results would also only change marginally if an SMC-like attenuation law is used. The results are listed in Table 6.2. The F110W imaging has a 3σ sensitivity of 27.3 AB magnitude in a $0.4''$ diameter, which corresponds to a limiting UV magnitude M$_{1500} > -19.5$ and a SFR$_{UV} < 4$ M$_\odot$ yr^{-1}.

---

[1] Without correcting the F110W photometry for the contribution from Lyα, we would obtain UV slopes of $\beta = -2.8 \pm 0.4, -1.5 \pm 1.0$ and -2.4 ± 0.8 for clump A, B and C. While the errors are still dominated by measurement uncertainty, systematic uncertainties due to ignoring potentially
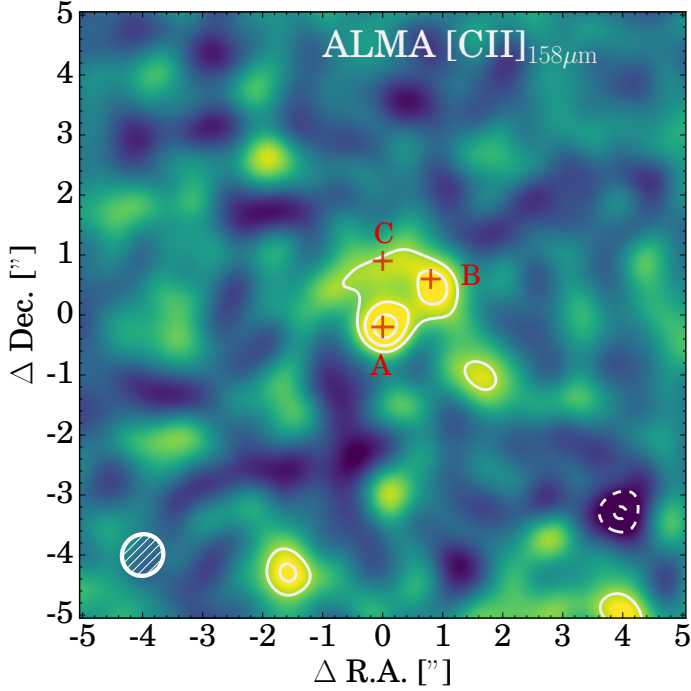
Figure 5.1: ALMA [CII] narrow-band image of CR7, collapsed for frequencies with -614 to $+96$ km s^{-1} with respect to the Lyα reference frame ($z = 6.604$). The image (54×54 kpc) is centred on the peak of Lyα position and the ALMA astrometry is shifted by $0.25''$ to the west to align it with *HST* imaging as described in §5.3.2. Contours are shown at the $3, 4, 5\sigma$ significance levels (with $1\sigma = 0.016$ Jy beam^{-1} km s^{-1}). Negative contours are shown as dashed lines. The beam size is shown in the bottom left corner and has FWHM $0.82'' \times 0.77''$. The red crosses mark the positions of the UV clumps of CR7. [CII] is clearly detected in CR7, indicating the presence of carbon.

5.3 ALMA data

5.3.1 Observations & data reduction

We observed CR7 (10:00:58.00 +01:48:15.3, J2000) in band 6 with ALMA during cycle 3 with configuration C43-4, aimed to achieve a $0.3''$ angular resolution (program ID #2015.1.00122.S). The target has been observed with between 35-43 antennas for a total on source integration time of 6.0h on 22, 23, 24 May and 4, 8 November 2016, with precipitable water vapor ranging from 0.3-1.4 mm. We observed in four spectral windows centred at 249.94592, 247.94636, 234.94917 and 232.9496 GHz with a bandwidth of 1875 MHz, of which the first is centred at [CII] line emission ($\nu_{z=6.604} = 249.9395$ GHz). The central frequencies of the spectral windows correspond to rest-frame frequencies between 1771.7 GHz and 1901.0 GHz, with a velocity resolution of 19.4 km s^{-1}. The phase calibrations have been performed on the source J0948+0022. The quasar J1058+0133 has been

_____

important contributions from Lyα could bias UV slope measurements to artificially bluer values.

observed regularly as a bandpass and flux calibrator, resulting in typical flux calibration errors of ~ 10 %. Data have been reduced using CASA version 4.7.0 (McMullin et al., 2007) with natural weighting and channel averaging resulting in a 38.8 km s^{-1} velocity resolution. We use uv tapering of the visibilities with a Gaussian width FWHM=0.7$''$ to optimise the S/N ratio. The observational set-up and data reduction results in a beam size of $0.35 \times 0.33''$ (gaussian σ; $0.82 \times 0.77''$ FWHM), with a position angle of -49.5 deg. We have also performed the reduction with uv tapering with different smoothing kernels ranging from $0.4 - 0.8''$, but find that all changes in luminosity, line-width and size measurements are consistent within the error-bars. A simple estimate of the noise level of the pixels within a radius of 20$''$ of the center results in rms=0.06 mJy beam^{-1} in 38.8 km s^{-1} channels.

5.3.2   Astrometry

As described in §5.4, we detect two separate clumps at high significance in the [CII] image collapsed over all velocities at which significant line-emission is detected, see Fig. 5.1. These [CII] clumps are offset by 0.25$''$ to the east with respect to the UV positions of clumps A and B, while the offset in declination is $< 0.10''$, respectively. The alignment of both clumps, and their separation is also similar in the UV and in [CII]. As these two [CII] clumps resemble the geometry of clumps A and B, we assume that the offsets between the UV positions and [CII] positions are due to errors in the astrometry. This offset is similar in magnitude as reported in e.g. Dunlop et al. (2017), but in the R.A. direction instead of the Dec. direction (see also Carniani et al. 2017 and references therein for offsets in $z \sim 6 - 7$ galaxies). For the rest of the analysis, we align the ALMA data with *HST* and Subaru narrow-band data by applying an offset of 0.25$''$ to the west. We note that the positions of two serendipitous IR continuum-detections of foreground galaxies are also in agreement with this offset (see §5.5.1 and Fig. 5.8).

5.3.3   Line-sensitivity measurements

As the noise is correlated spatially and spectrally, we measure the sensitivity of the observations and significance of detections as follows. In each collapsed image (which has a size of $51.2'' \times 51.2''$, centred on CR7), we measure the noise over the same spatial scales as those used for measurements (typically a beam-size, $r = 0.35''$). We place circular apertures on 100,000 random positions on the image and integrate the flux over the scales confined by these apertures. As the image size is much larger than the source size, we do not mask any central region. We then compute the 1σ detection significance using the r.m.s., which results in 16.9 mJy beam^{-1} km s^{-1} for beam-sized apertures on the collapsed image shown in Fig. 5.1.

As illustrated in Fig. 5.3, the distribution of fluxes measured on random positions approximately follows a gaussian. It can be seen that the negative image (where we have inverted all counts) has slightly lower number counts
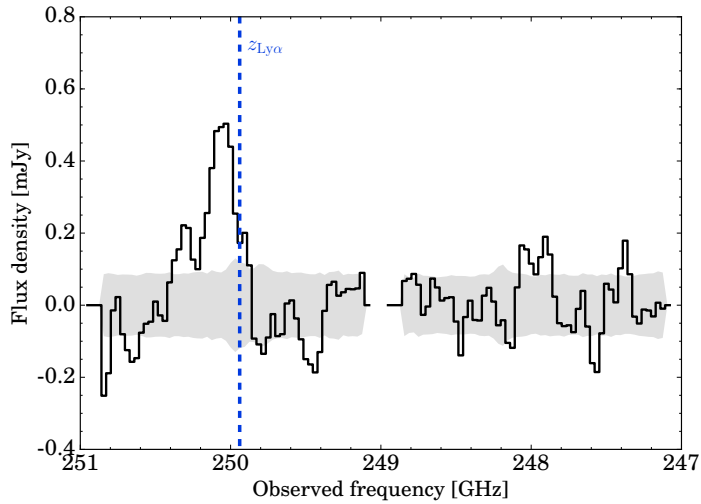
Figure 5.2: Integrated spectrum over the 3σ [CII] contour area in Fig. 5.1, in two observed spectral windows. The grey shaded region indicates the 1σ error estimated using apertures with the same geometry as the 3σ contour area, as a function of frequency. The blue dashed line indicates where [CII] would be detected at $z = 6.604$, the Lyα redshift of CR7. Lyα is redshifted by ≈ -170 km s^{-1} with respect to the systemic [CII] redshift.
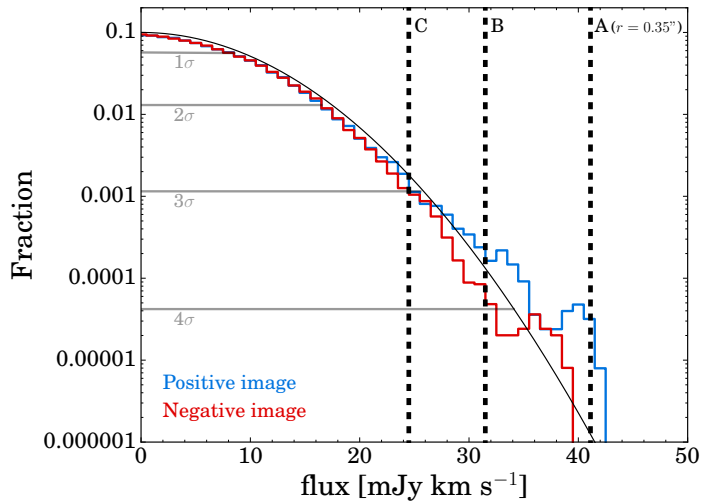

Figure 5.3: Histogram of the integrated [CII] fluxes measured over circular, beam-sized scales at random positions in the collapsed cube (with velocities from -614 to $+96$ km s^{-1} with respect to Lyα). The blue histogram shows positive fluxes, while the red histogram shows negative fluxes. We indicate the [CII] flux measured at the positions of *HST* clumps A, B and C with vertical lines. These correspond to $\approx 5, 4, 3\,\sigma$ detections, respectively. The grey curve shows the expected noise properties if the noise is gaussian with a 1σ dispersion.

than the positive image at high flux levels. This is due to random positions around the centre of CR7, or real sources around CR7. These sources (such as a $\sim 4\sigma$ detection $4''$ from the south-east of CR7, see Fig. 5.1) are discussed and investigated in a future paper. When integrating over a larger spatial scale, the noise estimate is slightly higher due to spatially correlated noise. The noise level is lower when data is collapsed over a smaller velocity range. In individual velocity channels (with resolution 38.8 km s^{-1}), we measure a 1σ sensitivity between 30-40 μJy when integrating flux over beam-sized scales. Throughout the paper, we convert measured fluxes to [CII] luminosities following e.g. Solomon et al. (1992) and Carilli & Walter (2013):

$$L_{[CII]}/L_\odot = 1.04 \times 10^{-3} \times S_\nu \Delta v \times \nu_{obs} \times D_L^2, \qquad (5.1)$$

where $S_\nu \Delta v$ is the flux in Jy km s^{-1}, ν_{obs} the observed frequency in GHz ($\approx$ 250.0 GHz for CR7) and D_L is the luminosity distance in Mpc (64457.8 Mpc at $z = 6.60$).

5.4   Resolved [CII] emission

5.4.1   Total luminosity

In order to search for [CII] emission around CR7, we inspect the data-cube of the spectral tuning centered at the frequency where [CII] is expected to be observed. As shown in Fig. 5.1, resolved [CII] emission is clearly detected.[2] We show the collapsed data-cube with velocities between -614 and $+96$ km s^{-1} with respect to the Lyα redshift, which includes the full velocity range over which we detect [CII] emission. Within the 3σ significance contours, we measure $L_{[CII]}$ = $2.17 \pm 0.36 \times 10^8$ L$_\odot$ in the collapsed image.[3] The spectrum extracted over this region is shown in Fig. 5.2 and is best-fitted with a line-width of $v_{FWHM} =$ 299 ± 27 km s^{-1} that is offset by -167 ± 27 km s^{-1} with respect to the Lyα redshift, see Table 6.2. The 3σ significance contours span a total area of 2.2 arcsec^2 and have a maximum diameter of $1.8''$, which corresponds to 9.7 kpc at $z = 6.60$. This detection of [CII] emission in a large region in/around CR7 clearly indicates the presence of metals, ruling out the possibility that a large fraction of the gas is primordial.

5.4.2   Multiple separated [CII] components

As illustrated in Fig. 5.1, the [CII] emission is clearly not homogeneous over the 3σ contour and reveals already two local peaks, resembling the rest-frame UV morphology as observed by *HST* (see Fig. 5.5). In order to show structure in both the spatial and spectral dimensions, we create collapsed [CII] maps in

---

[2] The individual [CII] channel maps with widths $\Delta v = 38.8$ km s^{-1} and frequencies from 249.83-250.42 GHz (corresponding to $z_{[CII]} = 6.607 - 6.589$) are shown in Fig. 5.12.

[3] This error has been estimated by measuring the flux in randomly located apertures with the same geometry as the 3σ contours.
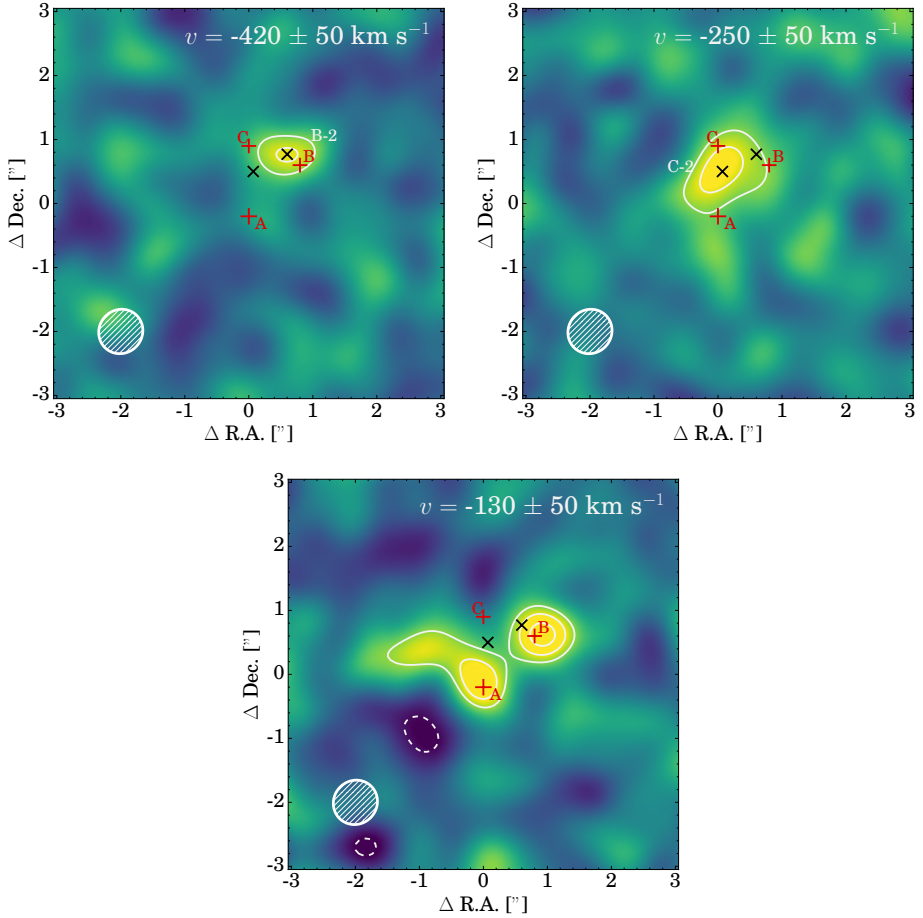
Figure 5.4: [CII] map in three velocity channels of 100 km s^{-1}, zoomed in on CR7 (with a scale of 32 × 32 kpc) and with velocities with respect to the Lyα redshift of $z = 6.604$. Contours mark the 3, 4, 5 σ levels, with sensitivities $\sigma \approx 5 - 6$mJy beam^{-1} km s^{-1}. Red crosses mark the positions of the UV clumps, while black crosses mark the positions of additional [CII] components B-2 and C-2. The most luminous [CII] components coincide with UV clumps A and B and have a similar peak velocity. Fainter [CII] flux is detected at $> 4\sigma$ in between clumps A, B and C offset by -120 km s^{-1} (clump C-2), and close to clump B at -290 km s^{-1} (clump B-2).

three different velocity ranges of 100 km s^{-1} each and show these in Fig. 5.4. As the noise level varies slightly at different velocities and is smaller for images that are collapsed over a smaller velocity range, we compute the noise level in each image independently as described in §5.3.3.

The three velocity channels reveal that the [CII] emission in CR7 consists of multiple, well separated components. Around the systemic velocity (-130 km s^{-1} with respect to Lyα), two sources are clearly detected at the UV positions of clumps A and B. At a blue-shift of ≈ 250 km s^{-1} a relatively faint, resolved component is detected in between the three UV clumps, but closest to clump C. No significant UV emission is detected at that ALMA position. We name this component C-2. Another compact sub-component is detected at an even larger blue-shift of ≈ 420 km s^{-1} close to the position of clump B (well within the beam radius), and hence named B-2. In these narrower velocity slices, all detections are at the $\gtrsim 4\sigma$ significance level, see Fig. 5.4.

Hence, we detect several components of [CII] emission in the CR7 system that are significantly offset in both the spatial and spectral dimension. Before discussing the implications of these detections in §5.7.1, we first measure their luminosities and [CII] line-profiles.

Measurements of individual clumps

Except for clumps A and C-2, all clumps are unresolved (see §5.4.3). For unresolved sources, we measure the [CII] luminosity within a circular aperture-region with radius of 0.35″ (corresponding to the beam semi-major axis). For clumps A and C-2, we use 0.55″ and 0.50″ apertures respectively to account for the fact that these sources are slightly extended. For these clumps, we find that these apertures retrieve the same fraction of the flux as is retrieved for modelled point sources with a 0.35″ aperture. Measurements at *HST*/UV positions are done on the collapsed image over the full velocity range (e.g. Fig. 5.1), while measurements at ALMA positions (B-2 and C-2) are done in the collapsed velocity range in which these clumps are detected (e.g. Fig. 5.4).

In Fig. 5.6 we show the ALMA spectra of the different clumps (extracted over their respective apertures) in the rest-frame of clump A ($z = 6.601$) and compare these to the Lyα profile measured with X-SHOOTER at the peak of Lyα emission (close to clump A). We measure the velocity offset between [CII] and Lyα and the [CII] line-width and amplitude by fitting gaussian profiles. All measurements are summarised in Table 6.2.

We find that clump A, which is the brightest in the UV and closest to the peak of Lyα emission, is also the brightest in [CII] line-emission, with $L_{[CII]} = (0.96 \pm 0.20) \times 10^8$ L$_\odot$. We caution that we measure a factor two lower luminosity if we measure the luminosity of clump A with a beam-sized aperture. Clump A is blue-shifted by 146 ± 27 km s^{-1} with respect to Lyα. This is slightly smaller than typical offsets between Lyα and nebular lines for sources with similar UV luminosities (e.g. Stark et al., 2017), although Carniani et al. (2017) shows a wide spread of velocity offsets in a compilation of ALMA detections (i.e. $-150 < \Delta v < +400$ km s^{-1} for galaxies with $10 < $ SFR < 100 M$_\odot$ yr^{-1}). The [CII]
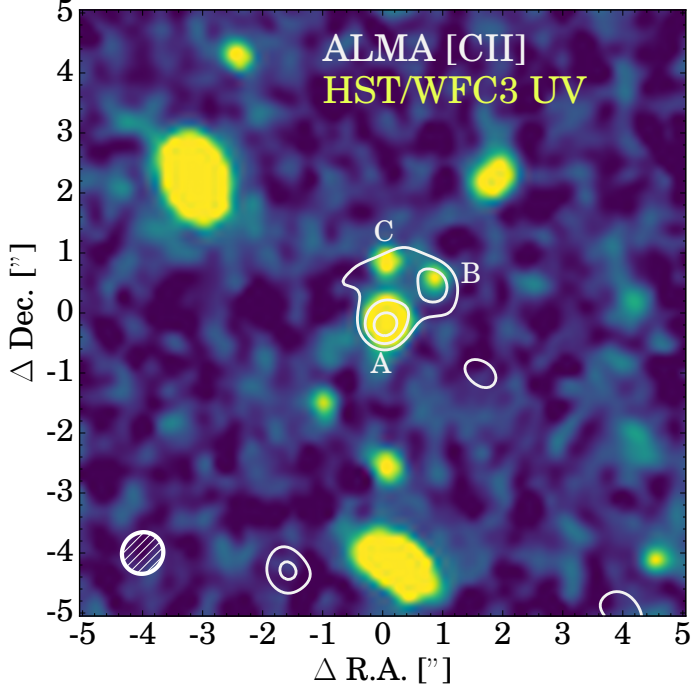
Figure 5.5: Rest-frame UV image (from *HST*/WFC3 F110W imaging) of CR7, overlaid with ALMA [Cɪɪ] 3, 4, 5σ contours at a scale of 54×54 kpc. The names of the three UV clumps are annotated in HST imaging. Relatively compact components of [Cɪɪ] emission are detected around clumps A and B, while there is diffuse [Cɪɪ] emission covering clump C, although at lower significance.

line-width is 259 ± 24 km s^{-1}, similar to the Lyα line-width (see e.g. Fig. 5.6).

At the UV position of clump B, we measure [Cɪɪ], with $L_{[CII]} = (0.34 \pm 0.09) \times 10^8$ L$_\odot$, which contains the contribution from both the ALMA detections B and B-2 (with ≈ 33 % of the flux being due to the sub-component B-2, see Table 6.2). The brightest [Cɪɪ] component of clump B is at $z = 6.600 \pm 0.001$, similar to the redshift of clump A, but has a narrower line-width. Clump B-2 is blue-shifted by 290 ± 30 km s^{-1} with respect to the systemic redshift and has a relatively narrow-line width of 92 ± 22 km s^{-1}.

At the position of clump C, we measure relatively faint [Cɪɪ] emission at the $\approx 3\sigma$ level, see Fig. 5.1 and Fig. 5.5. The aperture at the position of clump C is contaminated slightly by this clump B-2 (which may also be associated with C), explaining the bluest line, but the redder [Cɪɪ] component C-2 is offset spatially (see Fig. 5.4). At the position of C-2, we measure $L_{[CII]}=(0.27 \pm 0.07) \times 10^8$ L$_\odot$ with a line-width of 181 ± 30 km s^{-1} and an offset of -232 ± 27 km s^{-1} with respect to Lyα. This offset is bluer than clumps A and B, but redder than B-2. Due to its large blue-shift, component C-2 also dominates the velocity map shown in Fig. 5.7. Due to this strong contribution of component C-2 to the velocity map, we find that there is no clear evidence for ordered rotation over
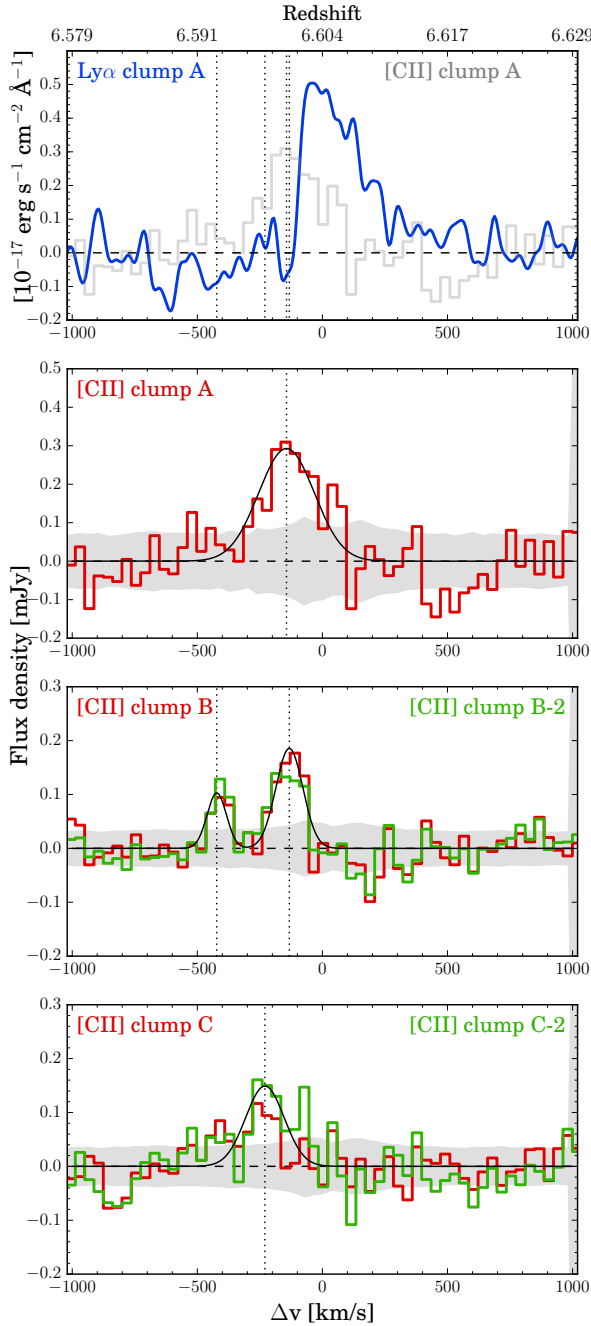
Figure 5.6: Flux densities of Lyα (from X-SHOOTER, centered at clump A) and [CII] at the HST positions of clumps A, B and C as a function of velocity with respect to the Lyα peak velocity at $z = 6.604$. We also measure [CII] line-profiles at the positions B-2 and C-2 (shown in green), based on [CII] detections, see Fig. 5.4. Gaussian fits are shown in black, and we highlight the central velocities with vertical dotted lines. Errors have been estimated for each velocity-slice and aperture as described in §5.3.3.
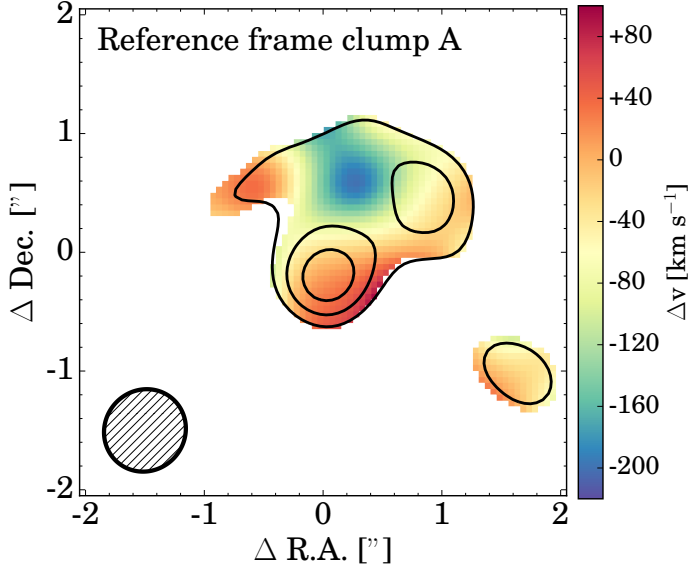
Figure 5.7: [Cii] velocity map (at a 22×22 kpc scale) in the rest-frame of clump A, based on the first moment map collapsed for frequencies with -614 to $+96$ km s^{-1} with respect to the Lyα redshift (see Fig. 5.1 for the corresponding [Cii] flux map). Contours show the 3, 4 and 5σ threshold and velocity maps are shown for $> 3\sigma$ detections. The map is driven by the the strongly blue-shifted component C-2.

the full [Cii] extent. This shows that the spatial resolution of our observations is crucial, as we may have not been able to distinguish clumps C-2 and B/B-2 with lower resolution, and could have mis-interpreted the velocity map as rotation. It is challenging to investigate whether ordered rotation is present inside individual clumps because they are either unresolved or only marginally resolved. Similarly as for clump A, we note that the [Cii] luminosity of clump C-2 would be reduced by a factor ≈ 2 if we use a smaller aperture of $0.35''$, which is used for unresolved sources. Therefore, the luminosities of clumps A and C-2 should be interpreted with caution. The total [Cii] luminosity that is associated to clumps is $(1.57 \pm 0.23) \times 10^8$ L$_\odot$, which is the sum of the aperture measurements at the *HST* positions. This corresponds to a fraction of 0.72 ± 0.18 of the total observed [Cii] luminosity.

5.4.3 Sizes and dynamical masses

Starting from the measured velocity width and size of the emitting regions, it is possible to obtain a rough estimate of the dynamical mass of the various [Cii] components (e.g. Wang et al., 2013). First, we measure the size by performing

two dimensional gaussian fits in the collapsed 2D image. Clumps A and B are simultaneously fitted in the image that is collapsed over the full velocity range, while clumps B-2 and C-2 are fitted in the collapsed image in the velocity range as shown in Fig. 5.4. In our fitting procedure, we fixed the position angle and the ratio between the dispersion in both dimensions corresponding to the those of the beam semi-major and semi-minor axis. We also fix the positions to those indicated in Fig. 5.4. Hence, the free parameters are the amplitudes and widths of the gaussian profiles. In order to take the (correlated) noise into account, we add the noise from a randomly selected cut-out region in the collapsed image, avoiding the source itself, before performing the fit. This is repeated 5000 times in order to estimate the statistical reliability of the fit. We find that more than $> 50\%$ of the measurements for clumps B and B-2 result in a size that is equal to or smaller than the beam, meaning that these clumps are unresolved and hence have a size $r_{1/2,[CII]} < 2.2$ kpc. We measure an observed size of $r_{1/2,[CII],obs} = 3.7^{+0.6}_{-0.6}$ kpc for clump A (4 % of the measurements result in an unresolved size, meaning that clump A is resolved at $\approx 2\sigma$ significance) and $r_{1/2,[CII],obs} = 4.4^{+0.9}_{-0.6}$ kpc for clump C-2 (resolved at $\approx 3.5\sigma$ significance). We deconvolve the sizes of A and C-2 to obtain the intrinsic size with $r_{\sigma,[CII]} = \sqrt{r^2_{obs} - 2.2^2}$. Resulting sizes are listed in Table 6.2. Dynamical masses are computed following Wang et al. (2013):

$$M_{dyn}/M_\odot (\sin i)^2 = 1.94 \times 10^5 \times v^2_{FWHM,[CII]} \times r_{1/2,[CII]}, \qquad (5.2)$$

where M_{dyn} is the dynamical mass in $M_\odot$, i is the inclination angle, $v_{FWHM,[CII]}$ the line-width in km s^{-1} and $r_{1/2,[CII]}$ the size in kpc (half-light radius). This results in dynamical masses (uncorrected for inclination) ranging from $(3.9 \pm 1.7) \times 10^{10}$ M$_\odot$ for component A, $(2.4 \pm 1.9) \times 10^{10}$ M$_\odot$ for clump C-2 and $< 0.7 \times 10^{10}$ M$_\odot$ for $< 0.4 \times 10^{10}$ M$_\odot$ for clumps B and B-2, respectively. These dynamical mass estimates are lower than typical quasar host galaxies at $z \approx 6$ (Wang et al., 2013), and comparable to star-forming galaxies at $z \approx 7$ with similar SFRs as CR7 (e.g. Pentericci et al., 2016; Smit et al., 2018).

5.5 IR continuum

5.5.1 Blind detections

We combine the flux in all four spectral windows from our ALMA coverage to search for dust continuum emission. In the entire image, we find two detections with S/N > 3, but they are not associated with CR7. One detection is 3.5″ north-east of CR7 (associated with ID number 339509 in the catalog from Laigle et al. 2016, photo$-z = 0.84$ and visible in Fig. 5.8), while the other is 18.5″ to the south-west (ID number 335753 in Laigle et al. 2016, $photo - z = 3.10$, not visible in the image). The positions of these foreground galaxies confirm the astrometric correction described in §5.3.2. We note that we detect a tentative (3σ) line at 250.484 GHz at the position of ID 339509 that is identified as CO(4-3) with $\nu_0 = 461.041$ GHz at $z = 0.841$, perfectly consistent with its photometric redshift.

Table 5.1: Properties of different components in CR7. Clumps B-2 and C-2 are based on [CII] detections, while A, B and C are based on *HST* detections (see §5.4.2). The 'Full' uses ground-based imaging and the 3σ contour levels from Fig. 5.1. ΔR.A.-HST and ΔDec.-HST are the difference between the *HST* and ALMA positions before shifting the ALMA R.A. by 0.25" to the east. For B-2 and C-2 the differences are between *HST* clumps B and C, and ALMA detections B-2 and C-2, respectively. M_{1500} is estimated from F110W imaging after correcting for the contribution of Lyα emission. SFRs assume a Salpeter IMF following Kennicutt (1998). Dust-attenuation of the UV SFR is estimated based on the UV slope β following Meurer et al. (1999). We provide [CII] luminosities measured from the collapsed image in a beam-sized aperture and [CII] luminosities obtained from the fitted gaussian line-profiles. Dynamical masses are estimated following Wang et al. (2013).

	Clump A	Clump B	Clump B-2	Clump C	Clump C-2	Full
ΔR.A.-HST	$-0.25''$	$-0.24''$	$-0.07''$	...	$+0.14''$	...
ΔDec.-HST	$-0.12''$	$-0.18''$	$-0.04''$	...	$+0.40''$	...
M_{1500}	-21.6 ± 0.1	-19.6 ± 0.2	...	-20.1 ± 0.1	>-19.5	-22.2 ± 0.1
β	-2.3 ± 0.4	-1.0 ± 1.0	...	-2.3 ± 0.8	...	-2.2 ± 0.4
$\mathrm{SFR_{UV,nodust}}/\mathrm{M_\odot\,yr^{-1}}$	27 ± 1	4 ± 1	...	7 ± 1	<4	44 ± 2
$\mathrm{SFR_{UV,Meurer}}/\mathrm{M_\odot\,yr^{-1}}$	29^{+23}_{-2}	38^{+182}_{-32}	...	7^{+19}_{-1}		50^{+55}_{-6}
$\mathrm{SFR_{UV+IR}}/\mathrm{M_\odot\,yr^{-1}}$	28^{+1}_{-1}	5^{+2}_{-1}	...	7^{+1}_{-1}	<4	45^{+2}_{-2}
$\Delta v_{Ly\alpha}/\mathrm{km\,s^{-1}}$	-146 ± 27	-152 ± 21	-422 ± 22	...	-232 ± 27	-167 ± 27
$z_{\mathrm{[CII]}}$	6.601 ± 0.001	6.600 ± 0.001	6.593 ± 0.001	...	6.598 ± 0.001	6.600 ± 0.001
$v_{\mathrm{FWHM,[CII]}}/\mathrm{km\,s^{-1}}$	259 ± 24	130 ± 21	92 ± 22	...	181 ± 30	299 ± 26
$S_{\nu,\mathrm{fit}}\Delta v\,/\mathrm{mJy\,km\,s^{-1}}$	81.1 ± 20.7	25.0 ± 5.3	10.0 ± 3.9	...	35.4 ± 10.9	185.2 ± 39.0
$L_{\mathrm{[CII],fit}}/10^8\,\mathrm{L_\odot}$	0.88 ± 0.23	0.26 ± 0.07	0.12 ± 0.03	...	0.27 ± 0.11	2.00 ± 0.43
$L_{\mathrm{[CII],aperture}}/10^8\,\mathrm{L_\odot}$	0.96 ± 0.20	0.34 ± 0.09	0.11 ± 0.03	0.26 ± 0.09	0.27 ± 0.07	2.17 ± 0.36
$r_{1/2,\mathrm{[CII]}}/\mathrm{kpc}$	3.0 ± 0.8	<2.2	<2.2	...	$3.8^{+1.1}_{-0.7}$	...
$M_{\mathrm{dyn}}/(\sin i)^2\,10^{10}\,\mathrm{M_\odot}$	3.9 ± 1.7	<0.7	<0.4	...	2.4 ± 1.9	...
$L_{\mathrm{UV}}/10^{10}\,\mathrm{L_\odot}$	9.1	1.4	...	2.3	<1.3	15.8
$\mathrm{rms_{cont},\lambda_0=160\text{-}m}/\mu\mathrm{Jy\,beam^{-1}}$	7	7	7	7	7	7
$L_{\mathrm{IR}}\,(T_d=35\mathrm{K})/10^{10}\mathrm{L_\odot}$	<3.14	<3.14	<3.14	<3.14	<3.14	<3.14
$\mathrm{SFR_{IR}}\,(T_d=35\mathrm{K})/\mathrm{M_\odot\,yr^{-1}}$	<5.4	<5.4	<5.4	<5.4	<5.4	<5.4
$M_{\mathrm{dust}}(T_d=35\mathrm{K})/10^6\mathrm{M_\odot}$	<8.1	<8.1	<8.1	<8.1	<8.1	<8.1

As visible in Fig. 5.8, there is a $\approx 2.7\sigma$ continuum detection $\approx 2''$ to the south-east of CR7, nearby a faint *HST* detection that we name potential clump D. This faint *HST* detection has F110W=27.2 ± 0.2 in a $0.4''$ aperture, similar to clump B. It is also detected at $\approx 3\sigma$ in the ACS/F814W filter (F814W= 27.5 ± 0.2) and F160W filter (F160W= 27.0 ± 0.3). It is not detected in NB921 and z' imaging, which have 3σ depths of 25.8 AB magnitude, hence consistent with the *HST* photometry. Potential clump D is not detected in the Subaru S-cam imaging in the B, V, R filters with 2σ upper limits of $\lesssim 28.5 - 29.0$. Therefore, the photometry is consistent with the Lyman-break falling in the F814W filter, such that $4.8 < z_{\text{phot}} < 6.9$. There is no significant [CII] detection at its position in any of the spectral tunings observed with ALMA. Further IFU observations are required to measure the redshift of clump D and test whether it is associated to CR7.

5.5.2 Upper limits for CR7

There is no IR continuum detected at the position of CR7's clumps A, B and C, see Fig. 5.8. Around the position of CR7, we measure an rms of 7 μJy beam^{-1} at $\lambda_0 \approx 160\mu$m. Note that we do not remove contamination from the [CII] line as we expect that this is negligible, as a result our upper limit is therefore somewhat on the conservative side. We follow Schaerer et al. (2015) to convert this limit into a 3σ upper limit on the infrared luminosity (between 8-1000 μm) of $L_{\text{IR}} < 3.14 \times 10^{10}$ $L_\odot$, under the assumption that the dust temperature is 35 K and a modified black body SED with a power-law slope of 2.9 in the Wien regime, $\beta_{\text{IR}} = 1.5$ and after removing the contribution of the CMB to the dust heating, see da Cunha et al. (2013). In the case that the dust temperature is 25 (45) K, the limit on the IR luminosity is $L_{\text{IR}} < 1.68(6.15) \times 10^{10}$ $L_\odot$. Combined with the total [CII] luminosity, we find a lower limit of the the ratio $\log_{10}(L_{\text{[CII]}}/L_{\text{IR}}) > -2.1$, which is similar to the highest values measured in local star-forming galaxies (e.g. Malhotra et al., 2001) and significantly higher than sub-mm galaxies and quasar host galaxies at $z > 3$ (see Ota et al. 2014 for a compilation). This could potentially indicate a lower dust-to-metal ratio, which in turn could result in a higher dust temperature due to the lower dust opacity (e.g. Cen & Kimm, 2014).

The ratio of the $\text{IR}_{160\mu\text{m}}$ to $\text{UV}_{0.15\mu\text{m}}$ flux density is constrained to $(\nu F_\nu)_{\text{IR}}/(\nu F_\nu)_{\text{UV}} < 0.04$ (3σ). This limit is almost an order of magnitude stricter than other $z \sim 7$ sources observed by Maiolino et al. (2015). In the local Universe, this ratio is related to metallicity (see the compilation and fitted relation in Maiolino et al. 2015), likely as a result of dust content increasing with metallicity (e.g. Rémy-Ruyer et al., 2014). If such a relation would be unchanged at $z = 7$ (e.g. Popping et al., 2017), the measurements imply a metallicity of $12 + \log(\text{O/H}) \lesssim 7.5$ (corresponding to $\lesssim 0.1$ $Z_\odot$), which is only found in dwarf galaxies in the local Universe with masses $M_{\text{star}} \lesssim 10^8$ $M_\odot$ (e.g. Izotov et al., 2015; Guseva et al., 2017).

We use the upper limits on the IR continuum to place an upper limit on the dust mass. We follow the method outlined in Ota et al. (2014), which assumes a dust mass absorption coefficient $k_\nu = 1.875(\nu/239.84)^{\beta_{\text{IR}}}$ m^2 kg^{-1} where ν
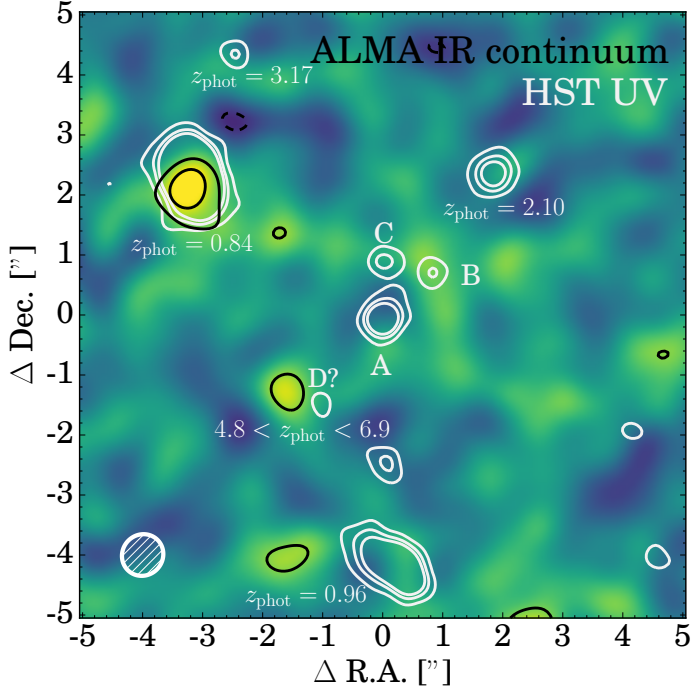
Figure 5.8: IR continuum map at 230-250 GHz centered on the position of CR7. The black contours show the 2, 3σ level, where $1\sigma = 7\mu$Jy beam^{-1}. We also show *HST* rest-frame UV (F814W+F110W+F160W) contours at the 2, 3, 4σ levels to highlight the positions of known (foreground) sources. Sources are annotated with their photometric redshifts estimated by Laigle et al. (2016). No dust continuum is detected at CR7, although a $\approx 2\sigma$ signal is detected around potential clump D. Dust continuum is also clearly detected in a foreground source at $z = 0.84$.

is in GHz and $\beta_{IR} = 1.5$ and removes the contribution from the CMB. This results in $M_{dust} < 8.1(27.5) \times 10^6$ M$_\odot$ if the dust temperature is 35 (25) K. These limits are consistent with expectations for CR7's UV luminosity, based on post-processed hydrodynamical simulations by Mancini et al. (2016), who find dust masses between $\approx 1 - 10 \times 10^5$ M$_\odot$.

Following the prescription from Kennicutt (1998), we measure a 3σ upper limit of the dust obscured SFR$_{IR} < 5.4$ M$_\odot$ yr^{-1} for a Salpeter (1955) IMF. This allows us to put a stronger constraint on the total SFR of different clumps. Because of these tight limits, the large errors in β (which for example allow relatively red UV slopes and hence relatively large dust obscurations) are mitigated. Combining these measurements (by constraining that the difference between dust-corrected SFR and dust-free SFR is < 5.4 M$_\odot$ yr^{-1} in each of the 10,000 realisations used to self-consistently compute the uncertainties as described in §5.2) results in SFR$_{UV+IR} = 28^{+1}_{-1}, 5^{+2}_{-1}, 7^{+1}_{-1}$ M$_\odot$ yr^{-1} for clump A, B and C, respectively. For the total (ground-based) photometry, we find SFR$_{UV+IR} = 45^{+2}_{-2}$ M$_\odot$ yr^{-1}, which is roughly consistent with the sum of the *HST* detected clumps and indicates no other significant source of star-formation.
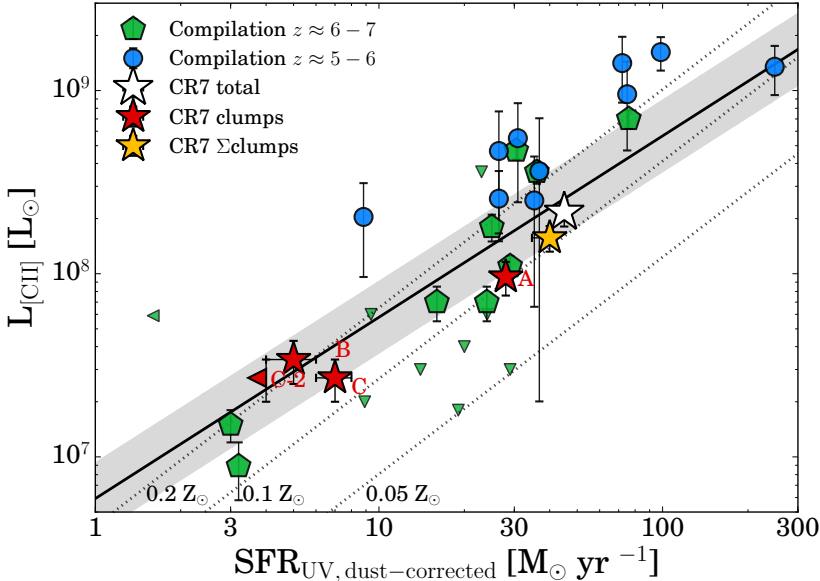
Figure 5.9: Dust corrected SFR(UV) versus [CII] luminosity for a compilation of galaxies at $z \sim 6$ (blue circles; Capak et al. 2015; Willott et al. 2015) and $z \sim 7$ (green pentagons; Kanekar et al. 2013; Ouchi et al. 2013; Ota et al. 2014; Maiolino et al. 2015; Schaerer et al. 2015; Knudsen et al. 2016; Pentericci et al. 2016; Bradač et al. 2017; Knudsen et al. 2017; Smit et al. 2018). We show the individual UV components of CR7 with red stars, and the sum of these component as an orange star. The integrated measurement over the full [CII] emitting region around CR7 is shown with an open star. Downward pointing triangles show galaxies with upper limits on the [CII] luminosity, while left-ward pointing triangles show [CII] detections with upper limits on SFR(UV). The black line shows the relation for local star-forming galaxies measured by De Looze et al. (2014), where the grey region shows the observed dispersion. The dotted lines are model-predictions from Vallini et al. (2015) on how the [CII] luminosity varies with metallicity. We find that the clumps in CR7 are within the scatter from the local relation. These measurements indicate metallicities $0.1 < Z/Z_\odot < 0.2$. Note that we have corrected published SFRs (including those from the local relation) to the Salpeter IMF.

5.6 The SFR-L$_{[CII]}$ relation

Due to its luminosity, the [CII] fine-structure cooling line has been proposed as a SFR tracer (see e.g. De Looze et al. 2014 and references therein), which is observable with ALMA at high-redshift, while other tracers such as Hα are currently unavailable. However, while [CII] is insensitive to dust attenuation, unlike (for example) UV emission, its luminosity is sensitive to metallicity (e.g. Vallini et al., 2013; Hemmati et al., 2017; Olsen et al., 2017). The [CII] luminosity is also dependent on the ionisation state of the gas and saturates at high temperatures (Kaufman et al., 1999; Decataldo et al., 2017; Vallini et al., 2017).

Early ALMA observations of galaxy samples at $z \approx 5 - 6$ (e.g. Capak et al., 2015; Willott et al., 2015) found that these galaxies have similar L$_{[CII]}$ to SFR(UV) ratios as local star-forming galaxies (De Looze et al., 2014). Galaxies at $z \approx 6 - 7$ were typically selected based on their Lyα redshifts and were initially observed

at fainter [CII] luminosities or luminosity limits (e.g. Kanekar et al., 2013; Ouchi et al., 2013; Ota et al., 2014; Maiolino et al., 2015; Schaerer et al., 2015). This was later confirmed in observations of lensed galaxies (Knudsen et al., 2016; Bradač et al., 2017). However, sources that have been selected independently of strong Lyα emission show a wider range in [CII] luminosities (e.g. Pentericci et al., 2016; Knudsen et al., 2017; Smit et al., 2018), although some may still be relatively luminous in Lyα (e.g. Laporte et al., 2017b).

In Fig. 5.9, we show how our [CII] measurements of the UV components of CR7, their sum, and the integrated CR7 measurements compare to samples at $z \sim 5 - 7$ and to the local relation. As we use the aperture measurements centred at the UV clumps, the [CII] luminosity of clump B includes that of sub-component B-2. We also show the upper limit of the UV SFR of clump C-2, if we do not associate its [CII] luminosity with the UV luminosity of clump C. Most sources that currently have been targeted are UV luminous (with SFR $\approx 20 - 30$ M$_\odot$ yr^{-1}, similar to clump A), while the two lensed sources have much lower SFRs.[4] CR7's clumps B and C lie roughly in the middle of the probed parameter space. All individual clumps in CR7, and the total luminosity are consistent within the observed scatter and their error-bars with the local relation, with only a marginal offset. This is in contrast with previously targeted luminous LAEs such as Himiko (Ouchi et al., 2013) and IOK-1 Ota et al. (2014).

Combining our measurements of clump A and CR7s total luminosity with sources from the literature, we confirm a large spread of an order of magnitude in [CII] luminosities at fixed UV SFR, indicating that these galaxies exhibit a range in metallicities and/or ionisation states (the dotted lines illustrate how the [CII] strength changes with metallicity in the model from Vallini et al. 2015). Using these models, we find that the components in CR7 would have gas-metallicities $0.1 < Z/Z_\odot < 0.2$, with relatively little variation between different components, although components A and C are consistent with being slightly more metal poor than B.

5.6.1 Are UV continuum, [CII] and Lyα related?

Because of the initial non-detections of [CII] emission in galaxies with strong Lyα emission (e.g. Ouchi et al., 2013; Ota et al., 2014), it has been speculated that the [CII] luminosity at fixed SFR is related to the strength of Lyα emission (e.g. Knudsen et al., 2016; Smit et al., 2018), as [CII] emission may be reduced in ISM conditions that favour high Lyα escape. Indeed, conditions that may lower the strength of [CII] emission are typically found in Lyα emitters. Compared to the general galaxy population, strong Lyα emitters at $z \approx 2 - 3$ are observed to have low metallicities and high ionisation states (e.g. Erb et al., 2016; Nakajima et al., 2016; Trainor et al., 2016; Kojima et al., 2017). Our results however do not agree with such scenario, as CR7 has an extremely high Lyα luminosity and EW, but has [CII] luminosities similar to those expected for the local relation (both integrated, and for individual clumps). Therefore, the strength of Lyα emission

---

[4] Note that we have also rescaled all published SFRs, including the local relation from De Looze et al. (2014), to a Salpeter IMF.

may not be the most important property driving the scatter in the SFR-L$_{[CII]}$ relation. Hence, indications of a potential relation between Lyα strength and [CII] luminosity may have reflected a more fundamental correlation.
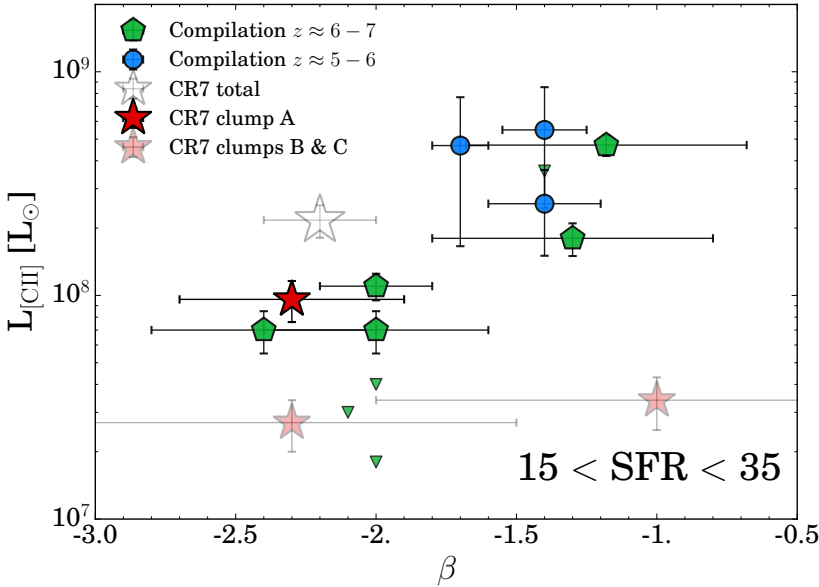

Figure 5.10: The relation between [CII] luminosity and UV slope, β, for galaxies with SFRs between $15 - 35$ M$_\odot$ yr^{-1}. Downward pointing triangles show galaxies with upper limits on the [CII] luminosity. Galaxies with redder colours are typically more evolved (older, higher metallicity), and consequently have higher [CII] luminosities. For reference, we show the measurements of clumps B, C and the total of CR7 in fainter colours.

A property that is related to the strength of Lyα emission in star-forming galaxies across $z \approx 0 - 5$ is the UV slope, with bluer galaxies being brighter in Lyα (e.g. Atek et al., 2008; Matthee et al., 2016; Oyarzún et al., 2017). The UV slope β is closely related to the age, metallicity and dust attenuation law (e.g. Bouwens et al., 2012; Duncan & Conselice, 2015; Mancini et al., 2016; Narayanan et al., 2018), and therefore indirectly with properties that determine the [CII] luminosity at fixed SFR. We illustrate this in Fig. 5.10, where we show the [CII] luminosity as a function of the UV slope for galaxies from the literature with SFR between 15 and 35 M$_\odot$ yr^{-1}. This is the range of SFRs in Fig. 5.9 that includes most galaxies at $z \approx 5 - 7$ that have currently been observed. We note that we explicitly investigate a relatively narrow range in SFR to prevent being diluted by relations between SFR and galaxy properties themselves (for example, it has been established that fainter galaxies have bluer colours, Bouwens et al. 2012). Although the error-bars on UV slope measurements are large[5], it can be seen that at fixed SFR, galaxies with redder colours (which are typically more evolved) have higher [CII] luminosities. Since β depends on several parameters, direct

---

[5] Note that for the sample at $z \approx 5 - 6$, we used the most recent UV slopes as measured by Barisic et al. (2017), which differ significantly from the ground-based estimates from Capak et al. (2015).
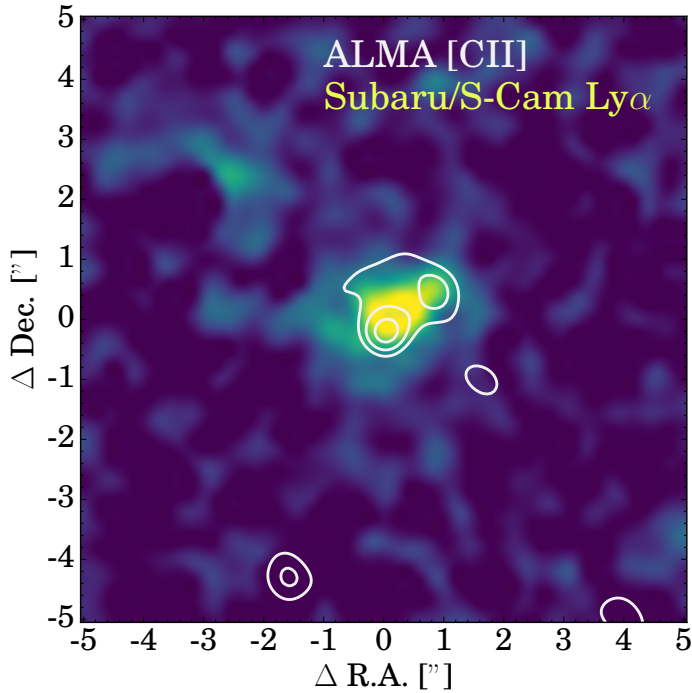
Figure 5.11: Rest-frame Lyα image (obtained by subtracting the (weak) contribution from the continuum in the NB921 image using the Subaru/S-Cam z' band image.) of CR7, overlaid with ALMA [CII] contours, with a scale of 54×54 kpc. The Lyα surface brightness is closely related to the [CII] surface brightness. At clump A, Lyα is redshifted with respect to [CII] by 127 ± 27 km s^{-1}.

measurements of these parameters (such as metallicity) are required to fully understand the origin of this trend, and which parameter is most important.

It is possible to compare our results in more detail to the results obtained for Himiko in Ouchi et al. (2013). Himiko consists of three UV components, with similar total UV and Lyα luminosity as CR7. Himiko has similar limits on its dust mass, but has not been detected in [CII], with a limiting luminosity L$_{[CII]} \lesssim 5 \times 10^7$ L$_\odot$ (Ouchi et al., 2013), which is well below the total [CII] luminosity from CR7. However, unlike CR7, the individual components in Himiko have SFRs of $\approx 7, 5$ and 8 M$_\odot$ yr^{-1} (Ouchi et al., 2013), and are hence likely of lower mass than CR7s clump A. The SFRs of Himiko's components are comparable to CR7 clumps B and C, that have lower [CII] luminosities than the existing [CII] limits for Himiko (and the clumps in Himiko are all very blue, with $\beta \lesssim -2.0$). Deeper [CII] observations at the resolution we obtained for CR7 could perhaps be able to detect those clumps. Another explanation could be that Himiko has a lower dynamical mass, such that supernova explosions disperse [CII] emitting gas over larger areas, decreasing its observability.

5.6.2   Spatial and spectral Lyα-[CII] connection in CR7

As shown in Fig. 5.11, the [CII] emission in CR7 coincides spatially with the Lyα emission. This may not be unexpected if both Lyα and [CII] originate from star-formation. Although [CII] is also emitted from gas that is (partly) neutral (due to its slightly lower ionisation energy than hydrogen; for example photo-dissociating regions), Lyα emission scatters in these neutral gas regions, such that it may also be observed from these regions.

Interestingly, the [CII] line-width and velocity offset of clump A are surprisingly similar to the best fitted-shell model to CR7's Lyα profile (Dijkstra et al., 2016a), which has an intrinsic line-width of 259 km s^{-1} and outflow velocity of 230 km s^{-1} (compare to Table 6.2). Their best fitted shell-model assumes a negligible dust content (consistent with our constraints on the IR luminosity), and the resulting shell-model parameters are similar to Lyα emitters and analogue galaxies at lower redshifts. Therefore, the resemblance of the shell-model parameters based on the Lyα profile with the observed velocity offsets indicates feedback processes are already present in CR7. Further detailed studies on how the Lyα and [CII] line-profiles are related spatially require high resolution Lyα IFU observations with e.g. MUSE, as our current Lyα spectral information is limited to clump A.

5.7   Discussion

5.7.1   Multiple velocity components: merger/satellites?

As shown in Figures 5.4 and 5.6, CR7 consists of several different components of [CII] emission, at different velocities. Similar clumpy structures are also observed in [OIII]$_{88\mu m}$ and [CII] emission in the $z = 7.1$ galaxy BDF3299 (Carniani et al., 2017), and also in [CII] emission in a relatively massive galaxy at $z = 6.1$ (Jones et al., 2017). Such relatively complex [CII] structures and the observed velocity offsets are also observed in hydro-dynamical simulations of galaxies at $z \approx 6 - 7$ with halo masses of $\sim 10^{11}$ M$_\odot$ (e.g. Vallini et al., 2013; Pallottini et al., 2017a). The line-profiles do not show evidence for broad-line components due to outflows (e.g. Gallerani et al., 2018). Therefore, we are likely observing satellites (B, B-2, C, C-2) falling into a more massive central galaxy. These satellites have velocity widths similar to those of satellites in simulations by Pallottini et al. (2017b,a), although simulated satellites typically have lower masses than those estimated for CR7's clumps. Clump A is the component that has the highest dynamical mass estimate (see Table 6.2, although we stress that these are rough estimates) and likely the central galaxy. The dynamical mass estimate of clump C-2 is on the same order of magnitude, potentially indicating a major merger. Observations at higher resolution and with improved sensitivity are required to robustly resolve different components and perform more detailed kinematical/dynamical analyses.

5.7.2   On the nature of CR7

Here, we investigate what our new measurements mean for the interpretation of CR7. For a more in depth discussion on the updated detection significance of HeII and limits on other high-ionisation UV lines we refer to Sobral et al. (2018a). The main conclusion from Sobral et al. (2018a) is that the most luminous component of CR7 is likely undergoing a recent burst of star-formation, with no clear evidence for AGN activity and no convincing detection of UV metal lines in clump A.

Initially, Sobral et al. (2015b) argued that different UV components in CR7 were in different evolutionary stages, with the majority of the stellar mass possibly being found in clumps B and C (see also Agarwal et al. 2016). This interpretation was mostly based on the different UV slopes, with clump A being the bluest and hence the youngest. However, there are two uncertainties related to this interpretation. The first is that UV slopes are relatively uncertain (see Table 6.2), and thus consistent with being the same for all sources. The second is that it is challenging to estimate where the majority of stellar mass is from *Spitzer*/IRAC observations, which has a relatively large PSF. For example, contrary to Sobral et al. (2015b), Bowler et al. (2017b) found that the majority of stellar mass is likely associated to clump A using a deconvolution of the IRAC data based on UV detections as a prior. The new observations point towards a scenario where most of the mass is in clump A as the dynamical mass estimate of clump A is higher than that of clumps B and C. Simultaneously, the constraints from the UV slope, IR continuum and the Lyα luminosity indicates that clump A is also the youngest.

As the SFR-[CII] ratio of different clumps are similar, there is evidence that all clumps have similar metallicities. However, [CII] luminosity may be reduced due to photo-evaporation by far-UV ($6-13.6$ eV) and ionising (> 13.6eV) photons emitted from young stars in the vicinity, which typically happens a few tens of Myrs after the burst of star-formation (e.g. Decataldo et al., 2017; Vallini et al., 2017), which can affect different clumps differently. The metallicities that we would infer from [CII] ($\approx 0.1-0.2Z_\odot$) are inconsistent with the metallicity inferred by Bowler et al. (2017b), which is $\approx 0.005Z_\odot$. However, their result depends on a HeII strength that is now ruled out (Sobral et al., 2018a). Based on upper limits on UV metal lines, the SFR and photoionization modelling, Sobral et al. (2018a) inferred a metallicity of $\approx 0.05-0.2$ Z$_\odot$, which is consistent with the metallicity indicated by the [CII] luminosity. Therefore, it is ruled out that the luminosity in all clumps in CR7 is dominated by PopIII-like stars, but note that small amounts of PopIII-like stars in unpolluted pockets of gas could still be present (e.g. Pallottini et al., 2015). The fact that the SFR-[CII] ratio is similar to other $z \approx 6-7$ galaxies and galaxies in the local Universe also indicates that photo-evaporation does not play a major role in lowering the [CII] luminosity.

Due to its extreme Lyα luminosity ($\approx 10L^\star$, Matthee et al. 2015), CR7 could be powered by an AGN, particularly as the AGN fraction of Lyα emitters with similar luminosities at $z = 2-5$ approaches 100 % (Calhau et al., 2017). However, these galaxies typically have (much) broader Lyα lines and CIV luminosities exceeding the observational limits for CR7 (e.g. Sobral et al., 2018c), such that

they are not fully comparable. The data presented in this paper do not favour an AGN explanation, particularly for clump A, because AGN typically have much lower $\log_{10}(L_{[CII]}/L_{IR})$ ratios (e.g. Ota et al., 2014). Furthermore, Bowler et al. (2017b) show that the UV emission in clump A is slightly extended, which could also be at odds with an AGN-dominated scenario. Therefore, it is likely that clump A in CR7 is powered by a burst of star-formation with moderately low metallicity. It is remarkable that there is no UV nor IR continuum emission observed at the position of the ALMA detection C-2, which has a similar dynamical mass estimate as clump A. If potential UV emission is obscured, the dust is likely at a higher temperature (such that our IR continuum luminosity limit would be weak).

In order to improve our understanding of the CR7 system and other similar systems at $z \sim 7$, it is most important to obtain more accurate constraints on the stellar masses, ages and metallicities of different clumps. While deeper *HST* imaging results in more strongly constrained UV slopes, the majority of progress will be made with integral field spectroscopic observations in the IR which can trace the rest-frame optical. Future adaptive optics assisted observations with MUSE can further map out the relation between the Lyα and [CII] kinematics, and simultaneously probe the large scale environment on $\sim 0.3 - 7$ Mpc scales.

5.8   Conclusions

In this paper, we have presented deep follow-up observations of the CR7 galaxy in band 6 with ALMA targeted at the [CII] fine-structure cooling line and the FIR dust continuum emission (on source integration time 6.0h). After the discovery of CR7 as the most luminous Lyα emitter at $z \sim 7$ (Matthee et al., 2015), the spectroscopic confirmation of Lyα (Sobral et al., 2015b), the evidence for a narrow and strong HeII line and the existence of several clumps seen in the *HST*/WFC3 imaging (Sobral et al., 2015b), numerous spectacular interpretations emerged. While a high HeII/Lyα ratio is now ruled out for clump A (Sobral et al., 2018a), our ALMA observations provide independent measurements of the properties of the structure of the ISM around the three UV clumps observed in CR7 and furthermore reveal the presence of metals in its ISM. Our main results are:

1. We detect extended [CII]$_{158^{-}m}$ line-emission around CR7, with a total luminosity of $(2.17 \pm 0.36) \times 10^8$ L$_\odot$ (Fig. 5.1). The [CII] emission is observed over an 2.2 arcsec^2 area with a typical blue-shift of -167 ± 27 km s^{-1} with respect to Lyα, consistent with simple shell-model parameters based on an outflowing shell of low column density hydrogen. A fraction of 0.72 ± 0.18 of the [CII] flux is associated with separate [CII] emitting clumps, see §5.4.

2. Within CR7, four separate components can be identified in the three dimensional [CII] data-cube, see §5.4.2. UV components A and B are associated to clumpy [CII] emission at a similar blue-shift of ≈ 130 km s^{-1} with respect to the Lyα redshift, see Table 6.2. A separate [CII] component, C-2,

is blue-shifted by ≈ 100 km s^{-1} with respect to the systemic redshift. This component is not clearly associated to a UV clump, but closest to clump C. Around clump B we detect another [CII] component blue-shifted by ≈ 300 km s^{-1} compared to the systemic.

3. The observed rich dynamical structure resembles the structure found in recent hydrodynamical simulations of $z \sim 6 - 7$ galaxies with halo masses $\sim 10^{11}$ M$_\odot$, and leads to the interpretation that these components are likely inflowing satellites. The measured line-widths and dynamical mass estimates (Table 6.2) indicate that clump A contains most of the mass and is likely the central galaxy of the halo, although the dynamical mass estimate of clump C-2 is on the same order of magnitude, potentially indicating a major merger.

4. We do not detect FIR continuum emission, resulting in a 3σ upper limit of L$_{IR}$ $< 2.8 \times 10^{10}$ L$_\odot$ (under the assumption that the dust temperature is 35 K), corresponding to M$_{dust}$ $< 2.7 \times 10^6$ M$_\odot$, see §5.5. The limiting FIR-to-[CII] ratio indicates a low dust-to-metal ratio, much higher than typical sub-mm and quasar host galaxies. We use the FIR constraints to mitigate large uncertainties in the SFRs (due to uncertainties in their UV slopes) and find SFRs of 28^{+1}_{-1}, 5^{+2}_{-1} and 7^{+1}_{-1} M$_\odot$ yr^{-1} for clumps A, B and C, respectively.

5. Based on spatially resolved [CII] measurements, we compare the positions of clumps A, B and C and CR7 in total on the SFR-L$_{[CII]}$ diagram with the literature, see §5.6 and Fig. 5.9. We find that all clumps and the total CR7 luminosity are consistent with the local relation (and other recent detections at $z \approx 6 - 7$) within the scatter. Comparison with hydrodynamical simulations (and with the caveat in mind that poorly constrained ionisation conditions may play an important role), these measurements indicate gas metallicities of $0.1 < Z/Z_\odot < 0.2$.

6. We find that for galaxies with SFRs between 15 and 35 M$_\odot$ yr^{-1}, the [CII] luminosity increases strongly with increasing UV slope, which is a tracer of dust, age and metallicity (Fig. 5.10). This explains why several Lyα emitters are offset towards lower [CII] luminosities, as the Lyα escape fraction increases towards bluer UV slopes.

The picture that emerges is that in CR7 we are likely witnessing the build up of a central galaxy in the early Universe through complex accretion of satellites. The strong Lyα emission is likely powered by a star-burst with young, metal poor stars. Major improvements will be made with resolved spectroscopy that can measure gas metallicities and ionisation states, which can be used to constrain the properties of stellar populations in the different components.

Acknowledgments

Figure 5.12: Channel maps of the [CII] emission around CR7 (54×54 kpc). Contours show the $\pm 2, 3, 4, 5\sigma$ levels, where $1\sigma \approx 0.06$ mJy beam^{-1}. Red crosses mark the positions of the UV clumps. Channels have widths $\Delta v = 38.8$ km s^{-1} or 30 MHz. The displayed channels range from $z_{[CII]} = 6.592 - 6.605$.

Chapter 6

Confirmation of double peaked Lyα emission at $z = 6.593$: witnessing a galaxy directly contributing to the reionization of the Universe

Distant luminous Lyman-α emitters (LAEs) are excellent targets for spectroscopic observations of galaxies in the epoch of reionisation (EoR). We present deep high-resolution ($R = 5000$) VLT/X-SHOOTER observations, along with an extensive collection of photometric data of 'COLA1', a proposed double peaked LAE at $z = 6.6$ (Hu et al., 2016). We rule out that COLA1's emission line is an [OII] doublet at $z = 1.475$ on the basis of i) the asymmetric red line-profile and flux ratio of the peaks (blue/red=0.31 ± 0.03) and ii) an unphysical [OII]/Hα ratio ([OII]/Hα > 22). We show that COLA1's observed B-band flux is explained by a faint extended foreground LAE, for which we detect Lyα and [OIII] at $z = 2.142$. We thus conclude that COLA1 is a real double-peaked LAE at $z = 6.593$, the first discovered at $z > 6$. COLA1 is UV luminous ($M_{1500} = -21.6 \pm 0.3$), has a high equivalent width ($EW_{0,Lyα} = 85^{+70}_{-30}$ Å) and very compact Lyα emission ($r_{50,Lyα} = 0.33^{+0.07}_{-0.04}$ kpc). Relatively weak inferred Hβ+[OIII] line-emission from *Spitzer*/IRAC indicates an extremely low metallicity of $Z < 1/20\,Z_\odot$ or reduced strength of nebular lines due to high escape of ionising photons. The small Lyα peak separation of 220 ± 20 km s^{-1} implies a low HI column density and an ionising photon escape fraction of $\approx 15 - 30\%$, providing the first direct evidence that such galaxies contribute actively to the reionisation of the Universe at $z > 6$. Based on simple estimates, we find that COLA1 could have provided just enough photons to reionise its own ≈ 0.3 pMpc (2.3 cMpc) bubble, allowing the blue Lyα line to be observed. However, we also discuss alternative scenarios explaining the detected double peaked nature of COLA1. Our results show that future high-resolution observations of statistical samples of double peaked LAEs at $z > 5$ are a promising probe of the occurrence of ionised regions around galaxies in the EoR.

Matthee, Sobral, Gronke, Paulino-Afonso, Stefanon and Röttgering
submitted to A&A (2018)

6.1   Introduction

The epoch of reionisation (EoR) is the last phase transition of the Universe. It occurred when the neutral hydrogen of the intergalactic medium (IGM) became reionised (e.g. Madau, 2017). In spite of the increasingly precise measurements of the global progress of reionisation and its patchiness (e.g. Becker et al., 2015; Davies et al., 2018; Bañados et al., 2018; Bosman et al., 2018), its evolution and drivers are still largely unknown. One of the main probes of reionisation is the Lyman-α (Lyα) line (see Dijkstra et al. 2007 for a review). Due to the low Lyα transmission in a partially neutral IGM, the progress of reionisation can be mapped out using the strength of detected Lyα emission. This is usually done through the equivalent width distribution among high-redshift galaxies (e.g. Pentericci et al., 2014; Schmidt et al., 2016), through the evolution in the luminosity function (e.g. Zheng et al., 2017) and/or its clustering signal (e.g. Jensen et al., 2014; Kakiichi et al., 2018).

Recently, wide-field narrow-band surveys have been highly efficient in identifying and confirming luminous Lyman-α emitters (LAEs) into the EoR ($z \approx 7$; e.g. Matthee et al. 2015; Hu et al. 2016; Santos et al. 2016; Bagley et al. 2017; Zheng et al. 2017; Shibuya et al. 2018). The number densities of extremely luminous LAEs at $z \sim 7$ ($L_{Ly\alpha} > 2 \times 10^{43}$ erg s^{-1}) are higher (Matthee et al., 2015; Bagley et al., 2017) than expected based on older, smaller surveys (e.g. Ouchi et al., 2010). While the number densities of faint LAEs decrease at $z > 6$, the number densities of the most luminous sources are relatively constant between $z \approx 5 - 7$ (e.g. Santos et al., 2016; Zheng et al., 2017; Konno et al., 2018). These luminous sources likely reside in early ionised bubbles (Stark et al., 2017), facilitating their Lyα observability during the EoR (e.g. Matthee et al., 2015; Weinberger et al., 2018).

Due to their luminosity, luminous LAEs are ideal for spectroscopic follow-up (e.g. Sobral et al., 2015b; Hu et al., 2016; Matthee et al., 2017d; Shibuya et al., 2018). The most Lyα-luminous example among these sources at $z \approx 6.6$ is CR7 (Sobral et al., 2015b, 2018a). CR7 has spectacular properties: strong, narrow Lyα emission (EW$_0 \approx 210$ Å), intense Hβ and/or [O$_{III}$] emission (Bowler et al., 2017a) and there are indications of strong high-ionisation rest-frame UV emission lines such as He$_{II}$ (Sobral et al., 2018a). High resolution *HST* and ALMA observations reveal multiple components in the rest-frame UV separated by ~ 5kpc and spatially and spectrally resolved [C$_{II}$] FIR cooling-line emission (Matthee et al., 2017e), indicating the build-up of a central galaxy through accretion of satellite galaxies.

Recently, Hu et al. (2016) presented the spectroscopic confirmation of a potentially even more luminous LAE at $z = 6.593$, 'COLA1', with an unexpected double peaked Lyα line-profile. The presence of multiple peaks in COLA1 had been unprecedented in $z > 6$ LAEs (e.g. Matthee et al., 2017d; Shibuya et al., 2018), but Songaila et al. (2018) show that roughly a third of a sample of extremely luminous LAEs at $z = 6.6$ may have such complex line shapes. The transmission on the blue part of the Lyα line is typically very low due to inflows of H$_I$ gas (e.g. Dijkstra et al., 2007; Laursen et al., 2011), residual neutral hydro-

gen in the halos of galaxies (e.g. Mesinger et al., 2015) and the increasing neutral fraction of the inter galactic medium (e.g. Hu et al., 2010).

Several effects help to increase the observability of Lyα at high redshift: (i) the redshift of the Lyα line with respect to the surrounding gas (e.g. due to outflows), and (ii) the Hubble expansion that may redshift the Lyα line out of the resonance frequency of the neutral gas, thus lowering the optical depth in case the galaxy is surrounded by a large, highly ionised region.

However, due to the large-scale infall of gas which shifts the absorption ~ 100 km s^{-1} towards the red, combined with the extended wing of the absorption profile of the highly neutral IGM, simulations and analytical models expect that even the red part of the Lyα emission is diminished significantly (e.g. Dijkstra et al., 2007; Laursen et al., 2011; Mesinger et al., 2015; Sadoun et al., 2017; Weinberger et al., 2018). Furthermore, radiative transfer processes in the interstellar medium (ISM) even shift the blue peak to lower velocities; e.g. Neufeld 1990. Therefore, a detection of intrinsically blue-shifted Lyα emission above $z \gtrsim 6$ is theoretically unexpected, or considered highly unlikely by theoretical models (e.g. Mason et al., 2018).

Since the transmission of the blue part of the Lyα line depends directly on the ionisation state of the environment of the emitting galaxy, COLA1 could open up a completely new probe of reionisation, if the detection of the blue Lyα line is confirmed. With a larger sample, the evolution of the Lyα line asymmetry (i.e., comparing the blue and red fluxes) can be quantified more robustly, adding an interesting additional observable to the evolution of LAE clustering and EW. Interestingly, the Lyα peak separation correlates strongly with the escape of Lyman-Continuum (LyC) radiation (e.g. Verhamme et al., 2015; Vanzella et al., 2018; Izotov et al., 2018). Therefore, COLA1 could also provide the first direct evidence that galaxies actively contribute to the reionisation of the Universe.

However, the double peaked line could also mean that COLA1 is an [O$_{II}$]$_{3727,3730}$ emitter at $z = 1.475$. We therefore test whether the line may have been misinterpreted, in which case COLA1 is a low-redshift interloper, and not a LAE at $z = 6.6$. Because of the unique potential of the COLA1 galaxy, we investigate its nature independently using our own narrow-band data (from Sobral et al. 2013, not used in Matthee et al. 2015), new high spectral resolution VLT/X-SHOOTER observations covering a wavelength range from 0.3 to 2.5μm and the wealth of public available data from the COSMOS survey which were not explored in Hu et al. (2016).

In this work, we first summarise the available photometric information and present the new X-SHOOTER observations in §6.2. We analyse the spectrum in detail and conclude on the redshift of COLA1 in §6.3. §6.4 presents the properties of COLA1 that we measure from the spectroscopic and photometric data available. We discuss the implications in §11.7 and summarise the results in §11.8. Throughout this work we adopt a flat ΛCDM cosmology with $\Omega_\Lambda = 0.7$, $\Omega_M = 0.3$ and H$_0 = 70$ km s^{-1} Mpc^{-1}, a Salpeter (1955) initial mass function and magnitudes in the AB system (Oke, 1974).

6.2   Data

6.2.1   Photometric measurements

COLA1 (Hu et al., 2016) is located in the COSMOS field (Capak et al., 2007; Scoville et al., 2007) and hence public imaging data are available in ≈ 30 filters from the UV to IR (e.g. Ilbert et al., 2009). This includes high resolution data in the F814W filter from the *Hubble Space Telescope (HST)*/Advanced Camera for Surveys (Koekemoer et al., 2007). COLA1 is located in a shallow region from the UltraVISTA survey (McCracken et al., 2012) and is covered by *Spitzer*/IRAC imaging from the SPLASH program (e.g. Steinhardt et al., 2014)[1]. We use optical data from Subaru/Suprime-cam (Taniguchi et al., 2007) and near-infrared data from UltraVISTA DR3. COLA1 is furthermore covered in Subaru/Suprime-cam NB921 images from Sobral et al. (2012, 2013), similar to the NB921 imaging from Hyper Suprime-Cam from Hu et al. (2016). We show thumbnail images in the u, B, z, NB921, F814W, Y, J, H, [3.6] and [4.5] bands in Fig. 7.11, where red contours illustrate the location of line-emission (measured from the NB921-z image). We note that we have confirmed the astrometric alignment of the different images using the position of ≈ 30 stars and galaxies around COLA1. Our photometric measurements are summarised in Table 6.1.

NB921 Narrow-band data

Combining the Suprime-cam NB921 narrow-band data (Sobral et al., 2013) with public z' band data, we measure a total line-flux of $5.8^{+1.2}_{-1.1} \times 10^{-17}$ erg s^{-1} cm^{-2}. As the full z' band flux can be explained by line-emission, we use the Y band ($Y = 25.2^{+0.4}_{-0.3}$, S/N ≈ 3, measured in a $2''$ diameter aperture and applying an aperture correction of -0.3 mag) to obtain a weak constraint on the observed equivalent width of EW$_{\mathrm{obs}} = 660^{+760}_{-350}$ Å assuming a UV slope $\beta = -2.0$. The Y band magnitude is in good agreement with the measurement in Hu et al. (2016) based on Subaru data. The line-flux we measure is a factor ≈ 2 lower than Hu et al. (2016), which is likely due to the use of a smaller aperture (they use apertures with a $3''$ diameter) and therefore less contaminated by a neighbouring object (see Fig. 7.11).

Ground-based optical data

Visual inspection of the thumbnail images reveals potential detections in the u and B filters. While the potential flux in the u band is offset, this is not as clear in the B band. We measure the significance of the flux in the B band by performing photometry centred on the NB921 detection in $1.2''$ diameter apertures. We choose such small aperture to optimise the S/N ratio (the PSF-FWHM of this data is $0.7 - 0.8''$) and minimise contamination from nearby objects. The noise level is measured from the standard deviation of 1000 empty aperture measurements located on random sky positions around COLA1. We measure flux at the $2.4 \, \sigma$ level with $B = 28.4^{+0.6}_{-0.4}$ (see Fig. 7.11, where we use a high contrast to

---

[1] http://splash.caltech.edu

Table 6.1: The coordinates and photometric measurements of COLA1. Magnitudes are in the AB system. Magnitude limits are at the 2σ level. *As the H band photometry is contaminated by ID 593625 we only provide it as a lower limit.

Coordinates	
R.A.	10:02:35.37 (J2000)
Dec.	+02:12:13.9 (J2000)
Photometry	
B	$28.4^{+0.6}_{-0.4}$
V	> 27.8
R	> 27.7
I	> 27.6
F814W	$26.6^{+0.4}_{-0.3}$
NB921	$23.6^{+0.1}_{-0.1}$
z'	$25.5^{+0.5}_{-0.3}$
Y	$25.2^{+0.4}_{-0.3}$
J	$24.8^{+0.5}_{-0.3}$
H	$> 24.8^*$
K_s	> 24.4
[3.6]	$24.4^{+0.2}_{-0.1}$
[4.5]	$24.6^{+0.3}_{-0.2}$

highlight potential detections). No flux above the 2σ level is detected in the u, V, R and I filters using the same aperture centered on COLA1. We measure flux at the 2σ level in the stacked $BVRI$ image. While the significance levels of these measurements is low, they may be troublesome for a galaxy at $z > 6.5$, motivating the need for careful spectroscopic analysis.

High resolution optical data

The *HST* imaging in the F814W filter (with > 20 % transmission between $\lambda = 6988 - 9577$ Å, $\lambda_{\text{eff}} = 7985$ Å, PSF-FWHM $= 0.095''$; Koekemoer et al. 2007) reveals a faint point-like detection at the position of COLA1 (Fig. 7.11). Similarly to the u and B imaging, F814W imaging also clearly shows another source 1.2" south-west of COLA (identified in the *HST* thumbnail in Fig. 7.11). This object has ID 593625 in the Laigle et al. (2016) catalogue (with photometric redshift $p_z = 1.9^{+0.2}_{-0.1}$) and we will refer to it with that ID from now on. COLA1 is detected at 3σ, with F814W $= 26.6^{+0.4}_{-0.3}$ measured in a 0.6" diameter aperture and corrected for aperture losses using tabulated encircled fluxes from Bohlin (2016).

Photometric redshift and the *Spitzer*/IRAC view

COLA1 is present in the public COSMOS2015 catalogue (Laigle et al. 2016; ID 593751), where it has a photometric redshift of $p_z = 0.99^{+0.12}_{-0.11}$. However, the photometry that is used to estimate this redshift is measured with 2" diameter apertures and may suffer contamination from ID 593625. We re-measure the
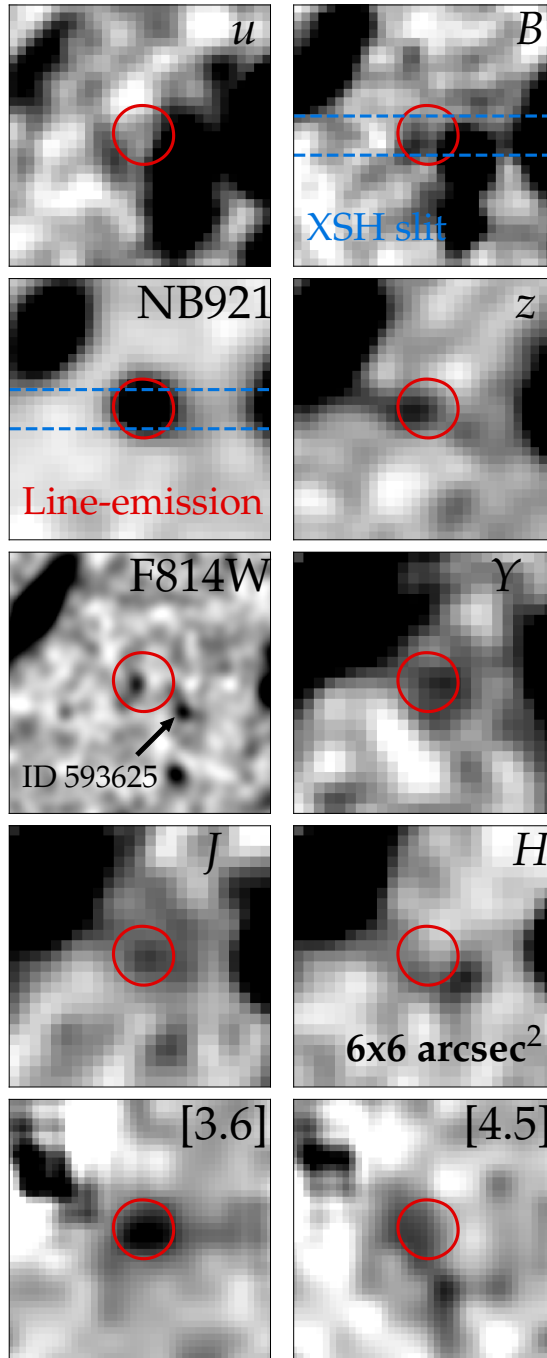
Figure 6.1: High contrast thumbnail images of 6×6 arcsec^2 (32×32 kpc^2) centered on the NB921 detection of COLA1. The red contour shows the 2σ level of the NB921-z' image (tracing line-emission). X-SHOOTER observations were performed with a slit alignment PA=0. A positional shift upwards along the slit corresponds to a shift to the right (west) in these thumbnails. The IRAC [3.6] and [4.5] images have been cleaned using *HST*/F814W as a prior following Stefanon et al. (2017).

photometry in the *Spitzer*/IRAC [3.6] and [4.5] filters using SPLASH data. We follow the procedure as last described in Stefanon et al. (2017), where the IRAC images are de-confused based on the *HST*/F814W images using the `mophongo` software (Labbé et al., 2006, 2015). We measure $[3.6] = 24.4^{+0.2}_{-0.1}$ and $[4.5] = 24.6^{+0.3}_{-0.2}$ in 1.2″ diameter apertures, see Fig. 7.11. This results in a moderately blue colour $[3.6] - [4.5] = -0.2 \pm 0.3$, although with significant uncertainties (see also Harikane et al. 2018, who measure $[3.6] - [4.5] = -0.2 \pm 0.1$).

6.2.2 X-SHOOTER spectroscopic observations & data reduction

We observed COLA1 with the X-SHOOTER echelle spectrograph on UT2 of the Very Large Telescope as part of ESO program 0100.A-0213 (PI Matthee). X-SHOOTER observes in three arms simultaneously: UVB ($\lambda = 0.30 - 0.55\mu$m), VIS ($\lambda = 0.55 - 1.02\mu$m) and NIR ($\lambda = 1.0 - 2.5\mu$m). Observations were performed on 19 January and 18-19 February 2018 with clear conditions and $0.6 - 0.8''$ seeing. GD71 was observed as telluric standard star. We used a 1.0″ slit in the UVB arm and 0.9″ slits in the VIS and NIR arms.

We first acquired on a $I = 13.5$ magnitude star and then applied a blind offset of 95.86″ to the position of COLA1 with a position angle of 0 degrees (see Fig. 7.11). We nodded between two positions along the slit (A and B, offset by 3″) using the `AutoNodOnSlit` procedure. Integration times were 700 and 780s for UVB and VIS arms respectively. Four shorter jitters with separations of 1″ along the direction of the slit were used for NIR exposures of 210s. This observing sequence was repeated ten times (split over two observing blocks with ABBA sequence and one with an AB sequence), resulting in total exposure times of 7.0, 7.8 and 8.4ks for the three arms respectively.

Data are reduced using standard procedures (bias and dark subtraction, flat-fielding, sky subtraction, wavelength calibration and flux calibration) incorporated in the X-SHOOTER pipeline (Modigliani et al., 2010). Individual exposures per observing block are combined using the pipeline. We then combine exposures over multiple observing blocks by computing the noise-weighted average as described in detail in Sobral et al. (2018d). Before extracting 1D spectra, we first smooth the spectrum with 2D gaussian kernels that corresponds to half the resolution $(\sigma_x, \sigma_y)_{\mathrm{UVB,VIS}} = (0.4$ Å, $0.32'')$ and $(\sigma_x, \sigma_y)_{\mathrm{NIR}} = (0.6$ Å, $0.21'')$, and bin it in the wavelength direction by 3 pixels (0.6 Å, half the resolution). The spatial extraction window in the VIS arm is 2.2″ which we find to optimise the S/N. Slit losses of the line at 922 nm are estimated using the NB921 image that is convolved to the PSF-FWHM of our spectroscopic observations. We measure the fraction of the total line-flux that is retrieved within the slit and extraction window. As COLA1's line-emission is compact in the NB921 data, the estimated slit losses are only 19 %. The spatial extraction windows in the UVB and NIR arms are 1.2″ and we do not apply slit loss corrections. Wavelengths are converted to vacuum wavelengths. We measure the effective spectral resolution using unresolved skylines on our extracted 1D spectrum. We find R ≈ 4000 at 0.5μm, R ≈ 5000 at 0.9μm and R ≈ 3800 at 1.6μm, corresponding to 75, 60 and 80 km s^{-1}, respectively.

Table 6.2: The details of the X-SHOOTER observations and spectroscopic measurements for COLA1. Flux measurements of the 923nm line are corrected for 19 % slit-losses. Upper and lower limits are at the 2σ level. Flux limits assume a line-width FWHM=200 km s^{-1}.

Observations	COLA1
Dates	19 Jan 2018, 18-19 Feb 2018
$R_{0.9\bar{}m}$	5000
$R_{1.6\bar{}m}$	3800
$t_{exp,UVB}$	7.0ks
$t_{exp,VIS}$	7.8ks
$t_{exp,NIR}$	8.4ks
923 nm line properties	
Flux	$5.90 \pm 0.24 \times 10^{-17}$ erg s^{-1} cm^{-2}
EW$_{obs}$	660^{+760}_{-350} Å
Peak separation	220 ± 20 km s^{-1}
FWHM$_{red}$	198 ± 14 km s^{-1}
FWHM$_{blue}$	150 ± 18 km s^{-1}
Flux$_{blue}$/Flux$_{red}$	0.31 ± 0.03
$S_{w,red}$	18.0 ± 0.9 Å
$S_{w,blue}$	-1.5 ± 0.4 Å
$S_{w,full}$	3.2 ± 0.2 Å
Flux limits of interest	
H$\alpha_{z=1.475}$	$< 5.2 \times 10^{-18}$ erg s^{-1} cm^{-2}
[O III]$_{4959,z=1.475}$	$< 9.8 \times 10^{-18}$ erg s^{-1} cm^{-2}
[O III]$_{5007,z=1.475}$	$< 9.0 \times 10^{-18}$ erg s^{-1} cm^{-2}
C IV$_{z=6.591}$	$< 1.6 \times 10^{-17}$ erg s^{-1} cm^{-2}
He II$_{z=6.591}$	$< 0.7 \times 10^{-17}$ erg s^{-1} cm^{-2}

6.2.3   Spectroscopic measurements

In our X-SHOOTER spectrum, we confirm COLA1's double peaked emission line at $\lambda_{obs,vac} = 9224, 9231$ Å (S/N $\approx$ 24), but we also detect faint emission-lines at $\lambda_{obs,vac} = 3821$ Å (S/N $\approx$ 10) and $\lambda_{obs,vac} = 15735$ Å (S/N $\approx$ 5). The centroid of these faint emission-lines is however shifted spatially by $1''$ to the west and are therefore not co-located with COLA1 (Fig. 7.11). We do not detect continuum emission. No other lines are detected in the $0.3 - 2.5\mu$m coverage above S/N > 2.

For the double peaked emission-line at 923nm, we measure a line-flux of $5.90 \pm 0.24 \times 10^{-17}$ erg s^{-1} cm^{-2} and a relative flux ratio between the blue and red component of 0.31 ± 0.03. The red line has a full width half maximum (FWHM) of 198 ± 14 km s^{-1}, while the blue line is narrower with FWHM=150 ± 18 km s^{-1}. While the red line is clearly asymmetric (with a weighted skewness of $S_w = 18.0 \pm 0.9$ Å; following the definition from Kashikawa et al. 2006), the blue line is not ($S_w = -0.2 \pm 0.3$ Å). Our measurements are summarised in Table 6.2.

The line at 3821 Å has a line-flux of $3.0 \pm 0.3 \times 10^{-17}$ erg s^{-1} cm^{-2} and FWHM= 350 km s^{-1}. The line that is observed at 15735 Å has a line-flux of

$1.5 \pm 0.3 \times 10^{-17}$ erg s^{-1} cm^{-2} and a width FWHM= 260 km s^{-1}. The spatial offset of $\approx 1''$ of these lines coincides with ID 593625.

6.3 Is COLA1 a LAE at $z = 6.59$ or an [OII] emitter at $z = 1.47$?

The tentative detection in the B band (although at the 2.4σ level) and the unlikelihood of observing Lyα flux blue-wards of the red asymmetric line indicate that COLA1 may not be a LAE at $z = 6.6$, but an [OII] emitter at $z = 1.47$ instead. Here, we assess the implications of each observed feature to test this hypothesis.

6.3.1 923nm line strength and consistency with F814W

If the 923nm line from COLA1 is [OII], it would yield $z = 1.475$ and it would have a typical luminosity (L$_{[OII]}$ = $1.5 \times L^\star$; Khostovan et al. 2015). The [OII] equivalent width would be extreme, EW$_0$ = 260^{+310}_{-140} Å, well above the typical EW for [OII] emitters (EW$_0$ = 50 ± 20 Å) at $z = 1.47$ (Khostovan et al., 2016).

We test whether the F814W photometry can be explained by pure line-emission. Assuming negligible contribution from continuum emission and by spreading the line-flux homogeneously over the full transmission region of F814W results in F814W= 26.8 ± 0.1. Hence, the F814W photometry (we measure F814W= $26.6^{+0.4}_{-0.3}$) can be perfectly explained by pure line-emission and does not indicate flux blue-wards of the emission-line. Therefore, the F814W detection does not rule out Lyα at $z = 6.6$.
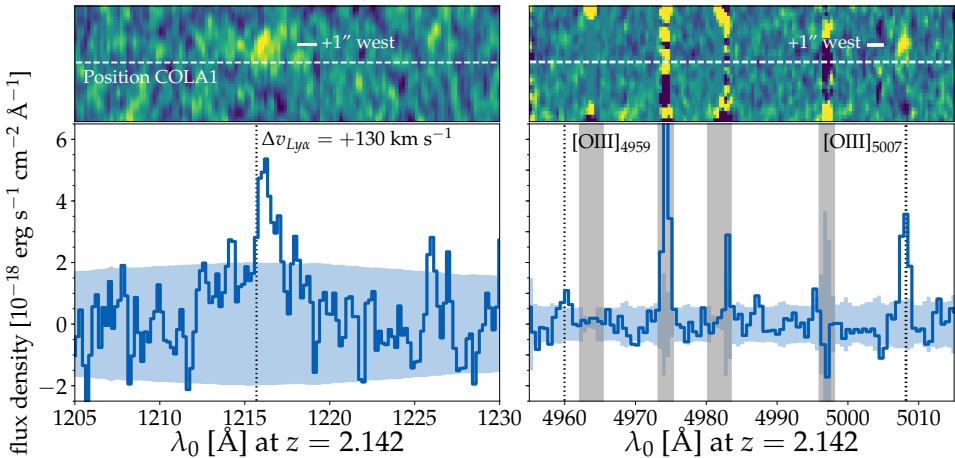
Figure 6.2: Lyα and [OIII]$_{5007}$ detections in the X-SHOOTER spectrum that are offset by $\approx 1''$ to the west. This confirms that a foreground source (ID 593625 in Laigle et al. 2016) is present at $z = 2.142$. Lyα emission is redshifted by $+130$ km s^{-1} compared to the systemic redshift based on [OIII]$_{5007}$.

6.3.2   Line-detections at 382nm and 1573.5nm

As described above, we detect two emission-lines that are offset by $\approx 1''$ to the west of COLA1. This corresponds roughly to the foreground source ID 593625 as can be seen in the B band thumbnail image (Fig. 7.11), which shows that outskirts of this galaxy fall in the X-SHOOTER slit. We identify the two lines as Lyα and [OIII]$_{5007}$ at $z = 2.142$, as illustrated in Fig. 6.2, where we have optimised the centroid of spatial extraction aperture for these lines. Lyα is redshifted by 130 km s^{-1} with respect to the systemic redshift, similar to other LAEs at $z \sim 2$ (Trainor et al., 2015; Sobral et al., 2018d). Without correcting for slit losses, we measure a Lyα luminosity of $1.0 \pm 0.1 \times 10^{42}$ erg s^{-1}, well below the typical Lyα luminosity at $z \approx 2.2$ ($\approx 0.4 \times L^\star$; Sobral et al. 2017). The B band magnitude corresponding to pure line-emission at this flux-level is $B = 28.2 \pm 0.1$. Lyα emission extends to close to the peak position of COLA1 and could thus contribute significantly to the faint B band detection ($B = 28.4^{+0.6}_{-0.4}$) at the COLA1 position. The [OIII]$_{5007}$ luminosity is $0.5 \pm 0.1 \times 10^{42}$ erg s^{-1}. We note that the centroid of the (low S/N) flux in the B- near COLA1 is shifted slightly towards a faint H band detection that could be explained by this [OIII] flux. Therefore, several detections in the images (in particular B and H) can be attributed to LAE 593625 at $z = 2.142$.
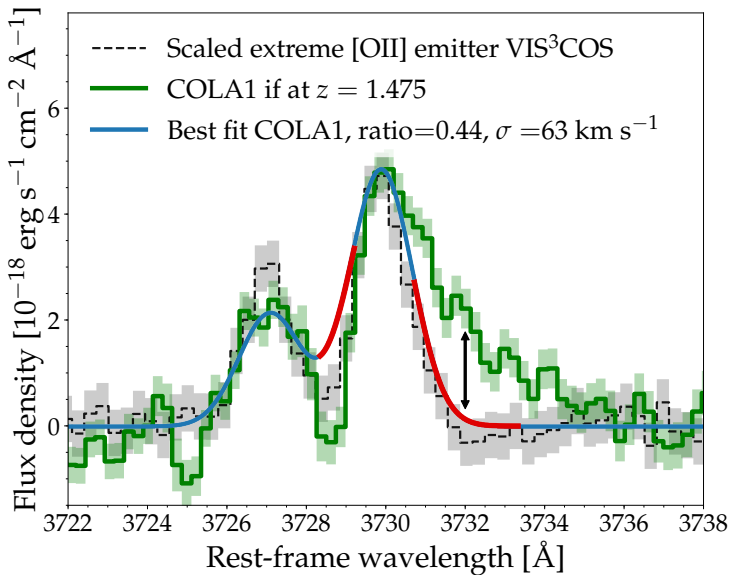
Figure 6.3: X-SHOOTER spectrum of COLA1, shifted to rest-frame wavelengths assuming it is an [OII] emitter at $z = 1.475$ (green). Dashed black lines show the median [OII] profile of the [OII] emitters in the VIS^{3}COS survey (Paulino-Afonso et al. 2018a) that are selected on having extreme blue/red ratios and asymmetric red lines. The blue line shows our fitted [OII] doublet to the spectrum of COLA1, and the red line indicates where the fit is $> 3\sigma$ away from the data. The asymmetry in the red line (not present in the blue line) and the absence of flux in between the lines are at odds with COLA1 being an [OII] emitter.

6.3.3   923nm line-profile

We show a detailed zoom-in figure of the line-profile of the 923nm line in Fig. 6.3. In this figure, we shift the spectrum to the rest-frame assuming COLA1 is at $z = 1.475$. We compare it to a median [OII] spectrum of galaxies with asymmetric red lines and high red/blue ratios from the VIS^{3}COS survey (Paulino-Afonso et al., 2018a) and also show the best fitted [OII] doublet. While the peak separation (220 ± 20 km s^{-1}) is fully consistent with the peak separation of the [OII] doublet, the asymmetry of the red line can not be fitted as an [OII] doublet. In particular, the blue line would have been expected to be asymmetric as well, similar to the red line. Moreover, the absence of flux between the two lines can also not easily be explained in the case of an [OII] doublet, unless lines are very narrow.

The skewness of COLA1's red line is high ($S_{w,\mathrm{red}} = 18.0 \pm 0.9$ Å; see Table 6.2), much higher than the typical maximum skewness of a low-redshift galaxy ($S_w = 3$ Å; Kashikawa et al. 2006), which is similar to the skewness of the full doublet. Finally, the line-ratio between [OII]$_{3726}$ and [OII]$_{3730}$ would be significantly lower than the line-ratio in our extreme [OII] emitter reference sample (with a blue-to-red fraction of > 0.65). In fact, the line-ratio of the blue and red lines of our best-fit (0.44) is significantly lower than the theoretical minimum line-ratio for electron densities as low as 1 cm^{-3} (≈ 0.65 for an electron temperature of 10^4 K; Sanders et al. 2016, but also for temperatures between 10^{3-5} K) and thus unphysical. Therefore, the line-profile strongly disagrees with COLA1 being an [OII] emitter at $z = 1.475$ even though the peak separation is in perfect agreement.
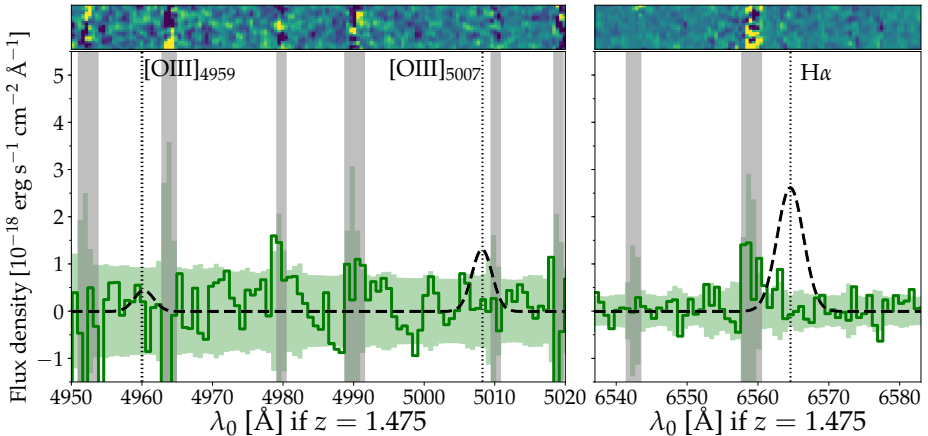
Figure 6.4: The wavelengths where [OIII] and Hα would be observed if COLA1 is at $z = 1.475$. The dashed lines indicate the minimum expected [OIII] and Hα fluxes based on known extreme line-ratios ([OIII]/[OII]=0.1 and [OII]/Hα = 0.2, shown with FWHM=200 km s^{-1}). These line-ratios are ruled out at $\approx 1\sigma$ and 4.7σ, respectively.

6.3.4   No line in the NIR associated with $z = 1.475$

As we show in Fig. 6.4, we do not detect Hα or [O$\textsc{iii}$]$_{5007}$ if COLA1 would be at $z = 1.475$. We illustrate how these lines would look in our data for the lowest empirical Hα/[O$\textsc{ii}$]$= 0.2$ and [O$\textsc{iii}$]/[O$\textsc{ii}$]$= 0.1$ line-ratios (e.g. Hayashi et al., 2013). These extreme line-ratios would imply both high metallicities and high ionisation states (properties that are typically anti-correlated; Nakajima & Ouchi 2014). If we assume a FWHM of 200 km s^{-1} (similar to the red line at 923nm), we measure a 1σ limit on the Hα flux of 2.6×10^{-18} erg s^{-1} cm^{-2} and a lower limit of 9.4×10^{18} erg s^{-1} cm^{-2} on the combined [O$\textsc{iii}$]$_{4959,5007}$ line. While the lowest [O$\textsc{iii}$]/[O$\textsc{ii}$] ratio is within the 1σ noise level, these data rule out Hα/[O$\textsc{ii}$]$= 0.2$ at 4.7σ, additional clear evidence against the interpretation that COLA1 is an [O$\textsc{ii}$] line at $z = 1.475$.

6.3.5   Concluding remarks on the redshift of COLA1

As the line-profiles of the red and blue lines differ, the double peaked emission line around 923nm can not be fitted by an [O$\textsc{ii}$] doublet, even though the peak separation is similar[2]. Photometric indications for COLA1 being at low-redshift (in particular B and F814W detections) are explained due to line-emission from COLA1 itself (F814W) and a foreground LAE at close separation (ID 593625 at $z = 2.142$). The relatively blue *Spitzer*/IRAC colours, combined with a optical to near-infrared break of $BVRI - Y > 3$ are also not indicative of a red dusty or old interloper at a lower redshift. Finally, if COLA1 would have been an [O$\textsc{ii}$] emitter at $z = 1.475$ the flux ratio of the lines in the [O$\textsc{ii}$] doublet and the limits on [O$\textsc{ii}$]/Hα indicate unphysical conditions. Combining all the observations from above, we conclude that COLA1 is best explained as a double-peaked LAE at $z_{\mathrm{Lyff,red}} = 6.593$, as initially claimed by Hu et al. (2016).

6.4   Properties of COLA1 – a unique LAE at $z = 6.6$

Now we have established that COLA1 is a real LAE at $z = 6.593$, we can have a better look at its properties based on the X-SHOOTER spectrum and available imaging data. The properties are summarised in Table 6.3.

6.4.1   Lyα luminosity and spectral energy distribution

The slit corrected line-flux measured in the X-SHOOTER spectrum implies a Lyα luminosity of $L_{\mathrm{Ly}\alpha} = 2.9 \times 10^{43}$ erg s^{-1}, which is among the most luminous LAEs know at $z \approx 5 - 7$ (see a compilation in Matthee et al. 2017d). The Lyα EW is high (EW$_0 = 85^{+70}_{-40}$ Å, based on the continuum estimated from the Y band flux), but this is a rather common property of LAEs at high-redshift (e.g. Hashimoto et al., 2017b; Sobral et al., 2018c) and we note that it is poorly constrained due

---

[2] As we show in Section 6.4, the Lyα line profile is well-fitted by a Lyα shell model and shows properties similar to normal LAEs at $z < 6$.
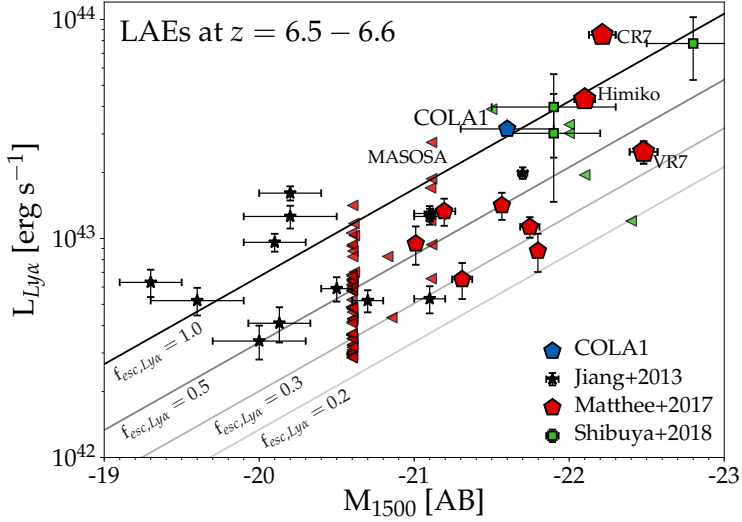
Figure 6.5: UV luminosity versus Lyα luminosity of known LAEs at $z = 6.5 - 6.6$ identified through narrow-band surveys (Jiang et al. 2013b; Matthee et al. 2017d; Shibuya et al. 2018). Left-ward pointing triangles indicate 2σ upper limits. Black lines show lines of constant escape fraction ($f_{esc,Ly\alpha}$; assuming a Salpeter IMF and a constant SFR for 100 Myr; e.g. Kennicutt 1998). COLA1 has a high Lyα escape fraction, similar to other LAEs known at $z = 6.6$.

to uncertainties on the continuum magnitude. The Lyα luminosity implies a comoving number density $\approx 1 \times 10^{-5}$ Mpc^{-3} (Matthee et al., 2015).

COLA1 is weakly detected in the Y and J bands (S/N ≈ 3 and 2.5, respectively), see Fig. 7.11. An off-centred H band detection is likely contaminated by strong [OIII]$_{4959,5007}$ emission from the foreground galaxy at $z = 2.14$, and we can only provide a 2σ limit on the magnitude of $H > 24.8$. COLA1 is undetected in the K_s band ($K_s > 24.4$). Due to the large uncertainties in the photometry no meaningful constraints can be obtained on the UV slope, and we assume a flat UV slope $\beta = -2$ in the rest of the paper (this is similar to other LAEs at $z = 6.6$; Ono et al. 2010; Matthee et al. 2017d).

The Y band magnitude implies an absolute magnitude $M_{1500} = -21.6 \pm 0.3$, slightly above $M_{1500}^\star$ at $z \approx 7$ (Bouwens et al., 2014), but fainter than other luminous LAEs at $z = 6.6$ (e.g. CR7 and VR7; Matthee et al., 2017d), see Fig. 6.5. Following Shibuya et al. (2015), such a UV luminosity indicates $M_{star} \approx 10^{10}$ $M_\odot$ at $z \sim 7$, although this could be significantly underestimated in case the source is strongly dust-obscured (which however is at odds with its strong Lyα emission; e.g. Matthee et al. 2016). The narrowness of the Lyα line indicates that COLA1 is likely a star-forming galaxy, as AGN typically have broader Lyα lines (e.g. Matsuoka et al., 2016). COLA1 is unlikely to be significantly magnified: no massive foreground structures are known and no distortions are seen on the images.

COLA1's colours in the shortest *Spitzer*/IRAC channels are blue, $[3.6] - [4.5] = -0.2 \pm 0.3$. This is likely a consequence of Hβ and/or [OIII] slightly

Table 6.3: Derived properties of COLA1 as described in §6.4. Limits are at the 2σ level.

Property	Best estimate
Spectral analysis	
$L_{Ly\alpha}$	$2.9 \pm 0.1 \times 10^{43}$ erg s^{-1}
$EW_{0,Ly\alpha}$	85^{+70}_{-40} Å
M_{1500}	-21.6 ± 0.3
M_{star}	$\approx 10^{10}$ M$_\odot$
r_{50}	$0.33^{+0.07}_{-0.04}$ kpc
$f_{esc,LyC}$	$\approx 15 - 30$ %
$SFR_{Ly\alpha}$	75^{+60}_{-35} M$_\odot$ yr^{-1}
$SFR_{UV,nodust}$	27^{+8}_{-7} M$_\odot$ yr^{-1}
$\Sigma_{SFR,UV,nodust}$	95^{+50}_{-35} M$_\odot$ yr^{-1} kpc^{-2}
Gas-phase metallicity Z	$\lesssim 10^{-3}(1/20\,Z_\odot)$
Shell model fitting	
v_{exp}	78^{+5}_{-6} km s^{-1}
$\log_{10}(N_{HI}/cm^{-2})$	$17.0^{+0.3}_{-0.3}$
$\log_{10}(T/K)$	$4.2^{+0.1}_{-0.2}$
$\sigma_{intrinsic}$	159^{+4}_{-4} km s^{-1}
τ_d	$4.2^{+0.5}_{-0.8}$
z_{sys}	$6.5930^{+0.0001}_{-0.0002}$

boosting the [3.6] flux more than Hα is boosting the [4.5] flux (which is in a low transmission wavelength of the [4.5] band). However, COLA1 is not nearly as blue as other confirmed galaxies at $z \sim 6.6$. For example, CR7 and Himiko have colours $[3.6] - [4.5] = -1.3 \pm 0.3$ and $[3.6] - [4.5] = -0.7 \pm 0.4$, respectively (Harikane et al., 2018). This could indicate that COLA1's [O III] line is relatively weaker due to a lower metallicity. When we compare this colour to the predicted colours at $z = 6.6$ using photoionisation analysis and BPASS SED models presented in Bowler et al. (2017a), we find that the implied metallicity lies between $Z \approx 10^{-4} - 10^{-3}$, but always consistent with $Z < 10^{-3}(< 1/20\,Z_\odot)$ within the uncertainties. Alternatively, the IRAC colour could also indicate that an older stellar population is present in COLA1, or that the strength of nebular lines is lower due to a high LyC escape fraction (e.g. Zackrisson et al., 2017).

6.4.2   Lyα size and star formation rate density

As discussed in §6.3, the detection of COLA1 in the F814W band can be explained by pure Lyα emission. As the *HST*/ACS imaging has a small PSF, we can therefore use these data to constrain the size of the Lyα emitting region in COLA1 accurately (e.g. Paulino-Afonso et al., 2018b). We use a non-parametric method to measure the median half-light radius ($r_{50,obs}$) for 5000 random realisations of the image, where each pixel count is drawn from a Poissonian distribution. Then, we correct for PSF-broadening using $r_{50} = \sqrt{r_{50,obs}^2 - r_{PSF}^2}$,

where $r_{PSF} = 0.38$ kpc. This results in $r_{50} = 0.33^{+0.07}_{-0.04}$ kpc. This size is smaller than typical UV-selected galaxies with $M_{1500} \approx -21$, similar to galaxies with $M_{1500} \approx -18.4$ in the UV luminosity - size relation from Shibuya et al. (2015) and similar to the largest star cluster complexes (Bouwens et al., 2017). As the UV sizes of galaxies are typically much smaller than the Lyα sizes (e.g. Wisotzki et al., 2016), it could be possible that the galaxy is even more compact in the UV. On the other hand, it is likely that more diffuse Lyα emission is resolved out in the broad, high resolution F814W image (similar to e.g. in CR7; more luminous, extended Lyα emission that is undetected in similar F814W data), and that the core Lyα profile resembles the UV profile. Lyα emission is expected to be compact in galaxies with a low HI column density and high $f_{esc,LyC}$ (Mas-Ribas et al., 2017) – conditions that are likely present in COLA1 as discussed next.

We can estimate the SFR of COLA1 from the UV continuum or from the Lyα luminosity. Assuming a UV slope $\beta = -2.0$ and a Meurer et al. (1999) attenuation law, we find a dust-corrected $SFR_{UV} = 40^{+12}_{-10}$ M$_\odot$ yr^{-1} (27^{+8}_{-7} M$_\odot$ yr^{-1} without correcting for dust). Alternatively, the Lyα luminosity indicates $SFR_{Ly\alpha} = 75^{+60}_{-35}$ M$_\odot$ yr^{-1} (assuming a 40 % Lyα escape fraction and 15 % LyC escape fraction; following Sobral & Matthee 2018).

If we assume that the UV size is similar to the Lyα size, these measurements imply a minimum average SFR surface density $\Sigma_{SFR,UV,nodust} = 95^{+50}_{-35}$ M$_\odot$ yr^{-1} kpc^{-2}. This number would be higher if the UV size is more compact or if significant dust attenuation is present. This Σ_{SFR} is significantly higher than other galaxies known at $z > 6$ (e.g. Carniani et al., 2018). The SFR surface density is well above the threshold required to drive galactic outflows (e.g. Heckman et al., 2001), hence such outflows may well be present.

6.4.3 Lyα line properties and modelling

In Fig. 6.6 we show COLA1's rest-frame spectrum assuming $z = 6.593$ (the redshift of the red peak) and compare it to the luminous LAE C-147 (a Lyα-selected star-forming galaxy at $z = 2.23$ for which a blue peak is also detected in the Lyα spectrum and the systemic redshift is confirmed through Hα and [OIII] emission; Sobral et al. 2017, 2018d). The red part of the Lyα line of C-147 resembles the red asymmetric line in COLA1 very well. C-147 has a broader blue line, but the peak separation and the fact that there is no significant flux at line-centre is similar to COLA1.

If we assume that the transmitted Lyα flux is zero at line-centre (in between the two peaks; e.g. Yang et al. 2017), we measure a systemic redshift $z = 6.591$ for COLA1. The peak separation of the blue and red Lyα lines is 220 ± 20 km s^{-1}. In LyC leaking galaxies in the local Universe, the peak separation is anti-correlated with the amount of leakage of LyC photons (Verhamme et al., 2015, 2017). If this correlation would hold up to $z = 6.6$, we would infer $f_{esc,LyC} \approx 15$ % for COLA1, but potentially up to $f_{esc,LyC} \approx 30$ % if we compare to the most recent results (Izotov et al., 2018). A comparison of the blue-to-red flux-ratio of local LyC leakers also indicates $f_{esc,LyC} \approx 15$ % (although we note that the IGM could absorb part of the blue line-flux, see §11.7). For the rest of the paper we thus
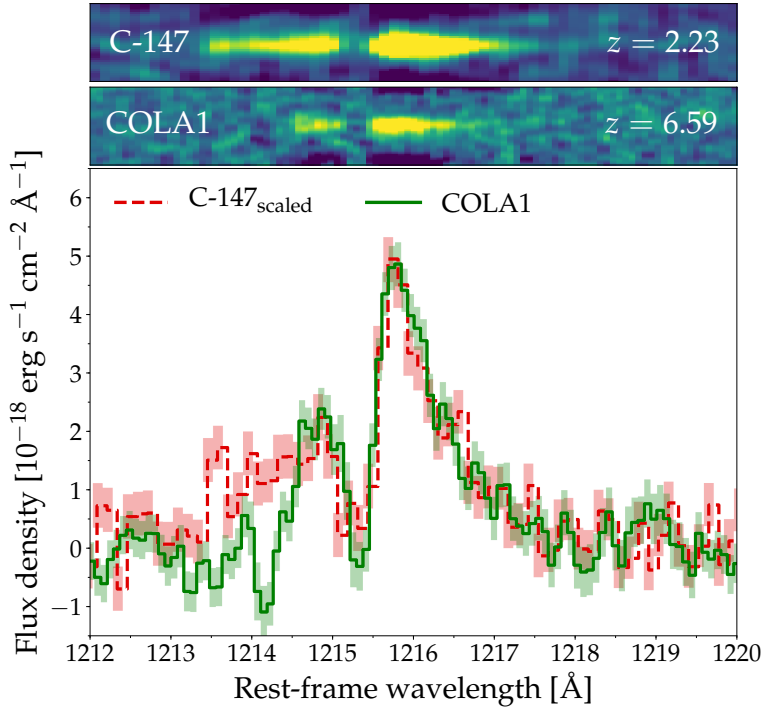
Figure 6.6: X-SHOOTER spectrum of COLA1, shifted to rest-frame Lyα at $z = 6.593$ (green), compared to spectra of C-147 (red dashed line, a double peaked LAE at $z = 2.23$ confirmed through Hα emission, scaled to the peak flux in the red line; Sobral et al. 2018d). The profile of the red line in COLA1 resembles the Lyα profile of C-147 remarkably well. The blue component of COLA1 is cut at $\Delta v \approx -250$ km s^{-1}, and thus narrower than C-147, potentially due to a higher optical depth at large distance from COLA1.

conservatively assume $f_{esc,LyC} \approx 15$ %. Therefore, the likely non-zero LyC escape fraction of COLA1 presents the best direct evidence to date that star-forming galaxies contributed to the reionisation of the Universe at $z \sim 7$. In fact, as we discuss in §11.7, such a contribution is required to ionise a large enough region to be able to detect the blue peak at its redshift. The prospects for directly detecting LyC photons at $z = 6.6$ are very low because of the typical opacity in the IGM is high at $z > 6$ (Inoue et al., 2014). Moreover, while foreground contamination is a major issue (Siana et al., 2015), measuring the Lyα peak separation may be a promising alternative.

Lyα spectral modelling

In order to get a more quantitative view of the ISM properties implied by the observed Lyα line, we fit the Lyα profile of COLA1 using a five-parameter shell model as in Dijkstra et al. (2016a). This model (e.g. Ahn et al., 2001; Verhamme et al., 2006) consists of a shell of neutral gas and dust around a central ionising source and parameters include the HI column density, expansion velocity, temperature and dust optical depth of the shell and the intrinsic width of the Lyα
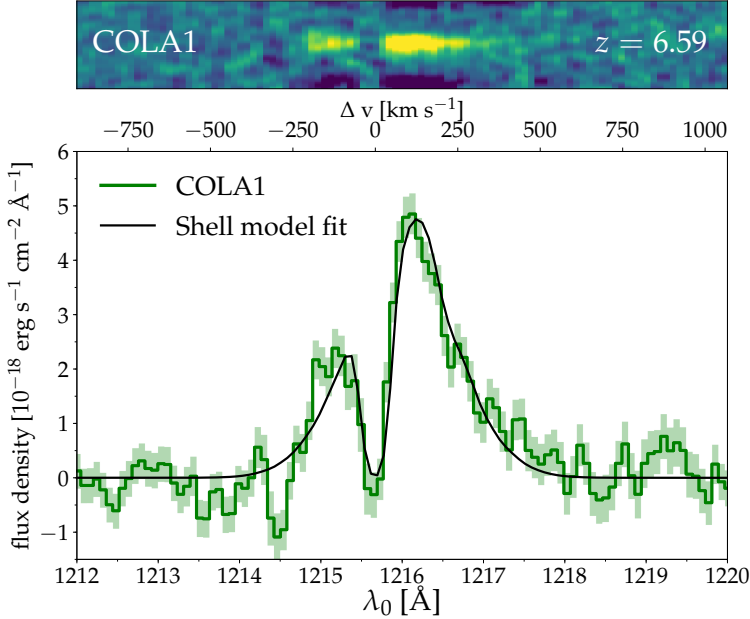
Figure 6.7: The observed Lyα profile of COLA1 (green) is well modelled by an expanding shell of neutral gas (black). The shell-model parameters indicate a low neutral hydrogen column density $N_{HI} = 10^{17.0\pm0.3}$ cm^{-2} and low expansion velocity $v_{exp} = 78^{+5}_{-6}$ km s^{-1}. We note that we have assumed here that the systemic redshift lies at line-centre (i.e. between the red and blue peak, where the flux is consistent with zero), or $z_{Ly\alpha} = 6.591$.

line (Gronke et al., 2015b). This fit does not include transmission through the IGM.

The best fitted parameters are listed in Table 6.3. Compared to $z \approx 3 - 5$ LAEs (Gronke, 2017), these parameters indicate a relatively low HI column density $N_{HI} = 10^{17.0\pm0.3}$ cm^{-2} and a high dust optical depth $\tau_d = 4.2^{+0.5}_{-0.8}$, while the other parameters are quite common for LAEs. The low HI column density is inferred from the low peak separation and suggests the possible escape of LyC photons. The high dust optical depth could alternatively be interpreted due to IGM opacity that could lower and narrow the blue peak. The HI column density and expansion velocity are also significantly lower than the inferred column density around CR7 (e.g. Dijkstra et al., 2016a). We note that the shell-model prediction of the systemic velocity of CR7 presented in Dijkstra et al. (2016a) agrees perfectly with recent [CII] measurements in Matthee et al. (2017e), suggesting that shell-model fitting is a good tool to recover the systemic redshift of a LAE at high redshift. The column density is also significantly lower than the column density inferred from absorption line measurements in local LyC leakers (Gazagnes et al., 2018), which lead these authors to conclude that the HI covering fraction in these galaxies is non-uniform. This is consistent with their larger Lyα peak separation compared to COLA1, and their typical escape fraction of ≈ 5 %.
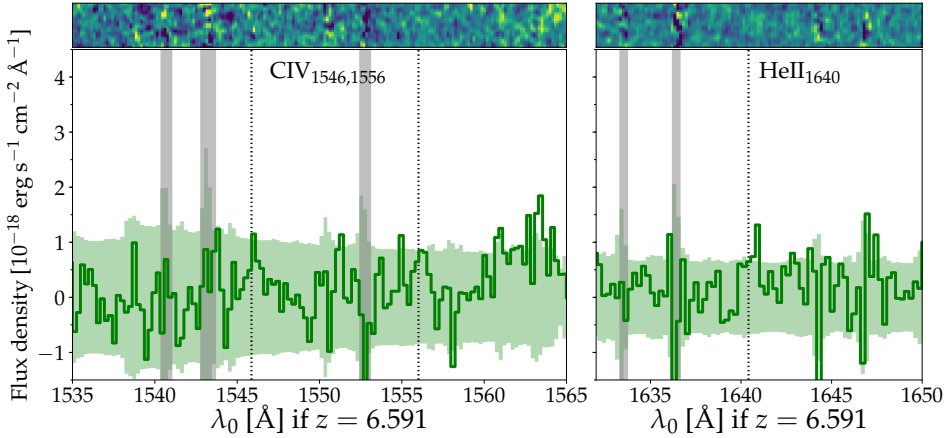
Figure 6.8: The wavelength coverage of the rest-UV CIV and HeII lines, redshifted to $z = 6.591$. We note that the background in a larger region around $\lambda_{0,z=6.591} = 1560 - 1565$ Å is boosted due to low atmospheric transmission and faint skylines. CIV and HeII lines are not significantly detected in COLA1, implying $EW_{0,CIV} < 25$ Å and $EW_{0,HeII} < 12$ Å.

As detailed in Verhamme et al. (2015), the Lyα line profile can be used as a tracer of $f_{esc,LyC}$ as both are sensitive to HI column density as $N_{HI} = -\ln(f_{esc,LyC})/\sigma_0$ where $\sigma_0 = 6.3 \times 10^{-18}$ cm^2 is the ionisation cross section. According to this equation, the column density derived from the shell-model fit (see Table 6.3) implies $f_{esc,LyC} \approx 50$ %. This is consistent with the result one would infer by using the correlation between Lyα EW_0 and $f_{esc,LyC}$ at $z \sim 3$ (Steidel et al., 2018), although we note this correlation has not been tested beyond $EW_0 \gtrsim 50$ Å and likely breaks down due to a reduced Lyα strength in the high $f_{esc,LyC}$ regime. It also points more towards a 30 % escape fraction as implied by comparison with the most recent measurements in local LyC leakers (Izotov et al., 2018). Such high escape fractions would also affect the strength of nebular emission lines such as Hα and Hβ and could therefore be tested with future spectroscopic observations with the *James Webb Space Telescope* (e.g. Jensen et al., 2016; Zackrisson et al., 2017). Indeed, the fact that COLA1 shows a $[3.6] - [4.5]$ colour that is much closer to zero than other luminous LAEs at the same redshift could potentially indicate a reduced strength of nebular emission lines, see §6.4.1.

6.4.4 High ionisation rest-UV emission-lines

Thanks to the wavelength coverage of the X-SHOOTER spectrum, we can inspect the spectrum for the presence of strong rest-UV emission line features (e.g. Stark et al., 2015a); see Fig. 6.8. We do not detect a significant feature besides Lyα. We measure 2σ limiting line-fluxes of 1.6 and 0.7×10^{17} erg s^{-1} cm^{-2} for the CIV$_{1546,1556}$ and HeII$_{1640}$ emission lines at $z = 6.591$, respectively (over 250 km s^{-1} extraction boxes), corresponding to $EW_{0,CIV} < 25$ Å and $EW_{0,HeII} < 12$ Å. These non-detections are not surprising given the fact that the limits are

shallower than other unsuccessful spectroscopic follow-up of LAEs at $z = 6.6$ (e.g. Shibuya et al., 2018), and EW limits are higher than detections in e.g. Stark et al. (2017).

6.5 Discussion: witnessing a galaxy reionising its surroundings

6.5.1 The unlikelihood of observing a blue Lyα line at $z > 6$

Lyα photons resonantly scatter in the presence of neutral hydrogen. Once Lyα photons are absorbed, they are re-emitted in a random direction in the rest-frame of the absorbing hydrogen atom, resulting in a diffusion process in real and frequency space. Analytical models show that this process results in a double peaked Lyα spectrum in a static medium (e.g. Neufeld, 1990). In the presence of outflows, Lyα photons see a larger optical depth towards the blue, resulting in a redshifted asymmetric spectrum. Hence, the Lyα profile is sensitive to the neutral hydrogen content and the velocity field of the gas in a galaxy (e.g. Loeb & Rybicki, 1999; Santos, 2004; Dijkstra et al., 2007).

After escaping from the ISM, Lyα photons are also affected by Hɪ in the circum-galactic medium (CGM). The CGM predominantly transmits red Lyα photons, enhancing the asymmetry between the red and the blue peak (e.g. Laursen et al., 2011). This is consistent with observations at high-redshift ($z > 2$), where high Hɪ column densities in the CGM result in a majority of Lyα profiles that consist of a single, red asymmetric line (e.g. Erb et al., 2014). Due to the increasing neutral fraction of the IGM, the asymmetry between the transmission of the red and blue line increases and the chances of observing double peaked emission decrease.

This is also found in semi-analytical and hydrodynamical models of the EoR, which typically predict negligible transmission bluewards of the systemic velocity at $z > 6$ (Dijkstra et al., 2007; Laursen et al., 2011; Weinberger et al., 2018). In the radiative transfer simulations from Laursen et al. (2011) the median IGM transmission at the blue peak is > 30 % only at $z < 4.5$, while it is < 0.1 % at $z > 5$ (similar to more recent simulations by Weinberger et al. 2018). Given that these models predict such low transmission bluewards of the systemic redshift, how is it possible that we observe a strong blue peak in the Lyα profile of COLA1 at $z = 6.59$, a redshift where this is highly unexpected? Here, we propose three scenarios that facilitate the transmission of blue Lyα photons and that may explain COLA1's Lyα profile.

6.5.2 Three scenarios to explain double peaked Lyα emission at $z = 6.6$

In Figs. 6.9 and 6.10 , we sketch three different physical scenarios that may explain the Lyα profile of COLA1. We first describe these models and then we propose observations that may test and differentiate between them. We note
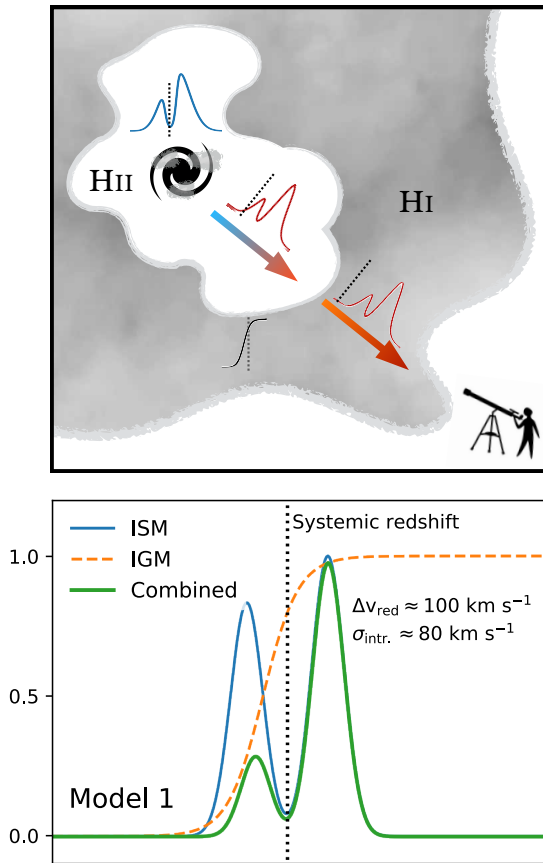
Figure 6.9: Sketch of a scenario that may explain the observed Lyα line-profile of COLA1. The top figure shows a sketch of the physical scenario and the bottom figure shows the emerging Lyα spectrum. Model 1 shows a double peaked emission line emerging from scattering in the ISM that is redshifted due to the expansion of the Universe before encountering the IGM, that preferentially attenuates the blue component.

that the transmission, line-widths and offsets in these figures are chosen for illustrative purposes.

In Model 1, COLA1 is surrounded by a highly ionised bubble that is large enough for Lyα photons to redshift out of resonance due to the expansion of the Universe before encountering a relatively neutral IGM. The Lyα profile is therefore only determined by the ISM conditions of the galaxy. In Model 2 the bubble itself is smaller, but is embedded in a larger relatively ionised region. The Lyα profile here is mostly affected by the gas in the CGM and IGM. Model 3 attempts to explain COLA1's Lyα profile without invoking IGM attenuation, but rather by an infalling self-shielded cloud of neutral hydrogen. This neutral hydrogen cloud absorbs part of the emitted Lyα line, resulting in a double peaked spectrum.

Model 1: Large, highly ionised bubble in a neutral IGM

If COLA1 resides in a large, highly ionised region, it is possible that blue Lyα photons redshift out of the resonance wavelength due to the Hubble expansion prior to encountering a neutral IGM (e.g. Malhotra & Rhoads, 2006). Depending on the size of this highly ionised region, it is possible that only (part of) the blue peak is attenuated. In Fig. 6.9, we illustrate this scenario where a double peaked Lyα line escapes from the ISM of the galaxy (resulting from resonant scattering effects, e.g. Neufeld 1990; Gronke et al. 2017), before the blue part of the line is attenuated by a sigmoid transmission function of the IGM.

The Lyα photons in the blue peak of COLA1 need to redshift out of the resonance wavelength by at least $\gtrsim 250$ km s^{-1} (the maximum velocity at which we observe blue Lyα flux compared to line-centre, see Fig. 6.7) before encountering significant amounts of neutral hydrogen. This requires a large ionised region. Ignoring peculiar velocities of inflowing gas, we can calculate the required size as follows:

$$d_{prop} = \frac{\Delta v}{H_{z=6.59}} \mathrm{Mpc}. \tag{6.1}$$

Here, d_{prop} is the proper distance photons are required to travel, Δv the required velocity offset and $H_{z=6.59}$ is the Hubble parameter at $z = 6.59$, which is $H_{z=6.59} = 803.85$ km s^{-1} Mpc^{-1} in our assumed cosmological model. Therefore, in order for Lyα photons to redshift by $\gtrsim 250$ km s^{-1} would require an ionised sightline/region of at least 0.3 pMpc; or $\gtrsim 2.3$ cMpc. Simulations indicate that this bubble-size is similar to the characteristic bubble size for a global ionised fraction of $x_{HI} \approx 50$ % (e.g. Furlanetto et al., 2006; Lin et al., 2016). As the ionised region needs to be *at least* 0.3 pMpc, and could be larger, this means the bubble size of COLA1 would correspond to a mean IGM $x_{HI} < 0.5$ at $z = 6.6$. On the other hand, the bubble around COLA1 may also be an outlier as COLA1 is likely a relatively massive galaxy. This could imply a higher neutral fraction.

Can such an ionised region be explained using the observed properties of COLA1? Following Haiman (2002), we estimate the maximum proper radius of the ionised region around a galaxy (in the absence of neighbouring ionising sources and ignoring recombinations):

$$R_s = 2.5 (f_{esc,LyC} \, Q_{ion} / 10^{54} \mathrm{s}^{-1})^{1/3} (t_{burst} / 10^7 \mathrm{yr})^{1/3} (1+z)^{-1} \mathrm{Mpc}. \tag{6.2}$$

Here, R_s is the radius of the Strömgren sphere, $f_{esc,LyC}$ the escape fraction of ionising photons, Q_{ion} the produced number of ionising photons per second and t the age of the burst of star formation. As listed in Table 6.4, we estimate $f_{esc,LyC} = 0.15$ (based on the Lyα peak offset), $Q_{ion} \approx 5 - 7 \times 10^{54}$ s^{-1} (based on either the Lyα luminosity, or based on the UV luminosity, combined with a ionising photon production efficiency of $\xi_{ion} = 10^{25.4}$ Hz erg^{-1}; Bouwens et al. 2016) and $t_{burst} = 10^7$ yr (based on the high Lyα EW; e.g. Charlot & Fall 1993) at $z = 6.591$. This results in $R_{s,max,Ly\alpha} = 0.33^{+0.07}_{-0.06}$ pMpc[3] and $R_{s,max,UV} =$

---

[3] We note that these uncertainties are the propagated errors corresponding to the UV and Lyα luminosities and ignore uncertainties in the age of the burst of star formation and the escape fraction.

Table 6.4: Parameters used in calculations of the ionised bubble around COLA1 at $z = 6.591$ (§6.5.2).

Property	Value	Motivation
$f_{\rm esc,LyC}$	15 %	(Conservative) Lyα peak separation and blue-to-red flux ratio in local LyC leakers
$f_{\rm esc,Ly\alpha}$	40^{+30}_{-20} %	Lyα EW calibration, tested at $z = 0 - 2.6$ (Sobral & Matthee 2018)
$Q_{\rm ion,Ly\alpha}$	$7^{+5}_{-3} \times 10^{54}$ s^{-1}	Lyα luminosity, $f_{\rm esc,LyC}$ and $f_{\rm esc,Ly\alpha}$ (Sobral & Matthee 2018)
$Q_{\rm ion,UV}$	$5^{+1}_{-1} \times 10^{54}$ s^{-1}	UV luminosity (no dust correction) and $\xi_{ion} = 10^{25.4}$ Hz erg^{-1}
$t_{\rm burst}$	10^7 yr	High Lyα EW (Charlot & Fall 1993)
$R_{s,\rm required}$	> 0.3 pMpc	Velocity offset $\gtrsim 250$ km s^{-1} due to expansion of the Universe
$R_{s,\rm max,Ly\alpha}$	$0.33^{+0.07}_{-0.06}$ pMpc	Eq. 2, assuming no recombinations and ionisation by the Lyα source of COLA1
$R_{s,\rm max,UV}$	$0.29^{+0.03}_{-0.03}$ pMpc	Eq. 2, assuming no recombinations and ionisation by the UV source of COLA1

$0.29^{+0.03}_{-0.03}$ pMpc, corresponding to ≈ 2.5 cMpc. The maximum radius would marginally increase by 0.03 pMpc when correcting the UV luminosity for a (high) attenuation $A_{\rm UV} = 0.45$.

Therefore, under basic assumptions, the star-formation in COLA1 may provide enough photons that can ionise a large enough region for allowing the blue peak to be observed up to ≈ -250 km s^{-1} from line-centre. However, there are important caveats that require attention. For example, our estimate conservatively assumes that the IGM does not affect Lyα photons red-wards of line-centre (as illustrated in Fig. 6.9) and the real required ionised region may have to be significantly larger.

Moreover, the calculation so far also ignores peculiar velocities that typically blueshift Lyα photons with respect to neutral gas in the IGM (Laursen et al., 2011). Our calculation also ignores self-shielded neutral regions in the CGM around galaxies, that could be challenging to ionise by the galaxy itself and therefore may form a major source of opacity (e.g. Mesinger et al., 2015; Sadoun et al., 2017). The recent simulations from Weinberger et al. (2018) suggest that these self-shielded regions may be more common for galaxies that reside in halos with $M_{\rm halo} \sim 10^{11}$ $M_{\odot}$, for which the fraction of sight-lines that has a significant transmission on the blue side of the systemic redshift is consequently extremely low. Sight-lines with high blue-transmission do exist in a significant fraction of low mass halos ($M_{\rm halo} \sim 10^9$ $M_{\odot}$). These simulations therefore suggest that COLA1 resides in a low mass halo, unless the ionisation from galaxies themselves have been under-estimated.

Finally, as noted in Haiman (2002), the radius of the ionised sphere is overestimated in case recombinations are important, for example when the clumping factor in the IGM is high ($C > 10$) or the age of the star formation burst is $> 10^8$ yr. It is thus unclear whether the ionised bubble can also be sustained, in par-
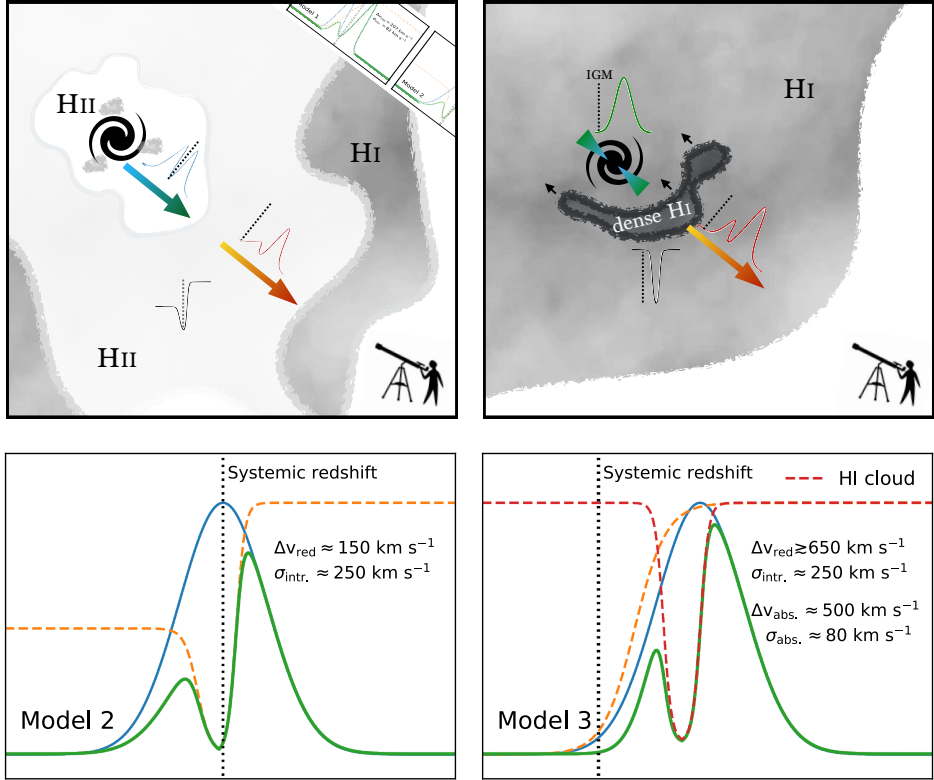
**Figure 6.10:** Sketches of alternative scenarios that may explain the observed Lyα line-profile of COLA1. The top row shows sketches of the physical scenarios and the bottom row shows the emerging Lyα spectrum. On the left, Model 2 shows that a double peak may originate due to a low transmission at line centre (due to neutral hydrogen in the CGM), while there is a relatively high transmission at further distances from the galaxy due to a large relatively ionised region (similar to the IGM transmission curve at $z \approx 4$ in Laursen et al. 2011). On the right, Model 3 shows that a double peaked profile can also arise without IGM attenuation in case there is an HI absorber slightly blue shifted with respect to the systemic Lyα velocity (which in this model is significantly redshifted with respect to the IGM).

ticular when the star formation rate of COLA1 would decline or if the escape fraction would decrease. A solution would be if a quasar or (faint) neighbouring galaxies contribute to the local ionising budget (e.g. Kakiichi et al., 2018). COLA1 is not located nearby a known quasar (Bañados et al., 2016). However, COLA1 is at a relatively close separation to CR7, the most luminous LAE known at $z = 6.6$. The projected distance on the sky of $34.17'$, which corresponds to a comoving distance of 77 Mpc (proper distance 10.1 Mpc) and the velocity difference is ≈ 350 km s^{-1}. No (faint) neighbouring galaxies are known around COLA1 (Bowler et al., 2014; Matthee et al., 2015), although the sensitivity to neighbouring galaxies is limited (corresponding to SFR$\gtrsim 25$ M$_\odot$ yr^{-1}) and deeper observations are required.

Model 2: Large mildly ionised region

In our second scenario, COLA1 resides in a relatively large ionised region with a high transmission away from line-centre, while the galaxy itself is not able to ionise gas clouds in its direct vicinity, causing the low transmission at line-centre. This scenario is illustrated in the left panel of Fig. 6.10. Here, the double peaked emission does not emerge from the galaxy itself, but is caused by the environment of COLA1 that transmits flux at different velocities differentially.

   Here, the gas in the CGM of the galaxy still contains significant amounts of neutral hydrogen (e.g. due to self-shielding), while the gas at larger distances from the galaxy is mildly ionised and has a transmission of ≈ 50 % at < -1000 km s^{-1} from the systemic redshift (similar to the simulated IGM properties at $z \approx 4$ in Laursen et al. 2011). The double peaked emission originates from residual hydrogen in the vicinity of COLA1, absorbing flux around the systemic velocity. In this scenario, the intrinsic Lyα profile (that escapes the ISM) is broader than the observed red Lyα line, but the resulting blue and red lines have similar widths. While this scenario still requires a highly ionised region (a transmission of 50 % corresponds to $\tau = 0.7$, or a mean neutral fraction of $\sim 2 \times 10^{-6}$ at $z = 6.6$), less ionising photons originating from COLA1 are required compared to Model 1.

   We point out that double peaked Lyα profiles with low flux at line centre are the norm among Green Pea galaxies in the local Universe ($z \approx 0.3$; e.g. Henry et al. 2015; Yang et al. 2017), emerging from scattering in the ISM. Therefore, for an emerging spectrum that has a similar profile at $z = 6.6$ (see also Fig. 6.6), but due to the effect of the IGM (and without scattering in the ISM) would be a remarkable coincidence.

Model 3: Large velocity offset and intervening absorber

The last scenario follows an alternative explanation which does not require a strong imprint from the IGM (either highly ionised, neutral, or partly ionised) in the vicinity of the emitting galaxy. Here, the emergent Lyα spectrum consists of a significantly redshifted broad peak (e.g. due to an outflow), such that line is not affected by H I in the CGM or IGM. The right panel of Fig. 6.10 shows that the double peaked profile originates from an absorbing system on top of this emission profile. This scenario is similar to the 'cold flow' scenario that is used to explain the Lyα profiles of high-redshift radio galaxies (e.g. van Ojik et al., 1997), but with the difference that the column density is much lower.

   The absorbing system could be interpreted as an inflow (e.g. Matsuda et al., 2006), or potentially a wall between two ionised regions (although we note that the IGM in model 3 can also be fully neutral), such as a filament that has not yet reionised (e.g. Finlator et al., 2009). We explore the H I column density that such an absorber would imply by fitting the line-profile with a voigt profile absorber on top of a gaussian emission line. The upper H I column density limit is mostly determined by the width of the absorber, which implies a marginally self-shielded column density $N_{HI} \lesssim 10^{17.7}$ cm^{-2}, blue shifted by ≈ 80 km s^{-1} with respect to the peak of the emission. The intrinsic line-width FWHM is

380 ± 20 km s^{-1}.

How likely is such a scenario? In this model, both observed lines are red-shifted with respect to the systemic redshift. This is not seen in $z = 0 - 3$ galaxies with double peaked Lyα emission, where the systemic redshift typically lies between peaks (e.g. Kulas et al., 2012; Henry et al., 2015; Sobral et al., 2018d). Vanzella et al. (2018) identify a luminous system at $z = 4$ (M$_{1500} = -22.2$, L$_{Ly\alpha} \approx 1.4 \times 10^{43}$ erg s^{-1}) that has four Lyα components, of which only one is redshifted by ≈ 350 km s^{-1}, while the others are either systemic or blueshifted. Multiple redshifted lines are seen in high-redshift radio galaxies (van Ojik et al., 1997), but these lines are typically much broader (FWHM $\gtrsim 1000$ km s^{-1}) and likely a consequence of large amounts of hydrogen present around the massive galaxies that harbour radio AGN. Therefore, unless particular conditions in the EoR are important, this scenario may be quite unlikely.

Summary and predictions

The sketched scenarios in Figs. 6.9 and 6.10 may be over-simplified and reality may be a combination of different aspects of the models. Even though Models 2 and 3 may be unlikely, some aspects of these models may be combined with the general scenario in Model 1. For example, the absorber from Model 3 could reside in the highly ionised region from Model 1. Other complications would arise if the galaxy is undergoing a major merger, with multiple emission line regions at different relative velocities (although there are currently no indications for this scenario). How can observations discriminate between the different explanations and make progress?

As illustrated in Figs. 6.9 and 6.10, it is clear that the key quantities that would allow to differentiate between the models are the intrinsic line-width and the systemic redshift. These properties can be measured from the Hα or the Hβ lines, accessible with the *James Webb Space Telescope*. The systemic redshift can alternatively also be measured using [CII] FIR emission with ALMA (e.g. Matthee et al., 2017e), which can also test whether a merger of multiple components is ongoing. Furthermore, if COLA1 is surrounded by a large ionised region, additional sources of ionising photons are likely present. It is therefore expected that COLA1 resides in a larger scale over-density of faint galaxies, potentially observable using deep Lyα observations with VLT/MUSE and/or with ALMA observations that can identify [CII].

6.5.3   Implications & considerations for surveys

Why are there no other LAEs known at $z = 5 - 7$ that have double peaked Lyα emission (c.f. Songaila et al., 2018)? Why do we find a double peaked LAE at a redshift where the IGM transmission towards the blue is likely very low, instead of around $z \approx 5 - 6$? Could it be that more double-peaked LAEs have been found, but they have been discarded as [OII] interlopers?

Observational biases against identifying double peaked LAEs?

As already noted in Dijkstra et al. (2007), LAEs with a strong blue peak show a relatively low asymmetry (quantified by skewness) and could thus be classed as low-redshift interlopers in the case of low resolution spectroscopy. Moreover, the range of observed peak separations in double peaked LAEs ($\Delta v \approx 200 - 400$ km s^{-1}; Verhamme et al. 2017) corresponds to observed wavelength differences $\Delta\lambda_{obs} = (1 + z_{Ly\alpha}) \times [0.8 - 1.6]$ Å, similar to the observed wavelength difference of the [OII] doublet $\Delta\lambda_{obs,[OII]} = (1 + z_{[OII]}) \times 2.79$ Å at all observed wavelengths in the optical. Therefore, 'single' line-identifications may be biased against confirming double peaked LAEs. This bias may particularly be important when spectral wavelength coverage is limited to the optical, but less important for $z_{Ly\alpha} \lesssim 4.8$, as potential interlopers of LAEs at these wavelengths will likely be detected in multiple lines (such as Hβ and [OIII], besides [OII]).

There are also other explanations of why the number of known double-peaked LAEs at $z = 5 - 6$ may be low. One explanation is that the fraction of double-peaked LAEs increases strongly with Lyα luminosity (as discussed in Hu et al. 2016) and current samples at $z = 5 - 6$ do not yet include enough luminous sources (as the majority of very wide-field surveys prioritised $z > 6$; e.g. Songaila et al. 2018). As the typical Lyα luminosity increases with redshift, this explanation would indirectly imply that the LyC escape fraction increases with Lyα luminosity and with redshift (as L$_{Ly\alpha}^{\star}$ increases; Sobral et al. 2018c).

Alternatively, it may be possible that spectroscopic follow-up observations and/or publication efforts may be biased towards $z > 6$ and double-peaked LAEs at $z = 3 - 6$ simply have not yet been observed spectroscopically or published; or that the typical S/N of spectroscopic observations at $z > 4$ is too low to identify similar blue peaks. The flux in the blue peak is a factor ≈ 0.3 lower than the brighter red component and can therefore only be detected at 3σ significance if the red peak is detected at $\approx 10\sigma$ significance, which is not always the case.

A preference for observing narrow peak separations only in luminous LAEs at $z > 5$?

Multiple peaked Lyα profiles have regularly been observed in LAEs at $z = 2 - 3$ (e.g. Kulas et al., 2012; Yamada et al., 2012; Trainor et al., 2015; Vanzella et al., 2016; Rivera-Thorsen et al., 2017), but also in quasars and in high-redshift radio galaxies (e.g. van Ojik et al., 1997; Miley & De Breuck, 2008). As COLA1 does not show evidence for AGN activity, we focus our comparison to LAEs at $z = 2 - 3$ (combining data from Yamada et al. 2012, Saez et al. 2015 and Sobral et al. 2018d) and Lyα analogues (i.e. Green Pea galaxies; GPs; Yang et al. 2017). The fraction of double peaked LAEs at $z = 2 - 3$ is $\approx 30 - 50$ % (Kulas et al., 2012; Yamada et al., 2012; Trainor et al., 2015), who find typical peak separations of $\sim 500 - 750$ km s^{-1}, although we note that the spectral resolution of these observations ($\approx 150 - 200$ km s^{-1}) may not identify peaks with low velocity separations. The peak separation in COLA1 is smaller than the peak separation of the ultra-faint
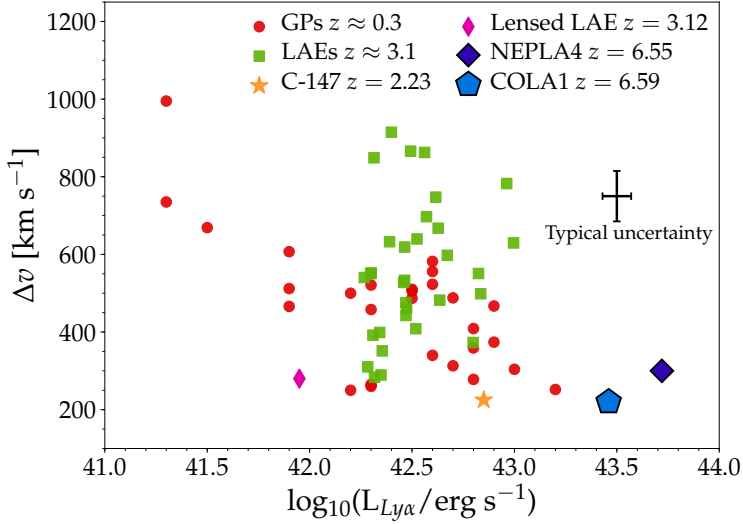
Figure 6.11: Lyα peak separation versus the observed Lyα luminosity of a compilation of star-forming LAEs. COLA1 (*blue pentagon*) has the lowest peak separation known, while NEPLA4 (*dark blue diamond*; Songaila et al. 2018) is the most luminous LAE known with a double peak. While there is no clear relation between the peak separation and Lyα luminosity at $z \approx 2-3$ (*orange star*: luminous LAE C-147 at $z = 2.23$, that is shown in Fig. 6.6; *green squares*: points based on published results from Yamada et al. 2012 and Saez et al. 2015; *magenta diamond*: a low mass $M_{star} < 10^7$ $M_\odot$ compact LAE presented in Vanzella et al. 2016), a clear anti-correlation is seen between peak separation and luminosity for Lyα emitting Green Pea galaxies (GPs; *red points*, Yang et al. 2017). This anti-correlation may be a selection effect, as GPs are selected on compactness and strong [OIII]/[OII] ratios that may trace density bounded HII regions, and not a pure Lyα selection.

($M_{1500} = -17$), lensed LAE at $z = 3.12$ identified in Vanzella et al. (2016), which is an extremely compact, highly ionising star-forming galaxy.

As shown in Fig. 6.11, there is no clear relation between peak separation and Lyα luminosity for LAEs at $z \approx 3$ (although the dynamic range is limited). On the other hand, a clear anti-correlation is seen between peak separation and luminosity for Lyα emitting GPs. COLA1, which is the most luminous LAE with the lowest known peak separation, seems to follow this relation. However, we note that this anti-correlation may be a selection effect, as GPs are selected on compactness and strong [OIII]/[OII] ratios (Cardamone et al., 2009), that may trace density bounded HII regions. For example, GPs may all have a similar intrinsic Lyα luminosity, but because of a correlation between the Lyα escape fraction and the peak separation (Yang et al., 2017) a strong anti-correlation is observed (Fig. 6.11).

If Lyα luminosity is anti-correlated with the peak separation at $z > 6$, this may explain why double peaked Lyα profiles may only be observed in the most luminous LAEs. As the IGM transmission strongly decreases towards the blue of the systemic redshift (e.g. Laursen et al., 2011; Weinberger et al., 2018), the blue lines of faint LAEs are more likely to be reduced. Luminous LAEs may however reside in larger ionised bubbles (because of a higher amount of ionising

photons), facilitating the observability of a blue peak. This would for example imply that NEPLA4 (Songaila et al., 2018) resides in a larger ionised bubble than COLA1. On the other hand, simulations argue that the blue peak transmission may be higher for fainter galaxies, as there is less self-shielded HI present in their CGM (e.g. Weinberger et al., 2018). The low *observed* peak separation in COLA1 could also indicate that the CGM/IGM attenuated a significant amount of the flux at even bluer wavelengths. Hence, it may simply be expected that observed peak separations at $z > 6$ are lower than at $z < 5$. A crucial test would therefore be to map out the evolution of the relation between peak separation and Lyα luminosity from $z \approx 5 - 7$ with high resolution spectroscopy, and explore how the blue-to-red flux ratio evolves with redshift.

6.6   Summary

We have presented a detailed analysis of the COLA1 galaxy, a double peaked LAE at $z = 6.59$ (Hu et al., 2016), using deep multi-wavelength photometry and new deep, high resolution optical and near infrared spectroscopy with VLT/X-SHOOTER. Due to the opacity of the CGM and IGM for blue Lyα photons, detecting a blue peak at $z > 6$ is highly unlikely. We therefore test whether the line profile is interpreted correctly as Lyα at $z = 6.6$ and study the properties of COLA1 and their implications. Our results are summarised as follows:

- We rule out that the double peaked line is [OII] emission at $z = 1.475$ based on 1) the shape of the line-profile: the asymmetric wing of the red line is not observed in the blue line and no flux is detected in the middle of the blue and red lines; 2) the extremely low blue-to-red flux ratio that is inconsistent with [OII] and 3) the non-detection of Hα at $z = 1.475$ ruling out even the lowest observed ratios with respect to [OII].

- A tentative detection in the B band is explained by a contribution from Lyα emission in a foreground LAE at $z = 2.142$, confirmed through [OIII]$_{5007}$ emission in addition to Lyα.

- We confirm that COLA1 is a double peaked LAE at $z_{\mathrm{Ly}\alpha,\mathrm{red}} = 6.593$ and summarise its properties in Table 6.3. The Lyα luminosity and EW are high ($L_{\mathrm{Ly}\alpha} = 2.9 \pm 0.1 \times 10^{43}$ erg s^{-1} and EW$_0 = 85^{+70}_{-40}$ Å) and the Lyα emission is compact ($r_{50} = 0.33^{+0.07}_{-0.04}$ kpc based on *HST* imaging).

- The Lyα peak separation is 220 ± 20 km s^{-1} and the flux of the blue peak is 0.31 ± 0.03 times the flux in the red peak. The Lyα lines are narrow (FWHM= 198 ± 14 km s^{-1} and 150 ± 18 km s^{-1} for the red and blue peak, respectively) and the full Lyα line-profile resembles the profile of a luminous LAE at $z = 2.2$ with a prominent blue peak (Fig. 6.6). Due to the narrowness of the Lyα line, COLA1 is unlikely to be powered by an AGN.

- By modelling the Lyα profile with a five-parameter shell model, we find that the line-profile is characterised by a very low HI column density

($N_{HI} = 10^{17.0 \pm 0.3}$ cm^{-2}), indicating a non-zero escape of ionising photons. Based on correlations between the escape fraction and the peak separation in LyC leaking galaxies, we infer an escape fraction of $\approx$ 15%, but potentially up to $\approx$ 30 %. Other inferences imply escape fractions up to $f_{esc,LyC} \sim$ 50 %. This means that we are witnessing a star-forming galaxy that is actively contributing to the reionisation of the Universe.

- COLA1 has a high UV luminosity, $M_{1500} = -21.6 \pm 0.3$, implying a SFR $\approx$ 30 M$_\odot$ yr^{-1}. The *Spitzer*/IRAC colours $[3.6] - [4.5] = -0.2 \pm 0.3$ imply relatively weak contribution from [OIII]/Hβ contributing to the [3.6] band, implying a metallicity as low as $Z < 10^{-3}(1/20\,Z_\odot)$ or reduced strength of nebular emission lines due to escaping ionising photons.

- The detectability of blue Lyα emission from COLA1 implies a low Lyα optical depth out to ≈ -250 km s^{-1} of the galaxy, potentially due to a surrounding $\gtrsim$ 0.3pMpc (2.3 cMpc) ionised region. Based on the observed properties of COLA1 and simple assumptions (detailed in Table 6.4), we find that enough ionising photons have escaped COLA1 to ionise a $\approx$ 0.3pMpc (2.3 cMpc) bubble. However, keeping this region ionised likely requires a contribution from faint neighbouring sources. No faint neighbouring galaxies are known, but COLA1 is likely in the same large scale over-density as CR7 with a separation of $\approx 30'$ ($\approx$ 10 pMpc) and ≈ 350 km s^{-1}.

As we have shown, the confirmation of COLA1 as a double peaked LAE at $z = 6.59$ allows us to witness directly that galaxies contribute to the reionisation of the Universe. Several assumptions made here can be overcome with future observations of the intrinsic line-profile and systemic redshift of COLA1. In particular, future high resolution spectroscopic observations of samples of LAEs may reveal the dependence on double peaked Lyα profiles on luminosity and redshift, providing a new probe of the reionisation process.

Acknowledgements

(Hunter, 2007; Astropy Collaboration et al., 2013a), the astronomical imaging tools `Swarp` (Bertin, 2010) and `ds9` and the `Topcat` analysis tool (Taylor, 2013).

The CALYMHA survey: Lyα escape fraction and its dependence on galaxy properties at $z = 2.23$

We present the first results from our CAlibrating LYMan-α with Hα (CA-LYMHA) pilot survey at the Isaac Newton Telescope. We measure Lyα emission for 488 Hα selected galaxies at $z = 2.23$ from HiZELS in the COSMOS and UDS fields with a specially designed narrow-band filter (λ_c = 3918 Å, $\Delta\lambda$= 52 Å). We find 17 dual Hα-Lyα emitters ($f_{Ly\alpha} > 5 \times 10^{-17}$ erg s^{-1} cm^{-2}, of which 5 are X-ray AGN). For star-forming galaxies, we find a range of Lyα escape fractions (f$_{esc}$, measured with 3$''$ apertures) from 2%−30%. These galaxies have masses from 3×10^8 M$_\odot$ to 10^{11} M$_\odot$ and dust attenuations E$(B - V) = 0 - 0.5$. Using stacking, we measure a median escape fraction of 1.6 ± 0.5% (4.0 ± 1.0% without correcting Hα for dust), but show that this depends on galaxy properties. The stacked f$_{esc}$ tends to decrease with increasing SFR and dust attenuation. However, at the highest masses and dust attenuations, we detect individual galaxies with f$_{esc}$ much higher than the typical values from stacking, indicating significant scatter in the values of f$_{esc}$. Relations between f$_{esc}$ and UV slope are bimodal, with high f$_{esc}$ for either the bluest or reddest galaxies. We speculate that this bimodality and large scatter in the values of f$_{esc}$ is due to additional physical mechanisms such as outflows facilitating f$_{esc}$ for dusty/massive systems. Lyα is significantly more extended than Hα and the UV. f$_{esc}$ continues to increase up to at least 20 kpc (3σ, 40 kpc [2σ]) for typical SFGs and thus the aperture is the most important predictor of f$_{esc}$.

7.1   Introduction

The Lyman-α (Lyα) emission line (rest-frame 1215.67 Å) has emerged as a powerful tool to study distant galaxies, since it is intrinsically the brightest emission line in H$_{II}$ regions and redshifted into optical wavelengths at $z > 2$. As a result, the Lyα line has been used to spectroscopically confirm the highest redshift galaxies (Oesch et al., 2015; Zitrin et al., 2015), select samples of galaxies with narrow-band filters (e.g. Ouchi et al., 2008; Matthee et al., 2015), find extremely young galaxies (e.g. Kashikawa et al., 2012; Sobral et al., 2015b), study the interstellar, circumgalactic and intergalactic medium (e.g. Rottgering et al., 1995; Cantalupo et al., 2014; Swinbank et al., 2015) and probe the epoch of reionization (e.g. Ouchi et al., 2010; Dijkstra, 2014).

However, due to the resonant nature of Lyα, it is unknown what the observed strength of the Lyα emission line actually traces. While Lyα photons are emitted as recombination radiation in H$_{II}$ regions, where ionising photons originate from star-formation or AGN activity, Lyα photons can also be emitted by collisional ionisation due to cooling (e.g. Rosdahl & Blaizot, 2012) and shocks. Most importantly, only a small amount of neutral hydrogen is needed to get an optical depth of 1 (with column densities of $\sim 10^{14}$ cm^{-2}; Hayes 2015). Therefore, Lyα photons are likely to undergo numerous scattering events before escaping a galaxy. This increases the likelihood of Lyα being absorbed by dust and also leads to a lower surface brightness (detectable as Lyα haloes, e.g. Steidel et al. 2011; Momose et al. 2014; Wisotzki et al. 2016) and diffusion in wavelength space, altering line profiles (e.g. Verhamme et al., 2008; Dijkstra, 2014).

In order to use Lyα to search for and study galaxies in the early Universe, it is of key importance to directly measure the fraction of intrinsically produced Lyα (the Lyα escape fraction, f_{esc}), and to understand how that may depend on galaxy properties. Under the assumption of case B recombination radiation, f_{esc} can be measured by comparing the Lyα flux with Hα. Hα (rest-frame 6563 Å) is not a resonant line and typically only mildly affected by dust, in a well understood way (e.g. Garn & Best, 2010). Measurements of both Lyα and Hα can thus improve the understanding of what Lyα actually traces by comparing f_{esc} with other observables as mass, dust content, kinematics, or Lyα line properties (such as the Equivalent Width (EW) and profile).

It is in principle possible to estimate the intrinsic Lyα production using other tracers of the ionising photon production rate (i.e. other star formation rate (SFR) indicators). However, these all come with their own uncertainties and assumptions. For example, studies using Hβ (e.g. Ciardullo et al., 2014) and UV selected samples (e.g. Gronwall et al., 2007; Nilsson et al., 2009; Blanc et al., 2011; Cassata et al., 2015) suffer from more significant and uncertain dust corrections, and may select a population which tends to be less dusty (e.g. Oteo et al., 2015). UV based studies are furthermore dependent on uncertainties regarding SED modelling, and on assumptions on the time-scales (UV typically traces SFR activity over a 10 times longer timescale than nebular emission lines, e.g. Boquien et al. 2014). Estimates using the far-infrared (Wardlow et al., 2014; Kusakabe et al., 2015) suffer from even larger assumptions on the time-scales. Remarkably though, most

studies find a consistent value of $f_{esc} \sim 30\%$ for Lyα emitters (LAEs), and lower for UV selected galaxies, $\sim 3 - 5\%$ (e.g. Hayes et al., 2011).

Locally, it has been found that the Lyα escape fraction anti-correlates with dust attenuation (Cowie et al., 2010; Atek et al., 2014), although the large scatter indicates that there are other regulators of Lyα escape, such as outflows (e.g. Kunth et al., 1998; Atek et al., 2008; Rivera-Thorsen et al., 2015). However, these locally studied galaxies have been selected in different ways than typical high redshift galaxies. Green pea galaxies (selected by their strong nebular [OIII] emission) have recently been studied as local analogs for high redshift LAEs (e.g. Henry et al., 2015; Yang et al., 2016). These studies find indications that the escape fraction correlates with HI column density, and that is also related to galactic outflows and dust attenuation. However, the sample sizes and the dynamic range are still significantly limited.

At higher redshift, it is challenging to measure the Lyα escape fraction, as Hα can only be observed up to $z \sim 2.8$ from the ground, while Lyα is hard to observe at $z < 2$. Therefore, $z \sim 2.5$ is basically the only redshift window where we can directly measure both Lyα and Hα with current instrumentation. This experiment has been performed by Hayes et al. (2010), who found a global average escape fraction of 5 ± 4 %. The escape fraction is obtained by comparing integrated Hα and Lyα luminosity functions (see also Hayes et al. 2011), so the results depend on assumptions on the shape of the luminosity function, integration limits, etc. Recently, Oteo et al. (2015) found that only 4.5% of the Hα emitters covered by Nilsson et al. (2009) are detected as LAEs, indicating a similar escape fraction.

In order to increase the sample size and study dependencies on galaxy properties, we have recently completed the first phase of our CALYMHA survey: CAlibrating LYMan-α with Hα. This survey combines the $z = 2.23$ Hα emitters from HiZELS (Sobral et al., 2013) with Lyα measurements using a custom-made NB filter (see Fig. 7.1). The observations from our pilot survey presented here cover the full COSMOS field and a major part of the UDS field, and are described in Sobral et al. (2017). The aim of this paper is to measure the escape fraction for the Hα selected sources, and measure median stacked escape fractions in multiple subsets in order to understand which galaxy properties influence f_{esc}.

The structure of this paper is as follows. In §7.2 we present the sample of $z = 2.23$ Hα emitters and the Lyα observations. We describe our method to measure Lyα line-flux and escape fraction and galaxy properties in §7.3, while §7.4 describes our stacking method. §7.5 presents the Lyα properties of individual galaxies. We explore correlations between f_{esc} and galaxy properties in §7.6 and study extended Lyα emission in §7.7. Our results are compared with other studies in §7.8 and we summarise our results and present our conclusions in §7.9.

Throughout the paper, we use a ΛCDM cosmology with H_0 = 70 km s^{-1}Mpc^{-1}, $\Omega_M = 0.3$ and $\Omega_\Lambda = 0.7$. Magnitudes are given in the AB system and measured in $3''$ diameter apertures, unless noted otherwise. At $z = 2.23$, $1''$ corresponds to a physical scale of 8.2 kpc. We use a Chabrier (2003) IMF to obtain stellar masses and star formation rates.
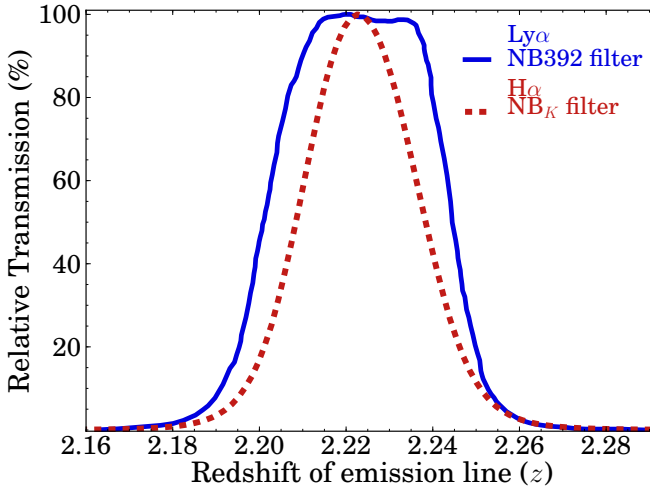
Figure 7.1: Filter transmission curves for the NBs used to measure Hα (NB$_K$) and Lyα (NB392). The NB392 filter is designed to provide complete coverage of the redshifts at which Hα emitters can be selected in NB$_K$, from $z = 2.20 - 2.25$. The Lyα emission for all our HAEs is covered even if it is shifted by ± 600 km s^{-1}. Depending on the specific redshift, the filter transmission varies between the two lines, such that Lyα is typically over-estimated with respect to Hα, see §7.3.4. We statistically correct for this in stacked or median measurements.

7.2   Sample and Observations

7.2.1   Sample of Hα emitters

We use a sample of Hα emitters (HAEs) at $z = 2.23$ in the COSMOS and UDS fields selected from the High-z Emission Line Survey (HiZELS; Geach et al. 2008; Sobral et al. 2009a; Best et al. 2013; Sobral et al. 2013) using narrow-band (NB) imaging in the K band with UKIRT. HAEs are identified using *BzK* and *BRU* colours and photometric redshifts, as described in Sobral et al. (2013). These HAEs are selected to have EW$_{0,\text{Hff}+[\text{NII}]} > 25$ Å. In total, there are 588 Hα emitters at $z = 2.23$ in COSMOS, of which 552 are covered by our Lyα survey area. We remove 119 HAEs because they are found in noisy regions of the Lyα coverage, resulting in a sample of 433 HAEs in COSMOS. The UDS sample consists of 184 HAEs, of which 55 are observed to sufficient S/N in the INT imaging (local background of 23.5, 3σ, or deeper). This means that our total sample includes 488 HAEs, shown in Fig. 7.2.

The multi-wavelength properties of the HAEs are discussed in Oteo et al. (2015), showing that the Hα selection incorporates the full diversity of star-forming galaxies (e.g. in their Fig. 5 and 6), while selections based on the Lyman break or the Lyα emission line miss significant parts of the star-forming galaxy population at $z = 2.23$. Furthermore, although our sample of galaxies contains strongly star-bursting systems, the majority is not biased towards these rare sources. Our sample is dominated by typical galaxies which are on the main relation between stellar mass and SFR (see Fig. 10 in Oteo et al. 2015, and e.g.
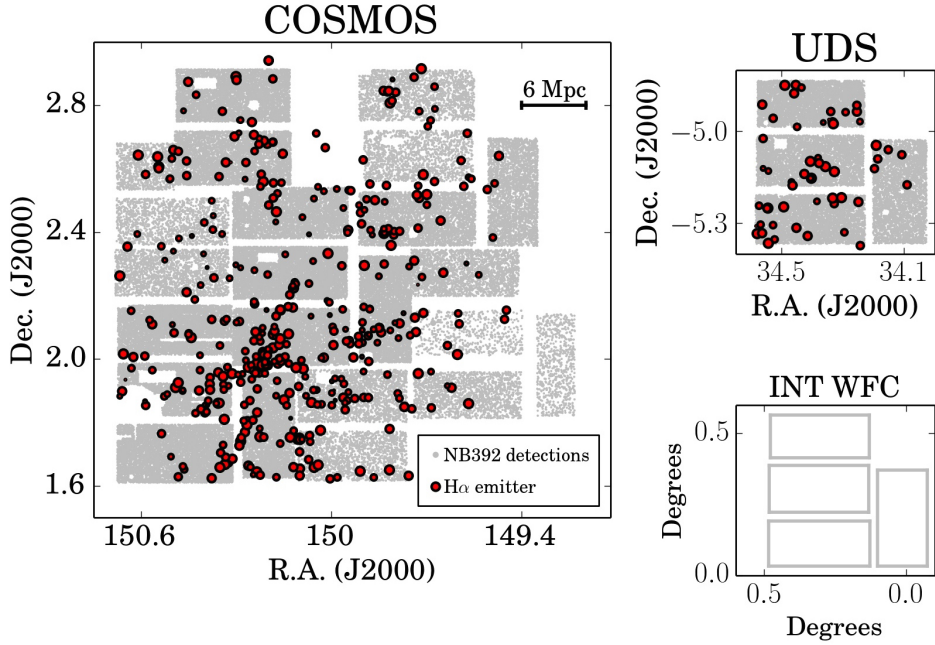
Figure 7.2: Coordinates of Hα emitters in the COSMOS and UDS fields are shown in red points, where the size of the symbols scales with observed Hα luminosity. The ∼ 2 deg² coverage includes a wide range of environments, with number density of sources on the sky varying over orders of magnitudes, overcoming cosmic variance (see e.g. Sobral et al. 2015a). The grey points show all detections in our NB392 observations, after conservative masking of noisy regions due to the dithering pattern. It can be seen that some pointings are shallower with a lower number density of sources, and that we masked regions around bright stars and severe damages to one of the chips. After our conservative masking, we use a total area of 1.208 deg² in COSMOS and 0.224 deg² in UDS. We also show the four detector chips of the WFC on the INT with a total field of view of ∼ 0.25 deg².

Rodighiero et al. 2014).

7.2.2 Lyα observations at $z = 2.23$

Lyα observations were conducted at the Isaac Newton Telescope (INT) at the Observatorio Roque de los Muchachos on the island of La Palma with a specially designed NB filter for the Wide Field Camera (WFC). This NB filter (NB392, $\lambda_c = 3918$Å, $\Delta\lambda = 52$Å) was designed for our survey such that it observes Lyα emission for all redshifts[1] at which Hα emitters can be selected with the NB$_K$ filter, see Fig. 7.1.

The details of the observations, data reduction and calibration are presented in Sobral et al. (2017), where we also present the Lyα luminosity function (LF), and other line-emitters detected in our NB data, such as CIV$_{1549}$ at $z \approx 1.5$ and [OII] at $z \approx 0.05$. For the purpose of this paper, we use the INT observations to

---

[1] Note that we investigate the effect of different filter transmissions between Lyα and Hα as a function of redshift and the effect of systematic velocity offsets between the lines in §7.3.4

measure the Lyα flux from Hα selected galaxies, by creating thumbnail images in NB392. For continuum estimation in COSMOS, we align publicly available *U* and *B* bands (from CFHT and Subaru respectively, Capak et al. 2007; McCracken et al. 2010) and measure the flux in these filters at the positions at which the Hα emission is detected. In UDS, we use CFHT *U* band data (PI: Almaini & Foucaud) from UKIDSS UDS (Lawrence et al., 2007) and Subaru *B* band data from SXDS (Furusawa et al., 2008).

We converted the *U*, *B*, NB_K and *K* images to the pixel scale of the INT WFC (0.33″/pixel). The astrometry of COSMOS images is aligned using SCAMP (Bertin, 2006), with a reference coordinate system based on *HST* ACS F814W band observations (as in the public COSMOS data, McCracken et al. 2010). The UDS images are aligned to 2MASS (Skrutskie et al., 2006). The accuracy of the astrometry is of the order of 0.1″. We match the full width half maximum (FWHM) of the point spread function (PSF) of all images to the FWHM of the NB392 observations (ranging from $1.8 - 2.0''$, depending on the particular pointing). The FWHM of reference stars was measured with SEXTRACTOR (Bertin & Arnouts, 1996), which fits a gaussian profile to the upper 80% of the light profile from each detected object. For NB392 imaging, we selected reference stars with magnitudes ranging from 16-18, resulting in ~ 20 stars per WFC detector. The reference stars in $U(B)$ are fainter because in $U(B)$ stars with magnitude $< 18(19)$ are saturated. For each frame, we find ~ 50 reference stars with magnitudes ranging from 19-21. PSF matching was then done by convolving images with a gaussian kernel. This procedure is based on the PSF matching procedure from the Subaru Suprime-Cam data reduction pipeline (Ouchi et al., 2004).

7.3 Measurements

7.3.1 Choice of aperture

Due to resonant scattering of Lyα photons, the choice of aperture can have an important consequence on the measured Lyα flux and escape fraction, particularly given the evidence of extended Lyα emission for a range of star-forming galaxies (e.g. Steidel et al. 2011; Momose et al. 2014 and which we confirm for our sample in §7.7). Previous surveys of Lyα emitters typically used MAG-AUTO photometry with SEXTRACTOR to measure Lyα fluxes (e.g. Hayes et al., 2010; Ouchi et al., 2010). However, the measured flux with MAG-AUTO will be dependent on the depth of the NB imaging. As we are measuring Lyα emission for Hα selected galaxies at the position of Hα detection, it is impossible to perform a similar MAG-AUTO measurement as Lyα selected surveys without uncontrolled bias. This is because we have no a priori knowledge of the optimal aperture to measure Lyα. In fact, we find in §7.5 that most Hα emitters are undetected in Lyα at the flux limit of our observations. We also note that MAG-AUTO measurements are dependent on the depth, and therefore are not suitable for an optimal comparison as the depth of our survey varies across the field and is different than other surveys.

Due to these considerations, we choose to use a fixed diameter aperture mea-

surements for individual sources. An aperture size of $3''$ was chosen for the following reasons. First, it corresponds to a radial distance of 12 kpc, which is larger than the exponential scale length of Lyα selected sources at $z = 2.2 - 6.6$ of $5 - 10$ kpc (Momose et al., 2014), and which is also similar to the reference scale used in the study of individual Lyα haloes (Wisotzki et al. 2016; although note that this survey has detected extended Lyα emission up to a radial distance of 25 kpc). Secondly, we find that $3''$ aperture magnitudes on the PSF convolved images of the U, B, NB_K and K band recover similar magnitudes as the $2''$ diameter apertures on the original Hα images (which typically have a PSF FWHM $\sim 0.8''$), with a standard deviation of 0.2 magnitudes. These magnitudes from $2''$ aperture measurements are used on most studies of the Hα emitters from our sample (e.g. Sobral et al., 2013; Oteo et al., 2015). For stacks of subsets of HAEs we vary the aperture, and discuss the difference in §7.7.

7.3.2   Measuring line-fluxes

We use fluxes in NB392, U and B band to measure the Lyα line-flux on the positions of the Hα emitters using dual-mode SExtractor. The NB392 flux is calibrated on U band magnitudes of photometrically selected galaxies (see Sobral et al. 2017), since stars have the strong $CaII_{3933}$ absorption feature at the wavelengths of the NB filter. After this calibration, we also make sure that the NB excess ($U - NB392$) is not a function of the $U - B$ colour, such that a very blue/red continuum does not bias line-flux measurements. This means that we empirically correct the NB magnitude using:

$$NB392_{corrected} = NB392 + 0.19 \times (U - B) - 0.09. \tag{7.1}$$

This correction ensures that a zero NB excess translates into a zero line-flux in NB392. For sources which are undetected in U or B we assign the median correction of the sources which are detected in U and B, which is $+0.02$. In the following, we refer to the broadband U as BB. Then, with the NB and continuum measurements, the Lyα line-flux is calculated using:

$$f_{Ly\alpha} = \Delta\lambda_{NB} \frac{f_{NB} - f_{BB}}{1 - \frac{\Delta\lambda_{NB}}{\Delta\lambda_{BB}}}. \tag{7.2}$$

Here, f_{NB} and f_{BB} are the flux-densities in NB392 and U and $\Delta\lambda_{NB}$ and $\Delta\lambda_{BB}$ the filter-widths, which are 52 Å and 758 Å respectively.

We measure Hα line-fluxes as described in Sobral et al. (2013). The relevant NB is NB_K and the continuum is measured in K band. The excess is corrected with the median correction of $+0.03$ derived from $H - K$ colours. For an HAE to be selected as a double Hα-Lyα emitter, we require the $U - NB392$ excess to be > 0.2 (corresponding to $EW_0 > 4$ Å) and a Lyα excess significance $\Sigma > 2$ (c.f. Bunker et al., 1995; Sobral et al., 2013), see the dashed lines in Fig. 9.2, which we base on local measurements of the NB and broadband background in empty $3''$ diameter apertures. This relatively low excess significance is only appropriate because we observe pre-selected Hα emitters. We note however that

all our directly detected sources are detected with at least 3σ significance in the
NB392 imaging.
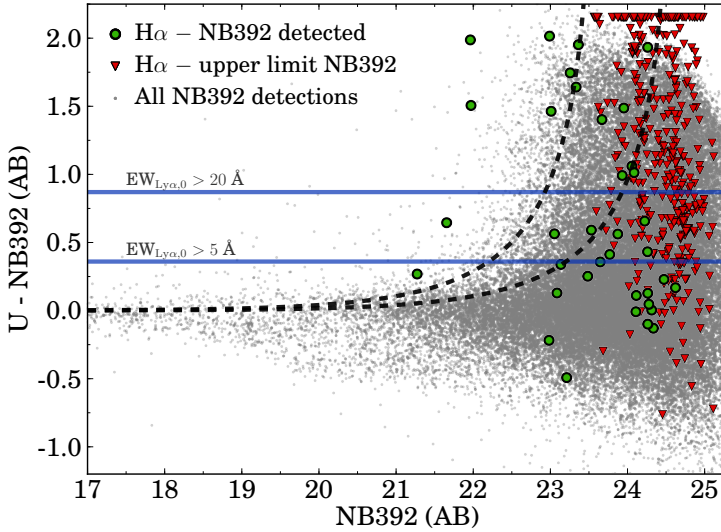
Figure 7.3: NB excess diagram of the sources in COSMOS and UDS. Grey points show all NB392
detections, where U has been measured in dual-mode. The green points show the Hα emitters
which are directly detected in the NB392 imaging, with measurements done at the position of the
HAEs. The red triangles are upper limits at the positions of the HAEs. The blue horizontal lines
show to which rest-frame Lyα EW a certain excess corresponds. Dashed black lines show the excess
significance for either the shallowest (left) or deepest (right) NB392 data. Note that some upper
limits on the NB392 magnitude are actually weaker than some detections. This is due to variations
in the depth of our NB392 observations across the field. Many stars have a negative excess due to
the Ca$\textsc{ii}_{3933}$ absorption feature.

7.3.3   Measuring the Lyα escape fraction

In order to measure the observed fraction of Lyα flux, we need to carefully esti-
mate the intrinsic Lyα line-flux. The intrinsic emission of Lyα due to recombina-
tion radiation is related to the Hα flux, and scales with the number of ionising
photons per second. Assuming case B recombination, a temperature T between
$5,000 - 20,000$K and electron density n_e ranging from $10^2 - 10^4$cm^{-3}, the in-
trinsic ratio of Lyα/Hα ranges from 8.1-11.6 (e.g. Hummer & Storey, 1987). For
consistency with other surveys (as discussed by e.g. Hayes 2015; Henry et al.
2015), we assume $n_e \approx 350$ cm^{-3} and $T = 10^4$K, such that the intrinsic ratio
between Lyα and Hα is 8.7. Therefore, we define the Lyα escape fraction as:

$$f_{esc} = \frac{f_{Ly\alpha,obs}}{8.7 f_{H\alpha,corrected}} \tag{7.3}$$

In the presence of an AGN, the assumption of case B recombination is likely in-
valid because e.g. collisional ionisation might play a role due to shocks, leading

to false estimates of the escape fraction. Among the sample of HAEs, we identify nine X-ray AGN in COSMOS using *Chandra* detections (Elvis et al., 2009), which are all spectroscopically confirmed to be at $z = 2.23$ (Civano et al., 2012). Eight of these are significantly detected in NB392 imaging. We exclude these AGN from stacking analyses, but will keep them in our sample for studying individual sources.

Note that since we measure line-fluxes in $3''$ apertures, f_{esc} is strictly speaking the escape fraction within a radius of 12 kpc. It is possible that the total escape fraction is higher, particularly in the presence of an extended low surface brightness halo due to resonant scattering (see also the discussion from a modellers point of view by Zheng et al. 2010).

7.3.4   Corrections to measurements

Although our matched NB survey requires less assumptions and uncertain conversions than escape fraction estimates based on UV or other emission-line measurements, we still need to take the following uncertainties/effects into account:

1. interlopers in the Hα sample

2. different filter transmissions

3. dust correction of the observed Hα flux

4. [NII] contributing to the flux in the Hα filter

Interlopers

Our Hα sample is selected using photometric redshifts and colour-colour techniques in a sample of emission line galaxies obtained from NB imaging (see Sobral et al. 2013). This means that galaxies with other emission lines than Hα can contaminate the sample if the photometric redshift is wrongly assigned (for example if the galaxy has anomalous colours). Spectroscopic follow-up shows a 10% interloper fraction, although this follow-up is so far limited to the brightest sources. These interlopers are either dusty low redshift ($z < 1$) sources, such as Paβ at $z = 0.65$, or Hβ/[OIII] emitters ($z \sim 3.2 - 3.3$, e.g. Khostovan et al. 2015). For the $z \sim 3.3$ emitters, the NB392 would only measure noise, as the NB392 filter observes below the Lyman break for higher redshift galaxies and the flux for the low redshift interlopers is typically much fainter than the NB392 limit. The identified interlopers do not occupy a particular region in the parameter space of the sample of HAEs. There may be small dependences of contamination with galaxy properties, but no trends are seen for our limited follow-up, thus we assume a flat contamination. For stacking, we increase our observed NB392 flux by 10% to account for these interlopers. For individual sources without NB392 detection, we are careful in our analysis as there is the risk of interlopers, even though the fraction is relatively small.

Table 7.1: Numbers and median properties with 1σ deviations of the sample of Hα-Lyα emitters with and without AGN. We show median upper limits for galaxies that are not detected in Lyα, which is the comparison sample. Line-fluxes are in 10^{-16} erg s^{-1} cm^{-2}. Hα and Lyα fluxes are the values observed in 3″ apertures. For completeness, we show the subsample of star-forming galaxies (SFGs) that we used for stacks (these are selected based on the depth of Lyα observations). We show the extinction using E($B-V$) from SED fitting and the Calzetti et al. (2000) law (see §7.3.5; A$_{H\alpha,C}$). The Hα attenuation from Garn & Best (2010), A$_{H\alpha,GB}$, is based on a calibration between dust, SFR and mass. The total sample consists of 488 HAEs, with a stacked median escape fraction of 0.9±0.1% (for 3″ diameter apertures), which is lower than the median escape fraction of individually detected source, because for individual sources we are observationally biased towards high escape fractions.

Hα sample	Nr.	$\langle f_{H\alpha} \rangle$	$\langle f_{Ly\alpha} \rangle$	A$_{H\alpha,C}$ [mag]	A$_{H\alpha,GB}$ [mag]	f$_{esc}$ [%]
SFG with Lyα	12	0.5±0.3	0.7±0.5	0.83±0.4	1.11±0.4	10.8±1.3
SFG no Lyα	468	0.4±0.3	< 0.7	0.83±0.5	0.86±0.4	< 20.1
AGN with Lyα	5	1.3±0.4	3.6±1.5	0.50±0.3	1.55±0.3	12.8±1.4*
SFGs for stacks	265	0.4±0.3	0.1±0.01	1.0±0.4	0.86±0.4	0.9±0.1

* This escape fraction is likely wrong, as in AGN there is likely a departure from case B recombination due to shocks. We still show this for comparison, indicating that Lyα is typically bright for AGN.

Filter transmissions

While the NB392 and NB$_K$ filters are very well matched in terms of redshift coverage, the transmission at fixed redshift varies between Hα and Lyα. This means that the measured escape fraction is influenced by the particular redshift of the galaxy and resulting different filter transmissions for Hα and Lyα. Furthermore, systematic velocity offsets between Lyα and Hα might increase this effect, as it has been found that Lyα is redshifted typically 200 (400) km s^{-1} with respect to Hα in Lyα (UV) selected galaxies (e.g. Steidel et al., 2010; McLinden et al., 2011; Kulas et al., 2012; Hashimoto et al., 2013; Erb et al., 2014; Shibuya et al., 2014; Song et al., 2014; Sobral et al., 2015b; Trainor et al., 2015).

We test the effect of the different filter transmissions and velocity shifts using a Monte Carlo simulation, similar to e.g. Nakajima et al. (2012). We simulate 1,000,000 galaxies with redshifts between the limits of the NB$_K$ filter, and with a redshift probability distribution given by the NB$_K$ filter transmission (as our sample is Hα selected). Then, we redshift the Lyα line w.r.t. Hα with velocity shifts ranging from $0-800$ km s^{-1}, and fold it through the filter transmission in NB392. Finally, we compute the average relative Hα-Lyα transmission. For a zero velocity offset, the average transmission is 20% higher for Lyα than Hα, because the NB392 filter is more top-hat like than the NB$_K$ filter. Increasing the velocity offset leads to an average lower Lyα transmission, as it is redshifted into lower transmission regions in the right wing of the filter. This effect is however very small, as it is constant up to a velocity shift of 400 km s^{-1}, and decreases to 11% for 800 km s^{-1}. Because of this, we decrease the Lyα-Hα ratio of stacks and individual sources by 20%. We add the 20% uncertainty of this correction to the error on the escape fractions in quadrature. Spectroscopic follow-up is required to fully investigate the effect of velocity offsets on our measured escape fractions.

Dust attenuation

Even though the Hα emission line is at red wavelengths compared to, for example, UV radiation, it is still affected by dust, such that we underestimate the intrinsic Hα luminosity. Correcting for dust typically involves a number of uncertainties, such as the shape and normalisation of the attenuation curve, the difference between nebular and stellar extinction (e.g. Reddy et al. 2015 and references therein) and the general uncertainties in SED fitting. For consistency with other surveys, we correct for extinction by applying a Calzetti et al. (2000) dust correction, using the estimated extinction, $E(B - V)_{star}$, measurements from the best fit SED model from Sobral et al. (2014). Note that we assume $E(B - V)_{star}$ = $E(B - V)_{gas}$, independent of galaxy property. Recent spectroscopic results at $z \sim 2$ (e.g. Reddy et al., 2015) indicate that this is reasonable when averaged over the galaxy population, although there are indications that the nebular attenuation is higher than the stellar attenuation for galaxies with high SFR, particularly for galaxies with SFR > 50 M$_\odot$ yr^{-1}. Therefore, if such a trend would be confirmed, our inferred relations between f_{esc} may be slightly affected. We discuss this when relevant in §7.6 and §7.8.2.

When stacking, we use the median dust correction of the sources included in the stacked sample, which is $A_{H\alpha} = 1.0$. This number has also been used for example by Sobral et al. (2013) in order to derive the cosmic star formation rate density, which agrees very well with independent measures. Ibar et al. (2013) showed this median attenuation also holds for a similar sample of HAEs at $z = 1.47$ by using Herschel data.

However, we also investigate how our results change when using the dust correction prescription from Garn & Best (2010), which is a calibration between dust extinction and stellar mass based on a large sample of spectroscopically measured Balmer decrements in the local Universe. This relation between Balmer decrement and stellar mass is shown to hold up to at least $z \sim 1.5$ (e.g. Sobral et al., 2012; Ibar et al., 2013).

For individual sources, the two different dust corrections explored here can vary by up to a factor five, as seen in Table 7.2. This results in large systemic errors which can only be addressed with follow-up spectroscopy to measure Balmer decrements. Throughout the paper, we add the error on the dust correction due to the error in SED fitting in quadrature to the error of the Hα flux, but note that the systematic errors in the dust-correction are typically of a factor of two.

[NII] contamination

Due to the broadness of the NB$_K$ filter used to measure Hα, the adjacent [NII] emission line doublet contributes to the observed line-flux. We correct for this contribution using the relation from Sobral et al. (2012), who calibrated a relation between [NII]/([NII]+Hα) and EW$_{0, H\alpha+[NII]}$ on SDSS galaxies. More recently, Sobral et al. (2015a) found the relation to hold at least up to $z \sim 1$. At $z = 2.23$, we use this relation to infer a typical fraction of [NII]/([NII]+Hα) = 0.17 ± 0.08, which is consistent with spectroscopic follow-up at $z \sim 2$ (Swinbank et al., 2012;

Sanders et al., 2015). We have checked that our observed trends between f_{esc} and galaxy properties do not qualitatively depend on this correction - if we apply the median correction to all sources, the results are the same within the error bars. We add 10 % of the correction to the error in quadrature. For stacks, we measure the $EW_{0, H\alpha+[NII]}$ and apply the corresponding correction, which is consistent with the median correction mentioned here, and we also add 10% of the correction to the error in quadrature.

7.3.5   Definitions of galaxy properties

We compare f_{esc} with a range of galaxy properties, defined here. SFRs are computed from Hα luminosity, assuming a luminosity distance of 17746 Mpc (corresponding to $z = 2.23$ with our cosmological parameters) and the conversion using a Chabrier (2003) IMF:

$$SFR(H\alpha)/(M_\odot yr^{-1}) = 4.4 \times 10^{-42} L(H\alpha)/(erg\,s^{-1}) \qquad (7.4)$$

where L(Hα) is the dust-corrected Hα luminosity and SFR(Hα) the SFR.

Stellar masses and extinctions (E$(B-V)$) are obtained through SED fitting as described in Sobral et al. (2014). In short, the far UV to mid-infrared photometry is fitted with Bruzual & Charlot (2003) based SED templates, a Chabrier (2003) IMF, exponentially declining star formation histories, dust attenuation as described by Calzetti et al. (2000) and a metallicity ranging from $Z = 0.0001 - 0.05$. While we use a mass defined as the median mass of all fitted models within 1σ of the best fit, we use the E$(B-V)$ value of the best fitted model. The errors on stellar masses and extinctions are computed as the 1σ variation in the fitted values from SED models that have a χ^2 within 1σ of the best fitted model. For stellar mass, these errors range from 0.2 dex for the lowest masses to 0.1 dex for the highest masses. The typical uncertainty on the extinction ranges from 0.12 at E$(B-V) \approx 0.1$, to 0.05 at E$(B-V) \approx 0.3$.

The UV slope β (which is a tracer for dust content, stellar populations and escape of continuum ionising photons, e.g. Dunlop et al. 2012) is calculated using photometry from the observed $g^+ - R$ colours. These bands were chosen such that there is minimal contribution from Lyα to the g^+ band (the transmission at the corresponding wavelength is $< 5\%$), and such that we measure the slope at a rest-frame UV wavelength of ~ 1500Å. We also chose to derive the slope from observed colours in stead of using the SED fit, as otherwise there might be biases (e.g. the SED based extinction correction is related to the UV slope). The error in β due to measurement errors in g^+ and R ranges from typically 0.5 at $\beta = -2.3$ to 0.3 at $\beta > 0$.

7.4   Stacking method

In order to reach deeper Lyα line-fluxes, we use stacking methods to combine observations of our full sample of observed galaxies, such that the exposure time is effectively increased by a factor of ~ 400. This however involves some

complications and assumptions. For example, we will use the median stacked value, rather than the mean stacked value, such that our results are not biased towards bright outliers. However, our results will still be biased towards the most numerous kind of sources in our sample. Stacking also assumes that all sources are part of a single population with similar properties - which may not always be the case, as indicated by the results in the previous section.

We divide our sample in subsets of various physical properties in §7.6 and study how these stacks compare with the results from individual galaxies. We discuss the effect of varying apertures in §7.7. The errors of the measured fluxes and resulting escape fractions in stacks are estimated using the jackknife method. The errors due to differences in the PSF of the NB and broadband are added as a function of aperture radius (see §7.4.1). We add all other sources of systematic error (see §7.3.4) in quadrature.

We obtain stacked measurements by median combining the counts in $1' \times 1'$ thumbnails in U, B, NB392, NB_K and K bands of the Hα emitters covered in our INT observations (see Fig. 7.2). From the stacked thumbnails (as for example shown in Fig. 7.11), we measure photometry in various apertures at the central position (defined by the position of the NB_K detection. Note that our typical astrometric errors are of the order $\sim 0.1''$, corresponding to ~ 1 kpc). With this photometry, we obtain line-fluxes for both Lyα and Hα. The Lyα flux is corrected using $U - B$ colours, and we account for the [NII] contribution to the NB_K flux using the relation with EW from Sobral et al. (2012) (see §7.3.4). We also add the error due to differences in the PSF of U and NB392 to the error of the Lyα flux (see §7.4.1). We apply the median dust correction of the Hα emitters, which is roughly similar for using the Calzetti or Garn & Best method: $A_{H\alpha} = 1.0$ or $A_{H\alpha} = 0.86$, respectively. For our full sample of 488 Hα emitters, we observe a median stacked Lyα line-flux of $3.5 \pm 0.3 \times 10^{-18}$ erg s^{-1} cm^{-2}, and an escape fraction of 0.3$\pm$0.06 % in $3''$ apertures, corresponding to a radial distance to the centre of ~ 20 kpc. The significance of these detections are discussed in §7.7.

The depth of our NB392 observations is inhomogeneous over the full fields (see Fig. 7.2). We therefore study the effect of limiting our sample based on the depth of the NB392 observations. We find that the photometric errors on the stacked NB392 image are minimised when we only include sources for which the local 3σ depth is at least 24.1 AB magnitude, which corresponds to the inclusion of 265 out of the 488 sources. For the remainder of this section, we only include sources which are among these 265. The median SFRs, stellar masses, and dust attenuations of this sample are similar to the average properties of the full sample (see Table 9.1). The 3σ depth of the NB392 stack of these 265 sources is 27.2 AB magnitude. In the case of a pure line and no continuum contributing to the NB392 flux, this corresponds to a limiting line-flux of $\sim 5 \times 10^{-18}$ erg s^{-1} cm^{-2}.

7.4.1 Empirical evaluation of different PSF shapes

The NB and broadband observations are taken with different telescopes, cameras and at different observing sites and under different conditions. Therefore, even
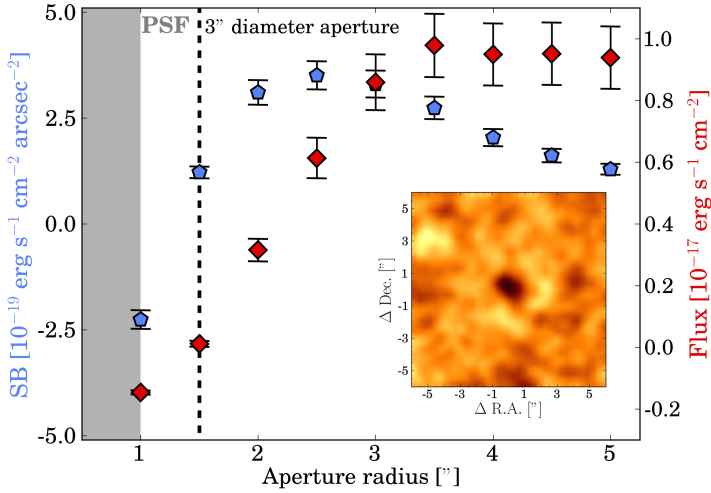
Figure 7.4: Surface brightness profile (blue) and integrated flux (red) of the stack of the reference sample, which should have a zero line-flux at a 1.5″ aperture radius by construction. The 1.5″ aperture radius is indicated with a dashed black line. The inset figure shows the 2D image obtained by subtracting the BB from the NB. We find a small residual signal which has central absorption and peak at a radial distance of 2.5″, attributed to differences in the PSF of the NB and the broadband. The typical signal measured for individually detected HAEs is 10-100 times higher than the signal due to the PSF differences, but it is of the same order of magnitude as stacked measurements.

though we match the PSF-FWHM of all images, the actual shape of the PSF might vary between NB and broadband. This might artificially influence the surface brightness profile of line-emission estimated from the difference between the two bands. This becomes particularly important when we study stacked images of over 300 sources, where errors on the percent level might dominate the measured signal.

We empirically evaluate the differences in NB and broadband PSF by performing the following sanity check: we first select line-emitters in NB_K imaging, which: i) are *not* selected as Hα emitters, ii) are *not* selected as higher redshift line-emitters, or iii) do *not* have a photometric redshift > 1 (from Ilbert et al. 2009). With this sample, we ensure that the NB392 photometry should measure (relatively flat) continuum by removing a handful of sources with an emission line in NB392. This leaves us with 245 sources, which have a similar NB_K magnitude distribution as the HAE sample. The U, B and NB392 images are stacked in the exact same way as we treat the HAEs. This is used to measure the resulting line-flux and surface brightness profile of the stack in the NB392 band (we estimate the continuum from U and B). Although the NB392 was photometrically calibrated to the U band in 3″ diameter apertures, we detect a small residual signal with a typical surface brightness profile of central absorption (with surface brightness $\sim -2 \times 10^{-19}$ erg s^{-1} cm^{-2} arcsec^{-2}, see Fig. 7.4), and peaking at a radial distance of 2.5″ (with a surface brightness of $\sim 4 \times 10^{-19}$ erg s^{-1} cm^{-2} arcsec^{-2}). We note that at the radial aperture of 1.5″, which we used for our

calibration, the integrated flux signal is consistent with zero, see Fig. 7.4. Corrections therefore only need to be applied for other aperture radii and surface brightness profiles. For individually detected Lyα sources, the residual signal at the $1 - 10\%$ flux level, but for stacks, it can be more important. The origin of this residual signal is likely because of differences in the inner part of the PSF, similarly as those reported by e.g. Momose et al. (2014). The uncertainty in our astrometry is of the order of $0.1''$ and therefore likely less important.

We thus conclude that the differences in PSF shapes of broadband and narrow-band have a small effect on stacked measurements, but we still take it into account by correcting all surface brightness profiles and any aperture measurements at values other than $3''$. We add the residual flux to the error of the total flux in quadrature.
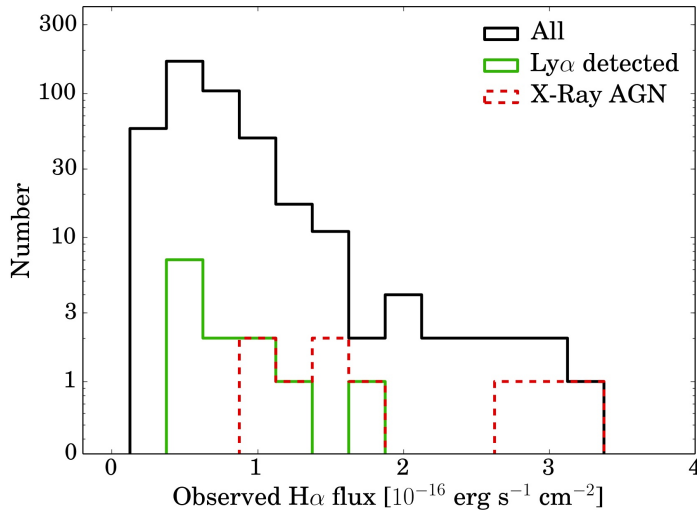
Figure 7.5: Histogram of Hα fluxes in our galaxy sample at $z = 2.23$. AGN are typically found among the brightest Hα emitters, and are also typically detected in NB392. We also show the distribution of Lyα detected star-forming galaxies. Not all brightest Hα emitters have been detected, indicating very low escape fractions or interlopers. On the other hand, some very faint Hα emitters are still detected in Lyα, indicating high Lyα escape fractions.

7.5 Direct measurements for individual galaxies

We directly detect ($> 3\sigma$) 43 out of our 488 HAEs in the NB392 imaging, which is a combination of UV continuum and Lyα line (see Table 9.1). The 3σ limit corresponds to limiting Lyα fluxes ranging from $3.8 - 7.4 \times 10^{-17}$ erg s^{-1} cm^{-2} (assuming the typical continuum level of 0.23 μJy, ~ 25.5 AB magnitude in the U band). Out of these robust detections, 17 show a significant Lyα line detection (excess significance $\Sigma > 2$), all in COSMOS. The properties of these sources and their IDs from the HiZELS catalog (Sobral et al., 2013) are listed in Table 7.2. The

Table 7.2: Properties of Hα emitters at $z = 2.23$ detected at 3σ in NB392 imaging and having a Lyα emission line. The IDs correspond to the last digits of the full HiZELS IDs, which can be retrieved by placing "HiZELS-COSMOS-NBK-DTC-S12B-" in front of them. The coordinates are measured at the peak of NB$_K$ (rest-frame R+Hα) emission. The observed line-fluxes (in 10^{-16} erg s^{-1} cm^{-2}), EW, dust extinction and escape fraction are measured with 3'' apertures. The escape fraction (f_{esc}) is computed under the assumptions explained in §7.3.4, thus using A$_{H\beta,C}$. [1]: SED: Dust correction using SED fitted E($B - V$) and a Calzetti et al. (2000) law. [2]: GB: Garn & Best (2010) dust correction based on stellar mass. [3]: codes in this column correspond to: 1: X-Ray AGN, 2: [OII] line detected in NB$_J$, 3: [OIII] line detected in NB$_H$.

ID	R.A. (J2000)	Dec. (J2000)	M$_{star}$ $\log_{10}(M_\odot)$	f$_{Ly\alpha}$ 10^{-16}	EW$_{0,Ly\alpha}$ Å	f$_{H\alpha}$ 10^{-16}	A$_{H\beta,C}$ SED[1]	A$_{H\beta,GB}$ GB[2]	f$_{esc}$ %	Note[3]
1057	10:00:39.6	+02:02:41.2	$10.6^{+0.1}_{-0.1}$	0.46	82	0.42	0.17	1.43	10.8 ± 1.4	
1073	10:00:44.2	+02:02:06.9	$11.1^{+0.1}_{-0.1}$	0.88	55	1.24	0.50	1.77	5.1 ± 0.6	1
1139	10:00:55.4	+01:59:55.4	$10.8^{+0.1}_{-0.1}$	4.55	63	1.03	0.17	1.56	43.7 ± 5.1	1, 2, 3
1993	10:02:08.7	+02:21:19.9	$8.6^{+0.1}_{-0.1}$	1.14	68	0.26	1.49	0.29	12.8 ± 1.5	3
2600	10:00:07.6	+02:00:13.2	$8.7^{+0.2}_{-0.2}$	1.32	80	0.53	1.00	0.29	11.4 ± 1.3	3
2741	10:01:57.9	+01:54:36.9	$10.1^{+0.1}_{-0.1}$	3.55	14	2.24	0.67	0.99	9.9 ± 1.0	1
4032	10:00:51.1	+02:41:16.9	$11.0^{+0.1}_{-0.1}$	0.46	28	0.34	0.83	1.67	7.3 ± 1.1	
4427	10:01:19.4	+02:07:32.6	$8.7^{+0.2}_{-0.4}$	0.57	12	0.58	1.16	0.29	3.8 ± 0.6	
4459	10:01:43.3	+02:11:15.7	$10.3^{+0.1}_{-0.1}$	1.41	93	0.41	0.50	1.18	24.8 ± 3.1	
4861	10:00:03.3	+02:11:04.4	$9.0^{+0.2}_{-0.2}$	0.31	16	0.28	0.0	0.34	12.4 ± 2.3	
5583	10:01:59.6	+02:39:32.7	$10.8^{+0.2}_{-0.2}$	1.73	244	0.41	0.50	1.54	30.4 ± 3.8	
5847	10:01:12.2	+02:53:25.9	$10.3^{+0.1}_{-0.1}$	0.70	60	1.03	0.50	1.11	4.9 ± 0.5	
7232	10:01:05.4	+01:46:11.6	$10.3^{+0.1}_{-0.1}$	0.42	15	0.74	1.33	1.11	1.9 ± 0.3	
7693	09:59:49.6	+01:50:24.7	$9.6^{+0.1}_{-0.1}$	0.75	10	0.84	0.67	0.65	5.5 ± 0.8	
7801	10:02:08.6	+01:45:53.6	$10.4^{+0.1}_{-0.1}$	2.38	5	1.35	0.50	1.24	12.8 ± 1.4	1
9274	10:00:26.7	+01:58:23.0	$11.0^{+0.1}_{-0.1}$	5.06	142	1.54	0.13	1.72	32.4 ± 3.6	1, 2
9630	10:02:31.3	+01:58:16.5	$9.7^{+0.2}_{-0.2}$	0.61	29	0.44	0.0	0.70	16.1 ± 2.2	
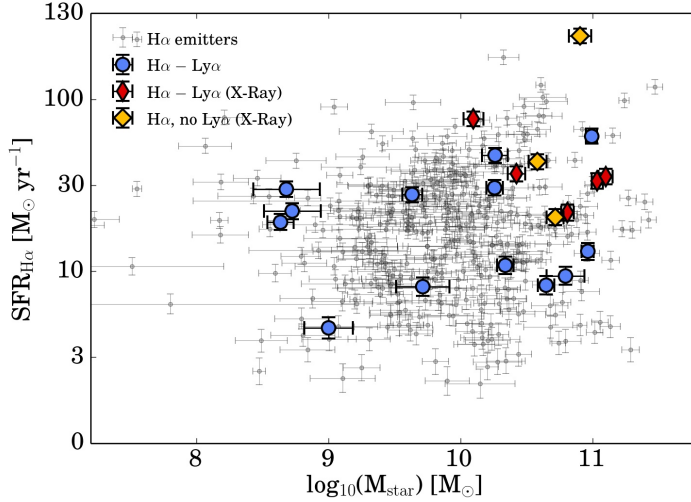
Figure 7.6: SFR(Hα) versus stellar mass for the observed Hα emitters. We obtained the SFR from dust corrected Hα and stellar mass from SED fitting (see §7.3.5). We show the position of sources with and without Lyα, AGN with Lyα and AGN without Lyα. There is no obvious difference in the SFRs or stellar masses between sources with or without Lyα. Since it is easier to observe Lyα for galaxies with higher SFR (at a given f_{esc}), this already indicates that f_{esc} is higher for galaxies with low SFR. Note that the SFR for the AGN is likely to be overestimated as AGN activity also contributes to the Hα flux.

other 26 robust NB392 detections are Hα emitters with strong upper limits on their Lyα flux, as we have detected the UV continuum in the NB392 filter.[2]

Five of the dual emitters are matched (within 3″) with an X-ray detection from *Chandra*. From spectroscopy with IMACS and from zCOSMOS (Lilly et al., 2009), these are all classed as BL-AGN. These AGN are among the brightest and most massive Hα emitters (Fig. 7.5): all have stellar masses above $10^{10.5}$ $M_\odot$ (Fig. 7.6), and the fraction of BL-AGN is consistent with the results from Sobral et al. (2016a). The ISM conditions surrounding the AGN might lead to other ionising mechanisms than case B photo-ionisation, such as shocks, making it more challenging to measure the Lyα escape fraction as the intrinsic Hα-Lyα changes.

Fig. 7.5 shows the distribution of Hα fluxes of our observed sample, of the AGN and also of the star-forming sources directly detected in Lyα. Whether a source is detected in Lyα does not clearly correlate with Hα flux, such that even very faint HAEs are detected. These very faint sources generally have high f_{esc}, although we note that it is possible that these sources are detected at a redshift where the transmission in the Hα filter is low. In the remainder of the paper, we will use the sample of 17 dual Hα-Lyα emitters for direct measurements of f_{esc},

---

[2] Note that these sources are unlikely higher-redshift interlopers, as the NB392 filter is below the Lyman break at $z > 3$, such that a NB392 detection rules out that the source is a $z \sim 3.3$ Hβ/[OIII] or $z = 4.7$ [OII] emitter (e.g. Khostovan et al., 2015). Moreover, 13 of these have detected [OIII], [OII] or both lines.

and use upper limits for the other 471 HAEs.
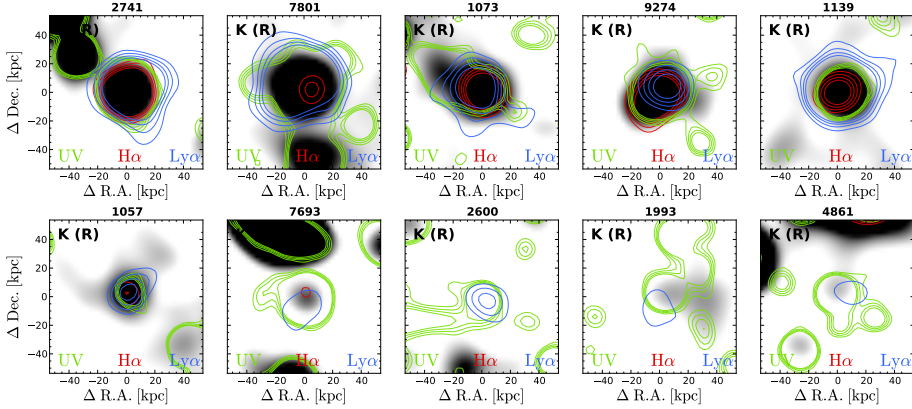
**Figure 7.7:** Lyα morphologies for the ten HAEs with most significant Lyα detections. All images (including *HST* ACS F814W) were smoothed to the PSF of the NB392 image and are centred on the position of peak Hα emission. The *top* row shows AGN, the *bottom* row SFGs. The sources are ordered by Hα flux, decreasing from left to right. Each panel shows a 100×100 kpc *K* band (which traces rest-frame *R*, and thus roughly stellar mass) thumbnail with contours of rest-frame Lyα (blue), UV (green, from ACS F814W) and Hα (red). The Lyα image was obtained by subtracting the continuum PSF matched *U* band from the NB392 image and correcting using the differential PSF image. The contours show 3, 4, 5 and 6 σ levels in each respective filter. For Lyα, the 3σ contour corresponds to a surface brightness ranging from $1.8 - 17$ (median 2.0)$\times 10^{-18}$ erg s^{-1} cm^{-2} arcsec^{-2}. The UV data is typically 3 magnitudes deeper than the Lyα data. Among the AGN, IDs 7801 and 1139 show evidence for extended Lyα emission. For the SFGs there is little convincing evidence for extended emission at the reached surface brightness limit. The faintest Hα emitters have no 3σ contour because of smoothing with the PSF of the Lyα image.

7.5.1 Lyα properties of dual Lyα-Hα emitters

After excluding the X-ray AGN, we find 12 robust dual Lyα-Hα emitters, which would translate in 2.5% of our star-forming galaxies being detected in Lyα down to our flux limit. However, if we only select the subset of HAEs with the deepest Lyα observations (194 star-forming galaxies, of which 8 have Lyα), we find a fraction of 4.1%. This is comparable to Oteo et al. 2015, who found a fraction of 4.5% and lower than the 10.9 % of Hayes et al. 2010, whose Lyα observations are a factor six deeper and Hα sample consists of fainter sources (by a factor of seven), but covers a volume which is ~ 80 times smaller than our survey.

Comparing our 12 Hα-Lyα emitters to HAEs without Lyα, we find that there are no clear differences in the SFR-M_{star} plane (Fig. 7.6). Since it is easier to observe Lyα for galaxies with higher SFR (at a given f_{esc}), this already indicates that f_{esc} is higher for galaxies with low SFR. We show the stellar masses, observed Hα and Lyα fluxes and dust attenuations of the Lyα detected sources in Table 7.2.

The median, dust-corrected Hα luminosity for the 12 SFGs with Lyα is 4.5×10^{42} erg s^{-1} (corresponding to a SFR of 20 M$_\odot$ yr^{-1}), and median stellar mass of 1.8×10^{10} M$_\odot$, such that they have specific SFRs which are typical to the

sample of HAEs, see Fig. 7.6. The median Lyα luminosity is 2.8×10^{42} erg s^{-1} and the Lyα escape fraction for these galaxies ranges from 1.9 ± 0.3 to 30 ± 3.8 % (although we note this does not take the uncertainty due to the filter transmission profiles into account, nor a statistical correction). The EW$_0$(Lyα) ranges from 10 to 244 Å. If we apply an EW$_0$(Lyα) cut of > 25 Å (similar to the selection of LAEs at high redshift, e.g. Matthee et al. 2014 and references therein), 7 out of 194 star-forming HAEs with deepest Lyα observations are recovered as LAEs, with luminosities $\sim 2 - 8 \times 10^{42}$ erg s^{-1}.

Morphology

In Fig. 7.7, we compare the Lyα surface brightness with rest-frame UV, *R* and Hα from *HST* ACS F814W (Koekemoer et al., 2007), *K* and NB$_K$ (continuum corrected with *K*) respectively. In order to be comparable, the PSF of the *HST* images is matched to that of the NB392 imaging on the INT, using a convolution with a gaussian kernel. As the PSF of our INT imaging is $1.8 - 2.0''$, this is a major limitation. However, for the most significantly detected sources (in Lyα), it is still possible to study differences qualitatively. Even though there is ground based *I* band data available, we use *HST* data because those are deeper.

The sources with IDs 2741, 7801 1073, 9274 and 1139 (see Table 7.2 for more information), shown in the first row are all AGN with mostly symmetrical Lyα morphology. Compared to the UV, IDs 7801 and 1139 show evidence for extended Lyα emission, while this is more evident when Lyα is compared to Hα. Note that the Lyα image is typically the shallowest, and that the outer contours of Lyα therefore typically represent a higher fraction of the peak flux than the UV contours.

The sources in the second row are undetected in the X-ray, and therefore classed as SFGs. 1057 is relatively massive (M$_{star}$ = $10^{10.6}$ M$_\odot$), and has f$_{esc}$ of 10.8 ± 1.6%. 7693 has an intermediate mass of $\sim 10^{9.5}$ M$_\odot$ and escape fraction of 5.5 ± 0.8%. From comparison with the Hα image, it can be seen that Lyα preferentially escapes offset to the south from the galaxy centre, which might be indicative of an outflow.

The sources with IDs 2600, 1993 and 4861, in the last three columns of Fig. 7.7 are the faintest HAEs for which we detect Lyα directly, such that there are no 3σ Hα contours due to smoothing the image with the PSF of the Lyα image. These HAEs have (possibly) little dust, blue UV slopes and Lyα EW$_0 > 30$ Å, such that they would be selected as Lyα emitters. The masses, SFRs and blue UV slopes are consistent with results from typical LAEs (e.g. Nilsson et al., 2009; Ono et al., 2010), and similar to simulated LAEs (e.g. Garel et al., 2012, 2015). The Lyα emission for ID 1993 and 4861 appears to be offset from the peak UV emission. This indicates that slit spectroscopy of UV or Hα selected galaxies might miss significant parts of Lyα. Note that we look at the stacked UV, Lyα, Hα and morphologies of these 12 SFGs and the full sample of SFGs in §7.7.
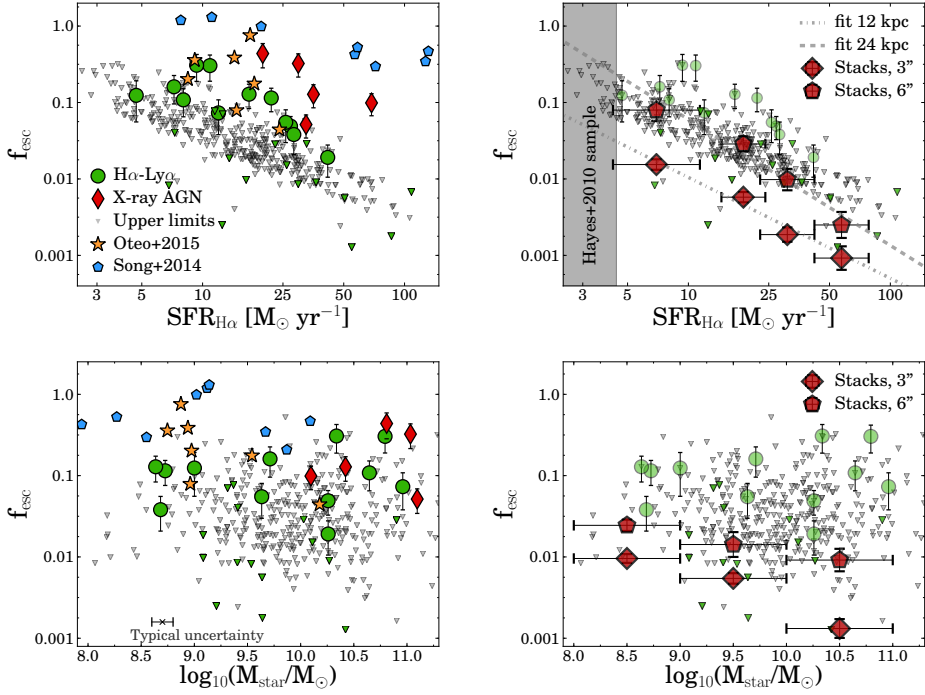
Figure 7.8: Lyα escape fraction versus SFR and stellar mass for galaxies without AGN for individual sources (left panels) and stacks (right panels). The green circles show our directly detected Hα-Lyα emitters, grey triangles highlight upper limits (green triangles have a UV detection in NB392) and our X-ray identified AGN with Lyα are shown in red diamonds. We also add the Hα selected sample from Oteo et al. (2015) in orange stars and the Lyα selected sample from Song et al. (2014) as blue pentagons. Our survey clearly extends the probed parameter space in galaxy properties. Stacked values are shown for two different radial distances to the center (corresponding to 3″ diameter apertures - diamonds, and 6″ diameter apertures - pentagons). The typical measurement uncertainty in stellar mass is indicated in the *bottom left* panel. *Top row*: The *left* panel shows the SFR obtained from Hα versus f_{esc} of individual sources. Although a correlation is expected by definition, it can be seen that on average, galaxies with a higher SFR have a lower escape fraction. The grey region in the *right* panel shows the SFRs typical for galaxies in the sample from Hayes et al. 2010, who inferred $f_{esc} = 5.3 \pm 3.8\%$. *Bottom row:* Escape fraction versus stellar mass. While f_{esc} can be relatively high for low mass galaxies, the stacked results indicate that f_{esc} might decrease weakly with increasing stellar mass. The large difference in f_{esc} between some massive individual sources and the stacked values indicate that there is likely significant scatter in the values of f_{esc} at this mass range.

7.5.2 [OII] and [OIII] emission lines

In addition to NB_K imaging, the HiZELS survey consists of NB_J and NB_H imaging in the same fields. These filters are designed such that they also cover the redshifted [OII] (in NB_J) and [OIII] (in NB_H) emission at $z = 2.23$, similar to e.g. Nakajima et al. (2012) and Sobral et al. (2012). Out of the 488 Hα emitters, 23 and 70 galaxies are detected in [OII] and [OIII], respectively. Two out of the 9 AGN are detected as line-emitters in both NBs, two as [OIII] emitters, and two AGN as [OII] emitters. The three remaining AGN all have a spectroscopic redshift at $z = 2.21 - 2.23$ (Sobral et al., 2016a). This means that all our AGN are either spectroscopically confirmed or have highly accurate photometric redshifts, with emission lines in at least two narrow-bands.

There are two star-forming HAEs with Lyα and [OIII] (ID 1993 and 2600, see Fig. 7.7 and Table 7.2). Compared to all HAEs with detection in [OIII] and similar limits on the Lyα flux and f_{esc}, these galaxies have the lowest mass and SFR ($\sim 10^{8.6}$ $M_\odot$, SFR $< 8 M_\odot$ yr^{-1}), most extreme UV slopes (either bluest, ID 2600, or reddest, ID 1993). They have $f_{esc} \sim 10\%$ and [OIII] EW$_0 \sim 100$ Å, resembling local Green pea galaxies (e.g. Henry et al., 2015). Their dust corrections are uncertain, because the two methods described in §7.3.4 give a factor 3-5 difference depending on the method. Compared to the other Lyα detected HAEs, these galaxies have the highest Lyα EWs. ID 2600 has very high Hα EW$_0$ of ~ 960 Å, similar to the most extreme emission line galaxies (e.g. Amorín et al., 2015), while the Lyα EW$_0$ is 80 Å. ID 1993, however, has a relatively low Hα EW$_0$ of 70 Å, and Lyα EW$_0$ of 68 Å. We note that if we use the Garn & Best (2010) dust correction, these two galaxies would have a factor 2-3 higher f_{esc}.

7.6 Correlations between Lyα escape and galaxy properties

We use our sample of dual Lyα-Hα emitters and upper limits for the other 468 star-forming HAEs to search for potential correlations between galaxy properties and the Lyα escape fraction, shown in Fig. 7.8 and Fig. 7.9. Our sample is compared with the Hα selected sample of Oteo et al. (2015) and the spectroscopically, Lyα-selected sample of Song et al. (2014). The main difference with our sample is that it has deeper Lyα observations than Oteo et al. (2015) and spans a wider range of galaxy properties. The major difference in respect to Song et al. (2014) is that their sample is selected on strong Lyα, and therefore biased towards sources with high f_{esc}.

In addition to studying correlations for individual sources, we also stack different subsets of galaxies. As described in §7.4, we will limit ourselves to the Hα emitters with the deepest NB392 observations. We divide our sample by SFR(Hα), stellar mass, dust extinction and UV slope and ensure that our results do not depend on our particular choice of bin limits and width by perturbing both significantly. The benefit from studying correlations in bins of galaxies

is that the results are less dependent on the systemic uncertainties in the dust corrections. While the systematic difference in dust corrections can be up to a factor of five for individual sources, the differences are much smaller over a statistical sample (compare for example Table 9.1 and 7.2).

7.6.1   Varying SFR(Hα) and Mass

In the top row of Fig. 7.8 we show that f_{esc} is anti-correlated with SFR. This is seen both in the individual sources and in stacks. As both f_{esc} and SFR involve the Hα measurement, we naively expected to find an anti-correlation between the two. Yet, the quantitative behaviour of this trend is not a priori trivial due to complex Lyα radiative transport. The qualitative trend is not strongly sensitive to the dust correction method applied. By fitting a linear relation to our stacked values (in logarithmic space), we obtain:

$$\log_{10}(f_{esc}/(\%)) = 1.34^{+0.12}_{-0.12} - 1.32^{+0.10}_{-0.10} \log_{10}(SFR/(M_\odot yr^{-1})) \qquad (7.5)$$

for a 12 kpc aperture radius, with $\chi^2_{red} = 1.96$. At a radius of 24 kpc, the normalisation is $2.43^{+0.15}_{-0.15}$ and slope $-1.65^{+0.08}_{-0.09}$, with a $\chi^2_{red} = 1.27$. This means that there is a $\sim 13\sigma$ anti-correlation between the escape fraction and the SFR (as a slope of zero is rejected at 13σ). According to this relation, a galaxy with a SFR of 4 $M_\odot$ yr^{-1} has a typical Lyα escape fraction of $\sim 3.5 \pm 1.8\%$ (in 12 kpc apertures). We note that this relation probably turns over at lower SFR than we probe (as f_{esc} would otherwise reach values > 100 %). The top-right panel of Fig. 7.8 also shows that the Lyα escape fraction is higher at larger radii at all SFRs, although the errors become a bit larger.

It can be seen that our directly detected sample occupies the region in parameter space which has highest escape fraction at fixed SFR. Compared to the Lyα selected sample from Song et al. (2014), we find a stronger anti-correlation between f_{esc} and SFR at a lower normalisation. This is because Lyα selected sources are biased towards high values of f_{esc}.

The bottom row of panels in Fig. 7.8 shows how f_{esc} is related to stellar mass. While the stacked values show a weak anti-correlation (although at very low significance), there is no evidence for a trend between f_{esc} and stellar mass for the individually detected sources even though our sample clearly extends the probed dynamic range up to higher masses. As massive galaxies would naively be expected to have a lower f_{esc}, since they tend to have a higher SFR and are dustier (e.g. Ibar et al., 2013), this means that the Lyα escape fraction is not only determined by the scale of a galaxy and it is likely that more subtle processes such as dust and gas dynamics play an important role. Interestingly, the individual detected sources with high stellar mass are at much higher f_{esc} than the stacked values, indicating that there is significant scatter in f_{esc} in this mass range.
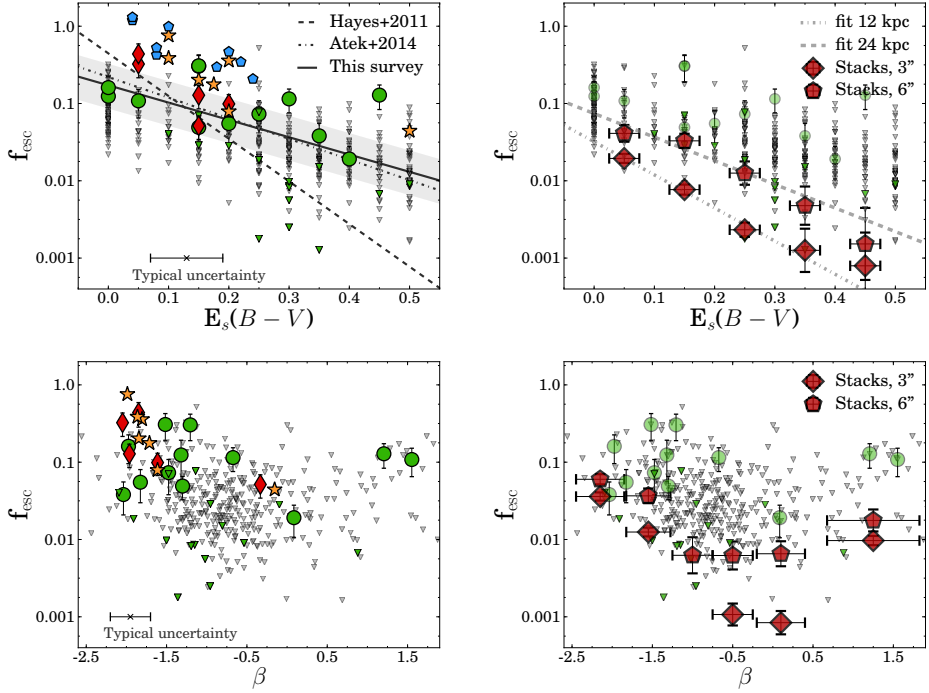
Figure 7.9: Correlations between f_{esc} and dust extinction, rest-frame $B - V$ colour and β, with symbols as defined in Fig. 7.8. We indicate the maximum typical uncertainties on extinction and β in the *left* panels. *Top row*: The *left* panel shows that f_{esc} is anti-correlated with the dust extinction, although there is significant scatter. This means that at fixed aperture, Lyα preferentially escapes galaxies with low dust content. For comparison, we show the relation at $z \sim 2 - 3$ from Hayes et al. (2011) and $z \sim 0.3$ from Atek et al. (2014). Our best fitted relation (to detections and upper limits, see text) resembles more that of local galaxies. The grey band shows the 1σ error of the normalisation of the fit. *Right:* Stacked values of escape fraction versus dust extinction. A similar trend is seen as for individual sources. However, because stacks are not biased towards high f_{esc} values, the normalisation is lower. *Bottom row:* Escape fraction versus β for individual sources (*left*), which confirms that there is a bimodal relation between f_{esc} and galaxy UV colour, such that either very blue or very red galaxies emit significant Lyα. As seen in stacks in the *right* panel, this bimodal trend is most clear at the largest apertures.

7.6.2   Dust extinction and UV slope

In the top row of Fig. 7.9 we show how f_{esc} is related to dust extinction. For individual sources and for stacks, we find that there is an anti-correlation between f_{esc} and dust extinction, although this relation contains significant scatter, caused in part by errors in our measurement of f_{esc} and $E(B - V)$. With our data, we are able to extend the previous found relation from Hayes et al. (2011) to lower escape fractions and higher dust extinctions. We fit the following linear relation:

$$f_{esc} = C \times 10^{-0.4E(B-V)k_{Ly\alpha}} \tag{7.6}$$

This fit is performed by simulating a large grid of normalisations and slopes and computing the χ^2 for each combination of normalisation and slope in $\log(f_{esc}) - E(B - V)$ space. Upper limits are taken into account by assigning them an f_{esc} of 0.01 % and using their upper limit as error. Since a fit to individual galaxies is mostly determined by the directly detected dual Hα-Lyα emitters, which are biased towards high f_{esc}, we also fit to the stacked values.

By minimising the χ^2 for individual galaxies, we find $C = 0.17^{+0.15}_{-0.09}$ and $k_{Ly\alpha} = 5.60^{+3.45}_{-2.90}$, such that a galaxy with $E(B - V) = 0$ has an escape fraction of 17%. This is lower in normalisation (although the errors are significant), and significantly shallower in slope than the fit from Hayes et al. (2011), who finds C is 0.445 and $k_{Ly\alpha} = 13.8$. The normalisation and slope are more similar to the $z = 0.3$ result from Atek et al. (2014) ($C = 0.22$, $k_{Ly\alpha} = 6.67$). A possible explanation could be that Hayes et al. (2011) misses dusty galaxies, such that they infer a steeper slope, which would be consistent with the discussion in Oteo et al. (2015). We discuss this further in §7.8.2.

For stacks, we find $C = 0.03^{+0.01}_{-0.01}$ and $k_{Ly\alpha} = 10.71^{+0.89}_{-1.01}$ for 12 kpc apertures and $C = 0.08^{+0.02}_{-0.01}$ and $k_{Ly\alpha} = 7.64^{+1.38}_{-1.36}$ for 24 kpc apertures. Our fit to stacked data is less biased towards high values of f_{esc} and therefore at a lower normalisation. The slope is slightly higher, although still not as high as the slope inferred by Hayes et al. (2011). Similar as seen for the stacks in bins of stellar mass, the individually detected galaxies at highest dust attenuations have much higher f_{esc} than the median stack. This means that there is a lot of scatter in the values of f_{esc} at the highest dust attenuations.

We furthermore note that part of the correlation between f_{esc} and $E(B - V)$ is expected because there is a dust correction in the Hα flux, and thus in f_{esc}. The fact that the correlation is rather weak (the slope is inconsistent with being zero at only 1.9σ and as there is significant scatter), indicates that dust is not the only regulator of Lyα escape, a result already found by Atek et al. (2008) at low redshift. We also note that the trend between f_{esc} and $E(B - V)$ becomes somewhat bimodal when using the Garn & Best (2010) dust correction, meaning that there are galaxies with high dust attenuation and high f_{esc}, which is virtually impossible with a Calzetti et al. (2000) dust correction. Galaxies with low $E(B - V)$ can in this case also have a lower f_{esc}, leading to a flattening of the relation.

The bottom row of panels in Fig. 7.9 shows how f_{esc} is related with the UV slope β. As the UV slope is also a tracer of dust attenuation, we also find
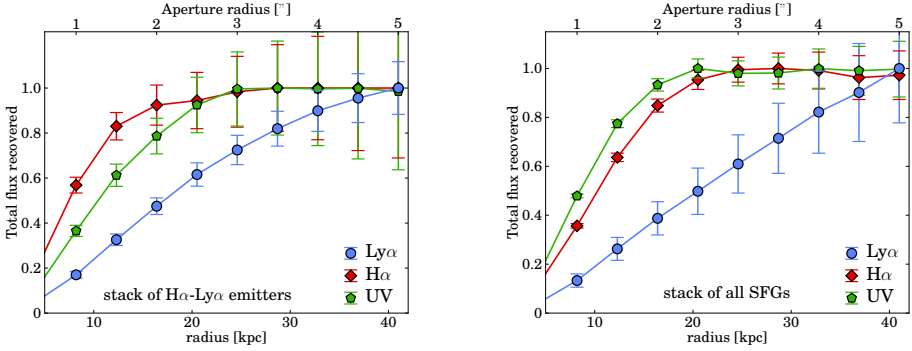
Figure 7.10: Fraction of the total retrieved flux (defined as the maximum flux within 5″ radius) as a function of aperture for the UV, Hα and Lyα and stack of direct detected Hα-Lyα emitters (*left*) and stack of all star-forming galaxies (*right*). It can be seen that while Hα and the UV (from PSF convolved HST F814W imaging) quickly reaches the total flux in both cases, the Lyα flux continues to increase. For the direct detected sources, the Lyα flux increases somewhat more rapidly because sources where selected on bright central Lyα. These sources also have more compact Hα than UV emission. For the stack of all SFGs, Lyα continues to increase (although the errors are significant), such that deeper observations are required to test whether we have captured the full extent of Lyα.

a tentative anti-correlation with escape fraction for galaxies with $\beta < 0$, but for stacks and individual sources, particularly when the HAEs from Oteo et al. (2015) are included. Surprisingly, the trend between f_{esc} and β seems to reverse for redder galaxies, leading to a bimodal relation which is particularly seen in measurements of f_{esc} with 3″ apertures. The (maximum) typical error of β is indicated in the bottom left panel of Fig. 7.9 and is sufficiently small to exclude measurement errors of β as the source of the observed bimodal behaviour. The bimodal behaviour is also seen when correcting for dust using the Garn & Best (2010) prescription.

7.7 Extended emission

As Lyα is a resonant emission line, scattering due to neutral hydrogen leads to a diffusion process similar to a random walk, which results in a lower surface brightness. Therefore, it is likely that in the presence of extended HI, Lyα emission will be more extended than the UV. Although our relatively large PSF FWHM and limited depth in NB392 ($\sim 1.8″$ and ~ 24 AB magnitude, respectively) limit the study of extended Lyα emission at low surface brightness, we can test how our measured escape fraction depends on the chosen aperture size. We do this by analysing the stacked images for the (biased) sample of 12 dual Hα-Lyα emitting SFGs, and for the stack of the 265 SFGs (see §7.5 and Table 9.1). We measure both Hα, Lyα and the rest-frame UV in apertures ranging from $2 - 10″$ in diameter.

As seen in Fig. 7.10 (and illustrated by Fig. 7.11), Lyα is significantly more extended than the UV (traced by convolved *HST* F814W imaging) and Hα for both stacks. The stack of all SFGs (right panel of Fig. 7.11) has extended Lyα

emission up to ~ 20 kpc distance from the center, at 3σ. At this significance, the stack of the 12 dual Hα-Lyα emitters (left panel of Fig. 7.11) is extended up to 30 kpc, and is clearly more extended than the aperture that we used for the sources individually.
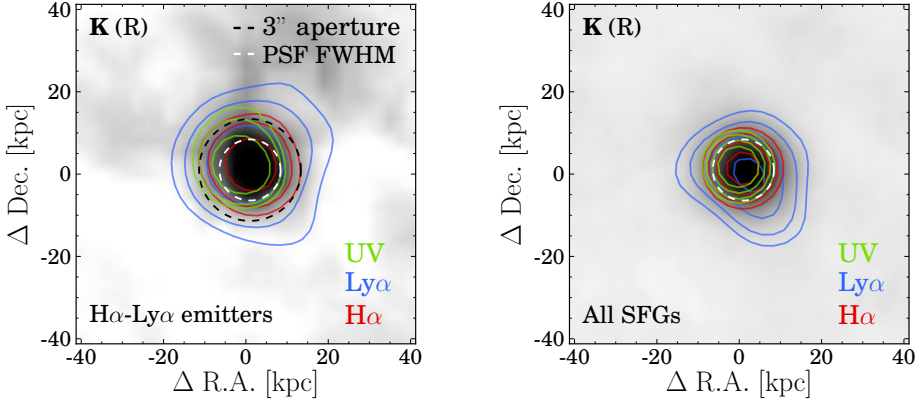

Figure 7.11: Thumbnails of the stacks of the 12 Hα-Lyα emitters (left) and full sample of SFGs (right). The background images shows the K band (where we removed the contribution from Hα using NB$_K$), which corresponds to rest-frame R. The Lyα emission is shown in blue contours, Hα emission is shown in red and UV (from observed F814W, corresponding to ~ 2000Å rest-frame) in green. In the left panel we also indicate the $3''$ diameter aperture used for measurements of individual sources in black dashed lines. The PSF FWHM is indicated with a white dashed circle in both panels. The contour levels are normalised to the peak flux in each band. The outer Lyα contour represents 7.5σ for the *left* panel, and 3σ for the *right* panel. This corresponds to 0.37 and 0.52 of the peak flux, respectively. The 1σ surface brightness limit in the two panels is 9.0 and 2.5×10^{-19} erg s^{-1} cm^{-2} arcsec^{-2}. Other contours correspond to a fraction of 0.5 and 0.75 of the peak flux in the *left* panel, and 0.6, 0.75 and 0.9 in the *right* panel. In both panels, it can be seen that Hα traces the UV light very well. Lyα is more extended than Hα and the UV for both the (biased) stack of direct detect Hα-Lyα and the full stack of SFGs, indicative of scattering. Lyα extends up to ~ 20 kpc distance from the center at the corresponding significances. The stack of the 12 Hα-Lyα emitters is extended up to 30 kpc at 3σ significance.

The growth curves for Hα and the UV are similar, quickly growing to the maximum at ~ 20 kpc. Lyα however continues to increase. The Lyα flux for the stack of the sample of 12 Hα-Lyα emitters peaks at $\sim 4''$ radial apertures, as further increase in the fraction of recovered flux with increasing aperture is within the errors. The f$_{esc}$ within this radius, ~ 30 kpc, is $14.2 \pm 1.9\%$. At a radius of $1.5''$ (similar to the aperture used for individual sources), we measure a stacked f$_{esc}$ of $7.7 \pm 0.9\%$. At this aperture, only $\sim 50\%$ of the maximum observed Lyα flux is retrieved. The Lyα flux for the stack of all SFGs also continues to increase up to at least 30 kpc. By fitting a linear relation between the fraction of the total recovered flux and radius, we find that r$_{90}$ (the radius at which 90 % of the flux is retrieved) for our stack of directly detected Hα-Lyα is 31.3 ± 1.5 kpc. For the stack of all SFGs, r$_{90} = 36.0 \pm 3.8$ kpc. For Hα, we find values of r$_{90} = 19.3 \pm 1.6$ kpc and r$_{90} = 21.0 \pm 0.5$ kpc, respectively.

We show the surface brightness (SB) profile of the full stack of SFGs in the top panel of Fig. 7.12, where we scaled Hα such that it has a similar SB as Lyα at

$5''$ radius, corresponding to an escape fraction of 2% (see also the right panel). The Hα profile follows an exponential (as the y-axis is logarithmic), decreasing with increasing radius. While the Lyα profile seems to be more complex, we note that the errors due to the different PSF shapes of broadband and NB are important, particularly in the centre part. Towards higher radii (> 30 kpc), the Lyα signal from the stack is significantly above the errors due to differences in the PSF, and is thus real. We find no evidence that the integrated Lyα flux does not continue to grow up to 40 kpc distance, indicating that it can be extended up to larger radii if deeper surface brightness limits are reached. This also means that we can not yet directly infer the total f_{esc}.

Comparing the Hα and Lyα profiles results in an increasing Lyα escape fraction with increasing aperture (see the bottom panel of Fig. 7.12). The f_{esc} increases from 0.3 ± 0.05% at 12 kpc distance to 1.6 ± 0.5% at ~ 30 kpc. Note that without dust correction f_{esc} is roughly a factor 2 higher. At the radius of 30 kpc, the Lyα surface brightness is $\sim 6 \times 10^{-19}$ erg s^{-1} cm^{-2} arcsec^{-2} (see also the left panel), such that the extended emission is detected at $\sim 2.4\sigma$ (at 2σ confidence level, extended emission is seen up to ~ 40 kpc). As seen in the right panel of Fig. 7.10 and illustrated in the right panel of Fig. 7.11, Lyα is extended up to ~ 20 kpc at 3σ confidence level. At 2σ significance, it is extended up to ~ 30 kpc. This means that aperture based measurements (including slit spectroscopy) might miss parts of Lyα emission, and that IFU's or specially designed NB filters are more suited.

7.8 Discussion

7.8.1 A consensus on the value of f_{esc}

To date, a number of papers have been published on measuring the Lyα escape fraction with different selections of galaxies and methods. Typically, Lyα selected galaxies at $z > 2$ have resulted in high escape fractions of ~ 30% (e.g. Blanc et al., 2011; Nakajima et al., 2012; Wardlow et al., 2014; Kusakabe et al., 2015; Trainor et al., 2015), even though techniques to estimate the intrinsic Lyα production range from UV to dual NB to FIR and spectroscopy. However, a Lyα selected sample of galaxies is not representative for the full (star-forming) galaxy population and estimates of f_{esc} are biased towards high values (as for example seen in Fig. 7.8).

With UV or rest-frame optical emission line selected galaxies, the typical f_{esc} at $z = 2 - 3$ is around $f_{esc} \sim 3$-5%, (e.g. Hayes et al., 2010; Kornei et al., 2010; Ciardullo et al., 2014), but f_{esc} is found to increase with increasing redshift, up to ~ 30% at $z = 5.7$ (e.g. Hayes et al., 2011). Our measured median value of 1.6 ± 0.5% of HAEs is lower than the value in these papers in the literature. However, we note that our measurement is the first which is independent of assumptions on the shape of the luminosity function and integration limits. Furthermore, as we will show now, the results are fully consistent with literature results when we account for different selections of galaxies and the different parameter spaces probed by different surveys.
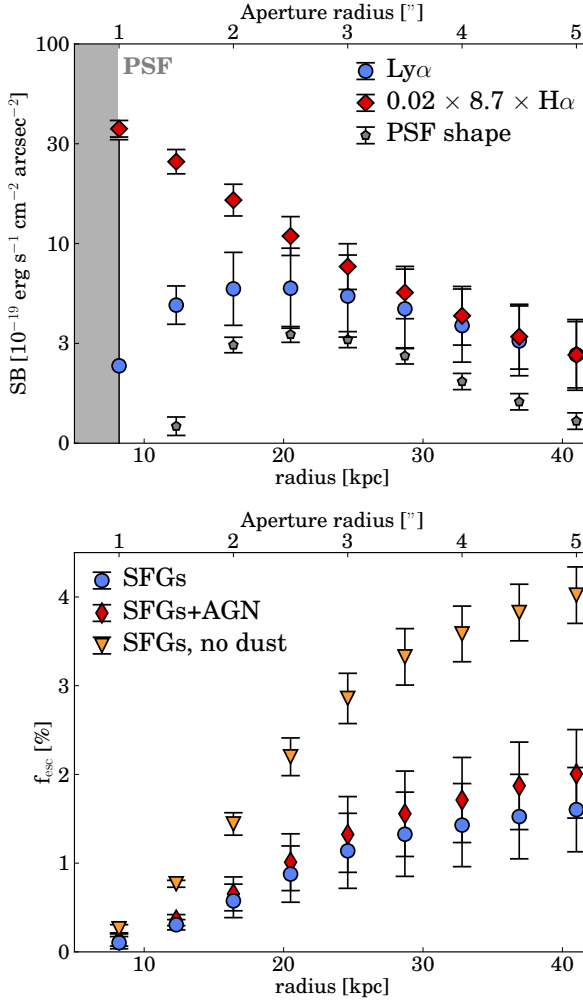
Figure 7.12: *Top*: Surface brightness of our full stack of star-forming galaxies for Hα and Lyα and we also show the surface brightness for the stack of the PSF control sample (§7.4.1), for which the stack of SFGs is corrected. The surface brightness that we observe is attributed to different shapes of the PSF of the NB and broadband. This surface brightness difference is added to the error of the Lyα surface brightness. We scaled the Hα flux such that it has the same surface brightness as Lyα at a radius of 5″, corresponding to 41 kpc. Note that this scaling corresponds to an escape fraction of 2 %, discussed in §7.7.1. *Bottom*: Escape fraction of the stack of all sources as a function of radial distance from the center. We compare stacking sources with and without removal of AGN, and we also show the escape fraction if we do not correct Hα for dust. The escape fraction at large radii is slightly higher without the removal of AGN, because the AGN are typically bright in Lyα and the haloes around them have a larger scale.

Most samples have either been UV selected or selected with emission lines bluer than Hα (e.g. [OIII]; Ciardullo et al. 2014), such that they might miss a population of dusty galaxies. This might cause a bias towards high f_{esc} values, as we show here that dustier galaxies typically have a lower f_{esc} (see Fig. 7.9, but note that we also observe significant f_{esc} for some dusty galaxies). On the contrary, Cassata et al. (2015) report a low fraction of UV selected galaxies with Lyα emission at $2 < z < 6$, corresponding to $f_{esc} < 1\%$, concluding that the bulk of the Lyα luminosity density is coming from fainter galaxies than the typically UV bright galaxies that were targeted. This is consistent with our results, as these galaxies have a typical SFR of $\sim 50 - 100$ M$_\odot$ yr^{-1} (Tasca et al., 2015), and we show that the typical escape fraction at these SFRs is very low ($< 0.5\%$).

The major difference between our survey and the matched Hα-Lyα survey at $z = 2.2$ from Hayes et al. (2010) is that our HAEs probe a larger range in SFRs and stellar masses, because our observations probe a much larger volume (~ 80 times larger, yet with shallower depth). We have shown in the top row of panel of Fig. 7.8 that the SFR anti-correlates with the escape fraction. If we compute SFRs from the Hα emitters from Hayes et al. (2010) as described in §7.3.5, we find that their SFRs are between 0.4-4.4 M$_\odot$ yr^{-1}, illustrated as the grey region in the top-right panel of Fig. 7.8. The difference between the inferred escape fraction of 5.3±3.8% by Hayes et al. (2010) and our stack of SFGs can be fully explained by the different parts of parameter space covered, and the anti-correlation between f_{esc} and SFR. This also means that the bulk of Lyα luminosity density at $z = 2.23$ is not emitted by star-forming galaxies of > 3 M$_\odot$ yr^{-1} (roughly the lower limit of the Hα survey), but by much fainter galaxies. We note that Konno et al. (2015) infer a global f_{esc} of $\sim 1.5\%$ based on more recent measurements of UV and Lyα luminosity functions.

7.8.2 Dependence on galaxy properties

In §7.6 we have shown that f_{esc} generally increases with decreasing SFR and dust attenuation (albeit with significant scatter), and that it shows bimodal behaviour with UV slope. The trends between f_{esc} and SFR and dust attenuation are also seen in the local Universe (Hayes et al., 2014). In this subsection we discuss how our inferred trends compare to previous results and speculate on the origin of bimodal relations.

Relation with dust attenuation

Other surveys have also established a correlation between f_{esc} and dust attenuation, both in the local Universe (Atek et al., 2008, 2014) and at high redshift (Verhamme et al., 2008; Kornei et al., 2010; Hayes et al., 2010; Blanc et al., 2011; Cassata et al., 2015). This trend is in line with the significantly lower observed f_{esc} in the low redshift Universe (e.g. $\sim 1\%$ at $z = 0.3 - 1$ Deharveng et al., 2008; Cowie et al., 2010; Wold et al., 2014), as the dust content of galaxies increases with cosmic time (c.f. Hayes et al., 2011).

We find a weak trend between f_{esc} and dust attenuation, both for stacks and individual galaxies. As shown in the top row of panels of Fig. 7.9, our trends

between f_{esc} and $E(B − V)$ are significantly shallower than the trend inferred by Hayes et al. (2011), and resembles the trend seen in the local Universe (Atek et al., 2014). However, note that comparison is limited by systematic uncertainties and differences between the methods used to estimate f_{esc} (for example, Atek et al. 2014 uses Balmer decrements to estimate the dust uncertainty, while our survey is dependent on SED fitting). While Hayes et al. (2010) only included Hα and Lyα selected galaxies in their analysis, Hayes et al. (2011) added the UV selected galaxies at $z \sim 3$ from Kornei et al. (2010) in order to have a larger sample. However, the UV selected sample requires additional uncertainties on the intrinsic production of Lyα and is biased towards lower dust attenuations (even though their mass and SFR distribution is similar to our Hα selected sample).

We speculate that the prime origin of the discrepancy between our fitted trend and the trends from Hayes et al. (2010) and Hayes et al. (2011) is the combination that we probe more luminous galaxies with higher masses and SFRs (compared to their Hα selected sub-sample) and more dusty galaxies (compared to their UV selected sub-sample), and therefore find a lower normalisation. As our parameter space also includes more dusty galaxies with significant f_{esc}, the relation is flattened. We also note that we find that at a fixed dust attenuation, galaxies with a relatively higher escape fraction have a higher SFR, and are thus also more likely to not be present in the Hayes et al. (2011) sample (as galaxies with higher SFR are rarer), and leading to a flattening of the relation. At the highest dust attenuations, we observe individual galaxies with f_{esc} over two orders of magnitude higher than the typical value for galaxies with similar dust attenuation, indicating that there is a lot of dispersion in the values of f_{esc}.

It is interesting to note that we find that the $E(B − V)$ values of HAEs are not dependent on Lyα EW. The relation we would infer between f_{esc} and $E(B − V)$ for HAEs with Lyα $EW_0 > 25$Å would be flatter than the relation inferred for our full sample of HAEs. This is because dusty HAEs with high f_{esc} tend to have high Lyα EW_0, which may be a sign of outflows. Note however that we do not include Lyα selected sources with faint Hα (and thus high f_{esc}) in this analysis.

There still exist large systematic uncertainties on the method to correct for dust attenuation at high redshift. For example, if the nebular extinction is indeed stronger than the stellar extinction at high SFRs (e.g. Reddy et al., 2015), this may influence our observed trends in Figures 7.8 and 7.9. We use the Garn & Best (2010) prescription for dust attenuation to evaluate how such a differential dust correction affects our results, as this prescription is based on stellar mass and thus qualitatively similar to a dust attenuation which varies with SFR. On a source-by-source basis, the f_{esc} can vary significantly (see for example the difference in attenuations in Table 7.2), however, the results for most stacks are very similar. The largest changes are seen for the stacks with either the highest or lowest SFRs, stellar masses and $E(B − V)$ values. We find that the relation between f_{esc} and $E(B − V)_{star}$ flattens somewhat, which is driven by a higher attenuation (and thus lower f_{esc}) for sources in the bin with lowest $E(B − V)$ values. The relations between f_{esc} and SFR and stellar mass would be steeper. Regardless of the method used to correct for dust, the trend we find between f_{esc} and $E(B − V)$ is relatively weak and there is a large dispersion in the val-

ues of f_{esc}. This indicates that dust attenuation alone is not the most important regulator of f_{esc}.

Absence of relations and bimodality?

Additional evidence that dust is not the most important (or at least not the only) regulator of f_{esc} is that there exists a significant population of red, dusty Lyα emitters (e.g. Blanc et al. 2011; Guaita et al. 2011; Nilsson et al. 2011; Oteo et al. 2015; Taniguchi et al. 2015 and this survey), particularly in the presence of strong outflows (e.g. Atek et al., 2008; Martin et al., 2015). We find tentative evidence that there are bimodal trends between f_{esc} and UV slope. This is supported by the observation that the two reddest galaxies in the sample (IDs 1057 and 1993) have a high f_{esc}. These sources are surprisingly different: while 1993 has low mass and high dust content, 1057 is massive with little dust. These two sources are not atypical, in fact, almost all Lyα detected HAEs are either bluer or redder than the average HAE without Lyα detection (which have $\beta \sim -1$). Apart from having high Lyα EW, we find no galaxy property which is related to having a red UV slope and high escape fraction. We note that this bimodal trend can only be seen for samples which include red, relatively massive objects. The trend is therefore still consistent with the results from Hagen et al. (2016), who find no statistical difference in the UV slopes of Lyα or [OIII] selected galaxies.

Fig. 7.8 shows that there is only a weak trend between f_{esc} and mass for stacks, such that high mass galaxies have lower f_{esc}. However, there are relatively massive galaxies which are detected with high f_{esc}. This means that there is a lot of dispersion in the values of f_{esc} at high stellar masses. This is also seen in the galaxies with highest dust attenuation. It is interesting to note that the mass scale at which we find higher f_{esc} for individual sources coincides with the point where our Hα selection starts picking out galaxies below the main relation between stellar mass and SFR, see also Fig. 7.6. Because of this, and with observations of local galaxies with strong outflows and Lyα emission in mind, we speculate that this enhanced f_{esc} might be related due to outflows of (dusty) gas. Outflows in turn redshift Lyα out of resonance wavelengths, which facilitate the escape of Lyα photons, as for example observed in local galaxies (e.g. Bik et al., 2015; Duval et al., 2016; Herenz et al., 2016; Rivera-Thorsen et al., 2015). This idea can be tested with spectroscopic follow-up.

7.8.3 Extended Lyα emission

There is increasing evidence that star-forming galaxies are surrounded by a low surface brightness Lyα halo, as indicated from stacks of UV selected galaxies (Steidel et al., 2011) and Lyα emitters (Matsuda et al., 2012; Feldmeier et al., 2013; Momose et al., 2014). Lyα haloes have also been detected around faint individual Lyα selected galaxies, both locally and at high redshift (Hayes et al., 2013; Wisotzki et al., 2016; Patrício et al., 2016; Caminha et al., 2016). Moreover, luminous Lyα emitters, without clear signs of AGN activity, can also be extended up to at least ~ 16 kpc (e.g. Hayashino et al., 2004; Ouchi et al., 2013; Sobral et al., 2015b).

As Lyα emission is observed to be more extended than the UV, it is usually attributed to resonant scattering (e.g. Zheng et al., 2010; Dijkstra & Kramer, 2012; Hayes et al., 2013), although simulations from Lake et al. (2015) indicate that collisional ionisation due to cooling flows might also contribute. Very extended Lyα emission on scales of ~ 100 kpc has been observed in Lyα blobs (e.g. Matsuda et al., 2004) and Lyα haloes around radio galaxies (e.g. Rottgering et al., 1995; Venemans et al., 2007; Swinbank et al., 2015), believed to be powered by either star formation or AGN activity (e.g. Geach et al., 2009; Overzier et al., 2013; Ao et al., 2015; Umehata et al., 2015).

We find that the average Hα selected, star-forming galaxy at $z = 2.23$ shows Lyα emission which is more extended than their Hα or the UV emission (see Fig. 7.10, Fig. 7.11 and Fig. 7.12). These galaxies are typically dustier than the sources from Steidel et al. (2011) (with our sample of HAEs having a median $A_{Ly\alpha} = 3.0$, compared to $A_{Ly\alpha} = 1.12$ from Steidel et al. 2011). The surface brightness of the stack of all sources is therefore fainter (roughly a factor two, at a radial distance of 20 kpc) than the stack by Steidel et al. (2011), but we note that the stack of galaxies with $E(B - V) \sim 0.1$ ($A_{Ly\alpha} = 1.2$) has similar Lyα surface brightness values as the stack from Steidel et al. (2011). We also note that our stack of SFGs is fainter in the UV by 0.5 magnitude, but has a dust corrected SFR of ~ 42 $M_{\odot}yr^{-1}$, compared to the typical SFR of ~ 34 $M_{\odot}yr^{-1}$ of the sample from Steidel et al. (2011), because of the higher dust attenuation of our sample.

With the current depth, we can not measure the maximum extent of Lyα for the stack of all SFGs or the stack of directly detected Hα-Lyα emitters (see Fig. 7.10). By comparing the ratio of r_{90} of Lyα and Hα for both stacks, we find that Lyα radii are larger than Hα radii with a factor of $1.6 - 1.7$. These values are comparable to those found for local Lyα analogs from Hayes et al. (2013), although that analysis used r_{20}, which is undesirable for our sample due to the limitations from the PSF. For these local analogs, the average ratio between the Lyα and Hα radii is however slightly higher than the ratio for our stack of SFGs, which may indicate that we have not yet observed the full extent of Lyα.

For the stack of directly detected Hα-Lyα emitters, we observed an escape fraction of $f_{esc} = 14.2 \pm 1.9\%$ at a radius of 30 kpc, twice the f_{esc} as the typical aperture used for photometry of Lyα selected galaxies. Assuming the Calzetti et al. (2000) dust law, we can estimate that attenuation of Lyα photons due to dust is a factor 9 ± 3 ($A_{Ly\alpha} = 2.4 \pm 0.3$). Hence, this predicts that f_{esc} before dust attenuation is $100/(9 \pm 3)$ %. This indicates that dust attenuation is sufficient to explain that f_{esc} is $\sim 15\%$. This may well be the case for the majority of Lyα selected galaxies. However, we note that the sample of directly detected Hα-Lyα emitters is obviously biased towards centrally peaked, high central f_{esc} Lyα emission, as otherwise they would not have been directly detected in Lyα. It is therefore likely that the typical SFG has a larger Lyα halo with a less peaked central surface brightness. The total inferred f_{esc} is roughly a factor two higher than f_{esc} measured with $3''$ diameter apertures. This means that, if we naively assume that this factor two is constant for all 12 SFGs used in the stack, the total escape fractions of our directly detected SFGs (see Table 7.2) range from $4 - 60\%$.

7.9 Conclusions

We have undertaken a panoramic matched Hα-Lyα NB survey to study the Lyα emission from a sample of 488 Hα selected star-forming galaxies at $z = 2.23$ and its dependence on radial scale and galaxy properties. Our conclusions are:

1. Out of the 488 observed Hα emitters, we detect 43 sources in the NB392 imaging. 17 of these have strong Lyα emission (of which 5 are X-ray AGN), and we measure the UV continuum for the other 26. We put limits on the escape fractions for these 26 and the other 445 undetected HAEs.

2. The observed Lyα escape fraction for individual detected sources ranges from $2 - 30\%$, and we find that these HAEs probe a wide range of star-forming systems: with masses from 3×10^8 M$_\odot$ to 10^{11} M$_\odot$ and dust attenuations E$(B - V) = 0 - 0.5$. We particularly note that some massive, dusty galaxies are clearly visible in Lyα, while they have no evidence for AGN activity from X-ray observations.

3. With matched NB observations in the J and H band from Sobral et al. (2013), we are also able to detect [O$\textsc{ii}$] and [O$\textsc{iii}$] emission-lines for 23 and 70 galaxies respectively. Two faint Lyα emitting galaxies are detected in [O$\textsc{iii}$]. Remarkably, these have relatively high escape fraction and have the lowest stellar mass and highest Lyα EW from our sample.

4. While Lyα morphologies of individual X-ray selected AGN are typically circularly symmetric, tracing the rest-frame UV light, the Lyα morphologies of star-forming galaxies are more irregular. Lyα can appear to be offset from the rest-frame UV and Hα emission, and also more extended, although we detect this only significantly for AGN.

5. Both for the individually detected sources and by stacking, we confirm existing trends between the Lyα escape fraction and SFR and dust attenuation and explore how they are extended to a larger range of parameter space - particularly more massive and dusty galaxies. Lyα escape increases for galaxies with lower SFR and low dust attenuation, albeit with significant scatter. The trend between f_{esc} and dust attenuation resembles that observed in local galaxies. The escape fraction shows bimodal behaviour with UV slope: f_{esc} increases for the bluest and reddest galaxies and is at a minimum UV slopes $\beta \sim -0.5$. At the highest masses and dust attenuations, we detect individual galaxies with f_{esc} much higher than the typical values from stacking, indicating significant scatter in the values of f_{esc} at the highest masses and dust attenuations.

6. We interpret apparently contradictory reported numbers of the escape fraction by various studies using our observed trends with galaxy properties. Deeper surveys over a smaller area infer a higher escape fraction as the SFRs of their galaxies are lower in general. As these studies miss rarer

galaxies with higher SFR and a higher dust attenuation, the inferred correlation between f_{esc} and dust content steepens. Studies based on UV selected galaxies report higher numbers of f_{esc} because the galaxies in their sample are biased towards galaxies with little dust, which tend to have higher f_{esc}, except if their typical SFR is higher.

7. The stack of our directly detected Hα-Lyα emitters reveals that Lyα is more extended than the UV and Hα, with an extent of at least $\sim$ 30 kpc. For Lyα, the radius at which 90 % of the flux is retrieved is $r_{90} = 31.3 \pm 1.5$ kpc, roughly 1.6 times larger than Hα. The median escape fraction for this biased sample increases up to 14.2 ± 1.9% at least. We suggest that the missing Lyα photons can be fully explained by dust absorption. At the typical apertures used for slit spectroscopy (e.g. 1″), only half of the Lyα flux is recovered, even for the sample which is biased towards centrally peaked Lyα emission. This means that slit spectroscopy might miss a significant fraction of Lyα.

8. By stacking our full sample of $z = 2.23$ SFGs, we find that Lyα extends up to at least 3″ (with $r_{90} = 36.0 \pm 3.8$ kpc) in radial distance at 3σ, corresponding to $\sim$ 20 kpc (30 kpc, 2σ), roughly twice the scale of star formation as traced by Hα and by the UV, with a Lyα surface brightness of $\sim 6 \times 10^{-19}$ erg s^{-1} cm^{-2} arcsec^{-2}. As a result, the Lyα escape fraction of our full sample of Hα emitters continues to increase with radius, up to at least 1.6 ± 0.5 % at 30 kpc distance from the centre. With the current depth, it is not yet possible to constrain the maximum extent of Lyα.

Two important questions regarding the escape of Lyα remain. First, what is the total f_{esc} for the typical SFG at $z = 2.23$? Deeper Lyα observations are required to fully answer this by measuring the full extent of Lyα. Second, properties which are not studied in this survey are likely equally or more important (for example the H$\textsc{i}$ covering fraction and geometry, e.g. Scarlata et al. 2009; H$\textsc{i}$ column density, Henry et al. 2015; outflows, Atek et al. 2008; ionisation state, Hayes et al. 2014). From the significant scatter in the relations and from the bimodal behaviour in for example the relation between f_{esc} and dust content and UV slope, it is clear that multiple mechanisms are likely together responsible for determining the Lyα escape fraction and its relation to extended Lyα emission.

It is crucial to improve the measurements of dust attenuation and to obtain precise measurements of redshifts and velocity offsets between Lyα and Hα, as these are responsible for the largest systematic errors which can go up to an order of magnitude when combined in unfortunate ways. However, the major downside is that this requires large, spectroscopic samples over a wide wavelength regime. Additional deeper Lyα NB observations are required in order to eliminate the biases caused by binning and stacking, and to be able to study the relation between galaxy properties and spatial extent of Lyα on a source-by-source basis.

Acknowledgments

CHAPTER 8

The production and escape of Lyman-Continuum radiation from star-forming galaxies at $z \sim 2$ and their redshift evolution

We study the production rate of ionizing photons of a sample of 588 Hα emitters (HAEs) and 160 Lyman-α emitters (LAEs) at $z = 2.2$ in the COSMOS field in order to assess the implied emissivity from galaxies, based on their UV luminosity. By exploring the rest-frame Lyman Continuum (LyC) with *GALEX/NUV* data, we find $f_{esc} < 2.8\,(6.4)\%$ through median (mean) stacking. By combining the Hα luminosity density with IGM emissivity measurements from absorption studies, we find a globally averaged $\langle f_{esc} \rangle$ of $5.9^{+14.5}_{-4.2}$ % at $z = 2.2$ if we assume HAEs are the only source of ionizing photons. We find similarly low values of the global $\langle f_{esc} \rangle$ at $z \approx 3-5$, also ruling out a high $\langle f_{esc} \rangle$ at $z < 5$. These low escape fractions allow us to measure ξ_{ion}, the number of produced ionizing photons per unit UV luminosity, and investigate how this depends on galaxy properties. We find a typical $\xi_{ion} \approx 10^{24.77 \pm 0.04}$ Hz erg^{-1} for HAEs and $\xi_{ion} \approx 10^{25.14 \pm 0.09}$ Hz erg^{-1} for LAEs. LAEs and low mass HAEs at $z = 2.2$ show similar values of ξ_{ion} as typically assumed in the reionization era, while the typical HAE is three times less ionizing. Due to an increasing ξ_{ion} with increasing EW(Hα), ξ_{ion} likely increases with redshift. This evolution alone is fully in line with the observed evolution of ξ_{ion} between $z \approx 2-5$, indicating a typical value of $\xi_{ion} \approx 10^{25.4}$ Hz erg^{-1} in the reionization era.

8.1   Introduction

One of the most important questions in galaxy formation is whether galaxies alone have been able to provide the ionizing photons which reionized the Universe. Optical depth measurements from the Planck satellite place the mean reionization redshift between $z \approx 7.8 - 8.8$ (Planck Collaboration et al., 2016b). The end-point of reionization has been marked by the Gun-Peterson trough in high-redshift quasars at $z \approx 5 - 6$, with a typical neutral fraction of $\sim 10^{-4}$ (e.g. Fan et al., 2006; McGreer et al., 2015). Moreover, recent observations indicate that there are large opacity fluctuations among various sight-lines, indicating an inhomogeneous nature of reionization (Becker et al., 2015).

Assessing whether galaxies have been the main provider of ionizing photons at $z \gtrsim 5$ (alternatively to Active Galactic Nucleii, AGN; e.g. Madau & Haardt 2015; Giallongo et al. 2015; Weigel et al. 2015) crucially depends on i) precise measurements of the number of galaxies at early cosmic times, ii) the clumping factor of the IGM (e.g. Pawlik et al., 2015), iii) the amount of ionizing photons that is produced (Lyman-Continuum photons, LyC, $\lambda < 912$Å) and iv) the fraction of ionizing photons that escapes into the inter galactic medium (IGM). All these numbers are currently uncertain, with the relative uncertainty greatly rising from i) to iv).

Many studies so far have focussed on counting the number of galaxies as a function of their UV luminosity (luminosity functions) at $z > 7$ (e.g. McLure et al., 2013; Bowler et al., 2014; Atek et al., 2015; Bouwens et al., 2015a; Finkelstein et al., 2015; Ishigaki et al., 2015; McLeod et al., 2015b; Castellano et al., 2016; Livermore et al., 2017). These studies typically infer luminosity functions with steep faint-end slopes, and a steepening of the faint-end slope with increasing redshift (see for example the recent review from Finkelstein 2016), leading to a high number of faint galaxies. Assuming "standard" values for the other parameters such as the escape fraction, simplistic models indicate that galaxies may indeed have provided the ionizing photons to reionize the Universe (e.g. Madau et al., 1999; Robertson et al., 2015), and that the ionizing background at $z \sim 5$ is consistent with the derived emissivity from galaxies (Choudhury et al., 2015; Bouwens et al., 2015b). However, without validation of input assumptions regarding the production and escape of ionizing photons (for example, these simplistic models assume that the escape fraction does not depend on UV luminosity), the usability of these models remains to be evaluated.

The most commonly adopted escape fraction of ionizing photons, f_{esc}, is 10-20 %, independent of mass or luminosity (e.g. Mitra et al., 2015; Robertson et al., 2015). However, hydrodynamical simulations indicate that f_{esc} is likely very anisotropic and time dependent (Cen & Kimm, 2015; Ma et al., 2015). An escape fraction which depends on galaxy properties (for example a higher f_{esc} for lower mass galaxies, e.g. Paardekooper et al. 2015) would influence the way reionization happened (e.g. Sharma et al., 2016). Most importantly, it is impossible to measure f_{esc} directly at high-redshift ($z > 6$) because of the high opacity of the IGM for ionizing photons (e.g. Inoue et al., 2014). Furthermore, to estimate f_{esc} it is required that the intrinsic amount of ionizing photons is measured accurately,

which requires accurate understanding of the stellar populations, SFR and dust attenuation (i.e. De Barros et al., 2016).

Nevertheless, several attempts have been made to measure f_{esc}, both in the local Universe (e.g. Leitherer et al., 1995; Deharveng et al., 2001; Leitet et al., 2013; Alexandroff et al., 2015) and at intermediate redshift, $z \sim 3$, where it is possible to observe redshifted LyC radiation with optical CCDs (e.g. Inoue et al., 2006; Boutsia et al., 2011; Vanzella et al., 2012; Bergvall et al., 2013; Mostardi et al., 2015). However, the number of reliable direct detections is limited to a handful, both in the local Universe and at intermediate redshift (e.g. Borthakur et al., 2014; Izotov et al., 2016b,a; De Barros et al., 2016; Leitherer et al., 2016), and strong limits of $f_{esc} \lesssim 5 - 10$ % exist for the majority (e.g. Grazian et al., 2016; Guaita et al., 2016; Rutkowski et al., 2016). An important reason is that contamination from sources in the foreground may mimic escaping LyC, and high resolution UV imaging is thus required (e.g. Mostardi et al., 2015; Siana et al., 2015). Even for sources with established LyC leakage, estimating f_{esc} reliably depends on the ability to accurately estimate the intrinsically produced amount of LyC photons and precisely model the transmission of the IGM (e.g. Vanzella et al., 2016).

The amount of ionizing photons that are produced per unit UV (rest-frame ≈ 1500 Å) luminosity (ξ_{ion}) is generally calculated using SED modelling (e.g. Madau et al., 1999; Bouwens et al., 2012; Kuhlen & Faucher-Giguère, 2012) or (in a related method) estimated from the observed values of the UV slopes of high-redshift galaxies (e.g. Robertson et al., 2013; Duncan & Conselice, 2015). Most of these studies find values around $\xi_{ion} \approx 10^{25.2-25.3}$ Hz erg^{-1} at $z \sim 8$. More recently, Bouwens et al. (2016) estimated the number of ionizing photons in a sample of Lyman break galaxies (LBGs) at $z \sim 4$ to be $\xi_{ion} \approx 10^{25.3}$ Hz erg^{-1} by estimating Hα luminosities with *Spitzer*/IRAC photometry.

Progress in the understanding of f_{esc} and ξ_{ion} can be made by expanding the searched parameter space to lower redshifts, where rest-frame optical emission lines (e.g. Hα) can provide valuable information on the production rate of LyC photons and where it is possible to obtain a complete selection of star-forming galaxies.

In this paper, we use a large sample of Hα emitters (HAEs) and Lyα emitters (LAEs) at $z = 2.2$ to constrain f_{esc} and measure ξ_{ion} and how this may depend on galaxy properties. Our measurements of ξ_{ion} rely on the assumption that f_{esc} is negligible (< 10 %), which we validate by constraining f_{esc} with archival *GALEX NUV* imaging and by comparing the estimated emissivity of HAEs with IGM emissivity measurements from quasar absorption lines (e.g. Becker & Bolton, 2013). Combined with rest-frame UV photometry, accurate measurements of ξ_{ion} are possible on a source by source basis for HAEs, allowing us to explore correlations with galaxy properties. Since only a handful of LAEs are detected in Hα (see Matthee et al. 2016), we measure the median ξ_{ion} from stacks of Lyman-α emitters from Sobral et al. (2017).

We describe the galaxy sample and definitions of galaxy properties in §9.2. §9.3 presents the *GALEX* imaging. We present upper limits on f_{esc} in §9.4. We indirectly estimate f_{esc} from the Hα luminosity function and the IGM emissivity in §9.6 and measure the ionizing properties of galaxies and its redshift evolution
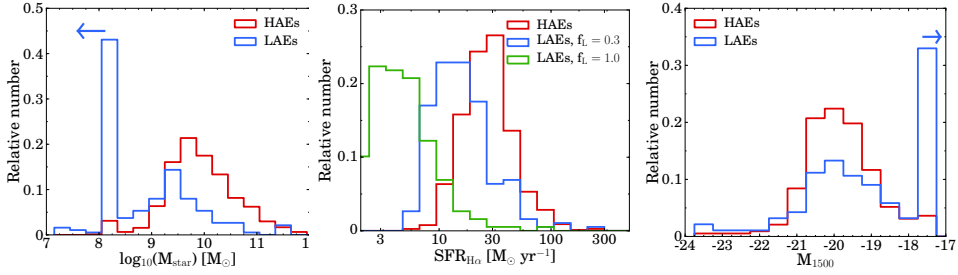
Figure 8.1: Histogram of the properties of HAEs and LAEs. Stellar mass is obtained through SED fitting (see §8.2.1). For HAEs, SFR(Hα) is obtained from dust-corrected Hα. LAEs that are undetected in broad-bands (and thus without SED fits) are assigned $M_{star} = 10^8$ $M_\odot$ and $M_{1500} = -17$, corresponding to a V band magnitude of 27 and we assumed those galaxies have no dust in computing SFR(Hα). For LAEs, we use the observed Lyα luminosity and convert this to Hα for two different Lyα escape fractions (f_L, the typical escape fraction for LAEs (30 %) and the maximum of 100 %, see Sobral et al. 2017). M_{1500} is obtained by converting the observed V magnitude to absolute magnitude. In general, LAEs trace a galaxy population with lower stellar masses and SFR and fainter UV magnitudes.

in §9.5. §9.6.3 discusses the implications for reionization. Finally, our results are summarised in §9.7. We adopt a ΛCDM cosmology with $H_0 = 70$ km s^{-1}Mpc^{-1}, $\Omega_M = 0.3$ and $\Omega_\Lambda = 0.7$. Magnitudes are in the AB system. At $z = 2.2$, $1''$ corresponds to a physical scale of 8.2 kpc.

8.2   Galaxy sample

We use a sample of Hα selected star-forming galaxies from the High-z Emission Line Survey (HiZELS; Geach et al. 2008; Sobral et al. 2009a) at $z = 2.2$ in the COS-MOS field. These galaxies were selected using narrow-band (NB) imaging in the K band with the United Kingdom InfraRed Telescope. Hα emitters (HAEs) were identified among the line-emitters using *BzK* and *BRU* colours and photometric redshifts, as described in Sobral et al. (2013), and thus have a photometric red-shift of $z = 2.22 \pm 0.02$ where the error is due to the width of the narrow-band filter. In total, there are 588 Hα emitters at $z = 2.2$ in COSMOS.[1]

HAEs are selected to have $EW_{0,Hα+[NII]} > 25$ Å. Since the COSMOS field has been covered by multiple narrow-band filters, a fraction of $z = 2.2$ sources are detected with multiple major emission lines in addition to Hα: [OIII], [OII] (e.g. Sobral et al., 2012; Nakajima et al., 2012; Sobral et al., 2013) or Lyα (e.g. Oteo et al., 2015; Matthee et al., 2016). Multi-wavelength photometry from the observed UV to mid-IR is widely available in COSMOS. In this paper, we make explicit use of V and R band in order to measure the UV luminosity and UV slope $β$, but all bands have been used for photometric redshifts (see Sobral et al.

---

[1] The sample of Hα emitters from Sobral et al. (2013) is publicly available through e.g. VizieR, http://vizier.cfa.harvard.edu.

2013, and e.g. Ilbert et al. 2009) and SED fitting (Sobral et al., 2014; Oteo et al., 2015; Khostovan et al., 2016).

We also include 160 Lyman-α emitters (LAEs) at $z = 2.2$ from the CAlibrating LYMan-α with Hα survey (CALYMHA; Matthee et al. 2016; Sobral et al. 2017). For completeness at bright luminosities, LAEs were selected with $EW_{0,Lyff} > 5$ Å, while LAEs are typically selected with a higher EW_0 cut of 25 Å (see e.g. Matthee et al. 2015 and references therein). Only 15 % of our LAEs have $EW_{0,Ly\alpha} < 25$ Å and these are typically AGN, see Sobral et al. (2017), but they represent some of the brightest. We note that 40 % of LAEs are too faint to be detected in broad-bands, and we thus have only upper limits on their stellar mass and UV magnitude (see Fig. 8.1). By design, CALYMHA observes both Lyα and Hα for Hα selected galaxies. As presented in Matthee et al. (2016), 17 HAEs are also detected in Lyα with the current depth of Lyα narrow-band imaging. These are considered as HAEs in the remainder of the paper.

We show the general properties of our sample of galaxies in Fig. 8.1. It can be seen that compared to HAEs, LAEs are typically somewhat fainter in the UV, have a lower mass and lower SFR, although they are also some of the brightest UV objects.

Our sample of HAEs and LAEs was chosen for the following reasons: i) all are at the same redshift slice where the LyC can be observed with the *GALEX NUV* filter and Hα with the NB_K filter, ii) the sample spans a large range in mass, star formation rate (SFR) and environments (Fig. 8.1 and Geach et al. 2012; Sobral et al. 2014) and iii) as discussed in Oteo et al. (2015), Hα selected galaxies span the entire range of star-forming galaxies, from dust-free to relatively dust-rich (unlike e.g. Lyman-break galaxies).

8.2.1 Definition of galaxy properties

We define the galaxy properties that are used in the analysis in this subsection. These properties are either obtained from: (1) SED fitting of the multi-wavelength photometry, (2) observed Hα flux, or (3) observed rest-frame UV photometry.

SED fitting

For HAEs, stellar masses (M_{star}) and stellar dust attenuations ($E(B-V)$) are taken from Sobral et al. (2014). In this study, synthetic galaxy SEDs are simulated with Bruzual & Charlot (2003) stellar templates with metallicities ranging from $Z = 0.0001 - 0.05$, following a Chabrier (2003) initial mass function (IMF) and with exponentially declining star formation histories (with e-folding times ranging from 0.1 to 10 Gyr). The dust attenuation is described by a Calzetti et al. (2000) law. The observed UV to IR photometry is then fitted to these synthetic SEDs. The values of M_{star} and $E(B-V)$ that we use are the median values of all synthetic models which have a χ^2 within 1σ of the best fitted model. The 1σ uncertainties are typically $0.1 - 0.2$ dex for M_{star} and 0.05-0.1 dex for $E(B-V)$.

The smallest errors are found at high masses and high extinctions. The same SED fitting method is applied to the photometry of LAEs.

We note that the SED fitting from Sobral et al. (2014) uses SED models which do not take contribution from nebular emission lines into account. This means that some stellar masses could be over-estimated. However, the SED fits have been performed on over > 20 different filters, such that even if a few filters are contaminated by emission lines, the χ^2 values are not strongly affected. Importantly, the *Spitzer*/IRAC bands (included in SED fitting and most important for measuring stellar mass at $z = 2.2$) are unaffected by strong nebular emission lines at $z = 2.2$.

We still investigate the importance of emission lines further by comparing the SED results with those from Oteo et al. (2015), who performed SED fits for a subsample ($\approx 60\%$) of the HAEs and LAEs, including emission lines. We find that the stellar masses and dust attenuations correlate very well, although stellar masses from Oteo et al. (2015) are on average lower by 0.15 dex. We look at the galaxies with the strongest lines (highest observed EWs) and find that the difference in the stellar mass is actually smaller than for galaxies with low Hα EW. This indicates that the different mass estimates are not due to the inclusion of emission lines, but rather due to the details of the SED fitting implementation, such as the age-grid ages and allowed range of metallicities. We therefore use the stellar masses from Sobral et al. (2014). Our sample spans galaxies with masses $M_{star} \approx 10^{7.5-12}$ M$_\odot$, see Fig. 8.1.

Intrinsic Hα luminosity

The intrinsic Hα luminosity is used to compute instantaneous star formation rates (SFRs) and the number of produced ionizing photons. To measure the intrinsic Hα luminosity, we first correct the observed line-flux in the NB$_K$ filter for the contribution of the adjacent [NII] emission-line doublet. We also correct the observed line-flux for attenuation due to dust.

We correct for the contribution from [NII] using the relation between [NII]/Hα and EW$_{0,H\alpha+[NII]}$ from Sobral et al. (2012). This relation is confirmed to hold up to at least $z \sim 1$ (Sobral et al., 2015a) and the median ratio of [NII]/(Hα+ [NII]) $= 0.19 \pm 0.06$ is consistent with spectroscopic follow-up at $z \approx 2$ (e.g. Swinbank et al., 2012; Sanders et al., 2015), such that we do not expect that metallicity evolution between $z = 1 - 2$ has a strong effect on the applied correction. For 1 out of the 588 HAEs we do not detect the continuum in the K band, such that we use the 1σ detection limit in K to estimate the EW and the contribution from [NII]. We apply the same correction to HAEs that are detected as X-ray AGN (see Matthee et al. 2016 for details on the AGN identification).

If we alternatively use the relation between stellar mass and [NII]/Hα from Erb et al. (2006) at $z \sim 2$, we find [NII]/(Hα+ [NII]) $= 0.10 \pm 0.03$. This different [NII] estimate is likely caused by the lower metallicity of the Erb et al. (2006) sample, which may be a selection effect (UV selected galaxies typically have less dust than Hα selected galaxies, and are thus also expected to be more metal poor, i.e. Oteo et al. 2015). The difference in [NII] contributions estimated either

from the EW or mass is smaller for higher mass HAEs, which have a higher metallicity. Due to the uncertainties in the [Nɪɪ] correction we add 50 % of the correction to the uncertainty in the Hα luminosity in quadrature.

Attenuation due to dust is estimated with a Calzetti et al. (2000) attenuation curve and by assuming that the nebular attenuation equals the stellar attenuation, $E(B-V)_{gas} = E(B-V)_{stars}$. This is in agreement with the average results from the Hα sample from MOSDEF (Shivaei et al., 2015), although we note that there are indications that the nebular attenuation is stronger for galaxies with higher SFRs and masses (e.g. Reddy et al., 2015; Puglisi et al., 2016) and other studies indicate slightly higher nebular attenuations (e.g. Förster Schreiber et al., 2009; Wuyts et al., 2011; Kashino et al., 2013). We note that we vary the method to correct for dust in the relevant sections (e.g. §8.6.3) in two ways: either based on the UV slope (Meurer et al., 1999), or from the local relation between dust attenuation and stellar mass (Garn & Best, 2010).

Star formation rates are obtained from dust-corrected L(Hα) and using a Chabrier (2003) initial mass function: SFR = 4.4×10^{-42} L(Hα) (e.g. Kennicutt, 1998), where the SFR is in $M_\odot$ yr^{-1} and L(Hα) in erg s^{-1}. The SFRs of galaxies in our sample range from $3-300$ $M_\odot$ yr^{-1}, with a typical SFR of ≈ 30 $M_\odot$ yr^{-1}, see Fig. 8.1.

Rest-frame UV photometry and UV slopes

For our galaxy sample at $z = 2.2$, the rest-frame UV (~ 1500Å) is traced by the V band, which is not contaminated by (possibly) strong Lyα emission. Our full sample of galaxies is imaged in the optical V and R filters with Subaru Suprime-Cam as part of the COSMOS survey (Taniguchi et al., 2007). The 5σ depths of V and R are 26.2-26.4 AB magnitude (see e.g. Muzzin et al. 2013) and have a FWHM of $\sim 0.8''$. The typical HAE in our sample has a V band magnitude of ≈ 25 and is thus significantly detected. 5-7 % of the HAEs in our sample are not detected in either the V or R band.

We correct the UV luminosities from the V band for dust with the Calzetti et al. (2000) attenuation curve and the fitted $E(B-V)$ values. The absolute magnitude, M_{1500}, is obtained by subtracting a distance modulus of $\mu = 44.97$ (obtained from the luminosity distance and corrected for bandwidth stretching with $2.5\log_{10}(1+z)$, $z = 2.23$) from the observed V band magnitudes. The UV slope β is measured with observed V and R magnitudes following:

$$\beta = -\frac{V-R}{2.5\log_{10}(\lambda_V/\lambda_R)} - 2 \tag{8.1}$$

Here, $\lambda_V = 5477.83$ Å, the effective wavelength of the V filter and $\lambda_R = 6288.71$ Å, the effective wavelength of the R filter. With this combination of filters, β is measured around a rest-frame wavelength of ~ 1800 Å.
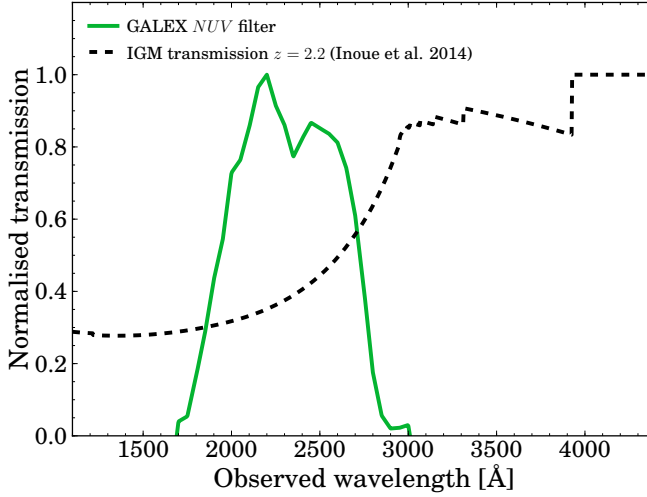
Figure 8.2: Filter transmission of the *GALEX NUV* filter (green line) and mean IGM transmission versus observed wavelength (dashed black line). We compute the IGM transmission at $z = 2.2$ using the models from Inoue et al. (2014). The bandpass-averaged IGM transmission is 40.4 %. As highlighted by a simulation from Vasei et al. 2016, the mean value of T_{IGM} is not the most common value. The distribution is bimodal, with a narrow peak at $T_{IGM} \approx 0.0$ and a broad peak around $T_{IGM} = 0.7$.

8.3   *GALEX* **UV data**

For galaxies observed at $z = 2.2$, rest-frame LyC photons can be observed with the *NUV* filter on the *GALEX* space telescope. In COSMOS there is deep *GALEX* data (3σ AB magnitude limit ~ 25.2, see e.g. Martin et al. 2005; Muzzin et al. 2013) available from the public Deep Imaging Survey. We stress that the full width half maximum (FWHM) of the point spread function (PSF) of the *NUV* imaging is 5.4″(Martin et al., 2003) and that the pixel scale is 1.5″ pix^{-1}. We have acquired *NUV* images in COSMOS from the Mikulski Archive at the Space Telescope Science Institute (MAST)[2]. All HAEs and LAEs in COSMOS are covered by *GALEX* observations, due to the large circular field of view with 1.25 degree diameter. Five pointings in the COSMOS field overlap in the center, which results in a total median exposure time of 91.4 ks and a maximum exposure time of 236.8 ks.

8.3.1   **Removing foreground/neighbouring contamination**

The large PSF-FWHM of *GALEX NUV* imaging leads to a major limitation in measuring escaping LyC photons from galaxies at $z = 2.2$. This is because the observed flux in the *NUV* filter could (partly) be coming from a neighbouring foreground source at lower redshift. In order to overcome this limitation, we

---

[2] https://mast.stsci.edu/

use available high resolution deep optical *HST*/ACS F814W (rest-frame $\approx$ 2500 Å, Koekemoer et al. 2007) imaging to identify sources for which the *NUV* flux might be confused due to possible foreground or neighbouring sources and remove these sources from the sample. In addition, we use visual inspections of deep ground-based *U* band imaging as a cross-check for the bluest sources which may be missed with the *HST* imaging. These data are available through the COSMOS archive.[3]

Neighbours are identified using the photometric catalog from Ilbert et al. (2009), which is selected on deep *HST*/ACS F814W data. We find that 195 out of the 588 HAEs in COSMOS have no neighbour inside a radius of 2.7″. We refer to this subsample as our Clean sample of galaxies in the remainder of the text. The average properties (dust attenuation, UV magnitude mass and SFR) of this sample is similar to the full sample of SFGs.

8.3.2 Transmission redward of 912 Å

For sources at $z = 2.22$, the *NUV* filter has non-negligible transmission from $\lambda_0 = 912 - 933$ Å of $\approx$ 1.5%. This limits the search for escaping LyC radiation. The fraction of the observed flux in the *NUV* filter that originates from $\lambda_0 > 912$ Å depends on the galaxy's SED, the IGM transmission and the filter transmission. In order to estimate this contribution, we first use a set of Starburst99 (Leitherer et al., 1999) SED models to estimate the shape of the galaxy's SED in the far UV. We assume a single burst of star formation with a Salpeter IMF with upper mass limit 100 $M_\odot$, Geneva stellar templates without rotation (Mowlavi et al., 2012) and metallicity $Z = 0.02$. Then, we convolve this SED with the filter and IGM transmission curves, to obtain the fraction of the flux in the *NUV* filter that is non-ionizing at $z = 2.2$ (compared to the flux in the *NUV* filter that is ionizing). By using the SED models with Hα EWs within our measured range, we find that 2.6 ± 0.4 % of the flux observed in the *NUV* filter is not-ionizing. This means that upper limits from non-detections are slightly over-estimated. For individually detected sources it is theoretically possible that the *NUV* detection is completely due to non-ionizing flux, depending on the SED shape and normalisation. This is analysed in detail on a source-by-source basis in Appendix A.

8.4 The escape fraction of ionizing photons

8.4.1 How to measure f$_{esc}$?

Assuming that LyC photons escape through holes in the ISM (and hence that H$_{II}$ regions are ionization bounded from which no ionizing photons escape), the escape fraction, f$_{esc}$, can be measured directly from the ratio of observed to produced LyC luminosity (averaged over the solid angle of the measured aperture).

---

[3] http://irsa.ipac.caltech.edu/data/COSMOS/

In this framework, produced LyC photons either escape the ISM, ionise neutral gas (leading to recombination radiation) or are absorbed by dust (e.g. Bergvall et al., 2006). The number of produced ionizing photons per second, Q_{ion}, can be estimated from the strength of the (dust corrected) Hα emission line as follows:

$$L_{H\alpha} = Q_{ion}\, c_{H\alpha}\, (1 - f_{esc} - f_{dust}) \qquad (8.2)$$

where Q_{ion} is in s^{-1}, $L_{H\alpha}$ is in erg s^{-1}, f_{esc} is the fraction of produced ionizing photons that escapes the galaxy and f_{dust} is the fraction of produced ionizing photons that is absorbed by dust. For case B recombinations with a temperature of $T = 10\,000$ K, $c_{H\alpha} = 1.36 \times 10^{-12}$ erg (e.g. Kennicutt, 1998; Schaerer, 2003). Since the dust attenuation curve at wavelengths below 912 Å is highly uncertain, we follow the approach of Rutkowski et al. (2016), who use $f_{dust} = 0.5$, which is based on the mean value derived by Inoue (2002) in local galaxies.

Rest-frame LyC photons are redshifted into the *NUV* filter at $z = 2.2$. However, the IGM between $z = 2.2$ and our telescopes is not transparent to LyC photons (see Fig. 8.2), such that we need to correct the observed LyC luminosity for IGM absorption. The observed luminosity in the *NUV* filter (L_{NUV}) is then related to the produced number of ionizing photons as:

$$L_{NUV} = Q_{ion}\, \epsilon\, f_{esc}\, T_{IGM,NUV} \qquad (8.3)$$

Here, ϵ is the average energy of an ionizing photon observed in the *NUV* filter (which traces rest-frame wavelengths from 550 to 880 Å, see Fig. 8.2). Using the STARBURST99 models as described in §8.3.2, we find that ϵ is a strong function of age, but that it is strongly correlated with the EW of the Hα line (which itself is also a strong function of age). For the range of Hα EWs in our sample, $\epsilon = 17.04^{+0.45}_{-0.26}$ eV. We therefore take $\epsilon = 17.0$ eV.

$T_{IGM,NUV}$ is the absorption of LyC photons due to the intervening IGM, convolved with the *NUV* filter. Note that $T_{IGM} = e^{-\tau_{IGM}}$, where τ_{IGM} is the optical depth to LyC photons in the IGM, see e.g Vanzella et al. (2012). The IGM transmission depends on the wavelength and redshift. According to the model of Inoue et al. (2014), the mean IGM transmission for LyC radiation at $\lambda \sim 750$ Å for a source at $z = 2.2$ is $T_{IGM} \approx 40$ %. We convolve the IGM transmission as a function of observed wavelength for a source at $z = 2.2$ with the normalised transmission of the *NUV* filter, see Fig. 8.2. This results in a bandpass-averaged $T_{IGM,NUV} = 40.4\%$.

Combining equations 2 and 3 results in:

$$f_{esc} = \frac{1 - f_{dust}}{\left(1 + \alpha \frac{L_{H\alpha}}{L_{NUV}}\right)} \qquad (8.4)$$

where we define $\alpha = \epsilon\, c_{H\alpha}^{-1}\, T_{IGM,NUV}$. Combining our assumed values, we estimate $\alpha = 8.09$. We note that ϵ and $c_{H\alpha}$ are relatively insensitive to systematic uncertainties, while f_{dust} and T_{IGM} are highly uncertain for individual sources.

In addition to the absolute escape fraction of ionizing radiation, it is common to define the relative escape fraction of LyC photons to UV (~ 1500 Å) photons,
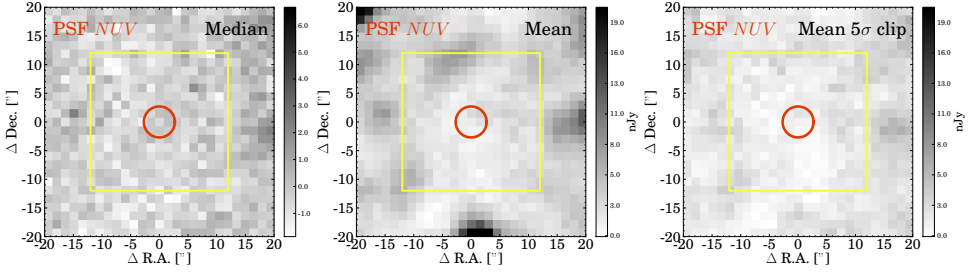
Figure 8.3: $20'' \times 20''$ thumbnail images of the *NUV* stack for CLEAN, star-forming HAEs in COSMOS, for three different stacking methods. The red circle shows the PSF-FWHM of *NUV* on the central position. The yellow box is the box which is used to measure the depth of the stack. Note that the range of the color-bar of the median stack is different than the color-bar of the mean stacks because the median stack is deeper.

Table 8.1: Stacked measurements for the CLEAN subsample (191 sources) of HAEs and LAEs at $z = 2.2$. The Hα luminosity is 1.6×10^{42} erg s^{-1}, the Hα extinction is $A_{H\alpha} = 1.23$, the median stellar mass is 3.5×10^9 M$_\odot$ and a median UV slope $\beta = -1.97$. The *NUV* column shows the limits on the *NUV* magnitude. L_{1500} is the rest-frame 1500 Å luminosity obtained from the *V* band. The absolute f_{esc} is measured from Hα and the *NUV* as described in §8.4.1. $f_{esc,rel}$ is the relative escape fraction of ionizing photons to UV photons and is measured from *NUV* and L_{1500}. Note that with a Calzetti law $A_{UV} = 3.1A_{H\alpha}$.

Subsample	NUV	L_{1500}	f_{esc}	f_{esc}^{rel}
	1σ AB	erg s^{-1}Hz^{-1}	%	%
Median stacking				
COSMOS no AGN	29.7	5.78×10^{28}	< 2.8	< 92.5
Mean stacking				
COSMOS no AGN	27.9	5.78×10^{28}	< 11.7	< 465.4
-5σ clip	28.7	5.78×10^{28}	< 6.4	< 231.0

since these are most commonly observed in high redshift galaxies. Following Steidel et al. (2001), the relative escape fraction, f_{esc}^{rel}, is defined as:

$$f_{esc}^{rel} = f_{esc}\, e^{\tau_{dust,UV}} = \frac{(L_{UV}/L_{NUV})_{int}}{(L_{UV}/L_{NUV})_{obs}} T_{IGM,NUV}^{-1} \qquad (8.5)$$

In this equation, L_{UV} is the luminosity in the observed *V* band, $e^{\tau_{dust,UV}}$ is the correction for dust (see §8.2.1) and we adopt an intrinsic ratio of $(L_{UV}/L_{NUV})_{int}$ = 5 (e.g. Siana et al., 2007). The relative escape fraction can be related to the absolute escape fraction when the dust attenuation for L_{UV}, A_{UV}, is known: $f_{esc} = f_{esc}^{rel} \times 10^{-0.4A_{UV}}$.

8.4.2 Individual *NUV* detections

By matching our sample of HAEs and LAEs with the public *GALEX* EM cleaned catalogue (e.g. Zamojski et al., 2007; Conseil et al., 2011), we find that 33 HAEs

and 5 LAEs have a detection with $NUV < 26$ within a separation of $1''$. However, most of these matches are identified as spurious, foreground sources or significantly contaminated inside the large PSF-FWHM of NUV imaging (see Appendix A). Yet, seven of these matches (of which five are AGN) are in the CLEAN subsample without a clear foreground source and could thus potentially be LyC leakers. Because it is known that foreground contamination has been a major problem in studies of LyC leakage at $z \sim 3$ (e.g. Mostardi et al., 2015; Siana et al., 2015), we can only confirm the reality of these candidate LyC leakers with high resolution UV imaging with HST. We list the individual detections in Appendix A, but caution the reader that any further investigation requires these candidates to be confirmed first.

8.4.3   Stacks of HAEs

The majority of our sources are undetected in the NUV imaging. Therefore, in order to constrain f$_{esc}$ for typical star-forming galaxies, we stack NUV thumbnails of our full sample of HAEs in COSMOS and also stack various subsets. We create thumbnails of $40'' \times 40''$ centered on the position of the NB$_K$ (Hα) detection and stack these by either median or mean combining the counts in each pixel. While median stacking results in optimal noise properties and is not dominated by outliers, it assumes that the underlying population is uniform, which is likely not the case. Mean stacking is much more sensitive to outliers (such as for example luminous AGN), but would give a more meaningful result as it gives the average f$_{esc}$, which is the important quantity in assessing the ionizing photon output of the entire galaxy population.

   We measure the depth by randomly placing 100,000 empty apertures with a radius of $0.67 \times$PSF-FWHM (similar to e.g. Cowie et al. 2009; Rutkowski et al. 2016) in a box of $24'' \times 24''$ around the centre of the thumbnail (see Fig. 8.3) and quote the 1σ standard deviation as the depth. Apertures with a detection of $NUV < 26$ AB magnitude are masked (this is particularly important for mean stacking). Counts are converted to AB magnitudes with the photometric zeropoint of 20.08 (Cowie et al., 2009). For mean stacking, we experiment with an iterative 5σ clipping method in order to have the background not dominated by a few luminous sources. To do this, we compute the standard deviation of the counts of the stacked sample in each pixel and ignore 5σ outliers in computing the mean value of each pixel. This is iterated five times, although we note that most of the mean values already converge after a single iteration.

   By stacking only sources from the CLEAN sample and by removing X-ray AGN, the limiting NUV magnitude of the stack of CLEAN HAEs is $NUV \approx 29.7$ AB (see Table 8.1), which translates into an upper limit of f$_{esc} < 2.8$ %. Mean stacking gives shallower constraints f$_{esc} < 11.7$ %) because the noise does not decrease as rapidly by stacking more sources, possibly because of a contribution from faint background or companion sources below the detection limit. This is improved somewhat by our iterative 5σ clipping (f$_{esc} < 6.4$ %), which effectively masks out the contribution from bright pixels. We show the stacked thumbnails of this sample in Fig. 8.3.

The median (mean) upper limit on the relative escape fraction, $f_{esc,rel}$, is much higher ($< 92.5(231)$ %). However, if we correct for the dust attenuation with the Calzetti et al. (2000) law, we find $A_{UV} \approx 3.8$ and a dust corrected inferred escape fraction of $< 2.8(7.0)$ %, in good agreement with our direct estimate from $H\alpha$, although we note that the additional uncertainty due to this dust correction is large.

We have experimented by stacking subsets of galaxies in bins of stellar mass, SFR and UV magnitude or LAEs, but all result in a non-detection in the NUV, all with weaker upper limits than the stack of Clean HAEs.

Systematic uncertainty due to the dust correction

In this sub-section, we investigate how sensitive our results are to the method used to correct for dust, which is the most important systematic uncertainty. In Table 8.1, we have used the SED inferred value of $E(B-V)$ to infer $A_{H\alpha}$: $A_{H\alpha} = E(B-V) \times k_{H\alpha}$, where $k_{H\alpha} = 3.3277$ following Calzetti et al. (2000), which results in $A_{H\alpha} = 1.23$. However, it is also possible to infer $A_{H\alpha}$ from a relation with the UV slope (e.g. Meurer et al., 1999), such that $A_{H\alpha} = 0.641(\beta + 2.23)$, for $\beta > -2.23$ and $A_{H\alpha} = 0$ for $\beta < -2.23$. Finally, we also use the relation between $A_{H\alpha}$ and stellar mass from Garn & Best (2010), which is: $A_{H\alpha} = 0.91 + 0.77X + 0.11X^2 - 0.09X^3$, where $X = \log_{10}(M_{star}/10^{10} M_\odot)$. Note that we assume a Calzetti et al. (2000) dust law in all these prescriptions.

It is immediately clear that there is a large systematic uncertainty in the dust correction, as for our full sample of HAEs we infer $A_{H\alpha} = 0.70$ with the Garn & Best (2010) prescription and $A_{H\alpha} = 0.19$ following Meurer et al. (1999), meaning that the systematic uncertainty due to dust can be as large as a factor 3. Thus, these different dust corrections result in different upper limits on f_{esc}. For the Clean, star-forming HAE sample, the upper limit on f_{esc} from median stacking increases to $f_{esc} < 4.4(6.6)$ %, using the attenuation based on stellar mass (β). With a simple 1 magnitude of extinction for $H\alpha$, $f_{esc} < 3.4$ % and without correcting for dust results in $f_{esc} < 7.7$ %.

In addition to the uncertainty in the dust correction of the $H\alpha$ luminosity, another uncertainty in our method is the f_{dust} parameter introduced in Eq. 8.2. The dust attenuation curve at wavelengths below 912 Å is highly uncertain, such that our estimate of f_{dust} is uncertain as well. However, because our limits on f_{esc} from the median stack are low, the results do not change significantly by altering f_{dust}: if $f_{dust} = 0.75(0.25)$, we find $f_{esc} < 1.4(4.1)$ %. This means that as long as the limit is low, our result is not very sensitive to the exact value of f_{dust}.

8.5 Constraining f_{esc} of HAEs from the ionizing background

In addition to constraining f_{esc} directly, we can obtain an indirect measurement of f_{esc} by using the ionizing emissivity, measured from quasar absorption studies, as a constraint. The emissivity is defined as the number of escaping ionizing

Table 8.2: Measurements of $\langle f_{esc} \rangle$, the escape fraction of ionizing photons averaged over the galaxy population at $z \approx 2 - 5$. Constraints on the IGM emissivity from absorption studies by Becker & Bolton (2013) have been used to infer the global escape fraction. For $z = 2.2$, we have used the Hα luminosity function from Sobral et al. (2013). We have used the analytical formula from Madau & Haardt (2015) to estimate the contribution from quasars to the ionizing emissivity, which assumes that $f_{esc,quasars} = 100$ %. At $z = 3.8$ and $z = 4.9$ we have used the SFR function from Smit et al. (2016).

Sample	Method	$\langle f_{esc} \rangle$
This paper		
HAEs $z = 2.2$	full SFR integration, $A_{H\alpha} = 1.0$	$4.4^{+7.1}_{-2.0}$ %
HAEs $z = 2.2$	SFR > 3 $M_\odot$/yr, $A_{H\alpha} = 1.0$	$6.7^{+10.8}_{-3.1}$ %
HAEs $z = 2.2$	full SFR integration, $A_{H\alpha} = 0.7$	$5.9^{+9.3}_{-2.6}$ %
HAEs $z = 2.2$	**final estimate: full integration, $A_{H\alpha} =$ 0.7, conservative systematic errors**	$5.9^{+14.5}_{-4.2}$ %
HAEs $z = 2.2$	full SFR integration, $A_{H\alpha} = 1.0$, QSO contribution	$0.5^{+3.6}_{-0.5}$ %
LBGs $z = 3.8$	full SFR integration, Hα from IRAC	$2.7^{+7.2}_{-2.3}$ %
LBGs $z = 3.8$	full SFR integration, Hα from IRAC, QSO contribution	$0.0^{+3.0}_{-0.0}$ %
LBGs $z = 4.9$	full SFR integration, Hα from IRAC	$6.0^{+13.9}_{-5.2}$ %
LBGs $z = 4.9$	full SFR integration, Hα from IRAC, QSO contribution	$2.1^{+6.2}_{-2.1}$ %
Literature		
Cristiani et al. (2016) $z = 3.8$	integrated LBG LF + contribution from QSOs	$5.3^{+2.7}_{-1.2}$ %

photons per second per comoving volume:

$$\dot{N}_{ion} = \langle f_{esc} \rangle \times \Phi(H\alpha) \times c_{H\alpha}^{-1} \qquad (8.6)$$

Here, $\dot{N}_{ion}$ is in s^{-1} Mpc^{-3}, $\langle f_{esc} \rangle$ is the escape fraction averaged over the entire galaxy population, $\Phi(H\alpha)$ is the Hα luminosity density in erg s^{-1} Mpc^{-3} and $c_{H\alpha}$ is the recombination coefficient as in Eq. 8.2.

We first check whether our derived emissivity using our upper limit on f_{esc} for HAEs is consistent with published measurements of the emissivity. The Hα luminosity density is measured in Sobral et al. (2013) as the full integral of the Hα luminosity function, with a global dust correction of $A_{H\alpha} = 1.0$. Using the mean limit on f_{esc} for our CLEAN sample of HAEs (so $f_{esc} \leq 6.4$ %), we find that $\dot{N}_{ion} \leq 1.3^{+0.2}_{-0.2} \times 10^{51}$ s^{-1} Mpc^{-3}, where the errors come from the uncertainty in the Hα LF. We note that these numbers are relatively independent on the dust correction method because while a smaller dust attenuation would decrease the Hα luminosity density, it would also raise the upper limit on the escape fraction, thus almost cancelling out. These upper limits on $\dot{N}_{ion}$ are consistent with the measured emissivity at $z = 2.4$ of Becker & Bolton (2013), who measured $\dot{N}_{ion} = 0.90^{+1.60}_{-0.52} \times 10^{51}$ s^{-1} Mpc^{-3} (combined systematic and measurement errors) using the latest measurements of the IGM temperature and opacity to Lyα and LyC

photons.

Now, by isolating $\langle f_{esc} \rangle$ in Eq. 8.6, we can estimate the globally averaged escape fraction. If we assume that there is no evolution in the emissivity from Becker & Bolton (2013) between $z = 2.2$ and $z = 2.4$ and that the Hα luminosity function captures all sources of ionizing photons, we find that $\langle f_{esc} \rangle = 4.4^{+7.1}_{-2.0}$ % for A$_{H\alpha} = 1.0$. There are a number of systematic uncertainties that we will address now and add to the error bars of our final estimate. These uncertainties are: i) integration limit of the Hα LF, ii) the dust attenuation to L(Hα), iii) the conversion from L(Hα) to ionizing numbers, and iv) the [NII] correction to the observed Hα luminosity.

Integrating the Hα LF only to SFR ≈ 3 M$_\odot$ yr^{-1}, we find $\langle f_{esc} \rangle = 6.7^{+10.8}_{-3.1}$ %, such that the systematic uncertainty is of order 50 %. If A$_{H\alpha} = 0.7$, which is the median value when we correct for dust using stellar mass, and which may be more representative of fainter Hα emitters (as faint sources are expected to have less dust), the escape fraction is somewhat higher, with $\langle f_{esc} \rangle = 5.9^{+9.3}_{-2.6}$ %. These numbers are summarised in Table 8.2. The uncertainty in c$_{H\alpha}$ is relatively small, as c$_{H\alpha}$ depends only modestly on the density and the temperature. For example, in the case of a temperature of T = 30000 K, c$_{H\alpha}$ decreases only by $\approx 10\%$ (Schaerer, 2002). This adds a 10 % uncertainty in the escape fraction. As explained in §8.2.1, there is an uncertainty in the measured Hα luminosity due to the contribution of the [NII] doublet to the observed narrow-band flux, for which we correct using a relation with observed EW. By comparing this method with the method from Erb et al. (2006), which is based on the observed mass-metallicity relation of a sample of LBGs at $z \sim 2$, we find that the inferred Hα luminosity density would conservatively be 10 % higher, such that this correction adds another 10 % systematic uncertainty in the escape fraction.

For our final estimate of $\langle f_{esc} \rangle$ we use the dust correction based on stellar mass, fully integrate the Hα luminosity function and add a 10 % error in quadrate for the systematic uncertainty in each of the parameters as described above, 50 % due to the uncertain integration limits and add a 40 % error due to the systematics in the dust attenuation. This results in $\langle f_{esc} \rangle = 5.9^{+14.5}_{-4.2}$ % at $z = 2.2$.

An additional contribution to the ionizing emissivity from rarer sources than sources with number densities $< 10^{-5}$ Mpc^{-3} such as quasars, would lower the escape fraction for HAEs. While Madau & Haardt (2015) argue that the ionizing budget at $z \approx 2 - 3$ is dominated by quasars, this measurement may be overestimated by assuming quasars have a 100 % escape fraction. Recently, Micheva et al. (2017) obtained a much lower emissivity (up to a factor of 10) from quasars by directly measuring f$_{esc}$ for a sample of $z \sim 3$ AGN. Using a large sample of quasars at $z = 3.6 - 4.0$, Cristiani et al. (2016), measure a mean $\langle f_{esc,quasar} \rangle \approx 70$ %, which means that quasars do not dominate the ionizing background at $z \approx 4$. When we include a quasar contribution from Madau & Haardt (2015) in the most conservative way (meaning that we assume f$_{esc} = 100$ % for quasars), we find that $\langle f_{esc} \rangle = 0.5^{+3.6}_{-0.5}$ %. If the escape fraction for quasars is 70 %, $\langle f_{esc} \rangle = 1.6^{+5.4}_{-1.3}$ %, such that a non-zero contribution from star-forming galaxies is not ruled out.
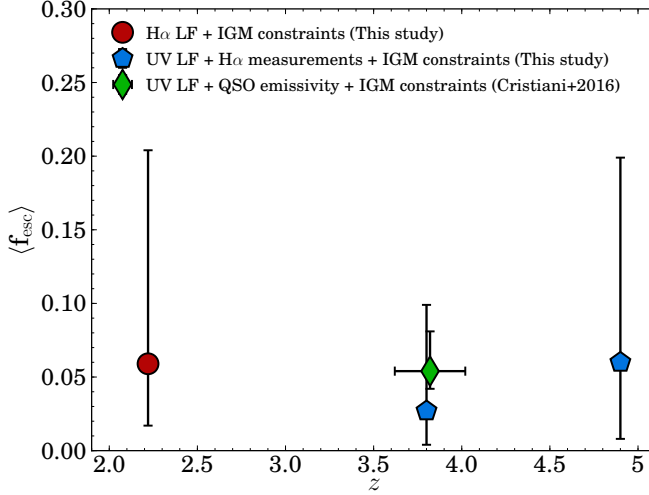
Figure 8.4: Evolution of the globally averaged $\langle f_{esc} \rangle$, which is obtained by forcing the emissivity of the integrated Hα ($z = 2.2$) and UV ($z \approx 4-5$) LF to be equal to the emissivity measured by IGM absorption models from Becker & Bolton 2013. The $z \approx 4-5$ results are based on a UV luminosity function which is then corrected to a SFR function with Hα measurements from *Spitzer*/IRAC, which implicitly means using a value of ξ_{ion} (SFR functions are presented in Smit et al. 2016, but see also Bouwens et al. 2016). The error bars of red and blue symbols include estimates of the systematic uncertainties. The green diamond shows the estimated value by Cristiani et al. 2016, who combined IGM constraints with a UV LBG and the emissivity of QSOs at $z = 3.6 - 4.0$.

We note that, these measurements of $\langle f_{esc} \rangle$ contain significantly less (systematic) uncertainties than measurements based on the integral of the UV luminosity function (e.g. Becker & Bolton, 2013; Khaire et al., 2016). This is because: i) UV selected galaxy samples do not necessarily span the entire range of SFGs (e.g. Oteo et al., 2015) and might thus miss dusty star-forming galaxies and ii) there are additional uncertainties in converting non-ionizing UV luminosity to intrinsic LyC luminosity (in particular the dust corrections in ξ_{ion} and uncertainties in the detailed SED models in $(L_{UV}/L_{NUV})_{int}$. An issue is that Hα is very challenging to observe at $z \gtrsim 2.8$ and that a potential spectroscopic follow-up study of UV selected galaxies with the *JWST* might yield biased results.

8.5.1 Redshift evolution

Using the methodology described in §8.5, we also compute the average f_{esc} at $z = 3.8$ and $z = 4.9$ by using the SFR functions of Smit et al. (2016), which are derived from UV luminosity functions, a Meurer et al. (1999) dust correction and a general offset to correct for the difference between SFR(UV) and SFR(Hα), estimated from *Spitzer*/IRAC photometry. This offset is implicitly related to the value of ξ_{ion} from Bouwens et al. (2016), which is estimated from the same measurements. We combine these SFR functions, converted to the Hα luminosity

function as in §8.2.1, with the IGM emissivity from Becker & Bolton (2013) at $z = 4.0$ and $z = 4.75$, respectively. Similarly to the Hα luminosity density, we use the analytical integral of the Schechter function. Similarly as at $z = 2.2$, we conservatively increase the error bars by a factor $\sqrt{2}$ to take systematic uncertainties into account. This results in $\langle f_{esc} \rangle = 2.7^{+7.2}_{-2.3}$ % and $\langle f_{esc} \rangle = 6.0^{+13.9}_{-5.2}$ % at $z \approx 4$ and $z \approx 5$, respectively, see Table 8.2. When including a (maximum) quasar contribution from Madau & Haardt (2015) as described above, we find $\langle f_{esc} \rangle = 0.0^{+3.0}_{-0.0}$ % at $z \approx 4$ and $\langle f_{esc} \rangle = 2.1^{+6.2}_{-2.1}$ %.

As illustrated in Fig. 8.4, the global escape fraction is low at $z \approx 2 - 5$. While dust has been corrected for with different methods at $z = 2.2$ and $z \approx 4 - 5$, we note that the differences between different dust correction methods are not expected to be very large at $z \approx 4 - 5$. This is because higher redshift galaxies typically have lower mass, which results in a higher agreement between dust correction methods based on either M$_{star}$ or β. One potentially important caveat is that our computation assumes that the Hα and UV luminosity functions include all sources of ionizing photons in addition to quasars. An additional contribution of ionizing photons from galaxies which have potentially been missed by a UV selection (for example sub-mm galaxies) would decrease the global f$_{esc}$. Such a bias is likely more important at $z \approx 3 - 5$ than $z \approx 2$ because the $z \approx 2$ sample is selected with Hα which is able to recover sub-mm galaxies. Even under current uncertainties, we rule out a globally averaged $\langle f_{esc} \rangle > 20$ % at redshifts lower than $z \approx 5$.

These indirectly derived escape fractions of ~ 4 % at $z \approx 2 - 5$ are consistent with recently published upper limits from Sandberg et al. (2015) at $z = 2.2$ and similar to strict upper limits on f$_{esc}$ at $z \sim 1$ measured by Rutkowski et al. (2016), see also Cowie et al. (2009); Bridge et al. (2010). Recently, Cristiani et al. (2016) estimated that galaxies have on average $\langle f_{esc} \rangle = 5.3^{+2.7}_{-1.2}$ % at $z \approx 4$ by combining IGM constraints with the UV luminosity function from Bouwens et al. (2011) and by including the contribution from quasars to the total emissivity. This result is still consistent within the error-bars with our estimate using the Madau & Haardt (2015) quasar contribution and Smit et al. (2016) SFR function. Part of this is because we use a different conversion from UV luminosity to the number of produced ionizing photons based on Hα estimates with *Spitzer*/IRAC, and because our computation assumes f$_{esc,quasars}$ = 100%, while Cristiani et al. (2016) uses f$_{esc,quasars}$ $\approx$ 70%.

Furthermore, our results are also consistent with observations from Chen et al. (2007) who find a mean escape fraction of 2 ± 2 % averaged over galaxy viewing angles using spectroscopy of the afterglow of a sample of γ-Ray bursts at $z > 2$. Grazian et al. (2016) measures a strict median upper limit of $f^{rel}_{esc} < 2$ % at $z = 3.3$, although this limit is for relatively luminous Lyman-break galaxies and not for the entire population of SFGs. This would potentially indicate that the majority of LyC photons escape from galaxies with lower luminosity, or galaxies missed by a Lyman-break selection, i.e. Cooke et al. (2014) or that they come from just a sub-set of the population, and thus the median f$_{esc}$ can even be close to zero. Khaire et al. (2016) finds that f$_{esc}$ must evolve from $\approx 5 - 20$ % between $z = 3 - 5$, which is allowed within the errors. However, we note
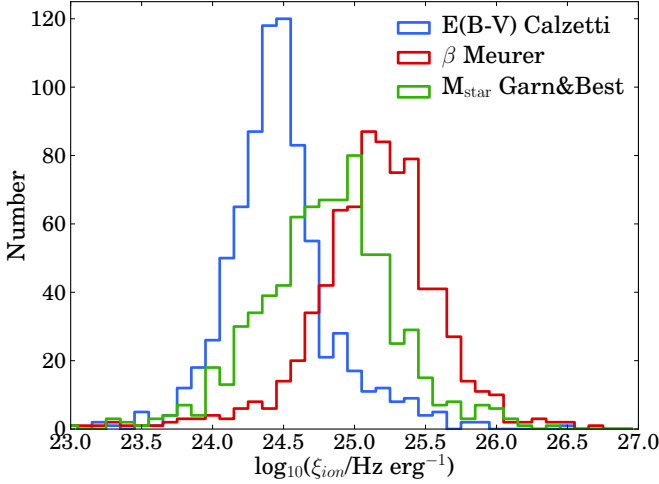
Figure 8.5: Histogram of the values of ξ_{ion} for HAEs with three different methods to correct for dust attenuation. The blue histogram shows values of ξ_{ion} when dust is corrected with the $E(B-V)$ value from the SED in combination with a Calzetti law (see §8.2.1). The red histogram is corrected for dust with the Meurer et al. 1999 prescription based on the UV slope and the green histogram is corrected for dust with the prescription from Garn & Best 2010 based on a relation between dust attenuation and stellar mass. As can be seen, the measured values of ξ_{ion} differ significantly, with the highest values found when correcting for dust with the UV slope. When the nebular attenuation is higher than the stellar attenuation, ξ_{ion} would shift to higher values.

that they assume that the number of produced ionizing photons per unit UV luminosity does not evolve with redshift. In §8.6.5 we find that there is evolution of this number by roughly a factor 1.5, such that the required evolution of f_{esc} would only be a factor ≈ 3. While our results indicate little to no evolution in the average escape fraction up to $z \approx 5$, this does not rule out an increasing f_{esc} at $z > 5$, where theoretical models expect an evolving f_{esc} (e.g. Kuhlen & Faucher-Giguère, 2012; Ferrara & Loeb, 2013; Mitra et al., 2013; Khaire et al., 2016; Sharma et al., 2016; Price et al., 2016), see also a recent observational claim of evolving f_{esc} with redshift (Smith et al., 2016a).

Finally, we stress that a low $\langle f_{esc} \rangle$ is not inconsistent with the recent detection of the high f_{esc} of above 50 % from a galaxy at $z \approx 3$ (De Barros et al., 2016; Vanzella et al., 2016), which may simply reflect that there is a broad distribution of escape fractions. For example, if only a small fraction (< 5 %) of galaxies are LyC leakers with $f_{esc} \approx 75$ %, the average f_{esc} over the galaxy population is ≈ 4 %, consistent with the indirect measurement, even if $f_{esc} = 0$ for all other galaxies. Such a scenario would be the case if the escape of LyC photons is a very stochastic process, for example if it is highly direction or time dependent. This can be tested with deeper LyC limits on individual galaxies over a complete selection of star-forming galaxies.

8.6 The ionizing properties of star-forming galaxies at $z = 2.2$

8.6.1 How to measure ξ_{ion}?

The number of ionizing photons produced per unit UV luminosity, ξ_{ion}, is used to convert the observed UV luminosity of high-redshift galaxies to the number of produced ionizing photons. It can thus be interpreted as the production efficiency of ionizing photons. ξ_{ion} is defined as:

$$\xi_{ion} = Q_{\text{ion}} / L_{UV,\text{int}} \tag{8.7}$$

As described in the previous section, Q_{ion} (in s^{-1}) can be measured directly from the dust-corrected Hα luminosity by rewriting Eq. 8.2 and assuming $f_{\text{esc}} = 0$. $L_{UV,\text{int}}$ (in erg s^{-1} Hz^{-1}) is obtained by correcting the observed UV magnitudes for dust attenuation. With a Calzetti et al. (2000) attenuation curve $A_{UV} = 3.1 A_{\text{H}\alpha}$.

In our definition of ξ_{ion}, we assume that the escape fraction of ionizing photons is ≈ 0. Our direct constraint of $f_{\text{esc}} \lesssim 6\%$ and our indirect global measurement of $f_{\text{esc}} \approx 5$ % validate this assumption. If the average escape fraction is $f_{\text{esc}} = 10\%$, ξ_{ion} is higher by a factor 1.11 (so only 0.04 dex), such that ξ_{ion} is relatively insensitive to the escape fraction as long as the escape fraction is low. We also note that the ξ_{ion} measurements at $z \approx 4 - 5$ from Bouwens et al. (2016) are validated by our finding that the global escape fraction at $z < 5$ is consistent with being very low, < 5 %.

8.6.2 ξ_{ion} at $z = 2.2$

We show our measured values of ξ_{ion} for HAEs in Fig. 8.5 and Table 8.3, where dust attenuation is corrected with three different methods based either on the $E(B - V)$ value of the SED fit, the UV slope β or the stellar mass. It can be seen that the average value of ξ_{ion} is very sensitive to the dust correction method, ranging from $\xi_{ion} = 10^{24.39 \pm 0.04}$ Hz erg^{-1} for the SED method to $\xi_{ion} = 10^{25.11 \pm 0.04}$ Hz erg^{-1} for the β method. For the dust correction based on stellar mass the value lies in between, with $\xi_{ion} = 10^{24.85 \pm 0.04}$ Hz erg^{-1}. In the case of a higher nebular attenuation than the stellar attenuation, as for example by a factor ≈ 2 as in the original Calzetti et al. (2000) prescription, ξ_{ion} increases by 0.4 dex to $\xi_{ion} = 10^{24.79 \pm 0.04}$ Hz erg^{-1} when correcting for dust with the SED fit.

We note that independent (stacking) measurements of the dust attenuation from *Herschel* and Balmer decrements at $z \sim 1 - 2$ indicate that dust attenuations agree very well with the Garn & Best (2010) prescription (e.g. Sobral et al., 2012; Ibar et al., 2013; Buat et al., 2015; Pannella et al., 2015), thus favouring the intermediate value of ξ_{ion}. Without correcting ξ_{ion} for dust, we find $\xi_{ion} = 10^{25.41 \pm 0.05}$ Hz erg^{-1}. With 1 magnitude of extinction for Hα, as for example used in the conversion of the Hα luminosity density to a SFR density in Sobral et al. (2013),

Table 8.3: Ionizing properties of HAEs and LAEs for various methods to correct for dust attenuations and different subsets. We show the median stellar mass of each subsample. Errors on ξ_{ion} are computed as $\sigma_{\xi_{ion}}/\sqrt{N}$, where $\sigma_{\xi_{ion}}$ is the median measurement error of ξ_{ion} and N the number of sources. For the Bouwens et al. (2016) measurements, we show only dust corrections with a Calzetti et al. (2000) curve. The subsample of 'low mass' HAEs has $M_{star} = 10^{9.0-9.4}$ $M_\odot$. 'UV faint' HAEs have $M_{1500} > -19$.

Sample	$\langle M_{star} \rangle$ $\log_{10} M_\odot$	$\log_{10} \xi_{ion}$ Hz erg^{-1}	Dust
This paper			
HAEs $z = 2.2$	9.8	24.39 ± 0.04	$E(B-V)$
		25.11 ± 0.04	β
		24.77 ± 0.04	M_{star}
		25.41 ± 0.05	No dust
		24.57 ± 0.04	$A_{H\alpha} = 1$
Low mass	9.2	24.49 ± 0.06	$E(B-V)$
		25.22 ± 0.06	β
		24.99 ± 0.06	M_{star}
UV faint	10.2	24.93 ± 0.07	$E(B-V)$
		25.39 ± 0.07	β
		25.24 ± 0.07	M_{star}
LAEs $z = 2.2$	8.5	24.84 ± 0.09	$E(B-V)$
		25.37 ± 0.09	β
		25.14 ± 0.09	M_{star}
		25.39 ± 0.09	No dust
Bouwens et al. (2016)			
LBGs $z = 3.8 - 5.0$	9.2	25.27 ± 0.03	β
LBGs $z = 5.1 - 5.4$	9.2	25.44 ± 0.12	β

$\xi_{ion} = 10^{24.57 \pm 0.04}$ Hz erg^{-1}.

Since individual Hα measurements for LAEs are uncertain due to the difference in filter transmissions depending on the exact redshift (see Matthee et al. 2016), we only investigate ξ_{ion} for our sample of LAEs in the stacks described in Sobral et al. (2017). With stacking, we measure the median Hα flux of LAEs convolved through the filter profile and the median UV luminosity by stacking V band imaging. As seen in Table 8.3, the median ξ_{ion} is higher than the median ξ_{ion} for HAEs for each dust correction. However, this difference disappears without correcting for dust. Therefore, the higher values of ξ_{ion} for LAEs simply indicate that the median LAE has a bluer UV slope, lower stellar mass and lower $E(B-V)$ than the median HAE. More accurate dust measurements are required to investigate whether ξ_{ion} is really higher for LAEs. We note that ≈ 40 % of the LAEs are undetected in the broad-bands and thus assigned a stellar mass of 10^8 $M_\odot$ and $E(B-V) = 0.1$ when computing the median dust attenuation. Therefore, the ξ_{ion} values for LAEs could be under-estimated if the real dust attenuation is even lower.
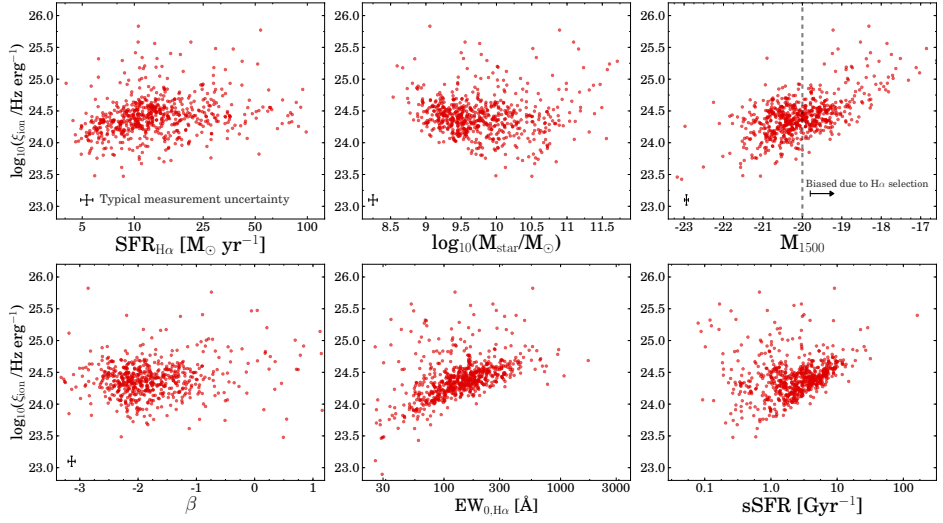
Figure 8.6: Correlations between ξ_{ion} and galaxy properties for HAEs, when dust is corrected using the SED fitted E$(B - V)$ values. ξ_{ion} does not clearly correlate with SFR(Hα), M$_{star}$ or β. A correlation between ξ_{ion} and M$_{1500}$ is expected of similar strength as seen, based on the definition of ξ_{ion}. ξ_{ion} increases strongly with Hα EW and sSFR. High values of ξ_{ion} at low sSFRs are mostly due to the dust correction.
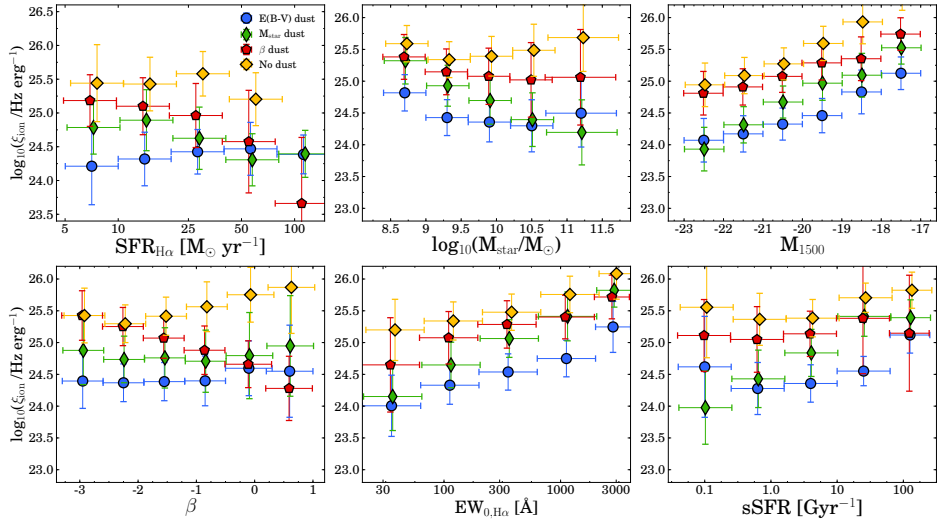
Figure 8.7: Correlations between ξ_{ion} and galaxy properties for different methods to correct for dust attenuation. To facilitate the comparison, HAEs were binned on the x-axis. The value of ξ_{ion} is the median value in each bin, while the vertical error is the standard deviation. Blue bins show the values where dust is corrected with the E$(B - V)$ value from the SED. The red bins are corrected for dust with the Meurer et al. (1999) prescription based on β and the green bins are corrected for dust with the prescription from Garn & Best (2010) based on stellar mass. Yellow bins show the results where we assume that there is no dust.

8.6.3   Dependence on galaxy properties

In this section we investigate how ξ_{ion} depends on the galaxy properties that are defined in §8.2.1 and also check whether subsets of galaxies lie in a specific parameter space. As illustrated in Fig. 8.6 (where we correct for dust with E($B -$ V)), we find that ξ_{ion} does not depend strongly on SFR(Hα) with a Spearman correlation rank (R$_s$) of R$_s = 0.11$. Such a correlation would naively be expected if the Hα SFRs are not related closely to UV SFRs, since $\xi_{ion} \propto L_{H\alpha}/L_{1500} \propto$ SFR(Hα)/SFR(UV). However, for our sample of galaxies these SFRs are strongly correlated with only 0.3 dex of scatter, see also Oteo et al. (2015), leading to a relatively constant ξ_{ion} with SFR.

   For the same reason, we measure a relatively weak slope of ≈ 0.25 when we fit a simple linear relation between $\log_{10}(\xi_{ion})$ and M$_{1500}$, instead of the naively expected value of $\xi_{ion} \propto 0.4M_{1500}$. At M$_{1500} > -20$, our H$\alpha$ selection is biased towards high values of Hα relative to the UV, leading to a bias in high values of ξ_{ion}. For sources with M$_{1500} < -20$, we measure a slope of ≈ 0.2. This means that ξ_{ion} does not increase rapidly with decreasing UV luminosity. This is because Hα luminosity and dust attenuation themselves are also related to M$_{1500}$. Indeed, we find that the Hα luminosity anti-correlates with the UV magnitude and E($B - V$) increases for fainter UV magnitudes.

   The stellar mass and β are not by definition directly related to ξ_{ion}. Therefore, a possible upturn of ξ_{ion} at low masses (see the middle-top panel in Fig. 8.6) may be a real physical effect, although we note that we are not mass-complete below M$_{star} < 10^{10}$ M$_\odot$ and an Hα selected sample of galaxies likely misses low-mass galaxies with lower values of ξ_{ion}.

   We find that the number of ionizing photons per unit UV luminosity is strongly related to the Hα EW (with a slope of ~ 0.6 in log-log space), see Fig. 8.6. Such a correlation is expected because of our definition of ξ_{ion}: i) the Hα EW increases mildly with increasing Hα (line-)luminosity and ii) the Hα EW is weakly anti-related with the UV (continuum) luminosity, such that ξ_{ion} increases relatively strongly with EW. Since there is a relation between Hα EW and specific SFR (sSFR = SFR/M$_{star}$, e.g. Fumagalli et al. 2012), we also find that ξ_{ion} increases strongly with increasing sSFR, see Fig. 8.6.

   In Fig. 8.7 we show the same correlations as discussed above, but now compare the results for different methods to correct for dust. For comparison, we only show the median ξ_{ion} in bins of the property on the x-axis. The vertical error on the bins is the standard deviation of the values of ξ_{ion} in the bin. As ξ_{ion} depends on the dust correction, we find that ξ_{ion} correlates with the galaxy property that was used to correct for dust in the case of β (red symbols) and M$_{star}$ (green symbols). Specific SFR depends on stellar mass, so we also find the strongest correlation between sSFR and ξ_{ion} when ξ_{ion} is corrected for dust with the Garn & Best (2010) prescription. We only find a relation between ξ_{ion} and β when dust is corrected with the Meurer et al. (1999) prescription. For UV magnitude only the normalisation of ξ_{ion} changes with the dust correction method.

   It is more interesting to look at correlations between ξ_{ion} and galaxy properties which are not directly related to the computation of ξ_{ion} or the dust correc-

tion. Hence, we note that irrespective of the dust correction method, ξ_{ion} appears to be somewhat higher for lower mass galaxies (although this is likely a selection effect as discussed above). Irrespective of the dust correction method, ξ_{ion} increases with increasing Hα EW and fainter M_{1500}, where the particular dust correction method used only sets the normalisation. We return to this relation between ξ_{ion} and Hα EW in §8.6.5.

8.6.4   Redshift evolution of ξ_{ion}

Because of its dependency on galaxy properties, it is possible that ξ_{ion} evolves with redshift. In fact, such an evolution is expected as more evolved galaxies (particularly with declining star formation histories) have a relatively stronger UV luminosity than Hα and a higher dust content, likely leading to a lower ξ_{ion} at $z = 2.2$ than at $z > 6$.

By comparing our measurement of ξ_{ion} with those from Bouwens et al. (2016) at $z = 4 - 5$, we already find such an evolution (see Table 8.3), although we note that the samples of galaxies are selected differently and that there are many other differences, such as the dust attenuation, typical stellar mass and the Hα measurement. If we mimic a Lyman-break selected sample by only selecting HAEs with $E(B - V) < 0.3$ (typical for UV selected galaxies, e.g. Steidel et al. 2011), we find that ξ_{ion} increases by (maximally) 0.1 dex, such that this does likely not explain the difference in ξ_{ion} at $z = 2.2$ and $z \approx 4 - 5$ of ≈ 0.5 dex. Furthermore, our Hα selection is likely biased towards high values of ξ_{ion} for $M_{1500} > -20$, which mitigates the difference on the median ξ_{ion}. If we select only low mass galaxies such that the median stellar mass resembles that of Bouwens et al. (2016), the difference is only $\approx 0.2 \pm 0.1$ dex, which still would suggest evolution.

We estimate the redshift evolution of ξ_{ion} by combining the relation between ξ_{ion} and Hα EW with the redshift evolution of the Hα EW. Several studies have recently noted that the Hα EW (and related sSFR) increases with increasing redshift (e.g. Fumagalli et al., 2012; Sobral et al., 2014; Smit et al., 2014; Mármol-Queraltó et al., 2016; Faisst et al., 2016; Khostovan et al., 2016). Furthermore, the EW is mildly dependent on stellar mass as EW $\sim M_{star}^{-0.25}$ (Sobral et al., 2014; Mármol-Queraltó et al., 2016). In order to estimate the ξ_{ion} using the Hα EW evolution, we:

i) Select a subset of our HAEs with stellar mass between $10^{9-9.4}$ M$_\odot$, with a median of $M_{star} \approx 10^{9.2}$ M$_\odot$, which is similar to the mass of the sample from Bouwens et al. (2016), see Smit et al. (2016),

ii) Fit a linear trend between $\log_{10}$(EW) and $\log_{10}(\xi_{ion})$ (with the Garn & Best (2010) prescription to correct for dust attenuation). We note that the trend between EW and ξ_{ion} will be steepened if dust is corrected with a prescription based on stellar mass (since Hα EW anti-correlates with stellar mass, see also Table 8.4). However, this is validated by several independent observations from either Herschel or Balmer decrements which confirm that dust attenuation increases with stellar mass at a wide range of redshifts (Domínguez et al., 2013; Buat et al., 2015; Koyama et al., 2015; Pannella et al., 2015; Sobral et al., 2016b).
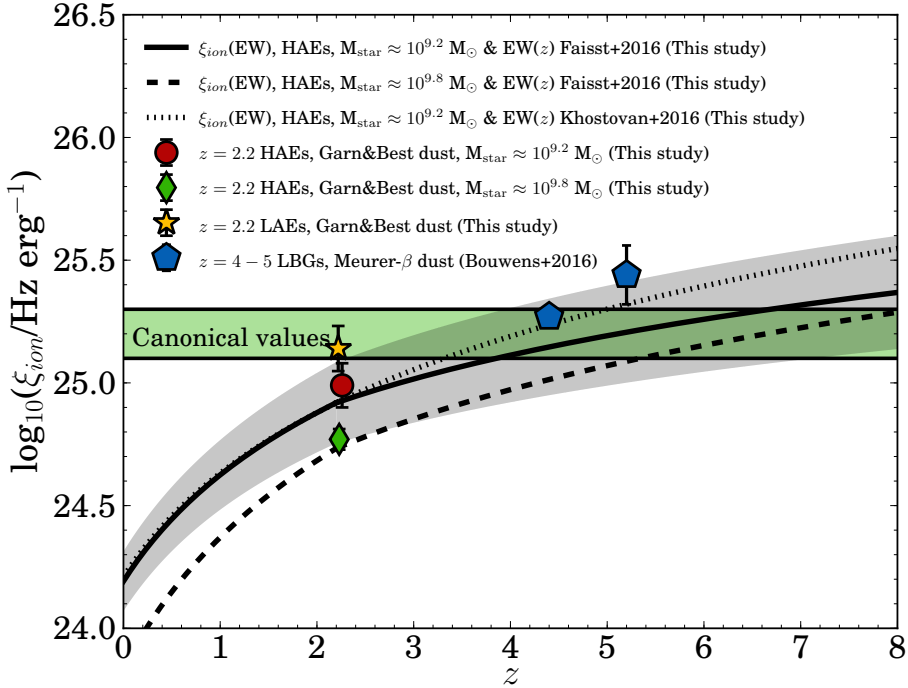
Figure 8.8: Inferred evolution of ξ_{ion} (corrected for dust with M_{star}) with redshift based on our observed trend between ξ_{ion} and Hα EW, for different stellar masses (compare the solid with the dashed line) and EW(z) evolutions (compare the solid with the dotted line). The grey shaded region indicates the errors on the redshift evolution of ξ_{ion}. The normalisation of ξ_{ion} is higher for lower mass galaxies or LAEs. The green region shows the typically assumed values. The estimated evolution of ξ_{ion} with redshift is consistent with the typically assumed values of ξ_{ion} in the reionization era and with recent measurements at $z = 4 - 5$.

Table 8.4: Fit parameters for $\log_{10} \xi_{ion} = a + b \log_{10} EW(H\alpha)$ for different selections and dust corrections

Sample	$\langle M_{star} \rangle$ $\log_{10} M_{\odot}$	a	b	Dust
All HAEs	9.8	23.12	0.59	$E(B-V)$
		23.66	0.64	β
		22.60	0.97	M_{star}
		23.59	0.45	$A_{H\alpha} = 1$
Low mass	9.2	22.64	0.78	$E(B-V)$
		23.68	0.64	β
		23.19	0.77	M_{star}
		22.77	0.75	$A_{H\alpha} = 1$

Using a simple least squares algorithm, we find:

$$\log_{10}(\tilde{\xi}_{ion}) = 23.19^{+0.09}_{-0.09} + 0.77^{+0.04}_{-0.04} \times \log_{10}(\text{EW}) \tag{8.8}$$

iii) Combine the trend between Hα EW and redshift with the trend between $\tilde{\xi}_{ion}$ and Hα EW. We use the redshift evolution of the Hα EW from Faisst et al. (2016), which has been inferred from fitting SEDs, and measured up to $z \approx 6$. In this parametrisation, the slope changes from EW$\approx (1+z)^{1.87}$ at $z < 2.2$ to EW$\approx (1+z)^{1.3}$ at $z > 2.2$. Below $z < 2.2$, this trend is fully consistent with the EW evolution from HiZELS (Sobral et al., 2014), which is measured with narrow-band imaging. Although HiZELS does not have Hα emitters at $z > 2.2$, the EW evolution of [OIII]+Hβ is found to flatten at $z > 2.2$ as well (Khostovan et al., 2016). We note that we assume that the slope of the Hα EW evolution with redshift does not vary strongly for stellar masses between $10^{9.2}$ M$_\odot$ and $10^{9.8}$ M$_\odot$, since the following equations are measured at stellar mass $\approx 10^{9.6}$ M$_\odot$ (Faisst et al., 2016), hence:

$$\text{EW}(z) = \begin{cases} 20 \times (1+z)^{1.87}, & z < 2.2 \\ 37.4 \times (1+z)^{1.3}, & z \geq 2.2 \end{cases} \tag{8.9}$$

This results in:

$$\log_{10}(\tilde{\xi}_{ion}(z)) = \begin{cases} 24.19 + 1.44 \times \log_{10}(1+z), & z < 2.2 \\ 24.40 + 1.00 \times \log_{10}(1+z), & z \geq 2.2 \end{cases} \tag{8.10}$$

where $\tilde{\xi}_{ion}$ is in Hz erg^{-1}. The error on the normalisation is 0.09 Hz erg^{-1} and the error on the slope is 0.18. For our typical mass of M$_{\text{star}} = 10^{9.8}$ M$_\odot$, the normalisation is roughly 0.2 dex lower and the slope a factor ≈ 1.1 higher compared to the fit at lower stellar masses. This is due to a slightly different relation between $\tilde{\xi}_{ion}$ and EW (see Table 8.4). The evolving $\tilde{\xi}_{ion}$ is consistent with the typically assumed value of $\tilde{\xi}_{ion} = 10^{25.2\pm0.1}$ Hz erg^{-1} (e.g. Robertson et al., 2013) at $z \approx 2.5 - 12$ within the 1σ error bars.

We show the inferred evolution of $\tilde{\xi}_{ion}$ with redshift in Fig. 8.8. The solid and dashed line use the EW(z) evolution from Faisst et al. (2016), while the dotted line uses the Khostovan et al. (2016) parametrisation. The grey shaded region indicates the errors on the redshift evolution of $\tilde{\xi}_{ion}$. Due to the anti-correlation between EW and stellar mass, galaxies with a lower stellar mass have a higher $\tilde{\xi}_{ion}$ (which is then even strengthened by a higher dust attenuation at high masses).

Relatively independent of the dust correction (as discussed in Fig. 8.11), the median $\tilde{\xi}_{ion}$ increases ≈ 0.2 dex at fixed stellar mass between $z = 2.2$ and $z = 4.5$. This can easily explain the 0.2 dex difference between our measurement at $z = 2.2$ and the Bouwens et al. (2016) measurements at $z = 4 - 5$ (see Fig. 8.8), such that it is plausible that $\tilde{\xi}_{ion}$ evolves to higher values in the reionization epoch, of roughly $\tilde{\xi}_{ion} \approx 10^{25.4}$ Hz erg^{-1} at $z \approx 8$. Interestingly, LAEs at $z = 2.2$ already have $\tilde{\xi}_{ion}$ similar to the canonical value in the reionization era.

8.7 Implications for reionization

The product of $f_{esc}\xi_{ion}$ is an important parameter in assessing whether galaxies have provided the photons to reionize the Universe, because these convert the (non-ionizing) UV luminosity density (obtained from integrating the dust-corrected UV luminosity function) to the ionizing emissivity. The typical adopted values are $\xi_{ion} \approx 10^{25.2-25.3}$ Hz erg^{-1} and $f_{esc} \approx 0.1 - 0.2$ (e.g. Robertson et al., 2015), such that the product is $f_{esc}\xi_{ion} \approx 10^{24.2-24.6}$ Hz erg^{-1}. This is significantly higher than our upper limit of $f_{esc}\xi_{ion} \lesssim 10^{23.5}$ Hz erg^{-1} (using $\langle f_{esc} \rangle$ and ξ_{ion} where dust is corrected with M_{star}, see §8.5 and §8.6). However, as shown in §8.6.5, we expect $\xi_{ion} \approx 10^{25.4}$ Hz erg^{-1} in the reionization era due to the dependency of ξ_{ion} on EW(Hα), such that escape fractions of $f_{esc} \approx 7$ % would suffice for $f_{esc}\xi_{ion} = 10^{24.2}$ Hz erg^{-1}. Becker & Bolton (2013) find an evolution in the product of $f_{esc}\xi_{ion}$ of a factor 4 between $z = 3 - 5$ (similar to Haardt & Madau 2012), which is consistent with our measurements.

Recently, Faisst (2016) inferred that f_{esc} may evolve with redshift by combining a relation between f_{esc} and the [O III]/[O II] ratio with the inferred redshift evolution of the [O III]/[O II] ratio. This redshift evolution is estimated from local analogs to high redshift galaxies selected on Hα EW, such that the redshift evolution of f_{esc} is implicitly coupled to the evolution of Hα EW as in our model of $\xi_{ion}(z)$. Faisst (2016) estimate that f_{esc} evolves from ≈ 2 % at $z = 2$ to ≈ 5 % at $z = 5$, which is consistent with our measurements of $\langle f_{esc} \rangle$ (see Fig. 8.4). With this evolving escape fraction, galaxies can provide sufficient amounts of photons to reionize the Universe, consistent with the most recent CMB constraints Planck Collaboration et al. (2016b). This calculation assumes $\xi_{ion} = 10^{25.4}$ Hz erg^{-1}, which is the same value our model predicts for ξ_{ion} in the reionization era.

In addition to understanding whether galaxies have reionized the Universe, it is perhaps more interesting to understand which galaxies have been the most important to do so. For example, Sharma et al. (2016) argue that the distribution of escape fractions in galaxies is likely very bimodal and dependent on the SFR surface density, which could mean that LyC photons preferentially escape from bright galaxies. Such a scenario may agree better with a late and rapid reionization process such as favoured by the new low optical depth measurement from Planck Collaboration et al. (2016b). We note that the apparent discrepancy between the f_{esc} upper limit from median stacking ($f_{esc} < 2.8$ %) and the average f_{esc} from the integrated luminosity density combined with IGM constraints ($\langle f_{esc} \rangle = 5.9$ %) can be understood in a scenario where the average f_{esc} is driven by a few galaxies with high f_{esc}, or by a scenario where f_{esc} is higher for galaxies below the Hα detection threshold (which corresponds to SFR> 4 M$_\odot$ yr^{-1}), contrarily to a scenario where each typical HAE has an escape fraction of $\approx 5 - 6$ %.

Dijkstra et al. (2016b) argue a connection between the escape of Lyα photons and LyC photons, such that LAEs could potentially be important contributors to the photon budget in the reionization era (particularly since we find that ξ_{ion} is higher for LAEs than for more normal star-forming galaxies at $z = 2.2$). Hence,

LAEs may have been important contributors of the photons that reionized the Universe.

To make progress we need a detailed understanding of the physical processes which drive f_{esc}, for which a significant sample of directly detected LyC leakers at a range of redshifts and galaxy properties is required. It is challenging to measure f_{esc} directly at $z > 3$ (and practically impossible at $z > 5$) due to the increasing optical depth of the IGM with redshift, such that indirect methods to estimate f_{esc} may be more successful (e.g. Jones et al., 2013; Zackrisson et al., 2013; Verhamme et al., 2015). However, the validity of these methods remains to be evaluated (i.e. Vasei et al., 2016).

8.8 Conclusions

We have studied the production and escape of ionizing photons (LyC, $\lambda_0 < 912$ Å) for a large sample of Hα selected galaxies at $z = 2.2$. Thanks to the joint coverage of the rest-frame LyC, UV and Hα (and, in some cases, Lyα), we have been able to reliably estimate the intrinsic LyC luminosity and the number of ionizing photons per unit UV luminosity (ξ_{ion}), for which we (indirectly) constrained the escape fraction of ionizing photons (f_{esc}). Our results are:

1. We have stacked the *NUV* thumbnails for all HAEs and subsets of galaxies in order to obtain constraints on f_{esc}. None of the stacks shows a direct detection of LyC flux, allowing us to place a median (mean) upper limit of $f_{esc} < 2.8 \,(6.4)$ % for the stack of star-forming HAEs (§8.4.3). A low escape fraction validates our method to estimate ξ_{ion}, the production efficiency of ionizing photons.

2. Combining the IGM emissivity measurements from Becker & Bolton (2013) with the integrated Hα luminosity function from Sobral et al. (2013) at $z = 2.2$, we find a globally averaged $\langle f_{esc} \rangle = 5.9^{+14.5}_{-4.2}$ % at $z = 2.2$ (§8.5), where the errors include conservative estimates of the systematic uncertainties. Combined with recent estimates of the QSO emissivity at $z \approx 2.2$, we can not fully rule out a non-zero contribution from star-forming galaxies to the ionizing emissivity. We speculate that the apparent discrepancy between the f_{esc} upper limit from median stacking and $\langle f_{esc} \rangle$ can be understood in a scenario where the average f_{esc} is driven by a few galaxies with high f_{esc}, or by a scenario where f_{esc} is higher for galaxies below the Hα detection threshold (SFR> 4 M$_\odot$ yr^{-1}).

3. Applying a similar analysis to published data at $z \approx 4 - 5$ results in a relatively constant f_{esc} with redshift (see Table 8.2 and Fig. 8.4). We rule out $\langle f_{esc} \rangle > 20$ % at redshifts lower than $z \approx 5$. An additional contribution of ionizing photons from rare quasars strengthens this constraint.

4. We find that ξ_{ion} increases strongly with increasing sSFR and Hα EW and decreasing UV luminosity, independently on the dust correction method. We find no significant correlations between ξ_{ion} and SFR(Hα), β or M$_{star}$.

On average, LAEs have a higher ξ_{ion} than HAEs, a consequence of LAEs having typically bluer UV slopes, lower masses and lower values of $E(B - V)$ (§8.6) – properties which are typical for galaxies at the highest redshift.

5. The median ξ_{ion} of HAEs at $z = 2.2$ is $\xi_{ion} \approx 10^{24.77 \pm 0.04}$ Hz erg^{-1}, which is ≈ 0.4 dex lower than the typically assumed values in the reionization era or recent measurements at $z \sim 4 - 5$ (Bouwens et al., 2016), see Table 8.3. Only half of this difference is explained by the lower stellar mass and dust attenuation of the galaxies in the Bouwens et al. (2016) sample.

6. For LAEs at $z = 2.2$ we find a higher $\xi_{ion} = 10^{25.14 \pm 0.09}$ Hz erg^{-1}, already similar to the typical value assumed in the reionization era. This difference is driven by the fact that LAEs are typically less massive and bluer and thus have less dust than HAEs.

7. By combining our trend between ξ_{ion} and Hα EW with the redshift evolution of Hα EW, we find that ξ_{ion} increases with ≈ 0.2 dex between $z = 2.2$ and $z = 4 - 5$, resulting in perfect agreement with the results from Bouwens et al. (2016). Extrapolating this trend leads to a median value of $\xi_{ion} \approx 10^{25.4}$ Hz erg^{-1} at $z \sim 8$, slightly higher than the typically assumed value in the reionization epoch (§8.7), such that a relatively low global f$_{esc}$ (consistent with our global estimates at $z \approx 2 - 5$) would suffice to provide the photons to reionize the Universe.

Acknowledgments

Appendix A: Individual *NUV* detections

We search for individual galaxies possibly leaking LyC photons by matching our CLEAN galaxy sample with the public *GALEX* EM cleaned catalogue (e.g. Zamojski et al., 2007; Conseil et al., 2011), which is *U* band detected. In total, we find 19 matches between CLEAN HAEs and *GALEX* sources with $NUV < 26$ within $1''$ (33 matches when using all HAEs), and 9 matches between LAEs and *GALEX* sources (four out of these 9 are also in the HAE sample and we will discuss these as HAEs). By visual inspection of the *HST*/ACS F814W and CFHT/*U* band imaging, we mark 8/19 HAEs and 2/5 LAEs as reliable *NUV* detections. The 14 matches that we discarded were either unreliable detections in *NUV* (9 times, caused by local variations in the depth, such that the detections are at 2σ level) or a fake source in *NUV* (5 times, caused by artefacts of bright objects). We note however that in most of the remaining 10 *NUV* detections (8 HAEs, 2 LAEs) the *NUV* photometry is blended with a source at a distance of $\approx 4''$, see Fig. 8.9.

In order to get a first order estimate of the contamination from neighbouring sources to the *NUV* flux, we perform the following simulation. First, we simulate the *NUV* flux of the candidate LyC leakers and all sources within $10''$ by placing Moffat flux distributions with the PSF-FWHM of *NUV* imaging and $\beta = 3$. These flux distributions are normalised by the *U* band magnitude of each source, since the catalog that we use to measure *NUV* imaging uses *U* band imaging as a prior. We then measure the fraction of the flux that is coming from neighbouring sources within an aperture with radius $0.67 \times$FWHM centred at the position of the *NUV* detection of the candidate LyC leaker. We find that contamination for most candidates is significant, and remove three candidates for which the estimated contamination is larger than > 50 %. The remaining candidates have contaminations ranging from 0-39 % and we subtract this contamination from the measured *NUV* flux when estimating their escape fractions. We estimate the uncertainty in our contamination estimate due to variations in the PSF and in the flux normalisation (due to $NUV - U$ colours) as follows: we first simulate the contamination with a gaussian PSF and Moffat PSFs with increasing β up to $\beta = 7$ and also by correcting the *U* band magnitude prior with the observed $U - B$ and $NUV - U$ colours. We then estimate the systematic uncertainty by measuring the standard deviation of the contamination rates estimated with the different simulations. For sources with little contamination, the systematic uncertainty in the contamination estimate is of the order 5 %.

We test whether the *NUV* detections for these sources could arise solely from flux at $\lambda_0 > 912$ Å in the far red wing of the *NUV* filter (see §8.3.2). For each galaxy, we obtain the best-fit STARBURST99 model by matching the Hα EW, as Hα EW is most strongly related to the SED shape around 900 Å. We redshift this model to a redshift of 2.22 and normalise the SED to reproduce the *V* band magnitude (we assume zero dust attenuation, which is a conservative assumption for this analysis, see below) and convolve the model with the mean IGM transmission at $z = 2.22$. Then, we measure the predicted *NUV* magnitude in the case that the flux is only non-zero at $\lambda_0 > 912$ Å. We find that, in all

cases, this magnitude is too faint to explain the NUV detections, ranging from $NUV = 30.1 - 32.5$, well below the detection limits. In the presence of dust, the attenuation at $\lambda \sim 912 - 930$ Å is stronger than at $\lambda \sim 1600$ Å (e.g. Reddy et al., 2016), such that the predicted NUV magnitude would be even fainter. We test the robustness of this estimate by varying the SED models (lowering the Hα EWs), neglecting the IGM absorption or by perturbing the redshift between $z = 2.20 - 2.24$, but find that this changes the result only by up to 1 magnitude if all effects are combined. For ID 1139 and 7801 we also test simple AGN power-law models ($f_\lambda \propto \lambda^\beta$) with UV slopes ranging from -2.0 to -2.7, but find that pure non-ionizing flux can not explain the NUV photometry. Therefore, it is unlikely that the NUV detections arise purely from flux at $\lambda_0 > 912$ Å, just because the filter transmission at these wavelengths is very low, and the wavelength range constitutes only a fraction of the full filter width.

For the five candidate LyC leakers with Hα measurements, we measure escape fractions ranging from $\approx 35 - 46$ %, see Table. 8.5, although we note that these escape fractions are still uncertain due to i) possible underestimated foreground contamination from sources not detected in U (or not detected as individual source due to blending) or with very blue $NUV - U$ colours, ii) uncertain dust attenuation of the Hα luminosity, iii) underestimated contribution from flux at $\lambda_0 > 912$ Å due to different SED shapes than expected or (photometric) redshift errors. Observations with higher spatial resolution and detailed spectroscopy are required in order to confirm whether these 7 candidates are really leaking LyC photons and at what rate.

Four isolated LyC leaker candidates (including two LAEs) are X-Ray AGN, and all have been spectroscopically confirmed at $z = 2.2$ (Lilly et al., 2009; Civano et al., 2012). HiZELS-ID 1993 is detected in two other narrow-bands than the Hα narrow-band: Lyα (EW$_{0,\mathrm{Ly}\alpha} = 67$ Å) and [OIII] (EW$_{0,\mathrm{[OIII]}} > 100$ Å), and is thus known to be at $z = 2.22 \pm 0.01$ robustly. ID 1872 and 2258 are selected as HAE at $z = 2.2$ based on their photometry (see Sobral et al. 2013), such that it is possible that they are interlopers (with the second most likely emission-line being [OIII] at $z \sim 3.3$, but other rarer possibilities such as Paschen series lines at $z < 1$). We show thumbnail images of our candidate LyC leakers in the NUV, $F814W$ and U bands in Fig. 8.9 and Fig. 8.10.

Appendix B: Redshift evolution of ξ_{ion} with different dust corrections

In Fig. 8.11 we show the inferred redshift evolution of ξ_{ion} when we apply different methods to correct ξ_{ion} for dust. Most of the differences are caused by a varying normalisation of ξ_{ion}, since we find that the slope of the fit between ξ_{ion} and Hα EW varies only mildly for various dust correction methods, see Table 8.4. However, we note again that most independent (stacking) observations from Balmer decrements and *Herschel* prefer dust attenuations similar to the dust attenuation we use when correcting for dust with stellar mass.

Table 8.5: Candidate LyC leakers among the HAE/LAE sample. ID numbers of HAEs refer to the IDs in the HiZELS catalog (Sobral et al. 2013). IDs indicated with a * are X-Ray AGN. The coordinates correspond to the peak of Hα/Lyα emission. The redshift is either spectroscopic (^{s}), photometric (^{p}) or from a dual-narrow band emission-line confirmation (^{d}). The *NUV* contamination fraction is estimated as described in the text. f$_{esc}$ is corrected for contamination from nearby sources to the *NUV* flux. Because of the absence of Hα measurements for LAEs, we do not estimate the SFR(Hα) or f$_{esc}$.

ID	R.A. (J2000)	Dec. (J2000)	Redshift	M$_{star}$ $\log_{10}$(M$_\odot$)	SFR(Hα) M$_\odot$ yr^{-1}	M$_{1500}$ mag	NUV mag	NUV contamination	f$_{esc}$ %
1139*	10:00:55.39	+01:59:55.39	2.219^s	10.1	34.8	-21.6	25.9	0.0	30
1872	10:01:56.39	+02:17:36.65	2.22±0.02^p	9.4	9.2	-21.0	25.7	0.14	43
1993	10:02:08.70	+02:21:19.88	2.22±0.01^d	9.6	8.2	-21.3	24.6	0.39	45
2258	10:01:29.69	+02:24:28.50	2.22±0.02^p	10.3	7.3	-21.0	25.1	0.21	43
7801*	10:02:08.55	+01:45:53.60	2.215^s	10.4	43.3	-23.5	24.9	0.05	37
C8*	09:59:34.82	+02:02:49.94	2.182^s	10.9		-22.5	24.6	0.03	
C10*	09:59:05.14	+02:15:29.86	2.222^s	10.6		-23.5	23.7	0.03	
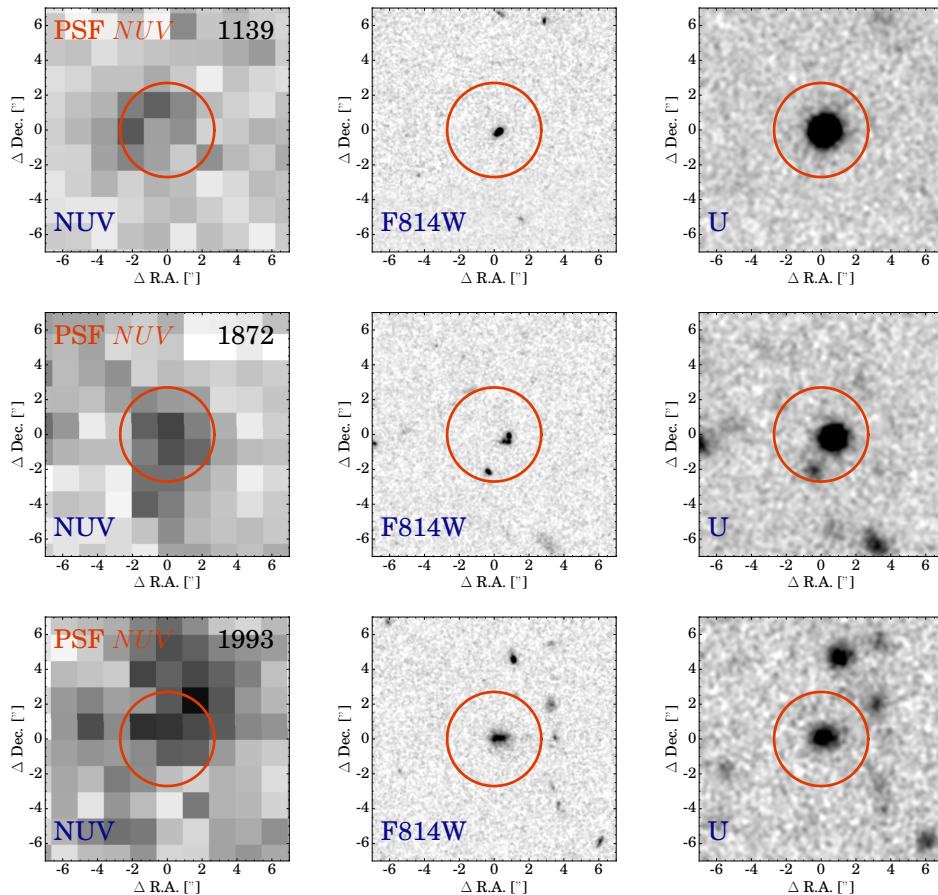
**Figure 8.9:** $15 \times 15''$ thumbnail images in *NUV*, *F814W* and *U* of candidate LyC leaking Hα and Lyα emitters at $z = 2.2$, centered on the positions of the HAE/LAE. The images are annotated with the IDs of the galaxies in the HiZELS catalogue (Sobral et al. 2013). Lyα emitters are identified with a "C". IDs 1139, 1993 and 7801 are detected in both Hα and Lyα. IDs 1139, 7801, C-8 and C-10 are X-ray AGN. All other sources than the central source seen in thumbnails have photometric redshifts of < 1.5.
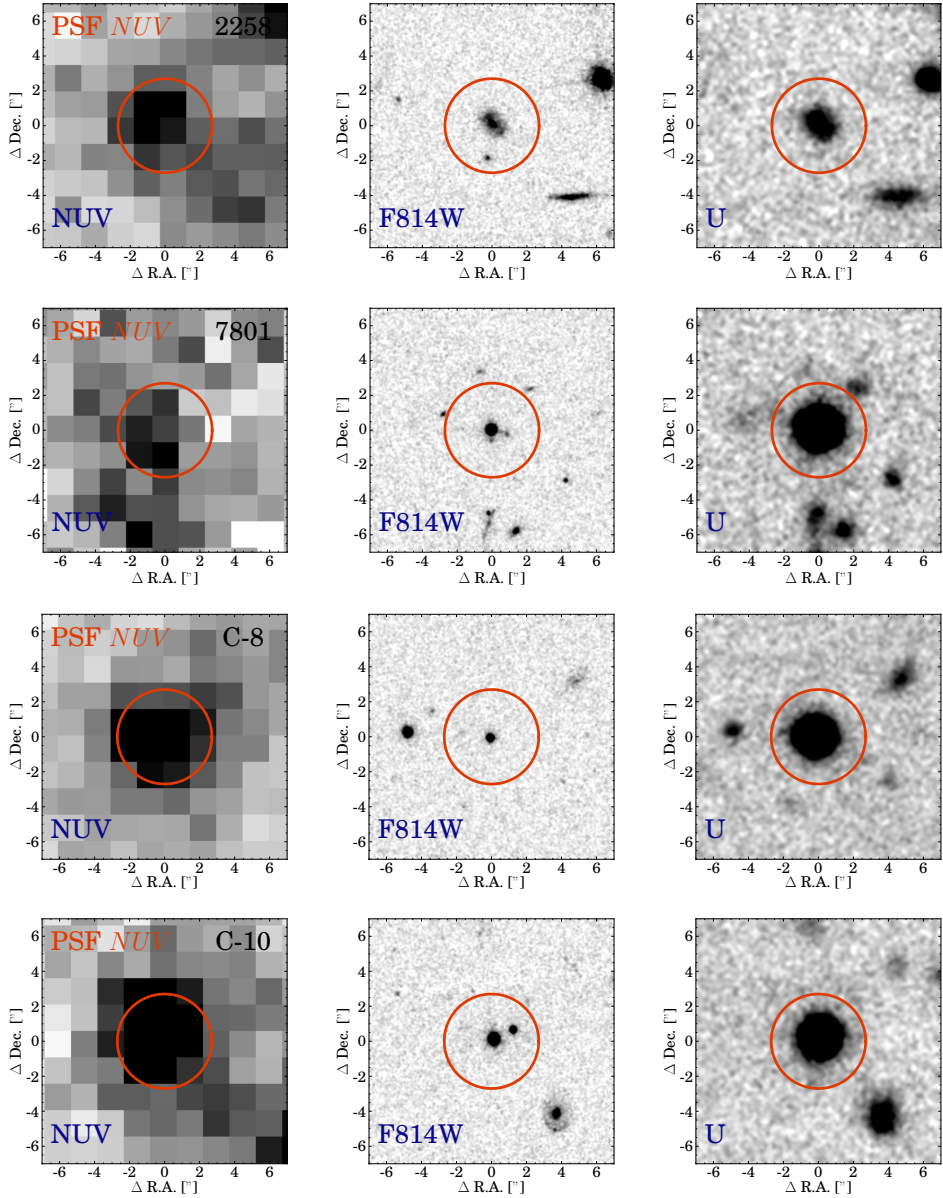
Figure 8.10: Continued from Fig. 8.9.
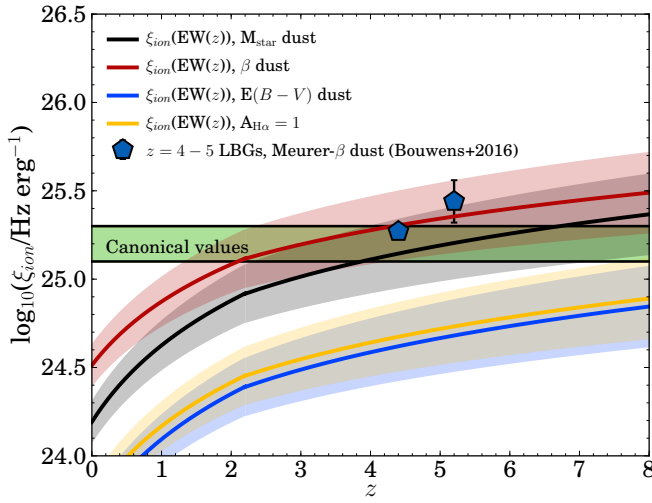
Figure 8.11: Inferred evolution of ξ_{ion} with redshift based on the EW(Hα) evolution from Faisst et al. (2016) and our observed trend between ξ_{ion} and Hα EW for HAEs with $M_{star} \sim 10^{9.2}$ $M_\odot$, for different methods to correct for dust. The black line shows the results when correcting for dust with M_{star}, the red line shows dust corrected with β, the blue line shows dust corrected with the E($B - V$) values from SED fitting and the yellow line shows the results when we apply a global correction of $A_{H\alpha} = 1$. The shaded regions indicate the errors on the redshift evolution of ξ_{ion}.

CHAPTER 9

Boötes-HiZELS: an optical to near-infrared survey of emission-line galaxies at $z = 0.4 - 4.7$

We present a sample of ~ 1000 emission line galaxies at $z = 0.4 - 4.7$ from the $\sim 0.7 \deg^2$ High-z Emission Line Survey (HiZELS) in the Boötes field identified with a suite of six narrow-band filters at $\approx 0.4 - 2.1$ μm. These galaxies have been selected on their Lyα (73), [OII] (285), Hβ/[OIII] (387) or Hα (362) emission-line, and have been classified with optical to near-infrared colours. A subsample of 98 sources have reliable redshifts from multiple narrow-band (e.g. [OII]-Hα) detections and/or spectroscopy. In this survey paper, we present the observations, selection and catalogs of emitters. We measure number densities of Lyα, [OII], Hβ/[OIII] and Hα and confirm strong luminosity evolution in star-forming galaxies from $z \sim 0.4$ to ~ 5, in agreement with previous results. To demonstrate the usefulness of dual-line emitters, we use the sample of dual [OII]-Hα emitters to measure the observed [OII]/Hα ratio at $z = 1.47$. The observed [OII]/Hα ratio increases significantly from 0.40±0.01 at $z = 0.1$ to 0.52±0.05 at $z = 1.47$, which we attribute to either decreasing dust attenuation with redshift, or due to a bias in the (typically) fiber-measurements in the local Universe which only measure the central kpc regions. At the bright end, we find that both the Hα and Lyα number densities at $z \approx 2.2$ deviate significantly from a Schechter form, following a power-law. We show that this is driven entirely by an increasing X-ray/AGN fraction with line-luminosity, which reaches ≈ 100 % at line-luminosities $L \gtrsim 3 \times 10^{44}$ erg s^{-1}.

Matthee, Sobral, Best, Smail, Bian, Darvish, Röttgering and Fan

9.1   Introduction

Understanding how and when galaxies grow their stellar mass and in some cases eventually stop forming stars are key goals of galaxy formation theory. However, since it is only possible to observe an individual galaxy at a single epoch, to assess their evolution it is crucial to homogeneously select equivalent samples of galaxies over a wide redshift range. Currently, different epochs in cosmic time are probed by different selections of galaxies. Moreover, the galaxy properties (such as star formation rates and estimates of dust attenuation) are measured with different tracers (e.g. Speagle et al., 2014). Therefore, it is important to understand whether local calibrations can be extrapolated to high redshift. This requires large samples of galaxies with a well understood selection function and a large dynamic range in galaxy properties.

Homogeneously selected samples of star-forming galaxies can be obtained with narrow-band (NB) surveys, that are very efficient in selecting emission-line galaxies. Using different NBs, galaxies can be selected on a particular emission-line across a range of redshifts with well defined line-luminosity and equivalent width limits. For example, in specific windows from the optical to the near-infrared, ground-based NB surveys can select $H\alpha_{\lambda6563}$ emission-line galaxies up to $z \sim 2.6$ (e.g. Bunker et al., 1995; Malkan et al., 1996; van der Werf et al., 2000; Ly et al., 2007; Geach et al., 2008; Tadaki et al., 2011; Lee et al., 2012; Drake et al., 2013; Sobral et al., 2013, 2015a; Stroe & Sobral, 2015). The $H\alpha$ recombination-line is a reliable tracer of star-formation rate on > 10 Myr time-scales (Kennicutt, 1998), and is less sensitive to attenuation due to dust than other shorter wave-length tracers (e.g. Garn et al., 2010; Ibar et al., 2013; Stott et al., 2013). At redshifts $z > 2.5$, the most commonly used rest-optical emission-lines are challenging to observe (but see e.g. Khostovan et al. 2015), while the rest-frame UV Lyman-$\alpha_{\lambda1216}$ (Lyα) line, intrinsically the strongest emission-line emitted in HII regions, is efficiently observed up to $z \sim 7$ (e.g. Rhoads et al., 2000; Dawson et al., 2007; Ouchi et al., 2008; Lee et al., 2014; Matthee et al., 2015; Santos et al., 2016), but is extremely sensitive to resonant scattering and dust attenuation (e.g. Hayes, 2015).

Our High-z Emission Line Survey (HiZELS, Geach et al. 2008; Best et al. 2013; Sobral et al. 2013) has been designed to observe multiple emission-lines in different NBs simultaneously. Hence, Sobral et al. (2012) used observations with NB921 at ≈ 920 nm and NB_H at ≈ 1620 nm to jointly observe [OII]$_{\lambda\lambda3726,3729}$ and $H\alpha$ at $z = 1.47$. At $z = 2.2$, matched NB surveys have observed (combinations of) Lyα+[OII]+[OIII]$_{\lambda\lambda4959,5007}$+$H\alpha$ at $z = 2.2$ (Lee et al., 2012; Nakajima et al., 2012; Oteo et al., 2015; Matthee et al., 2016; Sobral et al., 2017). One of the advantages of this dual (or multiple) NB technique is that identification of the specific emission-line is secure, such that dual-emitters may be used to fine-tune colour selection criteria (in particular in fields where only limited multi-wavelength data are available). Another advantage is that various SFR estimators, for example [OII] or (to lesser extent) Lyα, can be calibrated with joint $H\alpha$ observations.

Here we present the first results from Boötes-HiZELS, which is a survey of a central 0.7 deg^2 region in the Boötes field with a suite of six narrow-band filters,

split into two sets: three red filters at ≈921, 1620 and 2120 nm from HiZELS that select rest-optical lines such as Hα[1], Hβ/[OIII][2] and [OII], complemented by three blue filters at ≈ 392, 411 and 501 nm that select Lyα emitters. Using these narrow-band filters, we select samples of emission-line galaxies using their Hα line at $z = 0.4 - 2.2$, and from $z = 0.8 - 4.7$ with Hβ/[OIII], [OII] and Lyα. These samples are used as targets for ongoing detailed spectroscopic follow-up studies.

This paper presents the selection and classification of line-emitters, their global properties such as number densities, the number of dual-NB emitters and X-ray detections. We compare our number densities to published luminosity functions for samples in the range $z \approx 0.4 - 4.7$ and we study [OII]-Hα emitters at $z = 1.47$. These emitters can be used to measure whether the observed [OII]/Hα ratio changes with redshift (e.g. Hayashi et al., 2013), which is essential for studies employing [OII] as a SFR indicator at $z > 1$ (e.g. Ly et al., 2012). We also use the available deep X-ray coverage to study the X-ray fractions of line-emitters.

We present the observations and archival data used in this survey in §9.2. The data reduction, characteristics and catalog production and selection of emitters are presented in §9.3. §9.4 presents our procedure for classifying emission-line galaxies. We present the number densities of classed line-emitters and compare these to published luminosity functions in §9.5. In §9.6 we investigate the properties of dual-NB line-emitters, the observed [OII]/Hα ratio at $z = 1.47$ and the X-ray fractions of HAEs and LAEs. Finally, §9.7 presents our conclusions.

We adopt a ΛCDM cosmology with $H_0 = 70$ km s^{-1}Mpc^{-1}, $\Omega_M = 0.3$ and $\Omega_\Lambda = 0.7$. Magnitudes are in the AB system measured in 3″ apertures, unless noted otherwise.

9.2   Observations & data

We observed a 0.7 deg^2 region in the Boötes field with six narrow-band filters (NB392, stV, NB501, NB921, NB$_H$ and NB$_K$). The Boötes field was chosen for the availability of deep multi-wavelength data (see e.g. Lee et al. 2011; Bian et al. 2012, 2013; Beare et al. 2015) over a relatively large area, avoiding the galactic plane and its observability from La Palma and Hawaii. In addition to publicly available broad-band (BB) imaging in the *U*, *B*, *R*, *I*, *J* and *K* bands (described in §9.2.1), we also obtain the missing wavelength coverage with three broad-band filters *g*, *z* and *H* (see Table 9.1 for an overview).

---

[1] We note that narrow-band Hα measurements measure the line-flux and EW of the combined Hα and [NII] doublet depending on the precise redshift. Therefore, a correction needs to be applied to measured Hα EWs and line-fluxes. For simplicity, we refer to Hα+[NII] emitters as Hα emitters from now on.

[2] Typical photometric redshifts are not accurate enough to distinguish between Hβ line-emitters and a line-emitter with one of the [OIII] lines. Moreover, depending on the specific redshift, we either detect Hβ, or one or two of the [OIII] lines in the narrow-band filter. The majority of Hβ/[OIII] emitters are [OIII]$_{\lambda 5007}$ emitters, as this line is typically the stronger line; see Sobral et al. (2015a) and Khostovan et al. (2015) for details. Yet, to remind the reader of these caveats, we call these emitters Hβ/[OIII] emitters throughout the paper.

9.2.1   Public/archival multi-wavelength data

The Boötes field has been imaged in the optical by the NOAO Deep Wide Field survey[3] in *Bw*, *R* and *I* (Jannuzi & Dey, 1999) and by the LBT Bootes Field Survey in the *U* and *Y* bands (Bian et al., 2013). Near-infrared data in the *J*, *H* and *Ks* band are available from the Infrared Bootes Imaging Survey (Gonzalez et al., 2010), although we do not use the *H* band data as our data are deeper. The general characteristics of the archival data used in this paper are listed in Table 9.1. In addition, the field has been imaged in the X-ray by *Chandra* (Murray et al., 2005), in the UV by the *GALEX* Deep Imaging Survey (Martin et al., 2005), in the mid-infrared by *Spitzer*/IRAC (Ashby et al., 2009) and in the far-infrared by *Herschel* as part of the *Herschel* Multi-tiered Extragalactic Survey (Oliver et al., 2012). However, the X-Ray, UV and mid- and far-infrared data are not explicitly used in the selection of line-emitters. In addition, Williams et al. (2016) presented deep low-frequency (150 MHz) radio observations in this field. Finally, spectroscopic follow-up of mostly X-ray selected sources (and hence AGN) has been performed by Kochanek et al. (2012).

9.2.2   Optical observations

Optical observations in two narrow-band filters (NB392, NB501), a medium band filter (stV) and the *g* band were performed with the Wide Field Camera (WFC) on the 2.5m Isaac Newton Telescope, part of the Roque de los Muchachos Observatory on the island of La Palma, Spain. WFC has a mosaic of 4 CCDs with a combined field of view of 0.3 $\deg^2$ and a 0.33″ pixel scale, see Table 9.1. The survey was designed with four pointings, each with a C-NE-NW-SE-SW dither pattern (with 30″ offsets). Individual exposure times for narrow and medium-bands were either 0.2 or 1.0ks, depending on whether the telescope could successfully guide on a star (since the auto-guider CCD is behind the filter, this is challenging for narrow-band filters in extra-galactic fields) and the stability of the weather. The individual exposure times for the *g* band were 0.6ks.

Observations in the NB921 narrow-band filter and the *z* filter were performed with Suprime-Cam (S-cam) on the 8.0m Subaru telescope of the National Astronomical Observatory of Japan. S-cam consists of a mosaic of 10 CCDs with a combined field of view of 0.255 $\deg^2$ with a 0.2″ pixel scale. We imaged the field with the *z* (NB921) filter with five (three) pointings. For NB921, we used individual 360s exposures dithered either 7 (2 pointings) or 6 (1 pointing) times. For *z*, we used individual 150s exposures of the same pointings as NB921 dithered 14 times, and 3 times 100s in the other two pointings. Observations were done sequentially to avoid contamination of the emission-line sample by variable sources and/or supernova (i.e. Matthee et al., 2014).

---

[3] http://noao.edu/noao/noaodeep/

Table 9.1: Description of the available (archival and new) multi-wavelength data in Boötes-HiZELS, with narrow-band filters highlighted in bold. The abbreviations for the archival surveys are: LBFS – LBT Boötes Field Survey (Bian et al., 2013); NDWFS – NOAO Deep Wide Field Survey (Jannuzi & Dey, 1999); IBIS – Infrared Boötes Imaging Survey (Gonzalez et al., 2010). λ_c is the central wavelength of the filter and $\Delta\lambda$ is the width between the full width half maxima of the filter transmission. The full width half maximum (FWHM) of the point spread function has been measured as described in §9.2.2. We list the total exposure time per pixel and its variance. For NB921 and z, 60 % of the coverage has the highest exposure time listed. Depths are measured by measuring the sky value in 100,000 3$''$ apertures on blank regions in the images as described in §9.3.2. The coverage is after masking each individual filter for uncovered regions or regions with insufficient depth.

Filter	Telescope	Survey	λ_c [nm]	$\Delta\lambda$ [nm]	FWHM ['']	Exposure time [ks]	Dates	Depth [3σ, AB]	Coverage [deg^2]
U	LBT	LBFS	359	54	1.2			25.3	0.78
NB392	INT	This survey	392	5.2	1.8	12.4±2.0	2013 Jun 6-10; 2014 Feb 27, Mar 1-8,27	24.3	0.54
B_W	Mayall	NDWFS	464	110	1.4			25.4	0.78
stV	INT	This survey	410	16	1.9	3.8±0.8	2013 Jun 6-10; 2014 Mar 2, 5-7; 2016 Jun 11-13	24.1	0.63
g	INT	This survey	485	129	1.6	6.0±0.0	2016 Jun 6-8	24.9	0.78
NB501	INT	This survey	501	10	1.6	8.4±0.1	2015 Apr 11, 12, 16, 17; 2016 Jun 5, 6, 7, 10, 12	24.7	0.74
R	Mayall	NDWFS	602	160	1.1			25.0	0.78
I	Mayall	NDWFS	754	170	1.1			24.4	0.78
z	Subaru	This survey	878	113	0.8	1.0-2.1	2014 May 28, 29	24.3	0.76
NB921	Subaru	This survey	919	13	0.8	2.16-2.52	2014 May 28, 29	24.0	0.46
Y	LBT	LBFS	984	42	0.8			23.1	0.78
J	NEWFIRM	IBIS	1300	190	1.0			22.9	0.78
H	UKIRT	This survey	1600	200	0.8	1.2±0.1	2010 April 2-8	22.6	0.78
NB$_H$	UKIRT	This survey	1620	21	0.8	15.4±1.4	2010 April 2-6	22.1	0.74
K	NEWFIRM	IBIS	2260	280	1.2			22.1	0.78
NB$_K$	UKIRT	This survey	2120	21	1.2	20.2±0.0	2010 April 8, 9, 14, July 18-23; 2011 Feb 16, 27, 28, Mar 9, 12, 16, 20, 22-26	22.3	0.73

9.2.3   Near-infrared observations

Near-infrared observations in H, NB_H and NB_K were performed with WFCAM on the UK Infrared Telescope (UKIRT) on Mauna Kea as part of the High-z Emission Line Survey (HiZELS, e.g. Sobral et al. 2013). WFCAM has a "paw-print" configuration of four CCDs, with a total field of view of 0.21 deg^2 and a 0.4″ pixel scale. The field was imaged with 4 pointings in a dither sequence of 14 exposures with small offsets. Due to the high sky background in the near-infrared, the individual exposure times were 10s, 100s, and 60s for H, NB_H and NB_K, respectively, to avoid saturation. In order to obtain the final depth, this dither sequence was typically repeated 9, 11 and 24 times for the respective filters.

9.3   Data reduction & Catalogue production

9.3.1   Data reduction

Optical

We reduce data from the INT/WFC with a custom-made pipeline based on PYTHON described in detail in Stroe et al. (2014) and Sobral et al. (2017) and we reduce Subaru/S-Cam data similarly with SDFRED2 (Ouchi et al., 2004). In summary, we first bias subtract individual frames using a master bias from the median stack of bias frames for the corresponding night. We then create a master flat by median combining twilight flats and use it to flat-field the individual frames. Subsequently, we measure the FWHM of the PSF using unsaturated stars in individually reduced frames with SEXTRACTOR (Bertin & Arnouts, 1996), and reject frames with PSF FWHM above the chosen target FWHM listed in Table 9.1. This is particularly important for some exposures with the INT/WFC that have been observed in poor conditions. We then match the PSF of remaining frames before combining frames to the common mosaic by smoothing the images with a gaussian kernel.

Near-infrared

Near-infrared data from UKIRT/WFCAM have been reduced using PfHiZELS; see Sobral et al. (2009a) and Sobral et al. (2013) for full details. The steps are similar to the steps in the optical data reduction, except for dark subtraction instead of bias subtraction and the master flat that is based on an iterative self-flat method using the science frames themselves, instead of relying on twilight flats; see Sobral et al. (2013).

Astrometric alignment

The reduced frames are astrometrically registered to the 2MASS point source catalog (Skrutskie et al., 2006) with SCAMP (Bertin, 2006). Frames are then co-added, resampled to a pixel-scale of 0.33″ and mapped to the MOSAIC pointing

with Swarp (Bertin, 2010). We apply the same method for public data described in §9.2.1.

While extracting initial catalogues, we encountered significant astrometric distortions of up to $1.2''$ in the edges of the cameras of the public B_w, R and I data. These distortions significantly affect dual-mode photometry (described below in §9.3.2). In order to obtain a more accurate astrometric solution for these data, we used the Scamp software to remap the images to the SDSS DR7 astrometry (Abazajian et al., 2009). The astrometric differences between 2MASS and SDSS are minimal and no significant distortions affecting our photometry have been noticed after this correction.

Photometric calibration

We set the photometric zero-point (ZP) of the images to an arbitrary common $ZP = 30$ by matching the Mag-auto photometry in the combined images to the following available data: g and z are calibrated to SDSS and H and K to 2MASS. We then use the broad-bands available to calibrate the narrow-bands in the two following steps: we first calibrated NB921 to z, NB_H and NB_K are calibrated to H and K, NB501 to g from SDSS, and NB392 and stV to Bw. After this first step, we have to correct for the fact that most narrow-band central wavelengths are not in the center wavelength of the broad-band filters, which leads to a bias in line-flux measurements due to gradients in the continuum. This can be resolved by using colour information in adjacent broad-bands. For NB921, NB_H and NB_K we follow the corrections described in Sobral et al. (2013) and for NB392 we use the corrections from Matthee et al. (2016). We derive the following correction for stV: $stV_{cor} = stV - 0.23(U - B_w) + 0.24$. For sources undetected in U and B_w we apply the median correction of $+0.04$. We do not apply a correction for NB501 as it is close to the center of the g band.

9.3.2 Catalogue production

Photometry

Photometry of the optical-NIR filters listed in Table 9.1 is performed with SExtractor in dual-image mode. We create six catalogues, each with one of the six narrow-bands as detection image. Photometry is measured within circular apertures with a diameter of $3''$. For each narrow-band we measure the narrow-band and the corresponding broadband magnitudes from images with their PSF matched to the narrow-band imaging. We also measure the magnitudes in all broad-bands with their PSF matched to the g band PSF ($1.6''$ FWHM). The measurements with the PSF from the NB are used to select line-emitters and compute emission-line properties such as line-flux and equivalent width. The other measurements are used for colour-colour selections.

We have produced a mask for each narrow-band individually, where we mask regions around bright, saturated stars, CCD bleeding, cross-talk in near-infrared detectors and regions with low S/N or incomplete coverage (e.g. Sobral et al., 2009a; Santos et al., 2016).

Depths

We estimate the depth of images by measuring the standard deviation of the total counts in 100,000 apertures with a diameter of $3''$ placed at random (but avoiding sources) locations in our images. 3σ depths range from ~ 25 AB magnitude in blue broad-band filters to ~ 22 AB magnitude in the near-infrared filters, see Table 9.1.

9.3.3 Selecting Line-emitters

Line-emitters are selected based on two criteria: the narrow-band excess (the equivalent width, EW) must be high enough and the excess must be significant. For the narrow-band filters NB392, stV, NB501, NB921, NB_H and NB_K we use the corresponding broad-band filters U, B_w, g, z, H and K, see Fig. 9.2. In order to convert the photometric narrow-band excess to observed EW, we convert magnitudes (m_i) to flux densities in each filter (f_i) with the standard AB magnitude convention:

$$f_i = \frac{c}{\lambda_{i,\text{center}}^2} 10^{-0.4(m_i+48.6)}, \tag{9.1}$$

where c is the speed of light and $\lambda_{i,\text{center}}$ is the central wavelength in each filter. Next, we use the following equations to convert the narrow-band and their corresponding broad-bands to EW:

$$EW_{\text{obs}} = \Delta\lambda_{\text{NB}} \frac{f_{\text{NB}} - f_{\text{BB}}}{f_{\text{BB}} - f_{\text{NB}}\frac{\Delta\lambda_{\text{NB}}}{\Delta\lambda_{\text{BB}}}}. \tag{9.2}$$

Here, f_{NB} and f_{BB} are the flux-densities in the narrow-band and broad-band and $\Delta\lambda_{\text{NB}}$ and $\Delta\lambda_{\text{BB}}$ the filter-widths. In Eq. 10.3, the numerator is the difference in narrow-band and broad-band flux and the denominator is the continuum level, corrected for the contribution from the flux in the narrow-band. For sources without broad-band detection we set the EW to a lower limit. This lower limit ranges from 550 Å for NB392 and NB501 to 2500 Å for stV depending on the width of the NB filter and the depth of the BB data used to measure the continuum. The lower limit is around ≈ 1200 Å for near-infrared NBs.

The excess significance (Σ) quantifies whether a certain narrow-band excess is due to errors in the narrow-band and broad-band photometry or not. Hence, we follow the methodology presented in Bunker et al. (1995) and the equation from Sobral et al. (2013) to compute Σ:

$$\Sigma = \frac{1 - 10^{-0.4(BB-NB)}}{10^{-0.4(ZP-NB)}\sqrt{(\sigma_{\text{box,BB}}^2 + \sigma_{\text{box,NB}}^2)}}, \tag{9.3}$$

where BB is the broadband magnitude used for the continuum estimate, NB is the narrow-band magnitude and ZP is the zero-point of the images. σ_{box} is the root mean squared (rms) of background aperture values in the data of the respective filters (see §9.3.2).
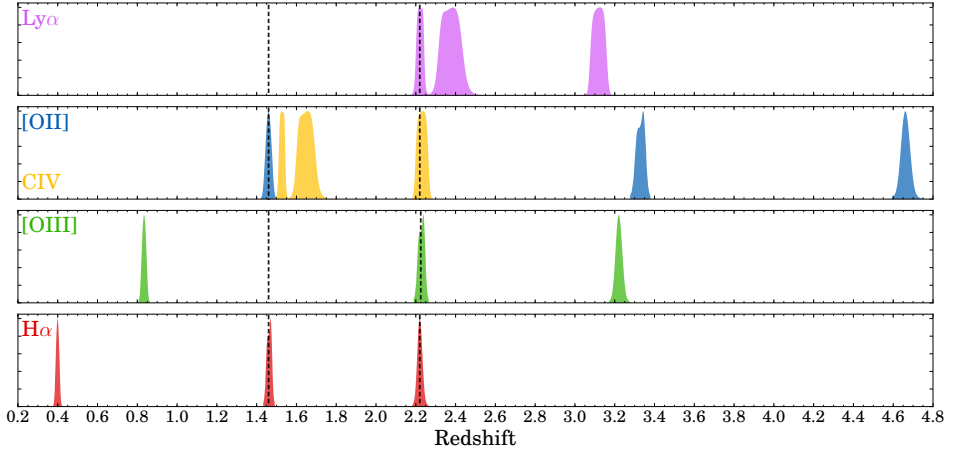
Figure 9.1: Redshift slices for different emission-lines probed by our Boötes-HiZELS survey. As highlighted by the dashed lines, there is joint coverage of [OII] and Hα at $z = 1.47$ and of Lyα, [OIII] and Hα at $z = 2.22$. By coincidence, there is also matched volume coverage of CIV at this redshift.

The line-flux is computed using:

$$f_{\text{line}} = \Delta\lambda_{\text{NB}} \frac{f_{\text{NB}} - f_{\text{BB}}}{1 - \frac{\Delta\lambda_{\text{NB}}}{\Delta\lambda_{\text{BB}}}}. \tag{9.4}$$

We select line-emitters among narrow-band selected sources in all six narrow-band filters with the criterion that $\Sigma > 3$. However, because each narrow-band has different filter characteristics, we do not apply a homogeneous excess (EW) selection threshold. For each filter, we apply the criterion that the observed EW is three times the standard scatter in observed EWs for sources detected at $> 15\sigma$. This means that we apply EW$> 30, 130, 50, 30, 85, 80$ Å for NB392, stV, NB501, NB921, NB_H and NB_K respectively.

Before obtaining our final list of line-emitters, in each filter, we visually inspect all the sources in the narrow-band images for remaining spurious sources such as artefacts from bright stars, cosmic rays or mis-identifications by SExtractor. This can happen when the noise properties vary strongly locally, which is the case in small regions of the coverage by the NB392, stV and NB921 filters.

9.4 Classifying line-emitters

Fig. 9.1 shows the redshift ranges where our narrow-band filters sample the brightest emission-lines seen in normal star-forming galaxies and AGN. By a combination of design and coincidence, the HiZELS narrow-band filters coincide with several different emission-lines at specific redshifts. At $z = 1.47$, the NB921/NB_H combination is sensitive to the [OII] and Hα lines (Sobral et al., 2012). At $z = 2.23$, the Lyα, [OIII] and Hα lines fall in the NB392/NB_H/NB_K

combination[4]. At $z = 2.23$, the NB501 filter is also sensitive to Civ emission. The redshifts of line-emitters detected in several narrow-bands (dual-emitters) can be estimated accurately and we refer to them as $z_{\mathrm{dual-NB}}$ in the remainder of this paper. As can be seen in Table 9.6, dual-emitters are found as faint as $I \approx 25$, three magnitudes fainter than typical available spectroscopic redshifts, which were mostly for X-ray selected sources.

Line-emitters that have no existing spectrosopic redshift or are not detected as dual-emitters are classified using colour-colour selections tuned to identify Lyman- and Balmer-breaks at various redshift intervals. For the blue narrow-bands, we use colour selections to identify Lyα-emitters. For the red filters we use colour selections to identify Hα emitters, Hβ/[Oiii] emitters and [Oii] emitters (see also similar selections in Sobral et al. 2013; Khostovan et al. 2015).

The main strategy to devise colour-criteria has been as follows: after removing stars (due to atmospheric features in the blue or the near-infrared, stars may be picked up with a narrow-band excess) using their uJK colours (e.g. Muzzin et al., 2013), we start with colour selections from the literature, which we slightly modify using the spectroscopically confirmed line-emitters and the dual-emitters. Colour-criteria are stated explicitly below and listed in Table 9.3. We summarise the number of emitters and classified line-emitters in Table 9.4.

Table 9.2: Spectroscopically and dual-NB confirmed emission-lines observed in narrow-band filters. We note that spectroscopic redshifts are highly biased towards AGN, and that the spectroscopic redshift distribution does not resemble the real redshift distribution, particularly for fainter line-emitters. Dual-NB redshifts are only available at $z = 1.47$ and $z = 2.23$, see Fig. 9.1.

Filter	Emission-line	Redshift	# z_{spec}	# z_{dualNB}
NB392	Mgii$_{\lambda 2798}$	0.39–0.41	8	-
	Ciii]$_{\lambda 1909}$	1.04–1.07	1	-
	Civ$_{\lambda 1549}$	1.51–1.55	2	-
	Lyα$_{\lambda 1216}$	2.20–2.24	2	5
stV	Mgii$_{\lambda 2798}$	0.42–0.50	1	-
	Ciii]$_{\lambda 1909}$	1.10–1.20	3	-
	Heii$_{\lambda 1640}$	1.44–1.56	1	-
	Civ$_{\lambda 1549}$	1.59–1.71	4	-
	Lyα$_{\lambda 1216}$	2.30–2.45	6	-
NB501	[Oii]$_{\lambda 3727}$	0.32–0.36	1	-
	Mgii$_{\lambda 2798}$	0.76–0.81	1	-
	Civ$_{\lambda 1549}$	2.19–2.27	1	3
	Lyα$_{\lambda 1216}$	3.06–3.17	5	-
NB921	Hα$_{\lambda 6563}$	0.39–0.41	5	-
	[Oiii]$_{\lambda\lambda 4959,5007}$	0.82–0.87	1	-
	[Oii]$_{\lambda 3727}$	1.44–1.48	0	20
	Mgii$_{\lambda 2798}$	2.25–2.31	1	3
NB$_{\mathrm{H}}$	Hα$_{\lambda 6563}$	1.44–1.48	6	21
	[Oiii]$_{\lambda\lambda 4959,5007}$	2.19–2.29	3	16
NB$_{\mathrm{K}}$	Hα$_{\lambda 6563}$	2.21–2.25	8	20

---

[4] In this case, it is certain that the emission-line in NB$_{\mathrm{H}}$ is [Oiii] and not Hβ.
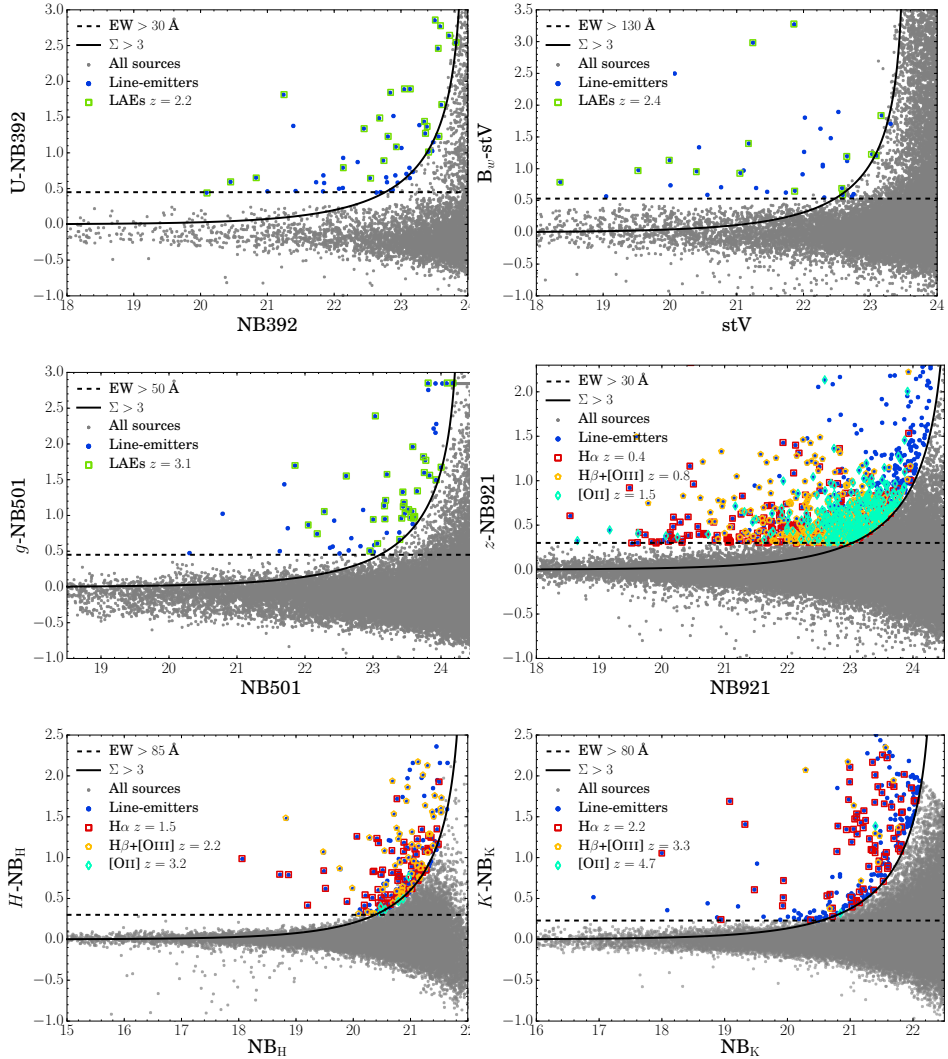
Figure 9.2: Narrow-band excess diagrams in NB392, stV, NB501,NB921, NB_H and NB_K. In grey we show all detected sources, while blue points are sources selected as line-emitters. The horizontal dashed line shows the imposed EW selection cut, while the solid line shows the excess significance criteria for the typical depth of the survey. In the three blue filters we mark Lyα selected sources with a green square. In the three red filters we mark Hα emitters with a red square, Hβ/[OIII] emitters with a yellow pentagon and [OII] emitters with a blue diamond.We note that we compute the excess significance locally, such that some sources may lie above the selection line, but are not selected as line-emitters because they are in shallower regions. It can be seen that LAEs detected in NB392 and NB501 are typically identified if a line-emitter has a high excess and faint magnitude (because most are likely faint star-forming galaxies with high EW), while this is not the case for LAEs identified in stV (which are typically bright AGN). In NB921 it can clearly be seen that most unidentified line-emitters are among the faintest magnitudes, and that there is a clear trend that higher redshift line-emitters are fainter and have higher observed EWs. In NB_H and NB_K Hα emitters and Hβ/[OIII] emitters have similar narrow-band magnitudes, but Hβ/[OIII] emitters tend to have higher excess because they are at higher redshift.

Table 9.3: Colour selection-criteria used to classify line-emitters. These criteria are based on the expected positions of the Lyman- and Balmer-breaks, see for example the *BzK* criterion from Daddi et al. (2004). These criteria are then fine-tuned using spectroscopic and dual-NB redshifts. In comparison to traditional criteria that use the *B* band, we adjust the B_w magnitude for the contribution from flux in the *U* band. For samples at $z > 2.4$, we also include a colour-criterion that removes very red objects for which the Lyman-break criterion has selected a strong Balmer break; see also Xue et al. (2017). The colour-colour selections are illustrated in the figures in Appendix 9.7.

Filter	Emission-line	Colour-criterion
NB392	Lyα $z = 2.2$	$(2B_w - U) - z < 0.2 + 0.7(z - K)$
stV	Lyα $z = 2.4$	$U - B_w > 0.3(B_w - g) + 0.2$ & $g - I < 1$
NB501	Lyα $z = 3.1$	$U - g > 1$ & $g - I < 1.5$
NB921	Hα $z = 0.40$	$(2B_w - U) - I > 0.4 + 0.4(Z - H)$
		$B_w - R > 1.3(R - I)$
	[OIII]/Hβ $z = 0.80$	$(2B_w - U) - I > 0.4 + 0.4(Z - H)$
		$B_w - R < 1.3(R - I)$
	[OII] $z = 1.47$	$(2B_w - U) - I < 0.4 + 0.4(Z - H)$
NB_H	$z > 1$	$(2B_w - U) - z < 0.4 + 0.8(z - K)$
		or $z - K > 2$
	Hα $z = 1.47$	$z > 1$ & $J - K < 2.1(I - J) - 1$
	[OIII]/Hβ $z = 2.23$	$z > 1$ & $J - K > 2.1(I - J) - 1$
	[OII] $z = 3.3$	Not Hα or [OIII]/Hβ in NB_H
		$U - g > 1$ & $g - I < 1.5$
NB_K	$z > 1$	$(2B_w - U) - z < (z - K) - 0.05$ or $z - K > 2$
	Hα $z = 2.23$	$z > 1$ & $U - R < 2$
	[OIII]/Hβ $z = 3.2$	$z > 1$ & $U - g > 1$ & $g - I < 1.5$
	[OII] $z = 4.7$	Not Hα or [OIII]/Hβ in NB_K & $g - I > 1.5$

9.4.1 Line-emitters in NB392

The narrow-band NB392 has specifically been designed to conduct a Lyα survey with a matched volume coverage to Hα emitters identified with the HiZELS NB_K filter (H₂S1) at $z = 2.23$ in order to study the Lyα escape fraction and its dependencies on galaxy properties, as described in detail in Matthee et al. (2016) and Sobral et al. (2017).

We select 57 line-emitters with an excess criterion of $EW_{obs} > 30$ Å (U-NB392 > 0.45). For LAEs at $z = 2.23$ this corresponds to $EW_0 > 9$ Å (it is possible to go to such low EWs because the width of NB392 is very narrow). Although Lyα surveys at $z \approx 2 - 3$ typically invoke a higher EW criterion of $\sim 25 - 30$ Å (e.g. Ouchi et al., 2008; Nakajima et al., 2012), we found that such a selection results in missing the most luminous LAEs at $z = 2.2$ in the COSMOS and UDS fields (Sobral et al., 2017). This is because these sources are typically AGN, which have bright Lyα emission on top of a bright UV continuum.

Using the spectroscopy available from AGES (Kochanek et al., 2012), we find 8 MgII emitters at $z = 0.4$ and 5 line-emitters at $z > 1$ (including two LAEs at $z = 2.2$), see Table 9.2. By matching the sample of line-emitters with the samples of line-emitters in NB_H and NB_K (see below), we add four other robust LAEs at $z = 2.2$. Other line-emitters are classed using the criteria described in Table

9.3. We spectroscopically identify four interlopers ($\approx 15 \pm 7$ % contamination, similar to the 10 ± 4 % from Sobral et al. 2017). These comprise two CIV emitters at $z = 1.53$ and two AGN for which we measure Lyman-Werner and Lyman-Continuum radiation in the NB392 filter at $z = 3.16$ and $z = 3.57$. We also identify two dual-emitters that are missed by the colour-colour selection (see Fig. 9.10). This results in a final sample of 25 LAEs at $z = 2.2$.

9.4.2   Line-emitters in stV

The stV medium-band filter is used to identify LAEs at $z \approx 2.4$. Because the width of the filter is relatively broad, it is sensitive to line-emitters over a larger redshift space (and thus covers a larger volume), at the cost of being only sensitive to lines with high EW. We apply a selection criterion of $EW_{obs} > 130$ Å (which corresponds to $B_w-\text{stV} > 0.54$). We note that due to the width of the filter, it is possible that multiple lines contribute to the observed EW and line-flux, such as the combination of Lyα+NV.[5] It is therefore not straightforward to interpret measured EWs and line-fluxes and caution must be taken.

   We find a total of 39 line-emitters, of which 15 have spectroscopic redshifts, see e.g. Table 9.2. As expected, these are dominated by LAEs at $z = 2.3 - 2.45$, but also contains high-ionization lines as CIII] and CIV at $z \approx 1.1 - 1.7$. After removal of one spectroscopic contaminant (a CIV emitter at $z = 1.613$) selected with the colour-criteria described in Table 9.3 and illustrated in Fig. 9.10), we obtain a sample of 16 LAEs.

9.4.3   Line-emitters in NB501

The NB501 filter is used to select Lyα emitters at $z = 3.1$. We apply $EW_{obs} > 50$ Å ($g-\text{NB501} > 0.45$), corresponding to a Lyα rest-frame EW of > 12 Å.

   We find a total of 65 line-emitters, of which only four have an archival spectroscopic redshift. This is because the majority of these line-emitters are faint with line-fluxes below 2×10^{-16} erg s^{-1} cm^{-2}. One spectroscopic confirmed line-emitter is a LAE, two are CIV emitters at $z = 2.24$ and $z = 2.26$ (these are the dual-emitters B-HiZELS_3 and B-HiZELS_15, Table 9.6, also detected as line-emitters in several other bands) and one is possibly [NeV] at $z = 0.426$.

   LAEs are selected as relatively blue U drop-outs (e.g. Hildebrandt et al., 2009) as described in Table 9.3 and illustrated in Fig. 9.11). One CIV emitter at $z = 2.24$ is mis-classed as a LAE and is removed from the sample. This leads to a sample of 31 LAEs. We note that our EW criterion of $EW_0 > 12$ Å is somewhat lower than the typical criterion used for selections of LAEs ($EW_0 > 25$Å, e.g. Ouchi et al. 2008; Yamada et al. 2012). However, more than 90 % of the identified LAEs have $EW_0 > 25$Å. Contrary to the properties of LAEs at $z \sim 2$, the additional LAEs with low EW are all faint in their UV continuum. This indicates an evolution in the properties of luminous LAEs from $z = 2 - 3$, with an increasing Lyα

---

[5] For example, for Type I AGN, NV/Lyα is typically ≈ 3 % (e.g. Vanden Berk et al., 2001), while for type II AGN (such as narrow-line Seyferts) NV/Lyα can be as high as 50 % (typically ≈ 20 %, e.g. Alexandroff et al. 2013).

EW_0 with redshift at fixed Lyα luminosity. Very recently, four additional LAEs from this sample have been confirmed at $z = 3.1$ from our spectroscopic follow-up campaign (to be presented in Sobral et al. in prep), including the brightest LAE in our sample with a Lyα luminosity of $\approx 10^{43.8}$ erg s^{-1} ($\sim 10 \times L^{\star}$ at $z = 3.1$, Ouchi et al. 2008) in a $3''$ aperture and an EW_0 of ~ 150 Å. To the current surface brightness limit, it is extended over $\sim 5''$ (40 kpc), and it may thus be classed a Lyα blob (e.g. Matsuda et al., 2004; Prescott et al., 2008; Dey et al., 2016). This follow-up spectroscopy also identifies two interlopers: a red [OII] emitter at $z = 0.35$ and a MgII emitter at $z = 0.81$, that we have removed from the sample.

9.4.4   Line-emitters in NB921

While the NB921 filter has been used to select LAEs at $z = 6.6$ (e.g. Matthee et al., 2015), it is also used to select Hα, Hβ/[OIII] and [OII] emitters at lower redshift (e.g. Ly et al., 2007; Drake et al., 2013; Sobral et al., 2013; Khostovan et al., 2015). We select 1161 line-emitters with the excess criterion of EW> 30 Å (corresponding to $z-$NB921> 0.3).

Since our sample of line-emitters is selected from relatively deep narrow-band imaging (compared to the other narrow-bands in this survey), it is dominated by sources with fluxes fainter than 2×10^{-16} erg s^{-1} cm^{-2} (> 94 % of line-emitters), down to fluxes of 2×10^{-17} erg s^{-1} cm^{-2}. Because of this, the number of spectroscopic redshifts is limited to only seven, of which five are Hα emitters at $z = 0.4$. However, the number of galaxies with a robust redshift due to emission-lines in multiple narrow-bands is significantly higher (23), see Table 9.2.

Among our sample of line-emitters, we use colour-criteria (Fig. 9.12; based on Sobral et al. 2013) to identify Hα emitters at $z = 0.40$, Hβ/[OIII] emitters at $z = 0.83$ and [OII] emitters at $z = 1.47$, see Table 9.3. We select 198 Hα emitters, 304 Hβ/[OIII] emitters and 277 [OII] emitters (see Table 9.4). Two MgII emitters at $z = 2.26$ are mis-identified as [OII] emitter, while one dual-emitter at $z = 1.47$ is mis-identified as Hβ/[OIII] emitters.

Due to their faintness, 359 out of the 1161 line-emitters are not detected in a sufficient number of broadbands required for classification and can thus not be classed. We expect that most of these sources are faint Hα, Hβ/[OIII] or [OII] emitters. Based on the fraction of emitters in different classifications as a function of line-flux, we expect an increasing fraction of [OII] emitters at low line-fluxes (see also Sobral et al. (2012)). As illustrated in the left panel of Fig. 9.3, the majority of sources indeed has $B_w - R$ colours similar to [OII] emitters (but could not be classed due to their faintness in other broadband filters). We discuss this 'identification-incompleteness' further in §9.5.1.

9.4.5   Line-emitters in NB$_H$

We select line-emitters detected in the NB$_H$ filter with a narrow-band excess of EW> 85 Å (corresponding to $H-$NB$_H > 0.3$). Since the near-infrared detectors

Table 9.4: Line-identifications of the total ~ 2000 emitters (as described in §9.4) in the Boötes-HiZELS narrow-band filters.

Filter	Sub-sample	# of sources
NB392	$\Sigma > 3$, EW> 30 Å	57
	Lyα at $z = 2.23$	25
stV	$\Sigma > 3$, EW> 130 Å	39
	Lyα at $z = 2.4$	16
NB501	$\Sigma > 3$, EW> 50 Å	65
	Lyα at $z = 3.1$	32
NB921	$\Sigma > 3$, EW> 30 Å	1161
	Hα at $z = 0.40$	198
	[OIII]/Hβ at $z = 0.8$	304
	[OII] at $z = 1.47$	277
NB$_H$	$\Sigma > 3$, EW> 85 Å	301
	Hα at $z = 1.47$	87
	[OIII]/Hβ at $z = 2.23$	72
	[OII] at $z = 3.3$	6
NB$_K$	$\Sigma > 3$, EW> 80 Å	255
	Hα at $z = 2.23$	77
	[OIII]/Hβ at $z = 3.2$	11
	[OII] at $z = 4.7$	2

of UKIRT/WFCAM contain significant amounts of crosstalk, we perform careful visual inspections of our sample of line-emitters, resulting in a sample of 301 line-emitters.

While the sample of line-emitters includes nine sources with spectroscopic redshifts (six Hα at $z = 1.4$ and three Hβ/[OIII] at $z = 2.2$), the NB$_H$ line-emitters are particularly suitable for identifying line-emitters with the dual-NB technique. These robustly identified line-emitters are used to adapt the colour selection criteria from Sobral et al. (2013) for the data available in this field. Using the criteria listed in Table 9.3, we select 87 Hα emitters at $z = 1.47$, 72 Hβ/[OIII] emitters at $z = 2.2$ and 6 [OII] emitters at $z = 3.3$, see Table 9.4. 99 sources are classed as low-redshift interlopers and 39 sources are too faint to be detected in the required broad-bands. Prior to the final identification, four spectroscopically confirmed Hβ/[OIII] emitters were classed as Hα emitters, while five Hα emitters were classed as Hβ/[OIII] emitter. These mis-identified emitters are typically very luminous and likely AGN, such that their colours are anomalous (see Fig. 9.13). There are no such identified contaminants among the fainter dual-emitters.

9.4.6 Line-emitters in NB$_K$

We select line-emitters detected in the NB$_K$ filter with EW> 80 Å (corresponding to $K-$NB$_K > 0.23$). In total, after visual inspections, we find 255 line-emitters, of which 18 have a spectroscopic redshift (including eight Hα at $z = 2.23$) and
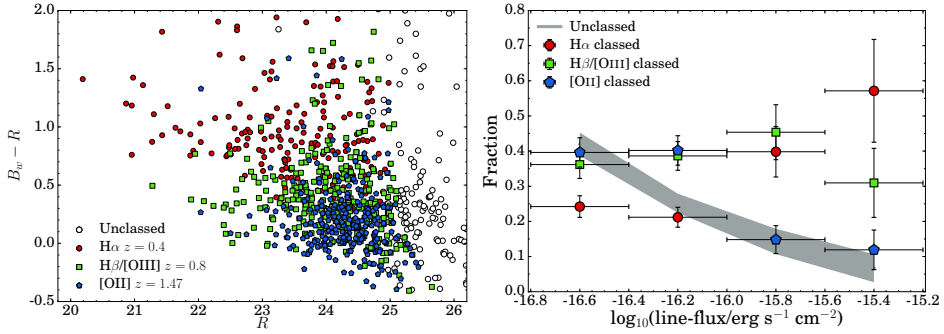
Figure 9.3: Left: $B_w - R$ versus R colour-magnitude diagram of line-emitters in NB921. This plot illustrates that the line-emitters that are not detected in enough broad-bands (such as I, z or H) in order to be classified, are typically faint ($R > 25.5$, note that these are low S/N detections) and lie most closely to the colour-magnitude parameter space probed filled with [OII] emitters. Right: The fraction of sources classed as Hα, Hβ/[OIII] and [OII] among the classed NB921 line-emitters in bins of line-flux. The grey shaded area shows the fraction of sources that is unclassed and its poissonian uncertainty. All emitters at higher line-fluxes are classed. These fractions are used to correct for identification incompleteness (§9.5.1).

20 are dual-emitters (all Hα at $z = 2.23$). Based on these robust redshifts and the colour selection criteria listed in Table 9.3, we select 77 Hα emitters at $z = 2.2$, 11 Hβ/[OIII] emitters at $z = 3.2$ and two [OII] emitters at $z = 4.7$ (see Table 9.4). 110 line-emitters are at $z < 1.5$ and 55 line-emitters are too faint to be classified. We have not identified any spectroscopically confirmed contaminants before the final classification. However, the colour-colour criteria missed two X-ray detected dual-emitters at $z = 2.23$ as illustrated in Fig. 9.14.

9.5   Number densities

9.5.1   Method

We measure the number densities of LAEs at $z = 2.2, 2.4$ and $z = 3.1$, Hα emitters at $z = 0.4, 1.47$ and $z = 2.23$, Hβ/[OIII] emitters at $z = 0.8, 2.2, 3.2$ and [OII] emitters at $z = 1.47, 3.3, 4.7$ as a function of their line-luminosity, in narrow luminosity bins (0.2-0.3 dex in this analysis). The luminosity is calculated using the line-flux (§9.3.3) and assuming the luminosity distance corresponding to the redshift of peak filter transmission for the relevant emission-line. We calculate the comoving volume for each line/filter combination using the redshifts of half peak transmission, see Table 9.5. For Hβ/[OIII], we compute the volume following Khostovan et al. (2015), who uses only the volume probed by the [OIII]$_{\lambda 5007}$ line. We refer to this work and Sobral et al. (2015a) for a detailed discussion on the contribution of Hβ and [OIII]$_{\lambda 4959}$. Luminosity-binned number densities were calculated by dividing the number of sources in each bin by the comoving volume, and then correcting these (as described in the following subsections) for the effects of the filter profile, flux incompleteness and identification incomplete-

Table 9.5: Survey volumes and flux completenesses for the various line-emitters in this survey.

Filter	Emission-line	Volume $[10^5 \, \text{Mpc}^3]$	50 % completeness $[\text{erg s}^{-1} \, \text{cm}^{-2}]$
NB392	Lyα $z = 2.2$	2.8	1.3×10^{-16}
stV	Lyα $z = 2.4$	9.5	4.7×10^{-16}
NB501	Lyα $z = 3.1$	7.2	1.1×10^{-16}
NB921	Hα $z = 0.4$	0.2	1.0×10^{-16}
	Hβ/[OIII] $z = 0.8$	1.2	1.0×10^{-16}
	[OII] $z = 1.47$	1.7	1.0×10^{-16}
NB$_\text{H}$	Hα $z = 1.47$	2.5	1.3×10^{-16}
	Hβ/[OIII] $z = 2.2$	5.2	1.3×10^{-16}
NB$_\text{K}$	Hα $z = 2.2$	2.7	0.5×10^{-16}

ness. Uncertainties on these number densities were estimated using Poissonian errors. To be conservative, we add in quadrature 20 % of the flux-completeness correction and 20 % of the identification-incompleteness correction (in the case of the red narrow-bands) to the error of each bin. We only show bins with > 40 % flux-completeness.

Filter profile correction

As described in Khostovan et al. (2015) and Sobral et al. (2013, 2015a), observed number densities have to be corrected for the fact that the filter transmission curves are not a perfect top-hat. Because of this, luminous sources may be observed as faint sources if they lie at a redshift corresponding to the wings of the filter. Furthermore, at fixed flux-limit, fainter sources can only be observed over a smaller volume than more luminous sources. Following the method described in these papers, we compute the number density corrections using a simulation. This simulation assumes that sources are distributed randomly in redshift space and computes their observed luminosities based on the relevant filter transmission. We then obtain a volume correction for each luminosity bin. These corrections typically increase the number densities of the most luminous bins by at most 0.3 dex, while the number densities of fainter bins stay constant, or are decreased by at most 0.05 dex.

Detection flux-completeness

The flux-completeness of our selection is measured as a function of line-flux as follows: for the relevant line, we select galaxies that are not selected as a line-emitter, but do fulfil the colour criteria from §9.4. We then artificially add line-flux (starting from 10^{-18} erg s^{-1} cm^{-2} in steps of 0.05 dex) and re-compute the line excess and excess significance for each step. After each step, we measure the fraction of sources that would be selected as line-emitter with the added line-flux. We tabulate the 50 % completeness in Table 9.5. Most narrow-band selections are 50 % complete at $\sim 1 \times 10^{-16}$ erg s^{-1} cm^{-2}, with the exception of
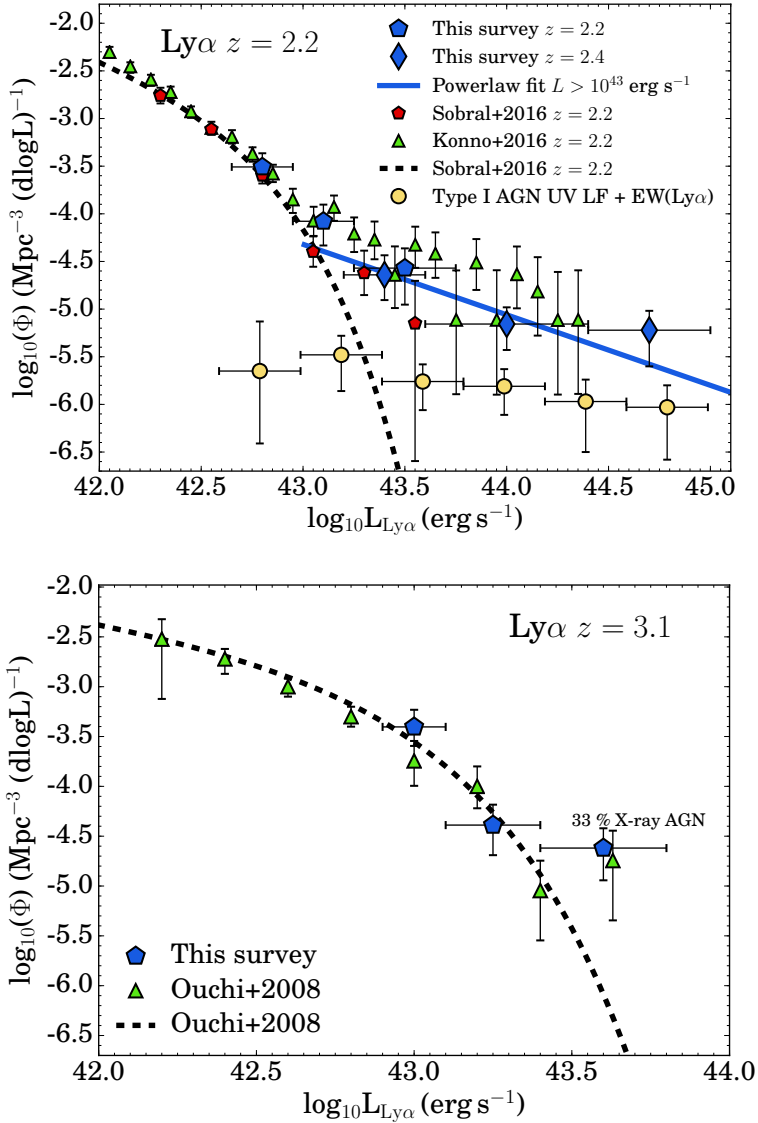
Figure 9.4: Number densities and luminosity functions of LAEs at $z \approx 2.2$ and $z = 3.1$. The power-law like behaviour at the bright end is due to the contribution from AGN (for which we provide a fit in §9.5.2). The yellow points show an estimate of the contribution from Type I AGN, based on the UV LF combined with a Lyα of 80 Å. At $z \approx 2.2$, we find good agreement between the luminosity function of LAEs in B-HiZELS and the luminosity function we measured in Sobral et al. (2017) and to the survey from Konno et al. (2016). The number density of LAEs at $z = 3.1$ is similar to that measured by Ouchi et al. (2008) in the UDS field.

stV, which is only sensitive to brighter emission-lines.

Identification incompleteness

For the red narrow-bands, we also take into account that the broad-band data is not deep enough for a robust classification of all faintest line-emitters, which we call identification-incompleteness. We estimate corrections for this effect as follows: for each narrow-band filter, we measure the fraction of line-emitters that is classed as either Hα, Hβ/[O$\textsc{iii}$] or [O$\textsc{ii}$] emitter or as lower redshift source, as a function of line-flux and assume that this fraction can be extrapolated to the line-fluxes of the sources that are not classable.

We find that for line-emitters in NB921 the fraction of classed Hα, Hβ/[O$\textsc{iii}$] and [O$\textsc{ii}$] emitters is 25 ± 5, 35 ± 5 and 40 ± 4 % respectively at fluxes $< 6.3 \times 10^{-17}$ erg s^{-1} cm^{-2} and 42 ± 10, 38 ± 10 and 20 ± 8 % respectively for fluxes between 6.3×10^{-17} erg s^{-1} cm^{-2} and 4×10^{-16} erg s^{-1} cm^{-2}, see Fig. 9.3. This is expected, as sources with fainter fluxes are expected to be at higher redshift. For line-emitters in NB$_\text{H}$, the corresponding fractions are 25 ± 5, 25 ± 7 and 4 ± 2 % at fluxes below 4×10^{-16} erg s^{-1} cm^{-2}. This means that ~ 40 % of the unclassed sources is likely at $z < 1$. Above this flux, all sources are classed. These fractions are in agreement with the estimate from Sobral et al. (2012). Finally, for line-emitters in NB$_\text{K}$, we estimate that below a flux of 1.5×10^{-16} erg s^{-1} cm^{-2} a fraction of 40 ± 8 % of the line-emitters is Hα, 7 ± 3 % is Hβ/[O$\textsc{iii}$] , while 55 ± 6 % is at low redshift. All sources with a larger line-flux have been classed. We note that maximally 40 % of the sources in a flux bin are unclassed. This maximum occurs in the faintest bin of the NB921 line-emitters (see Fig. 9.3). The typical fraction of unclassed sources at the discussed flux levels is 20 %. We use the estimates described above to obtain the identification-incompleteness for each luminosity bin for the relevant emission-line.

9.5.2 Comparison with previous surveys

Lyman-α emitters at $z = 2.2 - 3.1$

We show the measured luminosity function (LF) of LAEs at $z = 2.2 - 2.4$ and $z = 3.1$ in Fig. 9.4. The depth of our data allows us to constrain the LF to $\approx L^\star$. We find good agreement with earlier results from Sobral et al. (2017) and those from Konno et al. (2016) in different survey fields and slightly different colour-criteria (see also An et al. 2017). All surveys indicate that the Lyα LF at $z \approx 2.2$ deviates from a Schechter function at bright luminosities.[6] We note that all LAEs at $z = 2.2$ with a luminosity above 10^{44} erg s^{-1} are either spectroscopically confirmed or have a dual-NB redshift. As discussed in Sobral et al. (2017), the power-law behaviour of the luminosity function is likely due to the contribution of AGN in addition to the normal Schechter function. Indeed, most ($\sim 80 \pm 40$

---

[6] The Schechter (1976) shape of the luminosity function is expressed as $\Phi(L) \, \mathrm{d}L = \Phi^\star (\frac{L}{L^\star})^\alpha e^{-\frac{L}{L^\star}} d(\frac{L}{L^\star})$, where $\Phi^\star$ is the characteristic number density, $L^\star$ the characteristic luminosity and α the faint-end slope.
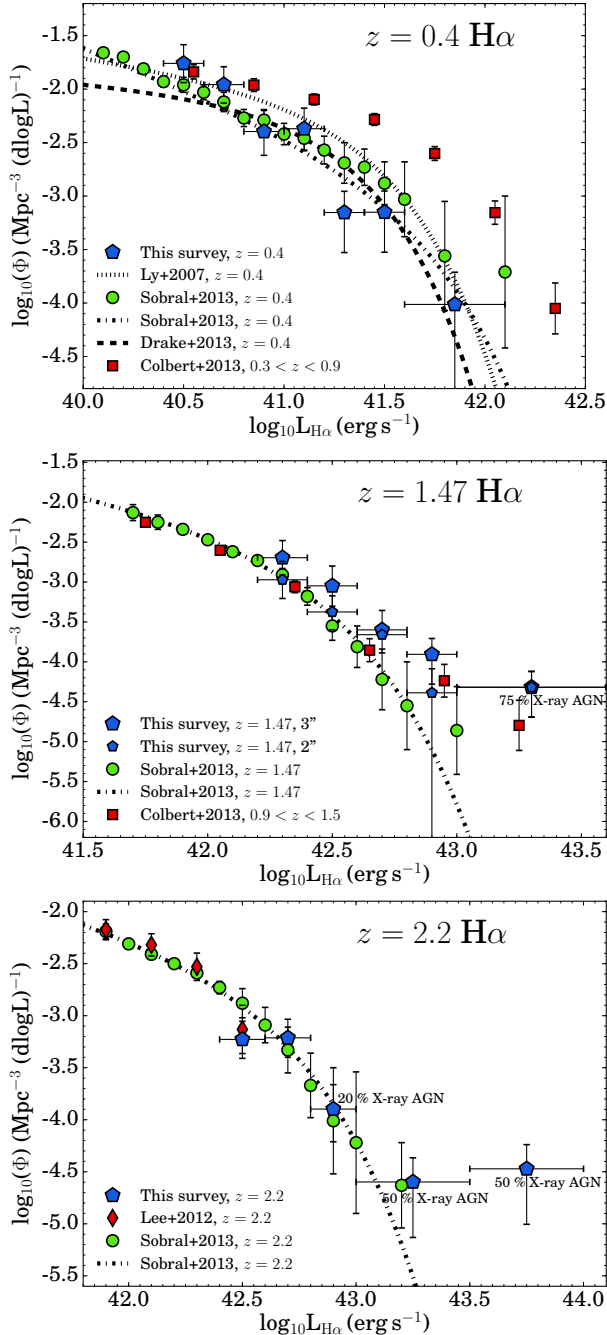
Figure 9.5: Measured Hα luminosity functions at $z = 0.4, 1.47, 2.2$. Hα luminosities are corrected for the [NII] contribution using a relation with Hα+[NII] EW (Sobral et al. 2012), but are not corrected for dust. At $z = 0.4$ the LF is compared to the narrow-band survey from Ly et al. (2007) in the SDF field and Drake et al. (2013) in the UDS field and with the survey from Lee et al. (2012) at $z = 2.2$. At all redshifts, the number densities are compared to the HiZELS survey results in the UDS+COSMOS fields from Sobral et al. (2013). We also compare the LFs with those measured in a blind grism survey by Colbert et al. (2013). Overall, there is reasonable agreement. The luminosity-offset at $z = 1.47$ may be explained by aperture effects (see §9.5.2). The brightest bin at $z = 2.2$ is due to X-ray AGN.
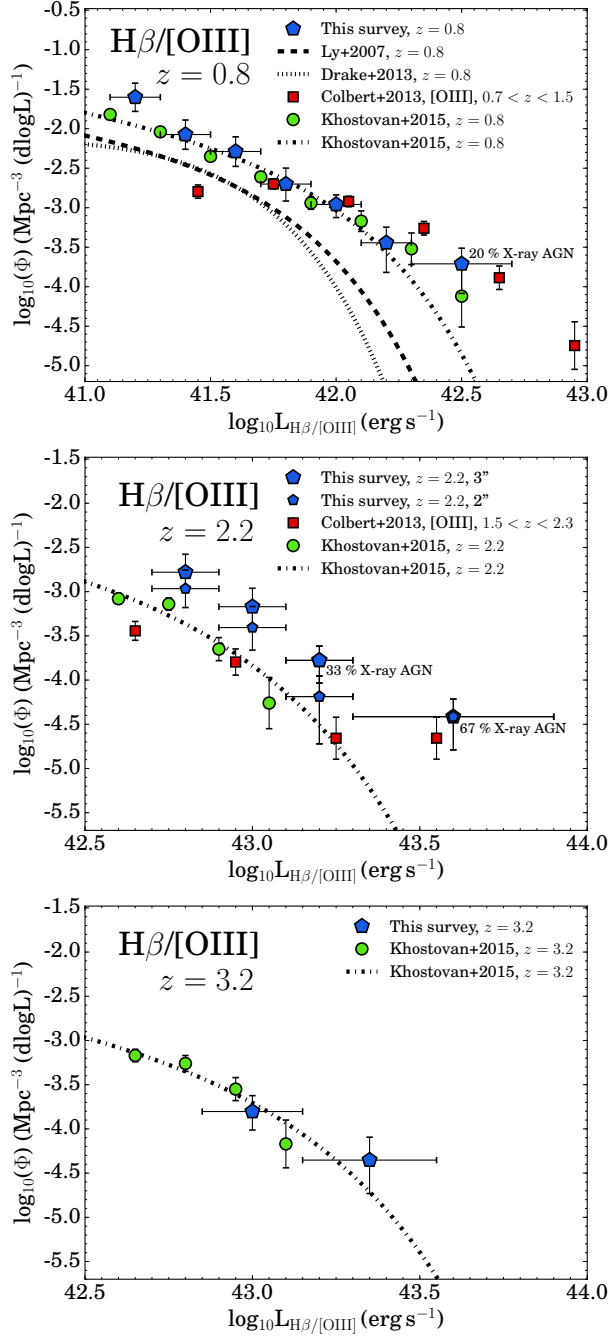
Figure 9.6: Measured Hβ/[OIII] luminosity functions at $z = 0.8, 2.2, 3.2$, compared to Ly et al. (2007) and Drake et al. (2013) at $z = 0.8$ and to Khostovan et al. (2015) and Colbert et al. (2013) at higher redshift. There is a luminosity-offset at $z = 2.2$ that is partially due to a larger aperture measuring a higher luminosity by ≈ 0.14 dex. The brightest bin at $z = 2.2$ contains the same AGN as in the brightest bin of the Hα luminosity function at $z = 2.2$.

%) luminous LAEs ($L_{Ly\alpha} > 10^{43}$ erg s^{-1}) are AGN (either due to X-Ray detection or CIV detection in NB501). We fully explore this in §9.6.4.

Due to its larger probed cosmic volume, the stV filter is mostly sensitive to very luminous LAEs. Although all LAEs with a luminosity above 10^{44} erg s^{-1} at $z = 2.4$ are spectroscopically confirmed, we expect that the sample with luminosities 10^{43-44} erg s^{-1} is contaminated, as the spectroscopic follow-up at these fluxes is not complete. Most importantly, we expect contaminants to be emission lines that are associated with AGN activity such as CIV, CIII] and HeII at $z = 1.15 - 1.65$ (e.g. Stroe et al., 2017), which are challenging to identify with these colour-colour selections. We estimate the contamination at these flux levels by mimicking the selection of this survey in a similar medium-band in the COSMOS field (IA427; Sobral et al. 2018b). We select LAEs at $z = 2.5$ with the same criteria (including broad-band depths) and estimate the number of interlopers using the most recent photometric redshifts (Laigle et al., 2016) and a compilation of spectroscopic redshifts. We find that at luminosities $\sim 10^{43-44}$ erg s^{-1} there is a non-negligible contamination due to CIV, CIII] and HeII emitters of 20±10 %. At higher luminosities the contamination decreases to 4±4 %. The plotted number densities are corrected for these contamination rates. We combine the $z = 2.2 - 2.4$ data to fit a power-law function to the number density of LAEs at the bright end ($L_{Ly\alpha} > 10^{43}$ erg s^{-1}), which results in: $\log_{10}(\Phi) = 27.5^{+7.3}_{-7.4} - 0.74^{+0.17}_{-0.17}\log_{10}(L_{Ly\alpha})$, with a reduced χ^2 of 1.1. This fit is slightly shallower than the power-law fitted by Sobral et al. (2017) based on a smaller volume, but consistent within 1σ.

We estimate the contribution of broad-line Type I AGN to the Lyα LF at $z \approx 2.2$ based on the UV LF of Type I AGN at $2.0 < z < 2.5$ from Bongiorno et al. (2007) and the typical UV slope and Lyα EW of these AGN. Assuming $f_\lambda \propto \lambda^{-1.5}$ and Lyα EW$_0 = 80$ Å (e.g. Vanden Berk et al., 2001; Hunt et al., 2004), we convert the number densities as a function of M_{1450} to number densities as a function of Lyα luminosity. As shown in Fig. 9.4, it is clear that the number density of LAEs is higher than the number density of Type I AGN at fixed Lyα luminosity. This indicates that only a fraction of the luminous LAEs are likely Type I AGN. This estimate suggests that at Lyα luminosities 10^{43-44} erg s^{-1} the fraction of Type I AGN is only ~ 10 %, while the fraction is $\sim 20 - 30$ % at higher Lyα luminosities. Because the AGN LF at the faintest UV magnitudes is relatively flat, these fractions do not depend strongly on the assumed values of the Lyα EW or UV slope. The low Type I AGN fraction indicates that the majority of luminous LAEs are narrow-line Type II AGN (see also §9.6.4), or star-forming galaxies.

At $z = 3.1$ we find that the Lyα LF agrees well with that from Ouchi et al. (2008), who performed a deep Lyα survey over a similar area. Compared to similar NB501 data in the COSMOS field (with deeper ancillary data and relatively more spectroscopic follow-up; Matthee et al. in prep), we also find that the fraction of line-emitters (with similar line-flux and EW distributions) that are classed as LAE is similar: 51 ± 9 % in Boötes against 46 ± 7 % in COSMOS. This also confirms evolution in L* between $z = 2.2 - 3.1$ from $L_{Ly\alpha} \approx 4 \times 10^{42}$ erg s^{-1} to $L_{Ly\alpha} \approx 9 \times 10^{42}$ erg s^{-1}. The number density of LAEs in the brightest

bin (three out of the four sources in this bin are spectroscopically followed-up and confirmed) lies above the Schechter fit from Ouchi et al. (2008) (similar to the actual data-points from that survey), indicating the presence of AGN among these luminous sources, similar to $z \sim 2$. Indeed, we find evidence for AGN activity for most LAEs in the most luminous bin, either due to an X-ray detection or due to the detection of high ionisation emission-lines as [Ne IV]$_{\lambda 2424}$ or broad Si IV and C IV absorption features in the spectrum (Sobral et al. in prep).

Hα emitters at $z = 0.4 - 2.2$

We show the number densities of Hα emitters as a function of their observed Hα luminosities. The Hα luminosities are corrected for the contribution due to [N II] following a method based on observed Hα+[N II] EW (Sobral et al., 2012). Hα luminosities are not corrected for attenuation due to dust and we compare our results with dust-uncorrected values from the literature. In case dust-uncorrected values are not provided, we convert dust-corrected values back using the prescriptions outlined in the relevant papers.

As illustrated in Fig. 9.5, we find that the Hα LF at $z = 0.4, 1.47$ and $z = 2.23$ are generally in good agreement with the number densities in the UDS+COSMOS parts of the HiZELS survey from Sobral et al. (2013). Within the errors, the LF agrees well with the fitted relations from Drake et al. (2013) and Ly et al. (2007). At $z = 2.23$, the number densities complement the number densities at fainter luminosities from Lee et al. (2012). This confirms strong evolution in $L_{H\alpha}^\star$ from $z = 0.4 - 2.23$. We note that at $z = 0.4$ there could be some contamination at the faintest luminosities due to identification-incompleteness (see §9.5.1). At $z = 1.47$ the luminosities seem to be systematically higher by $\approx 0.1 - 0.15$ dex, increasing slightly with luminosity. This offset can partly be explained by different apertures used in the photometry. While Sobral et al. (2013) uses $2''$ apertures for all measurements above $z > 0.5$, we use $3''$ measurements. Redoing the measurements with $2''$ apertures (smaller symbols in Fig. 9.5) results in good agreement at our faintest luminosities and reasonable agreement (within the error bars) at higher luminosities. At faint luminosities, the luminosity difference between the two apertures is typically 0.14 dex, while it is typically 0.1 dex at high luminosities. The highest luminosity bins at $z = 1.47 - 2.23$ show number densities diverging from a Schechter function, contributing to the difference as well. The sources in these bins are all spectroscopically confirmed or have dual-NB redshifts and most are X-ray detected, as indicated in the corresponding panels. We discuss this in more detail in §9.6.4.

Compared to the grism results at $0.3 < z < 0.9$ from Colbert et al. (2013), the number densities at $z = 0.4$ are offset (mostly in terms of luminosity). This can simply be explained by the evolution in the typical Hα luminosity between $z = 0.4$ and the median redshift of the Colbert et al. (2013) sample of $z \approx 0.6$, as $\log L_{H\alpha}^\star$ increases with $0.45 \times z$ over this redshift range (Sobral et al., 2013). The number densities at $z = 1.47$ are in good agreement with the grism results at $0.9 < z < 1.5$, even though the median grism redshift is $z \approx 1.2$. This indicates that there is little evolution in $L_{H\alpha}^\star$ between $z = 1.47$ and $z \approx 1.2$.

Hβ/[O III] emitters at $z = 0.8 - 3.2$

We also compare our idenfication of Hβ/[O III] at $z = 0.8, 2.2, 3.2$ with the analysis from Khostovan et al. (2015) in the COSMOS and UDS fields.

As illustrated in Fig. 9.6, the number densities of Hβ/[O III] emitters at $z = 0.8$ are in good agreement with those from Khostovan et al. (2015), and higher than those from Ly et al. (2007) and Drake et al. (2013), which could be due to cosmic variance or systematics such as different apertures and estimates of volume and completeness. Using a large 10 deg^2 Hα, Hβ/[O III] and [O II] survey, Sobral et al. (2015a) estimated empirically that the uncertainty in $L^\star$ and $\Phi^\star$ due to cosmic variance over the volume probed in these surveys at $z = 0.8$ is $\approx 40 - 50$ %. Such variance could easily explain the observed differences. At $z = 2.2$, the number densities are systematically higher in luminosity compared to the literature results. Similarly as in §9.5.2, we find that this is partly due to an aperture effect. As expected, the difference in luminosities measured with different apertures is slightly smaller at $z = 2.2$ than at $z = 1.47$, with a typical luminosity difference of 0.11 dex. As a consequence, even when matching apertures to Khostovan et al. (2015), we still find an offset at fainter luminosities, which we attribute to cosmic variance. Although the number of Hβ/[O III] emitters at $z = 3.2$ is limited, their number densities agree well with those from Khostovan et al. (2015).

Unlike the Hα number densities, the number densities of Hβ/[O III] emitters are in good agreement with those from Colbert et al. (2013), which could indicate that there is less evolution in the Hβ/[O III] luminosity function than in the Hα luminosity function between $0.7 < z < 1.5$. However, this could also be due to the contribution of Hβ emitters (see Sobral et al. 2015a and Khostovan et al. 2015 for detailed discussions). Except for luminosities $> 10^{43}$ erg s^{-1}, the number densities of Hβ/[O III] emitters at $z = 0.8$ are a factor 30 to 100 higher (at fixed [O III] luminosity) than the number densities of Type II AGN at $z \sim 0.71$ (Bongiorno et al., 2010).

[O II] emitters at $z = 1.47, 3.3, 4.7$

Fig. 9.7 compares the number density of [O II] emitters at $z = 1.47, 3.3, 4.7$ to the other published results. At $z = 1.47$, the number densities agree reasonably well with Drake et al. (2013) and Khostovan et al. (2015), except for the faintest bin, although identification-incompleteness is significant in this bin. At the bright end, the Schechter fit from Ly et al. (2007) indicates a lower number density, potentially due to a lack of bright sources in a small survey volume. We note that the sources in the brightest bin are not spectroscopically confirmed and thus could be interlopers (for this reason, these points have a lighter colour in Fig. 9.7). Although the number of [O II] emitters in our samples at $z = 3.3$ and $z = 4.7$ is limited to a handful, their number densities are slightly higher than Khostovan et al. (2015), potentially indicating either contamination or cosmic variance. A further hint of contamination in this sample is that some have relatively low colour-excess (Fig. 9.2), which is unexpected for high-redshift sources, although this would also be consistent with a drop in typical EWs for
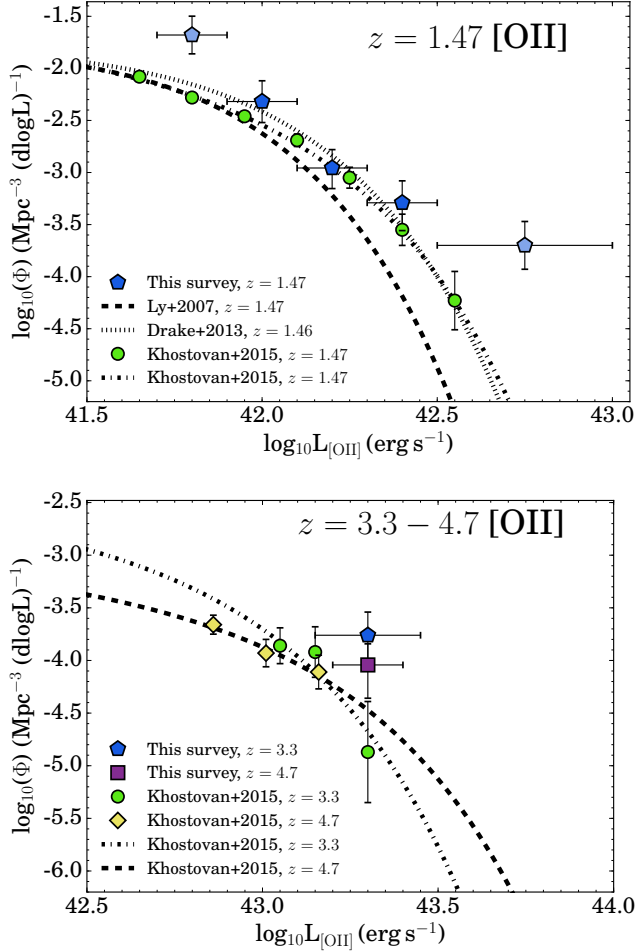
Figure 9.7: Measured [OII] luminosity functions at $z = 1.47, 3.3, 4.7$. At $z = 1.47$, the LF shows reasonable agreement with those from Ly et al. (2007), Drake et al. (2013) and Khostovan et al. (2015), except at the bright end. Since the sources in the brightest bin are not spectroscopically confirmed and identification-incompleteness in the faintest bin is large, we show these bins in a slightly lighter colour. We plot the number densities of [OII] emitters at $z = 3.3$ and $z = 4.7$ in a single panel. These number densities are slightly higher than Khostovan et al. (2015), potentially indicating some contamination or cosmic variance.

[OII] emitters (Khostovan et al., 2016).

9.6   Properties of line-emitters

9.6.1   Dual-emitters

In total, we detect 42 line-emitters that are line-emitters in multiple narrow-bands. We list the coordinates, redshifts and *I* band magnitude of these line-emitters in Table 9.6. The majority (20) of dual-emitters are Hα+[OII] emitters at $z = 1.47$ detected in NB921 and NB_H, followed by 17 Hα+[OIII] emitters at $z = 2.23$, of which two are also detected in Lyα, three in CIV and one in MgII. Three galaxies are identified as LAE in NB392 at $z \sim 2.2$–2.3 and are also detected in either NB_H ([OIII]) or NB_K (Hα), of which one is also detected in NB501 (CIV).

9.6.2   The most luminous Hα emitters at z = 2.23

B-HiZELS_1 is the most luminous Hα emitter known from HiZELS at $z = 2.23$ (i.e. Sobral et al., 2016a) and also detected as Lyα and [OIII] emitter. Although its high luminosity ($L_{H\alpha} = 7.9 \times 10^{43}$ erg s^{-1}) suggests that it is an AGN, it is X-ray undetected ($L_X < 3 \times 10^{44}$ erg s^{-1}, or $< L_X^\star$, La Franca et al. 2005). There is also a dual-emitter (B-HiZELS_27), detected in [OIII] and Hα at the same redshift only $6''$ away (a projected distance of ~ 50 kpc). This source has an estimated Hα EW_0 of $\gtrsim 400$ Å and [OIII] $EW_0 \gtrsim 375$ Å. This places it at the very high end of the Hα EW distribution at $z = 2.2$ (Fumagalli et al., 2012; Sobral et al., 2014), and the galaxy is thus likely a low mass extreme emission line galaxy (e.g. van der Wel et al., 2011). These strong emission-lines could indicate that this galaxy may be undergoing high interaction-induced SFR combined with little extinction due to dust, or is a shocked gas cloud.

The second most luminous Hα emitter at $z = 2.2$ is B-HiZELS_15 at $z = 2.244$ ($L_{H\alpha} = 3.6 \times 10^{43}$ erg s^{-1}). We also detect [OIII], Hα and CIV emission-lines (there are no Lyα observations at its position). Although B-HiZELS_15 also has a neighbouring galaxy (at $z = 2.242$ and a projected separation of ≈ 50 kpc) and the Hα luminosity is only a factor two lower than that of B-HiZELS_1, several other properties are different. B-HiZELS_15 is X-ray detected, has a higher Hα EW_0 (360 Å versus 120 Å) and is more than three magnitudes fainter in the optical and NIR continuum. This indicates a diversity in the properties of luminous Hα emitters, similar to the results from Sobral et al. (2016a).

9.6.3   [OII]-Hα view at z = 1.47

One strength of the Boötes-HiZELS survey is our sample of dual-emitters which can be used to study the relation between different star-formation rate indicators at $z = 1.47$ and $z = 2.23$, such as [OII], Hα and continuum tracers such as the rest-frame UV, FIR and radio. Compared to Hα, the [OII] emission-line and UV continuum are more sensitive to dust attenuation and effects from metallicity and gas density (e.g. Kennicutt, 1998; Jansen et al., 2001; Ly et al., 2012), which

may all evolve with redshift. We exploit this sample to derive the observed [OII]/Hα ratio at $z = 1.47$ and compare it to a reference sample from SDSS at $z = 0.1$, to test claims based on smaller samples by e.g. Hayashi et al. (2013) and Sobral et al. (2012).
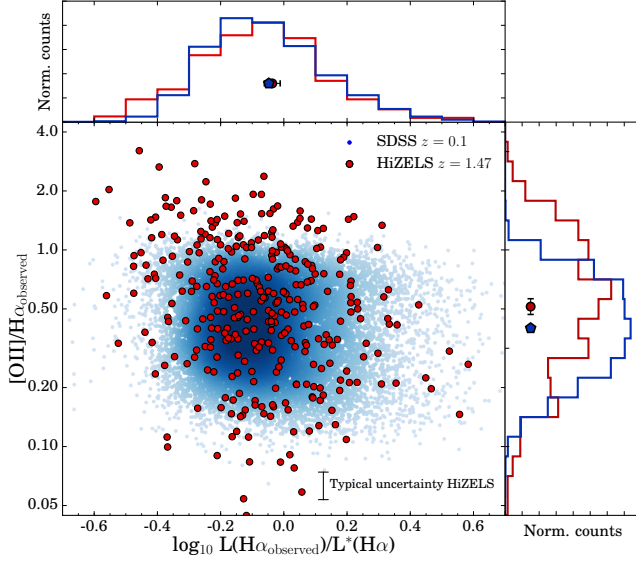

Figure 9.8: Observed [OII]/Hα ratio as a function of observed Hα luminosity, normalized by the typical luminosity ($L^\star$) at either $z = 1.47$ ($L^\star = 10^{42.16}$ erg s^{-1}, Sobral et al. 2013) or $z = 0.1$ ($L^\star = 10^{41.4}$ erg s^{-1}, Ly et al. 2007). The blue points (coloured by density) show the ratios observed in SDSS at $z = 0.1$, while the red points show the HiZELS measurements at $z = 1.47$. The distribution of $L/L^\star$ is similar at both redshifts, while the median observed [OII]/Hα increases from 0.40 ± 0.01 in the local Universe to 0.52 ± 0.05 at $z = 1.5$. A KS test confirms that this increase is statistically significant. This increase could be due to evolution of the dust attenuation, or an effect from fiber-measurements in SDSS.

We combine the sample of dual-emitters at $z = 1.47$ in Boötes with those from HiZELS in the UDS and COSMOS field (see Sobral et al. 2013 for details), and remove any source that is detected in the X-rays. In total, this results in a sample of 340 dual-emitters at $z = 1.47$. The majority of these are dominated by faint emitters observed in the deeper imaging in COSMOS. Hα luminosities are corrected for the contribution from the adjacent [NII] doublet using the relation with EW described in Sobral et al. (2012) (see also Sobral et al. 2015a for a spectroscopic validation). As a comparison sample at low redshift, we use a sample of emission-line measurements from a sample of star-forming galaxies at $z \approx 0.1$ drawn from data from SDSS DR7 (Abazajian et al., 2009) as described in Sobral et al. (2012). In short, a sample of 16414 galaxies were selected at $0.07 < z < 0.1$ with observed Hα luminosity $> 10^{40.6}$ erg s^{-1} and Hα EW > 20 Å. For consistency with our sample at $z = 1.47$, we do not remove AGN using the BPT diagnostic (Baldwin et al., 1981b). Aperture corrections to emission-line measurements have been done following Garn & Best (2010) based on the ratio
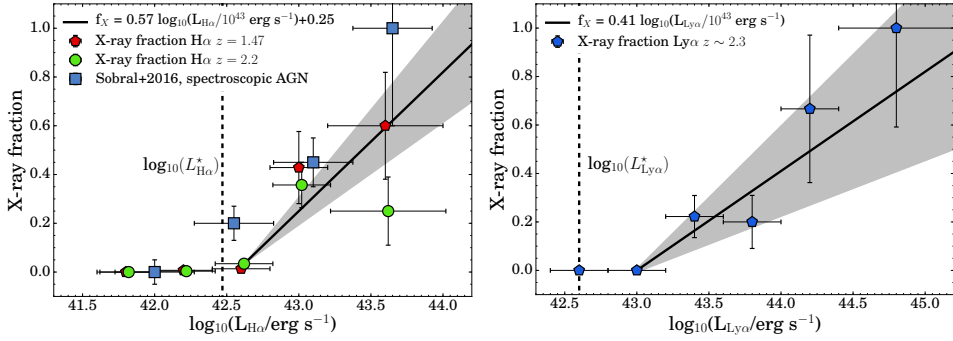
Figure 9.9: Left panel: X-ray fraction of HAEs combining Boötes-HiZELS and the sample of emitters from COSMOS from HiZELS (Sobral et al. 2013) as a function of Hα luminosity at $z = 1.47 - 2.23$, compared to the AGN fraction measured with spectroscopy in Sobral et al. (2016a). The AGN fraction increases strongly with Hα luminosity. At fixed Hα luminosity, the observed X-ray fraction does not evolve strongly between $z = 1.47 - 2.23$. Right panel: X-ray fraction of LAEs as a function of Lyα luminosity at $z \approx 2.3$. The AGN fraction increases strongly with Lyα luminosity. The luminosities above which the X-ray fraction exceeds 20 % correspond to the luminosities where the number densities start to diverge from Schechter, see e.g. Fig. 9.4.

between the stellar mass in the fiber and the total stellar mass. We note that these corrections do not change line-ratios.

In Fig. 9.8, we show the observed [OII]/Hα ratio as a function of observed Hα luminosity, normalized by the typical Hα luminosity ($L^{\star}_{H\alpha}$) at the specific redshift, both for the sample of dual-emitters and the local comparison sample. After correcting for the evolution in the typical Hα luminosity of a factor of ≈ 6, the distribution of Hα luminosities is remarkably similar. By computing the median ratio in 100,000 bootstrap resamples of the data, we measure [OII]/Hα = 0.40 ± 0.01 with 95 % confidence intervals at $z = 0.1$ (slightly lower than the measurement of 0.45 in Kennicutt 1998) and [OII]/Hα = 0.55 ± 0.07, such that there is a slight increase of the median value with redshift (although the increase is within the observed scatter of $\approx 0.2 - 0.3$ dex; see also Hayashi et al. 2013). We note that our survey may miss the galaxies with lowest [OII]/Hα ratio, in particular for the faintest Hα emitters, which may result in a bias towards finding a higher [OII]/Hα ratio at $z = 1.47$. However, if we restrict the analysis to brighter sources ($> 0.5 \times L^{\star}_{H\alpha}$), we find [OII]/Hα = 0.52 ± 0.05 at $z = 1.47$, while the SDSS results remain unchanged. This indicates that this selection effect is likely not driving the differences. A one dimensional Kolmogorov-Smirnov (KS) test of the observed [OII]/Hα ratios confirms that the distributions are significantly different, with a KS-statistic of 0.20 ($\approx 10^{-10}$ significance) and a P-value of 4×10^{-11}. This indicates that, even though the spread in values is relatively large ($\approx 0.4 - 0.5$ dex), the median observed [OII]/Hα ratio increases slightly, but statistically significantly, between $z = 0.1 - 1.47$.

We test whether the observed difference can be caused by systematic errors. At $z = 1.47$ there is a systematic uncertainty due to the relative filter transmissions at the different wavelengths, that leads to an increase in the scatter and a

small bias towards higher [OII]/Hα values. Based on the simulation that is discussed in detail in Sobral et al. (2012), we estimate that this systematic increase is only of the order of ≈ 5 %, insufficient to explain the offset of the median ratio. If we remove AGN in the SDSS sample using the BPT criterion as defined in Kauffmann et al. (2003), we find [OII]/H$\alpha = 0.42 \pm 0.01$. Finally, if we fully mimic the Hα measurement (and its correction for the contribution of the [NII] in the narrow-band), we measure [OII]/H$\alpha = 0.45 \pm 0.01$. Thus, none of these effects can explain the observed difference, but they further highlight that the evolution is small, and thus only our large statistical sample can measure evolution.

A higher observed [OII]/Hα ratio is expected when there is less attenuation due to dust, since [OII] is attenuated more than Hα (e.g. Reddy et al., 2015). For example, it could be that galaxies at $z = 1.47$ are less dusty. Indeed, if we restrict the sample of local galaxies to those with $A_{H\alpha} < 1.3$ (median $A_{H\alpha} = 0.82$, compared to a median $A_{H\alpha} = 0.91$ for the full sample), we find a similar observed [OII]/Hα ratio of 0.49 ± 0.01. However, results from *Herschel* stacking of Hα emitters at $z = 1.47$ (Thomson et al. 2017; see also Ibar et al. 2013) indicate that their extinction properties are similar to local galaxies, with a similar relation between stellar mass and $A_{H\alpha}$ (Garn & Best, 2010). We note that because the samples are matched in $L/L^{\star}_{H\alpha}$ there are likely no significant mass differences between the samples (e.g. Sobral et al., 2014). A more detailed analysis of the extinction properties of this sample is beyond the scope of this paper. Finally, another explanation is that the SDSS fiber-measurements are biased towards higher extinction (and thus lower [OII]/Hα ratios), because they measure the line-ratios in the central 3-4 kpc of galaxies, that are observed to be dustier/more evolved (e.g. Sánchez et al., 2014), while the $3''$ measurements at $z = 1.47$ measure flux out to radii of 8-13 kpc (depending on UDS/COSMOS or Boötes). Therefore, the observed offset between $z = 0.1$ and $z = 1.47$ could also be an observational effect due to dust, age and/or metallicity gradients within galaxy. These observational issues can be overcome with large IFU or matched NB surveys in the local Universe, as for example the J-PAS project (Benitez et al., 2014).

9.6.4 X-ray fraction & the power-law component of the luminosity function

We investigate the AGN fractions of Hα emitters at $z = 1.47$ and $z = 2.23$ and LAEs at $z = 2.4$ by matching our samples to source catalogs from X-ray (*Chandra*, 0.5–7.0 keV, depth 7.8×10^{-15} erg s^{-1} cm^{-2}, $1''$ resolution and matching radius, Kenter et al. 2005). In addition, we include the Hα emitters at $z = 1.47$ and $z = 2.23$ in the COSMOS field from Sobral et al. (2013) and match these with the *Chandra* COSMOS point source catalog (0.5–7.0 keV, 5.7×10^{-16} erg s^{-1} cm^{-2}, Elvis et al. 2009); see also Calhau et al. (2017) for their detailed properties. These X-ray flux limits correspond to luminosity limits of 0.3–3×10^{44} erg s^{-1}. If such an X-ray luminosity would have its origin in star formation, it would require SFRs of $> 10^{3.5-5}$ M$_\odot$ yr^{-1} (e.g. Lehmer et al., 2016), which is unlikely. This clearly indicates an AGN origin of all X-ray detections discussed in this section.

In total, we detect 21 HAEs in the X-ray, of which 10 are at $z = 1.47$ and 11 are at $z = 2.23$ and half of the X-ray detected HAEs are in Boötes. We find that the detection rate depends strongly on the Hα luminosity, see Fig. 9.9. This has also been observed using spectroscopic follow-up by Sobral et al. (2016a), who found that the majority (80 ± 30 %) of luminous HAEs are broad-line AGN. Relatively independent of redshift, roughly half of the most luminous HAEs are X-ray detected. Note that the other half may easily be undetected due to the short duty cycle of X-ray AGN (e.g. Shankar et al., 2009; Fiore et al., 2012), although it could also indicate that roughly half of the luminous HAEs are optically thick to X-rays. By combining the data-points above L* at $z = 1.47 - 2.23$, we find a best fit $f_X = 0.57^{+0.15}_{-0.15}\log_{10}(L_{H\alpha}/10^{43}$ erg s$^{-1}) + 0.25^{+0.06}_{-0.06}$, that we illustrate in Fig. 9.9.

We combine the sample of LAEs at $z = 2.2 - 2.4$ identified with the NB392 and the stV filter to investigate the X-ray fraction of LAEs as a function of luminosity. Out of the 41 LAEs, eight are X-ray detected (L$_X \gtrsim 3 \times 10^{44}$ erg s^{-1}). The X-ray fraction of LAEs increases strongly with line luminosity, from ≈ 0% at L$^\star_{Ly\alpha}$ to ≈ 100 % at $\gtrsim 3 \times 10^{44}$erg s^{-1}. We note that the Lyα luminosities at which the X-ray fraction exceeds 20 % correspond to the luminosities at which the number densities start to deviate from a Schechter function, as observed in Konno et al. (2016), Sobral et al. (2017) and this work (Fig. 9.4). For both Hα and Lyα, the X-ray fraction increases above L*. For Lyα, we find a best fit relation of: $f_X = 0.41^{+0.18}_{-0.18}\log_{10}(L_{Ly\alpha}/10^{43}$ erg s$^{-1})$ above L$_{Ly\alpha} > 10^{43}$ erg s^{-1}.

9.7   Conclusions

We presented the first results from the Boötes-HiZELS survey, which uses six narrow-bands to select emission-line galaxies from $z = 0.4 - 4.7$ in a 0.7 deg^2 region in the Boötes field. We described the observations, data-reduction, extraction of catalogs and selection of line-emitters, and how multi-wavelength data has been used to classify different populations of line-emitters. The main results are:

1. We identify 362 candidate Hα emitters (HAEs) at $z = 0.4, 1.47, 2.23$, 387 Hβ/[OIII] emitters at $z = 0.8, 2.23, 3.3$, 285 [OII] emitters at $z = 1.47, 3.3, 4.7$ and 73 Lyα emitters (LAEs) at $z = 2.23, 2.3, 3.1$.

2. Using a suite of matched narrow-band filters, we identify 42 galaxies with emission-lines in multiple narrow-bands, providing 22/18 new robust redshift identifications of [OII]/Hα and [OIII]/Hα emitters at $z = 1.47/2.23$, without pre-selection on AGN activity or I band magnitude, see §9.6 and Table 9.6. 56 additional line-emitters have a spectroscopic redshift.

3. In general, the number densities of line-emitters as a function of luminosity we derive agree remarkably well with luminosity functions observed in other survey fields (§9.5, Figures 9.4, 9.5, 9.6 and 9.7), confirming strong evolution in L$^\star_{H\alpha}$ from $z = 0.4 - 2.2$ and evolution in L$^\star_{Ly\alpha}$ from $z = 2.2 - 3.1$.

4. We confirm the result from Konno et al. (2016) and Sobral et al. (2017) that the luminosity function of LAEs at $z \approx 2.2$ diverges from a Schechter function at the bright end, $L_{Ly\alpha} \gtrsim 10^{43}$ erg s^{-1}. At these luminosities, the luminosity function follows $\log_{10}(\Phi) = 27.5 - 0.74\log_{10}(L_{Ly\alpha})$. Such a departure from a Schechter function is also clearly observed at the highest Hα luminosities ($L_{H\alpha} \gtrsim 10^{43.5}$ erg s^{-1}) at $z = 2.2$ (§9.5.2 and §9.5.2).

5. Combining our sample of dual-emitters with those from the COSMOS and UDS fields from HiZELS, we compare the observed [OII]/Hα ratio of 340 star-forming galaxies at $z = 1.47$ with those from a reference sample in the local Universe (§9.6.3). We measure a median ratio of [OII]/Hα = 0.40 ± 0.01 at $z = 0.1$ and [OII]/Hα = 0.55 ± 0.07 ([OII]/Hα = 0.52 ± 0.05 if we restrict the sample to sources with slightly higher S/N, see Fig. 9.8). The ≈ 0.1 dex offset can potentially be attributed to a lower dust attenuation at $z = 1.47$, or biases in the fiber-measurements in the local Universe, which measure the ratio at the central 3-4 kpc of galaxies, while the measurements at $z = 1.47$ are integrated over ≈ 10kpc.

6. By exploiting *Chandra* X-Ray data, we show that the Hα and Lyα luminosities at which the number densities start to diverge from pure Schechter form at similar luminosities to where the X-ray fractions start to increase, from ~ 20 % to ~ 100 % (Fig. 9.9). We also show that, under basic assumptions, the majority of luminous LAEs are not broad-line Type I AGN (Fig. 9.4), and more likely narrow-line Type II AGN.

The sample of identified line-emitters can be used to study various properties of star-forming galaxies. In particular, the relatively large sample of Hα emitters at $z = 1.5 - 2.2$ can be used to test various SFR indicators (Hα, rest-UV, radio, FIR) in future papers.

Acknowledgments

Appendix A: Photometric consistency check

In our catalogue production steps (§9.3.2), we only include objects in our catalogues that have a physically plausible NB excess. Because the BB covers the same wavelength as the NB, flux in the NB must also be observed in the BB, otherwise the object is either unreal (such as a cosmic ray, artefacts, etc.) or variable (such as variable stars, supernovae or AGN). It is fairly straightforward to compute the faintest possible BB magnitude given a NB magnitude:

$$BB_{max} = NB - 2.5\log_{10}(\frac{\lambda_{c,BB}^2 \Delta\lambda_{NB}}{\lambda_{c,NB}^2 \Delta\lambda_{BB}}) + 0.5 \qquad (9.5)$$

in this equation, $\lambda_{c,X}$ is the central wavelength of filter X, and $\Delta\lambda_X$ the width of filter X. We conservatively add 0.5 magnitude to take into account uncertainties in the photometry and relative filter transmissions. We remove any source for which the excess is larger than $BB_{max} - NB$. For example, for NB921 and z band, this equation results in $BB_{max} = NB + 3.4$. This means that if a source has a NB921 magnitude of 20, it must have a z magnitude of 23.4 or brighter. It is possible that the implied BB_{max} is below the background. In that case, we exclude sources for which the BB is not detected at 2σ. This consistency check removes most spurious objects such as cosmic rays and detector artefacts.

Appendix B: Colour-colour selections

In this section we illustrate the colour-colour selection criteria outlined in Table 9.3. In all figures (Fig. 9.10, 9.11, 9.12, 9.13 and 9.14), line-emitters with secure redshift-identifications from spectroscopy or dual-NB detections are shown with larger symbols. X-ray detected AGN are shown with a star symbol.
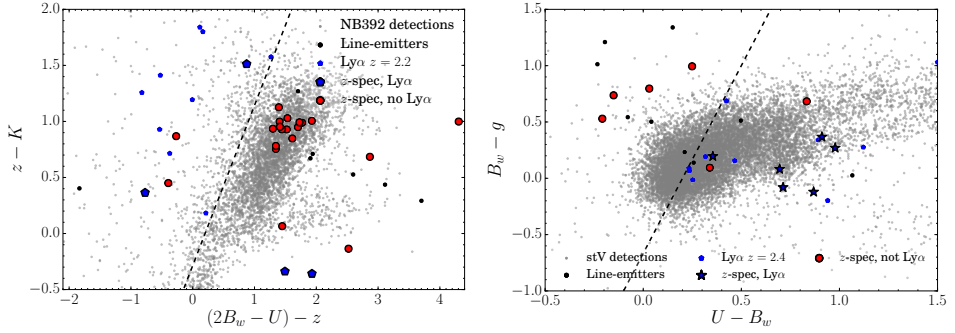
Figure 9.10: Colour selection criteria used to select LAEs at $z = 2.2$ and $z = 2.4$. These are based on the BzK criterion from Daddi et al. (2004). The B_w band magnitude is adjusted for the contribution to flux in the U band. We highlight the sources with spectroscopic redshifts in larger symbols.
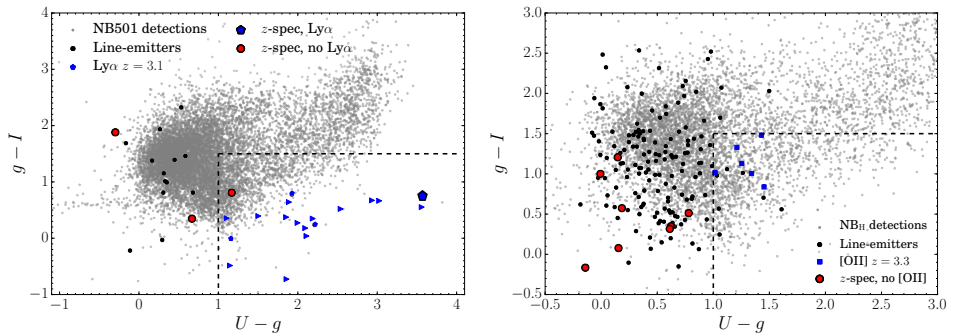

Figure 9.11: Colour selection criterion used to select LAEs at $z = 3.1$ (from NB501) and [OIII]/Hβ at $z = 3.2$ (from NB$_H$), based on the U drop-out criterion for Lyman-break galaxies at $z \approx 3$ from Hildebrandt et al. (2009). The $U - g$ colour identifies the Lyman-break, while the $g - I$ criterion removes any sources for which the Balmer break is mimicked by a strong Balmer break (particularly important in the case a galaxy is very dusty).
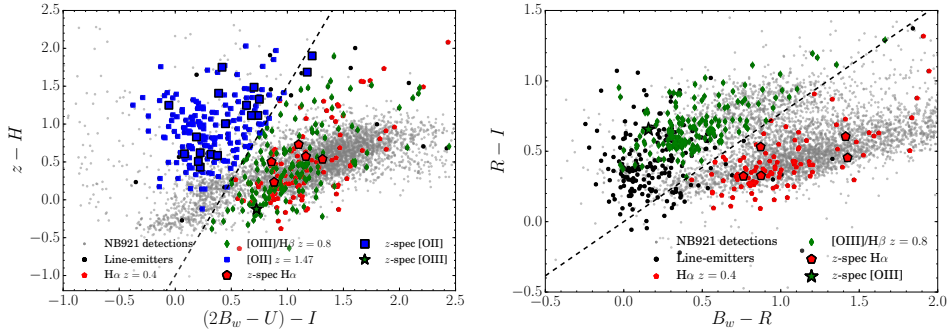
Figure 9.12: Colour selection criteria used to distinguish Hα, [OIII]/Hβ and [OII] emitters among the line-emitters identified with NB921. The criterion in the left panel identifies Balmer breaks at specific redshift intervals. Because this criterion can not distinguish between $z = 0.4$ and $z = 0.8$, we use the additional $B_w R I$ colours to distinguish between a Balmer break between B_w and R (around 600 nm, or $z \approx 0.5$) and between R and I (around 700 nm, or $z \approx 0.75$).
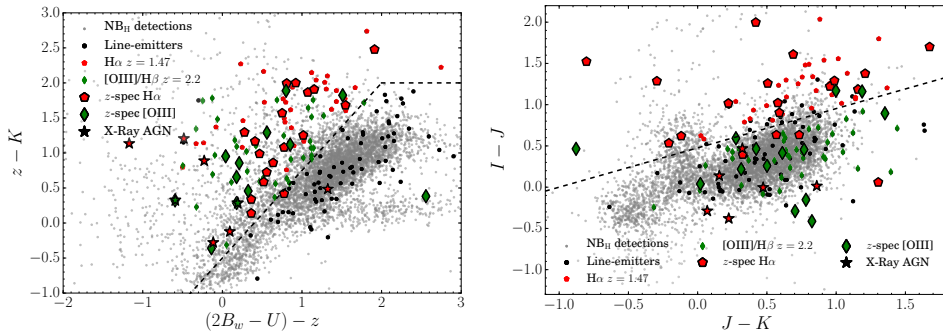
Figure 9.13: Colour criteria used to classify line-emitters identified with the NB_H filter. The modified $B_w z K$ criterion is used to distinguish $z > 1$ line-emitters from $z < 1$ line-emitters. We then distinguish between $z = 1.47$ and $z = 2.2$ based on the positions of Balmer breaks. At $z \approx 1.5$, the Balmer break lies around an observed 1000 nm, hence between $I - J$ (note that we use I rather than z because I is deeper and broader, see Table 9.1). At $z \approx 2.2$ the Balmer break lies between the J and K bands. Note that several X-ray detected Hα emitters at $z = 1.47$ mimic the colours of $z = 2.2$ [OIII]/Hβ emitters. These sources typically have high line-fluxes and their spectroscopic follow-up completeness is high. [OII] emitters at $z = 3.3$ are selected based on the position of their Lyman-break, similar to LAEs at $z = 3.1$ in Fig. 9.11.

Table 9.6: List of sources that are observed as dual-emitters (line-emitters in at least two narrow-bands). We present the coordinates, dual-NB redshifts (redshifts marked with a * are spectroscopic), I band magnitudes and the list of emission-lines that are detected. X-Ray and LOFAR detected sources are marked. We note that because the coverage in NB392, stV and NB921 is not homogeneous, the number of Lyα detections at $z = 2.23$ and [OII] at $z = 1.47$ is likely underestimated.

| ID	R.A.	Dec.	$z_{dual-NB}$	I	Note
B-HiZELS_1	14:33:19.29	+33:34:31.53	2.23*	18.9	Lyα+[OIII] + Hα.
B-HiZELS_2	14:32:58.85	+33:25:49.33	2.23	19.6	Hα + Lyα + Nv, X-Ray.
B-HiZELS_3	14:31:41.51	+33:49:11.27	2.26*	20.4	[OIII] + Hα + CIV +Lyα, X-Ray.
B-HiZELS_4	14:29:40.05	+33:33:32.13	2.27*	20.6	[OIII] + Hα + MgII, X-Ray.
B-HiZELS_5	14:32:01.52	+33:16:59.86	2.23	20.9	[OIII] + Hα
B-HiZELS_6	14:30:38.29	+33:20:17.85	2.23	21.3	[OIII]+Hα, X-Ray.
B-HiZELS_7	14:29:30.87	+34:05:44.85	2.23	21.7	[OIII]+Hα
B-HiZELS_8	14:32:13.88	+33:25:57.48	2.23	21.9	[OIII] + Hα + Lyα, LOFAR.
B-HiZELS_9	14:31:06.64	+33:46:19.18	2.23	22.1	[OIII] + Hα
B-HiZELS_10	14:33:07.48	+33:52:42.48	1.47	22.1	[OII] + Hα
B-HiZELS_11	14:32:37.05	+33:33:56.18	1.47	22.1	[OII] + Hα
B-HiZELS_12	14:30:51.00	+33:43:54.56	2.23	22.3	[OIII]+Hα
B-HiZELS_13	14:33:14.40	+33:46:53.17	1.47	22.4	[OII] + Hα
B-HiZELS_14	14:32:12.54	+33:22:26.15	1.47	22.4	[OII] + Hα
B-HiZELS_15	14:32:32.59	+33:59:03.32	2.24*	22.5	[OIII] + Hα + CIV, X-Ray & LOFAR.
B-HiZELS_16	14:30:40.31	+34:03:20.64	2.23	22.8	Lyα, CIV and Hα.
B-HiZELS_17	14:31:33.54	+34:02:48.52	2.23	22.8	[OIII] + Hα
B-HiZELS_18	14:32:52.90	+33:39:43.29	1.47	22.8	[OII] + Hα
B-HiZELS_19	14:30:16.12	+33:17:09.56	1.47	23.0	[OII] + Hα
B-HiZELS_20	14:30:28.28	+33:38:16.75	1.47	23.0	[OII] + Hα
B-HiZELS_21	14:30:19.38	+33:37:10.18	1.47	23.1	[OII] + Hα
B-HiZELS_22	14:33:15.16	+33:50:09.62	1.47	23.1	[OII] + Hα
B-HiZELS_23	14:32:37.05	+33:33:06.64	1.47	23.1	[OII] + Hα, LOFAR.
B-HiZELS_24	14:30:12.20	+33:51:57.33	2.23	23.3	[OIII] + Hα
B-HiZELS_25	14:30:26.29	+33:28:51.17	2.23	23.3	[OIII] + Hα
B-HiZELS_26	14:30:39.53	+33:57:09.60	1.47	23.3	[OII] + Hα
B-HiZELS_27	14:33:19.61	+33:34:36.66	2.23	23.4	[OIII] + Hα
B-HiZELS_28	14:31:50.68	+33:18:44.15	1.47	23.4	[OII] + Hα
B-HiZELS_29	14:30:28.56	+33:33:29.07	2.23	23.5	Lyα and Hα
B-HiZELS_30	14:30:54.03	+33:33:01.26	1.47	23.5	[OII] + Hα
B-HiZELS_31	14:31:19.33	+33:26:14.90	1.47	23.5	[OII] + Hα
B-HiZELS_32	14:32:48.04	+33:57:18.93	2.23	23.8	[OIII] + Hα
B-HiZELS_33	14:30:45.55	+33:23:50.12	1.47	23.8	[OII] + Hα
B-HiZELS_34	14:30:29.53	+33:20:49.91	1.47	23.8	[OII] + Hα
B-HiZELS_35	14:30:18.58	+34:03:24.88	2.23	23.9	[OIII] + Lyα
B-HiZELS_36	14:31:11.70	+33:41:28.69	1.47	24.0	[OII] + Hα
B-HiZELS_37	14:33:21.85	+33:54:50.65	1.47	24.2	[OII] + Hα
B-HiZELS_38	14:33:22.55	+33:48:04.57	1.47	24.3	[OII] + Hα
B-HiZELS_39	14:29:44.27	+33:50:43.84	1.47	24.3	[OII] + Hα
B-HiZELS_40	14:31:57.69	+33:16:37.87	2.23	24.9	[OII]+Hα
B-HiZELS_41	14:32:41.50	+33:26:18.45	2.23	25.5	[OIII] + Hα
B-HiZELS_42	14:30:39.05	+33:51:51.16	2.23	25.8	[OIII]+Hα
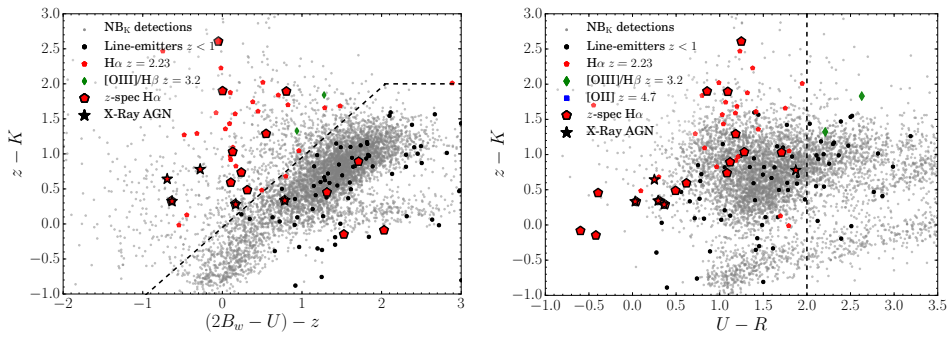
Figure 9.14: Colour criteria used to classify line-emitters identified with the NB$_K$ filter. Similarly to the line-emitters in the NB$_H$ filter, we use the modified $B_w zK$ criterion to selected line-emitters at $z > 1$ (left panel). We then distinguish those between Hα at $z = 2.23$ and [OIII]/Hβ emitters at $z = 3.2$ based on the positions of their Lyman-breaks.

CHAPTER 10

The origin of scatter in the stellar mass - halo mass relation of central galaxies in the EAGLE simulation

We use the hydrodynamical EAGLE simulation to study the magnitude and origin of the scatter in the stellar mass - halo mass relation for central galaxies. We separate cause and effect by correlating stellar masses in the baryonic simulation with halo properties in a matched dark matter only (DMO) simulation. The scatter in stellar mass increases with redshift and decreases with halo mass. At $z = 0.1$ it declines from 0.25 dex at $M_{200,\mathrm{DMO}} \approx 10^{11}$ $M_\odot$ to 0.12 dex at $M_{200,\mathrm{DMO}} \approx 10^{13}$ $M_\odot$, but the trend is weak above 10^{12} $M_\odot$. For $M_{200,\mathrm{DMO}} < 10^{12.5}$ $M_\odot$ up to 0.04 dex of the scatter is due to scatter in the halo concentration. At fixed halo mass, a larger stellar mass corresponds to a more concentrated halo. This is likely because higher concentrations imply earlier formation times and hence more time for accretion and star formation, and/or because feedback is less efficient in haloes with higher binding energies. The maximum circular velocity, $V_{\mathrm{max,DMO}}$, and binding energy are therefore more fundamental properties than halo mass, meaning that they are more accurate predictors of stellar mass, and we provide fitting formulae for their relations with stellar mass. However, concentration alone cannot explain the total scatter in the $M_{\mathrm{star}} - M_{200,\mathrm{DMO}}$ relation, and it does not explain the scatter in $M_{\mathrm{star}} - V_{\mathrm{max,DMO}}$. Halo spin, sphericity, triaxiality, substructure and environment are also not responsible for the remaining scatter, which thus could be due to more complex halo properties or non-linear/stochastic baryonic effects.

10.1   Introduction

The formation of structure in a universe consisting of dissipationless dark matter particles and dark energy is well understood and can be modelled with large *N*-body simulations, such that the halo mass function and the clustering of haloes can be predicted to high precision for a given set of cosmological parameters (e.g. Springel et al., 2006).

However, observations measure the masses and clustering of galaxies rather than dark matter haloes, so it is of utmost importance to connect stellar masses to dark matter halo masses. It is much more difficult for simulations to reproduce the observed stellar masses, as this requires a thorough understanding of the baryonic (feedback) processes involved, which are generally highly non-linear, complex and couple to a wide range of spatial scales. Therefore, a key goal of modern galaxy formation theory is to find the correlation or relation between the halo mass function and the stellar mass function.

The relation between stellar mass and halo mass is related to the efficiency of star formation, and to the strength of feedback from star formation (e.g. radiation pressure from hot young stars, stellar winds or supernovae) and Active Galactic Nuclei (AGN, e.g. quasar driven outflows or heating due to radio jets that prevent gas from cooling). By matching the abundances of observed galaxies and simulated dark haloes ranked by stellar and dark matter mass respectively, we can infer that the relation is steeper for low-mass centrals than for high mass central galaxies (e.g. Vale & Ostriker, 2004; Kravtsov et al., 2018). There is no tight relation between halo mass and stellar mass for satellite galaxies because of environmental processes such as tidal stripping, which is more efficient for the extended dark halo than for the stars. For the remainder of this paper, we therefore focus on central galaxies only.

The evolution of galaxies is thought to be driven by the growth of halo mass (e.g. White & Rees, 1978; Blumenthal et al., 1984), as assumed by halo models and semi-analytical models (SAMs, e.g. Henriques et al. 2015; Lacey et al. 2016) and related techniques such as abundance matching (e.g. Berlind & Weinberg, 2002; Yang et al., 2003; Behroozi et al., 2010; van den Bosch et al., 2013). However, both abundance matching models and observations suggest that there exists scatter in the stellar mass - halo mass (SMHM) relation (More et al., 2011; Moster et al., 2013; Behroozi et al., 2013b; Zu & Mandelbaum, 2015), meaning that halo masses alone cannot be used to predict accurate stellar masses. This could mean that there is also a second halo property which might explain (part of) the scatter in the stellar mass - halo mass (SMHM) relation, for example the formation time (e.g. Zentner et al., 2014), or that there is a halo property other than mass which is more strongly correlated to stellar mass, such as the circular velocity (e.g. Conroy et al., 2006; Trujillo-Gomez et al., 2011).

In this paper, we use simulated galaxies from the EAGLE project (Schaye et al., 2015; Crain et al., 2015) to assess which halo property can be used to predict stellar masses most accurately, and how it is related to the scatter in the stellar mass - halo mass relation, see Fig. 10.1. EAGLE is a hydrodynamical simulation for which the feedback from star formation and AGN has been cali-

brated to reproduce the $z = 0.1$ stellar mass function, galaxy sizes and the black hole mass - stellar mass relation. Because the simulation accurately reproduces many different observables and their evolution (e.g. Schaye et al., 2015; Furlong et al., 2015,?; Trayford et al., 2016), it is well suited for further studies of galaxy formation.

The properties of dark matter haloes can be affected by baryonic processes (e.g. Bryan et al., 2013; Velliscig et al., 2014; Schaller et al., 2015b). For example, efficient cooling of baryons can increase halo concentrations. For our purposes, it is therefore critical to connect stellar masses to dark matter halo properties from a matched dark matter only simulation. Otherwise, it would be impossible to determine whether a given halo property is a cause or an effect of efficient galaxy formation. In order to find which halo property is most closely related to stellar mass, we thus use halo properties from the dark matter only version of EAGLE, which has the same initial conditions, box size and resolution as its hydrodynamical counterpart.

An important caveat in studying the scatter in a galaxy scaling relation in general is that many properties are correlated. For example, the scatter in the SMHM relation by construction can not correlate strongly with any property that correlates strongly with halo mass. This way, an actual physical correlation can be hidden. As many halo properties are related to halo mass (e.g. Jeeson-Daniel et al., 2011), we should therefore be careful to only correlate the residuals of the SMHM relation to properties that are weakly or, ideally, not correlated with halo mass. We therefore use only dimensionless halo properties to study the origin of scatter in the SMHM relation.

This paper is organised as follows. The simulations and our analysis methods are presented in §10.2. In §10.3 we study which halo property is related most closely to stellar mass. We study the origin of scatter in the SMHM relation and the $M_{\mathrm{star}} - V_{\mathrm{max,DMO}}$ relation in §10.4. We show how we can predict more accurate stellar masses with a combination of halo properties in §10.5. In §10.6 we show the redshift evolution of the SMHM relation and its scatter. We discuss our results and compare with the literature in §10.7. Finally, §10.8 summarises the conclusions.

10.2 Methods

10.2.1 The EAGLE simulation project

In our analysis, we use central galaxies from the $(100 \ \mathrm{cMpc})^3$ reference EAGLE model at redshift $z = 0.101$, with a resolution such that a galaxy with a mass of $M_{\mathrm{star}} = 10^{10} \ \mathrm{M}_\odot$ (such as the Milky Way) is sampled by $\sim 10,000$ star particles. The hydrodynamical equations are solved using the smoothed particle hydrodynamics (SPH) N-body code Gadget 3, last described by Springel (2005), with modifications to the hydrodynamics solver (Hopkins, 2013; Dalla Vecchia, 2017; Schaller et al., 2015c), the time stepping (Durier & Dalla Vecchia, 2012) and new sub-grid physics. There are 2×1504^3 particles with masses $1.8 \times 10^6 \ \mathrm{M}_\odot$ (baryonic) and $9.7 \times 10^6 \ \mathrm{M}_\odot$ (dark matter). The resolution has been chosen to resolve
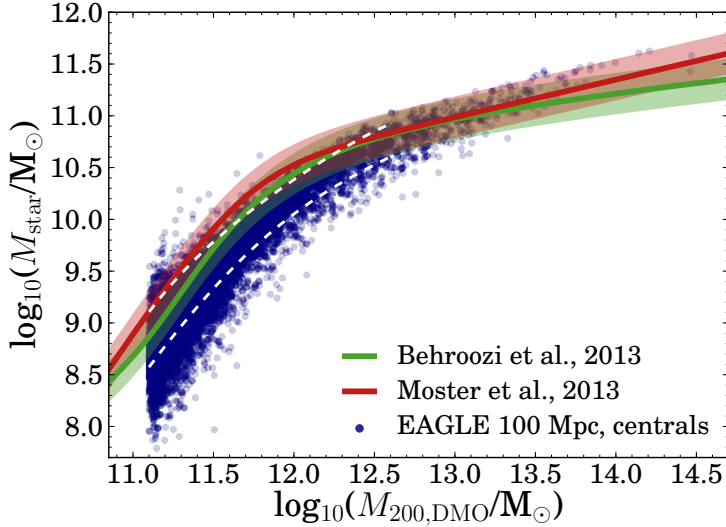
Figure 10.1: Relation between the stellar mass of central EAGLE galaxies and halo mass in the matched DMO simulation. The white dashed lines highlight the measured 1σ scatter in the region where individual points are saturated. Also shown are results obtained from abundance matching to observations (Behroozi et al., 2013b; Moster et al., 2013), including a shaded region indicating their 1σ scatter. It can be seen that the slope changes at a halo mass around 10^{12} $M_\odot$, which is the mass at which the galaxy formation efficiency peaks.

the Jeans scale in the warm (T$\sim 10^4$ K) interstellar medium (at least marginally). EAGLE uses a Planck cosmology (Planck Collaboration et al., 2014). The halo and galaxy catalogues and merger trees from the EAGLE simulation are publicly available (McAlpine et al., 2016).

For hydrodynamical simulations of galaxy formation, the implementation of sub-grid physics is critical (e.g. Schaye et al., 2010; Scannapieco et al., 2012). The included sub-grid models account for radiative cooling by the eleven most important elements (Wiersma et al., 2009a), star formation (Schaye & Dalla Vecchia, 2008) and chemical enrichment (Wiersma et al., 2009b), feedback from star formation (Dalla Vecchia & Schaye, 2012), growth of black holes (Springel et al., 2005b; Rosas-Guevara et al., 2015; Schaye et al., 2015) and feedback by AGN (Booth & Schaye, 2009). Galactic winds develop naturally without predetermined mass loading factors, velocities or directions, without any explicit dependence on dark matter properties and without disabling the hydrodynamics or the radiative cooling. This is achieved by injecting the feedback energy thermally using the stochastic implementation of Dalla Vecchia & Schaye (2012), which reduce numerical radiative losses. As discussed by Crain et al. (2015), the $z \approx 0$ galaxy stellar mass function can be reproduced even without tuning the feedback parameters. However, the feedback needs to be calibrated in order to simultaneously reproduce present-day galaxy sizes, which in turn leads to agreement with many other galaxy scaling relations.

Table 10.1: The properties of the simulated galaxies and haloes that are considered in our analysis. The stellar mass is from the reference EAGLE model, while the other properties are from the matched dark matter-only simulation. See §10.2.3 for detailed definitions of properties.

Property	Description
Dimensional	
M_{star}	Stellar mass inside 30 kpc, in $M_\odot$
$M_{200,DMO}$	Mass, in $M_\odot$
$M_{core,DMO}$	Mass within NFW scale radius, in $M_\odot$
$\sigma_{2500,DMO}$	Central velocity dispersion, in km/s
$V_{max,DMO}$	Maximum circular velocity, in km/s
$E_{2500,DMO}$	Binding energy, in $M_\odot$ km^2/s^2
$V_{peak,DMO}$	Highest V_{max} in a galaxy's history, in km/s
$V_{relax,DMO}$	Highest V_{max} while halo was relaxed, in km/s
Dimensionless	
$N_{2Mpc,DMO}$	Total number of subhalos within 2 Mpc
$N_{10Mpc,DMO}$	Total number of subhalos within 10 Mpc
$c_{200,DMO}$	Concentration
$\lambda_{200,DMO}$	Spin
s_{DMO}	Sphericity
T_{DMO}	Triaxiality
substructure	Mass fraction in bound substructures in a halo
$z_{0.5,DMO}$	Assembly redshift

10.2.2 Halo definition and matching between simulations

Haloes and galaxies are identified using the two step Friends-of-Friends (FoF) (e.g. Einasto et al., 1984) and subfind (Springel et al., 2001; Dolag et al., 2008) algorithms. First, the FoF-algorithm groups particles together using a linking length of 0.2 times the mean inter-particle distance (Davis et al., 1985). Then, subfind identifies subhalos as local overdensities whose membership is defined by the saddle points in the density distribution. The particles are then verified to be gravitationally bound to the substructure. The central galaxy is the subhalo at the minimum potential of the FoF-group. Following Schaye et al. (2015), we use a spherical 30 proper kpc aperture, centred on the central subhalo in each FoF-group, to measure the stellar masses of each central galaxy.

Dark matter halo properties are taken from the dark matter only version of EAGLE (DMO), which has the same initial conditions (phases and amplitudes of initial Gaussian field) and resolution as the reference model. Haloes in the DMO and EAGLE reference simulations were matched as described by Schaller et al. (2015a). In short, the 50 most-bound dark matter particles were selected for each halo in the reference model. These particles were located in the DMO model and haloes were matched if at least 25 of these particles belong to a single FOF halo in the DMO simulation. We note that for the halo masses discussed here (for the sample selection see §10.2.5), > 99% of the haloes are matched successfully.

10.2.3   Definitions of halo-properties

We study two classes of (dark matter) halo properties: dimensional and dimensionless. An overview of the properties, which are defined in this section, is given in Table 10.1.

Dimensional halo properties

In addition to stellar mass and halo mass ($M_{200,\mathrm{DMO}}$), dimensional properties that we consider are the core mass ($M_{\mathrm{core,DMO}}$), the maximum circular velocity at $z = 0.1$ (V_{max}) and in the halo's history (V_{peak}), the central velocity dispersion ($\sigma_{2500,\mathrm{DMO}}$) and the halo binding energy ($E_{2500,\mathrm{DMO}}$). While our main focus is on the stellar mass - halo mass relation, we use the other dimensional halo properties to investigate which halo property correlates best with stellar mass. Note that we vary our definition of stellar mass in Appendix A1.

$M_{200,\mathrm{DMO}}$ is used as the halo mass, which is the total mass contained within $R_{200,\mathrm{DMO}}$, the radius within which the enclosed over-density is 200 times the critical density. We study the effect of changing the definition to 500 and 2500 times the critical density in §10.3. V_{max} is the maximum circular velocity, $\max(\sqrt{\frac{GM(<R)}{R}})$. V_{peak} is the maximum circular velocity a halo had over its history (for central galaxies this is typically similar to the current V_{max}, as shown for EAGLE by Chaves-Montero et al. 2016). We also include V_{relax}, the maximum circular velocity of a halo during the part of its history when the halo was relaxed, which correlates most strongly with stellar mass Chaves-Montero et al. (2016)[1]. In this definition, a halo is relaxed when the formation time is longer than the crossing time (e.g. Ludlow et al., 2012). The formation time is defined as the time at which a fraction of 3/4 of the halo mass was first assembled in the main progenitor (although using a fraction of 1/2 leads to similar results, see Chaves-Montero et al. 2016).

Another definition of the halo mass is the halo core mass ($M_{\mathrm{core,DMO}}$), which is the mass inside the scale radius (r_s) of the NFW profile (e.g. Huss et al., 1999). As highlighted by Diemer et al. (2013), the evolution of $M_{200,\mathrm{DMO}}$ can be split into two stages: an initial growth of mass inside the $z = 0$ scale radius (growth of the core mass, e.g. Ludlow et al. 2013; Correa et al. 2015b), followed by "pseudo-evolution" due to the decreasing critical density of the Universe with cosmic time, during which the core mass remains nearly constant. We compute the core mass using the NFW fits of Schaller et al. (2015a) to obtain the scale radius. Typically, the core mass is $\approx 0.15 \times M_{200,\mathrm{DMO}}$, although there is significant scatter of 0.2 dex.

The halo binding energy is related to the halo mass and concentration. Galaxy formation may be more efficient in a halo with a higher binding energy (e.g. Booth & Schaye, 2010, 2011), since it will be harder for stellar and black hole feedback to drive galactic winds out of the galaxy. We compute the binding energy at three different radii: $R_{200,\mathrm{DMO}}$, $R_{500,\mathrm{DMO}}$ and $R_{2500,\mathrm{DMO}}$, using

---

[1] Note that Chaves-Montero et al. (2016) included satellites, whereas we only consider central galaxies.

$E_{200,DMO} = M_{200,DMO}\,\sigma^2_{200,DMO}$, where $\sigma_{200,DMO}$ is the velocity dispersion within $R_{200,DMO}$ (and similarly for $R_{500,DMO}$ and $R_{2500,DMO}$). As we are generally interested in stellar mass, which is concentrated in the centres of haloes, we focus on the binding energy and velocity dispersion of dark matter particles within $R_{2500,DMO}$. This radius ranges from $R_{2500,DMO} \approx 50$ kpc for $M_{star} = 10^{9.5}\ M_\odot$ to $R_{2500,DMO} \approx 350$ kpc for galaxies with $M_{star} = 10^{11.5}\ M_\odot$. $R_{2500,DMO}$ is typically $\approx 0.3 \times R_{200,DMO}$, and typically $\approx 2 \times r_s$, where r_s is the NFW scale radius.

Dimensionless halo properties

Dimensionless halo properties are generally related to the shape of the halo (such as triaxiality, sphericity, concentration and substructure), the environment (such as the number of neighbours) or its spin. These dimensionless properties are considered when we study the scatter in scaling relations.

The halo concentration was obtained by fitting a Navarro-Frenk-White (NFW) profile (Navarro et al., 1997) to the dark matter particles in the halo, as described by Schaller et al. (2015a). The concentration is defined as $c_{200,DMO} = R_{200,DMO}/r_s$.

The dimensionless spin parameter, $\lambda_{200,DMO}$, is defined as in Bullock et al. (2001), $\lambda_{200,DMO} = \frac{j}{\sqrt{2}V_{200,DMO}R_{200,DMO}}$, where $j = L/M$ is the specific angular momentum.

We quantify the shape of the halo with the sphericity, s, and triaxiality, T, parameters. The sphericity is defined as $s = c/a$, where c and a are the minor and major axes of the inertia tensor (e.g. Bett et al., 2007). The halo triaxiality is defined as $T = \frac{a^2-b^2}{a^2-c^2}$ (Franx et al., 1991).

The environment of the halo, $N_{X\,Mpc}$, is quantified by the number of neighbours within a distance of X Mpc. The number of neighbours, defined as the number of subhalos (including satellites) with a total dark matter mass above $10^{10}M_\odot$, is measured within spheres of 2 Mpc (N_{2Mpc}) and 10 Mpc (N_{10Mpc}).

The substructure parameter quantifies the environment of the central galaxy within the halo. It is defined as the fraction of the total mass of a FoF halo in bound substructures with dark matter mass above $10^{10}M_\odot$.

The assembly history of a halo is quantified by $z_{0.5,DMO}$, the redshift at which half of the halo mass has been assembled into a single progenitor subhalo. We use the EAGLE merger trees (McAlpine et al., 2016) to track the dark matter mass of the haloes from $z = 4$. For a halo at a fixed redshift, we select all the progenitors in the previous snapshot. The mass of the halo at that previous redshift is then the halo mass of its most massive progenitor. We thus obtain a mass assembly history for each halo and measure the formation redshift using a spline interpolation of the masses at the different snapshots.[2]

---

[2] The snapshot redshifts are $z = [0.10, 0.18, 0.27, 0.37, 0.50, 0.62, 0.74, 0.87, 1.00, 1.26, 1.49, 1.74, 2.01, 2.28, 2.48, 3.02, 3.53, 3.98]$.
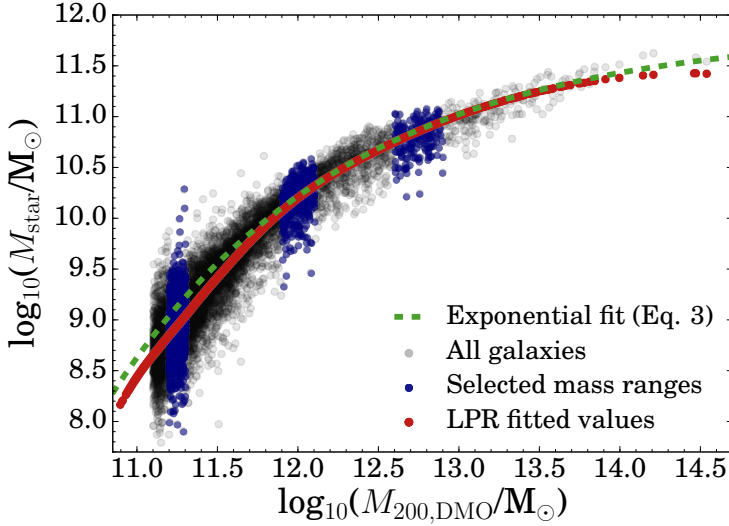
Figure 10.2: Relation between stellar mass in the EAGLE simulation and halo mass in the matched DMO simulation, illustrating the method to obtain residuals. The red points show the relation fitted using the non-parametric LPR method, see §10.2.4. The green line is the exponential fit specified by Eq. 10.3. The points marked in blue correspond to the three mass regimes mentioned throughout the text. Black points are galaxies not included in our analysis, but included in the LPR estimate of the relation.

10.2.4   Obtaining residuals of scaling relations

We quantify the scatter in scaling relations as the 1σ vertical offset from the mean relation (the residual). The mean relations are estimated in two ways: using non-parametric and parametric methods. The benefit of non-parametric methods is that they do not require an assumed functional form, but the downside is that they are less easily reproducible and perform less well at the limits of the dynamic range.

Non-parametric method: local polynomial regression

For the non-parametric approach, we use the local polynomial regression method (LPR, also known as locally-weighted scatterplot smoothing, LOWESS; Cleveland 1979). In short, for each data point $X_i = [x_i, y_i]$ a fitted value f_i is obtained using a local linear fit (described below), for which only the nearest half of the other data points is used. Our results are insensitive to changes in the fraction between 0.3 and 0.6 of the data that is used, except for the highest masses where a larger fraction results in an underestimate of the relation, or the lowest masses where smaller fractions result in greater noise. The following

Table 10.2: Fitted parameters for relations between stellar mass and the listed DMO halo properties using the functional form from Eq. 2.

Halo property	α	β	γ	χ^2_{red}
$M_{200,\mathrm{DMO}}$	$11.85^{+0.32}_{-0.18}$	$-0.68^{+0.13}_{-0.12}$	$8.65^{+1.17}_{-1.32}$	0.12
$V_{\max,\mathrm{DMO}}$	$11.56^{+0.62}_{-0.29}$	$-2.67^{+0.73}_{-0.76}$	$6.28^{+1.35}_{-1.35}$	0.08
$V_{\mathrm{peak},\mathrm{DMO}}$	$11.66^{+0.57}_{-0.32}$	$-2.46^{+0.62}_{-0.85}$	$5.92^{+1.53}_{-1.17}$	0.10
$V_{\mathrm{relax},\mathrm{DMO}}$	$11.62^{+0.59}_{-0.28}$	$-2.63^{+0.71}_{-0.76}$	$6.20^{+1.39}_{-1.30}$	0.11
$E_{2500,\mathrm{DMO}}$	$11.54^{+0.48}_{-0.17}$	$-0.54^{+0.11}_{-0.03}$	$8.77^{+0.36}_{-1.39}$	0.08
$\sigma_{2500,\mathrm{DMO}}$	$11.49^{+0.66}_{-0.32}$	$-2.77^{+0.78}_{-0.91}$	$5.94^{+1.52}_{-1.22}$	0.04

weight is then applied to each of the closest half of the data points:

$$w_{ij} = (1 - (\frac{d}{\max(d)})^3)^3, \tag{10.1}$$

where $d = \sqrt{(x_j - x_i)^2 + (y_j - y_i)^2}$ is the two-dimensional distance between points X_i and X_j. Finally, a linear relation is fitted to each selected data point using the least squares method:

$$f_i = \sum_j w_{ij} y_j / \sum_j w_{ij}. \tag{10.2}$$

From this linear relation, the fitted value, f_i, for X_i is obtained. This procedure is repeated for each point. This method is included in the R statistical language[3] by B. D. Ripley, and the reference for more information is Cleveland et al. (1992). The main benefit of this method is that it can handle non-trivial relations without assuming a functional form.

For the LPR procedure, we include all galaxies with a halo mass greater than 10^{11} M$_\odot$ in the matched DMO simulation (corresponding to stellar components with $\gtrsim 500$ star particles). The resulting values of f_i are shown using red symbols in Fig. 10.2. Note that there are as many red points as grey points, but that the red points appear as a line where they are close to each other. After this procedure, we find that the scatter, the 1σ standard deviation of the residuals $(y_i - f_i; \sigma(\Delta\log_{10} M_{\mathrm{star}}(M_{200,\mathrm{DMO}})))$, ranges from 0.15 dex to 0.27 dex, depending on the halo mass (see e.g. Table 10.3 and Fig. 10.3). A shortening of this method is that its accuracy depends on the number density of neighbouring points in the two dimensional plane. Therefore, it is less accurate at the highest masses ($M_{200,\mathrm{DMO}} > 10^{13.5}$ M$_\odot$, see Fig. 10.2) where there are fewer points and the available neighbours are strongly biased toward lower masses. Haloes of these masses are however not included in our analysis because of their small number in the simulation.

---

[3] https://www.r-project.org

Parametric method: functional fit

In addition to the non-parametric LPR fits, we perform parametric fits to the relations between stellar mass and dark matter halo properties. We use the following functional form in log-log space, which has three free parameters (α, β, γ):

$$\log_{10}(M_{\text{star}}/\text{M}_\odot) = \alpha - e^{\beta \log_{10}(M_{200,\text{DMO}}/\text{M}_\odot) + \gamma}. \tag{10.3}$$

In this equation, the halo property used is the halo mass ($M_{200,\text{DMO}}$), but it can be replaced by the other properties from §10.2.3. Because our sample of galaxies is dominated by the lowest-mass galaxies, we weight our fit, such that galaxies at all masses contribute equally. To do this, we compute the average stellar mass in halo mass bins of 0.1 dex and compute the standard deviation of the stellar masses in each bin. We only include bins that contain more than ten haloes (so up to $M_{200,\text{DMO}} \approx 10^{13.5}$ M$_\odot$). Using these bins and using the standard deviations as errors, we fit Eq. 10.3 by minimising the χ^2 value. We start with a large, but sparse, three dimensional grid of allowed values for the three parameters. After a first estimate of the values, we increase the resolution in a smaller range of allowed values to obtain our best-fit values. For the SMHM relation, we find best-fitting values of $\alpha = 11.85^{+0.32}_{-0.18}$, $\beta = -0.68^{+0.13}_{-0.12}$ and $\gamma = 8.65^{+1.17}_{-1.32}$.[4] The fit has a reduced χ^2 of 0.12 for 27 degrees of freedom. It can be seen in Fig. 10.2 that the parametric fit (green line) resembles the LPR values (red points) very well, except for the highest and lowest masses, for which the LPR method is less successful. This is because the LPR method is slightly biased towards the edges of parameter space, which can be overcome when the number density is sufficiently large to include a smaller fraction in the fit a larger number density without adding noise.

We also fit Eq. 10.3 to the relation between stellar mass and $E_{2500,\text{DMO}}$, $V_{\text{max,DMO}}$, $V_{\text{peak,DMO}}$, $V_{\text{relax,DMO}}$ and $\sigma_{2500,\text{DMO}}$ with the same method as described above. The results are summarised in Table 10.2. Using these equations, the dispersion in the residuals of the SMHM relation, $\sigma(\Delta \log_{10} M_{\text{star}}(M_{200,\text{DMO}}))$, is 0.15-0.26 dex, depending on the stellar mass range (see Fig. 10.3).

For infinitesimally small bins of halo mass, the dispersion in the residuals of the SMHM relation is equal to the scatter in stellar mass at fixed halo mass, $\sigma(\log_{10} M_{\text{star}}(M_{200,\text{DMO}}))$, and we will now therefore abbreviate this to $\sigma(\Delta \log_{10} M_{\text{star}})$ for simplicity in the remainder in the text.

10.2.5 Sample selection and mass range dependence

We initially select all central galaxies at $z = 0.1$ with a halo mass of $M_{200} > 10^{11}$ M$_\odot$ in the EAGLE simulation (and use these for fitting). However, due to small differences between M_{200} and $M_{200,\text{DMO}}$ we restrict our analysis to galaxies with $M_{200,\text{DMO}} > 10^{11.1}$ M$_\odot$ to avoid any biases which could arise from the influence

---

[4] We note that Eq. 10.3 can alternatively also be written as: $\log_{10}\left(\frac{M_{\text{star}}}{\text{M}_\odot}\right) = \alpha - e^\gamma \left(\frac{M_{200,\text{DMO}}}{\text{M}_\odot}\right)^{\beta \log_{10}(e)}$. In this case, our best fit can be written as:
$\log_{10}\left(\frac{M_{\text{star}}}{10^{10}\text{M}_\odot}\right) = 1.85 - 1.63\left(\frac{M_{200,\text{DMO}}}{10^{12}\text{M}_\odot}\right)^{-0.30}$.
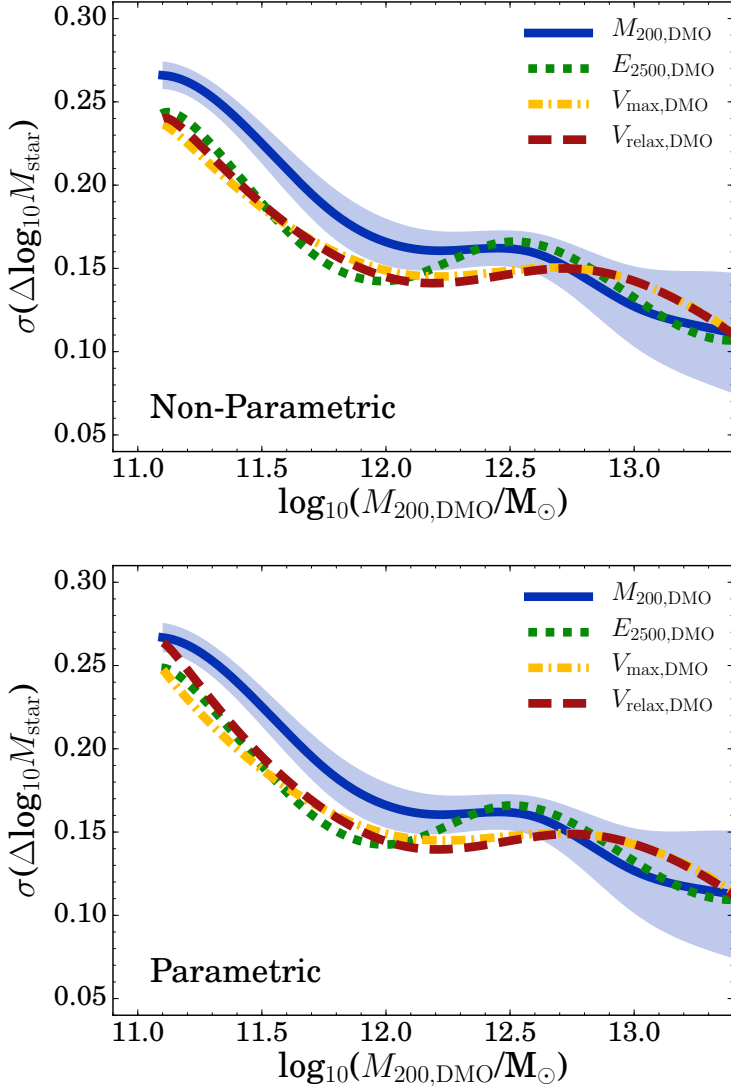
Figure 10.3: Scatter in the difference between true stellar masses (in the baryonic simulation) and stellar masses computed from the non-parametric (*top*) and parametric (*bottom*) fits to the relation between stellar mass and the different dark matter halo properties from the matched DMO simulation listed in the legend, as a function of DMO halo mass. We show the jackknife estimates of the errors in $\sigma(\log_{10} M_{\text{star}}(M_{200,\text{DMO}}))$ as a function of $M_{200,\text{DMO}}$ as a blue shaded region. The errors on $\sigma(\Delta\log_{10} M_{\text{star}})$ for the other halo properties are similar. We note that for halo properties other than $M_{200,\text{DMO}}$ we have binned $\sigma(\Delta\log_{10} M_{\text{star}})$ in bins of the specific halo property, and plot the result as a a function of the corresponding $M_{200,\text{DMO}}$ of that bin. In general, there is more scatter in the stellar mass - halo property relation at small stellar mass than at high stellar mass, irrespective of the halo property used. For $M_{200,\text{DMO}} < 10^{12.5}$ M$_\odot$, $M_{200,\text{DMO}}$ is a less accurate predictor of stellar mass than $V_{\text{max,DMO}}$, $V_{\text{relax,DMO}}$ and $E_{2500,\text{DMO}}$.

Table 10.3: Properties of the three halo mass samples. Different columns show different DMO halo mass ranges, the average stellar mass and the 1σ dispersion of the residuals of the stellar mass - halo mass relation, abbreviated as $\sigma(\Delta\log_{10}M_{\text{star}})$.

Halo mass range ($M_\odot$)	$< M_{\text{star}} >$ ($M_\odot$)	$\sigma(\Delta\log_{10}M_{\text{star}})$ (dex)
$11.2 < \log_{10}(M_{200,\text{DMO}}) < 11.3$	8.7×10^8	0.26
$11.9 < \log_{10}(M_{200,\text{DMO}}) < 12.1$	1.7×10^{10}	0.16
$12.6 < \log_{10}(M_{200,\text{DMO}}) < 12.9$	6.5×10^{10}	0.16

of baryons on the dark matter halo mass of the lowest halo masses.

In order to estimate the scatter in the SMHM relation as a function of halo mass, we perform the following steps: for each halo, we first obtain the residual relative to the main relation between stellar mass and the halo property (using either the non-parametric or parametric method). We then divide our sample of galaxies in bins (with width 0.4 dex for bins of halo mass, 0.6 dex for bins of $E_{2500,\text{DMO}}$ and 0.2 dex for bins of V_{max}), and compute the 1σ dispersion in the residual values of galaxies in each bin. We interpolate the values of the 1σ scatter as a function of halo mass and show this for the different halo properties in Fig. 10.3. Errors on $\sigma(\Delta\log_{10}M_{\text{star}})$ are estimated using the jackknife method. This means that we split the simulated volume in eight sub-domains of $(50\text{ cMpc})^3$ and compute the 1σ spread of residuals of the SMHM relation of the galaxies in each sub-box (for each bin of halo mass). Errors become significantly large at $M_{200,\text{DMO}} \gtrsim 10^{12.7}$ $M_\odot$ because of the limited number of massive haloes in the simulation.

As the correlations between halo properties and stellar mass might depend on the mass range, we also investigate how correlations between residuals and halo properties vary with halo mass (or circular velocity or binding energy, depending on the relevant halo property). We therefore compare galaxies in three narrow ranges of halo mass throughout the text. These intervals are listed in Table 10.3 and they are illustrated as blue points in Fig. 10.2. The lowest halo mass range is typical of dwarf galaxies, the middle of Milky Way like galaxies and the highest mass range of massive galaxies (the number of galaxies in a fixed range of halo masses declines quickly with mass, such that our bin widths increase with mass).

10.3   Correlations between stellar mass and DMO halo properties

In this section we explore which halo property correlates best with the stellar mass of central galaxies and is therefore the most fundamental.

In order to determine which halo property correlates most strongly with stellar mass, we perform a Spearman rank correlation (R_s) analysis. In a Spearman rank analysis, the absence of a relation between two properties results in $R_s = 0$

Table 10.4: Amount of scatter in stellar mass over all masses, as defined by the 1σ spread in the residuals from the non-parametric relation between stellar mass and the relevant DMO halo property. The column on the right shows the Spearman correlation rank coefficient for the relation between stellar mass and the halo property.

Halo-property	1σ scatter with M_{star}	R_s
$M_{200,\text{DMO}}$	0.24	0.92
$M_{500,\text{DMO}}$	0.22	0.93
$M_{2500,\text{DMO}}$	0.21	0.93
$M_{\text{core,DMO}}$	0.33	0.85
$M_{200,\text{mean,DMO}}$	0.24	0.91
$E_{200,\text{DMO}}$	0.23	0.92
$E_{500,\text{DMO}}$	0.22	0.93
$E_{2500,\text{DMO}}$	0.21	0.93
$\sigma_{200,\text{DMO}}$	0.25	0.91
$\sigma_{500,\text{DMO}}$	0.24	0.91
$\sigma_{2500,\text{DMO}}$	0.24	0.92
$V_{\text{max,DMO}}$	0.21	0.93
$V_{\text{peak,DMO}}$	0.24	0.93
$V_{\text{relax,DMO}}$	0.21	0.93

and a perfect (anti-)correlation results in $R_s = (-)1$. We will call a correlation 'strong' if $|R_s| > 0.3$. For this value, a correlation of 70 data points is statistically significant at 99% confidence. For our highest halo mass bin, consisting of 228 galaxies, a 99% confidence significance is obtained for $R_s = 0.17$ and higher.

We find that all dimensional halo properties are strongly correlated with stellar mass, with Spearman coefficients $R_s > 0.85$, see Table 10.4. The highest Spearman coefficients are found for $V_{\text{max,DMO}}$, $V_{\text{peak,DMO}}$, $V_{\text{relax,DMO}}$ and the halo mass and binding energy at $R_{2500,\text{DMO}}$ and $R_{500,\text{DMO}}$, which all give $R_s = 0.93$. This indicates that the central binding energy or maximum circular velocity are the most fundamental halo properties, although the differences are marginal.

Another way to study which halo property is the most fundamental, is by exploring how accurately a halo property can predict stellar masses, as a function of halo mass. By "accuracy" we mean the 1σ scatter in the difference between the predicted and true stellar masses, $\sigma(\Delta\log_{10}M_{\text{star}})$. Predicted stellar masses are obtained with both the non-parametric and the parametric relations between stellar mass and halo properties (see §10.2.4), and the true stellar masses are those measured in the baryonic simulation. The number density-weighted averaged results are listed in Table 10.4. The scatter is largest for the core mass (0.33 dex) and smallest (0.21 dex) for the halo mass measured at $R_{2500,\text{DMO}}$, $E_{2500,\text{DMO}}$, $V_{\text{max,DMO}}$ and $V_{\text{relax,DMO}}$. In Fig. 10.3 we show the mass dependence of the results for the halo properties with the least scatter in the difference between predicted and true stellar masses. Note that we vary the definitions of halo mass in Fig. 10.4 and of stellar mass in Appendix A.

Regardless of the halo property or fitting method, we find that $\sigma(\Delta\log_{10}M_{\text{star}})$ decreases from $\gtrsim 0.25$ dex at $M_{200,\text{DMO}} \approx 10^{11.2}$ M$_\odot$ to $\gtrsim 0.15$ dex at $M_{200,\text{DMO}} \approx$
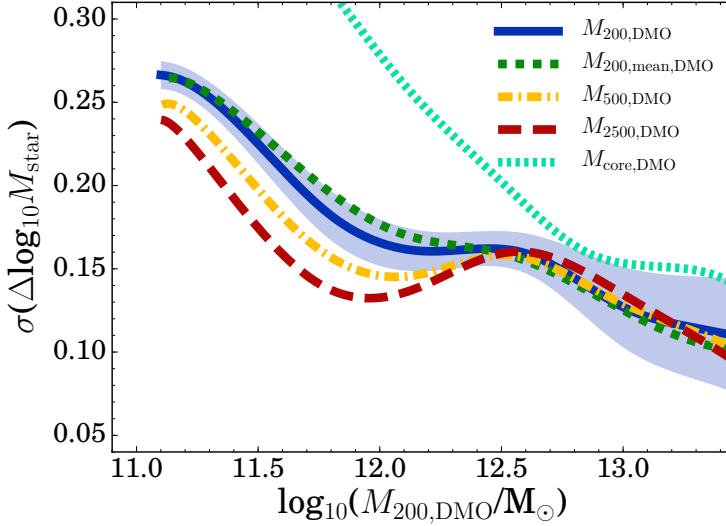
Figure 10.4: As Fig. 10.3, but now for varying definitions of halo mass. Bins are made in the respective halo property, but we plot the results as a function of the values of $M_{200,\mathrm{DMO}}$ corresponding to each bin. The halo mass within $R_{2500,\mathrm{DMO}}$ is most strongly related to stellar mass.

$10^{12.2}$ $M_\odot$. We show in Appendix B that this is not an effect of the limited simulation volume. This is in contrast with the typical assumptions in halo models, which use a mass-independent scatter of ~ 0.20 dex (i.e. Moster et al., 2013; van Uitert et al., 2016). Above $M_{200,\mathrm{DMO}} \gtrsim 10^{12.2}$ $M_\odot$, the uncertainties in $\sigma(\Delta\log_{10}M_\mathrm{star})$ are large enough (likely due to the limited simulation volume) that a constant scatter cannot be ruled out. Therefore, for the highest halo masses the decrease in the scatter with halo mass needs to be confirmed with larger simulation volumes.

We find that $V_{\mathrm{max,DMO}}$, $V_{\mathrm{relax,DMO}}$ and $E_{2500,\mathrm{DMO}}$ give similarly small $\sigma(\Delta\log_{10}M_\mathrm{star})$, while $M_{200,\mathrm{DMO}}$ performs somewhat worse for $M_{200,\mathrm{DMO}} < 10^{12.5}M_\odot$. However, using the parametric method, the differences are slightly smaller. This might mean that the chosen functional form is not optimal for V_{max}, V_{relax} and $E_{2500,\mathrm{DMO}}$ at low masses. Perhaps more striking is the fact that regardless of the halo property, there is at least 0.15 dex scatter in stellar masses at $M_{200} < 10^{12}M_\odot$, indicating that processes other than those captured by our halo properties are important. Another feature is that the slope changes at a mass of $\approx 10^{12}$ $M_\odot$, which coincides with the halo mass at which the galaxy bimodality arises and where feedback from AGN starts to become important (e.g. Bower et al., 2017).

In Fig. 10.4, we test whether our results depend on our specific choice of halo mass definition. Using $M_{200,\mathrm{mean,DMO}}$, which is based on the mass enclosed by the radius within which the mean density is 200 times the mean density of the Universe (as opposed to the critical density used before) results in a slightly
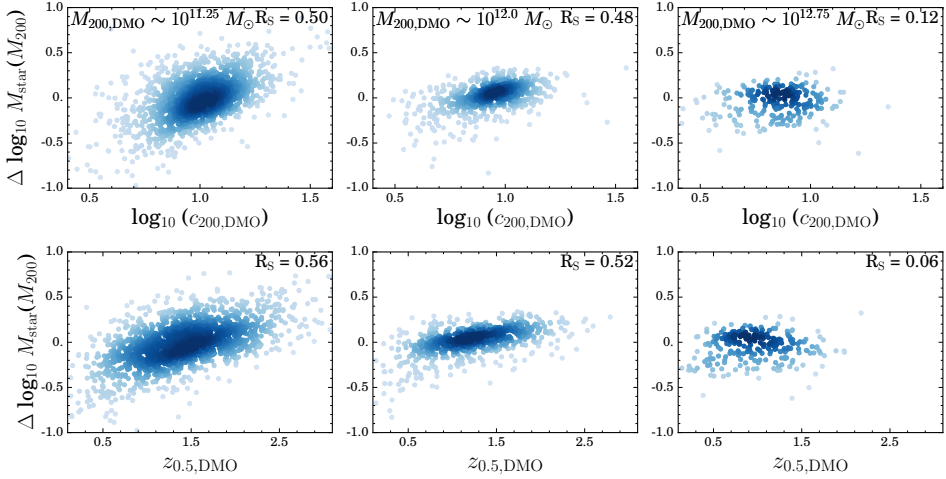
Figure 10.5: *Top:* Correlations between the residuals of the stellar mass - halo mass relation ($\Delta\log_{10} M_{\text{star}}(M_{200,\text{DMO}})$) and DMO halo concentration in the different halo mass ranges ($\log_{10}(M_{200,\text{DMO}}/\text{M}_\odot) \approx 11.2, 12.0, 12.6$, from left to right, respectively). The Spearman rank correlation coefficient (r_s) is shown in the corner of each panel. A strong correlation can be seen for the low- and intermediate-masses, showing that the scatter in the SMHM relation is partly due to the scatter in halo concentration at fixed mass. *Bottom:* Correlations between the residual and the formation time in different halo mass ranges. The results are similar to those for concentration.

larger scatter in the SMHM relation (by ~ 0.01 dex, with some dependence on halo mass, see Fig. 10.4). However, the scatter in the SMHM relation is much larger when using $M_{\text{core,DMO}}$. This is surprising, since the core mass is measured at a radius (r_s) which is typically half of $R_{2500,\text{DMO}}$, and thus more central. A possible explanation is that the NFW fits are inaccurate in the centres of haloes. Halo mass most accurately predicts stellar mass when it is measured at $R_{500,\text{DMO}}$ and $R_{2500,\text{DMO}}$, at least for $M_{200,\text{DMO}} < 10^{12.5}$ M$_\odot$. This is also the case for the binding energy. The halo properties measured at inner radii are more closely related to stellar mass. The same has been shown to hold for galaxy properties other than stellar mass (e.g. Velliscig et al., 2014; Zavala et al., 2016).

For comparison, we also have computed the scatter in stellar mass at fixed halo mass when using M_{200} and V_{max} from the baryonic simulation. We find that $\sigma(\Delta\log_{10} M_{\text{star}})$ is ≈ 0.015 dex smaller at masses $\lesssim 10^{12}$ M$_\odot$ when using M_{200} instead of $M_{200,\text{DMO}}$. The scatter in stellar mass at fixed rotational velocities is more sensitive to baryonic effects. At masses $\lesssim 10^{12}$ M$_\odot$, we find that $\sigma(\Delta\log_{10} M_{\text{star}})$ is ≈ 0.06 dex smaller when using V_{max} than $V_{\text{max,DMO}}$. There are no statistically significant differences between $\sigma(\Delta\log_{10} M_{\text{star}})$ in the baryonic and the DMO simulation at masses $> 10^{12}$ M$_\odot$.

10.4   Sources of scatter

In order to understand which processes are the source of scatter in the relations between stellar mass and dark matter halo properties, we investigate the scatter in two scaling relations: $M_{\text{star}} - M_{\text{200,DMO}}$ and $M_{\text{star}} - V_{\text{max}}$. We chose halo mass as this is most intuitive and widely used, and V_{max} as this property leads to the most accurate stellar masses (see Fig. 10.3). In this section we correlate the residuals of these scaling relations with the dimensionless DMO halo properties listed in Table 10.1 and discussed in §10.2.3. We quantify the strengths of the correlations using the Spearman rank correlation coefficient (R_s).

10.4.1   Sources of scatter in $M_{\text{star}} - M_{\text{200,DMO}}$

We find a strong correlation between the residuals of the SMHM relation and the concentration of the dark matter halo, $c_{\text{200,DMO}}$, implying that more concentrated haloes yield higher stellar masses. This effect is strong for both the low- and intermediate-mass ranges (R_s = 0.50, 0.48), see Fig. 10.5. We find a weaker correlation for the high halo mass range (R_s = 0.12, P-value 93%), indicating that there might be different physical processes operating at these halo masses. We have verified that the correlations in the low- and intermediate-mass ranges are not driven by the larger dynamic range in halo concentrations that is sampled thanks to a larger number of objects. By randomly resampling the numbers of galaxies in these mass ranges, such that we get the same number of galaxies as in the high-mass range, we find in all subsamples that $R_s \approx 0.5$, with a spread of 0.05.

The residuals of the relation between M_{star} and both $M_{\text{500,DMO}}$ and $M_{\text{2500,DMO}}$ are correlated weakly with concentration (not shown). This is because the mass in a more central part of the halo depends on both $M_{\text{200,DMO}}$ and concentration.

We investigate what fraction of the scatter in stellar masses at fixed halo mass is accounted for by concentration. This is done by fitting a linear relation between concentration and the residuals of the SMHM relation, for halo mass bins of 0.4 dex:

$$\Delta \log_{10} M_{\text{star}}(c_{\text{200,DMO}}) = a + b \log_{10}(c_{\text{200,DMO}}). \qquad (10.4)$$

The errors on the normalisation a and slope b of these fits are computed with the jackknife method, as described above. We then fit polynomial relations (with powers up to $\log_{10}(M_{\text{200,DMO}})^3$ to the relations in order to obtain the mass dependence of the normalisation and slope, $a(\log_{10}(M_{\text{200,DMO}}))$, and $b(\log_{10}(M_{\text{200,DMO}}))$). Then, $\Delta \log_{10} M_{\text{star}}(M_{\text{200,DMO}}, c_{\text{200,DMO}})$, the scatter after accounting for concentration, is computed as:

$$\Delta \log_{10} M_{\text{star}}(M_{\text{200,DMO}}, c_{\text{200,DMO}}) = \Delta \log_{10} M_{\text{star}}(M_{\text{200,DMO}})$$
$$+ a(\log_{10}(M_{\text{200,DMO}})) + b(\log_{10}(M_{\text{200,DMO}})) \times \log_{10}(c_{\text{200,DMO}}). \qquad (10.5)$$

At fixed halo mass, we fold the errors in the normalisation, Δa, and slope, Δb,

Figure 10.6: Scatter in the difference between the true and predicted stellar mass as a function of DMO halo mass, before and after using a dimensionless DMO halo property in addition to mass, in blue and red, respectively. Each panel corresponds to a different property. The shaded regions indicate the 1σ uncertainty. Only $c_{200,\text{DMO}}$ and $z_{0.5,\text{DMO}}$ are responsible for a statistical improvement in the scatter in stellar masses.

through the errors on the scatter in stellar masses, and obtain the halo mass dependence of the error in the scatter after taking account for concentration, $\sigma(\Delta\log_{10} M_{\text{star}}(M_{200,\text{DMO}}, c_{200,\text{DMO}}))$, with a spline interpolation.

The result is shown in the top-left panel of Fig. 10.6. At the lowest halo masses, 0.03 dex of the scatter in stellar masses is accounted for by concentration, while this is lower at higher masses. For $M_{200,\text{DMO}} > 10^{12.5}$ M$_\odot$ the inclusion of concentration does not reduce the scatter in stellar mass, again indicating that different physical processes are at play (i.e. Tinker, 2017).

It is interesting to note that Jeeson-Daniel et al. (2011) found from a principal component analysis of DMO simulations that halo concentration is the most fundamental halo property, being strongly related to many other dimensionless halo properties, and that halo mass only sets the scale of a system. This is consistent with our results, as we find that once the scale of the halo is factored out (by studying residuals at fixed halo mass), concentration is correlated with stellar mass. Furthermore, Booth & Schaye (2010) find that the black hole masses in
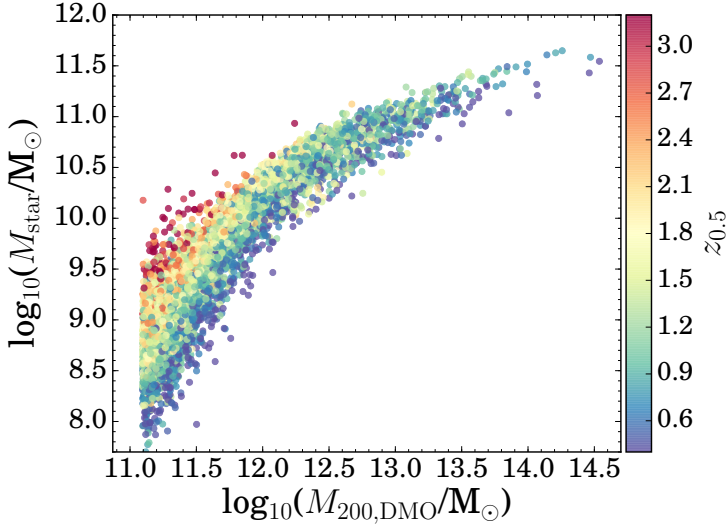
Figure 10.7: Stellar mass - halo mass relation in the EAGLE simulation colour-coded with the formation redshift of the halo. At low and intermediate halo masses, an earlier formation time corresponds to a higher stellar mass at fixed halo mass. This correlation is not seen at the highest masses. The transition occurs at masses slightly above 10^{12} $M_\odot$, where the SMHM relation also flattens.

their hydrodynamical simulation are set by halo mass with a secondary dependence on concentration, similar to our results for stellar mass, leading them to conclude that the halo binding energy is the most fundamental halo property in setting black hole masses. It could be that halo binding energy also determines stellar masses, as it is for example more difficult to drive galactic winds out of a galaxy in a halo with a steeper potential well. At the highest masses the correlation with binding energy may weaken because star formation is quenched and galaxies grow predominantly through mergers.

Since concentration is strongly correlated with formation time (e.g. Wechsler et al., 2002; Zhao et al., 2009; Jeeson-Daniel et al., 2011; Ludlow et al., 2014; Correa et al., 2015a), we expect galaxies with a large stellar mass at fixed halo mass to have formed earlier. We indeed find that the residuals of the SMHM relation correlate with $z_{0.5,\mathrm{DMO}}$, particularly for halo masses below $\sim 10^{12}$ $M_\odot$, as illustrated in Fig. 10.5. In Fig. 10.6 it can be seen that $z_{0.5,\mathrm{DMO}}$ is responsible for roughly the same amount of scatter in stellar masses, as concentration is. This is further illustrated in Fig. 10.7, which shows that haloes that form galaxies relatively efficiently generally form earlier.

Hence, another explanation for the correlation between concentration (and formation time) and the residuals of the SMHM relation is that haloes with a higher concentration started forming stars earlier and will thus be able to reach a higher stellar mass by a fixed redshift.

For halo masses $> 10^{12}$ $M_\odot$ there is almost no correlation between formation

time and the residuals of the SMHM relation. As was the case for concentration, a possible explanation for this is that in the most massive haloes stars have formed earlier than the assembly of their final halo, which is generally known as down-sizing (e.g. Cowie et al., 1996; De Lucia et al., 2006).

Fig. 10.6 shows that no halo property considered here, other than concentration and formation time, is responsible for the scatter in stellar mass at fixed halo mass. We find that there are weak correlations ($R_s \approx 0.3$) between the residuals of the SMHM relation and sphericity, substructure and $N_{2Mpc,DMO}$ for masses $< 10^{12}$ M$_\odot$. However, these might be explained by correlations between these quantities and concentration (e.g. Jeeson-Daniel et al., 2011). Since accounting for the concentration (or formation time) reduces the scatter in stellar mass by only $\lesssim 0.04$ dex, most of the scatter in the SMHM relation cannot be explained in terms of variations in the DMO halo properties.

It is interesting to measure how strongly the residuals of the SMHM relation are correlated with the concentration of the dark matter halo as measured in the full baryonic simulation. This correlation is much stronger for all halo mass ranges (R_s = 0.77, 0.79 and 0.47) than the correlation between the DMO concentration and the residuals of the SMHM relation (R_s = 0.50, 0.48 and 0.12). This implies that a higher concentration is both a cause of and an effect from efficient galaxy formation. For a given halo mass, efficient cooling (and thus star formation) leads to a higher concentration (e.g. Blumenthal et al., 1986; Duffy et al., 2010; Schaller et al., 2015b). However, the concentration from the dark matter only version of the simulation can only be a cause of more efficient galaxy formation. Thus, for a given halo mass, a higher dark matter halo concentration will lead to a higher stellar mass, which then results in an even more concentrated dark matter halo in the full baryonic simulation.

Robustness of results and varying definitions of concentration and formation time

The fact that halo concentration is itself weakly correlated with halo mass (e.g. Navarro et al., 1997; Avila-Reese et al., 1999; Duffy et al., 2008), with the parametric form $c_{200,DMO} \propto M_{200,DMO}^B$, with $B \approx -0.1$, can influence our results. We remove this dependence by correlating the residuals of the SMHM relation with the residuals of the $c_{200,DMO}$-$M_{200,DMO}$ relation obtained with the non-parametric method. We find that this does not change the Spearman coefficient for the correlation between $\sigma(\Delta \log_{10} M_{star})$ and concentration by more than 0.02, regardless of halo mass range.

We varied our definition of the concentration, as it might be important how we define the viral radius and because the use of an NFW profile to obtain the concentration might bias the results. Definitions that were tested are based on the circular velocity in the dark matter only version at various radii: $V_{max}/V_{200,DMO}$, $V_{max}/V_{500,DMO}$ and $V_{max}/V_{2500,DMO}$. However, all correlate slightly less or equally strong with the residuals of the SMHM relation than is the case for $c_{200,DMO}$. This suggests that our definition of concentration is close to optimal. A similar result is found when we vary the definition of formation
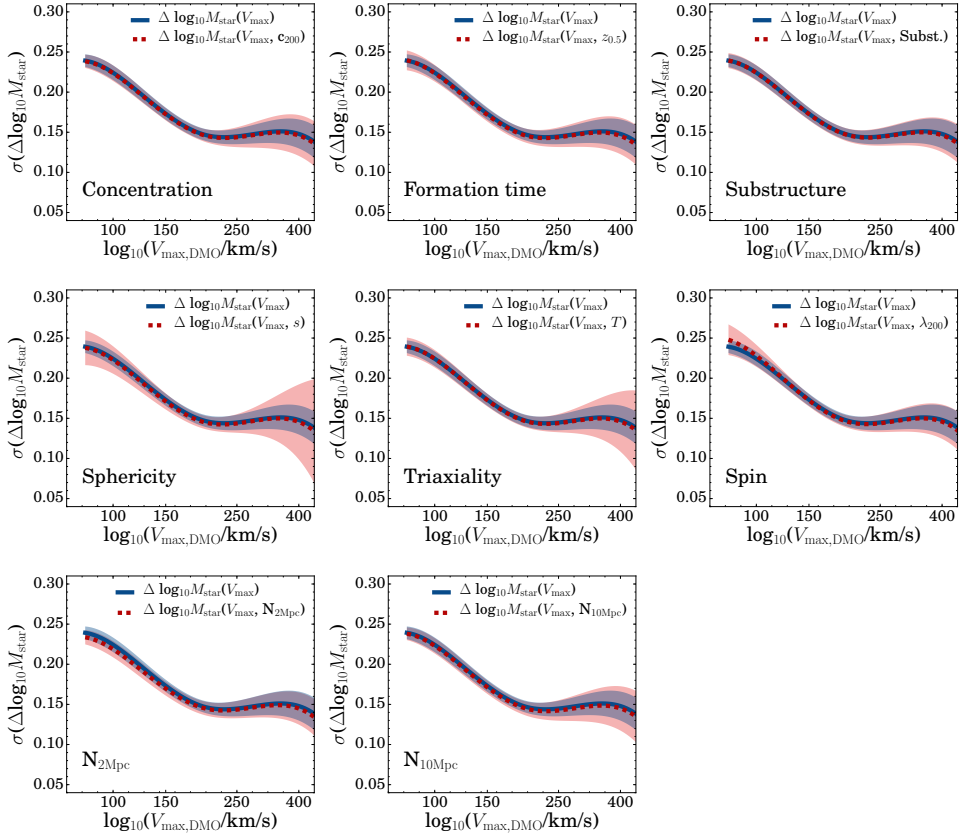
Figure 10.8: As Fig. 10.6 but now with the scatter in stellar mass as a function of $V_{\mathrm{max,DMO}}$ instead of $M_{200,\mathrm{DMO}}$. The addition of a dimensionless halo property to $V_{\mathrm{max,DMO}}$ does not result in statistically more accurate stellar masses.

time. The correlations between formation time and the residuals of the SMHM relation are slightly weaker if other assembly mass-fractions than 0.5 are chosen (we tested fractions of 0.33, 0.66 and 0.75). This indicates that our somewhat arbitrary choice of a mass fraction of 0.5 is close to optimal.

We also test the effect of selecting only relaxed haloes, using the definition from Duffy et al. (2008). This means that we only select haloes for which the distance between the centre of mass and the most bound particle is smaller than 0.07 times the virial radius. The fractions of relaxed halos in the low, intermediate and high halo mass range are 0.65, 0.55 and 0.52, respectively. For the highest halo mass range, we find that there are no differences. For the low- and intermediate-masses, the correlation between the scatter and concentration becomes slightly weaker (R_s = 0.45, 0.35, respectively). This is expected since the spread in concentration will be smaller, as concentration is correlated with relaxedness (e.g. Jeeson-Daniel et al., 2011).

To test the impact of recent interactions between haloes, we remove central

galaxies which have been satellite galaxies in the recent past (< 3 Gyr) or will become satellites between $z = 0.1$ and $z = 0.0$ (note that we carry out our analysis at $z = 0.1$). While some of these galaxies have either some of the highest or lowest stellar masses for their halo mass, there is little difference statistically. The $\sigma(\Delta \log_{10} M_{star})$ decreases by $\lesssim 0.01$ dex for all mass ranges and the correlation between $\sigma(\Delta \log_{10} M_{star})$ and formation time becomes slightly stronger for the low and intermediate mass ranges ($R_s = 0.57$ and 0.55, respectively), and similarly for concentration.

10.4.2   Sources of scatter in $M_{star} - V_{max,DMO}$

In §10.3 we showed that $V_{max,DMO}$ is somewhat more closely related to the stellar mass of central galaxies than $M_{200,DMO}$ is. However, there is still significant scatter in the $M_{star} - V_{max,DMO}$ relation. Therefore, we now investigate whether any dimensionless halo properties correlate with the residuals of the relation between stellar mass and $V_{max,DMO}$. Note that $V_{max,DMO}$ is very closely related to $E_{2500,DMO}$, with a scatter of only 0.05 dex.

Similarly as for $M_{200,DMO}$ in Fig. 10.6, Fig. 10.8 shows the 1σ spread in the residuals of the $M_{star} - V_{max,DMO}$ relation as a function of $V_{max,DMO}$, before and after correcting for the dependence on a dimensionless halo property. None of the investigated halo properties reduce the scatter in stellar mass. Indeed, we find no strong ($—R_s| > 0.3$) correlations between the residuals of the M_{star} - $V_{max,DMO}$ relation and dimensionless DMO halo properties. The fact that we find no correlation with concentration or formation time, means that the additional scatter in the SMHM relation due to concentration is already accounted for by V_{max}, which is related to both halo mass and concentration. This is also shown in Fig. 10.9, which compares the spread in stellar mass as a function of halo mass, where the stellar mass is computed either from $M_{200,DMO}$, $V_{max,DMO}$ or $E_{2500,DMO}$ alone, or from $M_{200,DMO}$ and either $c_{200,DMO}$ or $z_{0.5,DMO}$. Note that while we have binned in $V_{max,DMO}$ and $E_{2500,DMO}$, we show the halo masses corresponding to those bins respectively. By comparing the green curve (for V_{max}) with the dashed curves (using $M_{200,DMO}$ and an additional property), it is clear that $M_{200,DMO}$ performs less well than the other predictors.

10.5   A Parametric description for predicting stellar masses

As described in §10.4.1, up to 0.04 dex of scatter in stellar masses at fixed halo mass is attributed to variations in formation times and concentrations (where we measured the scatter in the SMHM relation with the non-parametric method). In this section, we use the parametric method to obtain fitting functions for stellar mass as a function of halo mass and concentration or formation time.

10.5.1   Halo mass and formation time

We correct the stellar mass at fixed $M_{200,\text{DMO}}$ using a fit between the scatter in the SMHM ($\Delta M_{\text{star}}(M_{200,\text{DMO}})$) and DMO formation time. As before, we use a simple linear least squares fit between the residuals of the SMHM and $z_{0.5,\text{DMO}}$, which results in:

$$\Delta \log_{10} M_{\text{star}}(M_{200,\text{DMO}}, z_{0.5,\text{DMO}}) = \\ a(\log_{10} M_{200,\text{DMO}}/\text{M}_\odot)\, z_{0.5,\text{DMO}} + b(\log_{10} M_{200,\text{DMO}}/\text{M}_\odot). \tag{10.6}$$

When including all galaxies (such that we average over all halo masses), we find best fitting parameters $a = 0.22^{+0.01}_{-0.01}$ and $b = -0.31^{+0.01}_{-0.01}$.

However, we have seen that the dependence on formation time varies with halo mass. We therefore need to fit the parameters a and b in a mass-dependent way. This mass dependence is obtained in the same way as we obtain the mass dependence of the scatter in the SMHM relation, which was described in §10.2.5.

The relations between the slope and normalisation of Eq. 10.6 and halo masses are fit with a cubic relation.

$$a(X) = -196.005 + 49.262\, X - 4.107\, X^2 + 0.114\, X^3, \tag{10.7}$$

where we define $X = \log_{10}(M_{200,\text{DMO}}/\text{M}_\odot)$, and

$$b(X) = 154.322 - 39.571\, X + 3.357\, X^2 - 0.094\, X^3, \tag{10.8}$$

Combining Equations 10.3, 10.6, 10.7 and 10.8, we find that we can predict stellar masses at $z = 0.1$ to a precision of $\approx 0.12 - 0.22$ dex from DMO halo properties with the following equation:

$$\log_{10}(M_{\text{star}}/\text{M}_\odot) = \alpha - e^{\beta\, X + \gamma} + a(X)\, z_{0.5,\text{DMO}} + b(X), \tag{10.9}$$

where α, β and γ are listed in the first line of Table 10.2. We note that the errors on the fits for $a(X)$ and $b(X)$ are large at $M_{200,\text{DMO}} > 10^{12.5}$ M$_\odot$. Above that halo mass, $a(X)$ and $b(X)$ should therefore be set to zero.

Using Eq. 10.9 instead of Eq. 10.3 reduces the 1σ scatter in the difference between predicted stellar masses and true stellar masses from 0.26 to 0.23 dex and from 0.16 to 0.14 dex in the low-mass and intermediate-mass ranges respectively by construction ($a = b = 0$ for $M_{200,\text{DMO}} > 10^{12.5}$ M$_\odot$. This is illustrated in Fig. 10.9, where we compile the scatter in the difference between true and predicted stellar mass as a function of DMO halo mass for various parametric fits.

10.5.2   Halo mass and concentration

Although formation time correlates slightly better with the residuals of the SMHM relation than concentration does, we can also use concentration as a secondary parameter to obtain more accurate stellar masses. We repeat the same steps as the previous section by using $\log_{10}(c_{200,\text{DMO}})$ in stead of $z_{0.5,\text{DMO}}$. The
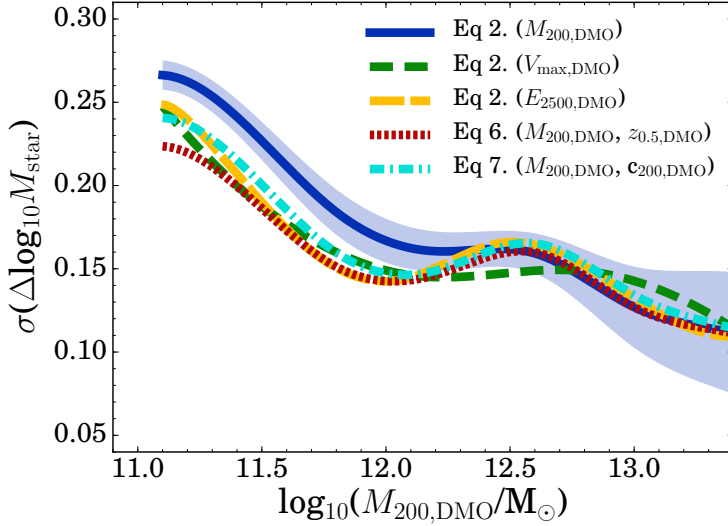
Figure 10.9: Scatter in the difference between true and predicted stellar mass from various parametric fits as a function of $M_{200,DMO}$. To first order, the stellar mass can be computed using halo masses and Eq. 10.3. A second order correction based on the relation between the scatter in the SMHM relation and formation time or concentration is applied using either Eq. 10.9 or Eq. 10.10. Since the scatter in the SMHM relation does not correlate with formation time at the highest halo masses, the scatter is only reduced for halo masses below $10^{12.6}$ M$_\odot$. It can be seen that using formation time is slightly more robust than using concentration. The scatter is then very similar to the scatter in stellar mass as a function of V_{max}.

benefit of using $\log_{10}(c_{200,DMO})$ is that we do not rely on the merger tree, and therefore only require the simulation output of a DMO simulation at a single snapshot. For the simulation output at $z = 0.1$, we obtain the following equation:

$$d(X) = -399.944 + 100.358\, X - 8.341\, X^2 + 0.230\, X^3, \qquad (10.10)$$

and,

$$e(X) = 296.274 - 75.165\, X + 6.307\, X^2 - 0.175\, X^3. \qquad (10.11)$$

Finally, this results in:

$$\log_{10}(M_{star}/M_\odot) = \alpha - e^{\beta X + \gamma} + d(X)\log_{10}c_{200,DMO} + e(X), \qquad (10.12)$$

where the relevant α, β and γ are listed in the first line of Table 10.2. We note again that above $M_{200,DMO} > 10^{12.5}$ M$_\odot$, $d(X)$ and $e(X)$ are set to zero because of the large errors.

When comparing the statistical corrections to stellar masses using formation time or concentration in Fig. 10.9, it is clear that using the formation time is only marginally better. One possible reason that the formation time performs slightly better than $c_{200,DMO}$ at low halo masses could be that there is some other scatter

in $c_{200,\mathrm{DMO}}$ at low halo mass that is due to numerical noise because the number of dark matter particles available to constrain the fitted NFW-profile is small.

10.6 Evolution

In this section we investigate the evolution of the SMHM relation and the scatter in stellar mass as a function of halo mass. As we did for $z = 0.1$, we fit the relation between stellar mass and $M_{200,\mathrm{DMO}}$ for central galaxies at different output redshifts from the EAGLE simulation using the non-parametric method.

We show $M_{\mathrm{star}}/M_{200,\mathrm{DMO}}$ versus $M_{200,\mathrm{DMO}}$ in the top panel of Fig. 10.10, as this better highlights the differences in comparison to showing stellar mass as a function of halo mass. There is almost no evolution between $z = 0$ and $z = 0.3$. At higher z, the evolution of the SMHM relation is, to first order, described by a decreasing normalisation: the ratio between stellar mass and halo mass decreases with increasing redshift, roughly independent of halo mass. At $M_{200,\mathrm{DMO}} \approx 10^{11}$ M$_\odot$, $M_{\mathrm{star}}/M_{200,\mathrm{DMO}}$ is roughly 0.15 dex lower at $z = 2.5$ than at $z = 0$. The evolution is largest at halo masses $\approx 10^{12}$ M$_\odot$, with M$_\odot$, $M_{\mathrm{star}}/M_{200,\mathrm{DMO}}$ decreasing by roughly 0.25 dex from $z = 0$ to $z = 2.5$. As a consequence, the peak in $M_{\mathrm{star}}/M_{200,\mathrm{DMO}}$ shifts to slightly higher masses with increasing redshift.

At fixed halo mass and $z = 0$ the normalisation of $M_{\mathrm{star}}/M_{200,\mathrm{DMO}}$ is about 0.2-0.3 dex lower in EAGLE than inferred from abundance matching by Behroozi et al. (2013b) and Moster et al. (2013). Similarly to Behroozi et al. (2013b), we find that the halo mass at which $M_{\mathrm{star}}/M_{200,\mathrm{DMO}}$ peaks increases only slightly ($\approx 0.1 - 0.2$ dex) between $z = 0$ and $z = 2.5$, while Moster et al. (2013) find a larger shift of ≈ 0.6 dex. Contrary to Behroozi et al. (2013b) (who find a constant or even increasing peak $M_{\mathrm{star}}/M_{200,\mathrm{DMO}}$ with redshift), we find that the peak $M_{\mathrm{star}}/M_{200,\mathrm{DMO}}$ decreases by ≈ 0.2 dex between $z = 0$ and $z = 2.5$, which is more similar to the trend found by Moster et al. (2013).

In the bottom panel of Fig. 10.10, we show the evolution of the scatter in the SMHM relation between $z = 0$ and $z = 2.5$. While we find a relatively constant scatter for $M_{200,\mathrm{DMO}} \approx 10^{11}$ M$_\odot$, there is significantly more scatter for $M_{200,\mathrm{DMO}} \approx 10^{11.5-12.0}$ M$_\odot$ at higher redshifts. This could be the caused by a larger spread in halo formation times at these higher redshifts. The evolution of the scatter in the SMHM relation at higher halo masses is unconstrained due to uncertainties stemming from limited number statistics in the EAGLE volume.

10.7 Discussion

10.7.1 Mass dependence of scatter

As shown in Fig. 10.3, the scatter in the difference between true stellar masses and stellar masses computed from fits to the SMHM relation, $\sigma(\Delta\log_{10}\mathrm{M}_{\mathrm{star}})$, decreases with increasing halo mass, at least up to a halo mass of $M_{200,\mathrm{DMO}} \approx 10^{12}$ M$_\odot$. This is not a result of the limited volume of the EAGLE simulation,
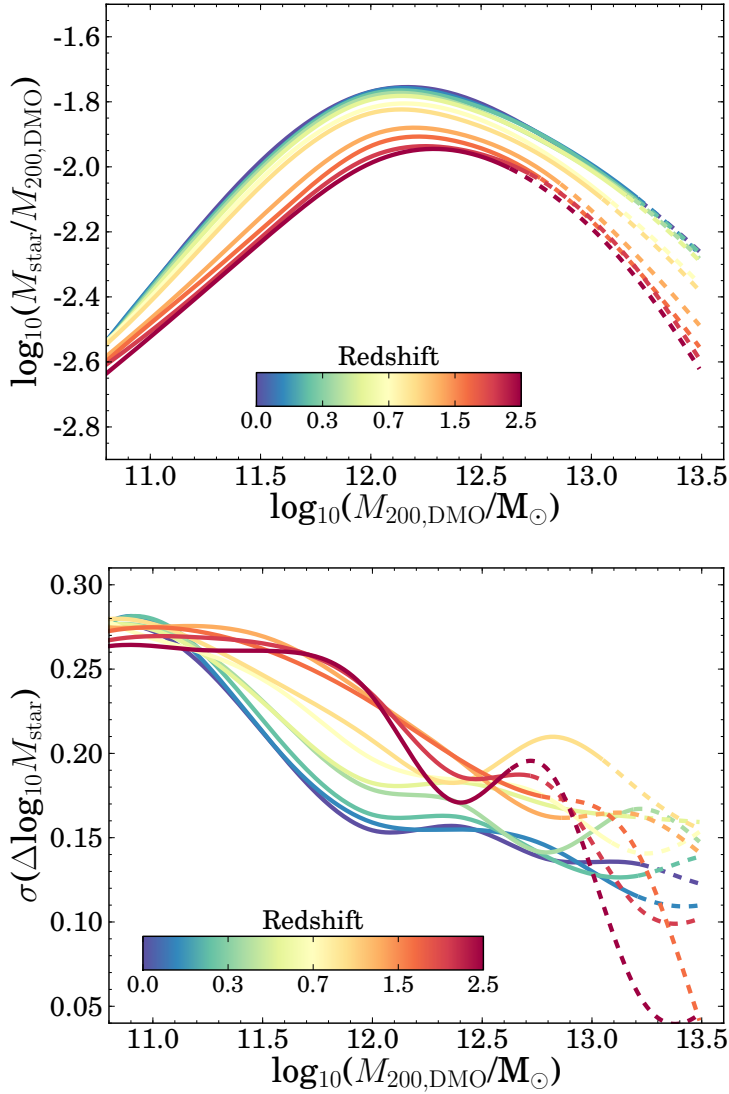
Figure 10.10: Evolution of the SMHM relation (left) and its scatter (right). Different from previous figures, we plot $M_{star}/M_{200,DMO}$ along the y-axis in order to increase the dynamic range. Dashed lines indicate where there are fewer than 100 galaxies per halo mass bin of 0.4 dex width. With increasing redshift the normalization of the SMHM drops and, except at the lowest halo masses, the scatter increases.

as shown in Appendix B. This is in contrast with the typical assumption that $\sigma(\log_{10}M_{\rm star})$ is not a strong function of halo mass, and roughly equals 0.2 dex (e.g. Leauthaud et al., 2012; Moster et al., 2013; van Uitert et al., 2016), which is often used in halo abundance matching modelling (e.g. Behroozi et al., 2013b). However, as noted by Vakili & Hahn (2016), abundance matching models that allow for assembly bias (see §10.7.2) indicate that the scatter can be significantly larger.

The most direct observational (yet model-dependent) constraints on the mass dependence of $\sigma(\log_{10}M_{\rm star})$ come from More et al. (2009) and Yang et al. (2009), who both measure a halo mass independent scatter of ≈ 0.17 dex. The observations from More et al. (2009) are based on the kinematics of satellite galaxies, while Yang et al. (2009) use a galaxy group catalog from the Sloan Digital Sky Survey (SDSS). However, for observational reasons, these constraints are mostly set at halo masses $M_{200,\rm DMO} > 10^{12}$ M$_\odot$ which are higher than the masses for which we find a significant trend. As illustrated in Fig. 10.11, EAGLE is consistent with these observational constraints, contrarily to some semi-analytical models of galaxy formation, which produce much greater scatter (Guo et al., 2016a). We note that the observational measurements of the scatter should be considered as upper limits due to errors in stellar mass measurements.

By fitting to lensing and clustering measurements, Zu & Mandelbaum (2015) simultaneously constrain the SMHM relation and its scatter at $z \sim 0.1$. In agreement with our results, they find that $\sigma(\log_{10}M_{\rm star})$ decreases with increasing halo mass: from $0.22^{+0.02}_{-0.01}$ dex at $M_{200} \lesssim 10^{12}$ M$_\odot$ to $0.18^{+0.01}_{-0.01}$ dex at $M_{200} \approx 10^{14}$ M$_\odot$ (see also Fig. 10.11 and the results from a semi-empirical approach by Rodríguez-Puebla et al. 2015). This scatter is similar to that we find in EAGLE at $M_{200} \lesssim 10^{12}$ M$_\odot$, but it decreases more slowly with halo mass than in EAGLE, which may be due to the constraints set by their assumption that the mass dependence of the scatter follows a simple linear relation. Tinker et al. (2017) report a $0.18^{+0.01}_{-0.02}$ dex scatter at $M_{200} \gtrsim 10^{12.7}$ M$_\odot$, slightly higher than the scatter in the SMHM in EAGLE. Combined with the result from Kravtsov et al. (2018) (who find that the scatter is 0.17 ± 0.02 dex for $M_{200} > 10^{14}$ M$_\odot$), the observations indicate that the scatter in the SMHM relation is insensitive of halo mass for haloes more massive than $M_{200} \gtrsim 10^{12.7}$ M$_\odot$.

In a recent combined analysis of *N*-body simulations and the fitted SMHM relation from Behroozi et al. (2013b), Gu et al. (2016) study the origin of scatter in the SMHM relation. Although their analysis is limited to haloes with masses $M_{200,\rm DMO} > 10^{12}M_\odot$, they argue that the constant scatter in the SMHM relation as a function of halo mass is due to an interplay of scatter due to ex-situ growth (i.e. accretion) and in-situ growth (i.e. star formation), and that the observed independence of the scatter in the SMHM relation on halo mass is a coincidence. In the analysis of Gu et al. (2016), hierarchical assembly leads to a scatter of ≈ 0.16 dex at high halo masses, which is roughly independent of the details of galaxy formation. Although the scatter due to ex-situ growth increases towards low halo masses, the relative importance of in-situ growth dominates below $M_{200,\rm DMO} < 10^{12}M_\odot$. Therefore, the scatter in the SMHM relation at lower masses is set mostly by the scatter in the in-situ growth at fixed halo mass,
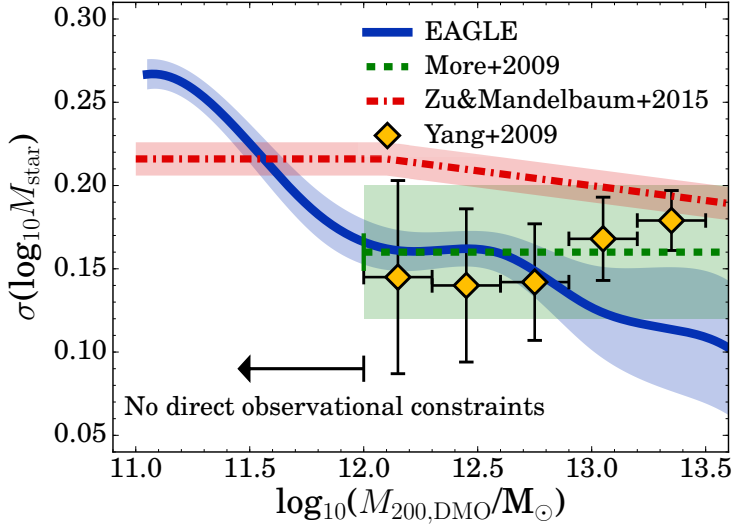
Figure 10.11: Scatter in the stellar mass at fixed halo mass as a function of halo mass. Yellow points show the binned results from the SDSS galaxy group catalog from Yang et al. 2009. The green shaded region shows the observational constraints from satellite kinematics (More et al. 2009). Both observational constraints are inferred for samples of galaxies with $M_{200,DMO} > 10^{12} M_{\odot}$ and are consistent with the results from EAGLE for this mass range. The red dashed line and shaded region shows the mass dependent scatter inferred by Zu & Mandelbaum (2015). We note that $\sigma(\Delta \log_{10} M_{star})$ in EAGLE is intrinsic, and does not take errors in stellar masses into account, which do affect the observations. Therefore, the observational constraints should be considered as upper limits.

which is more strongly related to the details of galaxy formation. Gu et al. (2016) assume the scatter in in-situ mass growth to be 0.2 dex for all halo masses. However, if this scatter were higher, or increases with decreasing halo mass, the resulting scatter in the SMHM relation will increase with decreasing halo mass. This would be consistent with our findings based on the EAGLE simulation, particularly since we find that at low halo masses the scatter in the SMHM relation depends strongly on halo formation time (which is likely related to in-situ star formation or binding energy).

More observational constraints on the scatter in the SMHM relation at low halo masses would be valuable. However, it is observationally challenging to measure halo masses for lower-mass central galaxies using methods such as satellite kinematics or galaxy-galaxy lensing (e.g. Mandelbaum et al., 2006; Zu & Mandelbaum, 2015). At lower stellar masses, halo masses may be estimated from measured rotational velocities (e.g. Blanton et al. 2008; Reddick et al. 2013 and see for example the compilation by Leauthaud et al. 2012). However, adiabatic contraction due to galaxy formation increases halo concentrations and thus also rotational velocities at fixed halo mass (e.g. Desmond & Wechsler, 2015). Thus, the measured scatter in stellar mass at fixed halo mass would be biased low if

halo masses were based on rotational velocities.

10.7.2   Relation to assembly bias & abundance matching

A commonly used technique to connect stellar masses to halo masses is abundance matching, which, in its simplest form, assumes that stellar mass increases monotonically with halo mass (or another halo property such as the maximum rotational velocity). This is related to the assumption that the halo clustering strength is fully determined by the halo mass. It may be plausible that a second halo property that is related to halo clustering is also a second parameter in determining galaxy stellar masses.

The existence of a second halo property that is related to the clustering strength of haloes is called assembly bias (e.g. Gao et al., 2005; Dalal et al., 2008; Lacerna & Padilla, 2011). These studies have shown that the clustering of dark matter haloes depends not only on halo mass, but also on their formation time. Chaves-Montero et al. (2016) showed that assembly bias significantly alters the clustering of galaxies in the EAGLE simulation, and that using V_{relax} as a halo property suffers significantly less from this effect. There is no consensus in observations of large sets of galaxies (such as 2dFGRS or SDSS) on the existence of assembly bias. While some authors claim a signal from assembly bias (Yang et al., 2006a; Wang et al., 2008), others (Blanton & Berlind, 2007; Tinker et al., 2008) argue little to no dependence of (for example) galaxy colour on large scale clustering (c.f. Hearin et al., 2016). More recently, Zentner et al. (2016) and Vakili & Hahn (2016) argue that significant assembly bias cannot be excluded from galaxy clustering data from SDSS.

The existence of scatter in the SMHM relation means that halo mass alone cannot predict stellar mass with an accuracy better than ≈ 0.2 dex, although we note again that this scatter decreases with increasing halo mass, see e.g. Fig. 10.9. The scatter in stellar masses can be slightly reduced by using information about the concentration or formation time of the haloes. This is similar to the approach by Lehmann et al. (2017) and Hearin et al. (2016), who extend the abundance matching method to halo properties that also depend on halo concentration. Thus, halo properties such as V_{max} or binding energy, which are related to both halo mass and concentration, are the most fundamental halo properties in determining stellar masses (see also Reddick et al. 2013). This resembles the conclusion from Booth & Schaye (2010), who argue that the halo binding energy determines black hole mass and indicates a co-evolution of galaxies and their massive black holes.

From an analysis of local galaxies from the SDSS, Lim et al. (2016) argued that there is a relation between the ratio of a central galaxy's stellar mass to its halo mass (from the Yang et al. 2009 group catalog) and the galaxy formation time. They find that galaxies with a high ratio of central stellar mass to halo mass are typically redder, older and more bulge-like: properties that are all associated with older stellar populations. In EAGLE, as illustrated in Fig. 10.7, such a relation also exists between DMO halo formation time and the ratio of stellar to halo mass. In this case, it certainly indicates a causal relationship, since the halo

formation time is measured in the independent DMO version of EAGLE.

10.7.3   The origin of the remaining scatter

Intriguingly, we find that there remains significant scatter in the SMHM relation after accounting for the effect of concentration, and that there is also scatter in the $M_{star} - V_{max}$ relation, which is not strongly related to any of the dimensionless DMO halo properties (see §10.4.2) studied. We consider possible explanations for the remaining scatter:

1. The scatter reflects noise due to the finite numerical resolution. We think this is unlikely since particularly the highest-mass galaxies are resolved using $> 10,000$ particles. In appendix B we compare with a higher-resolution 25 Mpc EAGLE simulation. Although this comparison is only possible for a volume that is too small to sample halo masses $\gtrsim 10^{12.5}$ M$_\odot$, we find no evidence for significant resolution effects.

2. The scatter is caused by a combination of weak correlations with halo properties that are uncorrelated with the halo properties we included. In particular, baryonic processes might be very non-linear and chaotic, such that only small differences in halo properties result in a substantial differences in the final stellar mass. Examples may include rare but explosive feedback or the interplay between dissipation, collapse and feedback.

10.8   Conclusions

We have used the EAGLE cosmological hydrodynamical simulation to study what drives the efficiency of galaxy formation in halos hosting central galaxies. In particular, we studied which dimensional dark matter halo property X is most closely related to stellar mass, and whether other dimensionless halo properties are responsible for driving the scatter in the stellar mass at fixed X for halo masses from $10^{11-13.5}$ M$_\odot$ (corresponding to $M_{star} \approx 10^{8-11.5}$ M$_\odot$). The investigated dimensional dark matter halo properties include different definitions of halo mass, binding energy and rotational velocity, see Table 10.1, while the investigated dimensionless halo properties are concentration, formation time, spin, sphericity, triaxiality, environment and substructure.

Since differences between haloes are ultimately determined by differences in the initial conditions, dominated by the initial density perturbations of (primarily) dark matter, we used halo properties from a matched DMO simulation. This is necessary since properties in the baryonic EAGLE simulation are affected by baryonic processes, making cause and effect impossible to separate. For example, if the baryonic simulations predicts a correlation between stellar mass and dark matter halo concentration, then it is not clear whether a higher concentration causes a higher stellar mass or vice versa.
The main conclusions of this work are:

1. The maximum circular velocity, $V_{\mathrm{max,DMO}}$, is the DMO halo property that is most closely related to stellar mass. The binding energy measured at $R_{2500,\mathrm{DMO}}$ is almost as strongly correlated with stellar mass. These halo properties are more fundamental than $M_{200,\mathrm{DMO}}$, for which there is more scatter in stellar mass, see Figs. 10.3 and 10.4. We have provided formulae to compute stellar masses based on dark matter halo properties (§10.5).

2. The scatter in stellar mass at fixed halo mass decreases with increasing halo mass, from ≈ 0.25 dex at $M_{200,\mathrm{DMO}} = 10^{11}$ M$_\odot$ to ≈ 0.12 dex at $M_{200,\mathrm{DMO}} = 10^{13}$ M$_\odot$. This is in contrast with the common assumption that the amount of scatter is independent of halo mass.

3. For halo masses $M_{200,\mathrm{DMO}} > 10^{12}$ M$_\odot$ the scatter in stellar mass decreases much less rapidly with halo mass than for $M_{200,\mathrm{DMO}} < 10^{12}$ M$_\odot$. This may be due to the transition from feedback dominated by star formation to feedback dominated by AGN, or due to the increased importance of mergers.

4. The measured scatter at $M_{200,\mathrm{DMO}} > 10^{12}$ M$_\odot$ is consistent with the most direct inferences from observations (Fig. 10.11). Future direct observations probing lower halo masses can test whether there is indeed more scatter in stellar mass at low halo mass.

5. The halo concentration, which is a good proxy for formation time, is responsible for part of the scatter in the stellar mass - halo mass relation up to a halo mass of $M_{200,\mathrm{DMO}} \sim 10^{12.5}$ M$_\odot$, see Figs. 10.5 and 10.6. Haloes with a higher concentration formed earlier and have been more efficient at forming stars (Fig. 10.7), probably because they are in a more advanced stage of their evolution and/or because it is harder for feedback to drive winds out of haloes with a higher concentration.

6. By correcting for concentration or formation time using a functional form, the scatter in the SMHM relation can be reduced by up to 0.04 dex (depending on the halo mass range), see Fig. 10.6. However, the remaining scatter in stellar mass is as large as the scatter in the M_{star} - V_{max} relation, see Fig. 10.9.

7. Empirical models, which assign stellar masses to haloes in DMO simulations are more reliable if halo properties based on both halo mass and concentration are used, such as V_{max}.

8. We find no DMO halo property that can account for the scatter in the SMHM relation after correcting for the effect of concentration (or formation time), or for the scatter the $M_{\mathrm{star}} - V_{\mathrm{max}}$ relation. This means that, except for properties related to the halo mass and concentration, other halo properties (such as spin, sphericity, triaxiality, environment and substructure) are statistically unimportant for determining the stellar mass of a galaxy. It is therefore likely that more complex (combinations of) halo properties and assembly histories are responsible for the remaining scatter in stellar masses by driving chaotic non-linear baryonic effects.

9. There is little evolution in the SMHM relation between $z = 0$ and $z = 0.3$. At higher redshift the evolution of the SMHM relation is approximately described by a decreasing normalisation, relatively independent of halo mass. The evolution is largest at halo masses $\approx 10^{12}$ $M_\odot$. As a consequence, the peak in $M_{\mathrm{star}}/M_{200,\mathrm{DMO}}$ shifts to slightly higher masses with increasing redshift. While the scatter in the SMHM is relatively constant between $z = 0$ and $z = 2.5$ for haloes with $M_{200,\mathrm{DMO}} \approx 10^{11}$ $M_\odot$, we find that there is significantly more scatter for $M_{200,\mathrm{DMO}} \approx 10^{11.5-12.0}$ $M_\odot$ at $z \gtrsim 1$ than at $z \approx 0$ (see Fig. 10.10). This is likely caused by the larger spread in halo formation times at these higher redshifts.

The efficiency of galaxy formation, defined as the scatter in the stellar mass - halo mass relation for central galaxies, is determined by the cosmological initial conditions. Haloes which reside in more over-dense regions collapse earlier, leading to a higher concentration and an earlier formation of stars and less efficient feedback due to deeper potential wells. Measures of the potential well depth, such as V_{max}, $M_{2500,\mathrm{DMO}}$ or a combination of these properties, correlate more strongly with stellar mass than $M_{200,\mathrm{DMO}}$ alone and are thus more fundamental properties governing the evolution of galaxies. However, this is only valid up to halo masses of $\sim 10^{12.5}$ $M_\odot$. Beyond this mass, additional physical processes play a role, as a more concentrated halo does not necessarily lead to a higher stellar mass.

Acknowledgments

Figure 10.12: The effect of scatter in stellar masses for varying definitions of stellar mass. The total stellar mass in a subhalo is slightly more closely related to halo mass than the aperture stellar mass is. There is negligible difference between the scatter in initial (i.e. corrected for stellar mass loss due to stellar evolution) and current with initial stellar mass.

Appendix A: Varying the definition of stellar mass

In this appendix, we vary the definition of stellar mass. In the main text, we used the total mass of star particles within 30 proper kpc of the minimum of the gravitational potential of a subhalo at $z = 0.1$. However, high-mass haloes contain substantial stellar mass at larger radii. We therefore use the stellar mass of all particles in the subhalo as identified by SUBFIND. As illustrated in Fig. 10.12, the spread in stellar mass as a function of halo mass becomes slightly lower for the highest halo masses.

Another variation that we investigate is the initial stellar mass (either within 30 kpc or of all star particles in the SUBFIND subhalo). This is the mass that a stellar particle had at the time it was formed, and using this mass removes the effects of stellar mass loss. Fig. 10.12 shows no significant differences when we use this definition. Although the typical stellar mass loss is $40 - 50$ %, the difference in stellar mass loss between the youngest and oldest galaxies is small, only ≈ 20 %, as the majority of stellar mass loss occurs on timescales $< 10^9$ yr due to the limited lifetimes of massive stars (e.g. Segers et al., 2016a). When using the initial stellar mass, the correlations between the scatter in the SMHM relation and concentration/formation time become slightly stronger ($\sim +0.02$ Spearman rank). This is easy to understand: the most concentrated haloes form the earliest, such that the effect of stellar mass loss will be highest, and this will therefore slightly weaken the trend that an earlier formation time leads to a higher redshift zero stellar mass (at fixed present-day halo mass).
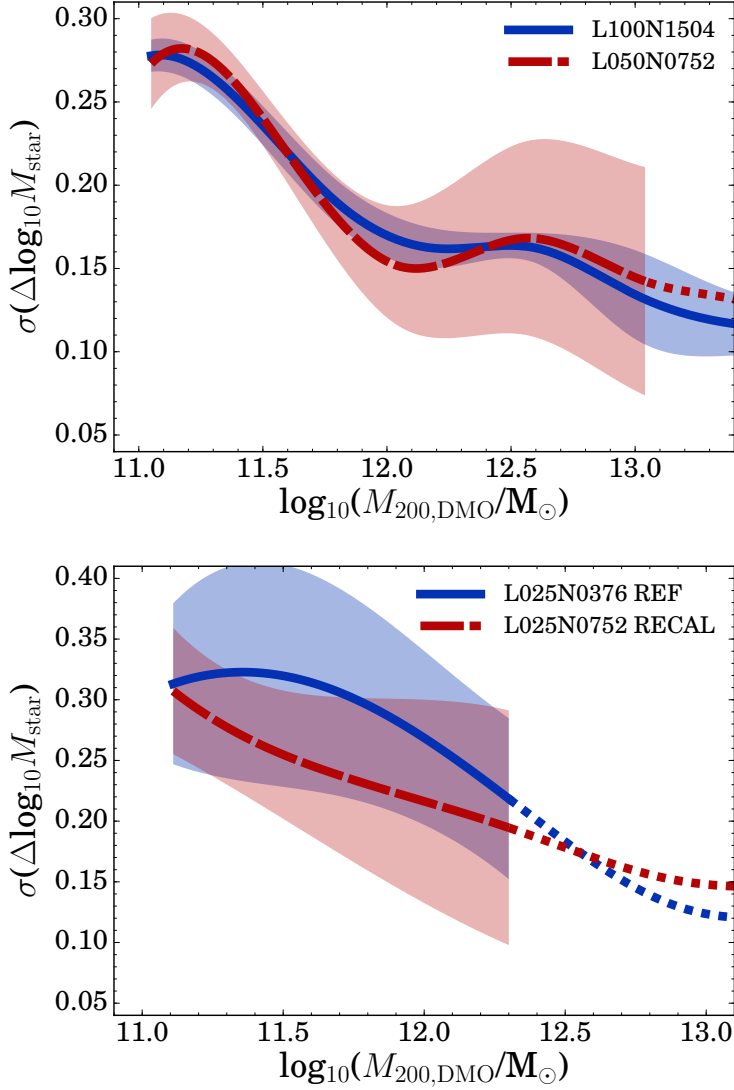
Figure 10.13: Box size and resolution test. Scatter in the difference between true stellar masses (in the baryonic simulation) and stellar masses computed from the non-parametric fits to the relation between stellar mass and DMO halo mass, as a function of DMO halo mass. The errors are estimated by jackknife resampling the data in sub-volumes with 1/8th times the total volume of the box. For halo mass ranges where there are less than 25 haloes per bin, we do not show the errors and only indicate the relation with a dashed line.

Appendix B: Dependence on box size and resolution

In this appendix, we test whether the scatter in the stellar mass - halo mass relation as a function of halo mass depends on the simulated volume or resolution. For the box size test, we compare the results from the $(100 \text{ Mpc})^3$ box with those from a $(50 \text{ Mpc})^3$ box with the same resolution. As shown in the top panel of Fig. 10.13, the spread in stellar mass as a function of halo mass is very similar between the two boxes. This means that our conclusions are not affected by the finite volume of our simulation. Small number statistics (in terms of number of galaxies and in terms of independent environments in the simulation volume) does increase the uncertainty in $\sigma(\Delta \log_{10} M_{\text{star}})$ with halo mass. The top panel of Fig. 10.13 shows that this effect is much stronger in the smaller box, such that the increase in uncertainty with mass may be due to the finite box size.

In the bottom panel of Fig. 10.13, we compare the spread in stellar mass as a function of halo mass in two simulations with a box size of $(25 \text{ Mpc})^3$. Note that we had to increase the bin-widths from 0.4 to 0.6 dex in order not to be dominated by errors. While one simulation has the *fiducial* resolution (L025N0376), the other uses a spatial (mass) resolution better by a factor two (eight). We note that the Recal model parameters differ slightly from those of the Reference model, see Schaye et al. (2015). It is hard to reliably investigate the effect of resolution on the statistical scatter in stellar mass, because the errors are very large due to the small numbers of galaxies per halo mass bin. While the differences are within the error bars, there might be less scatter in stellar mass at fixed halo mass in the simulation with higher resolution, particularly for $M_{200,\text{DMO}} < 10^{12.5} \text{ M}_\odot$.

The origin of scatter in the star formation rate - stellar mass relation in EAGLE

Observations have revealed that the star formation rate (SFR) and stellar mass (M_{star}) of star-forming galaxies follow a tight relation known as the galaxy main sequence. However, what physical information is encoded in this relation is under debate. Here, we use the EAGLE cosmological hydrodynamical simulation to study the mass dependence, evolution and origin of scatter in the SFR-M_{star} relation. At $z = 0$, we find that the scatter decreases slightly with stellar mass from 0.35 dex at $M_{star} \approx 10^9$ $M_\odot$ to 0.30 dex at $M_{star} \gtrsim 10^{10.5}$ $M_\odot$, in excellent agreement with observations. The scatter decreases from $z = 0$ to $z = 5$ by 0.05 dex at $M_{star} \gtrsim 10^{10}$ $M_\odot$ and by 0.15 dex for lower masses. We show that the scatter at $z = 0.1$ originates from a combination of (slightly dominant) fluctuations on short time-scales ($\lesssim$ 1 Gyr) that are presumably associated with self-regulation from cooling, star formation and outflows, and long time-scale ($\sim$ 10 Gyr) variations related to differences in halo formation times. At high masses, differences in black hole formation efficiency cause additional scatter, but also diminish the scatter caused by different halo formation times. While individual galaxies cross the main sequence multiple times during their evolution, they fluctuate around tracks associated with their halo properties, i.e. galaxies above/below the main sequence at $z = 0.1$ tend to have been above/below the main sequence for $\gg$ 1 Gyr.

11.1   Introduction

Observations of large samples of star-forming galaxies have shown that their star formation rate (SFR) and stellar mass (M_{star}) are closely related (e.g. Brinchmann et al., 2004; Elbaz et al., 2011; Rodighiero et al., 2014; Speagle et al., 2014; Schreiber et al., 2015). This relation is sometimes called the 'main sequence of galaxies' (Noeske et al., 2007). The existence of a main sequence (with a scatter of only ≈ 0.3 dex) indicates that the majority of galaxies (of fixed stellar mass) have SFRs that lie within a factor of two and it may be explained as an effect of the self-regulating nature of star-formation due to the interplay between gas accretion, star-formation and feedback driven outflows (e.g. Schaye et al., 2010; Davé et al., 2011; Haas et al., 2013; Lilly et al., 2013; Tacchella et al., 2016; Rodríguez-Puebla et al., 2016).

However, what information can be derived from the existence of the main sequence is still under debate (e.g. Kelson, 2014; Abramson et al., 2015). Is the main sequence some "attractor-solution", where galaxies fluctuate rapidly around the median relation because of stochasticity in star-formation events on short time-scales (e.g. Peng et al., 2010; Behroozi et al., 2013a), meaning that the star formation histories of galaxies with the same stellar mass are similar? Or does the main sequence simply show a "population average" at a certain age of the Universe (e.g. Gladders et al., 2013; Abramson et al., 2016), and do galaxies at fixed stellar mass have very diverse star formation histories (SFHs) on longer time-scales? Or is it a combination of both? Which effects are most important at different mass-scales and time-scales?

Crucial information may be encoded in the scatter in the SFR-M_{star} relation, and its dependence on stellar mass and cosmic time. What makes the growth rates of galaxies different, what are the important time-scales? Are the differences between galaxies at different positions along the main sequence systematic or stochastic? How important is the influence of the environment inside the halo (satellite galaxies) and at large radii (large-scale overdensity)? What is the role of the dark matter accretion history? These questions are the subject of this paper.

In order to investigate the physical origin of scatter in the SFR-M_{star} relation, we study galaxies in the cosmological hydrodynamical EAGLE simulation (Schaye et al., 2015; Crain et al., 2015; McAlpine et al., 2016). A benefit of using simulations is that we can trace galaxies during their evolution and also compare the evolution of the stellar mass with the evolution of the dark matter halo mass (particularly in matched dark matter only simulations) and the large-scale environment. EAGLE has been designed to reproduce the $z \approx 0$ galaxy stellar mass function and galaxy sizes, but simultaneously reproduces many other galaxy scaling relations (e.g. Crain et al., 2015; Lagos et al., 2016; Schaye et al., 2015; Bahé et al., 2016; Segers et al., 2016b). Importantly for this work, this includes the growth of the stellar mass density and the SFR-M_{star} relation (Furlong et al., 2015). A limitation from EAGLE is that short time-scale fluctuations in SFRs (particularly below 100 Myr) are challenging to measure due to the mass resolution and the time resolution of the simulation output. Likewise, frequently used observational SFR indicators also measure SFRs averaged over (at least) the past

100 Myr, such as the UV+IR that is used in e.g. Chang et al. (2015).

This paper is structured as follows. We first explain the methods in §12.2, including the simulation set-up and the way scatter is measured. We then characterise the scatter in the SFR-M_{star} relation in §11.3. This includes the dependence on mass, comparison with observations in the local Universe and the evolution of the scatter. We explore the relative importance of fluctuations in the SFRs on long and short time-scales in §11.4. Then, in §11.5, we investigate the relation between the scatter and the growth histories of galaxies and their dark matter haloes. We study the relation with supermassive black hole mass as a tracer of the impact of AGN feedback in §11.6. Our results are discussed in §11.7, including potential observational tests, and we summarise the paper in §11.8.

11.2   Methods

11.2.1   The EAGLE simulations

We study the properties of simulated galaxies from the EAGLE cosmological hydrodynamical simulation (Schaye et al., 2015; Crain et al., 2015)[1]. EAGLE is simulated with the smoothed particle hydrodynamic *N*-body code GADGET 3 (Springel, 2005), with extensive modifications in the hydrodynamic solver and time-stepping (Durier & Dalla Vecchia, 2012; Hopkins, 2013; Schaller et al., 2015c). We use the (100 cMpc)^3 reference model, which includes 2×1504^3 particles with masses 9.7×10^6 $M_\odot$ (dark matter) and 1.8×10^6 $M_\odot$ (initial baryonic). As several important physical processes are unresolved at these mass scales, the following sub-grid models are included: radiative cooling of gas (Wiersma et al., 2009a), the formation of star particles (Schaye & Dalla Vecchia, 2008), chemical enrichment by stellar mass loss (Wiersma et al., 2009b), feedback from star formation (Dalla Vecchia & Schaye, 2012), and the growth of black holes and the feedback associated with AGN activity (Springel et al., 2005a; Booth & Schaye, 2009; Rosas-Guevara et al., 2015; Schaye et al., 2015).

Galaxies have been identified as subhalos in Friends-of-Friends (FoF) halos (e.g. Einasto et al., 1984) using the SUBFIND (Springel et al., 2001; Dolag et al., 2008) algorithm. The subhalo that is at the minimum gravitational potential in a FoF halo is defined to be the central galaxy. The edges of subhalos are identified through saddle points in the density distribution and only gravitationally bound particles are members of a subhalo. We measure the evolution of halo masses by linking galaxies between redshift snap/snipshots with their most-massive progenitors using the merger-trees described in Qu et al. (2017). Following Schaye et al. (2015), we measure the stellar mass and SFR of a galaxy by summing over the particles within a 30 pkpc radius from the minimum of the gravitational potential, mimicking typical apertures used in observations. Similarly to other analyses, the *instantaneous* SFR in EAGLE is measured directly from the dense gas mass (Schaye & Dalla Vecchia, 2008). The density threshold for star formation increases with decreasing metallicity following the fits of Schaye (2004) for

---

[1] Galaxy catalogues and merger-trees are available through McAlpine et al. (2016).

the critical density required for the formation of a cold, molecular gas phase.

We compare the properties of the reference simulation (including baryon physics) with a matched dark matter only version of EAGLE (DMO). This version was run with the same initial conditions and resolution as the reference model. Halos are matched between the simulations by finding the DMO halo that includes the 50 most-bound dark matter particles in the reference model (see Schaller et al. 2015a for details). Halos are successfully matched if at least 25 of these particles are members of a single FoF group. More than 99% of the haloes that are included in our analysis are matched successfully.
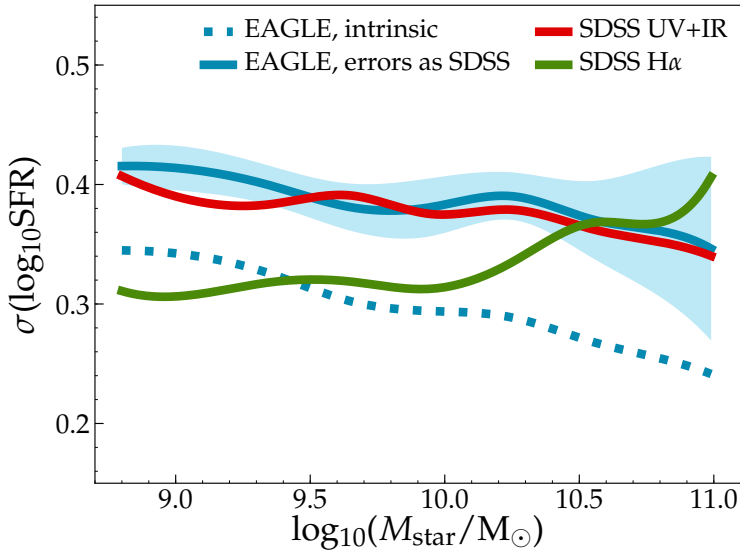
Figure 11.1: The mass dependence of the scatter in the SFR at fixed stellar mass for star-forming galaxies at $z = 0$ in EAGLE (blue) and observed at $0.02 < z < 0.04$ from SDSS (red; Chang et al. 2015). For a proper comparison, we apply the SDSS measurement uncertainties to EAGLE. The shaded region indicates the additional uncertainty in EAGLE due to cosmic variance. The dashed blue line shows the intrinsic scatter in EAGLE. The green line shows the scatter measured in the SDSS sample when using Hα SFRs (Brinchmann et al. 2004). The predicted scatter in SFR at fixed stellar mass decreases slowly with stellar mass, in excellent agreement with the observations.

11.2.2 Measuring scatter

As the goal of this paper is to study the origin of scatter in the SFR-M_{star} relation, we remove quenched galaxies from our analysis. While a significant fraction of quenched galaxies (in particularly quenched satellites) are devoid of star-forming gas (such that these galaxies formally have SFR=0 $M_\odot$ yr^{-1}), others still have a reduced, but non-zero SFR. In order to select star-forming galaxies that define the main relation between SFR and M_{star}, we select galaxies with

SFR/$M_{star} \equiv$ sSFR $> 10^{-11}$ yr^{-1} at $z = 0$. This selection threshold evolves with redshift to account for the overall change in specific SFRs as detailed in §12.3.3.

We measure the scatter from the residuals with respect to the relation determined using the non-parametric local polynomial regression (LPR) method (Cleveland et al., 1992). In this method, for each data point X = [$\log_{10} M_{star}$, $\log_{10}$ SFR] a fitted value is obtained using a local linear fit with the least squares method, for which only the nearest half in ($\log_{10} M_{star}$, $\log_{10}$ SFR) distance of the other data points are used and points are weighted by their distance in ($\log_{10} M_{star}$, $\log_{10}$ SFR) space to the data point X, see Matthee et al. (2017a) for full details. The residual is the vertical offset from the fitted value at the respective data point. The benefit of this method is that no assumption on the functional form of the relation is required. However, in practice the results are similar to a simple $\log_{10}$ SFR $\propto \log_{10} M_{star}$ relation. Therefore, the scatter in the residuals is very similar to the scatter in the specific SFR.

11.3   The amount of scatter

Before studying the physical origin of the scatter in the SFR-M_{star} relation, we measure the magnitude of the scatter as a function of stellar mass in both the EAGLE simulation and a sample of star-forming galaxies from the Sloan Digital Sky Survey (SDSS, e.g. Padmanabhan et al. 2008; Alam et al. 2015). For SDSS, we use the measurements from Chang et al. (2015), who combined the SDSS optical photometry with WISE infrared photometry and simultaneously and self-consistently modelled the dust attenuation and re-emission. As shown in Figure 5 of Schaller et al. (2015c), there is very good agreement between the normalisation and slope of the main sequence in Chang et al. (2015) and in the EAGLE simulation. As recommended by Chang et al. (2015), we only include galaxies that have FLAG = 1 (meaning they have reliable aperture corrections). As in EAGLE, we select star-forming galaxies with sSFR $> 10^{-11}$ yr^{-1}. In order to compare the measurements from Chang et al. (2015) with older SDSS measurements (DR7), we also perform our analysis on the same galaxy sample with Hα derived SFRs (and with SFR FLAG = 0) from Brinchmann et al. (2004). These are based on the flux measured with fibre-spectroscopy and thus rely on corrections to take emission at larger radii into account.

11.3.1   Mass dependence in EAGLE and SDSS

For EAGLE, we split the sample of galaxies at $z = 0$ in stellar mass bins of 0.3 dex from $\log_{10}(M_{star}/M_\odot) = 8.8$ to 11.2 and measure the 1σ standard deviation, $\sigma(\log_{10}$ SFR), from the residual values in each bin. The lower limit of the mass-range that we study is based on the resolution limit of EAGLE (such that galaxies are resolved with > 500 star particles). The upper limits are set by the simulation volume (10^6 cMpc^3), such that each bin includes at least 50 galaxies. Next, we shift bin edges by ± 0.1 dex, repeat the measurement, and interpolate the measured standard deviations in the bins to show how the 1σ scatter varies with

stellar mass. Choosing a smaller bin-width increases the uncertainty, while a larger bin-width smooths the trends.

For a proper comparison with the observations, we take the additional scatter due to measurement errors into account as follows. We assume that the uncertainties in the SFRs in EAGLE depend on sSFR similarly as in the observational sample from Chang et al. (2015). In practice, this results in uncertainties of $0.22^{+0.09}_{-0.07}$ dex. Then, we perturb the SFR of each galaxy in EAGLE 1000 times within the typical observational error (assuming the errors in $\log_{10}$ SFR are gaussian), and re-measure the scatter. This results in 1000 realisations of the mass-dependence of the scatter, from which we obtain the median and the 1σ confidence intervals. We account for cosmic variance due to the limited simulation volume by measuring the scatter in jackknife realisations of the galaxies in eight sub-boxes of $(50 \text{ cMpc})^3$. The intrinsic scatter in EAGLE is ≈ 0.30 dex, while the mimicked 'observed' scatter is ≈ 0.40 dex.

Several observational biases complicate the analysis of the SDSS sample. First, due to their limited sensitivity, observations suffer from incompleteness, particularly at low stellar masses. As the sensitivity limit is in observed flux, it is related to a complex combination of SFR, mass, dust attenuation and stellar age. It is therefore likely that incompleteness biases the measured scatter (e.g. Shimakawa et al., 2017). Second, observations are not performed within an infinitesimally small redshift slice. As the typical SFR of galaxies (at all masses) increases with redshift (e.g. Madau & Dickinson, 2014), this means that sources with a higher redshift will have a higher SFR at fixed stellar mass (increasing the observed scatter). Due to the shape of the galaxy luminosity function, the redshift-comoving volume relation and the redshift dependence of mass-incompleteness, the sample is dominated by slightly higher redshift galaxies at the high-mass end, and by slightly lower redshift galaxies at the low-mass end (see also Gunawardhana et al., 2013). Such biases can be overcome by restricting the sample to a narrow redshift slice, at the lowest redshift possible.

As motivated in Appendix 11.8, we select the subset of SDSS galaxies with redshifts between $z = 0.02$ and $z = 0.04$, which is complete at stellar masses $\gtrsim 10^{8.8}$ $M_\odot$. Combined with the survey footprint, this corresponds to a comoving volume of $\approx 4 \times 10^6$ Mpc^3. As a result, the SDSS sample consists of 33,769 galaxies. Using the same method as used for EAGLE, we find an observed scatter that decreases from ≈ 0.40 dex at $M_{\text{star}} = 10^9$ $M_\odot$ to ≈ 0.36 dex at $M_{\text{star}} > 3 \times 10^{10}$ $M_\odot$. This is similar to the results from Chang et al. (2015), who measure a scatter of 0.39 dex. When using Hα SFRs, we find a smaller scatter of ≈ 0.30 dex at $M_{\text{star}} < 10^{10}$ $M_\odot$ and find that it increases to 0.40 dex at higher masses. This is likely because the sSFR selection of the sample has been performed on UV+IR SFRs. Other potential reasons are underestimated dust-corrections or higher uncertainties in fibre-corrections at the high-mass end.

As shown in Fig. 11.1, we find that the scatter in the SFR-M_{star} relation decreases slightly with increasing stellar mass, both in EAGLE and in SDSS (but not when using Hα based SFRs). The slope and normalisation of the observed trend are remarkably similar to the predictions when we include observational errors to the EAGLE measurements. This implies that the intrinsic scatter in the
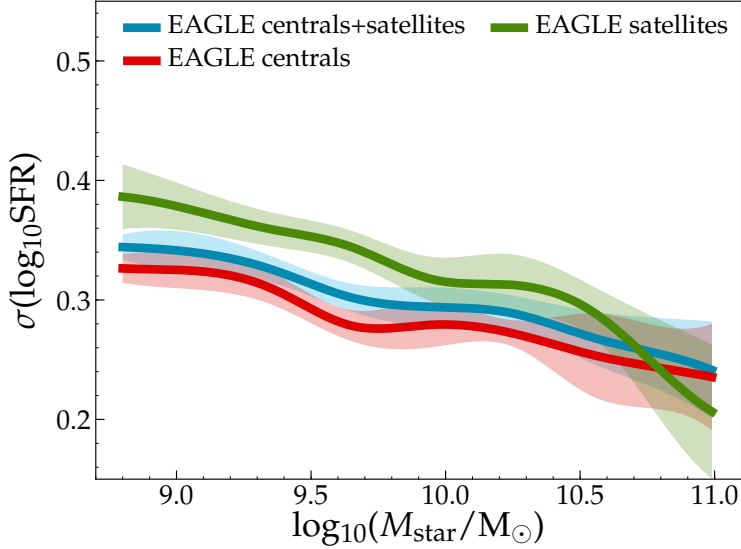
Figure 11.2: Scatter in SFR at fixed stellar mass of star-forming galaxies galaxies in EAGLE at $z = 0$. The blue line shows the analysis including all galaxies, while the red (green) line includes only central (satellite) galaxies. Star-forming satellites add only ≈ 0.02 dex of scatter to the SFR-M_{star} relation. This means that when becoming a satellite the SFR is either only mildly affected or so significantly that the satellite is removed from the star-forming galaxy sample.

SDSS sample is similar to the intrinsic scatter in EAGLE, which decreases from 0.35 dex at $M_{star} \approx 10^9 M_\odot$ to 0.30 dex at $M_{star} \approx 10^{10} M_\odot$ and higher.

We have tested the robustness of these results by changing the stellar mass binning, splitting the SDSS sample in four sub-regions on the sky, changing the upper redshift limit in SDSS (ranging from $z = 0.03 - 0.05$), measuring the scatter in $\log_{10}$ sSFR instead of using the residuals, but find that the results are unchanged. Finally, we note that the scatter in the SFR-M_{star} relation in EAGLE is slightly larger than the scatter in the Illustris simulation measured by Sparre et al. (2015), who finds a mass-independent scatter of ≈ 0.27 dex.

11.3.2   Scatter due to star-forming satellites

Galaxies that become satellites in a larger halo may experience several physical processes that influence their SFR, such as ram pressure stripping of gas, tidally induced star formation, harassment and/or strangulation (e.g. van den Bosch et al., 2008; Peng et al., 2012; Bluck et al., 2016). Thus, satellite interactions may both (temporally) increase or decrease their SFRs. We investigate the contribution of satellites to the scatter in the SFR-M_{star} relation by removing satellite galaxies from the EAGLE analysis. We show in Fig. 11.2 that the scatter decreases by only ≈ 0.02 dex up to masses of $M_{star} \approx 10^{10.5} M_\odot$ (at higher masses there are only a handful of star-forming satellite galaxies due to the limited sim-
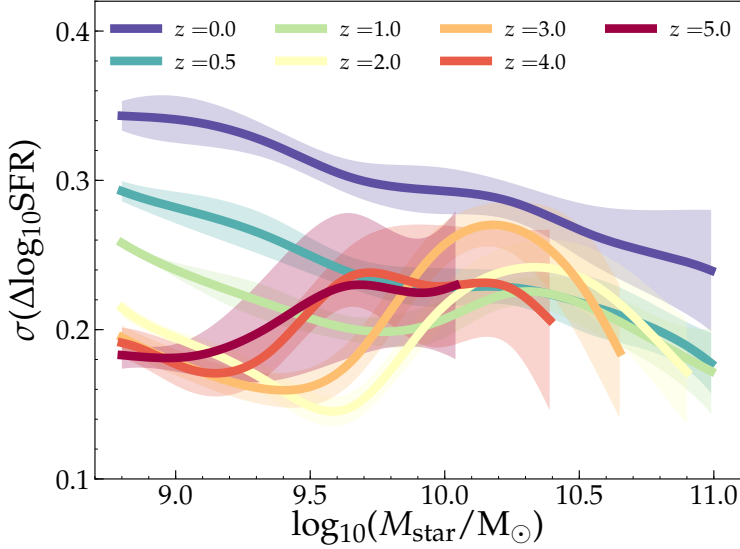
Figure 11.3: Evolution of the mass dependence of scatter in the SFR-M$_{star}$ relation. Star-forming galaxies are selected with an evolving sSFR threshold as described in the text and we only show mass-ranges where there are > 50 galaxies per bin of 0.3 dex width. The scatter decreases with increasing redshift, particularly at lower stellar masses. At high masses the decrease is less prominent and within the estimated uncertainty due to cosmic variance.

ulation volume). Recall that this scatter is measured for star-forming galaxies only. In EAGLE, the fraction of satellites that are quenched (i.e. sSFR $< 10^{-11}$ M$_\odot$ yr^{-1}) decreases from ≈ 50 % at M$_{star} = 10^9$ M$_\odot$ to ≈ 35 % at M$_{star} = 10^{10}$ M$_\odot$ and increases to ≈ 50 % at M$_{star} = 10^{11}$ M$_\odot$. Therefore, a significant fraction of satellites has not been included in this analysis. Our results indicate that satellite-specific processes are either weak, or strong and rapid (such that the satellites are not selected as star-forming galaxies anymore).

11.3.3 Evolution

We measure the evolution of the magnitude and mass dependence of the scatter in the SFR-M$_{star}$ relation in EAGLE in redshift slices with $z = 0 - 5$. As the typical SFR of galaxies increases at $z > 0$ (e.g. Whitaker et al., 2012; Sobral et al., 2013; Madau & Dickinson, 2014), we now change the threshold sSFR value that determines whether a galaxy is star-forming with redshift. At each redshift slice, we compute the median sSFR of all galaxies with M$_{star} > 10^9$ M$_\odot$ and set the threshold to $\log_{10}$(sSFR$_{median}$)-0.65. At $z = 0.0$, this threshold corresponds to sSFR $> 10^{-11}$ yr^{-1}, and it increases to sSFR $> 10^{-10.4, -10.0, -9.6, -9.4, -9.1, 9.0}$ yr^{-1} at $z = 0.5, 1, 2, 3, 4, 5$, respectively. We include both centrals and satellites.

As shown in Fig. 11.3, we find that the scatter decreases from $z = 0$ to $z = 5$ by 0.05 dex at M$_{star} \gtrsim 10^{10}$ M$_\odot$. This evolution occurs mostly between $z = 0$

and $z = 1$, although we note that the amount of evolution is of the same order as the uncertainties associated with cosmic variance. These results are roughly consistent with the observations from e.g. Whitaker et al. (2012), Shivaei et al. (2015), Schreiber et al. (2015), which typically are mass-complete (especially at $z > 2$) at $M_{star} > 10^{10}$ $M_\odot$ and who find a relatively constant scatter. On the other hand, Kurczynski et al. (2016) found observational indications that the scatter increases with cosmic time, while Pearson et al. (2018) finds that the scatter decreases strongly at $z > 2$.

At lower stellar masses, the scatter in the SFR-M_{star} relation in EAGLE decreases more strongly with increasing redshift, for example, it decreases from ≈ 0.35 dex at $z = 0$ to $\approx 0.25(0.20)$ dex at $z \approx 1(> 2)$ for $M_{star} \approx 10^9$ $M_\odot$. These results differ from those of Mitra et al. (2017), whose analytic model predicts that the scatter at these low masses increases with redshift under the assumption that fluctuations in the SFR follow fluctuations in halo accretion rates. The difference with Mitra et al. (2017) is mostly at low redshift, where they predict a scatter of ≈ 0.20 dex at $M_{star} = 10^{9-9.5}$ $M_\odot$ at $0.5 < z < 1.0$, significantly lower than EAGLE. At high-redshift the results are similar. We note that the scatter in the linear SFR at fixed mass, as opposed to the scatter in $\log_{10}$ SFR considered so far, increases towards higher redshift at low masses.

As we discuss and show in more detail in §11.6, the increasing scatter at $M_{star} \approx 10^{9.8}$ $M_\odot$ at high redshift is due to supermassive black hole growth impacting the SFHs, even after applying a relatively high sSFR threshold to remove quenched galaxies. The stellar mass above which the scatter rapidly increases (most clearly seen at $z > 1$) decreases slightly with increasing redshift. This indicates that the stellar mass above which AGN feedback becomes important is slightly lower at higher redshift.

11.4   How long galaxies remain above/below the main sequence

In this section, we investigate on what time-scales central, star-forming galaxies change their position relative to the evolving SFR-M_{star} relation. In particular, we measure the SFRs and stellar masses of the progenitors of galaxies that are star-forming centrals at $z = 0$ at multiple redshifts up to $z = 4$ and compare how the locations of galaxies in the SFR-M_{star} plane change relative to the main sequence at each specific redshift slice. We first focus on the *typical* (median) fluctuations depending on galaxies' present-day stellar mass and sSFR and then investigate the role of more stochastic fluctuations in individual galaxies.

11.4.1   Median fluctuations

The first results are shown in Fig. 11.4. In the top panel, we select the sub-set of galaxies that are above the main sequence at $z = 0.1$ (in bins of stellar mass), and measure the fraction of these galaxies that are also above the main sequence at other points in cosmic time. If the SFRs of galaxies had 'no memory' (i.e. if at
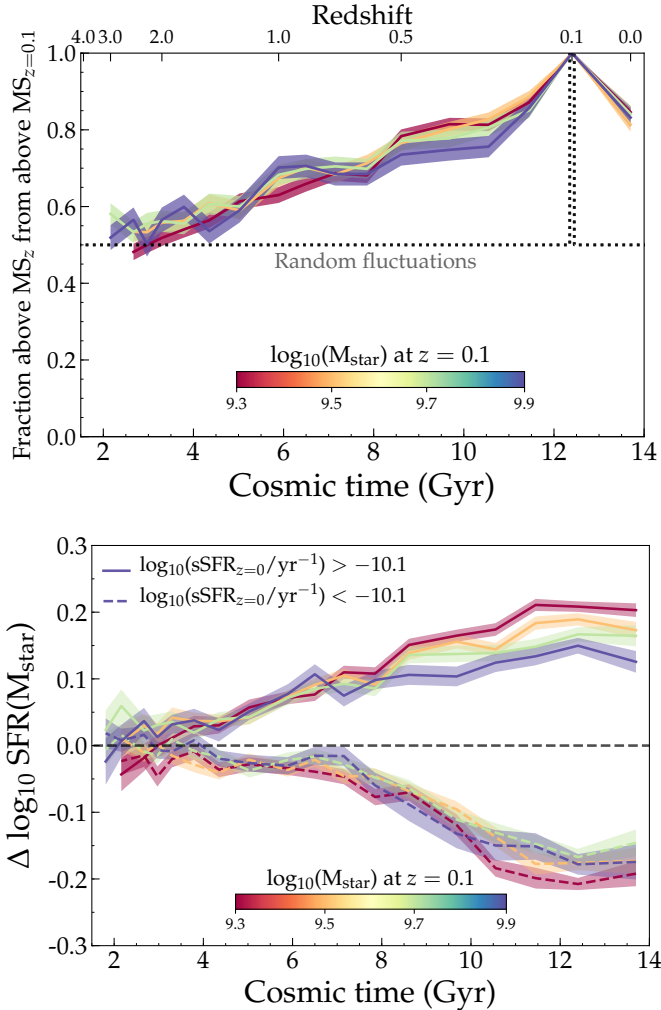
Figure 11.4: *Top*: The fraction of galaxies that are above the main sequence at a specific snapshot among the sample of central, star-forming galaxies that are above the main sequence at $z = 0.1$, in bins of $z = 0.1$ stellar mass. By definition, this fraction is 1.0 at $z = 0.1$. The shaded region shows the binomial uncertainty on the fraction. For each mass bin, we only show the results if the stellar mass of the median main progenitor in each bin is resolved with at least 100 star particles ($M_{star} > 10^8$ $M_{\odot}$). The horizontal dotted line indicates the expectation if SFRs have no 'memory' (i.e. the SFR of a galaxy at a certain redshift is drawn randomly from a normal distribution around the main sequence at the specific redshift). It is clear that there is a correlation between the SFRs of galaxies between different points in cosmic time. *Bottom*: Median difference to the SFR-M_{star} relation at each redshift for central star-forming galaxies binned by stellar mass and split into 'above' (solid) and 'below' (dashed) the main sequence at $z = 0.1$. The shaded region shows the uncertainty on the median. Relatively independently of stellar mass, the *median* galaxy that is above/below the main sequence has been above/below the main sequence for the prior ≈ 10 Gyr. Note that the medians wash out short time-scale fluctuations that are also present (see Fig. 11.5).
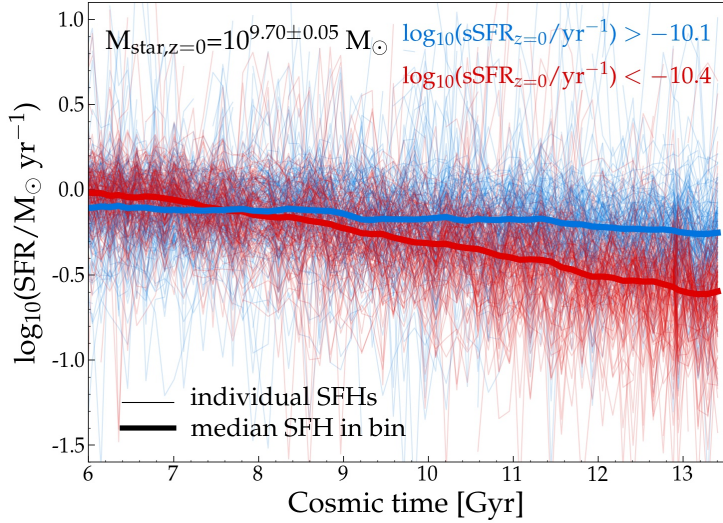
Figure 11.5: Star formation histories of galaxies with $M_{star} = 10^{9.70\pm0.05}$ $M_\odot$ at $z = 0$, split by their current SFR. Thin lines show paths of individual galaxies, while thick lines show the median in each bin of present-day sSFR. This figure highlights that median SFHs (like those shown in Fig. 11.4) smooth out short time-scale fluctuations of typically ≈ 0.3 dex. The median paths do recover the long time-scale variations that depend on the current SFR.

each point in cosmic time their SFR were drawn randomly from the distribution of sSFRs around the main sequence at its specific mass at that time), one would expect this fraction to be 50 % at $z \neq 0.1$. However, we clearly find that the majority of galaxies that lie above the main sequence at $z = 0.1$ are also above the main sequence at earlier times (up to $z \approx 2$, or ≈ 10 Gyr before $z = 0.1$). This means that *in the median*, a galaxy's SFR *remembers* its past SFR.

We note that the SFRs of individual galaxies do fluctuate between 'above' and 'below' the main sequence on shorter time-scales (see below), but that their population average displays a clear degree of long time-scale coherence depending on their location relative to the SFR-M_{star} relation (see also Abramson et al. 2016). That long time-scale fluctuations are present is also illustrated in the bottom panel of Fig. 11.4, which shows that the *median* galaxy above the main sequence has been above the main sequence for a long time, ≈ 10 Gyr. Similarly, the median galaxy below the main sequence (but with a sSFR$> 10^{-11}$ yr^{-1} at $z = 0.1$) has tended to be below the main sequence for most of the history of the universe.

These results show that 'oscillations' of galaxies through the 'main sequence' contain an oscillation-mode with a period similar to the Hubble time. This oscillation time-scale is longer than for galaxies in the hydrodynamical simulations presented in Tacchella et al. (2016), who find a typical time-scale of $\approx 0.4 \times t_{Hubble}$, where $t_{Hubble} \approx 14$ Gyr at $z = 0$.
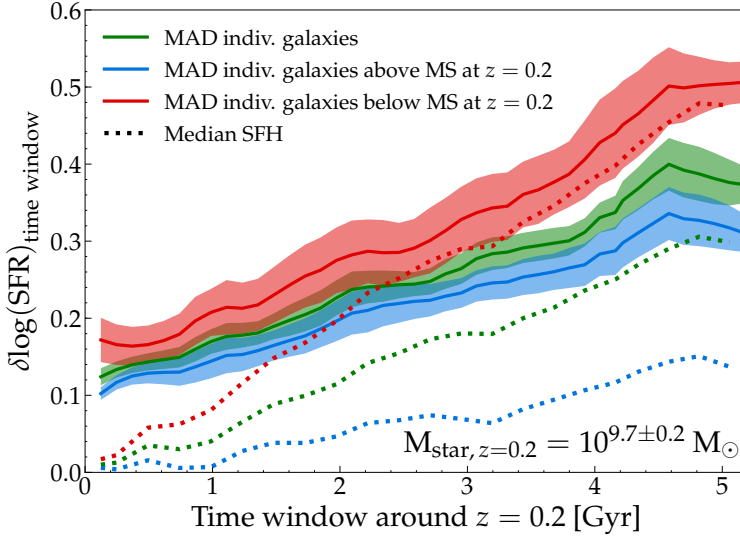
Figure 11.6: The rate at which SFRs typically change on different time-scales for galaxies with $M_{star} = 10^{9.7\pm0.2}$ $M_\odot$ at $z = 0.2$. The solid lines show the median absolute deviation of the change in $\log_{10}$ SFR measured on different time windows around $z = 0.2$. The green line includes all star-forming galaxies in the specified mass-range, while red and blue lines separate galaxies above and below the main sequence at $z = 0.2$. The dotted lines show the difference in the median $\log_{10}$ SFR of the galaxies in the specific bin (i.e. the thick solid line in Fig. 11.5). The SFRs of galaxies below the main sequence vary more (in log-space) than the SFRs of galaxies above the main sequence. Median SFHs only recover fluctuations on long time-scales.

11.4.2   The variety in SFHs of individual galaxies

A major limitation of our median[2] stacking method (e.g. Fig. 11.4) is that it may wash out short-time scale fluctuations in SFRs, such as those observed in high-resolution zoom-simulations (e.g. Hopkins et al., 2014; Muratov et al., 2015) and observations (e.g. Guo et al., 2016b). In particular, if the fluctuations for different galaxies in the same bin are not in phase, they will on average cancel (for an example of a similar effect occuring in stacked radial SF-profiles, see Orr et al. 2017). This would for example be the case if galaxies were to fluctuate around relatively parallel tracks in SFR-M_{star} space.

Indeed, we find that the SFRs of individual galaxies fluctuate significantly on short time-scales, with variations in $\log_{10}$SFR of $\approx 0.2 - 0.3$ dex, as illustrated in Fig. 11.5. In this figure, we show the SFRs of individual galaxies with $M_{star,z=0} = 10^{9.70\pm0.05}$ $M_\odot$ measured in the simulation *snipshots* (which have a spacing of ~ 100 Myr), coloured by their present-day sSFR. It is clear that the median SFH in bins of sSFR are insensitive to fluctuations on short time-scales, but that systematic differences on long time-scales can be identified with median SFHs.

We note that the SFRs in Fig. 11.5 are measured as $SFR_i = \frac{M_{i+1}-M_i}{\Delta t}$, where M_i

---

[2] We note that we find qualitatively similar results when using *mean* stacking.

is the sum of the birth (i.e. zero age main sequence) stellar mass of star particles in a galaxy at simulation output time i and Δt is the output spacing. This is different from the rest of the paper, where we measure SFR directly from the star-forming gas. The instantaneous SFRs were however not saved in the higher time-resolution output of the simulation. This means that mass growth due to (minor) mergers is included in the SFR as well, but as can be seen from Fig. 11.5, the highest SFRs are typically $< 2 - 3$ M$_\odot$ yr, corresponding to a typical maximum mass growth of $\approx 2 - 3 \times 10^8$ M$_\odot$ per timestep, i.e. maximum merger mass fractions of $\lesssim 1/25$. The presence of oscillations with frequencies higher than the snapshot spacing of 100 Myr cannot be tested. An additional source of scatter in these SFRs derived from the difference in stellar masses are Poisson fluctuations due to discreteness in star formation implementation (see Schaye & Dalla Vecchia 2008 for details). We calculate the contribution of Poisson noise to the scatter as follows: for a given SFR, the expected number of star particles formed per timestep is $N = \text{SFR}\frac{\Delta t}{m}$, where Δt=100 Myr and $m = 1.81 \times 10^6$ M$_\odot$, the birth mass of a star particle. Therefore, assuming Poisson noise, the scatter in the SFR measured over such a time step is $\sigma(\text{SFR}) = \sqrt{N}\frac{m}{\Delta t} = \sqrt{\text{SFR}\, m/\Delta t}$. As we study logarithmic SFRs, we convert this to $\sigma(\log_{10}\text{SFR})= \frac{1}{\ln 10}\sqrt{\frac{m}{\text{SFR}\Delta t}}$. For the typical SFRs in Fig. 11.5 the Poissonian noise is $0.05 - 0.10$ dex, meaning that Poisson fluctuations do not dominate the measured variation in $\log_{10}\text{SFR}$ of $\approx 0.2 - 0.3$ dex.

11.4.3 The relative importance of different time-scales

A more quantitative analysis of the rates at which SFRs typically change is shown in Fig. 11.6. Here, we select galaxies with M$_{\text{star}} = 10^{9.7\pm0.2}$ M$_\odot$ at $z = 0.2$ (when the age of the Universe is ≈ 11.2 Gyr) and measure $\delta\log_{10}\text{SFR}$ over different time-scales, the change in $\log_{10}\text{SFR}$ over a time difference centred around $z = 0.2$: $\delta\log_{10}\text{SFR}_{\Delta t} = \log_{10}\text{SFR}_{T_{0.2}-\Delta t/2} - \log_{10}\text{SFR}_{T_{0.2}+\Delta t/2}$, where $T_{0.2}$ is the age of the Universe at $z = 0.2$ (11.2 Gyr) and Δt is the time difference (i.e. 0.1-5 Gyr). For each time difference, we measure the median absolute deviation (MAD) of the $\delta\log_{10}$ SFR measurements of the individual galaxies in the mass bin and in sub-bins of sSFR at $z = 0.2$. For comparison, we also measure $\delta\log_{10}$ SFR for the median SFH of the bins. We find that the median SFHs underestimate the MAD of $\delta\log_{10}$ SFR on time-scales $\lesssim 1$ Gyr by more than an order of magnitude, but only by a factor $\lesssim 2$ on time-scales $\gtrsim 2$ Gyr.

Fig. 11.6 shows that typical fluctuations in $\log_{10}\text{SFR}$ on time-scales of $\lesssim 1$ Gyr are $\approx 0.10 - 0.25$ dex, and are slightly larger for galaxies with relatively low SFRs at $z = 0.2$. On longer time-scales, the fluctuations in SFRs are larger and they are recovered better by the median SFHs. On > 3 Gyr time-scales the typical changes are > 0.3 dex, i.e. larger than the scatter in the SFR - M$_{\text{star}}$ relation. However, on such time-scales, galaxies grow significantly in mass, meaning that the variation relative to the SFR - M$_{\text{star}}$ relation is reduced.

Fig. 11.7 summarises how the scatter in the SFR-M$_{\text{star}}$ relation depends on the time-scale over which the SFR is averaged. Here, time-averaged SFRs for individual galaxies are computed as in §11.4.2 using the difference in initial stellar
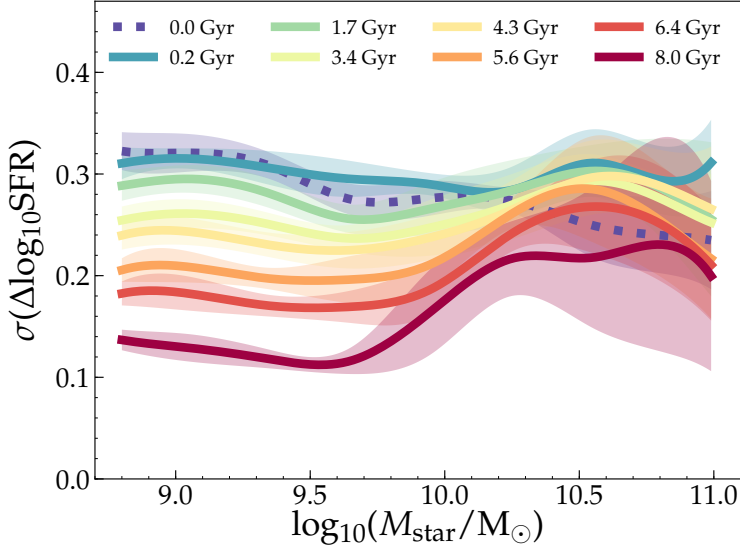
Figure 11.7: The dependence of the scatter in SFR(M_{star}) at $z = 0$ on the time-scale over which the SFR of each galaxy is averaged. The instantaneous SFR is shown as a dashed line, while averaged SFRs (computed using the merger-tree as in §11.4.2) are shown as solid lines. Time-averaged SFRs are corrected for Poisson noise associated with the SF recipe. We removed galaxies that underwent a major merger (1:4 ratio) during the time over which the SFR is averaged. We find that short time-scale fluctuations drive the scatter in the SFR-M_{star} relation, but long 8 Gyr fluctuations still contribute ≈ 0.15 dex of scatter at $M_{star} \lesssim 10^{10}$ $M_{\odot}$.

mass of the main progenitor between $z = 0$ and earlier times. We corrected the scatter for Poisson noise associated to the SF implementation. For each time-interval, we removed galaxies that underwent a major merger (1:4 ratio) in any 100 Myr interval during the time over which the SFR is averaged. This is necessary as the SFR is inferred from the change in stellar mass. The fraction of galaxies that underwent a major merger increases with stellar mass and with the time-scale over which SFR is averaged. For galaxies $M_{star} < 10^{10}$ $M_{\odot}$ a fraction of 10 (20) % is removed on 2 (8) Gyr time-scales, while 25 (60) % of the galaxies is removed on these respective time-scales at stellar masses $M_{star} > 10^{10}$ $M_{\odot}$. We find that the scatter is largest for the instantaneous SFR and short time-scales < 1 Gyr (≈ 0.3 dex) and decreases to a non-negligible scatter of ≈ 0.15 dex for long, 8 Gyr, time-scales, particularly at $M_{star} \lesssim 10^{10}$ $M_{\odot}$.

11.5   The origin of long time-scale correlations

What is driving the coherence in the long time-scale SFHs of galaxies and its dependence on their present-day sSFR? Star formation is fuelled by the inflow of (cold) gas. Naively, it is therefore expected that the star formation history of
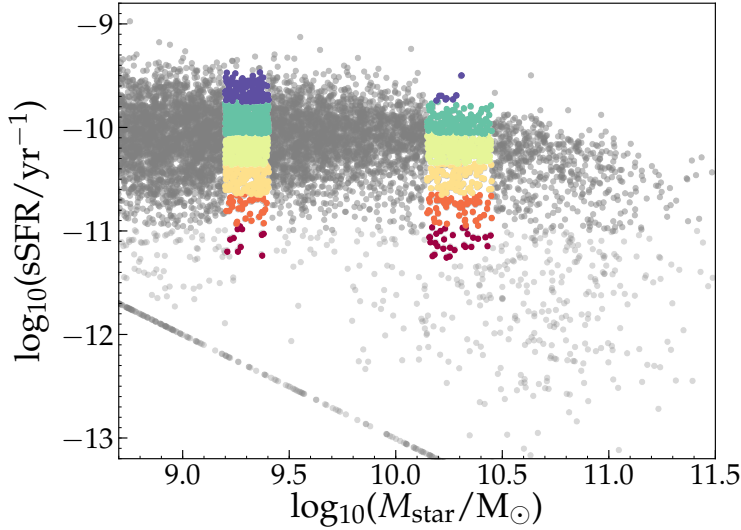
Figure 11.8: Relation between sSFR and stellar mass for central galaxies at $z = 0.1$. Galaxies that contain no star-forming gas particles are placed at a SFR of 0.001 $M_\odot$ yr^{-1} for visualisation purposes. We use color-coding to highlight the galaxies that have been binned in Fig. 11.9, where we show their median SFR, M_{star} and M_{200} histories.

a galaxy is related to its halo mass accretion history (e.g. Moster et al., 2013). In this section, we therefore explore how the halo and stellar mass assembly histories are related to the star formation histories of galaxies, and the positions of galaxies on the SFR - M_{star} plane. Specifically, we use the merger tree to map out the dark matter mass history of halos (in the matched DMO simulation, which is not affected by baryonic processes). We measure $z_{1/2}$, the redshift at which half of the halo mass (M_{200}) at $z = 0.1$[3] was first assembled in the main progenitor as a way to quantify formation time.

11.5.1 The joint evolution of SFR, M_{star} and $M_{200,DMO}$

We show the joint evolution of the median stellar mass, SFR and halo mass (in the matched DMO simulation) in bins of stellar mass and SFR (illustrated in Fig. 11.8) in Fig. 11.9. Here, each column shows a bin in stellar mass and in each panel different coloured lines correspond to different bins in specific SFR. We note that the stellar mass bins are chosen to be representative and that their exact values do not influence the results. We also note that for visualisation purposes we have binned galaxies by their mass and SFR at $z = 0.1$, while the plots show the history down to $z = 0$.

In general, for both masses shown here, the following characteristics can be seen for galaxies with high/low sSFR at $z = 0.1$: i) they have a SFH that peaks later/earlier and is more extended/compressed, ii) they have had

---

[3] For the remainder of the paper, we study central galaxies at $z = 0.1$ in the EAGLE simulation.
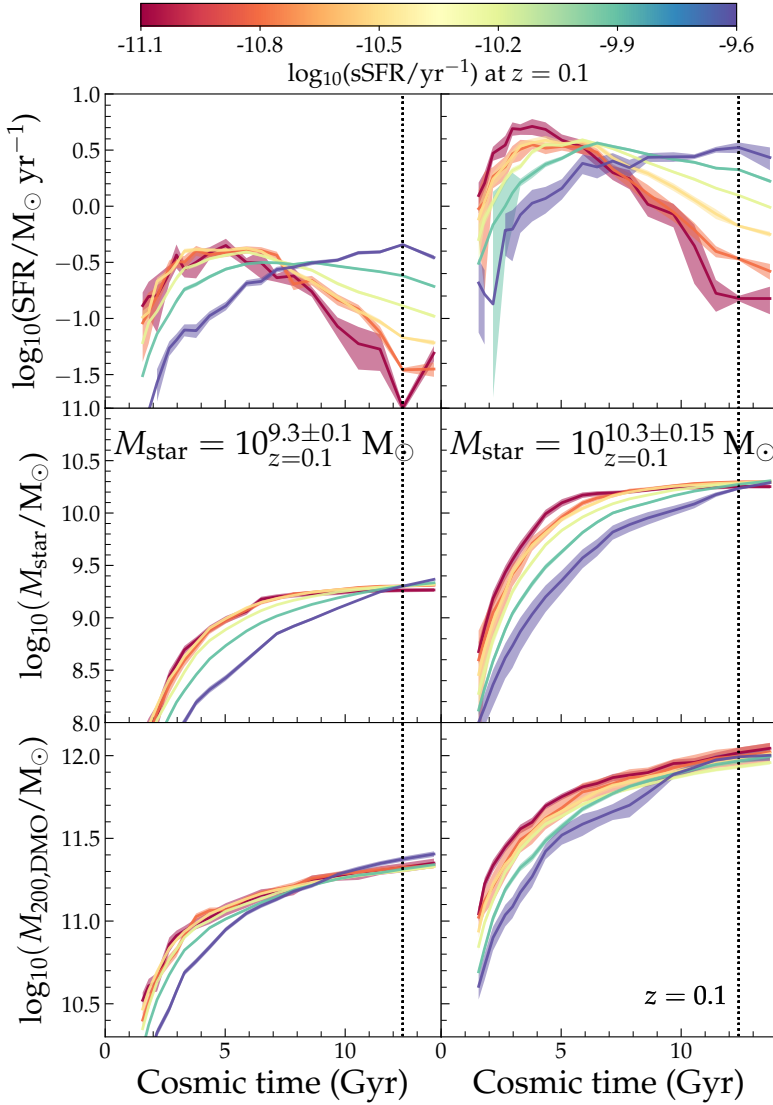
Figure 11.9: Evolution of the median SFR (*top row*), stellar mass (*middle row*) and DMO halo mass (*bottom row*) in bins of $z = 0.1$ stellar mass (*different columns*), sub-divided in bins of $z = 0.1$ sSFR (colour-coding). The shaded regions indicate the formal errors ($\sigma_{\mathrm{bin}}/\sqrt{N_{\mathrm{bin}}}$). At fixed stellar mass, galaxies with higher SFR at $z = 0.1$ have a delayed SFH compared to galaxies with low SFR at $z = 0.1$. Galaxies with a higher SFR at $z = 0.1$ typically have had a lower stellar mass throughout cosmic history, compared to other galaxies with the same final stellar mass. In the first ≈ 8 Gyr, their halo masses have also been lower than the typical halo mass of galaxies with similar $z = 0.1$ stellar mass.

a lower/higher stellar mass during most of the history of the Universe, compared to other galaxies that end up with the same stellar mass, iii) they had a relatively low/high halo mass during the first ≈ 8 Gyr of the Universe, but not necessarily at later times. These results clearly indicate that galaxies that occupy similar regions in the SFR-M_{star} plane have similar SFHs, confirming the results from §11.4.

Observationally, Pacifici et al. (2016) find similar results by measuring the SFHs of a large sample of galaxies in the local Universe (see also Pacifici et al. 2013). They find that low-mass galaxies formed their stars over a longer time-scale than massive galaxies ('downsizing'; e.g. Gallazzi et al. 2005; Thomas et al. 2005) and that at fixed stellar mass, galaxies with relatively low SFRs have a more compressed SFH than galaxies with relatively high SFRs (see also Dressler et al. 2016). More recently, Chauke et al. (2018) confirm this result with a detailed analysis of high-resolution spectra at $z = 1$. They find that at fixed stellar mass, star-forming galaxies have a SFH that is more extended and shifted towards later times compared to passive galaxies, and that the ongoing SFR is correlated with the SFH on ~ 3 Gyr time-scales, a significant fraction of the Hubble time at $z = 1$.

One subtle difference between the different mass bins in Fig. 11.9 is that galaxies in the higher stellar mass bin with a high sSFR at $z = 0.1$ have had a relatively low halo mass throughout cosmic history, instead of only during the first ≈ 8 Gyr, and vice versa for galaxies with low sSFRs. The explanation is that at these mass scales additional physical processes start to play a more prominent role, such as stellar mass growth due to merging and AGN feedback. These processes may result in a different relation between stellar and halo mass growth. We explore this further in §11.6.

11.5.2   The relation with halo accretion history

Next, we investigate in more detail how halo assembly influences the scatter in the SFR-M_{star} relation. In Fig. 11.10 we show that the sSFR[4] of galaxies at fixed M_{star} is related to $z_{1/2}$, the redshift at which the dark matter halo mass of the main progenitor had half its $z = 0.1$ mass (left panel). In this figure, we have created bins in 2D space of width 0.07 dex in M_{star} and 0.125 dex in sSFR and computed the median halo formation time of all galaxies in each bin. Galaxies with zero SFR are shown with a sSFR that would correspond to a SFR$= 10^{-3}$ $M_\odot$ yr^{-1}. For stellar masses $\lesssim 10^{10} M_\odot$, it is clear that haloes that form later tend to host galaxies with a higher sSFR. As discussed above, additional physical processes play a role at high masses (such as AGN feedback, see §11.6). We quantify the strength of the correlation between the residuals of the SFR-M_{star} relation and halo formation time using the Spearman rank correlation coefficient (R_S, where $R_S = (-)1$ for a perfect (anti-)correlation and $R_S = 0$ for no correlation). We find that $R_S \approx -0.45$ for stellar masses of $10^9 - 10^{10} M_\odot$, and

---

[4] We show sSFR instead of SFR as it visualises our results better, but we note that the same results are obtained for the residuals of the SFR-M_{star} relation.
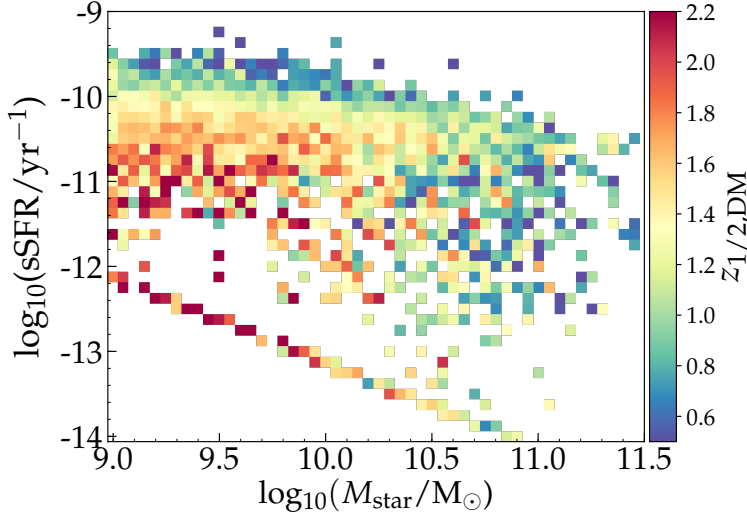
Figure 11.10: The relation between sSFR and stellar mass for central galaxies at $z = 0.1$, color-coded by the median halo formation time in the matched DMO simulation, in bins of sSFR and M_{star}. Galaxies that contain no star-forming gas particles are placed at a SFR of 10^{-3} $M_\odot$ yr^{-1} for visualisation purposes. The scatter in sSFR is related to halo formation time for stellar masses of $\lesssim 10^{10}$ $M_\odot$.

$R_S \approx -0.10$ at $M_{star} > 10^{10.5}$ $M_\odot$.[5]

Our results show that the scatter in the SFR-M_{star} relation is correlated with dark matter halo formation time. As halo formation time is related to halo clustering (e.g. Gao et al., 2005; Gao & White, 2007), the scatter in the SFR-M_{star} relation is (partly) connected to assembly bias (see also Tinker et al. 2018) and the formation of large-scale structure. These results are consistent with the results from the semi-analytical model of Dutton et al. (2010), who found that the scatter in the SFR-M_{star} correlates with halo concentration (which correlates strongly with $z_{1/2}$, see e.g. Matthee et al. 2017a). Our results are also consistent with observations from Coil et al. (2017), who found that at fixed stellar mass, galaxies with a higher sSFR are less clustered (indicating that they form later), although that could also be due to a lower halo mass.

Connecting these results with the results from Fig. 11.9, we find that the SFHs of haloes that form earlier also tend to peak earlier, while haloes that form later have a more extended SFH with a later peak. Quantitatively, we find that

---

[5] We test other ways to quantify the dark matter halo accretion history in Appendix 11.8, but find none that correlate more strongly with the scatter in SFR-M_{star} than $z_{1/2}$ does. We have also tested whether short time-scale fluctuations in the growth rate of M_{200} are related to the short time-scale fluctuations in the SFR that were discussed in §11.4 and illustrated in Fig. 11.5. Typical fluctuations in the halo growth rate on ~ 100 Myr time-scales have a spread of ≈ 0.4 dex, larger than fluctuations in SFRs. For the majority of galaxies, we do not find a strong correlation between the two growth rates, neither measured simultaneously nor measured with a time-delay between halo growth and stellar mass growth of $0 - 1$ Gyr in steps of 100 Myr.

the median SFR of a central galaxy in a halo with $M_{200} = 10^{11.8}$ $M_{\odot}$ within the earliest halo formation time quartile ($z_{1/2} \approx 2.5$) has increased by a factor ≈ 10 in the last 10 Gyr, while the median SFR of a galaxy within the latest halo formation time quartile ($z_{1/2} \approx 0.2$) has only increased by a factor ≈ 1.5 over the same period. Hence, part of the diversity in SFHs of galaxies at fixed halo mass is driven by differences in halo formation time. This drives a coherence in the long time-scale fluctuations in galaxies' SFRs that correlates with their current positions in the SFR-M_{star} diagram.

11.5.3   How much scatter can be explained?

What fraction of the scatter in the SFR-M_{star} relation can be attributed to variations in halo formation time? We measure this following the method described in detail in Matthee et al. (2017a): in each stellar mass bin, we fit a linear relation between the residuals in the SFR-M_{star} relation and halo formation time (in the matched DMO simulation). Hence, we compute the residual SFR (which is similar to residual sSFR) corrected for formation time:

$$\log_{10} \text{sSFR}_{\text{corrected}} = \log_{10} \text{sSFR} + \alpha + \beta \, z_{1/2}. \tag{11.1}$$

The normalisation α and slope β are weakly mass dependent, with (for example) $\alpha = 9.8$ at $\beta = 0.2$ at $M_{star} \approx 10^{9.5}$ $M_{\odot}$. We use this relation to compute $\Delta \log_{10}$ SFR ($M_{star}, z_{1/2}$), the residuals in the SFR-M_{star} relation after taking halo formation time into account. We then compute the standard deviation of these residuals in bins of stellar mass and show the results in Fig. 11.11. Note that this method is similar to measuring the scatter perpendicular to a three-dimensional plane of sSFR, M_{star} and $z_{1/2}$.

It can be seen that for stellar masses of $10^9 - 10^{10}$ $M_{\odot}$ the scatter is significantly reduced, by ≈ 0.05 dex, after taking halo formation time into account. Assuming that the total scatter can be written as $\sigma_{\text{tot}}^2 = \sigma_{z_{1/2}}^2 + \sigma_{\text{other}}^2$, we find that the scatter due to fluctuations in $z_{1/2}$ alone is ≈ 0.15 dex at $M_{star} < 10^{10}$ $M_{\odot}$. No significant reduction in the scatter is found for higher stellar masses. This result means that scatter in halo formation time is the cause of only part of the scatter in the SFR-M_{star} relation and its magnitude is similar to the scatter that we measured when SFRs were averaged on long time-scales (Fig. 11.7). We have varied our definition of formation time to mass fractions in the range 0.2-0.7 instead of 0.5, but found no significant difference. We have also tested whether the scatter is related to other DMO halo properties such as halo sphericity, triaxiality, spin or the number of neighbours within 2 and 10 Mpc (see Matthee et al. 2017a for their exact definitions), but find that they do not reduce the scatter by more than 0.01 dex. Similarly, neither of these properties is related strongly to the scatter in the stellar mass - halo mass relation in EAGLE (Matthee et al., 2017a).

As shown in Fig. 11.11, the stellar half-mass assembly time is (over the full mass-range) more closely related to the scatter in the SFR-M_{star} relation than halo formation time is. This is not surprising, as $z_{1/2,\text{stars}}$ is a measure of the star formation history and we already showed that the long-term SFH is cor-
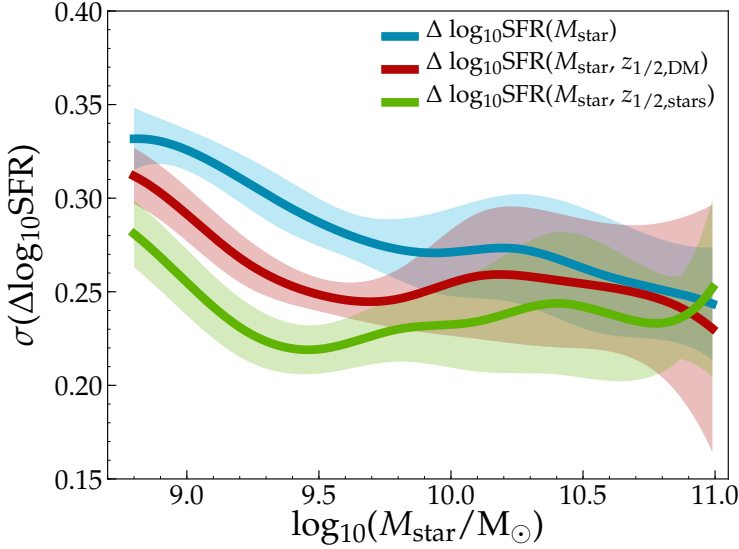
Figure 11.11: Scatter in SFR at fixed stellar mass for central star-forming galaxies at $z = 0.1$. The blue line shows the full scatter, while the red and green lines show the scatter after taking halo formation time (in the matched DMO simulation) and stellar mass assembly time into account, respectively. Shaded regions show the uncertainty associated to cosmic variance.

related with the scatter in SFR-M_{star}. Assuming that the total scatter in the SFR-M_{star} relation is due to $z_{1/2,\text{stars}}$ and additional 'stochastic' scatter combined in quadrature (see §11.4), we find that ≈ 0.20 dex of scatter can be attributed to fluctuations in $z_{1/2,\text{stars}}$ at fixed stellar mass at $M_{\text{star}} < 10^{10}$ $M_\odot$, and ≈ 0.10 dex at $M_{\text{star}} \approx 10^{10-11}$ $M_\odot$.

11.5.4 Connection to the M_{star}-M_{halo} relation

In this subsection, we explore how our results are related to the origin of scatter in the M_{star}-M_{halo} relation, which is a measure of the efficiency of galaxy formation. In Matthee et al. (2017a) we showed that at a fixed halo mass $M_{200} < 10^{12.6}$ $M_\odot$ in the matched DMO simulation, a galaxy with a relatively high stellar mass tends to reside in a halo that was assembled relatively early (such that the halo is relatively concentrated). This means that the haloes of these galaxies have a relatively low recent growth rate (and vice versa for haloes with relatively low stellar mass). Therefore, it is likely that the scatter in the stellar mass - halo mass relation is related to the scatter in the SFR-M_{star} relation. We show this in Fig. 11.12. For central galaxies with $M_{\text{star}} < 10^{10}$ $M_\odot$, we find that at fixed stellar mass galaxies with higher SFRs tend to have higher halo masses. This is consistent with the result of Matthee et al. (2017a), as these galaxies also have relatively late halo formation times, such that they have a relatively low stellar mass compared to their halo. This means that observational samples with a selection based on

SFR (and hence likely with relatively high sSFR) may yield samples with biased stellar mass to halo mass ratios. At $M_{star} > 10^{10}$ M$_\odot$, galaxies with a relatively high halo mass tend to have a relatively low SFR, inverting the trend between SFR and the relative halo mass to stellar mass. As we discuss in more detail in the next section, the stellar mass at which the transition occurs corresponds to the stellar mass where feedback associated to the growth of supermassive black holes starts to influence the star formation activity in galaxies.
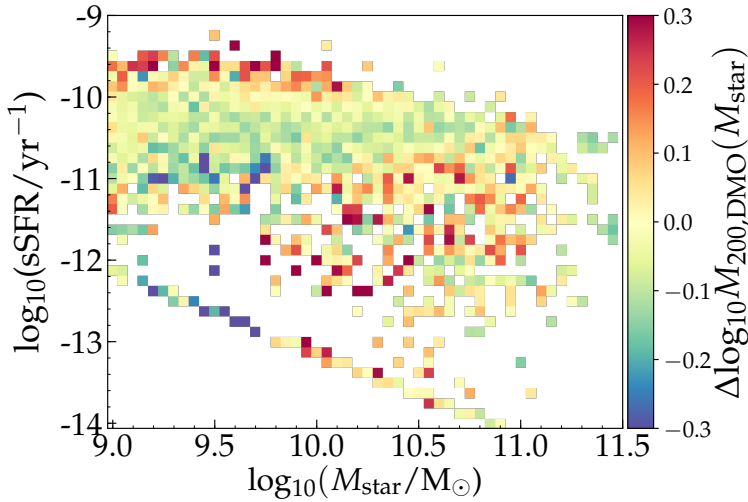
Figure 11.12: The relation between sSFR and stellar mass for central galaxies at $z = 0.1$, color-coded by the median deviation from the relation between halo and stellar mass. We find that galaxies with higher/lower SFRs at fixed stellar mass tend to have relatively high/low halo masses, for galaxies with stellar masses $\approx 10^9 - 10^{10}$ M$_\odot$. At $M_{star} > 10^{10}$ M$_\odot$ the trend reverses because galaxies with relatively massive haloes at fixed stellar mass tend to have higher black hole masses, reducing their SFRs (see §11.6).

11.6   Relation with the growth of black hole mass

In this section, we investigate how the mass of super-massive black holes influences the scatter in the SFR-M$_{star}$ relation. While correlations between the scatter and black hole mass do not imply causation, such correlations may still reveal clues with regards to the physical processes driving the scatter at high galaxy masses.

At the highest masses, the majority of galaxies have ceased their star formation and have much lower sSFRs than a typical main sequence galaxy. This means that the 'pseudo-equilibrium growth' of galaxies, where their SFR typically only fluctuates within a factor of two, ends at some mass-scale. Bower et al. (2017) show that, in the EAGLE simulation, this is due to the increasing importance of AGN feedback, as the hot corona around galaxies in haloes with mass
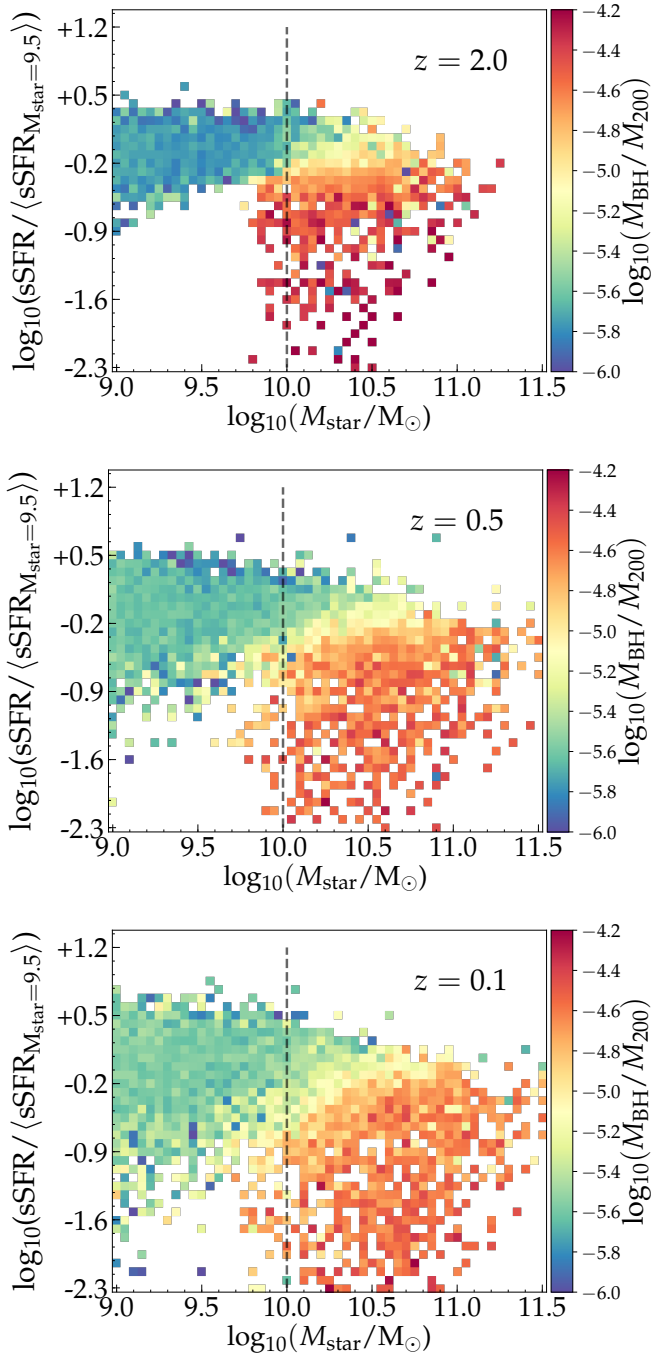
Figure 11.13: Relation between sSFR and stellar mass for central galaxies at $z = 2.0, 0.5, 0.1$ (*top*, *middle* and *bottom* rows, respectively). We normalise the sSFR to the median sSFR of galaxies with $M_{star} = 10^{9.50 \pm 0.05}$ $M_{\odot}$ and colour code the bins by the M_{BH}/M_{200} ratio, which highlights which halos have formed a BH efficiently. The vertically dashed line indicates a stellar mass of 10^{10} $M_{\odot}$.
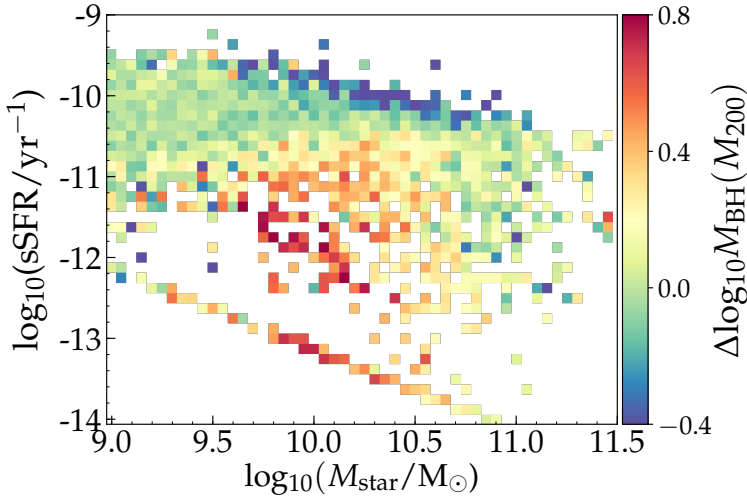
Figure 11.14: Relation between sSFR and stellar mass for central galaxies at $z = 0.1$. Here, we colour code the grid of bins with the median residual of the BH - halo mass relation ($\Delta\log_{10} M_{BH}(M_{200})$), which highlights the *relative* efficiency of BH formation. Part of the scatter at stellar mass $\gtrsim 10^{10}$ M$_\odot$ can be attributed to the mass of the BH relative to that of the halo.

$M_{200} \gtrsim 10^{12}$ M$_\odot$ traps winds driven by star formation, leading to runaway black hole growth until the AGN becomes sufficiently luminous to drive a large-scale outflow (see Trayford et al. 2016 for how this affects simulated galaxy colours).

Around the transition regime, some haloes grow their black holes earlier than others, influencing their galaxies' SFHs and hence their location on the SFR-M_{star} plane (e.g. Sijacki et al., 2015; Terrazas et al., 2016; McAlpine et al., 2017). The black hole (BH) mass is a measure for the accumulated amount of AGN feedback that was injected into a galaxy (assuming some of the released energy coupled efficiently to the gas). To first order, BH mass scales with halo mass and stellar mass, at least for halo masses $\gtrsim 10^{12}$ M$_\odot$. However, to second order more subtle effects can take place, for example in how the BH mass scales with stellar mass at fixed halo mass.

In Fig. 11.13 we show that the SFRs of central galaxies with $M_{star} \ll 10^{10}$ M$_\odot$ are uncorrelated with M_{BH}. However, galaxies with $M_{star} > 10^{10}$ M$_\odot$ residing in haloes that formed a BH efficiently (resulting in a high M_{BH}/M_{200} ratio) have relatively low SFRs at fixed stellar mass at $z = 0.1, 0.5$ and $z = 2.0$, and have thus stopped forming stars at the MS (or are in the process of ceasing their star formation). A relation between the relative BH growth and the SFH is also seen observationally by Martín-Navarro et al. (2018), who found that galaxies with over-massive black holes (at fixed velocity dispersion) formed their stellar mass earlier.

The stellar mass scale at which BH mass starts to drive scatter in the SFR-
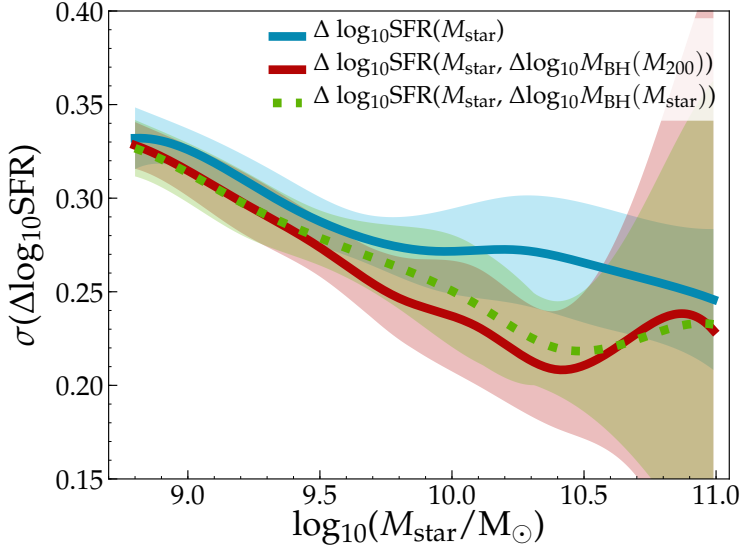
Figure 11.15: Scatter in SFR at fixed stellar mass for $z = 0.1$ central star-forming galaxies only (sSFR$> 10^{-11}$ yr^{-1}), and after correcting for the effect of the relative BH mass (using the residuals of the M_{BH}-M_{200} and M_{BH}-M_{star} relations). Although the uncertainties due to cosmic variance are high at large masses, we find clear indications that a significant part of the scatter in the SFR-M_{star} relation at $M_{star} > 10^{10}$ $M_\odot$ is due to the differences in the relative efficiency of BH growth. Note that the galaxies for which the residuals of the M_{BH}-M_{200} relation are the highest (around $M_{star} \approx 10^{10}$ $M_\odot$) are not included in this analysis as these are not classified as star-forming galaxies due to their reduced sSFR.

M_{star} relation is slightly smaller at $z = 2$. This likely reflects the fact that the stellar mass - halo mass relation in EAGLE is lower at $z = 2$ (see Matthee et al. 2017a), meaning that galaxies with $M_{star} \approx 10^{10}$ $M_\odot$ reside in higher-mass haloes at $z = 2$, compared to galaxies with this mass at $z = 0$. This effect explains why the scatter in the SFR-M_{star} relation increases with mass around $M_{star} \approx 10^{9.7}$ $M_\odot$ at high redshift (see Fig. 11.3), and why the transitioning stellar mass at which this happens decreases slightly with increasing redshift.

Fig. 11.13 also shows that a sample of galaxies selected above a simple sSFR threshold includes galaxies in which BH growth is already affecting galaxy properties, particularly at high masses. The selection of "main sequence galaxies" in a simulation, i.e. galaxies where AGN feedback is not yet important, could therefore additionally impose an additional selection threshold of $\log_{10}(M_{BH}/M_{200})$ > -5.0.

While the relation between the scatter in the SFR-M_{star} relation and BH growth shown in Fig. 11.13 illustrates mostly "first order effects" (i.e. at fixed stellar mass galaxies with lower SFRs tend to reside in higher-mass halos which tend to have higher BH to halo mass ratios), a "second order" effect of how BH growth affects galaxies SFRs is clearly illustrated in Fig. 11.14. Here, the colour coding shows the residuals of the M_{BH}-M_{200} relation, and thus highlights haloes
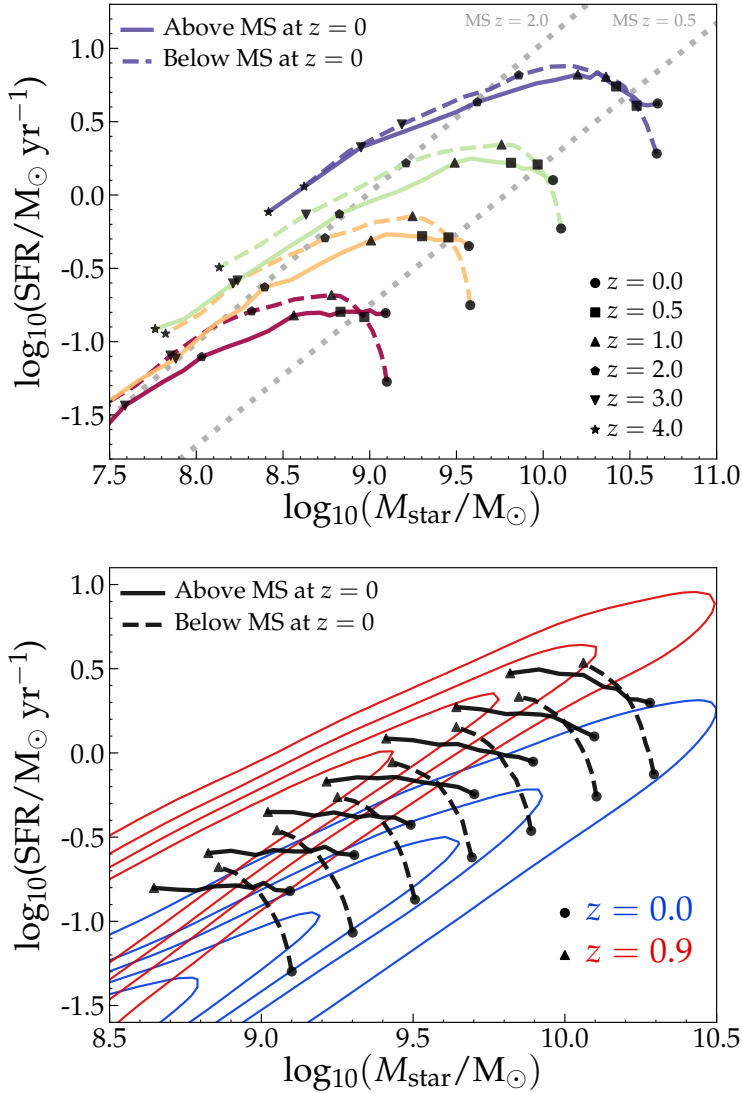
Figure 11.16: *Top:* The median tracks of central star-forming galaxies in stellar mass bins (different colours), split by their sSFR at $z = 0$ (different line-styles) in the SFR-M_{star} plane. The positions of galaxies at specific redshifts are indicated by different symbols. The grey dashed lines in the background show the median relations for star-forming galaxies at $z = 0.5$ and $z = 2.0$. There are clear differences between the median paths of galaxies at fixed mass, depending on their present-day SFR. *Bottom:* The median evolutionary tracks of galaxies in mass and SFR bins between $z = 0.0$ and $z = 0.9$ (roughly half of the history of the Universe). The contours show the full star-forming galaxy population at both redshifts. At all masses, the median SFR of the galaxies that are above/below the main sequence at $z = 0$ was also above/below the main sequence at $z = 0.9$.

that have grown their central super-massive black hole *relatively* efficiently. This figure shows that particularly at the transition (stellar) mass scale ($M_{star} \sim 10^{10}$ $M_{\odot}$, $z = 0.1$), haloes that have a higher BH mass relative to their halo mass tend to have a lower SFR at fixed stellar mass. For the highest and lowest stellar masses there is no clear relation with the relative black hole mass as galaxies typically have been quenched already (highest masses) or AGN feedback is unimportant (lowest masses).

As shown in Fig. 11.15, accounting for black hole mass reduces the scatter in the SFR of star-forming galaxies by ≈ 0.05 dex for masses $M_{star} \approx 1 - 3 \times 10^{10}$ $M_{\odot}$ (although the differences are within the uncertainties associated with cosmic variance). Assuming that the total scatter is the quadratic sum of the scatter due to relative BH formation efficiency and other sources of scatter, this means that variations in BH formation efficiency lead to ≈ 0.15 dex of scatter in the SFR-M_{star} relation at these mass scales. The results are similar when we compare the relative BH mass to stellar mass instead of to halo mass.

Which property determines whether halos grow a BH relatively efficiently? We find that the residuals of the M_{BH}-$M_{200,DMO}$ relation (particularly for halo masses $M_{200,DMO} > 10^{12}$ $M_{\odot}$) are correlated with halo formation time (and thus with concentration, see Booth & Schaye 2010, 2011). As a result, at fixed halo mass, haloes that form earlier typically end up receiving a larger amount of AGN feedback (once AGN feedback becomes efficient), resulting in a lower sSFR and eventually lower stellar mass. Simultaneously, at fixed M_{200}, but at $M_{200,DMO} < 10^{12}$ $M_{\odot}$, an earlier halo formation time tends to yield a larger M_{star} (see Matthee et al. 2017a). As a result, galaxies with high SFR at fixed M_{star} at stellar masses above 10^{10} $M_{\odot}$ tend to have a relatively low halo mass, while galaxies at lower stellar mass with high SFR typically have a high halo mass (see Fig. 11.12). The question that remains is: at fixed halo mass and fixed halo formation time, what determines whether a halo forms stars more efficiently? This is a topic for future investigations.

11.7 Discussion

11.7.1 What drives the scatter in the main sequence?

In the introduction, we posed the question whether the galaxy main sequence is an "attractor-solution", with the scatter originating from rapid fluctuations around a median relation, or whether it represents a "population-average", with the scatter reflecting the diversity in star formation histories. As presented in §11.4, we find that it most likely is a combination of both. Around ≈ 0.25 dex of scatter in the SFR-M_{star} relation is due to star formation burstiness on short $\lesssim 1$ Gyr time-scales, originating from the self-regulating interplay between gas cooling, star formation and feedback from star formation, and ≈ 0.15 dex of scatter is due to long ~ 10 Gyr time-scale differences related to the formation time of dark matter haloes (which originate from large-scale dark matter density fluctuations in the early universe). At masses $M_{star} > 10^{10}$ $M_{\odot}$ the residuals in the SFR-M_{star} relation are anti-correlated with the relative efficiency of BH
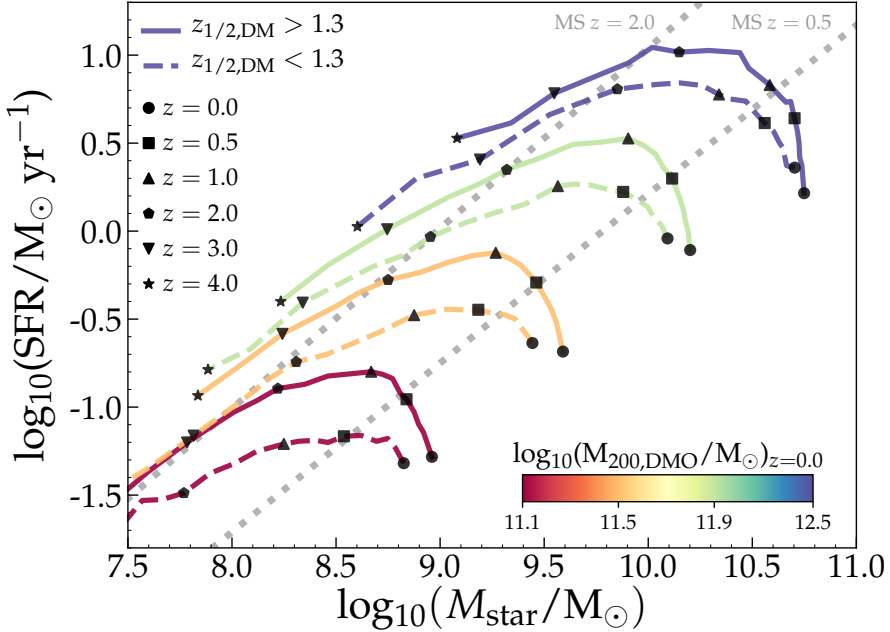
Figure 11.17: As Fig. 11.16, the paths of central star-forming galaxies at $z = 0$ through the SFR-M_{star} plane in bins of $z = 0$ DMO halo mass (colour scale) and halo formation time (different line-styles). At fixed final halo mass, haloes that assembled more than half of their mass at $z > 1.3$ (the median formation redshift of haloes included in this analysis) end up with a higher stellar mass (except for the highest halo masses). These early forming haloes had a higher SFR for most of the history of the Universe, but not at $z = 0$, where they have a lower SFR (except for the lowest halo masses).

growth (which is a proxy for the accumulated AGN feedback energy). Since the relative efficiency of BH growth is correlated with halo mass and formation time, see §11.6, this is an alternative manifestation of how halo assembly bias (i.e. variations in halo formation time at fixed mass) impacts the scatter in the SFR-M_{star} relation.

We illustrate the implications of these results for the *median* tracks of central star-forming galaxies in the SFR-M_{star} plane in Fig. 11.16. In the top panel, we show the tracks of galaxies that are binned by their $z = 0$ mass (line-colour) and sSFR (line-style). Their positions at specific redshifts are indicated by different symbols. The figure shows that there are clear differences between the median paths of galaxies at fixed mass, depending on their present-day SFR. For example, galaxies with $M_{star} = 10^{10}$ $M_{\odot}$ that are above the main sequence at $z = 0$ had a median stellar mass of $\approx 10^{9.4}$ $M_{\odot}$ at $z = 1$, while galaxies with the same mass at $z = 0$, but with a relatively low sSFR, already had a median stellar mass of $\approx 10^{9.7}$ $M_{\odot}$ at $z = 1$. As a result, the median tracks that galaxies follow are not parallel to the main sequence (which typically has a slope ≈ 1, as illustrated with grey dashed lines at $z = 0.5$ and $z = 2.0$) at specific redshifts.

The bottom panel of Fig. 11.16 shows another illustration of the long-term coherence of the median SFHs of galaxies depending on their position along the main sequence (see also Fig. 11.4). We show the positions of galaxies on the SFR-M_{star} relation at $z = 0.0$ and $z = 0.9$ (roughly half of the age of the Universe) and compare them to the general population of star-forming galaxies at these redshifts. At all masses, galaxies (at fixed mass at $z = 0$) that are above the main sequence at $z = 0$ have had a median SFR above the MS for roughly half of the age of the Universe, and vice versa for galaxies below the main sequence at $z = 0$. We emphasise that Fig. 11.16 shows median tracks. As discussed in §11.4, the SFRs of individual galaxies fluctuate around these tracks on shorter time-scales.

Fig. 11.17 illustrates that the origin of these long-term "fast-track" and "slow-track" SFHs lies in the different halo formation times and is thus a manifestation of assembly bias. At fixed halo mass, haloes that formed earlier end up with a higher stellar mass and underwent a period with a higher SFR in the past. While short time-scale fluctuations in the SFHs of individual galaxies that are not in phase cancel each other out when computing the median (as discussed in §11.4), we note that the typical fluctuations in $\log_{10}(SFR)$ are $\approx 0.2 - 0.3$ dex on time-scales of $\lesssim 1$ Gyr (see Fig. 11.5 and Fig. 11.6). Therefore, individual galaxies likely cross the main sequence multiple times, but they fluctuate around different median relations that are related to their halo formation times (resulting in differences in the median paths). Hence, at a specific snapshot in the history of the Universe, the scatter in the main sequence reflects a combination of the average paths of galaxies in the SFR-M_{star} plane related to their halo mass and formation time (see Fig. 11.17), and short time-scale fluctuations around these paths that are related to specific gas cooling and feedback events, bound by self-regulation.

11.7.2   Observational tests

While the EAGLE simulation reproduces several key global galaxy properties, such as the stellar mass function, galaxy sizes, build-up of stellar mass, passive fraction and the black hole mass - stellar mass relation (e.g. Schaye et al., 2015; Furlong et al., 2015, 2017), more detailed tests of the model can be performed using second order relations. Here we provide several second-order observational tests that can be performed to test the model:

1. As shown in Fig. 11.3, EAGLE predicts that there is significantly less scatter in the SFR-M_{star} relation at $z \gtrsim 1.5$ than at $z = 0$ for galaxies with stellar masses $M_{star} < 10^{9.5}$ $M_\odot$ (0.2 dex, versus 0.35 dex). At $z \approx 1.5 - 4$, the scatter is currently mostly constrained at higher masses (where observations find little evolution, similar to the results in the simulation). Deep surveys of mass-selected galaxies (we illustrate in Appendix 11.8 that a SFR-selected sample under-estimates the scatter significantly) that is complete down to these low masses with accurate measurements of their SFRs can test whether there is indeed less scatter at these redshifts.

2. As shown in Fig. 11.9, the SFHs of galaxies at fixed stellar mass depend strongly on their present-day sSFR. The median SFHs of galaxies with the lowest $z = 0$ sSFRs have been declining for more than ≈ 8 Gyr, while the SFHs of galaxies with high sSFR have a much more extended SFH. These qualitative trends can be tested with observationally inferred SFHs, for example based on detailed modelling of high-resolution spectra (e.g. Chauke et al., 2018). Detailed comparisons with observations would also require the mimicking of observational techniques on simulated galaxies.

3. An interesting consequence of the correlation between present-day sSFR and galaxies' SFHs is that the stellar and gas-phase α-enhancements of star-forming galaxies in the local Universe depend on sSFR (Matthee & Schaye, 2018b). Although the gas-phase iron abundance and α-enhancements of young stellar populations are challenging to measure, a correlation between sSFR and α-enhancement at fixed stellar mass would provide an independent constraint on differences in SFHs.

4. Most challenging to measure will be the relation between the scatter in the SFR-M_{star} relation and dark matter halo mass and black hole mass (such as the relative BH growth efficiency; Fig. 11.15). While (statistical) measurements of halo masses will be possible with lensing surveys such as *Euclid*, direct measurements of the masses of the supermassive black holes will remain challenging, particularly in non-active galaxies.

11.8   Summary

We have used the cosmological hydrodynamical EAGLE simulation to study the magnitude, mass dependence and origin of scatter in the SFR-M_{star} relation at $z = 0$, and its evolution. In order to allow for a proper comparison to observations, we have also measured the magnitude and mass dependence of the scatter in a sample of galaxies in the local Universe from the Sloan Digital Sky Survey.

At $z = 0$, we find that the scatter in the SFR of star-forming galaxies at fixed M_{star} decreases slightly with stellar mass (Fig. 11.1) from 0.35 dex at $M_{star} \approx 10^9$ $M_\odot$ to 0.30 dex at $M_{star} \gtrsim 3 \times 10^{10}$ $M_\odot$. Correcting for measurement errors in the data results in excellent agreement with the observed slope and normalisation of the scatter as a function of stellar mass. Consistent with observational constraints, there is little evolution in the scatter in SFR at fixed stellar mass for galaxies with masses $M_{star} \gtrsim 10^{10}$ $M_\odot$ between $z = 0$ and $z = 2$. At lower masses, however, the scatter is predicted to decrease from ≈ 0.35 dex at $z = 0$ to ≈ 0.20 dex at $z > 2.5$, see Fig. 11.3. Excluding star-forming satellite galaxies only removes ≈ 0.04 dex of scatter (Fig. 11.2). This indicates that satellite-specific processes are either weak, or strong and rapid (such that the satellites quickly drop out of the sample of star-forming galaxies).

We find that for galaxies that are 'above' the main sequence at $z = 0.1$ the median SFR tends to have been 'above' the main sequence for ~ 10 Gyr, see Figs. 11.4 and 11.16. On top of these long time-scale differences (of ≈ 0.15

dex) tracked by the median SFHs we find that the SFRs of individual galaxies typically fluctuate by $\approx 0.2 - 0.3$ dex on time-scales of $\lesssim 1$ Gyr (Figs. 11.5 and 11.6). As these short time-scale fluctuations in different galaxies are typically not in phase, median stacking analyses cannot identify them as sources of scatter. As a consequence, we find that the scatter in the SFR-M_{star} relation depends on the time-scale over which the SFR is averaged, particularly for $M_{star} \lesssim 10^{10}$ $M_\odot$. The scatter is ≈ 0.3 dex when SFR is averaged over 1 Gyr and it decreases to a non-negligibile ≈ 0.15 when SFR is averaged over 8 Gyr, highlighting the significant contribution of long-term SFHs to the scatter in the SFR-M_{star} plane (Fig. 11.7).

The origin of the long time-scale fluctuations lies in variations in dark matter halo formation times. For $M_{star} \lesssim 10^{10}$ $M_\odot$, scatter in the formation times of dark matter halos contributes 0.15 dex of scatter in the main sequence (at $z = 0.1$; central galaxies only), but its effect is smaller at higher stellar masses, see Figs. 11.10 and 11.11. As halo formation time is related to large-scale structure, this contribution to scatter in the SFR-M_{star} relation is a manifestation of assembly bias. Hence, while individual galaxies cross the main sequence multiple times during the history of the Universe, they fluctuate around different median relations that are related to their halo mass and their halo formation times (i.e. a fast-track associated to haloes that form relatively early and a slow-track for haloes that form relatively late, see Fig. 11.17).

At high masses the BH mass relative to the halo mass/stellar mass is strongly correlated with the scatter in the SFR-M_{star} relation (Figs. 11.13 and 11.15). Galaxies with a relatively high black hole mass for their halo/stellar mass tend to have a low SFR at fixed stellar mass (even when the galaxies are still classified as star-forming, see Fig. 11.14). As the relative BH formation efficiency is also higher in halos that assemble earlier, galaxies residing in haloes with a 'fast-track' evolution are affected earlier by AGN feedback.

Our results imply that the scatter in the SFR-M_{star} relation reflects the diversity in SFHs. Part of this scatter is driven by long time-scale (~ 10Gyr) differences related to halo mass and halo formation time (i.e. assembly bias), but the scatter is dominated by short ($\lesssim 1$Gyr) time-scale fluctuations that do not simply trace back to changes in halo accretion, but are likely controlled by self-regulation of star formation through feedback.

Acknowledgments
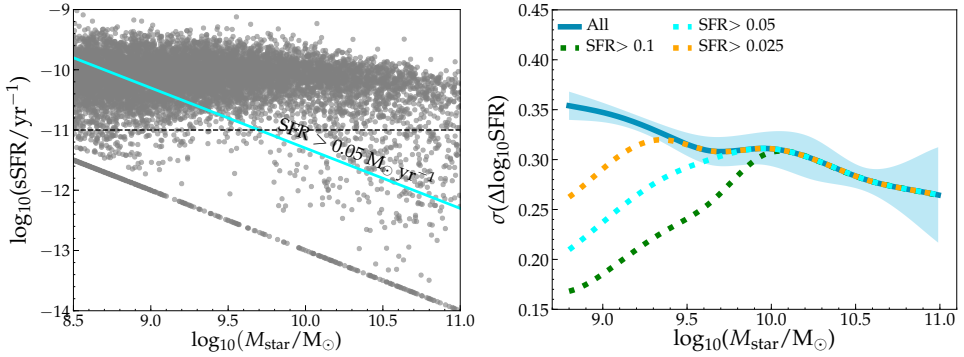
Figure 11.18: The effect of observational selection biases on the scatter in the SFR-M_{star} relation, mimicked using galaxies in EAGLE. The *left panel* illustrates a pure stellar mass selection (all grey points) and a SFR selection (cyan line). The *right panel* shows the scatter in the SFR-M_{star} relation that is measured from galaxy samples with these selection biases (note that we show various thresholds for SFR-selected samples).

Appendix A: On selection biases and the measured scatter

As discussed in the main text (§11.3.1), several observational biases complicate the measurement of scatter in the SFR-M_{star} relation for the observational sample from SDSS. Here, we motivate the redshift- and mass-limits of the sample used and explain why it is necessary to perform these cuts.

First, we use galaxies in the EAGLE simulation to show how sample incompleteness may influence the measured scatter in Fig. 11.18. In the left panel we illustrate two different selections of galaxies which depend on either SFR or stellar mass and in the right panel we show the corresponding scatter in the SFR-M_{star} relation measured with such selections. It is clear that any selection that is somewhat dependent on SFR results in an under-estimate of the scatter at low stellar masses, with the mass-scale at which this bias becomes important depending on the SFR threshold. In order to prevent such a bias from becoming important, the required SFR threshold can be computed as: $\log_{10}$sSFR > med($\log_{10}$sSFR) - 4σ(sSFR), where med($\log_{10}$sSFR) is the median sSFR (assuming a main sequence with a slope of 1) and σ(sSFR) the scatter. From this, it follows that the scatter can be measured reliably for a SFR threshold of > 0.05 at $M_{star} \approx 10^{9.7}$ $M_{\odot}$ and above.

Second, as observations are limited by observed flux, the mass above which at which a sample is complete increases with redshift. In Fig. 11.19, we show histograms of stellar masses for the SDSS galaxies of Chang et al. (2015) in three narrow redshift slices (left panel) and the corresponding measured scatter in the SFR-M_{star} relation in each redshift slice (right panel). We identify the lowest stellar mass at which each redshift slice is close to complete by the peak in the histogram, and show that indeed, due to the selection offset, the measured
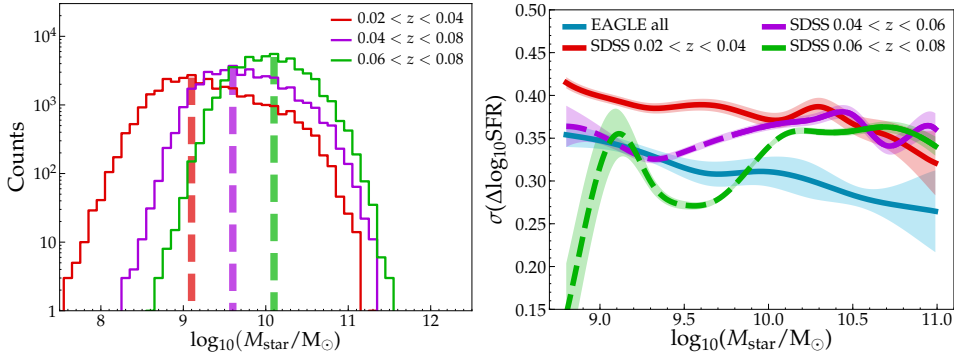
Figure 11.19: Galaxy counts in the SDSS sample as a function of stellar mass in three bins in redshift (*left panel*) and the measured scatter in the SFR-M_{star} relation in each redshift bin, where the line-style changes to dashed at masses below the completeness threshold (*right panel*). The left panel illustrates the stellar mass above which the bins are close to complete (which we define as the mass at which the histogram peaks, illustrated with a vertical dashed line). The right panel shows that incomplete galaxy samples result in an under-estimate of the scatter.

scatter is biased low at incomplete masses, similar to the mimicked observations in the right panel of Fig. 11.18. In the paper we therefore restrict the sample to $0.02 < z < 0.04$, which is complete at stellar masses $\gtrsim 10^9$ M$_\odot$.

Appendix B: Testing different measures of halo mass growth

In §11.5.2, we quantified the halo accretion history using $z_{1/2}$, the redshift at which half of the (dark matter) halo mass at $z = 0.1$ had been assembled in the main progenitor. In addition to only looking at $z_{1/2}$, which may be an overly simplistic parametrisation of the halo assembly history, we measure the halo mass growth averaged over a range of time-scales. We combine the low time-resolution (with resolution of 0.5-1 Gyr) merger tree up to $z = 4$ with a high time-resolution (with a resolution of ≈ 100 Myr) merger tree up to $z = 2$ and measure the halo mass growth averaged over $0.15 - 10$ Gyr. In Fig. 11.20 we examine the strength of the relation between the sSFR at $z = 0.1$ and the mass growth as a function of the time-scale over which the mass growth is averaged, in bins of stellar mass.

The most important result from Fig. 11.20 is that none of the time-scales yield a correlation with an absolute Spearman rank —$R_S| > 0.4$ (which is the strength of the correlation between the scatter in the SFR-M_{star} relation and $z_{1/2}$). This means that there is no simple measurement of accretion history that correlates better with sSFR at fixed stellar mass than $z_{1/2}$ ($R_S \approx -0.45$). For masses between 10^9 and 10^{10} M$_\odot$ we find that the strongest correlation is found when mass growth is averaged over long time-scales of ≈ 7 Gyr. Perhaps surpris-
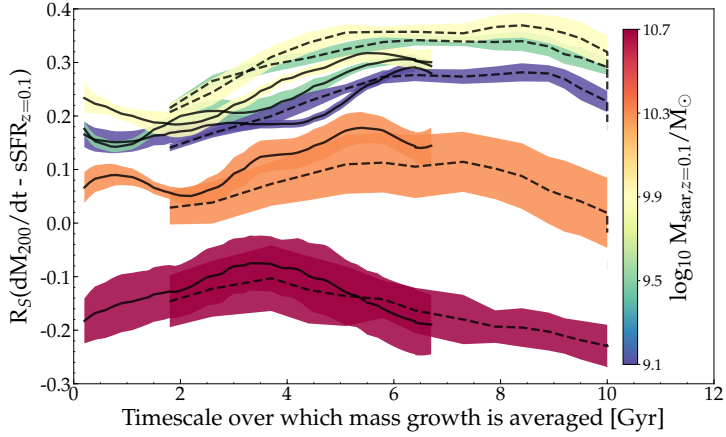
Figure 11.20: The strength of the correlation between the sSFR and the halo mass growth, where the latter is averaged over a range of time-scales, quantified by the Spearman correlation rank, R_S. Results are shown in bins of stellar mass at $z = 0.1$. Solid lines show the results for the high time-resolution merger tree, while dashed lines show the results for the low time-resolution merger tree. The shaded regions indicate errors that are estimated through jackknife resamples of eight sub-volumes in the simulation volume. At fixed stellar mass, the specific SFR is related most strongly to halo mass growth if it is averaged over long, ~ 7 Gyr time-scales.

ingly, on average, the current sSFR does not depend strongly on the most recent halo mass growth. This suggests that there is a gas reservoir in and/or around galaxies that dampens short time-scale fluctuations in the growth of M_{200} and weakens the direct influence of halo accretion on SFRs.

Chapter 12

Star-forming galaxies are predicted to lie on a fundamental plane of mass, star formation rate and α-enhancement

Observations show that star-forming galaxies reside on a tight three-dimensional plane between mass, gas-phase metallicity and star formation rate (SFR), which can be explained by the interplay between metal-poor gas inflows, SFR and outflows. However, different metals are released on different time-scales, which may affect the slope of this relation. Here, we use central, star-forming galaxies with $M_{star} = 10^{9.0-10.5}$ $M_\odot$ from the EAGLE hydrodynamical simulation to examine three dimensional relations between mass, SFR and chemical enrichment using absolute and relative C, N, O and Fe abundances. We show that the scatter is smaller when gas-phase α-enhancement is used rather than metallicity. A similar plane also exists for stellar α-enhancement, implying that present-day specific SFRs are correlated with long time-scale star formation histories. Between $z = 0$ and 1, the α-enhancement plane is even more insensitive to redshift than the plane using metallicity. However, it evolves at $z > 1$ due to lagging iron yields. At fixed mass, galaxies with higher SFRs have star formation histories shifted toward late times, are more α-enhanced and this α-enhancement increases with redshift as observed. These findings suggest that relations between physical properties inferred from observations may be affected by systematic variations in α-enhancements.

12.1   Introduction

One of the key goals of galaxy formation studies is to understand when and how the interstellar medium (ISM) was chemically enriched and how the metal abundances of stars evolved through cosmic time. A key observable is the metallicity of the ISM (Z_{gas}), which controls the metallicity of the stars that are being formed. Gas-phase metallicity is sensitive to gas accretion (pristine or recycled), chemical enrichment through stellar mass loss and supernovae, and outflows driven by feedback associated with the formation of stars and the growth of super-massive black holes.

Observationally, Z_{gas} is typically quantified by the (light-weighted) oxygen to hydrogen abundance in HII regions, (O/H). Can the choice for this ratio be theoretically motivated? In principle it can, as oxygen is the most abundant metal in the Universe and relatively easily observable.

However, in a gas-reservoir that evolves due to inflows and outflows, changes in $(O/H)_{gas}$ may simply reflect variations in the gas fraction. Indeed, variations in gas-phase metallicities at fixed galaxy mass are observed to be anti-correlated with variations in specific star formation rates (sSFRs; e.g. Ellison et al. 2008), a galaxy property that is closely related to the gas fraction (e.g. Bothwell et al., 2013). As a result, star-forming galaxies in the present-day Universe reside on a three dimensional relation between M_{star}, SFR and Z_{gas} (e.g. Lara-López et al., 2010; Mannucci et al., 2010), called the fundamental metallicity relation (FMR; Mannucci et al. 2010). This correlation weakens/breaks down at masses $M_{star} > 10^{10.5}\,M_\odot$ (e.g. Yates et al., 2012; Zahid et al., 2013; Salim et al., 2014), potentially due to the increased importance of AGN feedback (De Rossi et al., 2017).

The existence of a 3D metallicity relation is a well-understood property of galaxy equilibrium models (e.g. Finlator & Davé, 2008; Davé et al., 2012; Lilly et al., 2013; Rodríguez-Puebla et al., 2016) and is also reproduced by cosmological hydrodynamical simulations (e.g. Lagos et al., 2016; De Rossi et al., 2017). An increase in the accretion of (metal poor) gas both lowers the metallicity and fuels an increase in the SFR, as long as the time-scales on which the SFR and Z_{gas} evolve, are of the same order (Torrey et al., 2018). This means that the 3D metallicity relation reflects the time-scales of variations in the gas mass fraction (e.g. Bothwell et al., 2013; Forbes et al., 2014; Lagos et al., 2016; Brown et al., 2018).

What happens if we use another metal as the tracer of metallicity? Different metal species are produced on varying time-scales (e.g. Tinsley, 1979). The enrichment time-scale for oxygen is short (~ 10 Myr) as it is only produced in massive stars. Significant contributions (≈ 30 %) from AGB stars result in longer time-scales for carbon and nitrogen (~ 200 and 500 Myr, respectively; see Wiersma et al. 2009b). Significant iron enrichment occurs over the longest time-scale ($\gtrsim 2$ Gyr) as a substantial fraction (20-30 %) is produced in Type Ia supernovae (SNe). As a result, the different time-scales on which star formation histories (SFHs) and gas fractions change, drive variations in relative metal abundances.

In this letter, we use the EAGLE cosmological simulation to investigate which

chemical abundance is most closely related to stellar mass and SFR and which scaling relation evolves least between $z = 0 - 2$. This letter is structured as follows. We first discuss the simulation and the various definitions of metallicity in §12.2. §12.3 reports how much scatter there is in the 2-(3-)dimensional mass - metallicity (- SFR) relation for different element abundances and how this evolves with cosmic time. In §12.4 we discuss the implications of our results for the interpretation of observations and we discuss the prospects for testing our results observationally.

12.2   Methods

12.2.1   The EAGLE simulations

We use galaxies from the $(100 \text{ cMpc})^3$ reference model[1] from the EAGLE cosmological hydrodynamical simulation (Schaye et al., 2015; Crain et al., 2015; McAlpine et al., 2016). EAGLE uses a modified version of the smoothed particle hydrodynamics (SPH) code GADGET3 (Springel, 2005) with a modern formulation of SPH (see Schaller et al. 2015c).

Gas particles with sufficiently high density (depending on metallicity) are transformed into star particles following the pressure-dependent implementation of the Kennicutt-Schmidt law of Schaye & Dalla Vecchia (2008). Each star particle is a single stellar population with a Chabrier (2003) initial mass function and the metallicity inherited from the parent gas particle. As detailed in Wiersma et al. (2009b), the simulation tracks the enrichment of eleven elements as they are released into the ISM on their relevant time-scales. This model includes yields from type II SNe, mass loss from intermediate-mass AGB stars and winds from high mass stars and type Ia SNe. The cosmic type Ia SN rate follows an exponential distribution, where the normalisation and e-folding timescale of 2 Gyr are chosen to reproduce the evolution of observed SN Ia rates (see Schaye et al. 2015).[2] The radiative cooling rates are computed on an element-by-element basis (Wiersma et al., 2009a). Energy feedback from star formation is implemented stochastically (Dalla Vecchia & Schaye, 2012) and was calibrated to reproduce the present-day galaxy stellar mass function and sizes. The growth of black holes and the feedback associated with AGN activity are also modelled (Springel et al., 2005a; Rosas-Guevara et al., 2015; Schaye et al., 2015). The simulation uses baryonic particles with (initial) mass $1.8 \times 10^6 \text{ M}_\odot$ and a gravitational force resolution better than 0.7 physical kpc.

---

[1] We have verified that our conclusions remain unchanged when we use the higher-resolution $(25 \text{ cMpc})^3$ RECAL model of the EAGLE simulation. The mass-metallicity relation is steeper in the RECAL model (see also Schaye et al. 2015), the normalisation of abundances are lower (at fixed mass) and α-enhancement is higher by 0.1 dex. However, the slopes of the correlations between sSFR and chemical abundances at fixed mass remain unchanged.

[2] We note that the delay time distribution of SNIa in EAGLE is somewhat shifted to longer times compared to recent observations (e.g. Maoz et al., 2012; Friedmann & Maoz, 2018). As a result, α-enhancements in EAGLE may be somewhat over-estimated, though uncertainties in nucleosynthetic yields may be more important (e.g. Wiersma et al., 2009b).

Our analysis includes central galaxies[3] with $M_{star} = 10^{9-10.5}$ $M_{\odot}$ at all red-shifts and we select star-forming galaxies with sSFR $> 10^{(-11,-10.4,-10)}$ yr^{-1} at $z = (0.1, 1.0, 2.0)$, respectively. These cuts encompass the main sequence of star-forming galaxies as defined by Elbaz et al. (2007). They correspond to galaxies that have at least ≈ 500 star particles and ≈ 30 star-forming gas particles and ensure a sufficient number of galaxies (6201, 7046, 5487 at $z = 0.1, 1.0, 2.0$, re-spectively). The upper mass limit is chosen to ensure that the star formation histories are not yet significantly influenced by AGN feedback, which weakens 3D chemical enrichment correlations (De Rossi et al., 2017).

12.2.2   Definitions & choice of metal species

We use SPH-smoothed metallicities in stars and in the star-forming gas-phase (see Schaye et al. 2015 for details). Metal abundances are expressed relative to the Solar values.[4] We investigate the metals C, N, O and Fe, because of their abundance, observability and importance for determining the properties of stars.

Besides investigating the mass fractions of these metals, we also investigate their relative abundances. In the EAGLE model, the C/O ratio of stellar ejecta is sensitive to systematic changes in SFRs on ~ 200 Myr time-scales. Nitrogen is produced on longer time-scales than C and O and is a secondary element (increased stellar nitrogen abundance increases the nitrogen yields). Therefore, N/O is a measure of the integrated chemical evolution history. The O/Fe ratio ($\approx \alpha$-enhancement) traces even longer time-scales and is therefore sensitive to the entire SFH of a galaxy. As both nitrogen and iron trace relatively long time-scales, variations in the N/Fe ratio are sensitive to differences at early times that are amplified by the secondary nature of nitrogen. We do not explicitly discuss C/Fe as we find that this ratio is similar to O/Fe.

12.3   The scatter in 2D and 3D mass - metallicity relations

We first focus in §12.3.1 on 2D relations between mass and gas-phase metal abundances in the late Universe ($z = 0.1$), then in §12.3.2 measure the scatter in 3D relations that account for variations in sSFR and we finish in §12.3.3 with in-vestigating evolution. We measure scatter as the standard deviation of $\log_{10}(Z^i)$ in rolling bins of stellar mass (with bin-width 0.3 dex and with bin-centers in increasing steps of 0.1 dex) and interpolate these values to obtain a smoothed trend. Here, Z^i is either the metal mass-fraction or the relative metal abundance.

We account for variations in $\log_{10}$ sSFR by fitting a linear relation $\log_{10} Z^i = a + b \times \log_{10}$sSFR in each mass bin and measuring the scatter in $\log_{10} Z^i_{3D} = $

---

[3] To avoid strong environmental effects, we focus on central galaxies. See Bahé et al. (2017) for a study of the differences in the metallicities of central and satellite galaxies in EAGLE.

[4] We adopt a solar metallicity $Z_{\odot} = 0.012947$. We follow the standard notation of [O/Fe] = (O/Fe) - (O/Fe)$_{\odot}$. We adopt solar abundances of (O/Fe)$_{\odot} = \log_{10}(X^O_{\odot}/X^{Fe}_{\odot}) = 0.647$ and (N/O)$_{\odot} = \log_{10}(X^N_{\odot}/X^O_{\odot}) = -0.92$ (Asplund et al., 2009), where X^i is the mass-fraction of element i.
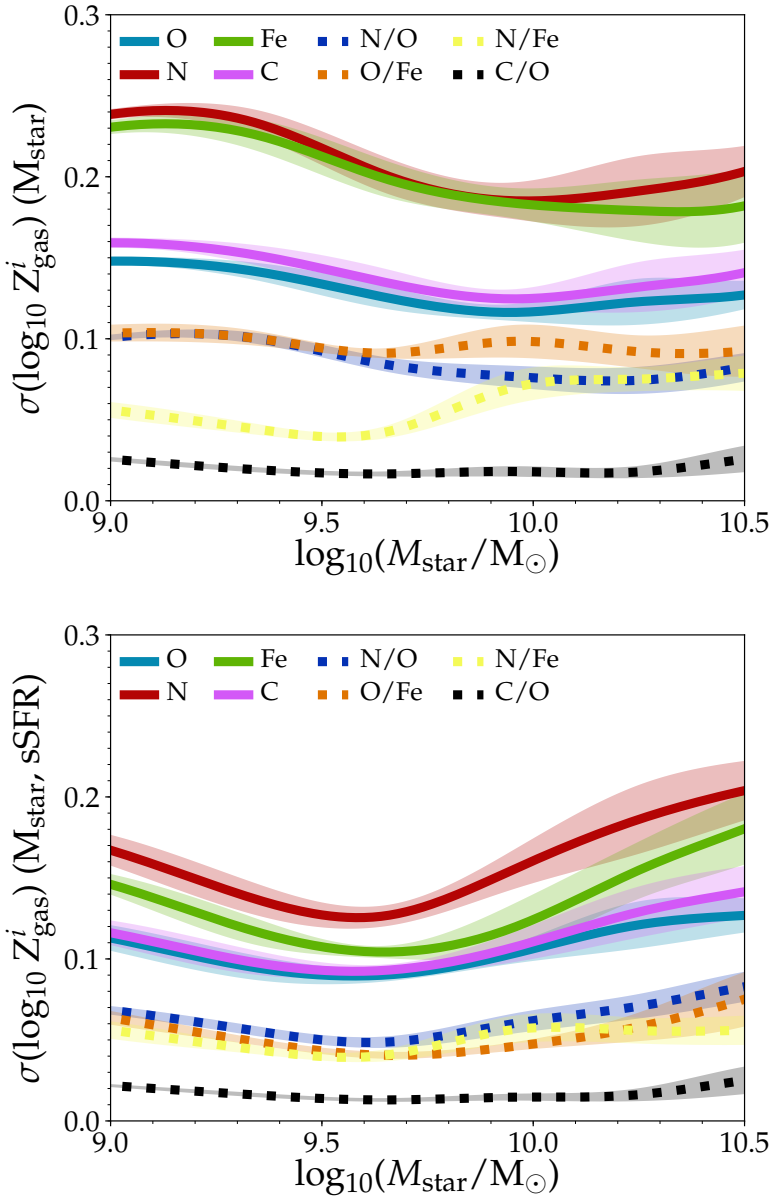
Figure 12.1: The scatter in the mass- gas metallicity relations for central star-forming galaxies at $z = 0.1$, as a function of stellar mass. The *top* panel shows the scatter in the 2D relation, while the *bottom* panel shows the scatter around the 3D relation (i.e. including $\log_{10}$ sSFR). Different colours show different metal abundances. Solid lines show absolute abundances, while dashed lines show relative abundances. All abundances are for the star-forming gas-phase.

$\log_{10}Z^i - [a(M_{\mathrm{star}}) + b(M_{\mathrm{star}}) \times \log_{10}\mathrm{sSFR}]$. We perform our measurements in eight separate sub-volumes of $(50\ \mathrm{cMpc})^3$ and show the median and its standard deviation to highlight variations due to cosmic variance. The results are shown in Figure 12.1, where we plot $\sigma(\log_{10} Z^i)$ as a function of stellar mass.

12.3.1 Absolute metal abundances

The top panel of Fig. 12.1 shows that among ISM metal abundances, there is least scatter in the oxygen mass fraction (≈ 0.15 dex, similar to observations of O/H abundances; Tremonti et al. 2004), followed closely by the C mass-fraction. There is significantly more scatter in the N and Fe fractions.[5]

The bottom panel of Fig. 12.1 shows the scatter in metallicities as a function of mass after accounting for the trend with sSFR. The scatter is reduced for all absolute abundances (i.e. mass fractions), but we find that it is most strongly reduced for Fe. This means that at fixed mass, fluctuations in sSFR are most closely related to the abundance of iron, and least strongly related to that of oxygen. However, the scatter in the 3D metallicity relation is still smallest for oxygen.

The differences in scatter shown in the top panel of Fig. 12.1 must arise from variations in the N/O and O/Fe ratios and are therefore a consequence of the different enrichment time-scales. If the gas fraction and hence sSFR increase, oxygen enrichment occurs almost simultaneously. This means that any increase in M_H, decreasing the O/H ratio, is rapidly followed by an increase in M_O and hence O/H. This processes limits the scatter in the O/H - M_{star} relation. As the enrichment time-scales of N and Fe are significantly longer, this scatter-reducing process is less effective for the N and Fe abundances, resulting in a larger scatter. This picture is supported by a comparison of the two panels of Fig. 12.2, which shows that at fixed mass, variations in N and Fe mass fractions are more sensitive to fluctuations in sSFRs than is the case for O.

12.3.2 Relative metal abundances

Relative metal abundances encode information about the chemical enrichment history and are less sensitive to present-day fluctuations in gas fractions. As a consequence, we find that N/O, C/O, N/Fe and O/Fe are more tightly correlated with M_{star} than any of the absolute abundances are (top panel of Fig. 12.1, consistent with observations from e.g. Andrews & Martini 2013b). There is very little variation in C/O and N/Fe at fixed mass. There is more variation in abundance ratios that trace both short and long time-scales (N/O and O/Fe), which is a result of galaxies at fixed stellar mass having different SFHs.

The scatter in the N/O and O/Fe abundance ratios decreases once fluctuations in sSFR are accounted for. This indicates that present-day sSFR is related to long-time-scale differences in chemical enrichment histories (and hence SFHs).

---

[5] We find qualitatively similar results for mass-weighted stellar abundances. The typical scatter in stellar abundances and the differences between different elements are smaller, but the rank-order is preserved.
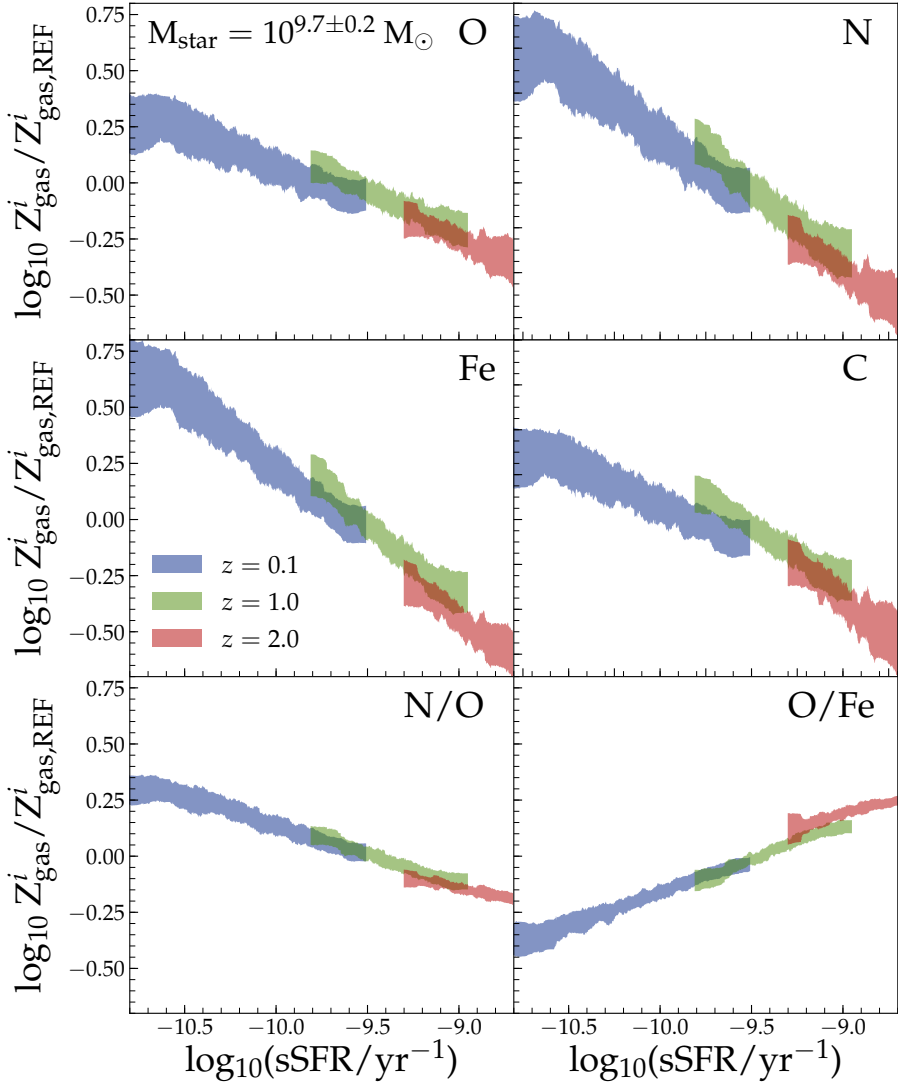
Figure 12.2: Evolution of the relations between the chemical enrichment of the ISM and sSFR for central star-forming galaxies with $M_{star} = 10^{9.7\pm0.2}\,M_\odot$. Each panel shows a different abundance ratio that is scaled to a *reference* median abundance at $\log_{10}(\mathrm{sSFR}_{z=1.0}/\mathrm{yr}^{-1}) = -9.5$ to facilitate the comparison. Absolute metal abundances show a weak evolution in the normalisation of the relation, particularly between $z = 0.1$ and 1.0. The N/O ratio correlates more weakly with sSFR, but the correlation evolves less. Fe/O does not evolve between $z = 0.1$ and 1.0, but shows an offset at $z = 2.0$ because the formation time-scale of iron is no longer small compared with the age of the Universe.

This can also be seen in Fig. 12.4, which shows that the mass-weighted stellar O/Fe correlates with sSFR. Because stellar O/Fe decreases with each cycle of star formation, this implies an anti-correlation between sSFR and the SFH. Moreover, at fixed mass, gas-phase O/Fe is strongly correlated with stellar O/Fe (with a Spearman rank correlation $R_S = 0.7$) and anti-correlated with mass-weighted stellar age ($R_S = -0.75$). The origin of the correlation between present-day sSFR and SFH lies in the fact that, at fixed mass, sSFR anti-correlates with the dark matter halo formation redshift. This manifestation of galaxy assembly bias is explored in more detail in Matthee & Schaye (2018a).
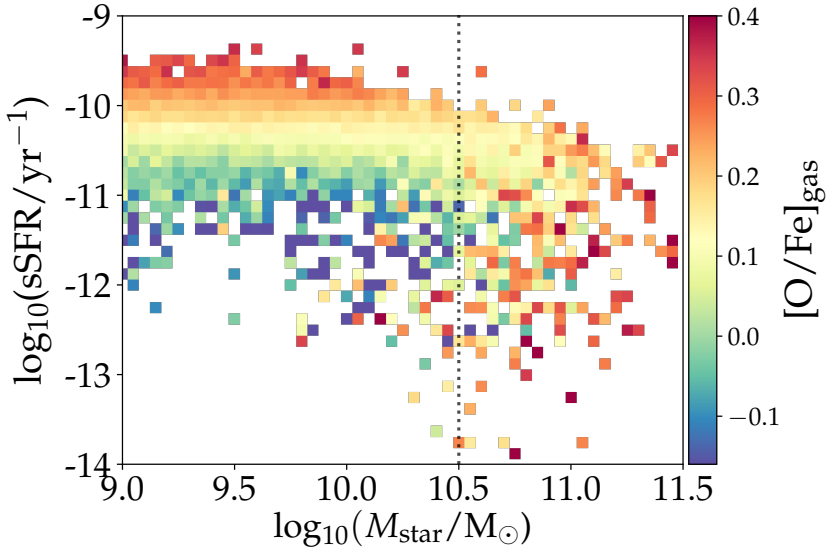
Figure 12.3: The correlation between the scatter in sSFR(M_{star}) and [O/Fe] clearly illustrates the 3D relation between M_{star} - sSFR - O/Fe, for $M_{star} < 10^{10.5}$ $M_\odot$. At higher masses the 3D correlation weakens and α-enhancement is mostly set by M_{star}.

Moreover, our results mean that the 3D relations M_{star} - sSFR - O/Fe or N/O have less scatter than the 'fundamental metallicity relation' with O/H. Although the scatter is even smaller if we use C/O or N/Fe, the residuals of their relations with mass do not correlate with sSFR. Hence, the small scatter merely reflects a similar nucleosynthetic origin and does not provide additional insight into galaxy evolution. We will therefore not consider these abundance ratios any further.

The reason for the tightness of the 3D α-enhancement relation is that O/Fe combines two physical effects that work in the same direction (unlike O/H, where these effects act oppositely). The first is rapid O enrichment in response to a recent increase in SFR. The second is the lower Fe abundance for galaxies with high SFRs due to such galaxies tending to have delayed SFHs. Both effects give rise to an increasing α-enhancement as a function of sSFR (this is also shown

in Fig. 12.2).

We show a 2D projection of the M_{star} - sSFR - [O/Fe] relation in Fig. 12.3, where the third dimension of the relation, [O/Fe], is illustrated with the color-coding. For $M_{star} < 10^{10.5}$ $M_\odot$, the scatter in the M_{star} - sSFR relation is correlated strongly with [O/Fe], while the relation weakens at higher masses. Fitting a 3D plane to these data-points at $z = 0.1$ using a least squares algorithm yields: $[O/Fe] = -0.282 \log_{10}(M_{star}/10^{10}M_\odot) + 0.290 \log_{10}(SFR/M_\odot yr^{-1}) + 0.163$.

12.3.3 Evolution through cosmic time

The results described above are for $z = 0.1$. What about higher redshifts? A key feature of the fundamental metallicity relation proposed by Mannucci et al. (2010), is that it seems to be redshift-invariant (see extended observational discussion in e.g. Stott et al., 2013; Maier et al., 2014; Sanders et al., 2015, 2018). De Rossi et al. (2017) show that there is no evolution in the gas fraction - metallicity relation between $z = 0 - 3$ in the EAGLE RECAL-L025N0752 simulation. To what extent does the same hold for the 3D α-enhancement relation or relations using other metal abundances?

Fig. 12.2 shows the correlation between sSFR and metal abundance (using different elements) at a fixed stellar mass of $M_{star} = 10^{9.7 \pm 0.2}$ $M_\odot$ and at $z = 0.1, 1.0$ and $z = 2.0$. We find that all absolute abundances anti-correlate with sSFR at all redshifts, but that the trends are slightly different for different elements (note that many trends identified in the previous subsection are clearly visible in this figure). To first order the different redshifts follow a single relation, but looking more closely, there is a slight shift in the normalisation between $z = 0$ and 1 for all absolute abundances. Such a shift is not visible for N/O and O/Fe, indicating that the differences are due to differences in the H gas masses at $z = 1$ compared to $z = 0$. Indeed, at $z = 1$ the galaxies are much smaller than at $z = 0.1$ (Furlong et al., 2017), which, combined with the non-linear star formation law, implies that less gas is required to obtain the same SFR. This can explain the higher metallicity (at $z = 1.0$ compared to $z = 0.1$) at fixed sSFR.

The normalisation and slope of the relation between O/Fe and sSFR do not evolve between $z = 0$ and $z = 1$, but the normalisation does shift slightly upwards at $z = 2$. This is because at high redshift the formation of iron is still lagging (the α-enhancement converges to the value for pure SNII yields at early times, see also Fig. 12.4). There is a similar enrichment-lag for N/O that becomes more prominent at $z > 3$ (not shown). Hence, at least for $z \lesssim 1$ the relation between mass, SFR and α-enhancement evolves even less than the "fundamental metallicity relation".

12.4 Discussion

12.4.1 Observational implications

In observations, Z_{gas} is typically measured using the relative strengths of strong emission lines from oxygen, nitrogen and hydrogen and calibrations based on
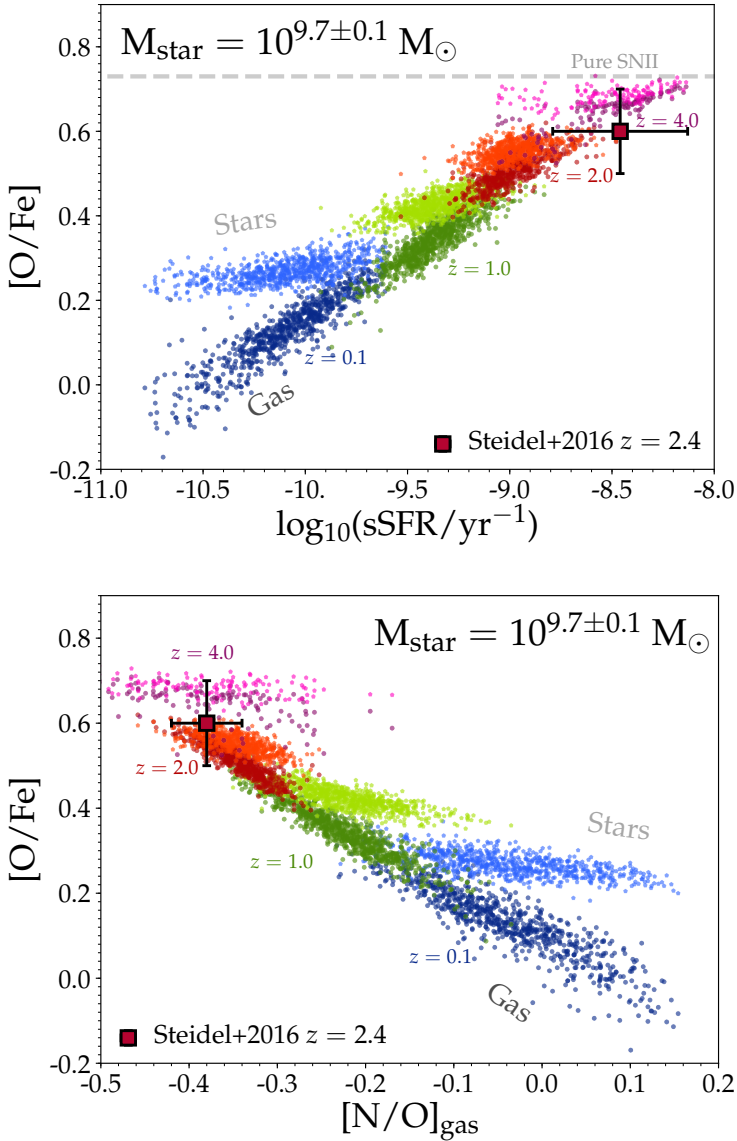
Figure 12.4: The relation between mass-weighted gas-phase and stellar α-enhancement versus specific SFR (*top*) and versus gas N/O ratio (*bottom*) for different redshifts (different colours) for central star-forming galaxies with $M_{star} = 10^{9.7\pm0.1}$ $M_\odot$. Light and dark colours correspond to stars and star-forming gas, respectively. At all redshifts, galaxies with a higher sSFR at fixed mass tend to be more α-enhanced. At higher redshift, when SFHs are necessarily more compressed, the differences between gas and stellar abundances become smaller, typical α-enhancements increase (similar to observational results from Steidel et al. 2016; data point) and the α-enhancement converges towards the theoretical yields for massive stars (dashed line; Nomoto et al., 2006).

local galaxies (e.g. Pettini & Pagel, 2004) or theoretical models. Besides metallicity, these line strengths implicitly depend on the ISM properties (density, temperature) and the ionising radiation, which depends on stellar age and iron abundance, among other properties (e.g. Eldridge et al., 2017). It is therefore important to understand how these properties differ among galaxies and how they evolve with cosmic time.

As the top panel of Fig. 12.4 shows, the gas-phase α-enhancement is a strong function of sSFR. As a result, galaxies at higher redshift are more α-enhanced. Such an increase has been inferred from observations (Steidel et al. 2016; data point in Fig. 12.4), in quantitative agreement with the EAGLE prediction. Galaxies that are α-enhanced have a lower iron abundance at fixed O/H, and hence have harder stellar spectra (as the hardness increases with lower iron abundance; see e.g. Figure 6 from Eldridge et al. 2017). The observed relative strengths of strong emission lines (such as Hα, [OIII] and [OII]) depend on the relative number of photons with ionisation energies corresponding to different line transitions. Therefore, variations in the hardness of the underlying ionisation field will result in different line ratios, even though oxygen abundances may be constant. Strong emission-line diagnostics may have to be revised, particularly when comparing samples with different redshifts.

Fig. 12.4 shows that the mass-weighted stellar α-enhancement of star-forming galaxies[6] is also correlated with sSFR. As discussed above, this is strong evidence for a correlation between the present-day sSFR and the SFH. This correlation may also lead to biases, because the stellar light predicted by population synthesis models depends (or should depend) on α-enhancement.

Fig. 12.4 also shows that biases are not only expected between galaxy samples at different redshifts, but also at a fixed cosmic time. Differences in the α-enhancements of galaxies add a systematic uncertainty correlated with the sSFR, which needs to be taken account in the applicability of emission line diagnostics.

12.4.2 Prospects

Can these predictions from the EAGLE simulation be tested observationally? Measuring the gas-phase α-enhancement in star-forming galaxies is challenging due to the faintness of iron emission lines and uncertainties in dust-depletion corrections. However, we show in the bottom panel of Fig. 12.4 that O/Fe is tightly related to N/O ([O/Fe] $\propto -1.2$ [N/O]; except at $z = 4$, when there is no strong correlation), which is slightly less challenging to observe (e.g. Andrews & Martini, 2013b; Masters et al., 2016). Promisingly, the observational results from Steidel et al. (2016) are quantitatively consistent, see the data point in Fig. 12.4. In EAGLE, at $z = 0.1$, the gas-phase N/O ratio in star-forming galaxies decreases weakly as [N/O]$\propto -0.3 \log_{10}(sSFR)$ at fixed stellar mass (see the bottom-center panel in Fig. 12.2). We note that Andrews & Martini (2013b) find a potentially contradictory result (higher N/O ratio for galaxies with a higher

---

[6] Observations are light-weighted rather than mass-weighted. Light-weighted stellar abundances likely lie closer to the gas abundances. At high redshift the light- and mass-weighted stellar abundances converge due to the high sSFRs.

SFR) at fixed mass $M_{star} \lesssim 10^9$ M$_\odot$, but Pérez-Montero et al. (2013) find no secondary dependence of N/O on SFR at fixed mass.

Stellar α-enhancement may be estimated using absorption-line measurements, as has been done for massive elliptical galaxies (e.g. Trager et al., 2000; Conroy, 2013). However, as the observed light from star-forming galaxies is dominated by hot massive stars, which typically have weaker metal absorption-lines, these measurements are more challenging for star-forming galaxies. An interesting approach could be to combine light-weighted stellar Fe/H abundances with gas-phase O/H abundances. This could be particularly useful at high sSFRs, where stellar and gas-phase α-enhancements are predicted to be similar. In any case, the model predictions could be based on the same approach.

In summary, we have shown that the EAGLE simulation predicts the existence of a tight three-dimensional relation between mass, SFR and gas-phase α-enhancement for galaxies with $M_{star} = 10^{9.0-10.5}$ M$_\odot$ due to a combination of rapid oxygen enrichment and delayed iron enrichment. A similar plane exists for stellar α-enhancement as galaxies with higher SFRs have compressed SFHs at fixed mass (Matthee & Schaye, 2018a). The gas-phase relation is tighter and, for $z < 1$, evolves less than the "fundamental metallicity relation" between mass, SFR and metallicity. These results illustrate the promise of using chemical abundances to constrain galaxy evolution in a cosmological environment, but also imply that trends between physical properties inferred from observations may be affected by systematic variations in α-enhancement.

Acknowledgments

Nederlandse samenvatting

Het onderwerp van dit proefschrift is het ontstaan van sterrenstelsels. Sterrenstelsels bestaan uit een verzameling van sterren en planeten, interstellair gas (gas tussen de sterren), supermassieve zwarte gaten en donkere materie. Het merendeel van de massa van een sterrenstelsel is in de vorm van donkere materie, waarvan de aard nog niet volledig doorgrond is. De massaverdeling van donkere materie domineert het zwaartekrachtsveld en daardoor volgt de groei van sterrenstelsels de groei van donkere materie structuren.

Sterrenstelsels zijn de plaatsen waar gas samenklontert en moleculaire wolken vormen. In deze wolken (zoals bijvoorbeeld de Adelaarsnevel, weergegeven in Figuur A) ontstaan sterren. Aan het eind van hun leven verrijken sterren het interstellair gas met metalen[7] dat in hun kernen geproduceerd is. Dit gebeurt door stellaire winden (extreme versies van zonnevlammen) en door de ontploffingen van massieve sterren die materiaal de ruimte in slingert (supernovae genaamd). In dit verrijkte gas kunnen vervolgens nieuwe generaties sterren ontstaan. Interstellair gas kan ook uit sterrenstelsels geblazen worden door galactische winden, aangedreven door supernova explosies, energetische straling of jet-stralen die ontstaan tijdens de groei van supermassieve zwarte gaten. Tegelijkertijd bereikt nieuw gas uit het intergalactisch medium (het gas tussen sterrenstelsels) het sterrenstelsel en levert nieuw materiaal om sterren uit te vormen. Allerlei verschillende fases van het gas in sterrenstelsels zenden verschillende soorten licht uit, zoals radio-straling van koud neutraal waterstof, röntgen-straling van de accretieschijven rondom zwarte gaten, UV straling van jonge sterren en infrarood licht van moleculen en stof. Al deze soorten licht kunnen waargenomen worden, elk met variërende gevoeligheid en met een verschillende techniek.

Waarneemmethoden

Moderne astrofysica is niet begrensd tot het golflengte bereik dat zichtbaar is voor het menselijk oog, maar spant het volledige elektromagnetische spectrum: van korte gamma-stralen tot lange radio-golven. Doordat de atmosfeer röntgen-straling en UV straling effectief tegenhoudt, kunnen waarnemingen in deze golflengten alleen efficient met ruimtetelescopen gedaan worden. Een ruimtetelescoop is ook nodig voor waarnemingen in het verre infrarood, omdat de atmosfeer zelf meer infrarood licht uitzendt dan het licht van sterren en sterrenstelsels

---

[7] In de sterrenkunde wordt elk element zwaarder dan helium een metaal genoemd, omdat elementen zwaarder dan helium niet in de oerknal, maar in sterren zijn geproduceerd (op uitzondering van kleine hoeveelheden lithium).

Figure A: Een valse-kleur compositie van een deel van de Adelaarsnevel (M16) op basis van eigen foto's gemaakt in Mei 2018 met de sloan *I*, NB501 en sloan *g* (RGB) filters met de WFC op de 2.5m Isaac Newton Telescope, onderdeel van het Roque de los Muchachos Observatorium op La Palma, Spanje. Groen licht accentueert de straling uitgezonden door dubbel geïoniseerd zuurstof en laat zien hoe de intense UV straling van een jonge, blauwe ster gaswolken aantast. De "Pillars of Creation" zijn gaswolken waarin nieuwe sterren gevormd worden. De linker "pilaar" is ongeveer 4 lichtjaar in lengte. Doordat interstellair stof met name blauw licht absorbeert, zien we met name het rode licht van sterren, in het bijzonder voor sterren die zich in dichte gaswolken bevinden.

dat ons bereikt (vergelijkbaar met de blauwe lucht die het overdags onmogelijk maakt sterren te zien). Zichtbaar licht en licht in het nabije infrarood kan vanaf de aarde waargenomen worden, idealiter in donkere gebieden met een stabiele atmosfeer, weinig wolken en een relatief droge lucht. Hierdoor zijn bergtoppen op eilanden of nabij grote oceanen ideaal, zoals Mauna Kea op Hawaii, Roque de los Muchachos op La Palma, of Cerro Paranal in het Andesgebergte in Chili. Waarnemingen op sub-mm golflengten vereisen met name een zeer lage luchtvochtigheid, waardoor de Atacamawoestijn in Chili de plek is waar de ALMA-telescoop gebouwd is.

In dit proefschrift heb ik onderzoek gedaan naar sterrenstelsels in UV licht, het zichtbare licht, nabije infrarood en sub-mm straling door middel van telescopen op bovengenoemde plekken en de *Hubble Space Telescope* in de ruimte. De relatieve helderheid van sterrenstelsels in verschillende golflengten (dat wil zeggen: de kleuren) bevat veel informatie over de eigenschappen van sterren en gas dat aanwezig is in sterrenstelsels. Een rode kleurt wijst op oude sterren en grote hoeveelheden stof, terwijl een blauwe kleur wijst op jonge sterren en weinig stof.

Specifieke eigenschappen kunnen nauwkeurig gemeten worden door de sterktes van verschillende emissie-lijnen te meten met spectroscopische technieken. Spectroscopische technieken zijn uitdagend, omdat het zwakke licht

van verre sterrenstelsels dat onze telescopen bereikt, verdeeld wordt over honderden golflengten. Hierdoor kunnen meestal alleen de helderste emissielijnen waargenomen worden, zoals emissie-lijnen die worden uitgezonden door (dubbel) geïoniseerd waterstof, helium, zuurstof, stikstof en koolstof, de meest voorkomende elementen in het heelal.

De relatieve sterktes van deze lijnen bevat informatie over het metaalgehalte, de ionisatie-toestand en dichtheid van interstellair gas in sterrenstelsels. Met behulp van deze informatie is het mogelijk om de eigenschappen van sterren, zoals hun temperatuur, te meten. Naast spectroscopie kan de sterkte van emissielijnen ook gemeten worden met behulp van foto's met smalband-filters, die de helderheid meten van het licht op specifieke golflengtes (zie bijvoorbeeld Figuur 9.1, dat laat zien welke emissie-lijnen er met een bepaalde combinatie van smalband-filters waargenomen kunnen worden voor sterrenstelsels die op verschillende afstanden staan). Door verschillende smalband-filters te combineren kunnen relatief veel objecten tegelijkertijd gemeten worden. Een voordeel is ook dat smalband-foto's gebruikt kunnen worden om sterrenstelsels te vinden die enkel licht uitzenden via specifieke golflengtes, en die niet op andere manieren gezien kunnen worden.

De emissie-lijn die het meest wordt bestudeerd in dit proefschrift is de Lyman-α (Lyα) lijn, die uitgezonden wordt wanneer een elektron rondom een waterstofatoom van een geïoniseerde toestand terugvalt naar de grondtoestand. Lyα straling wordt uitgezonden in UV licht met een golflengte van 121.6 nm en is intrinsiek de helderste emissie-lijn waarin sterrenstelsels stralen. Het licht van sterrenstelsels op een roodverschuiving[8] hoger dan $z = 2$ (dit komt overeen met licht dat meer dan 10 miljard jaar geleden is uitgezonden) is door de uitdijing van het heelal roodverschoven naar golflengtes in het zichtbare licht. Dit betekent dat Lyα straling relatief gemakkelijk waar te nemen is voor sterrenstelsels in het vroege heelal. Doordat Lyα straling in sterrenstelsels met veel jonge sterren erg helder is, kunnen verre sterrenstelsels efficiënt herkend worden door te zoeken naar hun Lyα straling met behulp van smalband-filters (veelvuldig gebruikt in dit proefschrift) of spectrografen.

Hoewel de Lyα lijn helder is, is de sterkte lastig te interpreteren. Dat komt doordat Lyα fotonen gemakkelijk door neutraal waterstof, dat op veel plaatsen in het heelal voorkomt, geabsorbeerd worden. Lyα fotonen zijn ook "resonant", wat betekent dat een waterstofatoom dat een Lyα foton absorbeert snel weer een nieuw Lyα foton in een willekeurige richting uitzendt. Als gevolg reizen Lyα fotonen bijna nooit in een rechte lijn tussen de plek waar het foton is uitgezonden

---

[8] Roodverschuiving is in de extragalactische sterrenkunde een maat voor zowel de afstand tot een object als de tijd die het licht erover heeft gedaan om ons te bereiken. Roodverschuiving, z, is gedefinieerd als $z + 1 = \frac{1}{a}$, waarbij a de schaalfactor van het heelal is. Dat betekent dat het heelal 10 keer kleiner was op een roodverschuiving $z = 9$ en twee keer zo klein op een roodverschuiving $z = 1$. Deze schaalfactor kan omgerekend worden naar een kosmologische leeftijd en afstand, afhankelijk van het kosmologische model dat gebruikt wordt. In dit proefschrift gebruik ik het meest gangbare en veruit best geteste vlakke ΛCDM model, waarin de energiedichtheid van het heelal wordt gedomineerd (70 %) door donkere energie en 30 % van de energiedichtheid in materie te vinden is (waarvan het overgrote deel donkere materie). Met deze inputparameters kan de uitdijingsgeschiedenis van het heelal en de relatie tussen roodverschuiving, leeftijd en afstand berekend worden met behulp van de Einstein vergelijking die de zwaartekracht beschrijft.
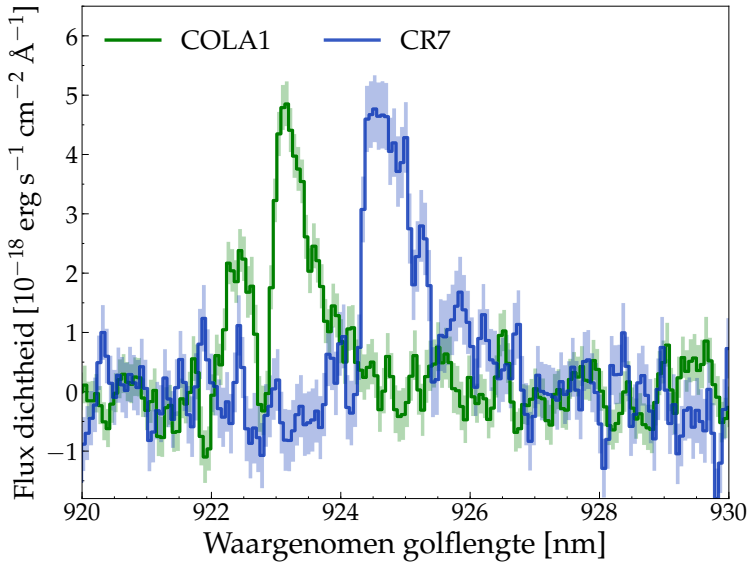
Figure B: De Lyα emissie-lijnen van verre sterrenstelsels CR7 (blauw) en COLA1 (groen), waargenomen in nabij-infrarood licht met het X-SHOOTER instrument op de VLT. De geschaduwde gebieden tonen de meet-onzekerheid per spectraalelement. Beide lijnen tonen een asymmetrische vleugel, de karakteristieke eigenschap voor de Lyα lijn. Aangezien de Lyα lijn op een golflengte van $\lambda = 121.6$ nm uitgezonden wordt, kunnen we meten dat de roodverschuivingen van beide objecten $z = 6.603$ en $z = 6.593$ zijn. Dit betekent dat het licht ongeveer 13 miljard jaar geleden verzonden is. De verschillen tussen de Lyα profielen van CR7 en COLA1 wijzen erop dat er minder neutraal waterstof aanwezig was rondom COLA1, omdat er een tweede piek op iets kortere golflengte zichtbaar is. Neutraal waterstof rondom CR7 heeft deze tweede piek geabsorbeerd.

en onze telescopen, maar hebben ze eerst een chaotisch pad afgelegd, telkens snel van richting veranderend in gebieden met veel neutraal waterstof. Dit proces wordt "resonant scattering" genoemd en zorgt ervoor dat de sterkte van Lyα straling moeilijk te interpreteren is, maar tegelijkertijd biedt dit ook mogelijkheden om iets over het neutraal waterstofgas in en rondom sterrenstelsels te leren (zie Figuur B).

Het reionisatie tijdperk

Ongeveer 300,000 jaar na de oerknal leidde de uitdijing van het heelal ertoe dat de temperatuur laag genoeg was voor waterstof atomen om te combineren met vrije elektronen. Op dit moment werd de kosmologische achtergrondstraling uitgezonden en was het heelal gevuld met donkere materie, neutraal waterstof en wat helium. Onder invloed van zwaartekracht groeiden de plaatsen waar de materie-dichtheid relatief groot was uit tot structuren van donkere materie waarin waterstofmoleculen konden vormen en waarin uiteindelijk de eerste sterren en sterrenstelsels ontstonden.

De geboorte van de eerste generaties sterren leidde tot de eerste verrijking van

het interstellair gas met zware elementen, die de vorming van latere generaties sterren vergemakkelijkte. In deze periode ontstonden ook de eerste supermassieve zwarte gaten, waarvan de hete accretieschijven fel schenen. Als gevolg van het ioniserende licht afkomstig van sterren en zwarte gaten werd het neutraal waterstof wederom geïoniseerd (net als voor het uitzenden van de kosmologische achtergrondstraling). Dit gebeurde ergens in de eerste miljard jaar in de geschiedenis van het heelal en dit tijdperk noemt men het reionisatietijdperk. Het is nog onduidelijk wanneer dit tijdperk precies startte en wanneer de eerste geïoniseerde regio's in het heelal verschenen. Het is ook onduidelijk welke objecten hoofdverantwoordelijk waren voor de ioniserende fotonen. Dit aantal hangt af van de hoeveelheid sterrenstelsels die bijdroegen, de mate waarin sterren ioniserende fotonen produceren en de fractie van ioniserende fotonen die uit sterrenstelsels zelf kan ontsnappen. De grootste onzekerheid is de zogenaamde "escape fractie", omdat het theoretisch lastig uit te rekenen is hoeveel ioniserende fotonen kunnen ontsnappen van de dichte moleculaire wolken waarin sterren geboren worden en hoeveel er uiteindelijk interstellair gas kunnen bereiken.

Aangezien directe metingen van de eigenschappen van neutraal waterstof in het reionisatie tijdperk een belangrijk doel zijn voor toekomstige radio-telescopen zoals de Square Kilometer Array, richten huidige observationele studies zich met name op het meten van de eigenschappen van sterren en sterrenstelsels die in het reionisatie tijdperk leefden. Aangezien de sterkte en het profiel van de Lyα emissie-lijn gevoelig zijn voor de hoeveelheid neutraal waterstof rondom sterrenstelsels, kunnen metingen van Lyα stralers[9] gebruikt worden om de hoeveelheid neutraal waterstof tijdens het reionisatie-tijdperk te meten.

Kosmologische computersimulaties

Grote observationele projecten hebben een aantal belangrijke eigenschappen over de evolutie van sterrenstelsels in het heelal blootgelegd. De populatie sterrenstelsels in het huidige heelal kan onderverdeeld worden in twee groepen: massive, rode elliptische sterrenstelsels die relatief weinig nieuwe sterren vormen en lichtere blauwe spiraalstelsels die nog actief bezig zijn om nieuwe sterren te vormen. De meeste sterrenstelsels vormden vroeger meer sterren dan nu en de kosmologische hoogtijdagen van stervorming vonden plaats toen het heelal ongeveer drie miljard jaar oud was.

Het verklaren van deze eigenschappen is een uitdaging voor complete theoriën over de vorming van sterrenstelsels, omdat complexe fysieke processen plaatsvinden op verschillende grootte- en tijdschalen, die niet analytisch berekend kunnen worden. De belangrijkste uitdaging is dat het door de lange tijdschalen die gepaard gaan met de grootte van sterrenstelsels onmogelijk is om veranderingen waar te nemen. Een voorspelling over hoe een bepaald

---

[9] Lyα stralers (Lyα emitters in het Engels) zijn objecten waarvoor sterke Lyα straling waargenomen wordt. De sterkte van de waargenomen Lyα straling is een combinatie van de hoeveelheid Lyα fotonen die geproduceerd wordt en het aantal dat de waarnemer kan bereiken. Beiden worden in detail bestudeerd in hoofdstukken 7 en 8.

sterrenstelsel zich zal ontwikkelen kan zodoende slecht bevestigd worden. Het is wel mogelijk om te vergelijken hoe de populatie van sterrenstelsels er nu uitziet en hoe die er 3, 7, 10 of zelfs 13 miljard jaar geleden eruit zag. De evolutie van een populatie zegt echter weinig over de evolutie van individuele objecten. Om deze redenen is het zinvol om grote computersimulaties te gebruiken die de evolutie van sterrenstelsels in een kosmologische omgeving (een gesimuleerd universum met dezelfde statistische eigenschappen als het Universum waarin wij leven) realistisch nabootst.
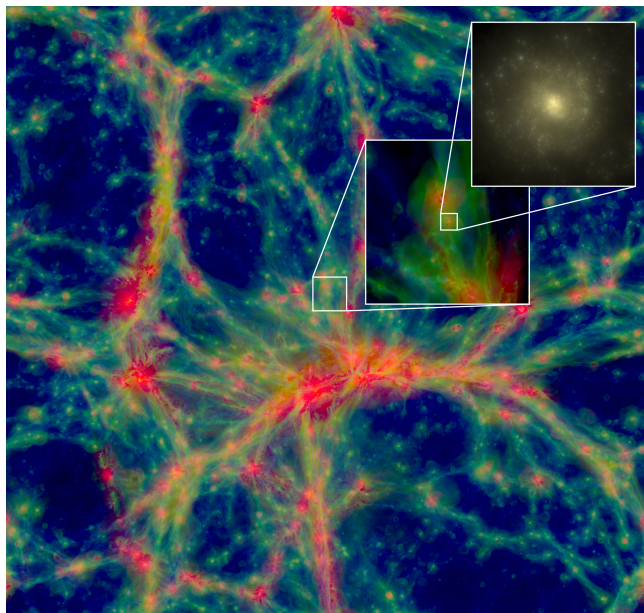
Figure C: De structuur van het heelal op grote schaal gesimuleerd in de EAGLE simulatie (100 x 100 x 20 cMpc, of 330 x 330 x 65 miljoen lichtjaar). De kleur illustreert de temperatuur van het gas, die varieert van 30,000 K (blauw) tot 300,000 K (rood). Sterrenstelsels bevinden zich in de knooppunten van het 'kosmische web'. De ingezoomde panelen laten het sterlicht van een gesimuleerd sterrenstelsel met vergelijkbare eigenschappen als de melkweg (rechtsboven) en het gas in diens directe omgeving (midden) zien. *Deze figuur is ook te vinden als Figuur 1.2 in de introductie en komt uit Schaye et al. (2015).*

Een van de meest succesvolle moderne kosmologische hydrodynamische simulaties is de EAGLE simulatie, dat staat voor "Evolution and Assembly of GaLaxies and their Environments", zie Figuur C. De EAGLE simulatie bevat een realistische populatie sterrenstelsels doordat zij efficiente 'feedback' implementeert die geassocieerd is met de vorming van nieuwe sterren en de groei van supermassieve zwarte gaten in het binnenste van sterrenstelsels. Sterrenstelsels vormen nieuwe sterren door de toevoer van nieuw, afgekoeld gas. Jonge sterren verhitten dit gas door hun ioniserende fotonen. Supernova ontploffingen en stellaire winden aan het eind van de levens van sterren zorgen ervoor dat gas uit sterrenstelsels gedreven wordt. Dit leidt tijdelijk tot een verminderde toevoer van nieuw gas waaruit nieuwe sterren gevormd kunnen worden en is dus een

vorm van feedback. Deze vorm van feedback zorgt ervoor dat er minder lage
massa sterrenstelsels zijn dan simpelweg verwacht wordt op basis van de groei
van donkere materie structuren. In zeer massieve sterrenstelsels leveren jonge
sterren niet meer genoeg energie om gas uit sterrenstelsels te drijven, waardoor
dit gas naar het centrum valt en ervoor zorgt dat supermassieve zwarte gaten
groeien. De hete accretieschijven en de hoog-energetische 'jets' die volgen op
de groei van supermassieve zwarte gaten leiden opnieuw tot galactische winden
die gas uit sterrenstelsels blazen. Uiteindelijk voegt de feedback die geassocieerd
is met de groei van supermassieve zwarte gaten ook energie toe aan het gas, wat
ertoe leidt dat massieve sterrenstelsels weinig nieuwe sterren vormen.

Dit proefschrift

Motivatie

Dit proefschrift is gemotiveerd door achterliggende fundamentele vragen van
de moderne astrofysica.

De eerste vraag, die de motivatie is voor hoofdstukken 2 tot 9, is *hoe ontstaan
sterrenstelsels?* Dit is een complexe vraag die opgesplitst kan worden in ver-
schillende deelvragen. Wanneer zijn de eerste generatie sterren ontstaan en wat
waren hun eigenschappen? Hoe is interstellair gas verrijkt met zware elementen
en hoe heeft dit de vorming van latere generaties van sterren beïnvloedt? Wan-
neer en hoe vond het reionisatie-tijdperk precies plaats en wat was de voor-
naamste oorzaak? Hoe zijn de eerste supermassieve zwarte gaten ontstaan en
wanneer gebeurde dit? Geen van deze vragen is volledig beantwoord in dit
proefschrift, maar het exploratieve karakter van de waarnemingen die in dit
proefschrift beschreven zijn, helpen om meer accurate vragen en hypotheses op
te stellen die getoetst kunnen worden in de toekomst.

De tweede set vragen is gerelateerd aan *hoe ontwikkelen sterrenstelsels zich
en waardoor ontwikkelen sommige sterrenstelsels zich anders dan anderen?* Dit is
de belangrijkste vraag achter hoofdstukken 10, 11 en 12, en deze wordt be-
naderd vanuit theoretisch perspectief. Sterrenstelsels hebben verschillen groot-
ten, kleuren, vormen en omgevingen. Waar komen deze verschillen vandaan?
Hoe kan het dat sterrenstelsels die even zwaar zijn (en dus een vergelijkbaar
zwaartekrachtsveld hebben) zeer verschillende kleuren, groeisnelheden en ster-
populaties kunnen hebben? In hoeverre is de vorming van sterrenstelsels een
chaotisch proces, waarin ogenschijnlijk verwaarloosbare verschillen in de initiële
condities (i.e. dichtheidsverschillen in het vroege heelal) tot grote verschillen
in sterrenstelsels kunnen leiden? Wat is de achterliggende oorzaak van "schal-
ingsrelaties", zoals die tussen de stellaire massa en de groeisnelheid van sterren-
stelsels?

Structuur van deze scriptie

De hoofdstukken in deze scriptie zijn onderverdeeld in drie onderwerpen: i) de
ontdekking, bevestiging en het spectroscopische onderzoek van heldere Lyman-

α stralers in het vroege heelal (hoofdstukken 2-6), ii) het kalibreren van ioniserende en Lyman-α straling van sterrenstelsels (hoofdstukken 7-9) en iii) het uitzoeken van de oorsprong van spreiding in schalingsrelaties van sterrenstelsels in de EAGLE simulatie (hoofdstukken 10-12).

Heldere Lyman-α stralers in het vroege heelal (Hoofdstukken 2-6)

Om sterrenstelsels in het reionisatie-tijdperk te kunnen bestuderen, is het belangrijk eerst een verzameling zeldzame objecten te identificeren die helder genoeg zijn om in detail te bekijken. Dit hebben we gedaan door publieke data-sets van verschillende telescopen te combineren met onze eigen waarnemingen om zo een relatief groot gebied aan de hemel in kaart te brengen. We hebben specifiek gezocht naar Lyα stralers op een roodverschuiving van $z = 6.6$. Dit was in 2014-2015 de grootste data-set die voor dit doeleinde gebruikt werd en daarom geschikt om zeldzame objecten te vinden. Deze zoektocht, beschreven in hoofdstuk 2, onthulde meer extreem heldere Lyα stralers dan verwacht werd op basis van eerdere, kleinere data-sets.

Door hun helderheid was het mogelijk om de afstand tot vier objecten nauwkeurig te meten door middel van gevoelige spectroscopische waarnemingen die beschreven zijn in hoofdstukken 3 en 4 (zie ook Figuur B). Het waargenomen licht is meer dan 12.5 miljard jaar geleden uitgezonden. Dit betekent dat we sterrenstelsels zien die in de eerste miljard jaar van het heelal ontstonden. In hoofdstukken 3 en 4 bespreken we ook de eigenschappen van deze sterrenstelsels die we kunnen meten met hoge resolutie afbeeldingen van de *Hubble Space Telescope* en spectroscopie in het nabije infrarood.

De resultaten in hoofdstukken 4 en 5 laten zien dat heldere Lyα stralers vaak uit meerdere losse componenten bestaan en dat ze bronnen van hete, ioniserende straling bevatten, zoals groepen van jonge, metaal-arme sterren of actieve supermassive zwarte gaten. Het helderste sterrenstelsel dat we gevonden hebben, COSMOS Redshift 7 (CR7) genaamd, bestaat uit drie losse sterpopulaties, omgeven door een grote wolk van neutraal waterstof die door een galactische wind wordt weggedreven (zie Figuur D). Toen we CR7 in 2015 voor het eerst in detail bekeken, wezen de waarnemingen erop dat CR7 zeer jonge sterren bevatte met extreem lage metaal-gehaltes. Daaropvolgende observaties met de ALMA-telescoop in 2017 (hoofdstuk 5) hebben echter aangetoond dat er wel degelijk zware elementen aanwezig zijn in de verschillende componenten van CR7, aangetoond door waarnemingen van koolstof in het interstellair gas. Dit wijst erop dat het gas in CR7 al chemisch verrijkt is door eerdere generaties van sterren. De gegevens van de ALMA-telescoop hebben tegelijkertijd ook twee extra componenten in CR7 onthuld die *HST* niet waar kon nemen (deze componenten bevinden zich ongeveer tussen componenten B en C in Figuur D). De meetgegevens van ALMA wijzen erop dat we getuige zijn van het ontstaan van een massief sterrenstelsel in het vroege heelal doordat verschillende kleinere sterrenstelsels fuseren.
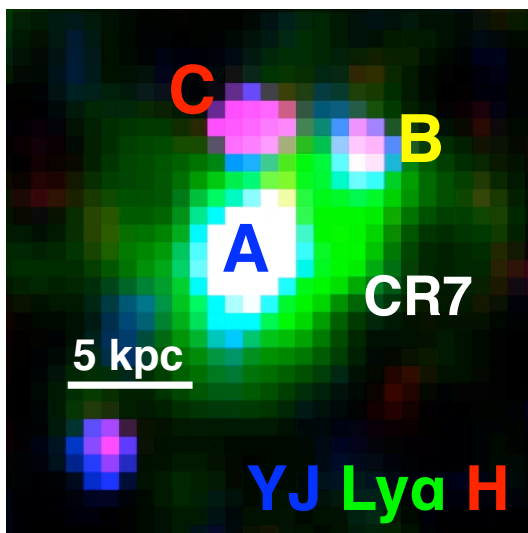
Figure D: Een valse-kleur compositie van CR7 op basis van foto's gemaakt met de NB921 filter op Subaru/Suprime-cam (Lyα straling, groen) en foto's met de F110W (*YJ*) en F160W (*H*) filters op *HST*/WFC3 (UV straling, rood en blauw). Deze Figuur laat zien dat de helderste en meest blauwe component A samenvalt met de piek van de Lyα straling. Tegelijkertijd spreidt Lyα straling zich ook uit naar (met name) component B, hetgeen zou kunnen wijzen op 'resonant scattering'. De verspreiding van Lyα straling wijst erop dat de drie componenten van CR7 omgeven zijn door een wolk neutraal waterstof. Hoewel de kleuren van componenten B en C onzeker zijn, wijzen ze erop dat component A het blauwst is (en daarom het jongst). De afstand tussen de verschillende componenten is ongeveer 5 kpc (16 duizend lichtjaar), ongeveer een zesde van de diameter van de huidige Melkweg. *Deze figuur is ook te vinden als Figuur 4.7 in hoofdstuk 4.*

Hoofdstuk 6 presenteert de eigenschappen van een ander eigenaardig, extreem helder sterrenstelsel dat zich relatief in de buurt van CR7 bevindt, COLA1 genaamd (Hu et al. 2016). Het complexe dubbel gepiekte Lyα profiel (weergegeven in Figuur B) van dit sterrenstelsel lijkt heel erg op de Lyα profielen die pas veel later in de geschiedenis van het heelal ontstaan. Het profiel wijst erop dat dit sterrenstelsel omgeven wordt door een grote regio van geïoniseerd waterstof waarin nauwelijks neutraal waterstof aanwezig is, iets dat voorheen onmogelijk geacht werd op de roodverschuiving waarop COLA1 waargenomen wordt. Dit sterrenstelsel is daardoor het eerste object dat direct bewijs levert dat het neutrale waterstofgas rondom sterrenstelsels geïoniseerd wordt door sterren in deze sterrenstelsels, en dat de eerste generaties sterren een belangrijke bijdrage hadden in het reionisatie-tijdperk.

Kalibratie van ioniserende en Lyman-α straling (Hoofdstukken 7-9)

Op dit moment zijn spectroscopische waarnemingen van sterrenstelsels in het vroege heelal ($z > 3$, de eerste 3 miljard jaar) vaak gelimiteerd tot de Lyα emissielijn, waarvan de helderheid lastig te interpreteren is omdat de escape fractie (het percentage van het geproduceerde Lyα licht dat uit sterrenstelsels ontsnapt) onbekend is. Bovendien is de gerelateerde Lyman-Continuum escape fractie

(het aantal ioniserende fotonen dat uit sterrenstelsels ontsnapt) een belangrijke eigenschap van sterrenstelsels om te beoordelen wat hun contributie is tot het reionisatie-budget. Beide escape fracties zijn extreem lastig te meten in de eerste 3 miljard jaar, doordat Lyα straling en ioniserende fotonen op hun weg tussen sterrenstelsels en onze telescopen geabsorbeerd worden door tussenliggend gas en doordat het lastig is de intrinsieke helderden nauwkeurig te bepalen. Het is daarom belangrijk om kalibraties te vinden tussen de escape fracties en andere eigenschappen van sterrenstelsels die wel eenvoudig gemeten kunnen worden.

Om dit te doen hebben we een project ontworpen dat zowel ioniserende fotonen, Lyα straling en Hα straling kan meten voor sterrenstelsels op een afstand van $z = 2.2$, het tijdperk waarop de stervormingsgeschiedenis in het heelal op haar hoogtepunt was. De sterkte van Hα straling is direct gerelateerd aan het aantal ioniserende fotonen dat een sterrenstelsel produceert en kan daarom gebruikt worden om de intrinsieke Lyα en Lyman-Continuum helderheid te meten, die vervolgens gebruikt wordt om de escape fractie te meten. Deze metingen gebruiken een specifieke combinatie van smalband filters, die speciaal voor dit project ontworpen zijn (zie hoofdstukken 7 en 9). De UV metingen zijn gedaan met behulp van de *GALEX* satelliet en zijn beschreven in hoofdstuk 8.

Deze hoofdstukken laten zien dat er individuele objecten bestaan met zeer hoge escape fracties (met name Lyα escape fracties). De gemiddelde escape fracties zijn echter erg laag, gemiddeld rond de 2 %. We vinden dat de Lyα escape fractie anti-correlateert met de massa en groeisnelheid van sterrenstelsels en dat de escape fractie hoger is voor sterrenstelsels waarin minder stof aanwezig is. Hoofdstuk 7 laat bovendien zien dat het merendeel van de Lyα fotonen op grote afstanden van sterrenstelsels ontsnapt door 'resonant scattering' in neutraal waterstof dat zich rondom sterrenstelsels bevindt. In hoofdstuk 8 presenteren we een voorspelling dat de efficiëntie waarmee sterrenstelsels ioniserende fotonen produceren hoger was in het vroege heelal, hetgeen de bijdrage van vroege sterrenstelsels tot het reionisatie-budget vergroot.

Spreiding in schalingsrelaties van sterrenstelsels (Hoofdstukken 10-12)

Grote waarneemprojecten hebben laten zien dat sterrenstelsels zich aan relatief nauwe schalingsrelaties houden, zoals de relatie tussen de stellaire massa en de metalliciteit en de relatie tussen stellaire massa en groeisnelheid.Volgens deze relaties kunnen de groeisnelheid en metalliciteit binnen een factor twee nauwkeurig geschat worden op basis van enkel de stellaire massa. Het is echter onduidelijk wat de oorsprong is van deze relaties.

Om schalingsrelaties beter te begrijpen, hebben we gekeken naar welke fysische processen er juist voor zorgen dat sterrenstelsels van schalingsrelaties af worden gedreven. Dit hebben we gedaan door te kijken naar de eigenschappen van gesimuleerde sterrenstelsels in de EAGLE simulatie.

In hoofdstuk 10 hebben we onderzocht welke eigenschap van donkere materie structuren het rendement van de vorming van sterren in sterrenstelsels beïnvloedt. Sterrenstelsels met een relatief grote stellaire massa (voor hun
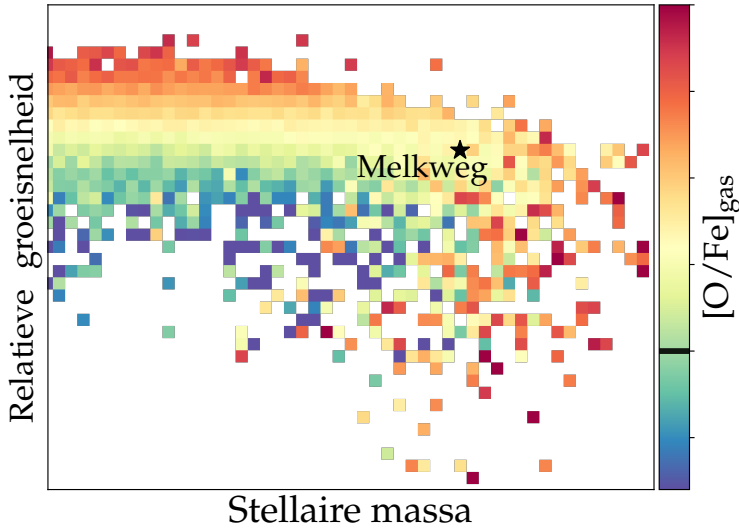
Figure E: De relatie tussen de relatieve groeisnelheid (de groeisnelheid gedeeld door de huidige stellaire massa) en huidige stellaire massa van sterrenstelsels in het hedendaagse heelal in de EAGLE simulatie. De kleur van elk vak toont de gemiddelde massa-fractie van zuurstof en ijzer in het interstellair gas waaruit nieuwe sterren ontstaan. De zuurstof/ijzer ratio in de zon is met een zwarte lijn in de kleurenbalk aangegeven. Deze figuur laat zien dat de sterren die nu gevormd worden in sterrenstelsels met een hoge massa (rechtsonder) of een relatief hoge groeisnelheid (linksboven) relatief veel zuurstof hebben in vergelijking met ijzer. De huidige massa en groeisnelheid van de Melkweg is aangegeven met een zwarte ster. *Deze figuur is ook te vinden als Figuur 12.3 in hoofdstuk 12.*

donkere materie massa) hadden een hoog rendement, terwijl sterrenstelsels met een laag rendement een relatief lage stellaire massa hadden. Om achter de oorzaak van verschil in rendementen te komen, hebben we het stervormingsrendement gecorreleerd met eigenschappen van 'sterrenstelsels' in een simulatie waarin enkel donkere materie aanwezig is. Deze simulatie heeft precies dezelfde initiële condities als de EAGLE simulatie (het is dus een simulatie van hetzelfde universum), maar er vindt geen stervorming plaats. Dit is noodzakelijk om oorzaak en gevolg te kunnen scheiden en te kunnen onderzoeken welke verschillen in donkere materie eigenschappen leiden tot verschillen in stellaire massa.

We vinden dat het stervormingsrendement sterk afhankelijk is van de massaverdeling van de donkere materie structuur en het tijdstip waarop de structuur gevormd is. Dit betekent dat zowel de massa van donkere materie als de verdeling van die massa (en dus de bindingsenergie) de meest fundamentele eigenschap is die de stellaire massa van sterrenstelsels bepaalt. We vinden echter ook dat een groot deel van de spreiding niet verklaard kan worden door eigenschappen van de "dark matter only" simulatie. Dit wijst erop dat de vorming van sterrenstelsels deels een chaotisch proces is.

De stellaire massa die een sterrenstelsel heeft in het hedendaagse heelal is het resultaat van een groei die 13.7 miljard jaar duurde. Dit zegt echter niet

direct iets over de mate waarin sterrenstelsels nu nieuwe sterren produceren (de groeisnelheid). In hoofdstuk 11 focussen we daarom op de spreiding in de relatie tussen de huidige stellaire massa van sterrenstelsels en hun groeisnelheid. We onderzoeken in dit hoofdstuk ook hoe de groei-geschiedenissen van sterrenstelsels verschillen. Hoewel de groeisnelheid van sterrenstelsels sterk varieert (met een factor $\approx$ 2) op relatief korte tijdschalen, is er een mate van coherentie tussen de huidige groeisnelheid en de historie van een sterrenstelsel, veroorzaakt door verschillen in formatie tijd van donkere materie structuren. Sterrenstelsels die op dit moment een relatief hogere groeisnelheid hebben (in vergelijking met sterrenstelsels met eenzelfde stellaire massa), hebben een grotere kans dat ze in de afgelopen $\sim$ 7 miljard jaar ook een relatief hogere groeisnelheid hebben gehad en vice versa.

Coherente groeisnelheden hebben gevolgen voor de chemische evolutie van sterrenstelsels doordat verschillende elementen op verschillende tijdschalen geproduceerd worden. In hoofdstuk 12 bekijken we met name hoe de verhouding tussen zuurstof (en andere zogenaamde α-elementen, waaronder ook magnesium en calcium) en ijzer verschilt per sterrenstelsel. Zuurstof wordt uitsluitend geproduceerd in de supernova explosies van sterren zwaarder dan acht zonsmassa's, terwijl ijzer ook een contributie heeft van sterren met lagere massa (in het bijzonder van type Ia supernovae die ontstaan in dubbelsterren). Aangezien massieve sterren relatief kort leven, wordt interstellair gas op relatief korte tijdschaal verrijkt met zuurstof. IJzer wordt deels geproduceerd door sterren die lang leven, waardoor de verrijking van ijzer langer duurt.

Sterrenstelsels die op dit moment relatief snel groeien, hebben dit ook in het verleden gedaan. Daardoor zijn ze in een relatief korter tijdsbestek gevormd in vergeleken met sterrenstelsels met een langzamere groeisnelheid. Hierdoor bevatten sterrenstelsels die snel groeien relatief weinig ijzer in vergelijking met zuurstof. Sterrenstelsels die relatief langzaam groeien bevatten juist relatief veel ijzer en hebben als gevolg een lage α-verrijking. Dit is weergeven in Figuur E. We voorspellen daarom dat sterrenstelsels in het huidige heelal op een nauwe drie dimensionale schalingsrelatie liggen tussen stellaire massa, groeisnelheid en α-verrijking. Deze relatie heeft belangrijke gevolgen voor de interpretatie van waarnemingen van sterrenstelsels. Terwijl zuurstof het eenvoudigst te meten is in het gas van verre sterrenstelsels, is het ijzer-gehalte het belangrijkst in het bepalen van de eigenschappen van sterren. Systematische variaties in de zuurstof-tot-ijzer ratio kunnen daarom tot belangrijke onzekerheden leiden. Het is daarom belangrijk om deze relatie te toetsen met toekomstige waarnemingen.

Conclusie & Vooruitblik

Tenslotte blikken we terug op wat we geleerd hebben en werpen we een blik vooruit naar wat er nog gedaan kan worden. In dit proefschrift hebben we een aantal zeldzame heldere sterrenstelsels gevonden die op extreem verre afstanden staan. Hierdoor zien we deze verre sterrenstelsels terwijl het heelal nog jong was en kunnen we metingen doen aan hoe de eerste sterren en sterrenstelsels ontstonden. Hoewel er al indicaties zijn dat de sterren die in deze

sterrenstelsels leefden groter, zwaarder en heter waren dan de sterren die we nu om ons heen zien, zijn hun precieze eigenschappen nog onduidelijk. De eigenschappen van sterren in deze sterrenstelsels zullen met toekomstige telescopen in detail bestudeerd kunnen worden, met name de *Extremely Large Telescope* die nu in Chili gebouwd wordt en de *James Webb Space Telescope* die binnen enkele jaren gelanceerd zal worden. Deze telescopen zullen ook onthullen of er zwarte gaten aanwezig zijn in deze jonge sterrenstelsels, en zo ja, hoe massief deze waren. Met behulp van de ALMA telescoop hebben we gezien dat sterrenstelsels ontstonden doordat verschillende kleinere sterrenstelsels samenklonterden in een redelijk chaotisch proces. De metingen met ALMA toonden ook aan dat er koolstof aanwezig was in het CR7 sterrenstelsel. Dit koolstof moet dus redelijk snel in de geschiedenis van het heelal zijn geproduceerd. In de toekomst is het belangrijk te meten in welke mate andere elementen als zuurstof, stikstof en ijzer in CR7 en andere sterrenstelsels aanwezig waren. Deze informatie kan gebruikt worden om de eigenschappen van de sterren die deze elementen geproduceerd hebben te berekenen.

Ik zal mij ook richten op gedetailleerde waarnemingen van sterrenstelsels die iets dichterbij staan, omdat hiervoor niet per se nieuwe telescopen nodig zijn. Dit zijn sterrenstelsels die we gevonden hebben met de *Isaac Newton Telescope* op La Palma. Hoewel deze sterrenstelsels erg lijken op de allereerste sterrenstelsels die in het heelal ontstonden, zien we deze sterrenstelsels terwijl het heelal al drie miljard jaar oud was. Met behulp van de *Very Large Telescope* is het mogelijk om te meten in hoeverre elementen als koolstof, zuurstof en stikstof aanwezig zijn in deze sterrenstelsels en wat voor soort sterren hiervoor verantwoordelijk waren.

Een ander onderdeel van dit proefschrift was de studie van de eigenschappen van sterrenstelsels in geavanceerde computersimulaties. We hebben gevonden dat een deel van de verschillen in sterrenstelsels terug te voeren zijn tot het tijdstip waarop sterrenstelsels begonnen te vormen, die weer teruggeleid kan worden tot de initiële condities in het zeer vroege heelal. Het is niet eenvoudig om de formatietijd te meten, maar met behulp van de simulatie heb ik wel een aantal gerelateerde voorspellingen kunnen doen die uit de resultaten volgden. Een van die voorspellingen is dat de huidige groeisnelheid van sterrenstelsels afhangt van de groei-geschiedenis en van de α-verrijking. Dit kan in de toekomst getest worden door de groei-geschiedenis van sterrenstelsels te reconstrueren en door de α-verrijking te meten. Dit kan zeker gedaan worden met behulp van gegevens van sterrenstelsels die andere internationale teams nu vergaren. Het is misschien zelfs al mogelijk om dit met huidige, publiek beschikbare data te doen. Op dit moment onderzoek ik of er ook connecties zijn tussen de formatietijd en de groei van supermassieve zwarte gaten. In de toekomst ga ik mij met name richten op het testen van voorspellingen omtrent de correlatie tussen de huidige groeisnelheid en de α-verrijking van sterrenstelsels.

Bibliography

Abadi M. G., Moore B., Bower R. G., 1999, MNRAS, 308, 947

Abazajian K. N., et al., 2009, ApJS, 182, 543

Abramson L. E., Gladders M. D., Dressler A., Oemler Jr. A., Poggianti B., Vulcani B., 2015, ApJL, 801, L12

Abramson L. E., Gladders M. D., Dressler A., Oemler Jr. A., Poggianti B., Vulcani B., 2016, ApJ, 832, 7

Adams T. F., 1972, ApJ, 174, 439

Agarwal B., Davis A. J., Khochfar S., Natarajan P., Dunlop J. S., 2013, MNRAS, 432, 3438

Agarwal B., Johnson J. L., Zackrisson E., Labbe I., van den Bosch F. C., Natarajan P., Khochfar S., 2016, MNRAS, 460, 4003

Agarwal B., Johnson J. L., Khochfar S., Pellegrini E., Rydberg C.-E., Klessen R. S., Oesch P., 2017, MNRAS, 469, 231

Ahn S.-H., Lee H.-W., Lee H. M., 2001, ApJ, 554, 604

Ajiki M., Mobasher B., Taniguchi Y., Shioya Y., Nagao T., Murayama T., Sasaki S. S., 2006, ApJ, 638, 596

Alam S., et al., 2015, ApJS, 219, 12

Alexandroff R., et al., 2013, MNRAS, 435, 3306

Alexandroff R. M., Heckman T. M., Borthakur S., Overzier R., Leitherer C., 2015, ApJ, 810, 104

Amorín R., et al., 2015, A&A, 578, A105

Amorín R., et al., 2017, Nature Astronomy, 1, 0052

An F. X., Zheng X. Z., Hao C.-N., Huang J.-S., Xia X.-Y., 2017, ApJ, 835, 116

Ando M., Ohta K., Iwata I., Akiyama M., Aoki K., Tamura N., 2006, ApJL, 645, L9

Andrews B. H., Martini P., 2013a, ApJ, 765, 140

Andrews B. H., Martini P., 2013b, ApJ, 765, 140

Ao Y., et al., 2015, A&A, 581, A132

Appenzeller I., Fricke K., Fürtig W., et al., 1998, The Messenger, 94, 1

Aravena M., et al., 2016, ApJ, 833, 71

Arrigoni Battaia F., Hennawi J. F., Cantalupo S., Prochaska J. X., 2016, ApJ, 829, 3

Ashby M. L. N., et al., 2009, ApJ, 701, 428

Asplund M., Grevesse N., Sauval A. J., Scott P., 2009, ARAA, 47, 481

Astropy Collaboration et al., 2013a, A&A, 558, A33

Astropy Collaboration et al., 2013b, A&A, 558, A33

Atek H., Kunth D., Hayes M., Östlin G., Mas-Hesse J. M., 2008, A&A, 488, 491

Atek H., Kunth D., Schaerer D., Mas-Hesse J. M., Hayes M., Östlin G., Kneib J.-P., 2014, A&A, 561, A89

Atek H., et al., 2015, ApJ, 800, 18

Avila-Reese V., Firmani C., Klypin A., Kravtsov A. V., 1999, MNRAS, 310, 527

Bañados E., et al., 2016, ApJS, 227, 11

Bañados E., et al., 2018, Nature, 553, 473

Bacon R., et al., 2015, A&A, 575, A75

Bacon R., et al., 2017, A&A, 608, A1

Bagley M. B., et al., 2017, ApJ, 837, 11

Bahé Y. M., et al., 2016, MNRAS, 456, 1115

Bahé Y. M., Schaye J., Crain R. A., McCarthy I. G., Bower R. G., Theuns T., McGee S. L., Trayford J. W., 2017, MNRAS, 464, 508

Baldry I. K., Driver S. P., Loveday J., Taylor E. N., Kelvin L. S., Liske J., Norberg P., Robotham A. S. G. e. a., 2012, MNRAS, 421, 621

Baldwin J. A., Phillips M. M., Terlevich R., 1981a, PASP, 93, 5

Baldwin J. A., Phillips M. M., Terlevich R., 1981b, PASP, 93, 5

Barisic I., et al., 2017, ApJ, 845, 41

Beare R., Brown M. J. I., Pimbblet K., Bian F., Lin Y.-T., 2015, ApJ, 815, 94

Becker G. D., Bolton J. S., 2013, MNRAS, 436, 1023

Becker G. D., Bolton J. S., Madau P., Pettini M., Ryan-Weber E. V., Venemans B. P., 2015, MNRAS, 447, 3402

Behroozi P. S., Conroy C., Wechsler R. H., 2010, ApJ, 717, 379

Behroozi P. S., Wechsler R. H., Conroy C., 2013a, ApJl, 762, L31

Behroozi P. S., Wechsler R. H., Conroy C., 2013b, ApJ, 770, 57

Bell E. F., et al., 2004, ApJ, 608, 752

Benitez N., et al., 2014, arXiv:1403.5237

Bennett C. L., et al., 2013, ApJS, 208, 20

Benson A. J., 2010, Physrep, 495, 33

Bergvall N., Zackrisson E., Andersson B.-G., Arnberg D., Masegosa J., Östlin G., 2006, A&A, 448, 513

Bergvall N., Leitet E., Zackrisson E., Marquart T., 2013, A&A, 554, A38

Berlind A. A., Weinberg D. H., 2002, ApJ, 575, 587

Bertin E., 2006, in Gabriel C., Arviset C., Ponz D., Enrique S., eds, Astronomical Society of the Pacific Conference Series Vol. 351, Astronomical Data Analysis Software and Systems XV. p. 112

Bertin E., 2010, SWarp, Astrophysics Source Code Library

Bertin E., Arnouts S., 1996, A&A, 117, 393

Best P. N., Kauffmann G., Heckman T. M., Brinchmann J., Charlot S., Ivezić Ž., White S. D. M., 2005, MNRAS, 362, 25

Best P., et al., 2013, Astrophysics and Space Science Proceedings, 37, 235

Bett P., Eke V., Frenk C. S., Jenkins A., Helly J., Navarro J., 2007, MNRAS, 376, 215

Bian F., et al., 2012, ApJ, 757, 139

Bian F., et al., 2013, ApJ, 774, 28

Bielby R. M., et al., 2016, MNRAS, 456, 4061

Bik A., Östlin G., Hayes M., Adamo A., Melinder J., Amram P., 2015, A&A, 576, L13

Blain A. W., Kneib J.-P., Ivison R. J., Smail I., 1999, ApJL, 512, L87

Blanc G. A., et al., 2011, ApJ, 736, 31

Blanton M. R., Berlind A. A., 2007, ApJ, 664, 791

Blanton M. R., Geha M., West A. A., 2008, ApJ, 682, 861

Bluck A. F. L., et al., 2016, MNRAS, 462, 2559

Blumenthal G. R., Faber S. M., Primack J. R., Rees M. J., 1984, Nature, 311, 517

Blumenthal G. R., Faber S. M., Flores R., Primack J. R., 1986, ApJ, 301, 27

Bohlin R. C., 2016, AJ, 152, 60

Bolton J. S., Haehnelt M. G., 2013, MNRAS, 429, 1695

Bolzonella M., Miralles J.-M., Pelló R., 2000, A&A, 363, 476

Bongiorno A., et al., 2007, A&A, 472, 443

Bongiorno A., et al., 2010, A&A, 510, A56

Booth C. M., Schaye J., 2009, MNRAS, 398, 53

Booth C. M., Schaye J., 2010, MNRAS, 405, L1

Booth C. M., Schaye J., 2011, MNRAS, 413, 1158

Boquien M., Buat V., Perret V., 2014, A&A, 571, A72

Borthakur S., Heckman T. M., Leitherer C., Overzier R. A., 2014, Science, 346, 216

Bosman S. E. I., Fan X., Jiang L., Reed S., Matsuoka Y., Becker G., Haehnelt M., 2018, MNRAS, 479, 1055

Bothwell M. S., Maiolino R., Kennicutt R., Cresci G., Mannucci F., Marconi A., Cicone C., 2013, MNRAS, 433, 1425

Boutsia K., et al., 2011, ApJ, 736, 41

Bouwens R. J., et al., 2011, Nature, 469, 504

Bouwens R. J., et al., 2012, ApJ, 754, 83

Bouwens R. J., et al., 2014, ApJ, 793, 115

Bouwens R. J., et al., 2015a, ApJ, 803, 34

Bouwens R. J., Illingworth G. D., Oesch P. A., Caruana J., Holwerda B., Smit R., Wilkins S., 2015b, ApJ, 811, 140

Bouwens R. J., Smit R., Labbé I., Franx M., Caruana J., Oesch P., Stefanon M., Rasappu N., 2016, ApJ, 831, 176

Bouwens R. J., van Dokkum P. G., Illingworth G. D., Oesch P. A., Maseda M., Ribeiro B., Stefanon M., Lam D., 2017, preprint

Bower R. G., McCarthy I. G., Benson A. J., 2008, MNRAS, 390, 1399

Bower R. G., Schaye J., Frenk C. S., Theuns T., Schaller M., Crain R. A., McAlpine S., 2017, MNRAS, 465, 32

Bowler R. A. A., et al., 2012, MNRAS, 426, 2772

Bowler R. A. A., et al., 2014, MNRAS, 440, 2810

Bowler R. A. A., et al., 2017a, MNRAS, 466, 3612

Bowler R. A. A., McLure R. J., Dunlop J. S., McLeod D. J., Stanway E. R., Eldridge J. J., Jarvis M. J., 2017b, MNRAS, 469, 448

Bradač M., et al., 2017, ApJL, 836, L2

Bradshaw E. J., et al., 2013, MNRAS, 433, 194

Brammer G. B., van Dokkum P. G., Coppi P., 2008, ApJ, 686, 1503

Bridge C. R., et al., 2010, ApJ, 720, 465

Brinchmann J., Charlot S., White S. D. M., Tremonti C., Kauffmann G., Heckman T., Brinkmann J., 2004, MNRAS, 351, 1151

Brinchmann J., Kunth D., Durret F., 2008, A&A, 485, 657

Brown T., Cortese L., Catinella B., Kilborn V., 2018, MNRAS, 473, 1868

Bruzual G., Charlot S., 2003, MNRAS, 344, 1000

Bryan S. E., Kay S. T., Duffy A. R., Schaye J., Dalla Vecchia C., Booth C. M., 2013, MNRAS, 429, 3316

Buat V., et al., 2015, A&A, 577, A141

Bullock J. S., Kolatt T. S., Sigad Y., Somerville R. S., Kravtsov A. V., Klypin A. A., Primack J. R., Dekel A., 2001, MNRAS, 321, 559

Bunker A. J., Warren S. J., Hewett P. C., Clements D. L., 1995, MNRAS, 273, 513

Burgarella D., Buat V., Iglesias-Páramo J., 2005, MNRAS, 360, 1413

Burkert A., et al., 2010, ApJ, 725, 2324

Cai Z., et al., 2011, ApJL, 736, L28

Cai Z., Fan X., Jiang L., Davé R., Oh S. P., Yang Y., Zabludoff A., 2015, ApJL, 799, L19

Calhau J., Sobral D., Stroe A., Best P., Smail I., Lehmer B., Harrison C., Thomson A., 2017, MNRAS, 464, 303

Calzetti D., Armus L., Bohlin R. C., Kinney A. L., Koornneef J., Storchi-Bergmann T., 2000, ApJ, 533, 682

Caminha G. B., et al., 2016, A&A, 595, A100

Cantalupo S., Arrigoni-Battaia F., Prochaska J. X., Hennawi J. F., Madau P., 2014, Nature, 506, 63

Capak P., et al., 2007, ApJS, 172, 99

Capak P. L., et al., 2015, Nature, 522, 455

Cardamone C., et al., 2009, MNRAS, 399, 1191

Carilli C. L., Walter F., 2013, ARAA, 51, 105

Carniani S., et al., 2017, A&A, 605, A42

Carniani S., et al., 2018, MNRAS, 478, 1170

Carroll S. M., 2001, Living Reviews in Relativity, 4, 1

Caruana J., Bunker A. J., Wilkins S. M., Stanway E. R., Lorenzoni S., Jarvis M. J., Ebert H., 2014, MNRAS, 443, 2831

Casali M., et al., 2007, A&A, 467, 777

Cassata P., et al., 2013, A&A, 556, A68

Cassata P., et al., 2015, A&A, 573, A24

Castellano M., et al., 2016, A&A, 590, A31

Cen R., Haiman Z., 2000, ApJL, 542, L75

Cen R., Kimm T., 2014, ApJ, 782, 32

Cen R., Kimm T., 2015, ApJL, 801, L25

Ceverino D., Dekel A., Bournaud F., 2010, MNRAS, 404, 2151

Chabrier G., 2003, PASP, 115, 763

Chang Y.-Y., van der Wel A., da Cunha E., Rix H.-W., 2015, ApJS, 219, 8

Charlot S., Fall S. M., 1993, ApJ, 415, 580

Chauke P., et al., 2018, arXiv:1805.02568

Chaves-Montero J., Angulo R. E., Schaye J., Schaller M., Crain R. A., Furlong M., Theuns T., 2016, MNRAS, 460, 3100

Chen H.-W., Prochaska J. X., Gnedin N. Y., 2007, ApJL, 667, L125

Choudhury T. R., Puchwein E., Haehnelt M. G., Bolton J. S., 2015, MNRAS, 452, 261

Ciardullo R., et al., 2014, ApJ, 796, 64

Cirasuolo M., et al., 2007, MNRAS, 380, 585

Civano F., et al., 2012, ApJS, 201, 30

Clément B., et al., 2012, A&A, 538, A66

Cleveland W. S., 1979, Journal of the American Statistical Association, 74, 829

Cleveland W., Grosse E., Shyu W., 1992, Local regression models. Technical Report, Bell Labs

Coil A. L., Mendez A. J., Eisenstein D. J., Moustakas J., 2017, ApJ, 838, 87

Colbert J. W., et al., 2013, ApJ, 779, 34

Cole S., Lacey C., 1996, MNRAS, 281, 716

Conroy C., 2013, ARAA, 51, 393

Conroy C., Wechsler R. H., Kravtsov A. V., 2006, ApJ, 647, 201

Conroy C., Graves G. J., van Dokkum P. G., 2014, ApJ, 780, 33

Conseil S., Vibert D., Amouts S., Milliard B., Zamojski M., Liebaria A., Guillaume M., 2011, in Evans I. N., Accomazzi A., Mink D. J., Rots A. H., eds, Vol. 442, Astronomical Data Analysis Software and Systems XX. p. 107

Cooke J., Ryan-Weber E. V., Garel T., Díaz C. G., 2014, MNRAS, 441, 837

Cooper M. C., Newman J. A., Davis M., Finkbeiner D. P., Gerke B. F., 2012, ASCL

Correa C. A., Wyithe J. S. B., Schaye J., Duffy A. R., 2015a, MNRAS, 450, 1514

Correa C. A., Wyithe J. S. B., Schaye J., Duffy A. R., 2015b, MNRAS, 450, 1521

Cowie L. L., Hu E. M., 1998, AJ, 115, 1319

Cowie L. L., Songaila A., Hu E. M., Cohen J. G., 1996, AJ, 112, 839

Cowie L. L., Barger A. J., Trouille L., 2009, ApJ, 692, 1476

Cowie L. L., Barger A. J., Hu E. M., 2010, ApJ, 711, 928

Crain R. A., et al., 2015, MNRAS, 450, 1937

Cristiani S., Serrano L. M., Fontanot F., Vanzella E., Monaco P., 2016, MNRAS, 462, 2478

Croton D. J., et al., 2006, MNRAS, 365, 11

Cuby J.-G., Le Fèvre O., McCracken H., Cuillandre J.-C., Magnier E., Meneux B., 2003, A&A, 405, L19

Cuby J.-G., Hibon P., Lidman C., Le Fèvre O., Gilmozzi R., Moorwood A., van der Werf P., 2007, A&A, 461, 911

Curtis H. D., 1917, PASP, 29, 206

Curtis-Lake E., et al., 2012, MNRAS, 422, 1425

Curtis-Lake E., et al., 2016, MNRAS, 457, 440

Daddi E., Cimatti A., Renzini A., Fontana A., Mignoli M., Pozzetti L., Tozzi P., Zamorani G., 2004, ApJ, 617, 746

Dalal N., White M., Bond J. R., Shirokov A., 2008, ApJ, 687, 12

Dalla Vecchia C., 2017, in prep

Dalla Vecchia C., Schaye J., 2012, MNRAS, 426, 140

Darvish B., Mobasher B., Sobral D., Scoville N., Aragon-Calvo M., 2015, ApJ, 805, 121

Davé R., Oppenheimer B. D., Finlator K., 2011, MNRAS, 415, 11

Davé R., Finlator K., Oppenheimer B. D., 2012, MNRAS, 421, 98

Davies F. B., Becker G. D., Furlanetto S. R., 2018, ApJ, 860, 155

Davis M., Efstathiou G., Frenk C. S., White S. D. M., 1985, ApJ, 292, 371

Dawson S., Rhoads J. E., Malhotra S., Stern D., Wang J., Dey A., Spinrad H., Jannuzi B. T., 2007, ApJ, 671, 1227

Dayal P., Ferrara A., 2012, MNRAS, 421, 2568

De Barros S., et al., 2016, A&A, 585, A51

De Breuck C., Röttgering H., Miley G., van Breugel W., Best P., 2000, A&A, 362, 519

De Looze I., et al., 2014, A&A, 568, A62

De Lucia G., Springel V., White S. D. M., Croton D., Kauffmann G., 2006, MNRAS, 366, 499

De Rossi M. E., Bower R. G., Font A. S., Schaye J., Theuns T., 2017, MNRAS, 472, 3354

Decarli R., et al., 2017, Nature, 545, 457

Decataldo D., Ferrara A., Pallottini A., Gallerani S., Vallini L., 2017, MNRAS, 471, 4476

Deharveng J.-M., Buat V., Le Brun V., Milliard B., Kunth D., Shull J. M., Gry C., 2001, A&A, 375, 805

Deharveng J.-M., et al., 2008, ApJ, 680, 1072

Desmond H., Wechsler R. H., 2015, MNRAS, 454, 322

Dey A., Lee K.-S., Reddy N., Cooper M., Inami H., Hong S., Gonzalez A. H., Jannuzi B. T., 2016, ApJ, 823, 11

Diemer B., More S., Kravtsov A. V., 2013, ApJ, 766, 25

Dijkstra M., 2014, PASA, 31, 40

Dijkstra M., 2017, Lecture notes, arXiv:1704.03416

Dijkstra M., Kramer R., 2012, MNRAS, 424, 1672

Dijkstra M., Lidz A., Wyithe J. S. B., 2007, MNRAS, 377, 1175

Dijkstra M., Mesinger A., Wyithe J. S. B., 2011, MNRAS, 414, 2139

Dijkstra M., Wyithe S., Haiman Z., Mesinger A., Pentericci L., 2014, MNRAS, 440, 3309

Dijkstra M., Gronke M., Sobral D., 2016a, ApJ, 823, 74

Dijkstra M., Gronke M., Venkatesan A., 2016b, ApJ, 828, 71

Ding J., et al., 2017, ApJL, 838, L22

Dolag K., Borgani S., Schindler S., Diaferio A., Bykov A. M., 2008, SSR, 134, 229

Domínguez A., et al., 2013, ApJ, 763, 145

Drake A. B., et al., 2013, MNRAS, 433, 796

Dressler A., 1980, ApJ, 236, 351

Dressler A., et al., 2016, ApJ, 833, 251

Duffy A. R., Schaye J., Kay S. T., Dalla Vecchia C., 2008, MNRAS, 390, L64

Duffy A. R., Schaye J., Kay S. T., Dalla Vecchia C., Battye R. A., Booth C. M., 2010, MNRAS, 405, 2161

Duncan K., Conselice C. J., 2015, MNRAS, 451, 2030

Dunlop J. S., McLure R. J., Robertson B. E., Ellis R. S., Stark D. P., Cirasuolo M., de Ravel L., 2012, MNRAS, 420, 901

Dunlop J. S., et al., 2017, MNRAS, 466, 861

Durier F., Dalla Vecchia C., 2012, MNRAS, 419, 465

Dutton A. A., van den Bosch F. C., Dekel A., 2010, MNRAS, 405, 1690

Duval F., Schaerer D., Östlin G., Laursen P., 2014, A&A, 562, A52

Duval F., et al., 2016, A&A, 587, A77

Einasto J., Klypin A. A., Saar E., Shandarin S. F., 1984, MNRAS, 206, 529

Elbaz D., et al., 2007, A&A, 468, 33

Elbaz D., et al., 2011, A&A, 533, A119

Eldridge J. J., Stanway E. R., Xiao L., McClelland L. A. S., Taylor G., Ng M., Greis S. M. L., Bray J. C., 2017, PASA, 34, e058

Ellis R. S., et al., 2013, ApJL, 763, L7

Ellison S. L., Patton D. R., Simard L., McConnachie A. W., 2008, ApJl, 672, L107

Elvis M., Civano F., Vignali C., et al., 2009, ApJS, 184, 158

Erb D. K., Shapley A. E., Pettini M., Steidel C. C., Reddy N. A., Adelberger K. L., 2006, ApJ, 644, 813

Erb D. K., Pettini M., Shapley A. E., Steidel C. C., Law D. R., Reddy N. A., 2010, ApJ, 719, 1168

Erb D. K., et al., 2014, ApJ, 795, 33

Erb D. K., Pettini M., Steidel C. C., Strom A. L., Rudie G. C., Trainor R. F., Shapley A. E., Reddy N. A., 2016, ApJ, 830, 52

Faisst A. L., 2016, ApJ, 829, 99

Faisst A. L., Capak P., Carollo C. M., Scarlata C., Scoville N., 2014, ApJ, 788, 87

Faisst A. L., et al., 2016, ApJ, 821, 122

Fan X., et al., 2006, AJ, 132, 117

Faucher-Giguère C.-A., Kereš D., Dijkstra M., Hernquist L., Zaldarriaga M., 2010, ApJ, 725, 633

Feldmeier J. J., et al., 2013, ApJ, 776, 75

Feltre A., Charlot S., Gutkin J., 2016, MNRAS, 456, 3354

Ferkinhoff C., Hailey-Dunsheath S., Nikola T., Parshley S. C., Stacey G. J., Benford D. J., Staguhn J. G., 2010, ApJL, 714, L147

Ferland G. J., et al., 2013, RMAA, 49, 137

Ferrara A., Loeb A., 2013, MNRAS, 431, 2826

Finkelstein S. L., 2016, PASA, 33, e037

Finkelstein S. L., Rhoads J. E., Malhotra S., Grogin N., Wang J., 2008, ApJ, 678, 655

Finkelstein S. L., et al., 2011, ApJ, 729, 140

Finkelstein S. L., Papovich C., Dickinson M., et al., 2013, Nature, 502, 524

Finkelstein S. L., et al., 2015, ApJ, 810, 71

Finlator K., Davé R., 2008, MNRAS, 385, 2181

Finlator K., Davé R., Oppenheimer B. D., 2007, MNRAS, 376, 1861

Finlator K., Özel F., Davé R., Oppenheimer B. D., 2009, MNRAS, 400, 1049

Fiore F., et al., 2012, A&A, 537, A16

Fontana A., et al., 2010, ApJL, 725, L205

Forbes J. C., Krumholz M. R., Burkert A., Dekel A., 2014, MNRAS, 443, 168

Förster Schreiber N. M., et al., 2009, ApJ, 706, 1364

Fort B., Mellier Y., 1994, AAPR, 5, 239

Franx M., Illingworth G., de Zeeuw T., 1991, ApJ, 383, 112

Friedmann M., Maoz D., 2018, arXiv:1803.04421

Fumagalli M., et al., 2012, ApJL, 757, L22

Furlanetto S. R., Zaldarriaga M., Hernquist L., 2004, ApJ, 613, 1

Furlanetto S. R., McQuinn M., Hernquist L., 2006, MNRAS, 365, 115

Furlong M., et al., 2015, MNRAS, 450, 4486

Furlong M., et al., 2017, MNRAS, 465, 722

Furusawa H., et al., 2008, ApJs, 176, 1

Furusawa H., et al., 2016, ApJ, 822, 46

Fynbo J. U., Möller P., Thomsen B., 2001, A&A, 374, 443

Gallazzi A., Charlot S., Brinchmann J., White S. D. M., Tremonti C. A., 2005, MNRAS, 362, 41

Gallerani S., Pallottini A., Feruglio C., Ferrara A., Maiolino R., Vallini L., Riechers D. A., Pavesi R., 2018, MNRAS, 473, 1909

Gao L., White S. D. M., 2007, MNRAS, 377, L5

Gao L., Springel V., White S. D. M., 2005, MNRAS, 363, L66

Garel T., Blaizot J., Guiderdoni B., Schaerer D., Verhamme A., Hayes M., 2012, MNRAS, 422, 310

Garel T., et al., 2015, MNRAS, 450, 1279

Garn T., Best P. N., 2010, MNRAS, 409, 421

Garn T., et al., 2010, MNRAS, 402, 2017

Gawiser E., et al., 2007, ApJ, 671, 278

Gazagnes S., Chisholm J., Schaerer D., Verhamme A., Rigby J. R., Bayliss M., 2018, arXiv:1802.06378

Geach J. E., Smail I., Best P. N., Kurk J., Casali M., Ivison R. J., Coppin K., 2008, MNRAS, 388, 1473

Geach J. E., et al., 2009, ApJ, 700, 1

Geach J. E., Sobral D., Hickox R. C., Wake D. A., Smail I., Best P. N., Baugh C. M., Stott J. P., 2012, MNRAS, 426, 679

Genel S., et al., 2014, MNRAS, 445, 175

Giallongo E., et al., 2015, A&A, 578, A83

Gladders M. D., Oemler A., Dressler A., Poggianti B., Vulcani B., Abramson L., 2013, ApJ, 770, 64

Gnat O., Sternberg A., 2007, ApJS, 168, 213

Gonzalez A. H., et al., 2010, in American Astronomical Society Meeting Abstracts #216. p. 415.13

González V., Bouwens R., Illingworth G., Labbé I., Oesch P., Franx M., Magee D., 2014, ApJ, 781, 34

Götberg Y., de Mink S. E., Groh J. H., 2017, A&A, 608, A11

Gräfener G., Vink J. S., 2015, A&A, 578, L2

Grazian A., et al., 2016, A&A, 585, A48

Gronke M., 2017, A&A, 608, A139

Gronke M., Dijkstra M., 2014, MNRAS, 444, 1095

Gronke M., Dijkstra M., 2016, ApJ, 826, 14

Gronke M., Dijkstra M., Trenti M., Wyithe S., 2015a, MNRAS, 449, 1284

Gronke M., Bull P., Dijkstra M., 2015b, ApJ, 812, 123

Gronke M., Dijkstra M., McCourt M., Oh S. P., 2016, ApJL, 833, L26

Gronke M., Dijkstra M., McCourt M., Peng Oh S., 2017, A&A, 607, A71

Gronwall C., et al., 2007, ApJ, 667, 79

Gu M., Conroy C., Behroozi P., 2016, ApJ, 833, 2

Guaita L., et al., 2011, ApJ, 733, 114

Guaita L., Francke H., Gawiser E., Bauer F. E., Hayes M., Östlin G., Padilla N., 2013, A&A, 551, A93

Guaita L., et al., 2016, A&A, 587, A133

Gunawardhana M. L. P., et al., 2013, MNRAS, 433, 2764

Gunn J. E., Gott III J. R., 1972, ApJ, 176, 1

Guo Q., et al., 2011, MNRAS, 413, 101

Guo Q., et al., 2016a, MNRAS, 461, 3457

Guo Y., et al., 2016b, ApJ, 833, 37

Guseva N. G., Izotov Y. I., Fricke K. J., Henkel C., 2017, A&A, 599, A65

Haardt F., Madau P., 2012, ApJ, 746, 125

Haas M. R., Schaye J., Booth C. M., Dalla Vecchia C., Springel V., Theuns T., Wiersma R. P. C., 2013, MNRAS, 435, 2931

Hagen A., et al., 2016, ApJ, 817, 79

Haiman Z., 2002, ApJL, 576, L1

Haiman Z., Cen R., 2005, ApJ, 623, 627

Hamana T., Ouchi M., Shimasaku K., Kayo I., Suto Y., 2004, MNRAS, 347, 813

Harikane Y., et al., 2018, ApJ, 859, 84

Hartwig T., et al., 2016, MNRAS, 462, 2184

Hashimoto T., Ouchi M., Shimasaku K., Ono Y., Nakajima K., Rauch M., Lee J., Okamura S., 2013, ApJ, 765, 70

Hashimoto T., et al., 2017a, MNRAS, 465, 1543

Hashimoto T., et al., 2017b, A&A, 608, A10

Hayashi M., Sobral D., Best P. N., Smail I., Kodama T., 2013, MNRAS, 430, 1042

Hayashino T., et al., 2004, AJ, 128, 2073

Hayes M., 2015, PASA, 32, 27

Hayes M., Östlin G., Atek H., Kunth D., Mas-Hesse J. M., Leitherer C., Jiménez-Bailón E., Adamo A., 2007, MNRAS, 382, 1465

Hayes M., et al., 2010, Nature, 464, 562

Hayes M., Schaerer D., Östlin G., Mas-Hesse J. M., Atek H., Kunth D., 2011, ApJ, 730, 8

Hayes M., et al., 2013, ApJL, 765, L27

Hayes M., et al., 2014, ApJ, 782, 6

Hearin A. P., Zentner A. R., van den Bosch F. C., Campbell D., Tollerud E., 2016, MNRAS, 460, 2552

Heckman T. M., Sembach K. R., Meurer G. R., Leitherer C., Calzetti D., Martin C. L., 2001, ApJ, 558, 56

Hemmati S., Yan L., Diaz-Santos T., Armus L., Capak P., Faisst A., Masters D., 2017, ApJ, 834, 36

Henriques B. M. B., White S. D. M., Thomas P. A., Angulo R. E., Guo Q., Lemson G., Springel V., 2013, MNRAS, 431, 3373

Henriques B. M. B., White S. D. M., Thomas P. A., Angulo R., Guo Q., Lemson G., Springel V., Overzier R., 2015, MNRAS, 451, 2663

Henry A., Scarlata C., Martin C. L., Erb D., 2015, ApJ, 809, 19

Herenz E. C., et al., 2016, A&A, 587, A78

Herrera-Camus R., et al., 2015, ApJ, 800, 1

Hibon P., et al., 2010, A&A, 515, A97

Hildebrandt H., Pielorz J., Erben T., van Waerbeke L., Simon P., Capak P., 2009, A&A, 498, 725

Hildebrandt H., et al., 2017, MNRAS, 465, 1454

Hill G. J., et al., 2008, in Kodama T., Yamada T., Aoki K., eds, Panoramic Views of Galaxy Formation and Evolution. p. 115

Hirashita H., Ferrara A., Dayal P., Ouchi M., 2014, MNRAS, 443, 1704

Hopkins P. F., 2013, MNRAS, 428, 2840

Hopkins A. M., Beacom J. F., 2006, ApJ, 651, 142

Hopkins P. F., Hernquist L., Cox T. J., Di Matteo T., Robertson B., Springel V., 2006, ApJs, 163, 1

Hopkins P. F., Hernquist L., Cox T. J., Kereš D., 2008, ApJs, 175, 356

Hopkins P. F., Kereš D., Oñorbe J., Faucher-Giguère C.-A., Quataert E., Murray N., Bullock J. S., 2014, MNRAS, 445, 581

Horne K., 1986, PASP, 98, 609

Hu E. M., Cowie L. L., Barger A. J., Capak P., Kakazu Y., Trouille L., 2010, ApJ, 725, 394

Hu E. M., Cowie L. L., Songaila A., Barger A. J., Rosenwasser B., Wold I. G. B., 2016, ApJL, 825, L7

Huang K.-H., et al., 2016, ApJ, 817, 11

Hubble E. P., 1926, ApJ, 64

Hummer D. G., Storey P. J., 1987, MNRAS, 224, 801

Hunt M. P., Steidel C. C., Adelberger K. L., Shapley A. E., 2004, ApJ, 605, 625

Hunter J. D., 2007, Computing in Science and Engineering, 9, 90

Huss A., Jain B., Steinmetz M., 1999, ApJ, 517, 64

Hutter A., Dayal P., Partl A. M., Müller V., 2014, MNRAS, 441, 2861

Ibar E., et al., 2013, MNRAS, 434, 3218

Ilbert O., et al., 2009, ApJ, 690, 1236

Ilbert O., et al., 2013, A&A, 556, A55

Iliev I. T., Mellema G., Pen U.-L., Merz H., Shapiro P. R., Alvarez M. A., 2006, MNRAS, 369, 1625

Inoue A. K., 2002, ApJL, 570, L97

Inoue A. K., Iwata I., Deharveng J.-M., 2006, MNRAS, 371, L1

Inoue A. K., Shimizu I., Iwata I., Tanaka M., 2014, MNRAS, 442, 1805

Inoue A. K., et al., 2016, Science, 352, 1559

Ishigaki M., Kawamata R., Ouchi M., Oguri M., Shimasaku K., Ono Y., 2015, ApJ, 799, 12

Iye M., et al., 2006, Nature, 443, 186

Izotov Y. I., Guseva N. G., Fricke K. J., Henkel C., 2015, MNRAS, 451, 2251

Izotov Y. I., Schaerer D., Thuan T. X., Worseck G., Guseva N. G., Orlitová I., Verhamme A., 2016a, MNRAS, 461, 3683

Izotov Y. I., Orlitová I., Schaerer D., Thuan T. X., Verhamme A., Guseva N. G., Worseck G., 2016b, Nature, 529, 178

Izotov Y. I., Worseck G., Schaerer D., Guseva N. G., Thuan T. X., Fricke A. V., Orlitová I., 2018, MNRAS, 478, 4851

Jannuzi B. T., Dey A., 1999, in Weymann R., Storrie-Lombardi L., Sawicki M., Brunner R., eds, Photometric Redshifts and the Detection of High Redshift Galaxies. p. 111

Jansen R. A., Franx M., Fabricant D., 2001, ApJ, 551, 825

Jeeson-Daniel A., Dalla Vecchia C., Haas M. R., Schaye J., 2011, MNRAS, 415, L69

Jensen H., Hayes M., Iliev I. T., Laursen P., Mellema G., Zackrisson E., 2014, MNRAS, 444, 2114

Jensen H., Zackrisson E., Pelckmans K., Binggeli C., Ausmees K., Lundholm U., 2016, ApJ, 827, 5

Jiang L., Bian F., Fan X., Krug H. B., McGreer I. D., Stark D. P., Clément B., Egami E., 2013a, ApJL, 771, L6

Jiang L., et al., 2013b, ApJ, 772, 99

Jiang L., et al., 2013c, ApJ, 773, 153

Jimenez R., Haiman Z., 2006, Nature, 440, 501

Johnson J. L., Khochfar S., Greif T. H., Durier F., 2011, MNRAS, 410, 919

Jones E., Oliphant T., Peterson P., et al., 2001, SciPy: Open source scientific tools for Python

Jones T. A., Ellis R. S., Schenker M. A., Stark D. P., 2013, ApJ, 779, 52

Jones G. C., Willott C. J., Carilli C. L., Ferrara A., Wang R., Wagg J., 2017, ApJ, 845, 175

Kakiichi K., et al., 2018, MNRAS, 479, 43

Kanekar N., Wagg J., Chary R. R., Carilli C. L., 2013, ApJL, 771, L20

Karman W., et al., 2015, A&A, 574, A11

Kashikawa N., et al., 2006, ApJ, 648, 7

Kashikawa N., et al., 2011, ApJ, 734, 119

Kashikawa N., et al., 2012, ApJ, 761, 85

Kashino D., et al., 2013, ApJL, 777, L8

Kauffmann G., et al., 2003, MNRAS, 346, 1055

Kaufman M. J., Wolfire M. G., Hollenbach D. J., Luhman M. L., 1999, ApJ, 527, 795

Kelson D. D., 2014, arXiv:1406.5191

Kennicutt Jr. R. C., 1998, ARAA, 36, 189

Kenter A., et al., 2005, ApJS, 161, 9

Kewley L. J., Ellison S. L., 2008, ApJ, 681, 1183

Khaire V., Srianand R., Choudhury T. R., Gaikwad P., 2016, MNRAS, 457, 4051

Khostovan A. A., Sobral D., Mobasher B., Best P. N., Smail I., Stott J. P., Hemmati S., Nayyeri H., 2015, MNRAS, 452, 3948

Khostovan A. A., Sobral D., Mobasher B., Smail I., Darvish B., Nayyeri H., Hemmati S., Stott J. P., 2016, MNRAS, 463, 2363

Kim M., Dunlop J. S., Lonsdale C. J., Farrah D., Lacy M., Sun M., SpUDS Team 2011, in American Astronomical Society Meeting Abstracts #217. p. 335.51

Knudsen K. K., Richard J., Kneib J.-P., Jauzac M., Clément B., Drouart G., Egami E., Lindroos L., 2016, MNRAS, 462, L6

Knudsen K. K., Watson D., Frayer D., Christensen L., Gallazzi A., Michałowski M. J., Richard J., Zavala J., 2017, MNRAS, 466, 138

Kochanek C. S., et al., 2012, ApJS, 200, 8

Koekemoer A. M., et al., 2007, ApJS, 172, 196

Kojima T., Ouchi M., Nakajima K., Shibuya T., Harikane Y., Ono Y., 2017, PASJ, 69, 44

Konno A., et al., 2014, ApJ, 797, 16

Konno A., Ouchi M., Nakajima K., Duval F., Kusakabe H., Ono Y., Shimasaku K., 2015, preprint

Konno A., Ouchi M., Nakajima K., Duval F., Kusakabe H., Ono Y., Shimasaku K., 2016, ApJ, 823, 20

Konno A., et al., 2018, PASJ, 70, S16

Koo D. C., 1986, in Spectral Evolution of Galaxies. pp 419–438

Koo D. C., Kron R. T., 1980, PASP, 92, 537

Kormendy J., Richstone D., 1995, ARAA, 33, 581

Kornei K. A., Shapley A. E., Erb D. K., Steidel C. C., Reddy N. A., Pettini M., Bogosavljević M., 2010, ApJ, 711, 693

Koyama Y., et al., 2015, MNRAS, 453, 879

Kravtsov A. V., Vikhlinin A. A., Meshcheryakov A. V., 2018, Astronomy Letters, 44, 8

Krug H. B., et al., 2012, ApJ, 745, 122

Kuhlen M., Faucher-Giguère C.-A., 2012, MNRAS, 423, 862

Kulas K. R., Shapley A. E., Kollmeier J. A., Zheng Z., Steidel C. C., Hainline K. N., 2012, ApJ, 745, 33

Kunth D., Mas-Hesse J. M., Terlevich E., Terlevich R., Lequeux J., Fall S. M., 1998, A&A, 334, 11

Kurczynski P., et al., 2016, ApJL, 820, L1

Kurucz R. L., 1992, in The Stellar Populations of Galaxies. p. 225

Kusakabe H., Shimasaku K., Nakajima K., Ouchi M., 2015, ApJL, 800, L29

La Franca F., et al., 2005, ApJ, 635, 864

Labbé I., Bouwens R., Illingworth G. D., Franx M., 2006, ApJL, 649, L67

Labbé I., et al., 2015, ApJS, 221, 23

Lacerna I., Padilla N., 2011, MNRAS, 412, 1283

Lacey C. G., et al., 2016, MNRAS, 462, 3854

Lagos C. d. P., et al., 2016, MNRAS, 459, 2632

Laigle C., et al., 2016, ApJS, 224, 24

Lake E., Zheng Z., Cen R., Sadoun R., Momose R., Ouchi M., 2015, ApJ, 806, 46

Laporte N., et al., 2017a, ApJL, 837, L21

Laporte N., Nakajima K., Ellis R. S., Zitrin A., Stark D. P., Mainali R., Roberts-Borsani G. W., 2017b, ApJ, 851, 40

Lara-López M. A., et al., 2010, A&A, 521, L53

Laursen P., Sommer-Larsen J., Razoumov A. O., 2011, ApJ, 728, 52

Lawrence A., et al., 2007, MNRAS, 379, 1599

Leauthaud A., et al., 2012, ApJ, 744, 159

Lee K.-S., et al., 2011, ApJ, 733, 99

Lee J. C., et al., 2012, PASP, 124, 782

Lee K.-S., Dey A., Hong S., Reddy N., Wilson C., Jannuzi B. T., Inami H., Gonzalez A. H., 2014, ApJ, 796, 126

Lehmann B. V., Mao Y.-Y., Becker M. R., Skillman S. W., Wechsler R. H., 2017, ApJ, 834, 37

Lehmer B. D., et al., 2016, ApJ, 825, 7

Leitet E., Bergvall N., Hayes M., Linné S., Zackrisson E., 2013, A&A, 553, A106

Leitherer C., Ferguson H. C., Heckman T. M., Lowenthal J. D., 1995, ApJL, 454, L19
Leitherer C., et al., 1999, ApJS, 123, 3
Leitherer C., Hernandez S., Lee J. C., Oey M. S., 2016, ApJ, 823, 64
Lewis I., et al., 2002, MNRAS, 334, 673
Lidman C., Hayes M., Jones D. H., Schaerer D., Westra E., Tapken C., Meisenheimer K., Verhamme A., 2012, MNRAS, 420, 1946
Lilly S. J., Le Fevre O., Hammer F., Crampton D., 1996, ApJl, 460, L1
Lilly S. J., et al., 2009, ApJS, 184, 218
Lilly S. J., Carollo C. M., Pipino A., Renzini A., Peng Y., 2013, ApJ, 772, 119
Lim S. H., Mo H. J., Wang H., Yang X., 2016, MNRAS, 455, 499
Lin Y., Oh S. P., Furlanetto S. R., Sutter P. M., 2016, MNRAS, 461, 3361
Livermore R. C., Finkelstein S. L., Lotz J. M., 2017, ApJ, 835, 113
Loeb A., 2006, Scientific American, 295
Loeb A., Barkana R., 2001, ARAA, 39, 19
Loeb A., Rybicki G. B., 1999, ApJ, 524, 527
Lowenthal J. D., Hogan C. J., Leach R. W., Schmidt G. D., Foltz C. B., 1990, ApJ, 357, 3
Ludlow A. D., Navarro J. F., Li M., Angulo R. E., Boylan-Kolchin M., Bett P. E., 2012, MNRAS, 427, 1322
Ludlow A. D., et al., 2013, MNRAS, 432, 1103
Ludlow A. D., Navarro J. F., Angulo R. E., Boylan-Kolchin M., Springel V., Frenk C., White S. D. M., 2014, MNRAS, 441, 378
Ly C., et al., 2007, ApJ, 657, 738
Ly C., Malkan M. A., Kashikawa N., Hayashi M., Nagao T., Shimasaku K., Ota K., Ross N. R., 2012, ApJ, 757, 63
Ma X., Kasen D., Hopkins P. F., Faucher-Giguère C.-A., Quataert E., Kereš D., Murray N., 2015, MNRAS, 453, 960
Madau P., 1995, ApJ, 441, 18
Madau P., 2017, ApJ, 851, 50
Madau P., Dickinson M., 2014, ARAA, 52, 415
Madau P., Haardt F., 2015, ApJL, 813, L8
Madau P., Haardt F., Rees M. J., 1999, ApJ, 514, 648
Magnelli B., et al., 2014, A&A, 561, A86
Magorrian J., et al., 1998, AJ, 115, 2285
Maier C., Lilly S. J., Ziegler B. L., Contini T., Pérez Montero E., Peng Y., Balestra I., 2014, ApJ, 792, 3
Mainali R., Kollmeier J. A., Stark D. P., Simcoe R. A., Walth G., Newman A. B., Miller D. R., 2017, ApJL, 836, L14
Maiolino R., et al., 2015, MNRAS, 452, 54
Malhotra S., Rhoads J. E., 2002, ApJL, 565, L71
Malhotra S., Rhoads J. E., 2004, ApJL, 617, L5
Malhotra S., Rhoads J. E., 2006, ApJL, 647, L95
Malhotra S., et al., 2001, ApJ, 561, 766
Malkan M. A., Teplitz H., McLean I. S., 1996, ApJL, 468, L9
Mallery R. P., et al., 2012, ApJ, 760, 128
Mancini M., Schneider R., Graziani L., Valiante R., Dayal P., Maio U., Ciardi B., Hunt L. K., 2015, MNRAS, 451, L70
Mancini M., Schneider R., Graziani L., Valiante R., Dayal P., Maio U., Ciardi B., 2016, MNRAS, 462, 3130
Mandelbaum R., Seljak U., Kauffmann G., Hirata C. M., Brinkmann J., 2006, MNRAS, 368, 715
Mannucci F., Cresci G., Maiolino R., Marconi A., Gnerucci A., 2010, MNRAS, 408, 2115
Maoz D., Mannucci F., Brandt T. D., 2012, MNRAS, 426, 3282
Mármol-Queraltó E., McLure R. J., Cullen F., Dunlop J. S., Fontana A., McLeod D. J., 2016, MNRAS, 460, 3587
Martín-Navarro I., Brodie J. P., Romanowsky A. J., Ruiz-Lara T., van de Ven G., 2018, Nature, 553, 307
Martin C., et al., 2003. pp 336–350
Martin D. C., et al., 2005, ApJL, 619, L1
Martin C. L., Dijkstra M., Henry A., Soto K. T., Danforth C. W., Wong J., 2015, ApJ, 803, 6

Mas-Ribas L., Dijkstra M., 2016, ApJ, 822, 84

Mas-Ribas L., Dijkstra M., Forero-Romero J. E., 2016, ApJ, 833, 65

Mas-Ribas L., Hennawi J. F., Dijkstra M., Davies F. B., Stern J., Rix H.-W., 2017, ApJ, 846, 11

Maseda M. V., et al., 2017, A&A, 608, A4

Mason C. A., Treu T., Dijkstra M., Mesinger A., Trenti M., Pentericci L., de Barros S., Vanzella E., 2018, ApJ, 856, 2

Masters D., Faisst A., Capak P., 2016, ApJ, 828, 18

Matsuda Y., et al., 2004, AJ, 128, 569

Matsuda Y., Yamada T., Hayashino T., Yamauchi R., Nakamura Y., 2006, ApJL, 640, L123

Matsuda Y., et al., 2012, MNRAS, 425, 878

Matsuoka K., Nagao T., Maiolino R., Marconi A., Taniguchi Y., 2009, A&A, 503, 721

Matsuoka Y., et al., 2016, ApJ, 828, 26

Matthee J., Schaye J., 2018a, arXiv:1805.05956

Matthee J., Schaye J., 2018b, MNRAS, 479, L34

Matthee J. J. A., et al., 2014, MNRAS, 440, 2375

Matthee J., Sobral D., Santos S., Röttgering H., Darvish B., Mobasher B., 2015, MNRAS, 451, 400

Matthee J., Sobral D., Oteo I., Best P., Smail I., Röttgering H., Paulino-Afonso A., 2016, MNRAS, 458, 449

Matthee J., Schaye J., Crain R. A., Schaller M., Bower R., Theuns T., 2017a, MNRAS, 465, 2381

Matthee J., Sobral D., Best P., Khostovan A. A., Oteo I., Bouwens R., Röttgering H., 2017b, MNRAS, 465, 3637

Matthee J., Sobral D., Best P., Smail I., Bian F., Darvish B., Röttgering H., Fan X., 2017c, MNRAS, 471, 629

Matthee J., Sobral D., Darvish B., Santos S., Mobasher B., Paulino-Afonso A., Röttgering H., Alegre L., 2017d, MNRAS, 472, 772

Matthee J., et al., 2017e, ApJ, 851, 145

McAlpine S., et al., 2016, Astronomy and Computing, 15, 72

McAlpine S., Bower R. G., Harrison C. M., Crain R. A., Schaller M., Schaye J., Theuns T., 2017, MNRAS, 468, 3395

McCracken H. J., et al., 2010, ApJ, 708, 202

McCracken H. J., et al., 2012, A&A, 544, A156

McGreer I. D., Mesinger A., D'Odorico V., 2015, MNRAS, 447, 499

McLeod D. J., McLure R. J., Dunlop J. S., Robertson B. E., Ellis R. S., Targett T. A., 2015a, MNRAS, 450, 3032

McLeod D. J., McLure R. J., Dunlop J. S., Robertson B. E., Ellis R. S., Targett T. A., 2015b, MNRAS, 450, 3032

McLinden E. M., et al., 2011, ApJ, 730, 136

McLure R. J., et al., 2006, MNRAS, 372, 357

McLure R. J., et al., 2013, MNRAS, 428, 1088

McMullin J. P., Waters B., Schiebel D., Young W., Golap K., 2007, in Astronomical Data Analysis Software and Systems XVI. p. 127

McQuinn M., Zahn O., Zaldarriaga M., Hernquist L., Furlanetto S. R., 2006, ApJ, 653, 815

McQuinn M., Hernquist L., Zaldarriaga M., Dutta S., 2007, MNRAS, 381, 75

Mesinger A., Aykutalp A., Vanzella E., Pentericci L., Ferrara A., Dijkstra M., 2015, MNRAS, 446, 566

Meurer G. R., Heckman T. M., Calzetti D., 1999, ApJ, 521, 64

Michałowski M. J., 2015, A&A, 577, A80

Micheva G., Iwata I., Inoue A. K., 2017, MNRAS, 465, 302

Miley G., De Breuck C., 2008, AAPR, 15, 67

Milvang-Jensen B., et al., 2013, A&A, 560, A94

Miralda-Escudé J., 1998, ApJ, 501, 15

Mitra S., Ferrara A., Choudhury T. R., 2013, MNRAS, 428, L1

Mitra S., Choudhury T. R., Ferrara A., 2015, MNRAS, 454, L76

Mitra S., Davé R., Simha V., Finlator K., 2017, MNRAS, 464, 2766

Miyazaki S., et al., 2002, PASJ, 54, 833

Miyazaki S., Komiyama Y., Nakaya H., et al., 2012, in Society of Photo-Optical Instrumentation Engineers (SPIE) Conference Series.

Modigliani A., et al., 2010, in Observatory Operations: Strategies, Processes, and Systems III. p. 773728

Møller P., Warren S. J., 1998, MNRAS, 299, 661

Momose R., et al., 2014, MNRAS, 442, 110

More S., van den Bosch F. C., Cacciato M., Mo H. J., Yang X., Li R., 2009, MNRAS, 392, 801

More S., van den Bosch F. C., Cacciato M., Skibba R., Mo H. J., Yang X., 2011, MNRAS, 410, 210

Mortlock D. J., et al., 2011, Nature, 474, 616

Morton D. C., 1991, ApJS, 77, 119

Mostardi R. E., Shapley A. E., Steidel C. C., Trainor R. F., Reddy N. A., Siana B., 2015, ApJ, 810, 107

Moster B. P., Naab T., White S. D. M., 2013, MNRAS, 428, 3121

Mowlavi N., Eggenberger P., Meynet G., Ekström S., Georgy C., Maeder A., Charbonnel C., Eyer L., 2012, A&A, 541, A41

Muratov A. L., et al., 2015, MNRAS, 454, 2691

Murayama T., et al., 2007, ApJS, 172, 523

Murray S. S., et al., 2005, ApJS, 161, 1

Muzzin A., et al., 2013, ApJs, 206, 8

Muzzin A., et al., 2014, ApJ, 796, 65

Nagao T., et al., 2008, ApJ, 680, 100

Nakajima K., Ouchi M., 2014, MNRAS, 442, 900

Nakajima K., et al., 2012, ApJ, 745, 12

Nakajima K., Ouchi M., Shimasaku K., Hashimoto T., Ono Y., Lee J. C., 2013, ApJ, 769, 3

Nakajima K., Ellis R. S., Iwata I., Inoue A. K., Kusakabe H., Ouchi M., Robertson B. E., 2016, ApJL, 831, L9

Narayanan D., Davé R., Johnson B. D., Thompson R., Conroy C., Geach J., 2018, MNRAS, 474, 1718

Navarro J. F., Frenk C. S., White S. D. M., 1997, ApJ, 490, 493

Neufeld D. A., 1990, ApJ, 350, 216

Neufeld D. A., 1991, ApJL, 370, L85

Newman J. A., et al., 2013, ApJS, 208, 5

Nilsson K. K., et al., 2007, A&A, 471, 71

Nilsson K. K., Tapken C., Møller P., Freudling W., Fynbo J. P. U., Meisenheimer K., Laursen P., Östlin G., 2009, A&A, 498, 13

Nilsson K. K., Östlin G., Møller P., Möller-Nilsson O., Tapken C., Freudling W., Fynbo J. P. U., 2011, A&A, 529, A9

Noeske K. G., et al., 2007, ApJL, 660, L43

Nomoto K., Tominaga N., Umeda H., Kobayashi C., Maeda K., 2006, Nuclear Physics A, 777, 424

Oesch P. A., et al., 2015, ApJL, 804, L30

Oke J. B., 1974, ApJS, 27, 21

Oliver S. J., et al., 2012, MNRAS, 424, 1614

Olsen K., Greve T. R., Narayanan D., Thompson R., Davé R., Niebla Rios L., Stawinski S., 2017, ApJ, 846, 105

Ono Y., Ouchi M., Shimasaku K., Dunlop J., Farrah D., McLure R., Okamura S., 2010, ApJ, 724, 1524

Ono Y., et al., 2012, ApJ, 744, 83

Oppenheimer B. D., Davé R., Kereš D., Fardal M., Katz N., Kollmeier J. A., Weinberg D. H., 2010, MNRAS, 406, 2325

Orr M. E., et al., 2017, ApJL, 849, L2

Orsi Á., Padilla N., Groves B., Cora S., Tecce T., Gargiulo I., Ruiz A., 2014, MNRAS, 443, 799

Osterbrock D. E., 1989, Astrophysics of gaseous nebulae and active galactic nuclei

Ota K., et al., 2010, ApJ, 722, 803

Ota K., et al., 2014, ApJ, 792, 34

Oteo I., Sobral D., Ivison R. J., Smail I., Best P. N., Cepa J., Pérez-García A. M., 2015, MNRAS, 452, 2018

Ouchi M., et al., 2003, ApJ, 582, 60

Ouchi M., et al., 2004, ApJ, 611, 660

Ouchi M., et al., 2005, ApJL, 635, L117

Ouchi M., et al., 2008, ApJs, 176, 301

Ouchi M., et al., 2009, ApJ, 696, 1164

Ouchi M., et al., 2010, ApJ, 723, 869

Ouchi M., et al., 2013, ApJ, 778, 102

Ouchi M., et al., 2018, PASJ, 70, S13

Overzier R. A., Nesvadba N. P. H., Dijkstra M., Hatch N. A., Lehnert M. D., Villar-Martín M., Wilman R. J., Zirm A. W., 2013, ApJ, 771, 89

Oyarzún G. A., Blanc G. A., González V., Mateo M., Bailey III J. I., 2017, ApJ, 843, 133

Paardekooper J.-P., Khochfar S., Dalla Vecchia C., 2015, MNRAS, 451, 2544

Pacifici C., Kassin S. A., Weiner B., Charlot S., Gardner J. P., 2013, ApJL, 762, L15

Pacifici C., Oh S., Oh K., Lee J., Yi S. K., 2016, ApJ, 824, 45

Pacucci F., Pallottini A., Ferrara A., Gallerani S., 2017, MNRAS, 468, L77

Padmanabhan N., et al., 2008, ApJ, 674, 1217

Pallottini A., et al., 2015, MNRAS, 453, 2465

Pallottini A., Ferrara A., Gallerani S., Vallini L., Maiolino R., Salvadori S., 2017a, MNRAS, 465, 2540

Pallottini A., Ferrara A., Bovino S., Vallini L., Gallerani S., Maiolino R., Salvadori S., 2017b, MNRAS, 471, 4128

Pannella M., et al., 2015, ApJ, 807, 141

Parsa S., Dunlop J. S., McLure R. J., 2018, MNRAS, 474, 2904

Partridge R. B., Peebles P. J. E., 1967, ApJ, 147, 868

Patrício V., et al., 2016, MNRAS, 456, 4191

Paulino-Afonso A., Sobral D., Darvish B., Ribeiro B., Stroe A., Best P., Afonso J., Matsuda Y., 2018a, arXiv:1805.07371

Paulino-Afonso A., et al., 2018b, MNRAS, 476, 5479

Pawlik A. H., Schaye J., Dalla Vecchia C., 2015, MNRAS, 451, 1586

Pearson W. J., et al., 2018, preprint

Peng Y.-j., et al., 2010, ApJ, 721, 193

Peng Y.-j., Lilly S. J., Renzini A., Carollo M., 2012, ApJ, 757, 4

Pentericci L., et al., 2011, ApJ, 743, 132

Pentericci L., et al., 2014, ApJ, 793, 113

Pentericci L., et al., 2016, ApJL, 829, L11

Pérez-Montero E., et al., 2013, A&A, 549, A25

Pettini M., Pagel B. E. J., 2004, MNRAS, 348, L59

Pillepich A., et al., 2018, MNRAS, 473, 4077

Planck Collaboration et al., 2014, A&A, 571, A16

Planck Collaboration et al., 2016a, A&A, 594, A13

Planck Collaboration et al., 2016b, A&A, 596, A108

Popping G., Somerville R. S., Galametz M., 2017, MNRAS, 471, 3152

Portinari L., Chiosi C., Bressan A., 1998, A&A, 334, 505

Prescott M. K. M., Kashikawa N., Dey A., Matsuda Y., 2008, ApJL, 678, L77

Prescott M. K. M., Dey A., Jannuzi B. T., 2009, ApJ, 702, 554

Price L. C., Trac H., Cen R., 2016, arXiv:1605.03970

Pritchet C. J., 1994, PASP, 106, 1052

Pritchet C. J., Hartwick F. D. A., 1987, ApJ, 320, 464

Puglisi A., et al., 2016, A&A, 586, A83

Qu Y., et al., 2017, MNRAS, 464, 1659

Raiter A., Schaerer D., Fosbury R. A. E., 2010, A&A, 523, A64

Reddick R. M., Wechsler R. H., Tinker J. L., Behroozi P. S., 2013, ApJ, 771, 30

Reddy N. A., et al., 2015, ApJ, 806, 259

Reddy N. A., Steidel C. C., Pettini M., Bogosavljević M., 2016, ApJ, 828, 107

Reichardt C. L., 2016, in Understanding the Epoch of Cosmic Reionization: Challenges and Progress. p. 227

Rémy-Ruyer A., et al., 2014, A&A, 563, A31

Rhoads J. E., Malhotra S., Dey A., Stern D., Spinrad H., Jannuzi B. T., 2000, ApJL, 545, L85

Rhoads J. E., et al., 2003, AJ, 125, 1006

Ribeiro B., et al., 2016, A&A, 593, A22

Richard J., Kneib J.-P., Ebeling H., Stark D. P., Egami E., Fiedler A. K., 2011, MNRAS, 414, L31

Riechers D. A., et al., 2013, Nature, 496, 329

Riechers D. A., et al., 2017, ApJ, 850, 1

Ritter J. S., Safranek-Shrader C., Gnat O., Milosavljević M., Bromm V., 2012, ApJ, 761, 56

Ritter J. S., Sluder A., Safranek-Shrader C., Milosavljevic M., Bromm V., 2014, MNRAS, 451, 1190

Rivera-Thorsen T. E., et al., 2015, ApJ, 805, 14

Rivera-Thorsen T. E., et al., 2017, A&A, 608, L4

Robertson B. E., et al., 2013, ApJ, 768, 71

Robertson B. E., Ellis R. S., Furlanetto S. R., Dunlop J. S., 2015, ApJL, 802, L19

Rodighiero G., et al., 2014, MNRAS, 443, 19

Rodríguez-Puebla A., Avila-Reese V., Yang X., Foucaud S., Drory N., Jing Y. P., 2015, ApJ, 799, 130

Rodríguez-Puebla A., Primack J. R., Behroozi P., Faber S. M., 2016, MNRAS, 455, 2592

Rosas-Guevara Y. M., et al., 2015, MNRAS, 454, 1038

Rosdahl J., Blaizot J., 2012, MNRAS, 423, 344

Rosdahl J., et al., 2018, MNRAS, 479, 994

Rottgering H. J. A., Hunstead R. W., Miley G. K., van Ojik R., Wieringa M. H., 1995, MNRAS, 277, 389

Rousselot P., Lidman C., Cuby J.-G., Moreels G., Monnet G., 2000, A&A, 354, 1134

Rutkowski M. J., et al., 2016, ApJ, 819, 81

Sadoun R., Zheng Z., Miralda-Escudé J., 2017, ApJ, 839, 44

Saez C., et al., 2015, MNRAS, 450, 2615

Salim S., Lee J. C., Ly C., Brinchmann J., Davé R., Dickinson M., Salzer J. J., Charlot S., 2014, ApJ, 797, 126

Salpeter E. E., 1955, ApJ, 121, 161

Sánchez S. F., et al., 2014, A&A, 563, A49

Sandberg A., Östlin G., Melinder J., Bik A., Guaita L., 2015, ApJL, 814, L10

Sanders R. L., et al., 2015, ApJ, 799, 138

Sanders R. L., et al., 2016, ApJ, 816, 23

Sanders R. L., et al., 2018, ApJ, 858, 99

Santos M. R., 2004, MNRAS, 349, 1137

Santos S., Sobral D., Matthee J., 2016, MNRAS, 463, 1678

Scannapieco E., Schneider R., Ferrara A., 2003, ApJ, 589, 35

Scannapieco C., et al., 2012, MNRAS, 423, 1726

Scarlata C., et al., 2009, ApJL, 704, L98

Schaerer D., 2002, A&A, 382, 28

Schaerer D., 2003, A&A, 397, 527

Schaerer D., Pelló R., 2005, MNRAS, 362, 1054

Schaerer D., de Barros S., 2009, A&A, 502, 423

Schaerer D., de Barros S., 2010, A&A, 515, A73

Schaerer D., de Barros S., Stark D. P., 2011, A&A, 536, A72

Schaerer D., Boone F., Zamojski M., Staguhn J., Dessauges-Zavadsky M., Finkelstein S., Combes F., 2015, A&A, 574, A19

Schaerer D., Izotov Y. I., Verhamme A., Orlitová I., Thuan T. X., Worseck G., Guseva N. G., 2016, A&A, 591, L8

Schaller M., et al., 2015a, MNRAS, 451, 1247

Schaller M., et al., 2015b, MNRAS, 452, 343

Schaller M., Dalla Vecchia C., Schaye J., Bower R. G., Theuns T., Crain R. A., Furlong M., McCarthy I. G., 2015c, MNRAS, 454, 2277

Schaye J., 2004, ApJ, 609, 667

Schaye J., Dalla Vecchia C., 2008, MNRAS, 383, 1210

Schaye J., et al., 2010, MNRAS, 402, 1536

Schaye J., et al., 2015, MNRAS, 446, 521

Schechter P., 1976, ApJ, 203, 297

Schenker M. A., Stark D. P., Ellis R. S., Robertson B. E., Dunlop J. S., McLure R. J., Kneib J.-P., Richard J., 2012, ApJ, 744, 179

Schenker M. A., Ellis R. S., Konidaris N. P., Stark D. P., 2014, ApJ, 795, 20

Schmidt K. B., et al., 2016, ApJ, 818, 38

Schmidt K. B., et al., 2017, ApJ, 839, 17

Schreiber C., et al., 2015, A&A, 575, A74

Scoville N., et al., 2007, ApJS, 172, 38

Scoville N., et al., 2016, ApJ, 820, 83

Scoville N., et al., 2017, ApJ, 837, 150

Segers M. C., Crain R. A., Schaye J., Bower R. G., Furlong M., Schaller M., Theuns T., 2016a, MNRAS, 456, 1235

Segers M. C., Schaye J., Bower R. G., Crain R. A., Schaller M., Theuns T., 2016b, MNRAS, 461, L102

Shankar F., Weinberg D. H., Miralda-Escudé J., 2009, ApJ, 690, 20

Sharma M., Theuns T., Frenk C., Bower R., Crain R., Schaller M., Schaye J., 2016, MNRAS

Shibuya T., Kashikawa N., Ota K., Iye M., Ouchi M., Furusawa H., Shimasaku K., Hattori T., 2012, ApJ, 752, 114

Shibuya T., et al., 2014, ApJ, 788, 74

Shibuya T., Ouchi M., Harikane Y., 2015, ApJS, 219, 15

Shibuya T., et al., 2018, PASJ, 70, S15

Shimakawa R., Koyama Y., Prochaska J. X., Guo Y., Tadaki K.-i., Kodama T., 2017, arXiv:1705.01127

Shimasaku K., et al., 2006, PASJ, 58, 313

Shirazi M., Brinchmann J., 2012, MNRAS, 421, 1043

Shivaei I., et al., 2015, ApJ, 815, 98

Siana B., et al., 2007, ApJ, 668, 62

Siana B., et al., 2015, ApJ, 804, 17

Sijacki D., Vogelsberger M., Genel S., Springel V., Torrey P., Snyder G. F., Nelson D., Hernquist L., 2015, MNRAS, 452, 575

Skrutskie M. F., et al., 2006, AJ, 131, 1163

Smidt J., Wiggins B. K., Johnson J. L., 2016, ApJL, 829, L6

Smit R., et al., 2014, ApJ, 784, 58

Smit R., et al., 2015, ApJ, 801, 122

Smit R., Bouwens R. J., Labbé I., Franx M., Wilkins S. M., Oesch P. A., 2016, ApJ, 833, 254

Smit R., et al., 2018, Nature, 553, 178

Smith B. M., et al., 2016a, preprint

Smith A., Bromm V., Loeb A., 2016b, MNRAS, 460, 3143

Sobral D., Matthee J., 2018, preprint

Sobral D., et al., 2009a, MNRAS, 398, 75

Sobral D., et al., 2009b, MNRAS, 398, L68

Sobral D., Best P. N., Matsuda Y., Smail I., Geach J. E., Cirasuolo M., 2012, MNRAS, 420, 1926

Sobral D., Smail I., Best P. N., Geach J. E., Matsuda Y., Stott J. P., Cirasuolo M., Kurk J., 2013, MNRAS, 428, 1128

Sobral D., Best P. N., Smail I., Mobasher B., Stott J., Nisbet D., 2014, MNRAS, 437, 3516

Sobral D., et al., 2015a, MNRAS, 451, 2303

Sobral D., Matthee J., Darvish B., Schaerer D., Mobasher B., Röttgering H. J. A., Santos S., Hemmati S., 2015b, ApJ, 808, 139

Sobral D., Kohn S. A., Best P. N., Smail I., Harrison C. M., Stott J., Calhau J., Matthee J., 2016a, MNRAS, 457, 1739

Sobral D., Stroe A., Koyama Y., Darvish B., Calhau J., Afonso A., Kodama T., Nakata F., 2016b, MNRAS, 458, 3443

Sobral D., et al., 2017, MNRAS, 466, 1242

Sobral D., et al., 2018a, arXiv:1710.08422

Sobral D., et al., 2018b, MNRAS, 476, 4725

Sobral D., Santos S., Matthee J., Paulino-Afonso A., Ribeiro B., Calhau J., Khostovan A. A., 2018c, MNRAS, 476, 4725

Sobral D., et al., 2018d, MNRAS, 477, 2817

Solomon P. M., Downes D., Radford S. J. E., 1992, ApJL, 398, L29

Song M., et al., 2014, ApJ, 791, 3

Songaila A., Hu E. M., Barger A. J., Cowie L. L., Hasinger G., Rosenwasser B., Waters C., 2018, ApJ, 859, 91

Sparre M., et al., 2015, MNRAS, 447, 3548

Speagle J. S., Steinhardt C. L., Capak P. L., Silverman J. D., 2014, ApJS, 214, 15

Springel V., 2005, MNRAS, 364, 1105

Springel V., White S. D. M., Tormen G., Kauffmann G., 2001, MNRAS, 328, 726

Springel V., Di Matteo T., Hernquist L., 2005a, MNRAS, 361, 776

Springel V., et al., 2005b, Nature, 435, 629

Springel V., Frenk C. S., White S. D. M., 2006, Nature, 440, 1137

Stark D. P., Ellis R. S., Chiu K., Ouchi M., Bunker A., 2010, MNRAS, 408, 1628

Stark D. P., Ellis R. S., Ouchi M., 2011, ApJL, 728, L2

Stark D. P., Schenker M. A., Ellis R., Robertson B., McLure R., Dunlop J., 2013, ApJ, 763, 129

Stark D. P., et al., 2014, MNRAS, 445, 3200

Stark D. P., et al., 2015a, MNRAS, 450, 1846

Stark D. P., et al., 2015b, MNRAS, 454, 1393

Stark D. P., et al., 2017, MNRAS, 464, 469

Stefanon M., et al., 2017, ApJ, 851, 43

Steidel C. C., Giavalisco M., Pettini M., Dickinson M., Adelberger K. L., 1996, ApJL, 462, L17

Steidel C. C., Adelberger K. L., Shapley A. E., Pettini M., Dickinson M., Giavalisco M., 2000, ApJ, 532, 170

Steidel C. C., Pettini M., Adelberger K. L., 2001, ApJ, 546, 665

Steidel C. C., Erb D. K., Shapley A. E., Pettini M., Reddy N., Bogosavljević M., Rudie G. C., Rakic O., 2010, ApJ, 717, 289

Steidel C. C., Bogosavljević M., Shapley A. E., Kollmeier J. A., Reddy N. A., Erb D. K., Pettini M., 2011, ApJ, 736, 160

Steidel C. C., Strom A. L., Pettini M., Rudie G. C., Reddy N. A., Trainor R. F., 2016, ApJ, 826, 159

Steidel C. C., Bogosavlevic M., Shapley A. E., Reddy N. A., Rudie G. C., Pettini M., Trainor R. F., Strom A. L., 2018, arXiv:1805.06071

Steinhardt C. L., et al., 2014, ApJL, 791, L25

Stott J. P., et al., 2013, MNRAS, 436, 1130

Strateva I., et al., 2001, AJ, 122, 1861

Stroe A., Sobral D., 2015, MNRAS, 453, 242

Stroe A., Sobral D., Röttgering H. J. A., van Weeren R. J., 2014, MNRAS, 438, 1377

Stroe A., Sobral D., Matthee J., Calhau J., Oteo I., 2017, MNRAS, 471, 2558

Swinbank A. M., Sobral D., Smail I., Geach J. E., Best P. N., McCarthy I. G., Crain R. A., Theuns T., 2012, MNRAS, 426, 935

Swinbank A. M., et al., 2015, MNRAS, 449, 1298

Tacchella S., Dekel A., Carollo C. M., Ceverino D., DeGraf C., Lapiner S., Mandelker N., Primack Joel R., 2016, MNRAS, 457, 2790

Tadaki K.-I., Kodama T., Koyama Y., Hayashi M., Tanaka I., Tokoku C., 2011, PASJ, 63, 437

Taniguchi Y., et al., 2005, PASJ, 57, 165

Taniguchi Y., et al., 2007, ApJS, 172, 9

Taniguchi Y., et al., 2015, ApJL, 809, L7

Tasca L. A. M., et al., 2015, A&A, 581, A54

Taylor M. B., 2006, in Gabriel C., Arviset C., Ponz D., Enrique S., eds, Astronomical Data Analysis Software and Systems XV. p. 666

Taylor M., 2013, Starlink User Note, 253

Taylor J., Lidz A., 2014, MNRAS, 437, 2542

Terrazas B. A., Bell E. F., Henriques B. M. B., White S. D. M., 2016, MNRAS, 459, 1929

Thomas D., Maraston C., Bender R., Mendes de Oliveira C., 2005, ApJ, 621, 673

Thomson A. P., et al., 2017, ApJ, 838, 119

Tilvi V., et al., 2010, ApJ, 721, 1853

Tilvi V., et al., 2014, ApJ, 794, 5

Tilvi V., et al., 2016, ApJL, 827, L14

Tinker J. L., 2017, MNRAS, 467, 3533

Tinker J. L., Conroy C., Norberg P., Patiri S. G., Weinberg D. H., Warren M. S., 2008, ApJ, 686, 53

Tinker J. L., et al., 2017, ApJ, 839, 121

Tinker J. L., Hahn C., Mao Y.-Y., Wetzel A. R., 2018, MNRAS, 478, 4487

Tinsley B. M., 1979, ApJ, 229, 1046

Tornatore L., Ferrara A., Schneider R., 2007, MNRAS, 382, 945

Torrey P., et al., 2015, MNRAS, 454, 2770

Torrey P., et al., 2018, MNRAS, 477, L16

Trager S. C., Faber S. M., Worthey G., González J. J., 2000, AJ, 119, 1645

Trainor R. F., Steidel C. C., Strom A. L., Rudie G. C., 2015, ApJ, 809, 89

Trainor R. F., Strom A. L., Steidel C. C., Rudie G. C., 2016, ApJ, 832, 171

Trayford J. W., Theuns T., Bower R. G., Crain R. A., Lagos C. d. P., Schaller M., Schaye J., 2016, MNRAS, 460, 3925

Tremonti C. A., et al., 2004, ApJ, 613, 898

Treu T., Schmidt K. B., Trenti M., Bradley L. D., Stiavelli M., 2013, ApJL, 775, L29

Trujillo-Gomez S., Klypin A., Primack J., Romanowsky A. J., 2011, ApJ, 742, 16

Tumlinson J., Giroux M. L., Shull J. M., 2001, ApJL, 550, L1

Turner O. J., et al., 2017, MNRAS, 471, 1280

Umehata H., et al., 2015, ApJL, 815, L8

Vakili M., Hahn C. H., 2016, arXiv:1610.01991

Vale A., Ostriker J. P., 2004, MNRAS, 353, 189

Vallini L., Gallerani S., Ferrara A., Baek S., 2013, MNRAS, 433, 1567

Vallini L., Gallerani S., Ferrara A., Pallottini A., Yue B., 2015, ApJ, 813, 36

Vallini L., Ferrara A., Pallottini A., Gallerani S., 2017, MNRAS, 467, 1300

Van Der Walt S., Colbert S. C., Varoquaux G., 2011, arXiv:1102.1523

Vanden Berk D. E., et al., 2001, AJ, 122, 549

Vanzella E., et al., 2010, A&A, 513, A20

Vanzella E., et al., 2011, ApJL, 730, L35

Vanzella E., et al., 2012, ApJ, 751, 70

Vanzella E., et al., 2014, A&A, 569, A78

Vanzella E., et al., 2016, ApJL, 821, L27

Vanzella E., et al., 2017, ApJ, 842, 47

Vanzella E., et al., 2018, MNRAS, 476, L15

Vasei K., et al., 2016, ApJ, 831, 38

Velliscig M., van Daalen M. P., Schaye J., McCarthy I. G., Cacciato M., Le Brun A. M. C., Dalla Vecchia C., 2014, MNRAS, 442, 2641

Venemans B. P., et al., 2007, A&A, 461, 823

Verhamme A., Schaerer D., Maselli A., 2006, A&A, 460, 397

Verhamme A., Schaerer D., Atek H., Tapken C., 2008, A&A, 491, 89

Verhamme A., Orlitová I., Schaerer D., Hayes M., 2015, A&A, 578, A7

Verhamme A., Orlitová I., Schaerer D., Izotov Y., Worseck G., Thuan T. X., Guseva N., 2017, A&A, 597, A13

Vernet J., et al., 2011, A&A, 536, A105

Visbal E., Haiman Z., Bryan G. L., 2016, MNRAS, 460, L59

Vogelsberger M., et al., 2014, MNRAS, 444, 1518

Wang Y., Yang X., Mo H. J., van den Bosch F. C., Weinmann S. M., Chu Y., 2008, ApJ, 687, 919

Wang R., et al., 2013, ApJ, 773, 44

Wardlow J. L., et al., 2014, ApJ, 787, 9

Watson D., Christensen L., Knudsen K. K., Richard J., Gallazzi A., Michałowski M. J., 2015, Nature, 519, 327

Wechsler R. H., Bullock J. S., Primack J. R., Kravtsov A. V., Dekel A., 2002, ApJ, 568, 52

Weigel A. K., Schawinski K., Treister E., Urry C. M., Koss M., Trakhtenbrot B., 2015, MNRAS, 448, 3167

Weinberger L. H., Kulkarni G., Haehnelt M. G., Choudhury T. R., Puchwein E., 2018, MNRAS, 479, 2564

Westra E., et al., 2006, A&A, 455, 61

Whitaker K. E., van Dokkum P. G., Brammer G., Franx M., 2012, ApJL, 754, L29

White S. D. M., Rees M. J., 1978, MNRAS, 183, 341

Wiersma R. P. C., Schaye J., Smith B. D., 2009a, MNRAS, 393, 99

Wiersma R. P. C., Schaye J., Theuns T., Dalla Vecchia C., Tornatore L., 2009b, MNRAS, 399, 574

Williams W. L., et al., 2016, MNRAS, 460, 2385

Willis J. P., Courbin F., 2005, MNRAS, 357, 1348

Willis J. P., Courbin F., Kneib J.-P., Minniti D., 2008, MNRAS, 384, 1039

Willott C. J., et al., 2009, AJ, 137, 3541

Willott C. J., et al., 2013, AJ, 145, 4

Willott C. J., Carilli C. L., Wagg J., Wang R., 2015, ApJ, 807, 180

Wisotzki L., et al., 2016, A&A, 587, A98

Wold I. G. B., Barger A. J., Cowie L. L., 2014, ApJ, 783, 119

Wold I. G. B., Finkelstein S. L., Barger A. J., Cowie L. L., Rosenwasser B., 2017, ApJ, 848, 108

Wuyts S., et al., 2011, ApJ, 738, 106

Xue R., et al., 2017, ApJ, 837, 172

Yamada T., Nakamura Y., Matsuda Y., Hayashino T., Yamauchi R., Morimoto N., Kousai K., Umemura M., 2012, AJ, 143, 79

Yang X., Mo H. J., van den Bosch F. C., 2003, MNRAS, 339, 1057

Yang X., Mo H. J., van den Bosch F. C., 2006a, ApJL, 638, L55

Yang Y., Zabludoff A. I., Davé R., Eisenstein D. J., Pinto P. A., Katz N., Weinberg D. H., Barton E. J., 2006b, ApJ, 640, 539

Yang X., Mo H. J., van den Bosch F. C., 2009, ApJ, 695, 900

Yang H., Malhotra S., Gronke M., Rhoads J. E., Dijkstra M., Jaskot A., Zheng Z., Wang J., 2016, ApJ, 820, 130

Yang H., et al., 2017, ApJ, 844, 171

Yates R. M., Kauffmann G., Guo Q., 2012, MNRAS, 422, 215

Zabl J., Nørgaard-Nielsen H. U., Fynbo J. P. U., Laursen P., Ouchi M., Kjærgaard P., 2015, MNRAS, 451, 2050

Zackrisson E., Inoue A. K., Jensen H., 2013, ApJ, 777, 39

Zackrisson E., et al., 2017, ApJ, 836, 78

Zahid H. J., Yates R. M., Kewley L. J., Kudritzki R. P., 2013, ApJ, 763, 92

Zamojski M. A., et al., 2007, ApJS, 172, 468

Zavala J., et al., 2016, MNRAS, 460, 4466

Zentner A. R., Hearin A. P., van den Bosch F. C., 2014, MNRAS, 443, 3044

Zentner A. R., Hearin A., van den Bosch F. C., Lange J. U., Villarreal A., 2016, preprint

Zhao D. H., Jing Y. P., Mo H. J., Börner G., 2009, ApJ, 707, 354

Zheng Z., Cen R., Trac H., Miralda-Escudé J., 2010, ApJ, 716, 574

Zheng Z.-Y., et al., 2017, preprint

Zitrin A., et al., 2015, ApJL, 810, L12

Zu Y., Mandelbaum R., 2015, MNRAS, 454, 1161

da Cunha E., et al., 2013, ApJ, 766, 13

da Cunha E., et al., 2015, ApJ, 806, 110

van Breukelen C., Jarvis M. J., Venemans B. P., 2005, MNRAS, 359, 895

van Dokkum P. G., et al., 2010, ApJ, 709, 1018

van Ojik R., Roettgering H. J. A., Miley G. K., Hunstead R. W., 1997, A&A, 317, 358

van Uitert E., et al., 2016, MNRAS, 459, 3251

van den Bosch F. C., et al., 2008, MNRAS, 387, 79

van den Bosch F. C., More S., Cacciato M., Mo H., Yang X., 2013, MNRAS, 430, 725

van der Wel A., et al., 2011, ApJ, 742, 111

van der Wel A., et al., 2014, A, 788, 28

van der Werf P. P., Moorwood A. F. M., Bremer M. N., 2000, A&A, 362, 509

Publications

First-author publications

1. *A 10 deg^2 Lyman-α survey at z=8.8 with spectroscopic follow-up: strong constraints on the LF and implications for other surveys*
J. Matthee, D. Sobral, M. Swinbank, I. Smail, P. Best, J-W. Kim, M. Franx, B. Milvang-Jensen & J. Fynbo
2014, MNRAS, 440, 2375.

2. *Identification of the brightest Lyα emitters at z=6.6: implications for the evolution of the luminosity function in the re-ionisation era*
J. Matthee, D. Sobral, S. Santos, H. Röttgering, B. Darvish & B. Mobasher
2015, MNRAS, 451, 400.

3. *The CALYMHA survey: Lyα escape fraction and its dependence on galaxy properties at z = 2.23*
J. Matthee, D. Sobral, I. Oteo, P. Best, I. Smail, H. Röttgering & A. Paulino-Afonso
2016, MNRAS, 458, 449.

4. *The origin of scatter in the stellar mass - halo mass relation of central galaxies in the EAGLE simulation*
J. Matthee, J. Schaye, R. Crain, M. Schaller, R. Bower & T. Theuns
2017, MNRAS, 465, 2381.

5. *The production and escape of Lyman-Continuum radiation from star-forming galaxies at z ∼ 2 and their redshift evolution*
J. Matthee, D. Sobral, P. Best, A. Khostovan, I. Oteo, R. Bouwens & H. Röttgering
2017, MNRAS, 465, 3637.

6. *Boötes-HiZELS: an optical to near-infrared survey of emission-line galaxies at z = 0.4 − 4.7*
J. Matthee, D. Sobral, P. Best, I. Smail, F. Bian, B. Darvish, H. Röttgering & X. Fan
2017, MNRAS, 471, 629.

7. *Spectroscopic properties of luminous Lyman-α emitters at z ≈ 6 − 7 and comparison to the Lyman-break population*
J. Matthee, D. Sobral, B. Darvish, S. Santos, B. Mobasher, A. Paulino-Afonso, H. Röttgering & L. Alegre
2017, MNRAS, 472, 772.

8. *ALMA reveals metals yet no dust within multiple components in CR7*
   J. Matthee, Sobral, D., F. Boone, H. Röttgering, D. Schaerer, M. Girard, A. Pallottini, L. Vallini, A. Ferrara, B. Darvish & B. Mobasher
   2017, ApJ, 851, 145.

9. *Star-forming galaxies are predicted to lie on a fundamental plane of mass, star formation rate and α-enhancement*
   J. Matthee & J. Schaye
   2018, MNRAS Letters, 479, 34.

10. *The origin of scatter in the star formation rate - stellar mass relation*
    J. Matthee & J. Schaye
    submitted to MNRAS, arXiv:1805.05956.

11. *Confirmation of double peaked Lyman-α emission at $z = 6.593$: Witnessing a galaxy directly contributing to the reionisation of the Universe*
    J. Matthee, D. Sobral, M. Gronke, A. Paulino-Afonso, M. Stefanon & H. Röttgering
    submitted to A&A, arXiv:1805.11621.

Co-authored publications

1. *The Dynamics of z = 0.8 Hα-selected Star-forming Galaxies from KMOS/CF-HiZELS*
   D. Sobral, M. Swinbank, J. Stott, **J. Matthee**, R. Bower I. Smail, P. Best, J. Geach & R. Sharples
   2013, ApJ, 779. 139.

2. *A relationship between specific star formation rate and metallicity gradient within $z \sim 1$ galaxies from KMOS-HiZELS*
   J. Stott, D. Sobral, M. Swinbank, I. Smail, R. Bower, P. Best, R. Sharples, J. Geach. & **J. Matthee**
   2014, MNRAS, 443, 2695.

3. *CF-HiZELS, a 10 deg^2 emission-line survey with spectroscopic follow-up: Halpha, [OIII]+Hbeta and [OII] luminosity functions at z=0.8, 1.4 and 2.2*
   D. Sobral, **J. Matthee**, P. Best, I. Smail, A. Khostovan, B. Milvang-Jensen, J-W. Kim, J. Stott, J. Calhau, H. Nayyeri & B. Mobasher
   2015, MNRAS, 451, 2303.

4. *Evidence for PopIII-like stellar populations in the most luminous Lyman-α emitters at the epoch of re-ionisation: spectroscopic confirmation*
   D. Sobral, **J. Matthee**, B. Darvish, D. Schaerer, B. Mobasher, H. Röttgering, S. Santos & S. Hemmati
   2015, ApJ, 808, 139.

5. *The brightest Lyα emitter: Pop III or black hole?*
   A. Pallottini, A. Ferrara, F. Pacucci, S. Gallerani, S. Salvadori, R. Schneider, D. Schaerer, D.Sobral & **J. Matthee**
   2015, MNRAS, 453, 2465.

6. *The CALYMHA survey: Lya luminosity function and global escape of Lyα photons at z=2.23*
D. Sobral, **J. Matthee**, P. Best, A. Stroe, H. Röttgering, I. Oteo, I. Smail, L. Morabito & A.Paulino-Afonoso
2017, MNRAS, 466, 1242.

7. *The most luminous Hα emitters at z = 0.8-2.23 from HiZELS: evolution of AGN and star-forming galaxies*
D. Sobral, S. Kohn, P. Best, I. Smail, C. Harrison, J. Stott, J. Calhau & **J. Matthee**
2016, MNRAS, 457, 1739.

8. *The Fundamental Plane of star formation in galaxies revealed by the EAGLE hydrodynamical simulations*
C. Lagos, T. Theuns, J. Schaye, M. Furlong, R. Bower, M. Schaller, R. Crain, J. Trayford & **J. Matthee**
2016, MNRAS, 459, 2632.

9. *The Lyman-α luminosity function at z=5.7-6.6 and the steep drop of the faint end: implications for reionization*
S. Santos, D. Sobral & **J. Matthee**
2016, MNRAS, 464, 1678.

10. *The KMOS Deep Survey (KDS) - I. Dynamical measurements of typical star-forming galaxies at z ≈ 3.5*
O. Turner, M. Cirasuolo, C. Harrison, R. McLure, J. Dunlop, M. Swinbank, H. Johnson, D. Sobral, **J. Matthee** & R. Sharples
, 2017, MNRAS, 471, 1280.

11. *A 1.4 deg2 blind survey for C II], C III] and C IV at z ∼ 0.7 − 1.5 - I. Nature, morphologies and equivalent widths*
A. Stroe, D. Sobral, **J. Matthee**, J. Calhau & I. Oteo
2017, MNRAS, 471, 2558.

12. *A 1.4 deg2 blind survey for C II], C III] and C IV at z ∼ 0.7 − 1.5 - II. Luminosity functions and cosmic average line ratios*
A. Stroe, D. Sobral, **J. Matthee**, J. Calhau & I. Oteo
2017, MNRAS, 471, 2575.

13. *Slicing COSMOS with SC4K: the evolution of typical Lya emitters and the Lya escape fraction from z ∼ 2 to z ∼ 6*
D. Sobral, S. Santos, **J. Matthee**, A. Paulino-Afonso, B. Ribeiro, J. Calhau & A. Khostovan
2018, MNRAS, 476, 4725.

14. *On the UV compactness and morphologies of typical Lyman-a emitters from z ∼ 2 to z ∼ 6*
A. Paulino-Afonso, D. Sobral, B. Ribeiro, **J. Matthee**, S. Santos, J. Calhau, A. Forshaw, A. Johnson, J. Merrick, S. Perez & O. Sheldon
2018, MNRAS, 476, 5479.

15. *The nature of luminous Lyman-α emitters at z ∼ 2 − 3: maximal dust-poor starbursts and highly ionising AGN*
D. Sobral, **J. Matthee**, B. Darvish, I. Smail, P. Best, L. Alegre, H. Rttgering, B. Mobasher, A. Paulino-Afonso, A. Stroe & I. Oteo
2018, MNRAS, 477, 2817.

16. *Kiloparsec-scale gaseous clumps and star formation at z = 5 − 7*
S. Carniani, R. Maiolino, R. Amorin, L. Pentericci, A. Pallottini, A. Ferrara, C. Willott, R. Smit, **J. Matthee**, D. Sobral, P. Santini, M. Castellano, S. De Barros, A. Fontana, A. Grazian & L. Guaita
2018, MNRAS, 478, 1170.

17. *The clustering of Hβ+[OIII] and [OII] emitters since z ∼ 5: dependencies with line luminosity and stellar mass*
A. Khostovan, D. Sobral, B. Mobasher, P. Best, I. Smail, **J. Matthee**, B. Darvish, H. Nayyeri, S. Hemmati & J. Stott
2018, MNRAS, 478, 2999.

18. *On the nature of the luminous Lyα emitter CR7 and its UV components: physical conditions and JWST predictions*
D. Sobral, **J. Matthee**, G. Brammer, A. Ferrara, L. Alegre, H. Rottgering, D. Schaerer, B. Mobasher & B. Darvish
submitted to MNRAS, arXiv:1710.08422.

19. *Predicting Lyman-alpha escape fractions with a simple observable: Lyman-alpha in emission as an empirically calibrated star formation rate indicator*
D. Sobral & **J. Matthee**.
submitted to A&A, arXiv:1803.08923.

Curriculum Vitae

I was born on 19 May 1990 in the city of Utrecht, son of Toon Matthee and Bertheke Matthee-Ruijs. Together with my brother Wouter and sister Annelotte, I grew up in the city of Roermond in the southern parts of the Netherlands where I attended primary school and high school. During my childhood I developed a strong interest in topics as mythology, ancient history, mathematics, physics, astronomy and philosophy and was often caught devouring books in stores and libraries. My first experience with astronomy was when I tried to find constellations as a young kid stargazing during dark nights in summer holidays – to little avail.

During my penultimate year in high school, I participated in the first Dutch Astronomy Olympiad in 2007, resulting in a third place after an intensive week of workshops in Leiden. Yet, I moved back to Utrecht in 2008 to enrol in the 'Liberal arts & sciences' bachelor program, allowing me to pursue a broad curriculum ranging from philosophy, writing and history to mathematics and theoretical physics. After attending a course on galaxy formation and cosmology, I realised I wanted to focus fully on astronomy. I obtained my BSc degree with a focus on theoretical physics and obtained my first research experience with a BSc project on the observability of multiple stellar generations in globular clusters under supervision of Søren Larsen at Sterrekundig Instituut Utrecht. During my studies I have been active in student sports associations on cycling and speedskating.

I continued my studies with the astronomy MSc program at the Leiden Observatory in 2012. I was fortunate to arrive in a stimulating environment with enthusiastic co-students, engaged teachers and a strong emphasis on research. I worked with David Sobral on finding the most distant galaxies and joined for observing runs on La Palma in 2013 and Hawaii in 2014. My MSc thesis was performed under supervision of Joop Schaye and Rob Crain on analysing the multi-dimensional properties of simulated galaxies in the state-of-the-art EAGLE simulation using advanced statistical techniques.

I was awarded a Huygens PhD fellowship by Leiden University to work on my own research project under supervision of David Sobral and Huub Röttgering at Sterrewacht Leiden. This allowed me to continue my observational studies of distant galaxies, but also to continue theoretical analysis with Joop Schaye that eventually led to the final three Chapters of this thesis. Throughout my PhD, I was responsible for acquiring own observational data, both from publicly available archives, but also through new observations. I (co-)authored more than 60 observing proposals for telescopes throughout the world and in space, I observed for 60 nights on the INT and WHT on La Palma and I prepared

observing instructions for 106 hours of remote observations with the MUSE and X-SHOOTER instruments on the VLT and with ALMA.

I had the opportunity to present my results to international colleagues during conferences and workshops in Sintra (Portugal), Groningen (NL), Paris (France), Kolymbari (Greece), Nunspeet (NL), Heidelberg (Germany), Salt Lake City (Utah, USA), Cambridge (UK), Leiden (NL), Liverpool (UK), Garching (Germany), Strasbourg (France) and Noordwijk (NL). I also presented my research during visits to astronomy departments in Hilo (Hawaii, USA), Lisbon (Portugal), Santa Cruz de La Palma (Spain), Riverside (California, USA), Pasadena (California, USA), Lancaster (UK) and Nijmegen (NL).

During my PhD, I was a teaching assistant for the second year BSc course 'Sterren' for three years and supervised the research projects of a MSc student and a summer student. I (co)-organised biweekly PhD talks and the Galaxies journal club for a year. I have been the referee for seven scientific articles published in MNRAS and ApJ and wrote several articles that appeared in Dutch popular science magazines. Three press releases followed from my research (based on Chapters 4, 5 and 7, respectively), of which our discovery of the CR7 galaxy had the most impact appearing in for example the New York Times, the news sections from Nature and Science magazines and being the subject of a dedicated documentary from the Japanese NHK broadcaster.

I will continue my research in astronomy as an independent Zwicky fellow at ETH in Zürich in October 2018.

Acknowledgements

'If I have seen further it is by standing on the shoulders of giants'
– Isaac Newton

This thesis would certainly have been be a bit heavier had I listed the names of the numerous 'giants' that contributed directly or indirectly, but unfortunately there is limited space available. On the other hand, perhaps it may not be the few 'giants' that helped me the most in being able to finish this thesis, but rather the numerous modest contributions from many, sometimes not even noticeable. Where to start? Who should I thank explicitly?

I could start thanking the people that helped me get to the position to be able to start a PhD project in the first place. Such as my grandparents, who taught me already early on how much fun it is to learn and to enjoy the beauty in nature and in numbers, until they were not longer able to do so. I could think of thanking my parents for their unconditional support, for being an example of what can be achieved through hard work and for raising us in an environment where each question was allowed to be asked. I could thank my close family, my brother and sister, my uncles, aunts and cousins for always showing their interest and open-mindedness. I could also pay tribute to my high school friends, whom I hope to keep for a very long time. Together we built confidence in being different, started and finished bold projects and found out that it is fine to speak out being proud about that. This mentality helped me a lot over the past few years.

I should definitely be grateful for the welcoming and stimulating environment at the Leiden Observatory that I joined when I started my MSc in 2012. The resources have been excellent – I have never been slowed by bureaucracy or computer issues, which is remarkable given the amount of time I spent behind a computer. Thanks to the support staff for making this possible, in particular to Alexandra Schouten and Erik Deul. Perhaps I could even expand this to a 'thank you' for the astronomical community in general. We should cherish excellent resources such as the arXiv, ADS and the widespread availability of data, such as the databases from Subaru, ESO and STScI, that I used extensively. While it could always be improved, astronomy is an example for other scientific disciplines due to availability of raw data and the open access to preprints that are submitted to a well defined and limited number of journals. I thank the reviewers of my thesis for their time going through these many pages. I also thank the majority of anonymous referees for the articles I (co-)authored for their constructive comments and willingness to contribute to the advancement of science without directly benefitting themselves.